Crack Growth Resistance in Nuclear Graphite

Shahed Fazluddin

Submitted in accordance with requirements for the degree of Doctor of Philosophy

Professor Brian Rand

Department of Materials

School of Process, Environmental and Materials Engineering

The University of Leeds

July 2002

The candidate confirms that the work submitted is his own and that appropriate credit has been given where reference has been made to the work of others.

ABSTRACT

R-curve behaviour is often used for evaluating crack growth resistance in quasi-brittle materials but few studies have focused on polycrystalline graphite. In this study, *R*-curve behaviour in three commercial grade nuclear graphites, of varying structure and properties, is compared using an optical method, a theoretical compliance method, and, a potential drop (PD) technique to measure crack length. Two graphites are coarse-grained and the third a fine grained graphite. Both 3-point bend and compact tension specimens are used.

The fine-grain graphite shows lowest resistance, with the coarse-grained materials displaying similar *R*-curves. The compliance method is simplest but assumes the material is linear elastic, producing similar *R*-curves to the optical method. The PD method seriously underestimates the crack length due to crack face bridging, causing the *R*-curves to show a falling behaviour. The shortfall in the PD measurements presents a novel way of physically measuring the bridging zone length. The graphites display similar variation in the apparent bridging zone length despite the difference in grain size.

Higher resistance in the coarser material results from increased crack path deflection, coupled with stronger grain bridging traction within the bridging zone. The bridging zone length is longer in compact tension specimens than in 3-point bend specimens, explaining partly why higher fracture energy is recorded in compact tension. In oxidised graphite, the crack growth resistance reduces but the coarser materials still show useful resistance. The fine-grain graphite shows a tendency toward flat *R*-curve behaviour with increasing oxidation. The mechanisms responsible for toughening in non-oxidised graphite prevail in oxidised material but diminish with increasing porosity and loss of binder phase.

A preliminary study of the nano-indentation behaviour of the nuclear graphites reveals a similar response in all the materials. Anelastic hysteresis in the load-unload response is found with little residual deformation. There is also evidence of a creep effect during the dwell period at the maximum load. Comparison of the average indentation modulus with the bulk flexural and sonic modulus indicates that the nano-indentation technique is unable to sense bulk modulus changes such as occur with oxidation or the forming process. Instead, the method is susceptible to localised structural inhomogeneities.

ACKNOWLEDGEMENT

I would like to take this opportune moment to express my appreciation to my supervisor, Professor Brian Rand for his advice and guidance. The mentorship of Dr Barry Marsden and assistance of Dr Steve Preston (formerly of AEA Technologies, UK) is highly appreciated. The sponsorship of Eskom (South Africa) and the PBMR Company (South Africa), which made this wonderful opportunity possible, is gratefully acknowledged. Particular recognition is due to the following people within Eskom and the PBMR Company:

Dave Nicholls for captaining the ship through stormy waters
Wynn Roscoe for his advice and help in numerous instances
Thabang Makubire for his valuable support
Danie Smith for his HR work par excellence

The valuable assistance of university staff, members of the department and colleagues is also acknowledged, especially that of the following people:

Rod Holt for his excellent help in the electronics workshop
Austin Wilson for helping to set-up the mechanical tests
Diane Bavester for her assistance in the laboratories
Dr David Wright who assisted with the XRD work
John Harrington for his assistance with the SEM
David Squires for assistance in the machining workshop

The invaluable discussions and debates with Anton Arulrajah and Peter Ramos, my colleagues in the Carbon Group, and the exchange of ideas that helped to deepen our understanding of *R*-curve behaviour cannot be forgotten.

This is a most wonderful moment to express my sincere gratitude to my parents whose hard work and nurturing throughout these years I am unable to fully acknowledge. I am grateful to my family for their love and support over the years, the value of which I have come to fully realise during these three years spent away from them. Finally, I am grateful to my loving wife, Zakkiyah, for her support during this trying period and the nurturing of our two-year old baby Nabeel, whose repeated question “why did daddy go to work?” I will not forget.

DEDICATION

"And she conceived him and withdrew with him to a far place.

And the pangs of childbirth drove her unto the trunk of the palm tree. She said: Oh, would that I had died ere this and had become a thing of naught, forgotten!

Then one cried unto her from below her, saying: Grieve not! Thy Lord has placed a rivulet beneath thee,

And shake the trunk of the palm-tree toward thee, thou wilt cause ripe dates to fall upon thee.

So eat and drink and be consoled. And if thou meetest any mortal, say: Lo! I have vowed a fast unto the Beneficent, and may not speak this day to any mortal.

Then she brought him unto her own folk, carrying him. They said: O Mary! Thou hast come with an amazing thing. Oh sister of Aaron! Thy father was not a wicked man nor was thy mother a harlot.

Then she pointed to him. They said: How can we talk to one who is in the cradle, a young boy?

He spake: Lo! I am the slave of Allah. He hath given me the Scripture and hath appointed me a Prophet,

And hath made me blessed wheresoever I may be, and hath enjoined on me prayer and alms-giving so long as I remain alive,

And hath made me dutiful toward her who bore me, and hath not made me arrogant, unblest.

Peace on me the day I was born, and the day I die, and the day I shall be raised alive!

Such was Jesus, son of Mary: this is a statement of the truth concerning which they doubt.

It befitteth not the Majesty of Allah that He should take unto himself a son. Glory be to Him! When He decreeth a thing, He saith unto it only: Be! And it is."

The Holy Koran
Chapter 19: Mary
Verses 22 - 35

CONTENTS

Chapter 5

Chapter 6

List of Tables

List of Abbreviations

ACPD	Alternating current potential drop
DCPD	Direct current potential drop
PC	Personal computer
C/C	Carbon/carbon
XRD	X-ray diffraction
FWHM	Full width at half-maximum
SEM	Scanning electron microscope
GPIB	General-purpose interface board
LEFM	Linear elastic fracture mechanics
COD	Crack opening displacement
STCA	Straight-through crack assumption
AGR	Advanced gas-cooled reactor
PBMR	Pebble-bed modular meactor
JAERI	Japanese Atomic Energy Research Institute
IUPAC	International Union of Physical and Applied Chemistry

List of Symbols

a	unit cell parameter for graphite [Å], instantaneous crack length [mm], radius of punch or indenter [mm]
a_0	initial notch length or length of starter crack [mm]
da, Δa	difference in crack length or amount of crack increment [mm]
Δa^*	crack increment corresponding with the establishment of a steady-state bridging zone length or a plateau region in the *R*-curve
a_1,a_2	dimensions of the chevron notch on either side of the notch [mm]
a_{11}	average of the two side lengths a_1 and a_2 [mm]
a_{ACPD}	crack length measured by ACPD method [mm]
$a_{optical}$	crack length obtained by optical measurement [mm]
$a_{compliance}$	crack length derived from a compliance technique [mm]
α	relative crack length, included angle of indenter [°]
α_{min}	relative crack length corresponding to Y^*_{min}
α_{ACPD}	relative crack length obtained by the ACPD method
$\alpha_{optical}$	relative crack length measured by the optical method
$\alpha_{compliance}$	relative crack length derived by the compliance method
A	cross-sectional area of specimen [mm^2]
A_a	apparent, indenter contact area
b	instrumental broadening, width of crack front in trapezoidal notch [mm]
B	width of test specimen [mm]
β	true width of peak [radians]
B_{int}	integral line breadth [radians]
B_m	measured peak width at half-maximum intensity [radians]
B_s	peak width at half-maximum of a standard substance [radians]
c	interlayer distance of basal planes in the graphite unit cell [Å]
C_0	initial compliance or compliance of un-notched specimen
C	instantaneous compliance
C_{tr}	compliance of specimen with a trapezoidal-shaped notched
d	half the interlayer distance in graphite unit cell (*c/2*) [Å], grain size
ε	strain, fractional porosity, geometric shape factor for indenter
E	elastic modulus [GPa]
E_f	elastic modulus derived from flexural testing [GPa]
E_{sonic}	elastic modulus obtained by the sonic resonance technique [GPa]
f	frequency [Hz]
λ	wavelength [nm]
θ	critical diffraction angle [°]
θ_b	base angle of chevron notch [°]
g	degree of graphitisation
γ	surface tension of mercury [mJ m^{-2}]
γ_e	elastic, fracture surface energy [Jm^{-2}]
γ_{WOF}	actual fracture surface energy or work of fracture [Jm^{-2}]
Φ_p	plastic component of the total fracture energy
G	shear modulus [GPa], elastic energy release rate [Jm^{-2}], elastic component of the total fracture energy, grain size
G_C, G_{IC}	critical, elastic energy release rate in Mode I loading [Jm^{-2}]
G_R	linear, energy-based crack growth resistance parameter [Jm^{-2}]
h, h_{max}	penetration depth of indenter, maximum penetration depth [nm]
$h_{residual}$	residual depth of indentation after unloading [nm]
ib	instrumental broadening factor
I, i	current (DC or AC) [A]
I, I_{max}	intensity, maximum intensity in XRD spectrum
J_R	energy-based fracture toughness parameter [Jm^{-2}]
K	stress intensity factor [$MPam^{1/2}$]
K_α	characteristic peak in the X-ray radiation spectrum of materials

K_C	critical stress intensity factor [MPam$^{1/2}$]
K_{IC}	critical stress intensity factor in Mode I loading conditions [MPam$^{1/2}$]
K_{IVB}	critical stress intensity factor in chevron-notch specimen [MPam$^{1/2}$]
K_R	linear stress-intensity based crack growth resistance [MPam$^{1/2}$]
$K_{R,plat}$	plateau value of the crack growth resistance parameter K_R [MPam$^{1/2}$]
l_{br}	length of apparent bridging zone [mm]
L	gauge length [mm]
L_a, L_c	apparent diameter, thickness of crystallites [nm]
m	spring constant or slope of tangent to deformation curve, mass [g]
n	order of critical reflection in XRD
p	fraction of disordered in graphite crystallites
p_m	mean indentation pressure or hardness (H) [GPa]
Δp	difference in applied pressure in mercury porosimetry test
ρ	density [g cm^{-3}], electrical resistivity [µohm m]
ρ_B	bulk density [g cm^{-3}]
ρ_S	apparent solid density [g cm^{-3}]
ρ_T	true density [g cm^{-3}]
ρ_{Hg}	mercury density [g cm^{-3}]
P_A	apparent porosity [%]
P_C	closed porosity [%]
P_T	true porosity [%]
P, P_{max}	load, maximum load [N]
P_r	dimensionless load
r	pore entrance radius [m]
R	electrical resistance [ohm]
R	non-linear, energy based crack growth resistance [Jm^{-2}]
R_{plat}	apparent plateau value of energy-based toughness parameter R [Jm^{-2}]
$\overline{R}$	energy envelope defined by the area under the R-curve [Jm^{-2}]
σ, σ_{ys}	stress, yield stress [MPa]
σ_{br}	bridging stress [MPa]
S	strength, sensitivity, load span, stiffness (slope of tangent to unload curve)
t	thickness [mm]
μ	shear modulus [GPa]
u	displacement [mm]
u_r	dimensionless displacement
U	fracture energy defined by area under the P-u curve [Nm]
v	velocity of sound, Poisson's ratio
V_b	bulk volume [cm^3]
V, V_0	voltage, initial voltage or voltage of un-notched specimen [mV]
V_{ref}	voltage across reference probes [mV]
W	thickness of test specimen [mm]
y	spacing across voltage probes in theoretical model
$Y(\alpha)$	geometric correction factor for straight-through notched specimen
Y^*	geometric correction factor for chevron-notched specimen
Y^*_{min}	minimum or critical value of the parameter Y^*

CHAPTER 1

INTRODUCTION

From its humble and misunderstood beginning as a writing material, graphite has developed into an engineering material with advanced applications. Today, graphite is used as a refractory material and as electrodes for electro-discharge machining. In the steel manufacturing industry, the anisotropy of graphite electrodes for arc furnaces is one of the desired properties, providing the electrode with adequate flexural strength along its length.

The variety of properties offered by graphite, some of these being unique, make it suitable for numerous advanced applications. Its excellent thermal shock resistance makes graphite suitable for use in rocket nozzles. In the nuclear industry, graphite has found place amongst the limited number of practically useful and economical moderator materials available. The need for high purity graphite, referred to as nuclear graphite, was recognised with the birth of the graphite-moderated reactor in 1942. Impurities raise the neutron capture cross-section of graphite, fouling its efficiency as a moderator, making it necessary to scale-up reactor core size to an uneconomical level.

Extensive advances have been made in understanding the behaviour of nuclear graphite under a variety of conditions. Advances have also been made in understanding the structure-property relationships governing the behaviour of polycrystalline graphite and carbon materials in general. Graphite-moderated reactor technology has advanced considerably from its early stages and future reactor designs seek to operate at far higher temperatures than the first air-cooled piles.

Given the global need to reduce air-borne emissions and meet rising energy demand, interest into the high-temperature, gas-cooled reactor (HTGR) technology has been re-kindled, much of this interest having died in the 1970's. A number of countries, including South Africa, have begun research and development into HTGR technology with a view to constructing a reactor before 2010. Given the vital role of the graphite moderator in the performance and life of the reactor, the development and application of nuclear graphite technology is crucial to the success of the HTGR, including its long-term sustainability.

The need to address problems related with advanced HTGR technology has therefore become an important issue. Furthermore, the performance and cost effectiveness of nuclear graphite to be used in any future reactors is key to their success. Advances in materials technology and analytical techniques provide a means of improving the present state of understanding of nuclear graphite and finding solutions to the problems that may arise.

Extensive studies have been performed in an attempt to understand the deformation and fracture mechanisms that control failure in polycrystalline graphite. Several models have been developed to predict the conditions under which failure of polycrystalline graphite does occur. However, the complexity of the operating variables imposed on moderator graphite makes this task difficult with the result that many of the models find limited applicability. Coupled to this is the need to quantify the various mechanisms that contribute to failure in polycrystalline graphite.

There remains some speculation as to the precise mechanism by which inherent flaws in polycrystalline graphite grow to macroscopic size and lead to failure. There is also a need to understand better the non-linear, non-elastic deformation behaviour of polycrystalline graphite and the mechanisms which give rise to crack growth resistance, i.e. *R*-curve behaviour. *R*-curve behaviour is often used to evaluate toughening mechanisms in ceramic materials and compare different ceramic materials in terms of their crack growth resistance.

The application of the *R*-curve concept has become commonplace in recent years. It is now used routinely to compare fracture behaviour in engineering materials, particularly in ceramics and other materials that are generally classed as brittle materials. *R*-curve behaviour is observed in polycrystalline graphite, but only a limited number of studies have been carried out in this area. These studies have not really compared the *R*-curve behaviour of nuclear graphites with varying structural characteristics. This study focuses on the comparison of *R*-curve behaviour in nuclear graphites with varying structures in terms of, grain size, grain shape, method of forming, pore size and distribution, and, physical and mechanical properties.

The materials selected in this study cover a wide range of nuclear graphite properties, allowing a deeper insight into the toughening mechanisms that contribute to *R*-curve behaviour in polycrystalline graphite. These materials are also of commercial importance, one of these materials being currently used as a moderator in modern British AGR's (Advanced Gas-cooled Reactors). The other test materials are candidate materials for the intended South African PBMR, one of these being currently tested in the JAERI High Temperature Reactor (HTR) programme.

As a starting point, a detailed description of the graphite structure and its development, as well as, the conceptual models used to define the graphite crystallite structure is presented. This is followed by a review of various models proposed for predicting failure in polycrystalline graphite with a consideration of the micro-fracture processes that are thought to cause macro-failure. The initial part of this study therefore characterises various physical and mechanical properties of the selected materials. This provides a baseline from which to better evaluate differences in the *R*-curve behaviour of the nuclear graphites.

The *R*-curve concept and numerous ideas surrounding the origin of toughening processes in ceramics are also reviewed in some detail. Methods proposed for extracting the non-linear fracture energy or the energy-based *R*-curve are also reviewed. Some consideration is given to the methods used to measure the crack length, which is an integral part of deriving the *R*-curve.

Differences in the degree of toughening observed between these materials are explained in relation to their structural differences and the various crack growth resistance mechanisms that are thought to contribute to R-curve behaviour. The *R*-curve response of oxidised material is also assessed to a limited degree, in order to obtain an insight into the impact of oxidation in this regard.

An exploratory study was made of the nano-indentation behaviour of the nuclear graphite materials. Of particular interest was the potential of the technique in affording a measure of the elastic modulus on small samples. It may also afford the opportunity to study irradiation damage on a localised scale. The method is also applied to oxidised nuclear graphite material.

CHAPTER 2

LITERATURE REVIEW

SECTION 2.1: STRUCTURE OF GRAPHITIC MATERIALS

Graphite derives its name from Abraham Gottlob Werner (1750-1817). He named the mineral after the Greek word meaning 'to write'. To understand the graphite structure, it must be recognised that graphite refers to a particular structure found in carbon materials. This structure can be found in close association with other forms of carbon such as chars, soot, and lampblack. Elemental carbon consists of about 98.9% of the C^{12} isotope and 1.1% of C^{13}. Natural carbon also contains C^{14} and other unstable isotopes (Reynolds, 1968).

Natural graphite however, is a carbon-containing mineral (30-90% C) consisting of graphitic carbon. Synthetic graphite is synonymous with artificial graphite, referring to graphitic carbon formed by certain processes, for example, the graphitization heat treatment of non-graphitic carbon material. Graphite may therefore be defined as a crystalline form of carbon. Along with diamond, graphite constitutes one of the allotropic forms of carbon (Wege, 1984).

2.1.1. Crystal Structure of Graphite

The hexagonal crystal structure of graphite was first proposed by J D Bernal in 1924 (see Figure 2.1.1). It is characterised by large sheets or layers of inter-connected, co-planar hexagonal carbon rings in which the electrons are mobile, with a large atomic spacing between these layers of hexagonal carbon rings. The layers of co-planar carbon rings, or basal planes, are spaced at 3.3539 Å in the perfect, graphite crystal lattice. Successive basal planes are not superimposed on each other, so an alternating stacking sequence coded ABABAB... of the layers occurs is in the hexagonal graphite structure. The atoms of A-layers are located directly in the centre of the hexagonal rings of the adjacent B-layers. Each carbon atom in the ring is bonded covalently (energy = 600 kJ mol^{-1}) to its three nearest neighbour atoms at a bond length of about 1.415 Å. A fourth valence electron serves as a weak, inter-planar bond (energy = 4 kJ mol^{-1}) as well as a charge carrier (Nightingale, 1962).

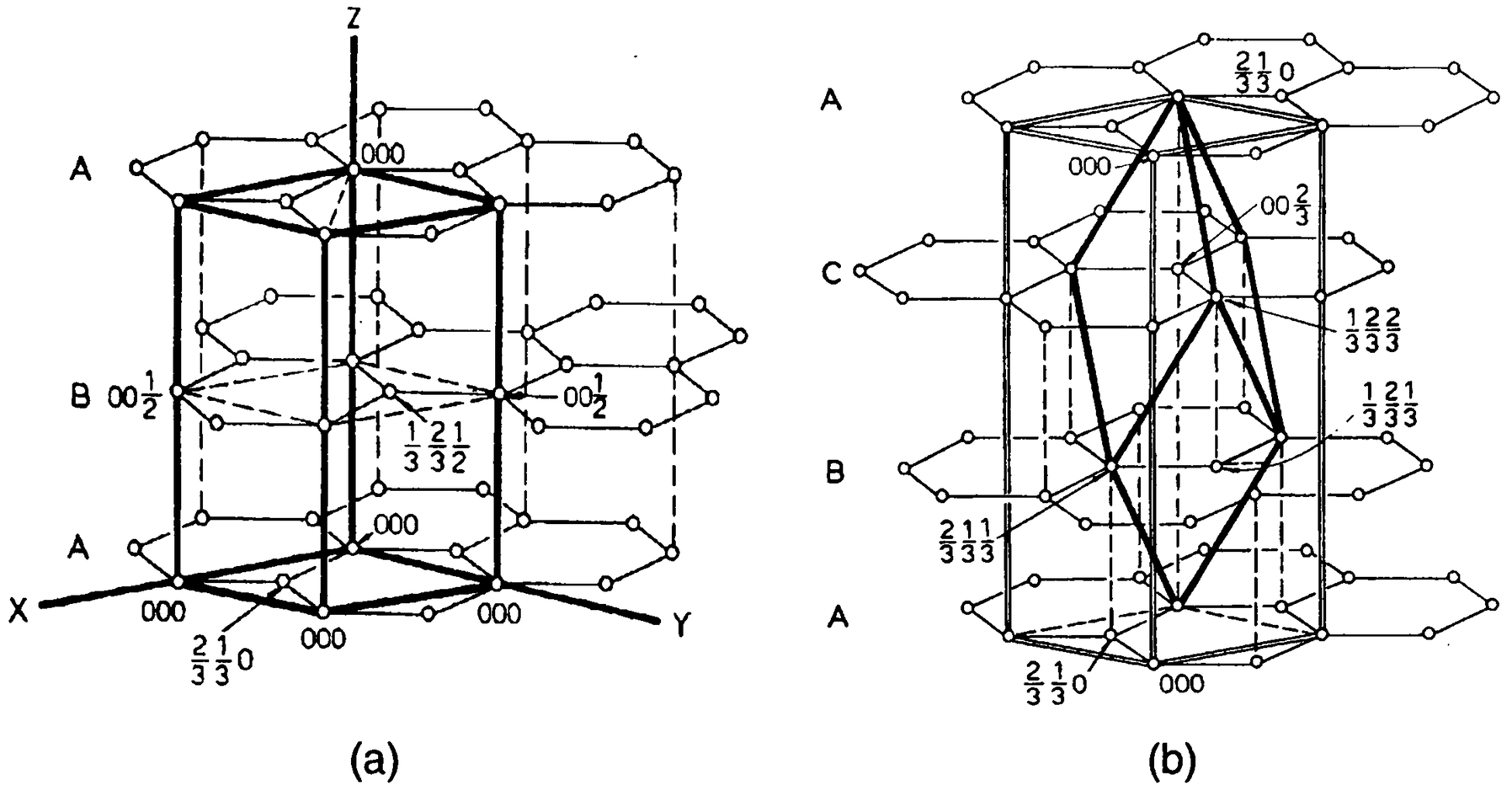

(a) (b)

Figure 2.1.1. Unit cell of (a) hexagonal (b) rhombohedral graphite (Nightingale, 1962).

The unit cell of hexagonal graphite is defined by second nearest neighbour atoms as indicated in Figure 2.1.1. A pair of basal plane vectors at 60° to each other defines the basal plane structure with a basal plane lattice constant of a = 2.456 Å. Each unit cell contains four atoms with a perfect crystal density of 2.256 gcm^{-3}. The c-axis lattice spacing, c, is taken as twice the inter-planar spacing, d, because adjacent basal planes cannot be superimposed over each. At room temperature, this distance is about 6.7078 Å, but changes with temperature and inter-layer defects.

The large inter-atomic distance between the basal plane atoms, i.e. 1.415 Å, and the interlayer distance of 3.3539 Å renders the graphite crystal extremely anisotropic lending the graphite crystal physical and mechanical properties that are directionally oriented. Lipton and Stokes detected the rhombohedral form of graphite (see Figure 2.1.1) in 1942. It is said to occur when, the graphite lattice is highly strained or undergoes shear by the selective, cumulative gliding of pairs of atomic planes. The preferred directions for gliding are the atomic planes parallel to the basal layers.

2.1.1.1. Determination of the Crystal Lattice Dimensions

X-ray diffraction studies have played an instrumental role toward understanding the changes in polycrystalline graphite structure with varying heat treatment and neutron irradiation. Diffraction profiles are useful for deriving various

crystallographic data, one of the most important parameters being the unit cell dimensions or lattice spacing. The unit cell dimensions of polycrystalline graphite can be measured quite accurately using XRD provided allowance is made for factors that influence the diffraction profile.

Both the *a*-spacing and *c*-spacing of the graphite unit cell are obtained using the critical diffraction angles defined by the Bragg equation (Cullity, 1956)

$$n\lambda = 2d \sin \theta \qquad [2.1.1]$$

n = order of reflection

λ = wavelength of incident X-ray radiation

d = inter-planar spacing

θ = critical angle between incident and diffracted X-rays, i.e. the Bragg angle

The magnitude of *d*, defines half the interlayer distance between consecutive (00*l*) planes in the graphite lattice and is calculated from the (002), (004), or (006) reflections. The *c*-spacing, which defines the vertical height of the graphite unit cell is then simply twice the value of *d*. The *a*-spacing defining the dimensions of the unit cell in the hexagonal plane is derived from the (110) and (112) reflections (Nightingale, 1962).

Often, significant variation is found in the lattice dimensions measured in polycrystalline graphite. Variations occur within a single bar of material and within a specific grade of material (Nightingale, 1962). The lattice constant *c* is sensitive to lattice imperfections. Even the best of graphite crystals show some imperfection.

2.1.2 Degree of Ordering in Graphitic Structures

The inter-basal distance of the hexagonal graphite structure varies with heat treatment such that at low temperatures, the stacking arrangement of the basal planes is 'turbostratic' (completely random), with the inter-planar distance increasing to about 3.44 Å. The 'turbostratic' structure in 2-dimensional. XRD profiles of turbostratic carbons only display (00*l*) lines and (*hk*) lines ($h,k \neq 0$). As the material becomes more graphitized, these XRD lines become less

asymmetric, tending toward the (*hkl*) line system for a 3-dimensional graphite structure. In graphitic carbons therefore, a 3-dimensional crystalline structure, of long-range order becomes detectable by XRD. This qualifies the material as being graphitic (Ruland, 1968).

In highly graphitic carbons, the main defect is a scatter, within a limited range, of the interlayer distance. Almost all natural and artificial graphite can be said to be comprised only of 'defective' graphite crystals, that is containing a significant portion of disordered carbon, of lower order than the graphite crystallites making up the material. The extent of this inherent disorder depends on the precursor material and processing conditions used in fabricating the material. The less ordered regions are said to be randomly oriented within the graphite structure. Natural graphite flake shows higher structural order than artificial graphite given the narrowness of the X-ray diffraction peaks and smaller interlayer spacing. Bacon (1958), however, showed that artificial graphite could attain a higher degree of order than natural graphite.

The graphite crystallites in graphitic carbons are often conceptualised in terms of layer stacks, arranged in the *c*-direction, with these stacks arranged parallel to each other. The crystallites are viewed as anisometric disc-like or cylindrical structures, with the discs oriented relative to each other. The degree of ordering of the crystallites is reduced by layer translation and rotation within the stacks, including structural defects such as vacancies, interstitials, and, dislocations. Increasing disorder increases the inter-layer distance measured by XRD. An increase in the lattice strain also reduces the degree of ordering (Ergun, 1976), as evidenced in irradiated graphite where the XRD profiles become diffuse, due to increasing lattice strain caused by interstitials (Nightingale, 1962).

Therefore, the crystallinity of graphitic carbons is viewed in terms of the stacking perfection of the layers of carbon atoms within the crystallites, and, the structural perfection within these layers (Reinoso, 1997). The range of ordering is also determined by the crystallite orientation (Figure 2.1.2). When crystallites are favourably oriented relative to each other, a higher degree of ordering results compared with that defined by the crystallite size alone (Edwards, 1989).

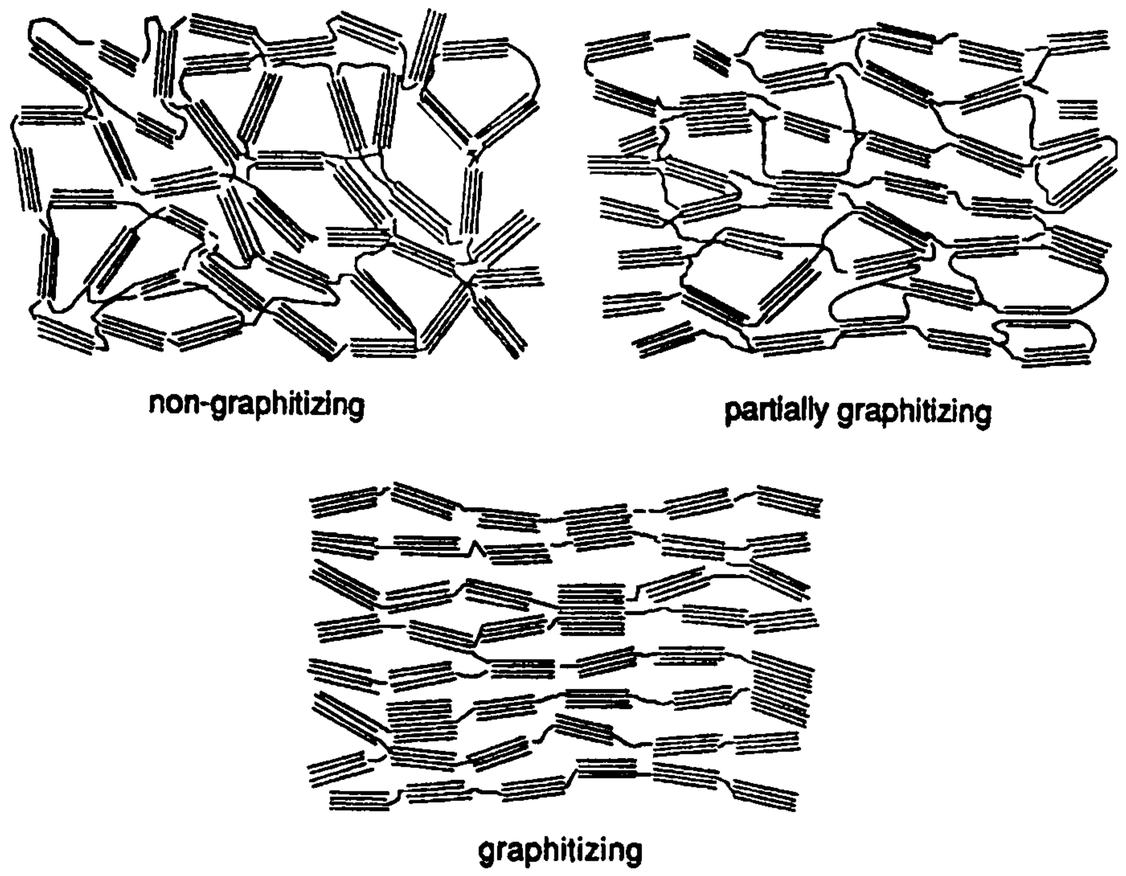

Figure 2.1.2. Models of crystallite arrangement in graphitizing & non-graphitizing carbon structures proposed by Franklin (1951).

Non-graphitizing carbons develop extensive cross-linking during heat treatment producing a structure that is a highly defective form of the graphite lattice. They include all carbon-containing substances which cannot be transformed into graphitic carbon by heat treatment at temperatures up to 2700 °C under atmospheric or low pressure conditions (Reinoso, 1997). Franklin (1951) indicated that the apparent height and diameter of the conceptualised, disc-shaped crystallites in graphitic carbons was much larger than that in the non-graphitic types. Non-graphitic carbons are said to have 2-dimensional long-range order where the carbon atoms are arranged into planar hexagonal networks. These planar networks have no crystallographic arrangement perpendicular to these layers, i.e. in the *c*-direction, except for a random parallel stacking arrangement of the layers (Edwards, 1989).

2.1.2.1. Determination of the Crystallite Size

In addition to the graphite crystal lattice dimensions, many researchers find it useful to measure the 'apparent' graphite crystallite size when comparing the degree of crystallinity, or extent of graphitic order, in different carbon or graphite materials. The term 'apparent' is used because the cylindrical crystallite shape is a conceptual one. The dimensions of this apparent cylinder being defined by the parameters L_a and L_c, such that L_a is the apparent radius of the cylindrical crystallite and L_c is its apparent height or thickness. The highly anisotropic graphite lattice makes it necessary to use these definitions.

In isotropic crystal structures, the average crystallite shape can be viewed as spherical with dimensions defined by the radius of a sphere. It is now more appropriate to refer to these conceptual crystallite dimensions as X-ray coherence lengths in the *a*- or *c*-directions given that these dimensions derive from XRD measurements. Physically, the *L*-dimensions represent the number of basal or graphite layers that are coherently aligned to the X-ray path, and, the length or radius of the basal plane area that defines these coherent regions.

The apparent crystallite dimensions are determined using the same diffraction peaks used to measure the unit cell dimensions. Average crystallite height or thickness, L_c, is commonly derived from the (002) peak, and, the mean crystallite diameter, L_a, from the (110) peak. However, 2nd, 3rd, and, 4th order reflections of the (00*l*) peaks could also be used to calculate L_c, while the (100) peak can also be used to obtain L_a. The classical equation derived by Scherrer (Cullity 1956, Ruland 1968) relates the width of the relevant diffraction peak (β) to the apparent crystallite dimension (L_a or L_c), i.e.

$$L = \frac{K\lambda}{\beta \cos\theta} \qquad [2.1.2]$$

K = crystallite shape factor (usually ≈1)

β = true width of peak in radians, i.e. due to crystallite broadening only

λ = wavelength of the incident X-ray radiation; θ = Bragg angle

It is important to recognise that the Scherrer equation provides an approximate estimate of the average crystallite size, unlike the lattice parameter, which is more closely related to the actual crystal lattice structure. The calculated crystallite size becomes less meaningful due to uncertainty in the exact value of *K*, broadening of the diffraction line due to lattice distortion, and, inaccuracy in the value of β, the true width of the diffraction peak. The degree of uncertainty in the value of *K* can be 20% or more (Alexander and Klug, 1974). In theory, the Scherrer equation is used to determine the size of very small crystallites from the true width, β, i.e. the broadening of the diffraction curve due to crystallite size only. To obtain a more accurate measure of the peak width, it is necessary to account for line broadening phenomena. Some consideration of line broadening effects in relation to the graphitic structure is given below.

Line Broadening Effects caused by Graphitic Structures

The phenomenon of broadening of XRD lines when crystallite size becomes smaller than ~10^{-6} m (~1μm) is well known and was discovered by Scherrer in 1920. X-ray line broadening occurs because ideal diffraction conditions never really exist. Crystal imperfections and non-monochromatic radiation cause measurable intensities of the diffracted X-rays, at angles very close to the Bragg angle, to be recorded. Ideally, X-rays are diffracted at the Bragg angle so that the observed diffraction profile is a straight line. Non-ideal conditions cause the intensity of beams diffracted near the Bragg angle to be recorded, so that the intensity ranges between zero and I_{max}, giving rise to the 'broadened' diffraction profile observed in practice (Figure 2.1.3) (Cullity, 1956).

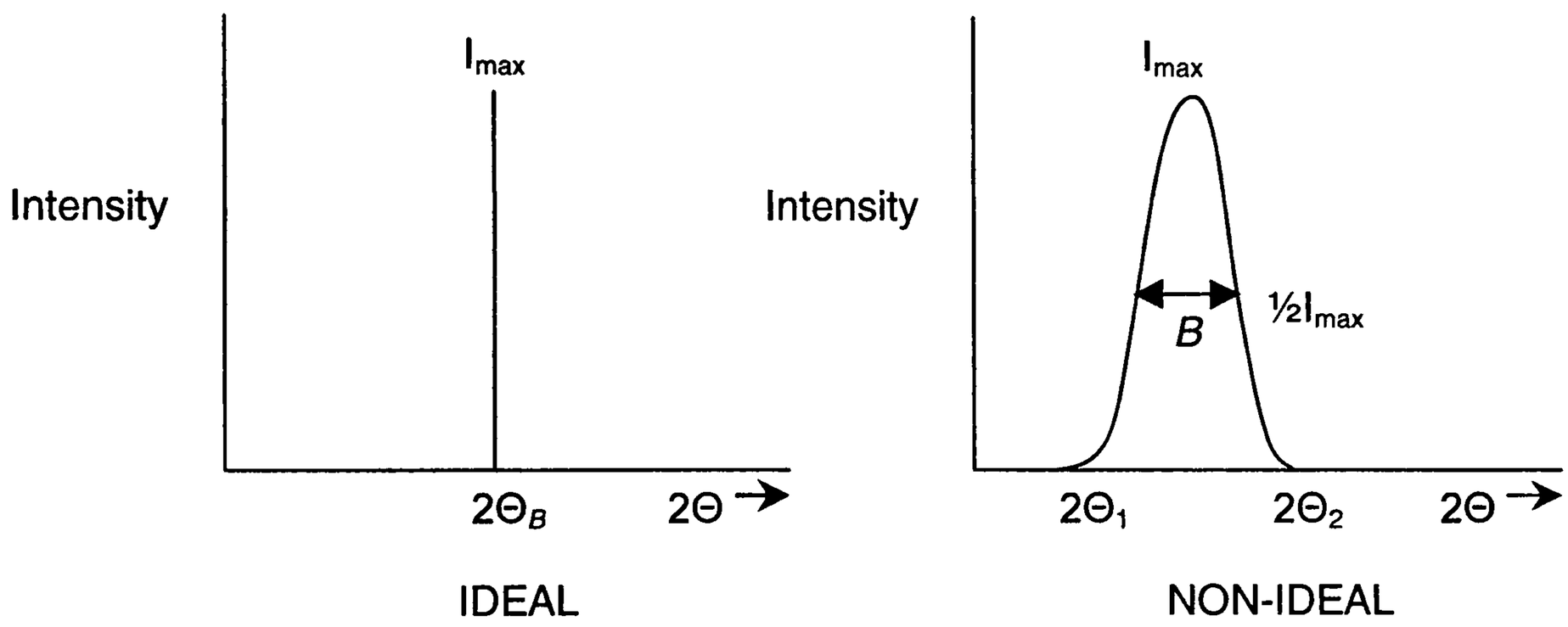

Figure 2.1.3. Broadening of diffraction lines (Cullity, 1956).

X-ray line broadening effects have proven useful in understanding structural development during graphitization, and the structural changes that occur in graphite under irradiation. The broadness of diffraction peaks is influenced by instrumental broadening (or geometrical broadening), as well as intrinsic broadening. Instrumental broadening is caused by geometrical factors related to the equipment used (Cullity, 1956). Intrinsic broadening stems mainly from limited crystallite size, i.e. <100 nm, and, short-range lattice distortions of the crystal lattice. The natural spectral width of the X-ray radiation comprises a *Kα*-doublet made up of α_1 and α_2 components superimposed on the continuous spectrum which also contributes to line broadening. Crystallite mis-orientation also causes broadening. To measure the crystallite size accurately, it is therefore necessary to derive the true or intrinsic line width, which is that due to the crystallite size only, from the experimentally obtained line width.

In graphitic carbons, a prime source of line broadening is fluctuation in the interlayer spacing, i.e. inherent disorder. The (00*l*) lines used to determine L_c are also subject to line broadening caused by crystal lattice imperfections. Franklin (1951) showed that the apparent crystallite thickness (L_c) decreased when measured using higher order (00*l*) lines. In more graphitic material therefore, the XRD peaks are narrower and more sharply defined, with the angular position of the peaks approaching the ideal position (Nightingale, 1962).

Many researchers have attempted to relate the degree of disorder in graphitic carbons to the structural parameters measured by XRD in an attempt to quantify the effect of disorder on the observed line broadening. Most workers have used the value of d_{002}, the interlayer spacing calculated from the position of the 002 peak, as an indicator of the degree of disorder. Franklin (1951) first attempted to quantify the extent of disorder, proposing a relation between the fraction of mis-oriented layers in the stack (p) to the average interlayer spacing:

$$\frac{c}{2} = 3.440 - 0.086(1 - p^2) \qquad \text{\{for all } p\} \qquad [2.1.3]$$

Similar relations were derived by other workers (Ruland, 1968):

$$\text{(for } p>0.25) \qquad \frac{c}{2} = 3.440 - 0.086(1 - p) - 0.064\,p(1 - p) \qquad [2.1.4]$$

Ruland (1968) argues that the definition of p according to these equations implies a linear decrease in d with increasing disorder although, the relations derived by them, are of a non-linear form. Franklin (1951) really derived her expression on the basis that it fit her experimental data well. Babu and Seehra (1996) agree that Franklin's model is inconsistent in its assumption that two discrete interlayer spacings form the border between order and disorder in carbons. That is, 3.354 Å at the ordered end, and 3.440 Å at the disordered end, whilst her equation represents a non-linear relation. They add that this inconsistency is probably due to the way in which p is defined, making the model unsuitable for a complete description of disorder in carbons. In their study of the disorder in a range of carbons using a computational model for describing the degree of graphitic order in carbons, they include additional disorder parameters such that:

$$\frac{c}{2} = 3.354 + \alpha p + \beta p^2 \qquad [2.1.5]$$

The value of α and β vary with the parameters chosen to describe the model. Interestingly, Aladekomo & Bragg (1990) hold the view that the interlayer spacing of graphite increases continuously in the range 3.354 – 3.375 Å as in a solid solution. That is carbon exists as a continuous solid solution of carbon interstitials in graphite. Above 3.375 Å, a mixture of metastable, graphite interstitial phases make up the disordered graphite structure. The value of 3.375 Å marks a very stable, limiting interlayer spacing at which there is maximum solubility for the solid solution type structure. This idea is supported by neutron irradiation studies, which show that the interlayer spacing takes on discrete values with increasing neutron dose.

2.1.3. Structure of Polycrystalline Graphite

Graphitization of the baked compact of petroleum coke filler grains and coal-tar pitch binder at temperatures above 2500 °C produces a graphitized article comprised of inter-connected filler grains and a binder phase, both of which are graphitic. The article is termed polycrystalline due to the array of tiny, sub-microscopic graphite crystallites making up the graphitized filler and binder phase, the crystallites being of different size and varying degrees of order. Crystallite size ranges from 20-50 Å to a few 1000 Å in the polycrystalline material. Regions within the graphitized coke grains may contain highly aligned crystallites, these crystallites being inter-connected by chemical bonds and weaker long-range forces (Reynolds, 1968).

The term ‘structure’ in polycrystalline graphite therefore extends beyond that of the graphite crystal lattice. It includes grain size and shape, pore size, and shape, pore size distribution, and, the degree of ordering within the tiny graphite crystallites contained in the polycrystalline phases. Grain size usually refers to the apparent size of the coke filler particles observed in the structure. Coke particle size can vary between 0.074-6.0mm and particles below 0.074mm size are labelled ‘flour’ (Nightingale, 1962). The distinction between binder and filler is not always clear in polycrystalline graphite, and, little is known about the nature of the binder-filler bridges, their size, and, shape. It is thought that a mechanical keying-in of the filler surface by the binder occurs, thereby bridging the binder and filler phase (Marsh & Fiorino, 1997).

2.1.3.1. Porosity in Polycrystalline Graphite

Pores form an important part of the graphite structure, adding to the defective nature of the graphite. Pores form in defective sites between crystallites and where the packing between binder and filler phase, is imperfect. They can be either closed or open to the atmosphere. Generally, it is not only the type of pore which is important to the properties of carbons but also the size, shape, and distribution of pores. Porosity is generally classed into three categories, i.e. macropores (>50nm), mesopores (2-50nm), and, micropores (<2nm).

In polycrystalline graphite made from a mixture of coal-tar pitch and petroleum-coke filler particles, pores originate from various sources (Rand et al, 1989). Macropores may be considered part of the external surface area given that they usually function as transport pores to the interior of particles that make up the porous material. In polycrystalline nuclear graphites, macropores are usually of most concern since they influence graphite properties the most. Micropores can be located between crystallites, graphitized coke particles and disorganised carbon, ranging from ~10 Å to several tens of microns (Nightingale, 1962).

McEnaney & Mays (1995) point out that the macropores often provide access to meso- and micropores although they have a low surface area to volume ratio. They emphasise the importance of pore shape on properties. For example, long, crack-like pores promote internal stress-concentration in nuclear graphite. It is also necessary to determine the total porosity, i.e. both open and closed, to fully evaluate the effect of porosity on thermal, physical, and, mechanical properties. The open porosity is especially relevant when oxidation takes place.

McEnaney & Mays (1995) also stress the importance of differentiating between the various types of macropores. A range of macropore types form during graphite manufacture (Rand et al, 1989). Volumetric shrinkage cracks (~100 μm wide by 1mm long) form in needle-coke particles during calcination and are usually closed. Open, globular macropores form during the baking stage as the pitch binder is converted to carbon. These globular macropores usually form an open, macroporous network.

SECTION 2.2: DEFORMATION & FRACTURE IN GRAPHITIC MATERIALS

In characterising the fracture behaviour of polycrystalline graphite and for developing a means of predicting failure in graphite components, in reactor environments for example, fracture mechanics is most useful. Studies have focused on trying to obtain a quantitative link between the mechanism of crack initiation and growth of the macro-crack, and, the conditions leading to ultimate failure. This is a complex task given the need to account for widely varying environmental conditions in the analysis. Before discussing the fracture behaviour of polycrystalline graphite, it is essential to outline the underlying principles of the fracture mechanics approach.

2.2.1. Principles of Fracture Mechanics

Linear Elastic Fracture Mechanics (LEFM) was born out of Irwin's stress intensity approach which aimed at characterising fracture in linear elastic materials. Irwin modified Griffith's classical failure theory, which stated that a crack propagates if the total energy of the system in which the crack lies is reduced by crack propagation. Griffith's energy-based approach held that the energy of the system was kept in balance by the energy release associated with crack propagation, and, the energy consumed in enlarging crack surface area. (see Lawn & Wilshaw 1975, Ewalds & Wanhill 1984, Hellan 1985).

Griffith proved experimentally that the product of the critical stress (σ) required to fracture glass specimens, and, the square root of the length of pre-cracks ($\sqrt{a}$) in these specimens was a constant, that was characteristic of brittle materials (Lawn & Wilshaw, 1975). That is,

$$\sigma\sqrt{a} = \left(\frac{2E\gamma_e}{\pi}\right)^{\frac{1}{2}} \qquad [2.2.1]$$

E = elastic modulus

γ_e = elastic surface energy

Griffith's theory was limited in assuming that the material was completely brittle and showed no plasticity, hence the crack tip was ideally sharp, with the fracture process being completely reversible (Ewalds & Wanhill, 1984). In reality, these assumptions were not valid.

Irwin tried to accommodate for plasticity effects with the understanding that a portion of the energy spent in crack propagation would be consumed by plastic deformation processes. He defined the parameter *G* as the elastic energy release rate, or, the 'crack driving force' representing the total energy absorbed during crack propagation per unit increase in crack surface area. So, the value of *G* in ductile materials would be low due to the extensive plasticity, while in brittle materials, *G* would be high due to their ability to release greater elastic strain-energy during crack extension. Irwin related G to the elastic surface energy (γ_e), according to the relation:

$$G = \frac{\pi\sigma^2 a}{E} = 2\gamma_e \qquad [2.2.2]$$

According to this relation, unstable crack propagation occurred when *G* exceeded a critical value, i.e. $G_{crit} > 2\gamma_e$, in an ideally brittle material. However, this concept only applied to unstable crack propagation from an ideally sharp crack, and, was not applicable when slow, stable crack growth occurred, e.g. fatigue. Irwin then developed the stress intensity approach by modelling the elastic stress-distribution ahead of the crack tip, as illustrated in Figure 2.2.1. By showing that failure occurred when the stress distribution at the tip reached a critical level, Irwin proved that there was, a critical, crack tip stress intensity that governed fracture.

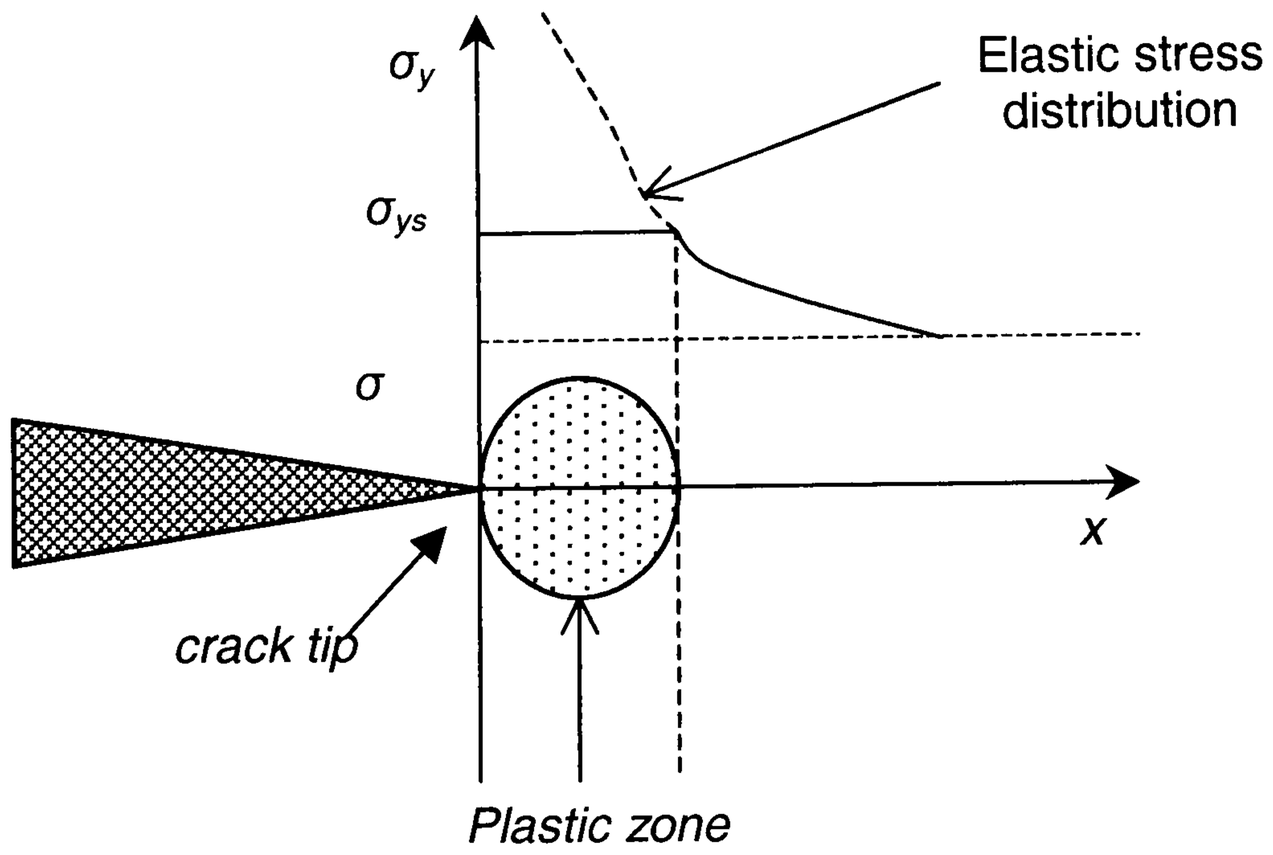

Figure 2.2.1. Irwin's stress intensity profile at the crack tip (Ewalds&Wanhill, 1984).

He found the stress intensity at the crack tip (K) to be a constant that is related to applied stress (σ), the crack length (a), and, the geometry of the crack relative to the body in which it lay, i.e.

$$K = \sigma\sqrt{\pi a}.f\left(\frac{a}{W}\right) \qquad [2.2.3]$$

W = width of cracked body

$f(a/W)$ = dimensionless geometric factor

There was therefore a critical combination of stress (σ_c) and crack length (a_c) at which K reach a critical value, K_c, and failure occurred, i.e.

$$K_c = \sigma_c\sqrt{\pi a_c}.f\left(\frac{a_c}{W}\right) \qquad [2.2.4]$$

This was consistent with Griffith's findings which showed that failure occurred when the product of the applied stress and the square root of the crack length, i.e. $\sigma\sqrt{a}$, attained a constant critical value. Irwin further proved the consistency of this approach by showing that the critical stress intensity (K_c) was related to the critical value for the 'crack driving force', i.e. the elastic energy release rate (G_c). That is,

Plane stress: $$K_c^{\,2} = EG_c \qquad [2.2.5a]$$

Plane strain: $$K_c^{\,2} = \frac{EG_c}{(1-\nu^2)} \qquad [2.2.5b]$$

Irwin recognised that these relations only applied for an elastic stress field at the crack tip, with the concentration of stress at the crack tip causing the material to deform plastically at the tip. The concept of an atomically sharp crack tip also remained a problem. He accounted for these shortcomings by assuming a circular plastic zone formed at the crack tip. This simply made the crack behave as if it was longer (Figure 2.2.2). The assumption of a circular plastic zone however had no physical basis because, the location of the plastic zone relative to the tip was speculative. In fact, an accurate description of the plastic zone is extremely difficult. Another model of the plastic zone by Dugdale (see Hellan, 1985), represents the plastically deformed zone as an additional strip of crack length, along which the stress is uniformly distributed.

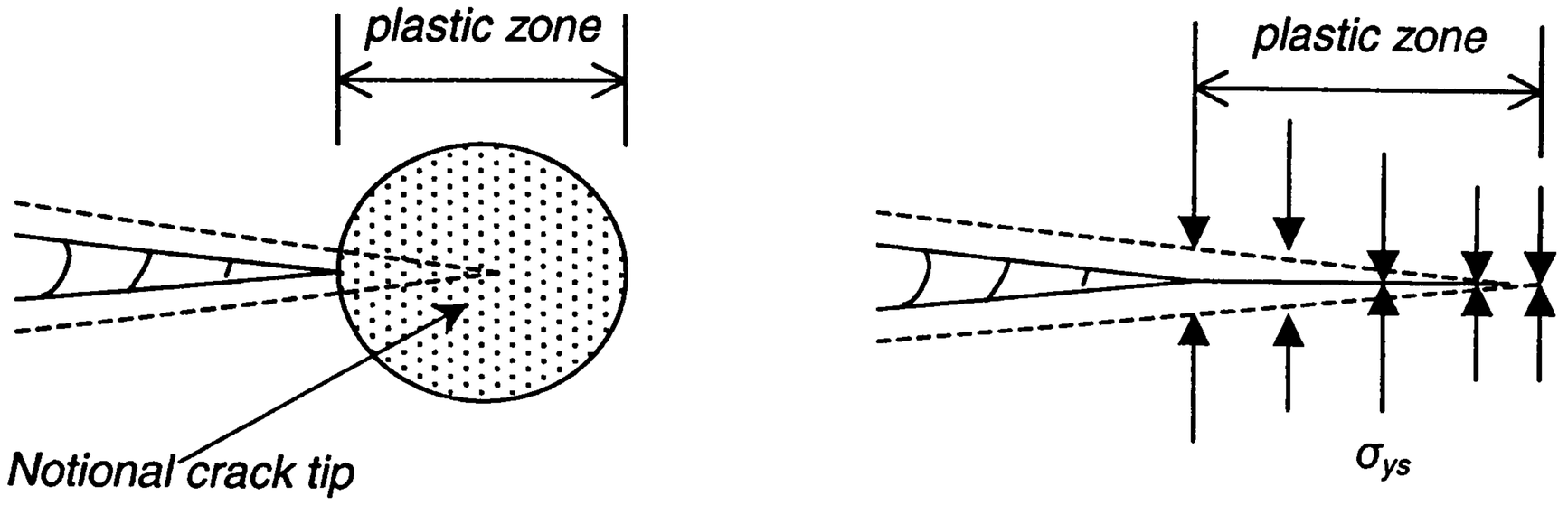

Figure 2.2.2. The plastic zone according to Irwin or Dugdale (Ewalds&Wanhill, 1984).

The stress intensity approach could therefore be applied as long as crack tip plasticity was limited and the stress field at the crack tip was approximately elastic. That is, where the size of plastic zone was small compared to the crack length, and, the cracked body behaved in a more or less elastic manner. Irwin's approach provided a breakthrough over the simpler, critical stress approach, which held that there was a well-defined stress limit, below which, materials do not fail. This critical stress criterion was not universally applicable.

The stress intensity approach, which forms the backbone of Linear Elastic Fracture Mechanics (LEFM), provided a means of evaluating the critical defect size in materials that showed elastic or approximately elastic behaviour. The usefulness of this approach is that the critical combination of stress and crack length is used to determine the fracture strength of different materials. The parameter K_c therefore characterises a material's resistance to cracking and is commonly referred to as the fracture toughness of the material. Tests on specimens of suitable shape and size allow the fracture toughness of materials to be measured for a given application.

The value of K is found experimentally to depend on the specimen constraint and thickness at a given temperature. The mode of loading is also relevant. The critical stress intensity factor (K_{Ic}) is defined by Mode I loading (tensile opening). Test specimens contain starter notches or pre-cracks, the aim being to obtain an 'ideal' plane crack that meets the assumptions of LEFM. Although test specimens derive from the ASTM standard for testing metallic materials, they are widely applied for testing non-metallic materials, e.g. ceramics.

2.2.2. Deformation Behaviour of Polycrystalline Graphite

An understanding of the deformation behaviour of polycrystalline graphite is a prerequisite to understanding its fracture behaviour since the initiation and growth of the critical defect occurs during the early stages of deformation. Considerable insight into the structural response of graphitized carbons under deformation has been acquired from studies of their behaviour under tension, compression, and, other complex modes of loading. Brocklehurst (1978) provides a detailed, pre-1980 review of fracture in polycrystalline graphite, some aspects of which are included in this discussion.

Graphite generally displays non-linear deformation behaviour such that the apparent elastic modulus (defined by the tangent to the elastic portion of the curve) decreases with increasing stress (Figure 2.2.3). Upon unloading to zero load, the material shows permanent set, even at very small strains. There is also a hysteresis effect such that the unloading curve does not coincide with the loading curve. Some workers state that the material remains elastic because cyclic loading and unloading between the same stress limits produces identical superimposed hysteresis loops (Jenkins, 1962). However, Greenstreet et al (1970) classify this behaviour as non-linear, non-elastic because the unloading curve does not retrace the loading curve.

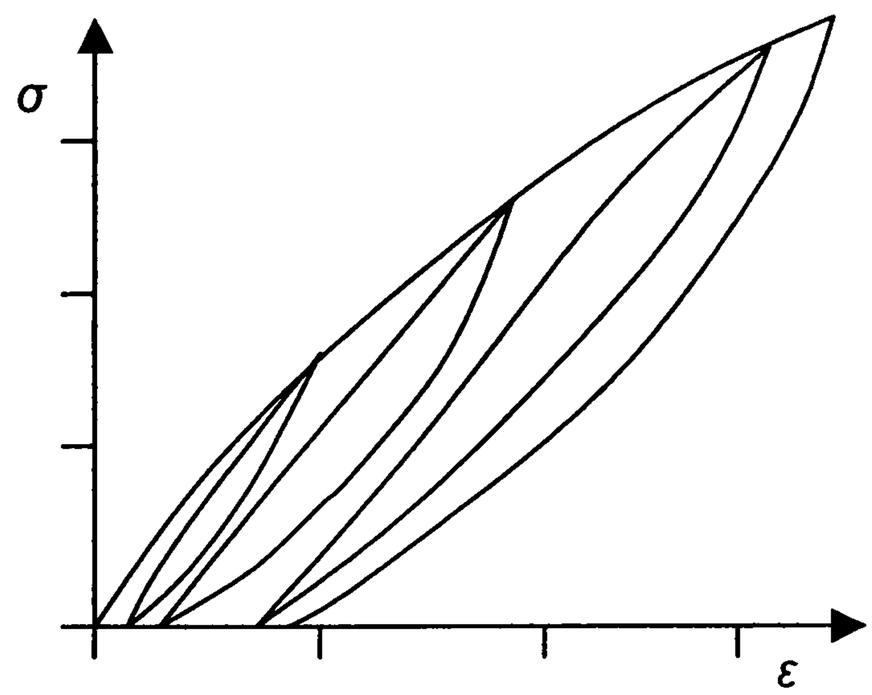

Figure 2.2.3. Typical stress-strain response of polycrystalline graphite.

Jenkins' (1962, 1965, 1973) 'friction-block' model was amongst the first to describe this somewhat unique behaviour of polycrystalline graphite. In this model, Jenkins' (1962, 1965) envisaged the graphite structure to comprise a continuous network of carbon atoms surrounding the filler grains.

Elastic restraint from the network controls the extent of plastic deformation experienced by the grains, for a given strain. As the stress increases, the restraint of this network diminishes and more grains deform plastically. The low restraining ability of the carbon network, or, inter-connected 'carbon springs' as Jenkin's (1962) called it, allows non-linear deformation even at very small strains. This gives the impression of a continuous decrease in the elastic modulus, with a non-linear stress (σ)-strain (ε) response such that,

$$\varepsilon = A\sigma + B\sigma^2 \qquad [2.2.6]$$

Jenkin's model deviates from the actual behaviour at high stresses, apparently due to a reduction in the apparent modulus, caused by an increased micro-crack density at high stress. Other deformation models follow a similar concept, with varying accuracy in the prediction of the strain at a given stress.

2.2.3. Micro-Failure Mechanisms in Polycrystalline Graphite

Two mechanisms, which both occur simultaneously, are generally, held to be responsible for the deformation response and ultimate failure of polycrystalline graphite, i.e. dislocation movement and microcracking. The microcracks form an inherent part of the graphite structure, with the volume of cracks ranging between 4-6% at room temperature. They are usually fine enough to be viewed only by electron microscopy, but grow to optical visibility under applied stress. The larger their number and the closer their spacing, the greater the probability that these cracks will align to form a fracture path, and, hence the lower the graphite strength (Smith, 1964).

Jenkins (1965) stated that the mechanical properties of polycrystalline graphite are influenced by the behaviour of dislocations that make up the crystals at the boundary between the filler and binder grains. The high dislocation density in polycrystalline graphite (~10^{14} cm^{-2}) was attributed to be responsible for much of the strain taken up by the material. Since no work hardening effects were observed, Jenkins (1965) concluded that the deformation response of polycrystalline graphite must be due to inherent barriers, to dislocation movement, and not the formation of additional barriers. Most of the strain was attributed to dislocation movement and their interaction, without the need to look

for nucleation mechanisms. In his non-linear deformation model (Equation 2.2.6) therefore, Jenkins (1973) adds that the constant 'A' accounts for the elastic strain defined by the elastic lattice compliance of the graphite crystallites. The parameter 'B' accounts for the non-linear strain component, which arises from dislocation motion and interaction.

Jenkins (1965) showed that polycrystalline graphite deforms by sliding along basal layers defined by striations within the filler particles, these striations being regions of a highly graphitic nature. This slip of the basal layers is obstructed at mis-orientations between the filler and binder particles. This obstruction is enhanced by the random orientation of the binder particles around the filler grains. Localised internal stress also opposes slip (Seldin 1966), the origin of these stresses being the thermal expansion anisotropy of the graphite crystallites when it is cooled during heat treatment.

Although Jenkins (1965) was of the opinion that the extent to which dislocations influenced the deformation behaviour of polycrystalline graphite is low (~10%), other studies have revealed a strong influence. Increased dislocation pinning in irradiated graphite raises the shear modulus of polycrystalline graphite and increases the linearity of the stress-strain response, thus confirming the strong effect of dislocations on the deformation behaviour (Taylor et al, 1967).

Microcracking has been detected both microscopically and via acoustic emission (AE) studies of polycrystalline graphite under deformation. Ioka et al (1990) used AE to study basal slip under compressive loading in polycrystalline graphite, with the premise that AE response has been shown to coincide with dislocation movement in solids. They associated an initial increase followed by a decrease, in the AE signal, with dislocation movement and pile up, mainly at grain boundaries. By oxidising the material, they envisaged a reduction in the ability of the grain boundary to obstruct dislocation movement, due to the preferential oxidation of the boundary regions. The increase in dislocation movement and in the extent of microcracking, following oxidation, produced a continuous increase in the AE signal and a reduction in fracture strength, meeting their expectations.

Ioka and Yoda (1990) further showed that the electrical resistivity of polycrystalline graphite was reduced under compressive loading, which for them, was a clear indication of the dominant role of microcracks and porosity in the fracture process. They point out that the change in resistivity parallel and perpendicular to extrusion of the graphite would be similar if dislocation density was a controlling factor. The closure of microcracks and pores aligned parallel to the compressive stress explain the decrease in resistance in this direction.

The influence of microcracks is also confirmed by the increase and decrease in the thermal expansion coefficient of polycrystalline graphite with compressive and tensile pre-loading respectively. The respective closure or opening of microcracks under compression or tension, effectively increases or decreases material density, with the result that the microcracks lose their ability to accommodate thermal expansion (Hart, 1972).

Microscopy has also helped to reveal the mechanism of crack initiation and growth in polycrystalline graphite. In a coarse needle-coke graphite, Jenkins (1962) found that cracks grew between the interlamellar regions within the filler grains, particularly when the grains were aligned at an angle to the maximum strain direction, indicating that a shear mechanism was responsible. Knibbs (1967) also noted the ordered structure within coarse and medium grain graphites to be a weakness due to interlamellar cleavage within the grains.

2.2.4. Micro-failure Mechanisms in Relation to Graphite Failure Models

Numerous studies have attempted to develop models that describe and predict failure in polycrystalline graphite. An underlying theme of these models is the coincidental alignment of micro-defects initiated from pores and cleavage planes along the basal direction in filler particles (Figure 2.2.4). This coincidental alignment of defects varies with pore size and distribution, and, also with grain size and orientation, leading ultimately to a sizeable macro-defect and failure (Brocklehurst, 1978). Tucker et al (1986) provide an excellent review of six fracture models that have been used to predict graphite failure, including the 'Rose-Tucker' model. This model is based on the probability that adjacent grains cleave to form a critical Griffith flaw leading to failure.

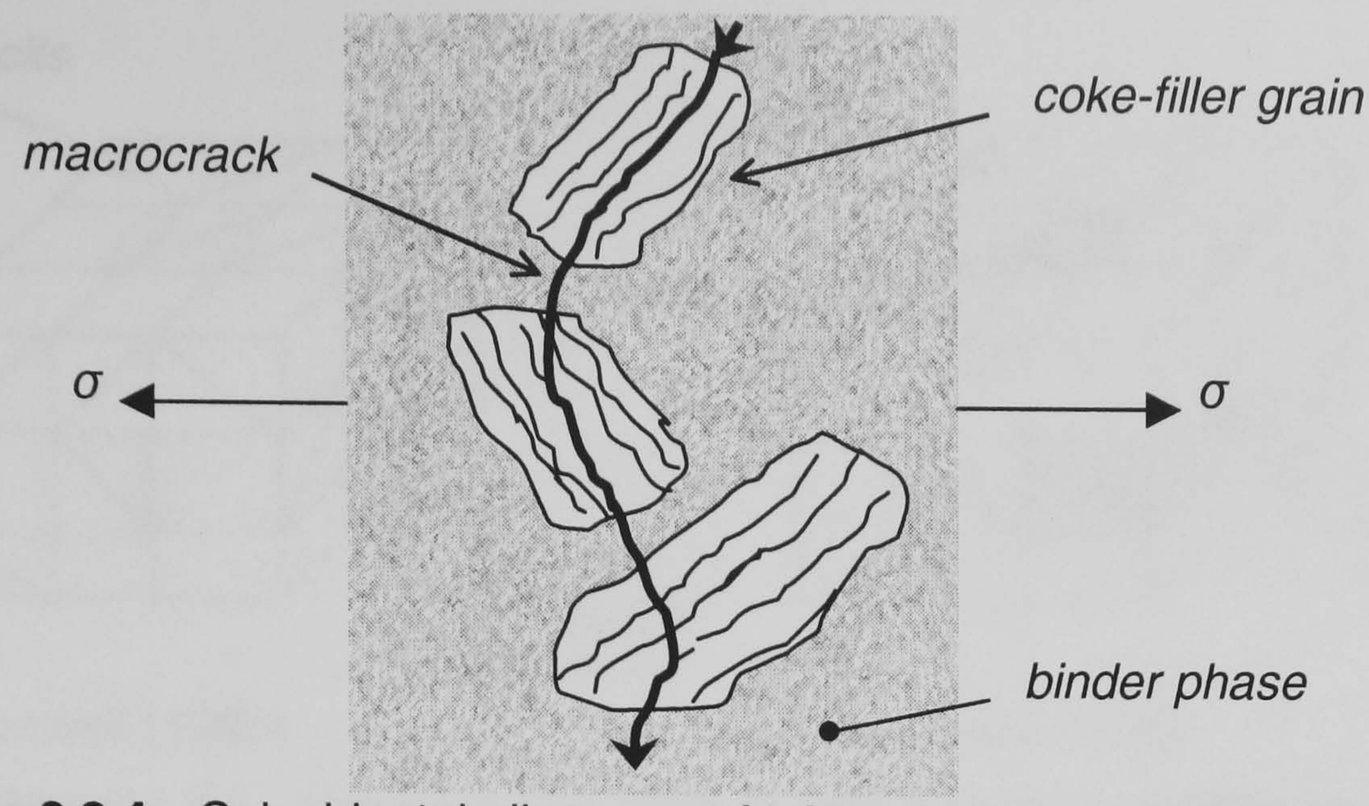

Figure 2.2.4. Coincidental alignment of microcracks to form the Griffith flaw.

They expose the failure of existing models, including their own model, in not accounting for microstructural interactions in the failure process, as well as, material changes due to the environment, e.g. oxidation. One of their main limitations of four commonly applied failure models, viz. the critical stress, critical strain, critical strain-energy density, and, the Weibull model is their treatment of the graphite structure as a defect-free, homogeneous continuum. Weibull's statistical model also falls short in accommodating for the non-linear stress-strain behaviour of polycrystalline graphite, and, predicts a greater dependence of strength on volume than is experimentally observed. Marshall & Priddle (1973) found the fracture mechanics to be more reliable for strength prediction than the Weibull model.

Microscopic observations by Tucker et al (1986) also found crack development to occur after random sub-critical defect formation, often with incorporation of pores into their developing structure, leading ultimately to interconnected grain cleavage. An important aspect of the fracture mechanics model is its ability to predict failure from an artificial notch, provided the notch length exceeds that of the largest inherent flaw. In contrast, other models failed to do so.

An earlier model by Buch (1976) and a recent model by Burchell (1986) have been more successful in predicting graphite failure behaviour. These models include microstructural characteristics in the analysis as shown in Figure 2.2.5. The model of Buch (1976) describes the graphite structure in terms of a 3-D array of grains and pores. Failure develops by cleavage of the grains when the resolved applied stress exceeds the grain cleavage strength.

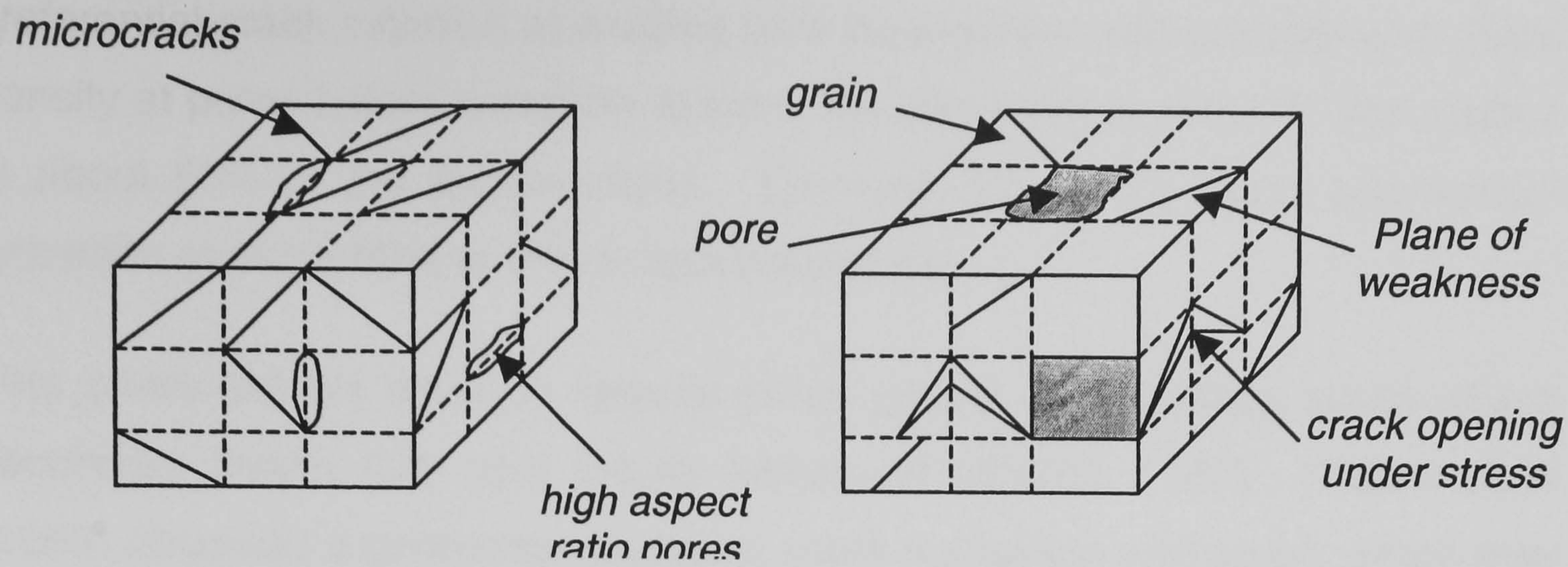

Figure 2.2.5. Conceptual models of polycrystalline graphite structure.

Burchell's model (1986) is similar in that, it includes high aspect ratio pores that are aligned favourably to the applied stress, as sites of stress concentration, from which cracks initiate at relatively low stress levels. Ouagne (2000) points out that, existing models fail in predicting the failure behaviour of oxidised, or, irradiated graphite, because these models do not account for changes in the corresponding stress-strain curves of the materials. Existing models have also failed to exploit the use of energy-based failure parameters in trying to predict graphite failure behaviour. Ouagne (2000) used crack growth resistance curves (*R*-curves) to develop a failure prediction model for reactor graphite.

2.2.4.1. Role of Porosity

Polycrystalline graphite contains a variety of pore types, ranging from extremely small microcracks to large pores caused by evolution of volatiles during manufacture. The role of these pores in the fracture behaviour can be quite complex, and is often perceived to be different. Some workers view the pores as crack blunting sites where stress intensity is reduced. Pores are also viewed as having the ability to accommodate deforming elements within their space, hence delaying the onset of fracture. However, many researchers see pores as stress concentrators that help initiate cracks.

Jenkins (1962) noted that cracks travelled between pores, with isolated cracks appearing before major fracture. Taylor et al (1967) also observed crack initiation at pores, with the major fracture path linking the larger pores. Large pores were regarded as a source of weakness. Slagle (1967) observed

preferential crack initiation at existing pore boundaries, with a build-up in crack density at pores before complete failure. He noted micro-cracks to first appear at about 50% of the tensile stress. Oku and Eto (1973) noted micro-crack formation at about 60% of the compressive stress.

Fine pores did not seem to impede crack growth, unlike larger pores where secondary cracks form and cracks branch off (Knibbs, 1967). Tucker et al (1986) observed a connection between crack nucleation and pores, which they attributed to the stress-concentrating effect of the pores. They indicate that the distribution of pore size, orientation, and, aspect ratio maybe needed in a complete failure model for graphite. Tucker et al (1986) describe the often observed phenomenon of crack growth into pores in terms of a perforation mechanism, similar to the “tearing of a postage stamp”.

2.2.5. Relation between Strength, Grain Size, and, Porosity

As with most materials, graphite strength depends strongly on grain size, but this dependence is not singular given the influence of other factors such as porosity, degree of anisotropy, etc on strength. There is a difference in perception between workers regarding the influence of grain size or porosity as the critical defect controlling strength, in that expressions relating the strength to both porosity and grain size are rarely reported. Various expressions have been derived to describe the relation between graphite strength (S) and grain size (d) or porosity (ε) as outlined by Knibbs (1967):

Hutcheon & Price: $S \propto \varepsilon^{-q}$

Knudsen: $S \propto e^{(-m\varepsilon)}$

Orowan: $S = K \,.d^{-1/2}$

Petch: $S = K_1 + K.d^{-1/2}$

Griffith: $S = \left(\frac{4E\gamma}{\pi}\right)^{1/2} .d_{max}^{-1/2}$

Knibbs: $\overline{S} = c.e^{(-m\varepsilon)} .d^{-1/2}$

Perhaps the most interesting expression are those of Griffith and Knibbs (1967), the latter linking both porosity and grain size with strength, and, the former linking the grain size to the strength.

These relations strongly implicate both porosity and the filler grains as the main strength controlling defects. Tucker et al (1986) explain that the reduction in strength with increasing grain size is related to the fact that fewer grains need to be cleaved to form the critical Griffith crack when the grain size is large. This was evident from the strain at which microcracking became apparent. In coarse grain materials, this critical strain occurred at about 0.1%. However, in fine grain material the strain increased by about 3 times.

The Griffith energy balance criterion is said to hold for polycrystalline graphite, because failure occurs due to stress concentration at inherent crack-like defects, which are adequately found in polycrystalline graphite at the macro and micro-level (Brocklehurst, 1978). Consideration of relevant material properties in the Griffith relation also produces defect sizes that are realistic in relation to the structural features. McEnaney (2000) indicates that the critical flaw size in graphites typically range between 0.5-1.5mm. He cautions, however, that the application of linear fracture mechanics is dubious given the non-linear stress-strain response of graphite. Another practical consideration in applying FM, is the ability to measure the fracture toughness based on the inherent random defects in the material, rather than machined artificial flaws. Artificial defects can exceed the dimensions of the inherent defects.

Another aspect is the influence of the type of test on the measured failure strength. Ishiyama and Eto (1996) demonstrate that the failure probability of fine-grain graphite (IG-110) depends strongly on the test method. Tensile tests give the highest failure probability, followed by 4-point and 3-point bending. It is also observed that graphites with similar elastic modulus and density show different strengths. This is explained by the dependence of strength on the maximum flaw size. According to (Brocklehurst), several cracks may exist simultaneously in graphite and these can influence each other. As the applied external stress increases, the density of these cracks increases, reaching a critical point at which coincidental alignment of these cracks leads to a flaw that is sufficiently large to cause failure. Controlling and measuring the generation and growth of multiple cracks, many of which exist internally, is clearly difficult. Graphite strength is therefore not a unique material property but varies with the test used to determine this strength.

SECTION 2.3: *R*-CURVE BEHAVIOUR IN QUASI-BRITTLE MATERIALS

It was discussed in the previous section, how the fracture behaviour of polycrystalline graphite is inadequately described by fracture mechanics and how other failure models are limited in this respect. In this section, an important failing of LEFM is described in that many materials do not develop a catastrophic defect at the maximum load. This makes it necessary to characterise the fracture behaviour of quasi-brittle materials such as graphite in terms of the crack growth resistance curve or *R*-curve. Methods used to measure *R*-curve behaviour are outlined. Toughening mechanisms that are thought to cause this behaviour in ceramics and carbon materials are reviewed.

2.3.1. The *R*-Curve Concept

In brittle materials, LEFM is adequate for predicting failure. The fracture toughness, K_{IC}, is a characteristic material property, independent of the crack length, specimen geometry, and test method. Carbon materials, however, do not behave as ideally brittle materials but are elasto-plastic, and do not fail abruptly from an initial crack at a critical load. Instead, they absorb a significant portion of the energy required for crack extension, requiring additional energy to increase the crack surface area. The energy needed for complete fracture of the material is thus higher than that needed for crack initiation.

Upon initiation, cracks remain stable up to a certain load beyond which, additional energy is needed to cause further crack propagation. The maximum fracture toughness is higher than predicted mainly because cracking initiates at loads below the critical load defined by LEFM. The fracture behaviour of such materials is thus not adequately described in terms of a single toughness parameter such as K_{IC}, G_{IC}, or, J_{IC}. Whilst K_{IC} represents the linear elastic form of the fracture toughness, which is directly related to the critical elastic energy-release rate (G_{IC}), J_{IC} is used as a measure of fracture toughness in non-linear, elasto-plastic materials. The *R*-curve relates the crack growth resistance parameters such as K_R, G_R, or, J_R to the extent of crack growth (Δa). The crack growth resistance curve or *R*-curve thus provides a more realistic view of the fracture behaviour of quasi-brittle materials.

The energy needed for crack extension rises because the energy needed to propagate the crack exceeds that available at the crack tip. The energy required to cause a unit increase in crack surface area is, therefore, a definitive parameter according to which 'energy absorbing' materials may be compared. An energy-based *R*-curve can therefore be defined in terms of *R* [Jm^{-2}] and constitutes the sum of the elastic energy and pseudo-plastic energy (Allard et al, 1991) involved in fracturing the specimen. *R*-curves are commonly used to compare the fracture resistance of many ceramics. Ahlborn et al (1993) class *R*-curve behaviour into three categories as illustrated in Figure 2.3.1.

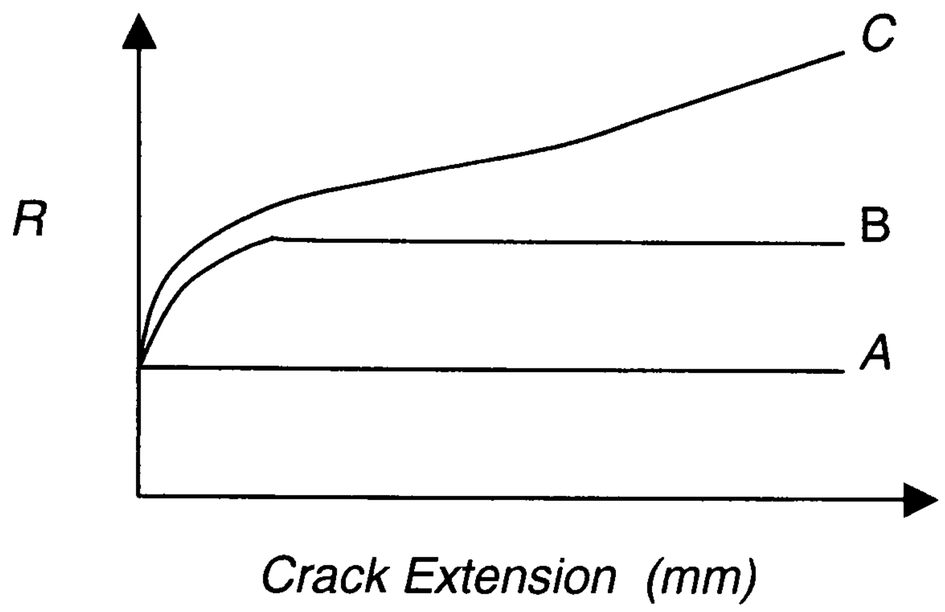

Figure 2.3.1. Different types of *R*-curve behaviour (Ahlborn et al, 1993).

Group A covers homogeneous materials that behave close to ideally brittle materials showing no resistance, e.g. glass. Group C covers materials that show a steady increase in crack growth resistance or fracture toughness as the crack propagates, e.g. C/C-composites. Group B materials display a short-range increase in fracture toughness followed by a plateau in the resistance as the crack extends. It is in category B that Ahlborn et al (1993) class polycrystalline graphite.

Group B behaviour is usually characterised by three stages. Stage I is an increase in crack growth resistance, which is historically related to process zone development. Stage II is a plateau corresponding to steady-state crack propagation. Stage III corresponds to changes in crack growth resistance related to specimen end effects. It is usually considered the stage where the process zone coincides with the back end of the specimen. There is some conflicting evidence regarding the nature of this final stage in that some studies show a plateau, while others show a rise or fall in *R*-curve behaviour.

Mazzei et al (2000) consider Group B, *R*-curve behaviour to be indicative of a material where toughening is associated with a wake zone of constant size. This typically occurs with stress-induced phase transformations and bridging effects. Group C behaviour exemplifies materials where crack branching is the main toughening process such that the wake zone extends indefinitely. They state that the main toughening mechanism can be deduced from the *R*-curve profile. However, this analysis is often clouded by the influence of test parameters on the *R*-curve profile, making it necessary to eliminate the influence of these parameters so that the main toughening mechanism can be ascertained.

Another important aspect of applying the *R*-curve concept highlighted by Sakai et al (1988) is the use of the stress-intensity based K_R-curve and the energy-based *R*-curve (G_R-curve) by researchers when comparing different materials. Sakai et al (1988) caution that the K_R-curve has its basis in Irwin's similarity rule which requires that the material shows a linear elastic return to the origin upon unloading. Since there are few materials which fulfil this criterion, there is no physical basis for using the energy toughness parameter (G_R) derived from the K_R-curve. Sakai et al (1988) extend this argument by showing that a large K_c-value gives high fracture energy, and vice versa, when the material is linear elastic. However, this does not apply for non-linear materials. Many refractories materials have low K_c-values but large fracture energy.

There is also some contention as to whether the *R*-curve is a material characteristic curve given that the fracture toughness, K_{IC}, is not a material constant independent of the crack length, test specimen geometry, and, the test method. Some evidence of this has been demonstrated by Munz (1980) who showed that K_{IC} varied widely with differences in specimen geometry, pre-cracking methods, and the type of notch (chevron or straight-through). Sakai & Kurita (1995) state that the *R*-curve only becomes a material constant for steady-state crack propagation conditions in which the height and length of the wake zone and bridging zone respectively, are small compared to the specimen geometry. This is akin to the requirement that the plastic zone be small relative to the specimen thickness in plane-strain conditions.

2.3.2. Influence of the Geometric Factor on the *R*-curve Profile

It is widely recognised that the *R*-curve profile is largely affected by test parameters. A particular aspect in this regard, is the influence of the geometric factor on the experimental *R*-curve profile. For both the straight-through notched and chevron-notched specimen, *R*-curve profiles usually show a steep rise in stress-intensity over the latter part of the crack extension range, typically when $a/W \approx 0.8$. There has been some contention as to why this steep rise occurs. Many workers cite the strong influence of the geometric factor as the cause of the steep rise. Other researchers attribute the strong rise towards the end of the profile to a compressive loading effect as the crack approaches the backend of the specimen. For instance, Kostopoulos et al (1998) reported a rise in *R*-curve behaviour for C/C-composite, compact tension specimens. They attributed this to a compressive shielding of the crack tip due to the loading configuration towards the backend of the specimen.

Mazzei et al (2000) make an important contribution in resolving this problem by testing refractory material under both 3-point and 4-point bending, and, commercial glass specimens under similar conditions using identical specimen geometry. They show that the refractory samples had almost identical *R*-curve behaviour in both 3-point and 4-point bending except at $a \approx 0.8W$ when variations in the curves began to appear. They also showed that chevron-notched commercial glass specimens, which should display a flat *R*-curve, showed a rise in *R* when $a \approx 0.8W$. This was unambiguous evidence of the strong and rather erroneous influence of the geometric factor on the *R*-curve profile since commercial glass has no toughening mechanism that could cause a rise in *R*.

Mazzei et al (2000) further demonstrated the influence of the geometric factor by comparing *R*-curves for identical materials using the straight-through notch and chevron-notch configuration in 3-point bending. The *R*-curves of both specimen types show a rise after $\alpha \approx 0.8$. The chevron-notch profile was flatter than the straight-through profile over the region $0.4<\alpha<0.9$ (see Figure 2.3.2). It is worth noting that the compact tension specimen configuration presents an even steeper rise in $Y(\alpha)$, which occurs at $\alpha \approx 0.6$.

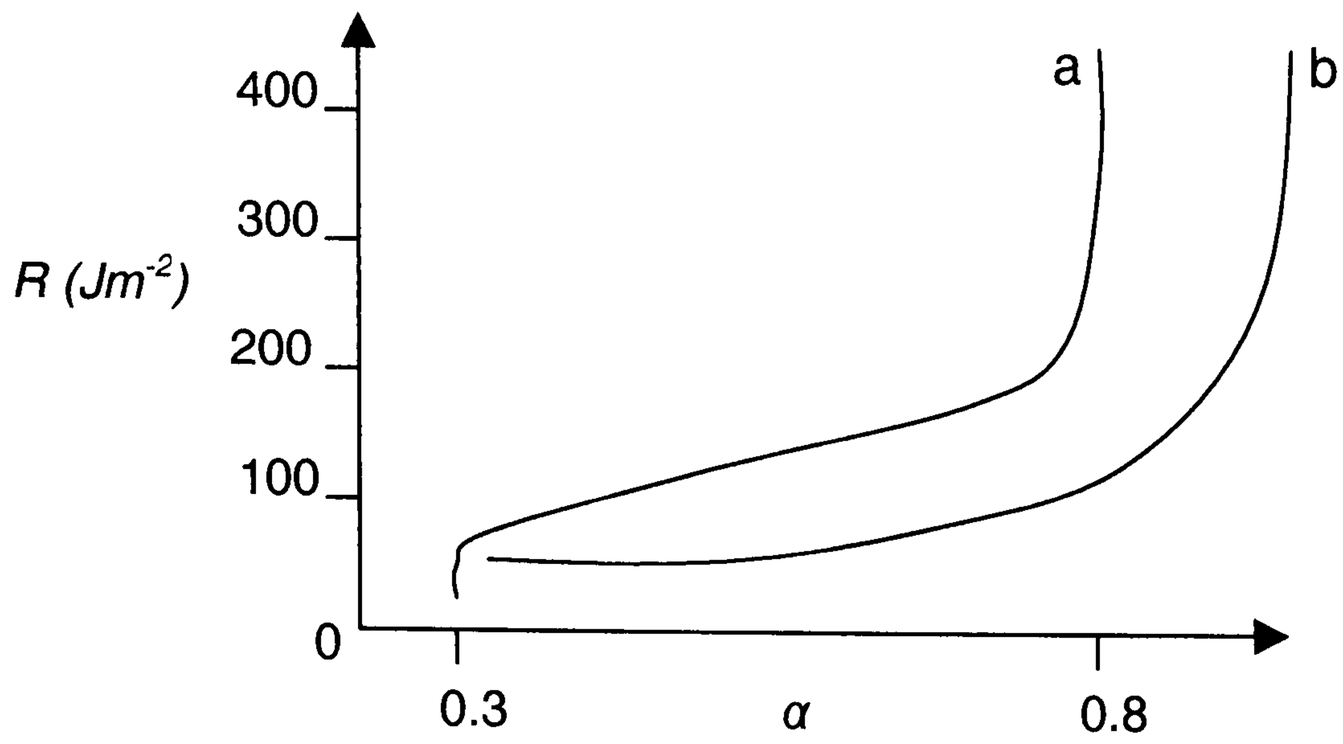

Figure 2.3.2. Comparison of *R*-curves for the same material using (a) straight-through notched; (b) chevron-notched specimens (Mazzei et al, 2000).

2.3.3. Methods Used to Measure the *R*-curve Behaviour

Sakai (1989) states that there is currently no standardised method for determining the *R*-curve behaviour of quasi-brittle materials. Various techniques may be used to obtain a measure of the *R*-curve behaviour in carbon and ceramic materials, each having their own advantages and disadvantages. A crucial aspect of all the methods, regardless of their sophistication, is their reliance on the method used to measure the crack length. Crack length measurement techniques therefore form a crucial part of *R*-curve measurement. As will be seen, even the graphical methods used to derive the *R*-curve depend on accuracy in the crack length, measurement technique.

2.3.3.1. The Optical Method

In this method, a travelling microscope or optical measuring device is employed to measure crack length. In making the optical measurements, it is desirable to use a very non-compliant (stiff) loading machine and low test speed to promote stable crack growth. The accuracy of the method depends on the precision with which the crack tip is resolved. The method can be complicated by crack path tortuosity and pore-crack tip interactions. Stress intensity equations are based on an idealised view that the crack is infinitesimally thin and straight, adding to scatter in the *R*-curve obtained by the optical method. Despite these difficulties, Hiramatsu & Okada (1998) favour the method citing its advantages to be simplicity, the need for a single specimen, and its intrinsic accuracy and reliability.

2.3.3.2. Compliance Methods

Since the compliance of a cracked elastic body depends on the crack length, compliance techniques allow an indirect way of measuring the crack length. An experimental or analytical compliance method can be used. Experimental measurement involves measuring the compliance of a series of notched specimens to increasing depths to simulate an increasing crack length (Sakai and Bradt, 1993). A calibration curve of the compliance change with crack length is obtained, providing an estimate of the crack length based on the compliance change of the test specimen (Ewalds and Wanhill, 1984).

Analytical methods are based on numerical analysis of the compliance change of the cracked body, where the compliance is taken from the slope of the unloading line taken to the origin, or, to the point of residual displacement (Figure 2.3.3). That is, the body is treated as elastic or non-elastic. The crack increment is obtained analytically (Allard et al 1991, Kostopoulos et al 1998):

$$\alpha_n = \alpha_{n-1} + \frac{b_{n-1}}{2} \cdot \frac{C_n - C_{n-1}}{C_n} \qquad [2.3.1]$$

α_n, α_{n-1} = crack length after two successive cycles

C_n, C_{n-1} = corresponding unloading compliance at n and $(n-1)$

b_n = uncracked ligament of the specimen after n-cycles

A shortcoming of the method is insensitivity to small compliance changes that occur in the early stages of crack growth. This produces scatter in the data (Ouagne, 2000). Fett and Munz (1998) state that the method underestimates the crack length due to constraint from the wake and frontal process zone, making the crack appear shorter than it physically is (Fett, 1991).

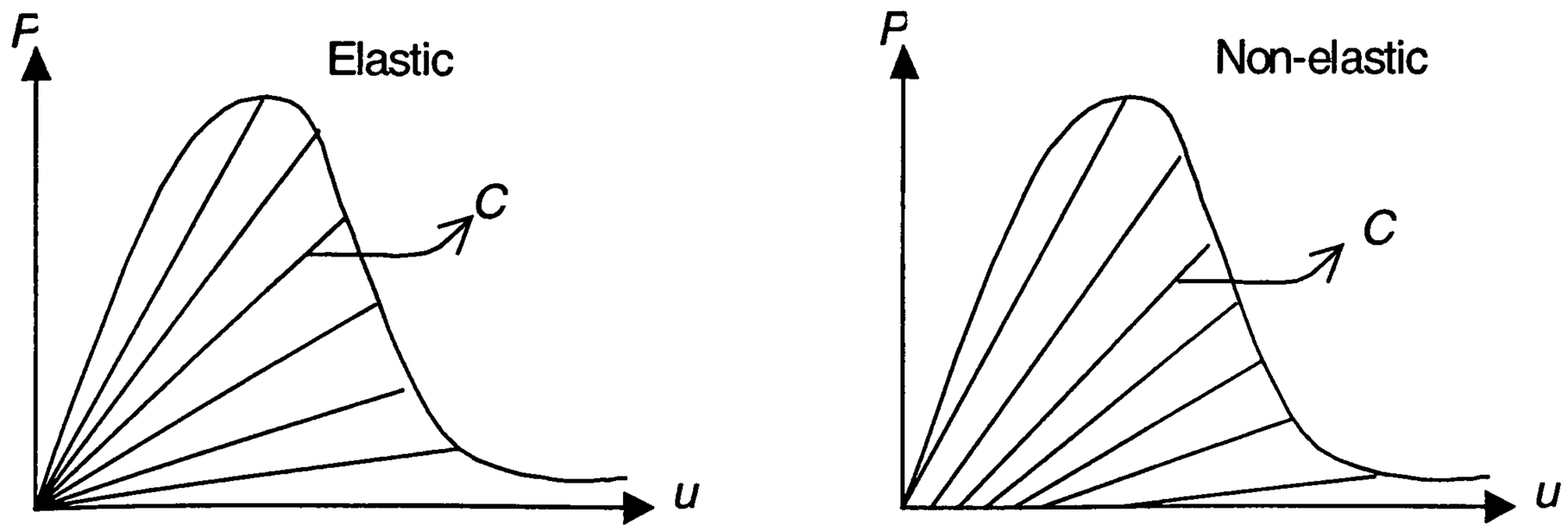

Figure 2.3.3. Compliance of an elastic and non-elastic body (Allard et al, 1991).

2.3.3.3. Graphical Methods for determining the Energy-based *R*-curve

Classical linear elastic mechanics based on continuum theory does not fully account for the non-elasticity and heterogeneity of many ceramics. The conventional stress intensity parameter is based on the linear hypotheses and shows a strong dependence on specimen geometry, specimen dimensions, and the test method. Sakai (1988) is of the opinion that the physical meaning of K_{IC} for such materials, no matter how accurately determined, is obscure and meaningless. For this reason, he prefers to compare the fracture resistance of different materials based on energy principles.

The energy approach is based on macroscopic thermodynamics. It considers both the kinetic energy and plastic energy dissipated in the material. In theory, the energy required to fracture a specimen consists of two components, an elastic part and a pseudo-plastic portion. Therefore, the total energy needed (R) is equal to the sum of the elastic energy (G) and the plastic energy (Φ_p), i.e. $R = G + \Phi_p$. The value of the elastic part (G) can be determined graphically from the *P-u* curve (see Figure 2.3.3) where G is given by:

$$G = \frac{dU}{(a_2 - a_1)B} \quad \text{or} \quad G = \frac{dU}{(W - a)B} \qquad [2.3.2]$$

dU = area between adjacent load-displacement curves at crack initiation corresponding to initial notch lengths a_1 and a_2 ($a_2 > a_1$), or, the area under the load-displacement curve at crack initiation

(W-a) = ligament of the fracture specimen

The elastic part is defined by the slope of the unloading line taken to the origin. The plastic component is more complex and difficult to extract as it is dictated by the extent of residual displacements that occur upon unloading to zero load. Various methods have been proposed to determine separately the elastic and plastic components of the fracture energy. Clearly, these methods still require that the crack length be known at various displacement intervals. Sakai and Bradt (1986, 1993) have described in detail graphical techniques for deriving the energy-based *R*-curves. These graphical methods each have advantages and limitations and only pertinent aspects of the methods are outlined below.

Loading-unloading Method

This method involves loading and unloading the specimen at various intervals along the *P-u* curve once the crack initiates (see Figure 2.3.4). By considering the area between consecutive unloading or loading lines (*dU*), and, the crack increment (*da*) over this interval, the energy-based *R*-curve can be determined using the relation (Sakai et al, 1988):

$$R = \frac{dU}{dA} = \frac{dU}{Bda} \qquad [2.3.3]$$

The method requires that the crack length be known at each *P-u* interval. The problems with this method stem from the fact that the unloading compliance differs from the theoretical because the unloading procedure involves additional energy dissipation effects due to frictional forces in the bridging zone. Thus, more energy is consumed in the load-unload process. This effect is said to be worse for materials with rough fracture surfaces or extensive micro-cracking. It also relies on the assumption that inelastic deformation or crack growth does not occur during unloading. It may also be that damage is caused to bridging elements in the following wake during unloading.

Superposition Method

This technique avoids the problems of the load-unload method but is limited by the requirement of multiple test specimens. An assumption is made that the material is a completely brittle, linear elastic body such that, the critical load-point for each specimen, which has a different initial crack length, falls on the single curve shown in Figure 2.3.5b. The shift in the *P-u* curve defined by the shortfall in the critical displacement for the individual specimens (Figure 2.3.5a) is taken as the extent of residual displacement (Figure 2.3.5b). This residual displacement is then used to define the unloading compliance of the material as if it were non-elastic. Using the area defined by successive unloading lines and the measured crack lengths, the *R*-curve can be derived by Equation [2.3.3]. The assumption of a brittle, linear elastic body and the use of an apparent residual displacement must introduce some error. The use of notched specimens to simulate the growing crack is also likely to misrepresent the compliance of a specimen with a fully-bridged crack.

Dimensionless Load-Displacement Method

The experimental *P-u* curve is redefined in terms of a dimensionless load-displacement curve. The re-defined curve is matched against a universal dimensionless *P-u* curve that is said to describe the load-displacement behaviour of all linear elastic materials (see Figure 2.3.6). As shown by Figure 2.3.6, the required area under the *P-u* curve is obtained by relating the compliance lines on the universal curve to those on the experimental curve. Using the measured crack lengths, the *R*-curve can be obtained using Equation 2.3.3. The method is described in detail by Sakai and Bradt (1986, 1993). A shortcoming of this method is the assumption that the experimental P-u curve behaves perfectly linear-elastic up to maximum load because this is the point from which the experimental and theoretical curves are compared. Therefore, the portion of stable crack growth preceding the maximum load appears to be ignored in the derivation of the *R*-curve, and this is a crucial part of the *R*-curve, typically forming the rising part of the *R*-curve.

2.3.4. *R*-curve Behaviour in Carbon and Ceramic Materials

Although numerous studies have focused on crack growth resistance in ceramics and C/C-composite materials, only a handful of studies focus on polycrystalline graphite. In the case of composite materials, studies mostly involve the use of compliance methods for comparing the crack growth resistance of the materials. The purpose of these studies has mainly been to evaluate changes in the fracture toughness of the composites with variation in fibre orientation, surface texture, manufacturing process, etc. The compliance method has proven useful in comparing *R*-curve behaviour of C/C-composites, even though these materials do not lend themselves ideally to LEFM theory.

The fibrous nature of C/C-composites makes a physical assessment of the crack length difficult, particularly if the potential drop method is applied given the extensive fibre bridging that occurs. The potential drop method exploits the change in material resistance with crack growth to obtain a measure of the crack length (see Section 2.4). Arulrajah (2002) recently applied the potential drop method to compare K_R-curve behaviour in short and long-fibre C/C-composites.

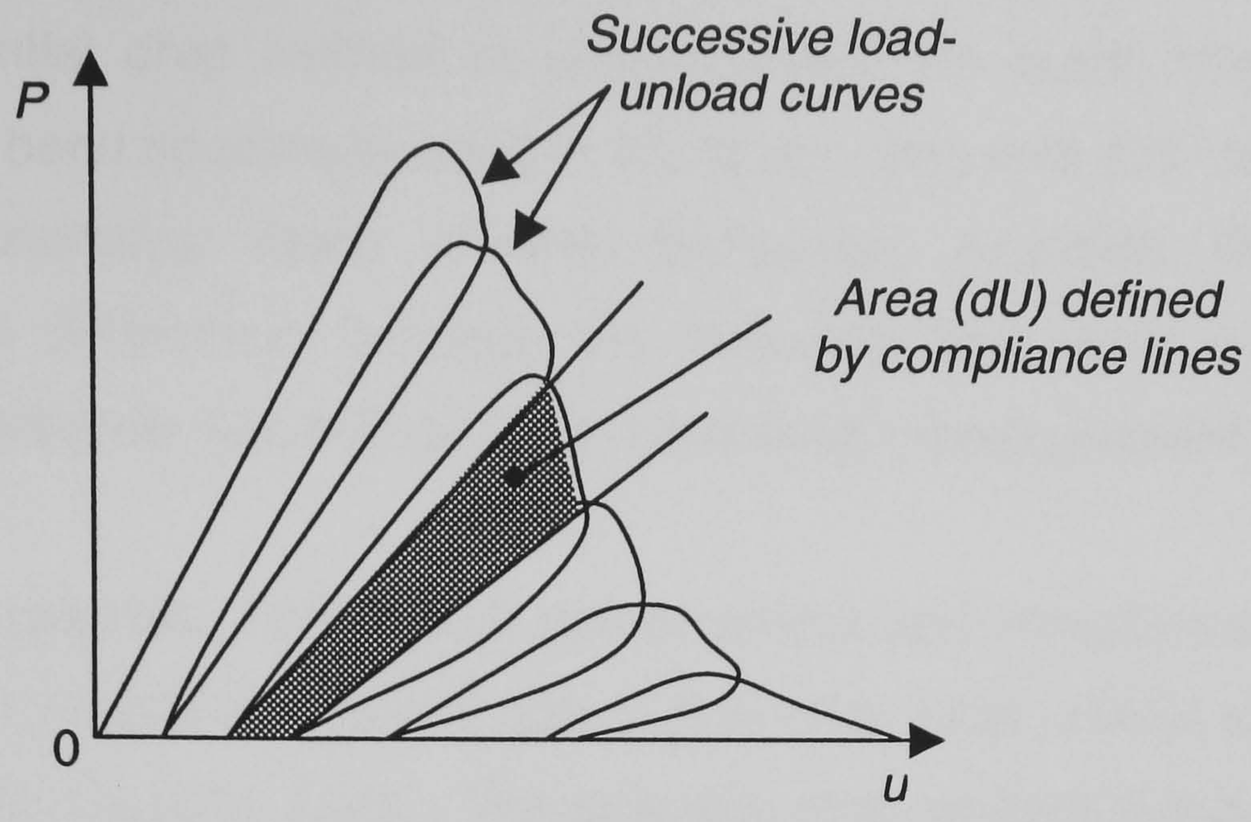

Figure 2.3.4. Schematic description of the load-unload method (Sakai & Bradt, 1986).

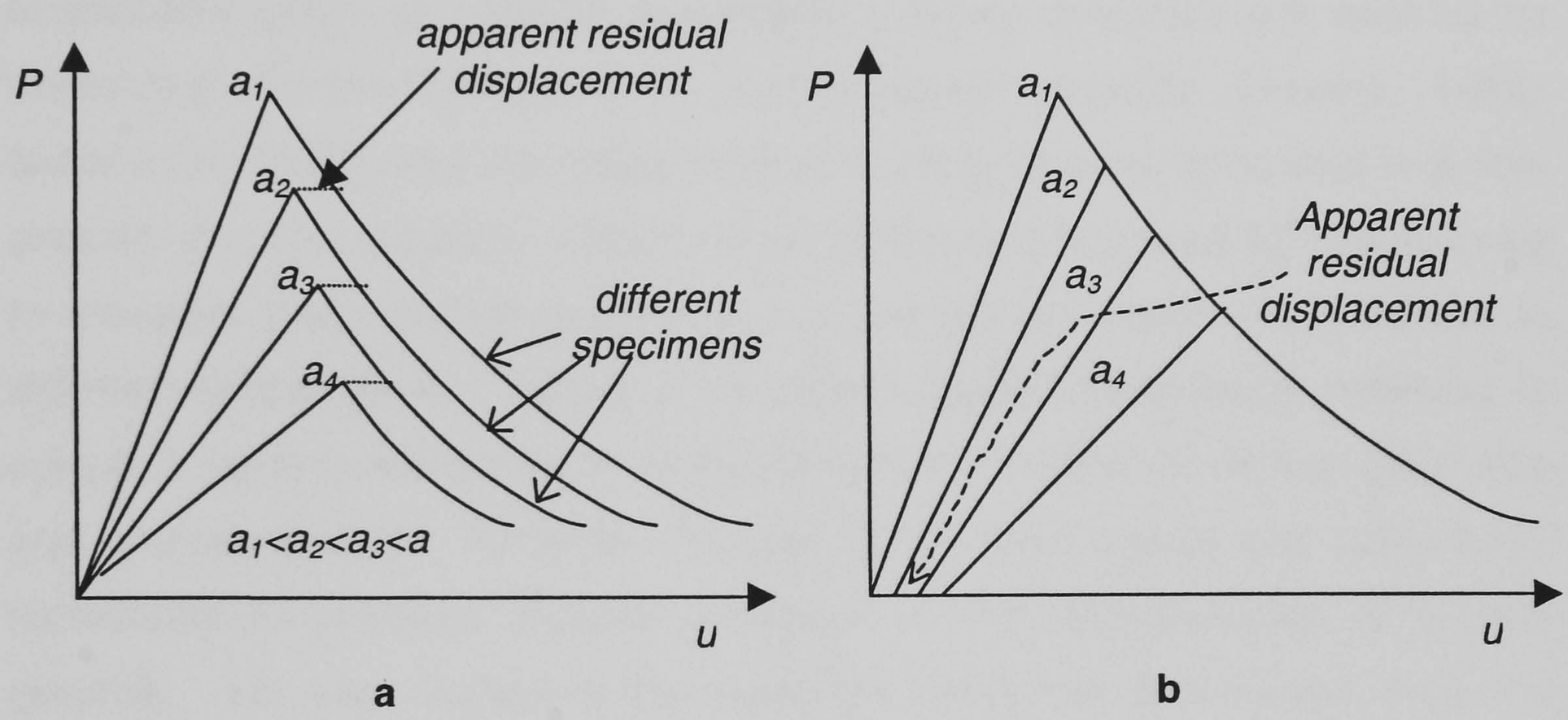

Figure 2.3.5. Schematic of the superposition method (Sakai & Bradt, 1986).

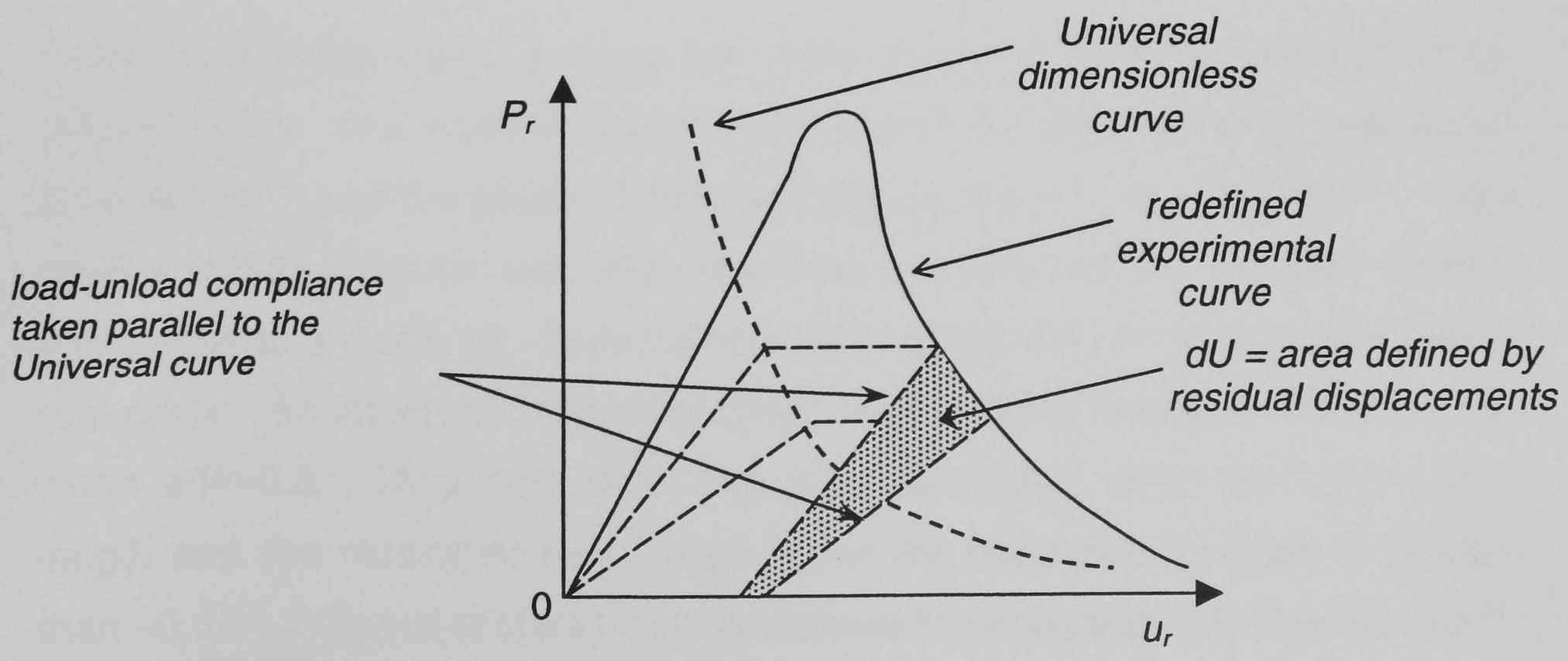

Figure 2.3.6. Schematic of the universal dimensionless load-displacement method; P_r, u_r = dimensionless load, displacement (Sakai & Bradt,1986).

Arulrajah (2002) found problems associated with fibre-bridging effects, which caused the potential drop method to underestimate the crack length in the chevron-notched bend specimens used in his study. Because C/C composites usually show extensive, rising *R*-curve behaviour, Arulrajah (2002) still managed to find differences between the materials that were qualitatively equivalent to differences revealed by other crack length measurement methods.

In polycrystalline graphite, both optical measurement and compliance methods have been used to measure crack length (Sakai et al 1988, Allard et al 1991, Ahlborn et al 1993, Ouagne 2000). The potential drop method has been given little consideration. One study used the potential drop method on an unspecified grade of graphite to validate a newly designed test method for measuring *R*-curve behaviour in coarse-grained ceramics (Browne, 1989). Sakai et al (1988) used the optical method to study *R*-curve behaviour in a fine-grained, isotropic graphite. Ahlborn et al (1993) used polarised light microscopy to measure crack growth resistance in a fine-grained carbon heat treated to different temperatures. Allard et al (1991) applied compliance methods to compare fracture resistance in anthracite-based carbons of varying grain size and graphite content. Recently, Ouagne (2000) used optical and compliance techniques to compare *R*-curve behaviour in two coarse-grades of nuclear graphite. He also compared the materials using the load-unload, and, the universal dimensionless methods.

Sakai et al (1988) found a steep rise in the K_R-curve following crack initiation (Figure 2.3.7). The initiation toughness ($K_{c,init}$) of the IG-11 graphite was about 0.74 MPam$^{1/2}$, and the plateau toughness ($K_{R,plat}$) about 1.1-1.2 MPam$^{1/2}$. They used a stiff load frame, and, sharpened the notch tips of the compact tension specimens to a depth of ~1mm using a razor sharp disc in order to simulate a real crack. An important feature of Sakai et al's (1988) results is the fall in K_R when $a/W \approx 0.6$. They also show that $K_{c,init}$ calculated using the initial notch length and the maximum load, drops when the initial notch length is greater than ~0.6W. Sakai et al (1988) also compared the energy-based *R*-curve (Jm^{-2}) derived by Irwin's similarity principle and by the dimensionless load-displacement technique. Using the similarity rule, they obtained $R_{plat} \approx 150$ Jm^{-2}. However, by graphical methods they obtained $R_{plat} \approx 220$ Jm^{-2}.

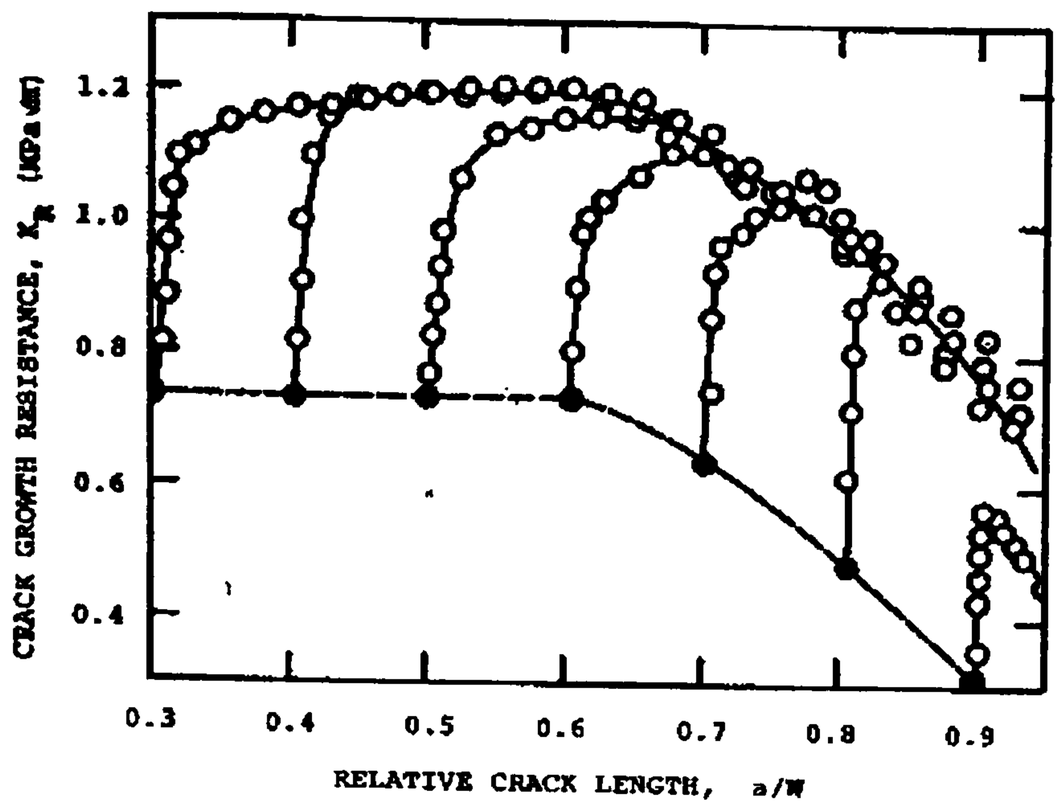

Figure 2.3.7. K_R-curve of IG-11 graphite: compact tension specimens with different, initial notch lengths (Sakai et al, 1988).

Sakai et al (1988) stress that this discrepancy highlights the need to compare materials in terms of the *R*-curve rather than the K_R-curve as the former accounts for non-linear energy consumption during the fracture process.

Using TCB (tapered cantilever beam) specimens, Ahlborn et al (1993) examined the change in crack growth resistance of a fine-grained (~5μm) carbon with increasing heat treatment temperature. They notched samples with a 0.1mm thick blade. Their work shows less clearly the initial rise in stress intensity factor but complies with Sakai's results in that both show a plateau in the K_R-curve, following the initial rise (Figure 2.3.8). In Ahlborn et al's (1993) case however, the K_R-curve does not fall but remains at the plateau level. Both studies indicate that the initial rise in fracture toughness is a short-range phenomenon occurring over a crack increment of about 1.0-2.0 mm only. For the fine-grain carbon heat treated at 2000 °C, they obtained $K_{c,init} \approx 1.15$ MPam$^{1/2}$ and $K_{R,plat} \approx 1.3$ MPam$^{1/2}$ (see Figure 2.3.8).

The investigation of Allard et al (1991) on anthracite-based carbons also shows an initial rise in the energy-based *R*-curve (Jm^{-2}) followed by a plateau region (Figure 2.3.9). In their case, the initial rise in fracture toughness was also not clearly resolved, due to the poor resolution of the compliance method to small changes in the initial compliance. Unlike Sakai et al (1988), and, Ahlborn et al (1993), the *R*-curves of Allard et al (1991) show a steep rise in *R* towards the end of the crack extension range. The reason for this difference is not clear.

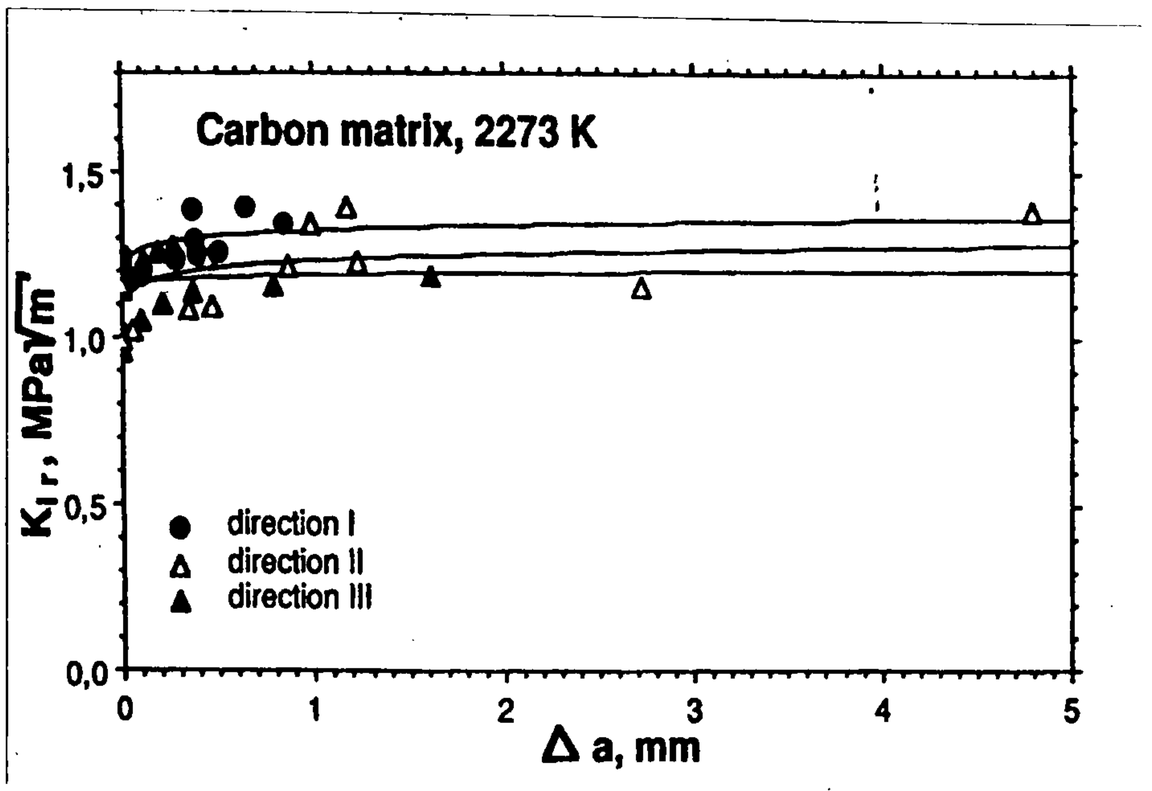

Figure 2.3.8. K_R-curve of fine grain carbon (Ahlborn et al, 1993).

Ouagne (2000) is of the opinion that this may be related to the use of compact tension specimens by Sakai et al (1988) and 3-point bend specimens by Allard et al (1991). He views the bend specimen as having a more extensive back end surface along which the frontal process zone is able to expand, compared to compact tension specimens where the back end surface is smaller.

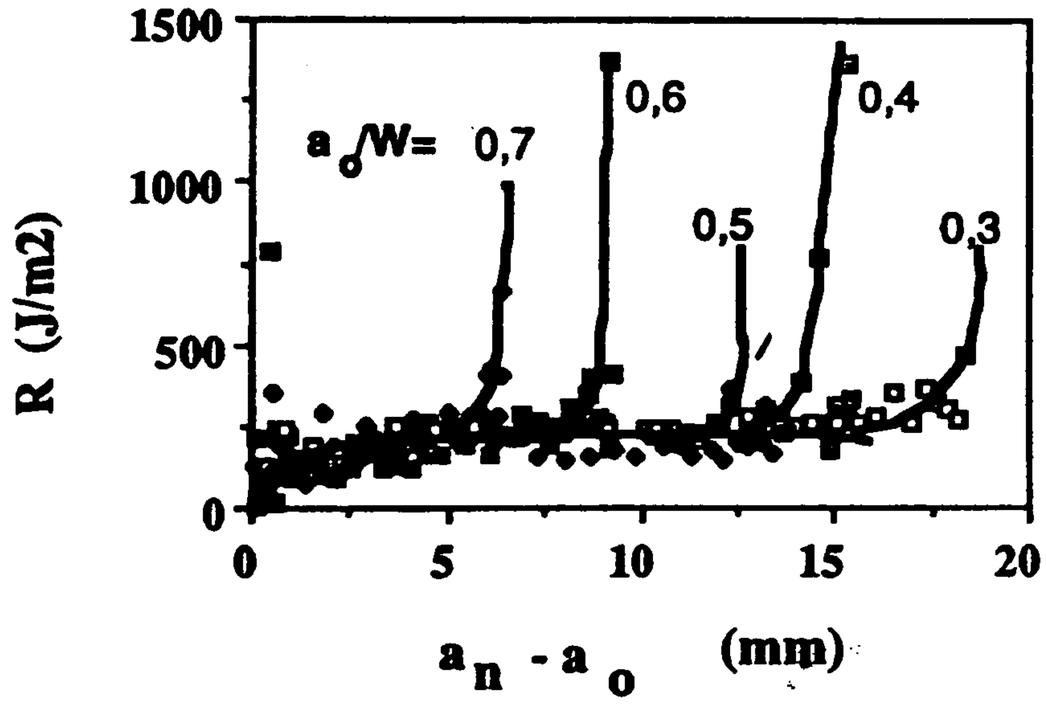

Figure 2.3.9. *R*-curve behaviour of anthracite-based carbon, showing the effect of initial notch length on the profile of the curve (Allard et al, 1991).

Ouagne's study (2000) compares the K_R-curve and *R*-curve behaviour of two moderator graphites, a Gilsocoke graphite and a needle-coke graphite. The *R*-curves obtained by Ouagne (2000) using the load-unload method and the universal dimensionless technique were somewhat anomalous. They show a very sharp rise in R (Jm^{-2}) followed by as rapid a drop in R and a levelling off at a low value. Ouagne (2000) cites various reasons for this anomaly, one being the use of a compliance calibration method that simulates crack length by saw-cutting specimens, which ignored the effects of bridging on the specimen compliance.

Using the optical method, Ouagne (2000) found an initial rise in the *R*-curve of both nuclear graphites. This was followed by a plateau region and a falling behaviour towards the end of the crack extension range, at ~0.7*a/W*. However, in contrast to the *R*-curves, the K_R-curves obtained by Ouagne (2000) show a rise in K_R at $a/W \approx 0.7$ (see Figure 2.3.10). He re-emphasises the view that the stress intensity derived K_R-curve is really descriptive of an ideally elastic material, whereas the energy-based *R*-curve accounts for both the elastic and plastic deformation that graphite undergoes as an elasto-plastic material. For Gilsocarbon graphite, Ouagne (2000) obtained $K_{R,plat} \approx 1.7\text{-}2.0$ MPam$^{1/2}$ and $R_{plat} \approx 200–300$ Jm^{-2} using compact tension specimens.

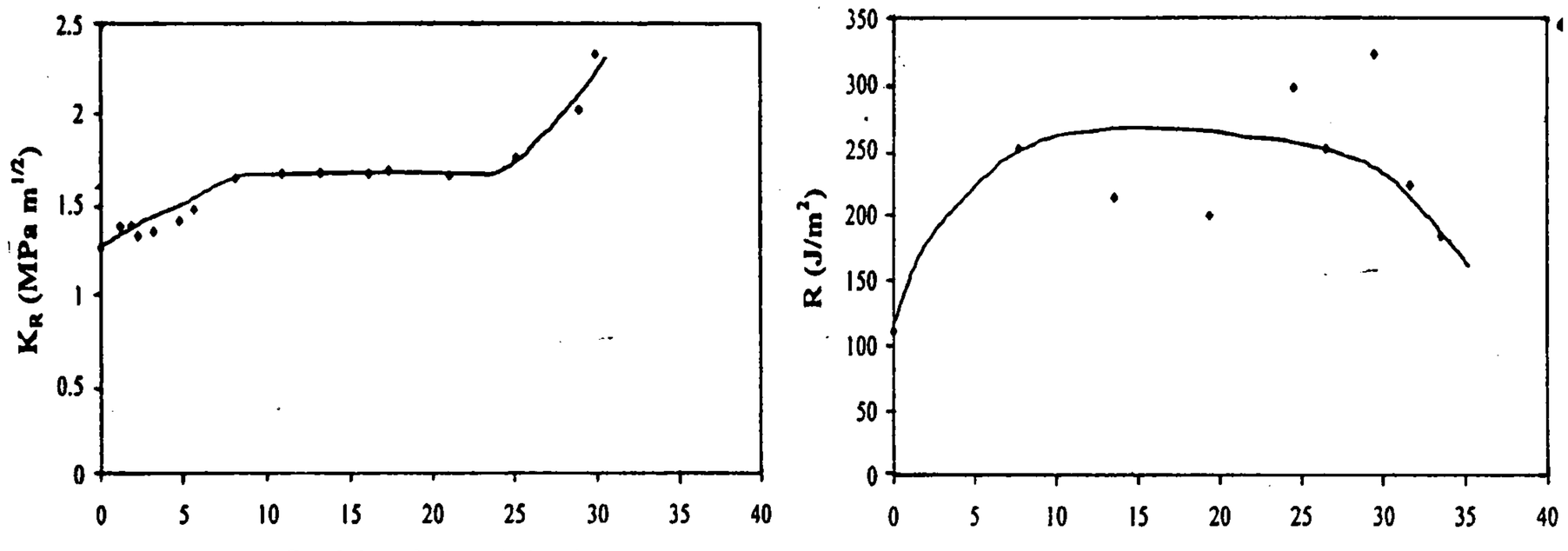

Figure 2.3.10. K_R-curve and *R*-curve profiles for Gilsocarbon (Ouagne, 2000).

Using an unspecified graphite to validate a newly developed test method (Browne and Chandler, 1987), Browne (1989) found a rising K_R-curve for the graphite. With this test method, K_R rose above 2.0 MPam$^{1/2}$ after the crack had extended more than 20mm (Figure 2.3.11). The crack length was estimated by a potential drop method using a calibration curve obtained by saw-cutting.

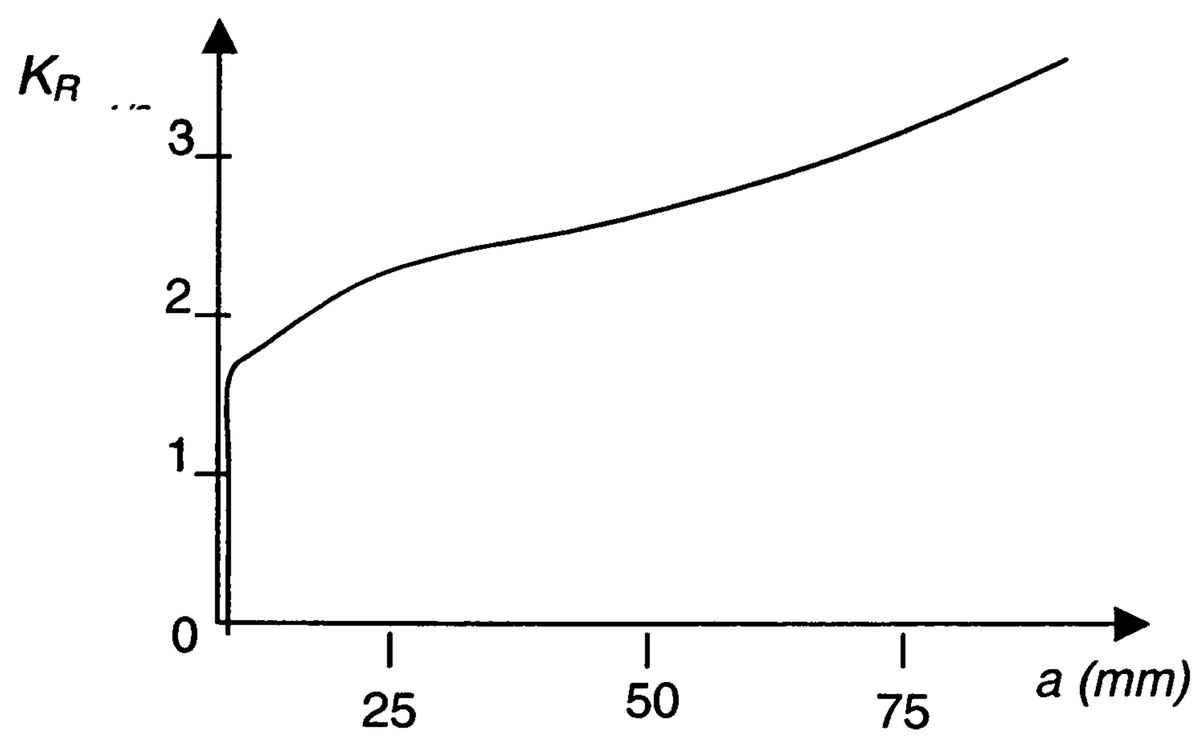

Figure 2.3.11. *R*-curve profile for graphite according to Browne (1989).

However, the method is unsuited to measuring the initial rising part of the *R*-curve, but has the advantage that very large specimens are used, offering an extensive crack growth ligament (>100mm). Over this extensive ligament, Browne (1989) found a continuous rise in K_R for the graphite.

These studies indicate that a variation in *R*-curve behaviour has been reported for polycrystalline graphite. The test method also influences the R-curve profile. This raises the need to understand better the test parameters and material characteristics that influence the *R*-curve profile.

2.3.5. Toughening Mechanisms in Relation to *R*-curve Behaviour

There has been considerable investigation into the mechanisms, which contribute to crack growth resistance. Different mechanisms have been forwarded to explain rising *R*-curve behaviour. The primary toughening mechanism is thought to comprise the development and growth of a frontal, micro-cracked process zone and a bridging zone in the following wake of the crack. These concepts are reviewed in detail in the sections that follow.

2.3.5.1. Development of the Process Zone and Bridging Zone

Initially, the toughening behaviour displayed by many ceramics and other brittle materials was thought to originate mainly from the development of a micro-cracked frontal process zone. This frontal process zone lowered the effective modulus of the material around the crack tip, shielding it from the applied stress. Fracture surface energy was consumed in the generation of this process zone with the toughness increasing for larger process zone sizes. This mechanism accounts for the toughness observed in transformation toughening ceramics. However, efforts to identify micro-crack regions of sufficient scale and density to account for the extent of toughening observed have not really succeeded (Grimes et al, 1990).

Although micro-crack formation in the process zone and the wake is responsible for toughening, it is now a more commonly held view that grain bridging and frictional interaction in the wake is the primary mechanism responsible for *R*-curve behaviour. Strong evidence for this is provided by re-notching experiments.

A dramatic reduction in the stress intensity factor occurs, or, the energy required to propagate the crack is reduced, when a sharp propagating crack is blunted by machining a notch in place of the existing crack. The reduction in toughness after re-notching provides a clear indication of the toughening contribution from crack face bridging, as many workers have shown (Sakai et al 1988, Evans & Faber 1984, Ouagne 2000).

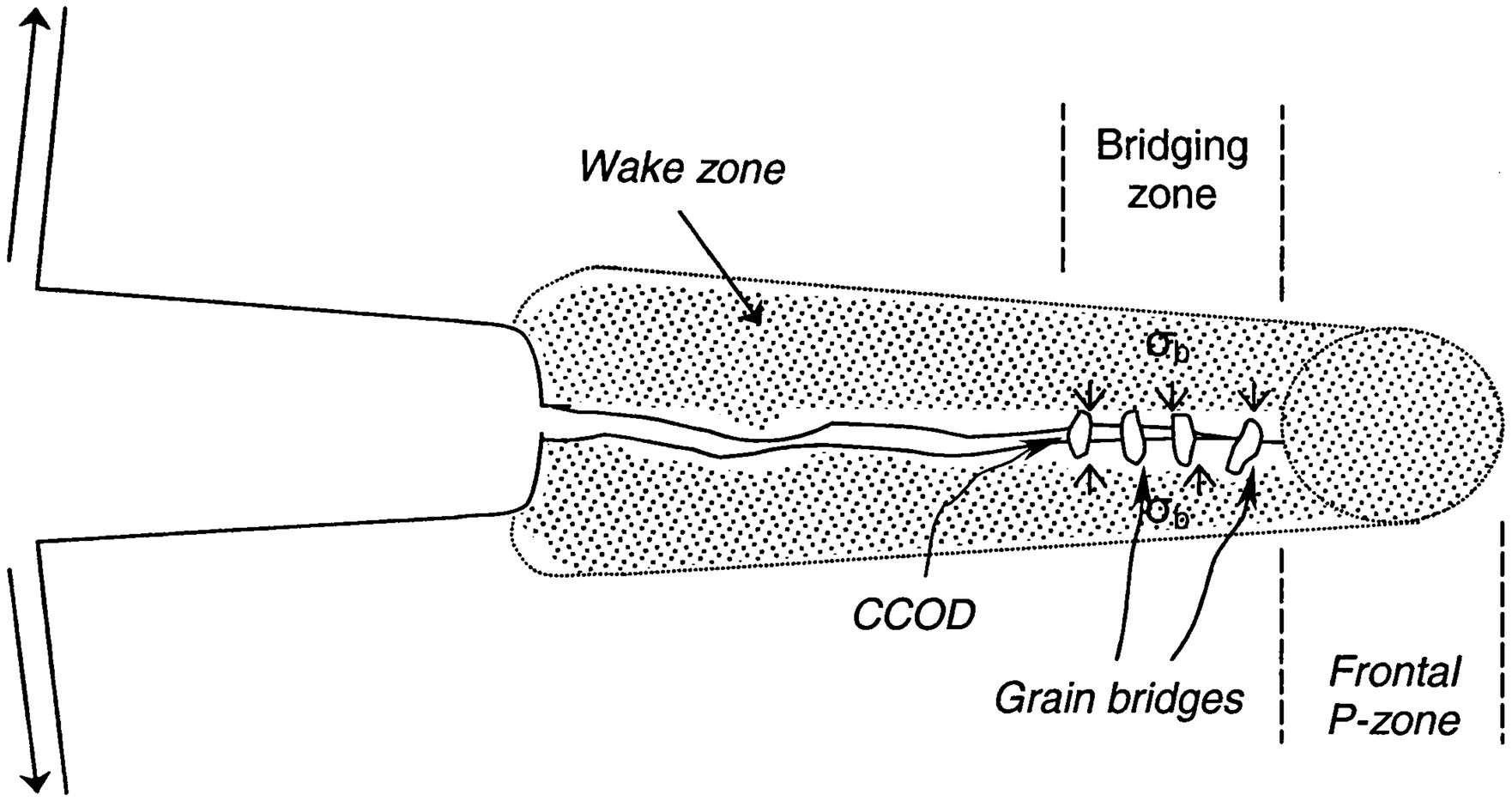

Figure 2.3.12. Schematic view of the frontal process zone and bridging zone.

The location, and relative proportions, of the process zone and its following wake, as well as the relative interactions between these regions, are shown schematically in Figure 2.3.12. Also indicated in the figure are the perceived bridging stresses behind the crack tip due to grain bridging and interlocking traction. The process zone includes both the frontal process zone and the wake region. It is said to contain extensive microcracks. The process zone may also contain material that has undergone phase transformation. The concept of a critical crack opening displacement (CCOD) is also illustrated in Figure 2.3.12. This is sometimes related to microstructural constituents, e.g. the filler grains (Sakai et al, 1988).

The initial rise in the *R*-curve, or, the increase in fracture energy demand, has generally been considered to be due to the onset of microcracking. The development of the process zone is associated with microcracking and the rise in toughness has been attributed to the growth of the process zone and development of the macrocrack. However, some bridging effects are also thought to contribute to this early rise in toughness (Allard et al, 1991).

In the second stage of the *R*-curve, i.e. the plateau region, the crack is said to propagate in a steady-state. At this juncture, the process zone is said to have reached a critical size and does not grow larger. Instead, its size remains constant and it moves forward, increasing in proportion relative to the steady-state propagation of the crack. The final stage of the *R*-curve is also said to reflect the interaction between the process zone and the specimen backend.

Allard et al (1991) reported a rising *R*-curve profile in coarse-grained anthracite-based carbons. They indicate that the rise in *R*-curve may be due to a lateral extension of the process zone along the back surface of the specimen, which consumes more energy (Figure 2.3.13) and causes the *R*-curve to rise. Crack branching also consumes energy in this final stage. It is not clear however, how this idea can be reconciled with a fall in the latter part of the *R*-curve that is sometimes reported.

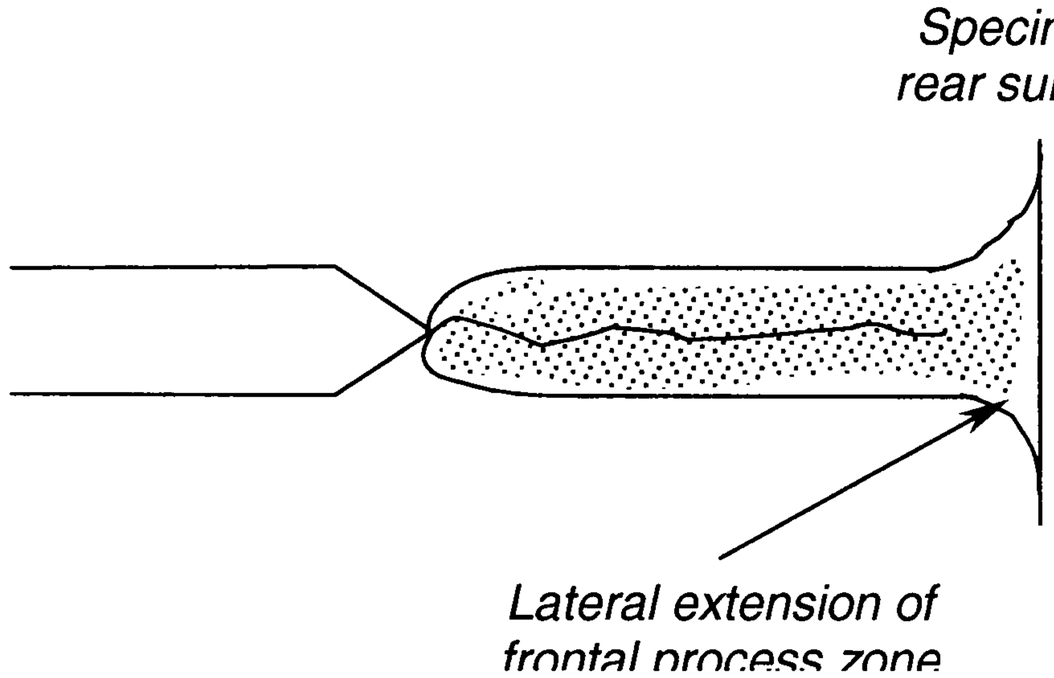

Figure 2.3.13. Interaction between process zone and backend (Allard et al, 1991).

In some ceramics such as $Zr0_2$, rising *R*-curve behaviour stems from phase transformations within the frontal process zone. Transformation of graphite crystallites within the frontal process zone, i.e. hexagonal to rhombohedral transformation, may also be likely (Sakai et al, 1988). The contribution from transformation toughening is found to exceed microcrack toughening (Evans & Faber, 1984). In polycrystalline graphite, studies indicate that fracture is accompanied by extensive micro-cracking and irreversible slip deformation along the basal planes of graphite crystallites. Sakai et al (1988) view pre-existing micro-cracks, i.e. Mrozowsky cracks, as likely sites for the development of a large-scale process zone.

Sakai et al (1988) used in-situ SEM on mini-CTS specimens (25x20x10mm) that were screw-loaded to study grain bridging and microcracking in a fine grain graphite (average grain size~15μm). They found that microcracks (1-20μm long) were generated in region ahead of the 'sharpened' notch tip, at ~60% of the failure load. During fracture, some of the microcracks combined to form longer cracks. Cracks nearer the centre-line of the notch tip tended to join the main crack as fracture progressed. By observing these microcracks as fracture progressed, Sakai et al (1988) showed that partial closure of these cracks occurred as the crack tip advanced. The cracks are transformed from elements in the process zone to elements in the wake region. They concluded that a finite amount of residual strain is generated in the wake region. However, estimates of the contribution from such residual strain could only account for less than 40% of the total increment in toughness that was observed.

Sakai et al (1988) therefore attributed the main toughening mechanism in the fine-grained graphite to grain bridging. Further proof of this was provided by re-notching. Re-notching only removed the bridging zone and not the wake region containing these partially closed cracks, due to the thinness of the blade used for re-notching. The drop in fracture toughness to its initial low value following re-notching therefore indicated a weak contribution by any compressive residual strain effects on the overall toughening.

Knehans and Steinbrech (1982) also showed that there is a large discrepancy between the measured toughness values for a sharp propagating crack and a machined sharp notch. Freiman (1988) indicates that toughening due to microcracking alone will not usually promote strengthening because micro-cracks can act as precursors to the formation of larger flaws. Grimes et al (1990) showed a marked difference in the load at which, the specimen was unloaded for re-notching, and, the maximum load achieved with the re-notched specimen. The compliance of the re-notched specimen was also lower than the unloading compliance of the specimen before it was re-notched. Both factors provided evidence of toughening from the wake region, not the frontal process zone.

Recently, Li et al (1999) evaluated the toughening contribution of grain bridging/interlocking. They pre-cracked notched specimens to obtain specimens with an active crack-face contact region, since pre-cracking leaves an active contact face region behind the crack tip. The stress-intensity needed to drive the pre-crack should then be larger than that for an as-notched specimen given the absence of the toughening zone in the as-notched sample. They obtained an increase in K_{IC} of ~0.42 MPa $m^{1/2}$ for pre-cracked specimens.

Sakai & Kurita (1995) state that micro-deformation mechanisms and fracture processes in the process zone, e.g. dislocation movement, twinning, micro-cracking, etc, shield the crack tip from the far-field applied stresses reducing them to a finite level. Evans & Faber (1984) state the process zone and wake region both contribute to crack tip shielding, reducing the crack tip stress intensity. The lower modulus of the process zone assists in toughening.

2.3.5.2. Microstructure and Grain Size Effects on Toughening Behaviour

Ahlborn et al (1993) agree that the dominant toughening process is bridging, as noted from the need to apply some force to separate specimens even when the crack has traversed the entire specimen width. On a microscopic level, crack extension occurs when the fracture surface energy is exceeded at the crack tip. This depends on the strength of atomic bonds ahead of the crack tip. Covalent bonding within the basal plane offers more resistance than the weak Van der Waal's forces between these layers so that the crack growth resistance parallel to the graphite extrusion direction is lower than that perpendicular to it.

Ebrahimi et al (2000) report a strong influence of grain size on the crack growth resistance of alumina ceramics. Their study showed that the crack initiation toughness, which is independent of grain bridging effects, for alumina materials of varying grain size (2, 5, and, 13 μm) was higher in the coarse grained materials. They also noted that the increase in the crack growth resistance of the coarse-grained material was more marked towards the end of the fracture test, i.e. when the crack was several millimetres long, and, that the relative increase in the toughness (ΔK_R) with crack extension was much higher in the coarse-grained alumina. Both these effects were said to be direct effects of grain bridging which is enhanced in the coarser material.

Tandon & Faber (1998) found that loading rate influenced the steady-state fracture toughness in coarse-grained alumina ceramic (18μm) but has little influence on fine-grain material (7μm). An increase in loading rate caused the steady-state fracture toughness ($K_{R,plat}$) to drop but did not affect the initial fracture toughness ($K_{c,init}$). They observed that loading rate affected the development of the bridges within the bridging zone. Intergranular fracture occurred at slow loading rates in the coarse-grained material. At higher rates, mixed-mode fracture occurred and the bridging effect was reduced.

Tandon & Faber (1998) are of the opinion that intergranular fracture is a prerequisite for grain bridging. They state that toughening from bridging grains occurs as a combination of two events, de-bonding of the grains followed by pullout of these grains. The effective toughening contribution from bridging grains is reduced by transgranular fracture since a smaller crack opening displacement (COD) is required for transgranular fracture compared to when a bridging grain is debonded and pulled-out without fracturing.

Reichl and Steinbrech (1988) explain that the size of the interaction zone in the wake is generally considered to be due to the roughness of the crack surfaces and the development of the crack opening displacement (COD). They note that the COD is a function of the type of test and crack geometry. When the COD at a particular interaction site is larger than the crack surface roughness, which is related to the grain size of the material, bridging is no longer possible. This limiting value in the COD, commonly referred to as the CCOD, defines the end of the bridging zone and hence the bridging interactions in the wake (See Figure 2.3.12).

Grimes et al (1990) add that the critical component governing the bridging traction is not the crack length, but, the local COD instead. They state that the dependence of a grain bridging-toughening mechanism on a characteristic microstructural feature, e.g. grain size, and, the COD is to be expected. They explain that a small COD, relative to a coarse grain size gives a rising *R*-curve.

Allard et al (1991) found the crack growth resistance of anthracite-based carbon to increase with increasing proportions of graphite, mainly because the

anthracite grains were easily traversed by the growing crack whilst graphite grains deflected the crack. They observed that the path taken by cracks that were obstructed by the anthracite grains depended on the size and orientation of these grains. Shorter grains were easily bypassed but longer grains were fractured. Sakai (1988) cites the importance of grain size and aspect ratio in refractories, stating that bridging traction is extended along the crack surface at higher aspect ratios.

Allard et al (1991) regarded the nature of the filler-binder interface to also be relevant, since the graphite-pitch interface was considered to be stronger than the anthracite-pitch interface. They also noted that porosity played a dual role of either stopping cracks or assisting their growth. Due to the variability in pore shape and size it was difficult to generalise the role of porosity.

Freiman (1988) lists crack deflection as one of the simpler toughening mechanisms in polycrystalline ceramics. Misorientation of the easy fracture paths at each grain along the crack front encourages crack deflection. The roughness of the fracture surface thus becomes a function of the degree of deflection produced by the microstructure. In materials where crack deflection is the primary mechanism, toughness increases up to 40% have been observed, independent of the grain size of the material. Freiman (1988) describes a model which predicts the toughening due to crack deflection around second phase particles, showing that elongated particles make a stronger contribution than equiaxed grains. However, the model failed to predict the high toughness of many polycrystalline ceramics, possibly due to its inability to account for the bridging effects.

Sakai and Bradt (1993) mention that it is only recently acknowledged that processes behind the crack tip also promote shielding. Importantly, they hold that crack deflection and other crack meandering processes by fibres, or, grains are not the main cause of rising *R*-curve behaviour because these processes have a non-cumulative effect on the overall toughening process. Sakai and Bradt (1993) conclude that the mechanisms in the wake complicate the fracture behaviour of ceramics, raising many critical issues and obstacles in the characterisation of the fracture resistance of quasi-brittle materials.

SECTION 2.4: THE POTENTIAL DROP METHOD

The potential drop method provides one of the simpler means of monitoring crack growth in conductive materials. Developed for metals, it has found wide ranging application in both research and general materials testing, and, continuous monitoring of industrial plant and machinery. One of its attractions is the capability for unattended monitoring of structures and components over long duration. The method has been applied successfully in a variety of environments including vacuum, air, seawater, and, gaseous (Austen, 1980). Recently, the technique has been applied for monitoring pipework in nuclear power plant, reducing the need for conventional ultrasonic and radiographic techniques and the total exposure to radiation of personnel (Opperman, 1997).

2.4.1. Principle of the Potential Drop Method

A growing crack causes a reduction in the cross-sectional area of a conductive material, changing the potential field produced in the material by the current. Four contact points are normally used in materials testing applications (Figure 2.4.1).

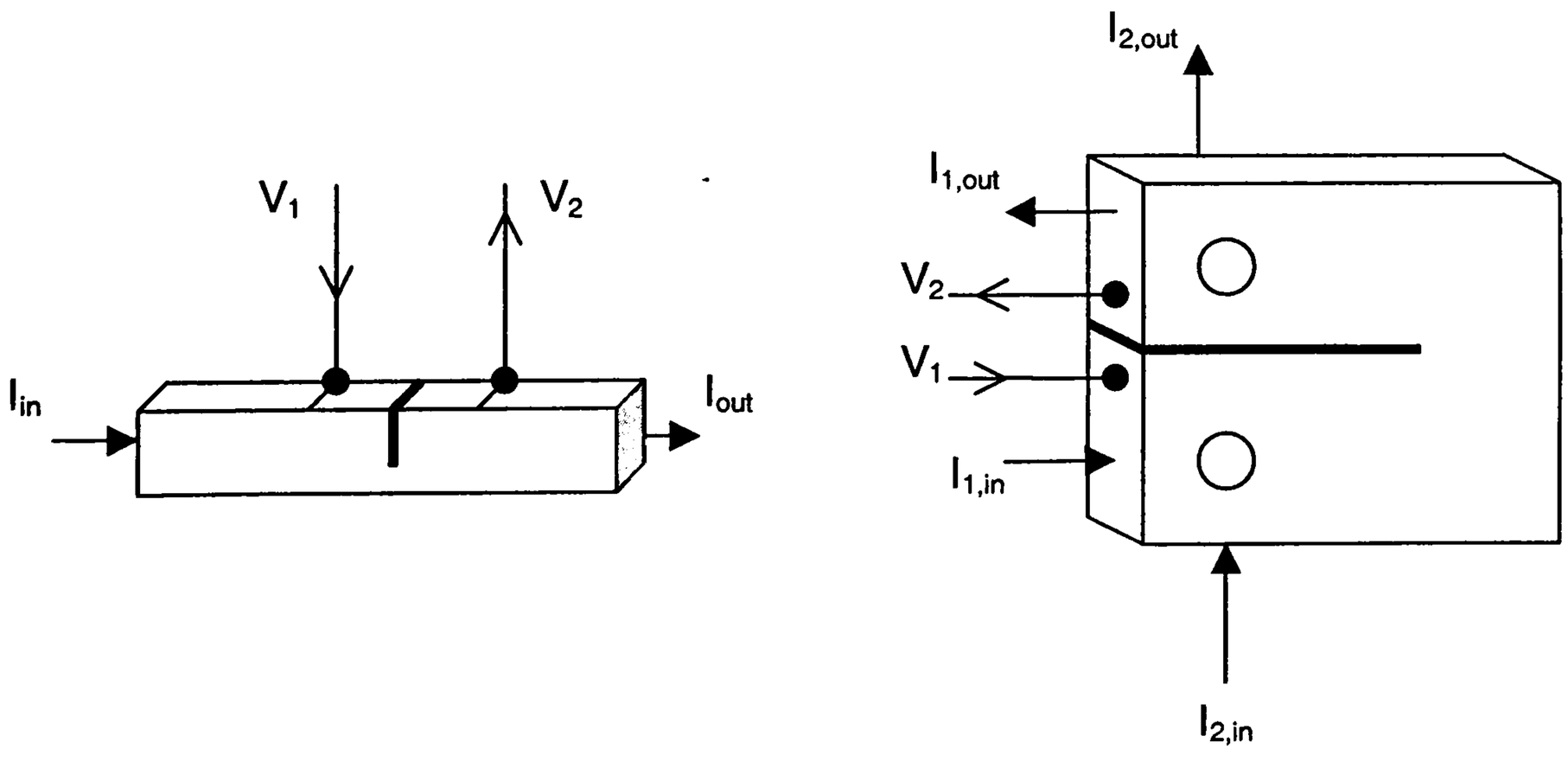

Figure 2.4.1. Typical current-voltage probe locations used in potential drop method.

Two leads supply current and two leads measure the potential across a section of the material. The potential field varies with conductor shape and is uniform or non-uniform depending on the current input-output points (Figure 2.4.2).

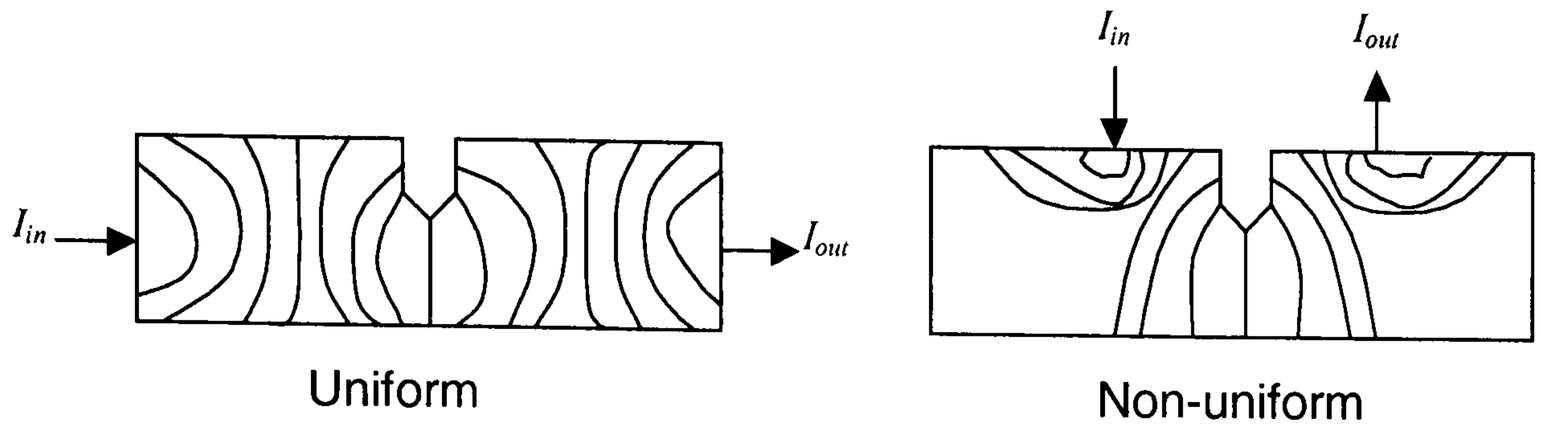

Figure 2.4.2. Uniform and non-uniform potential distributions (Knott, 1980).

A uniform current configuration cannot be obtained in the compact tension specimen. The presence of loading holes and a long, wide notch interferes with the uniform potential distribution that may otherwise prevail. Various current-lead positions therefore produce different calibrations. The basic procedure involves a measurement of the potential change across the portion of the material containing the crack and relating the potential change to the crack length using a calibration. Accuracy depends largely on the calibration used, which can be derived experimentally or theoretically.

2.4.2. Potential Drop Calibration Techniques

2.4.2.1 Experimental Calibration

Experimental or 'empirical' calibration is used when component geometry is complex, and, as an alternative to theoretical analyses. A calibration curve of the potential change with crack length of a dedicated specimen is required. The lead attachment points on the calibration specimen must mimic those on the test specimen. The calibration is made independent of variations in material resistivity and applied current by normalising the potential drop with respect to the initial potential across the cracked specimen (Wei & Brazill, 1980).

Druce and Booth (1980) state that a disadvantage of the empirical calibration is the reliance on an initial potential measurement that is used to normalise the potential change. This initial potential is usually small. Errors in this initial potential can thus magnify errors in the measured crack length, especially with longer cracks. This problem may be overcome by using a reference potential gradient, or, reduce the current probe distance which raises the absolute value of the potential obtained for a given crack length. However, the actual potential increase attainable is very small because there is a limit to the closeness of the current lead spacing imposed by the specimen dimensions (Knott, 1980).

2.4.2.2. Theoretical Calibration

Theoretical calibrations are based on mathematical models of the cracked specimen. Cracks are regarded as thin slits emerging from the plane (2-D) surface of a specimen that disrupt the uniform potential field. A common model is Johnson's (1965), which describes the potential field in a sheet of uniform thickness with a central, infinitesimally thin slit.

$$\frac{V(a)}{V(a_0)} = \frac{Cosh^{-1}\left(\frac{\cosh\frac{\pi y}{2W}}{\cos\frac{\pi a}{2W}}\right)}{Cosh^{-1}\left(\frac{\cosh\frac{\pi y}{2W}}{\cos\frac{\pi a_0}{2W}}\right)} \qquad [2.4.1]$$

a_0 = initial slit length; a = different slit length; W = specimen thickness
V = voltage between two points spaced a distance y either side of the slit

This is often adapted to the bend specimen configuration. A condition of Johnson's model is that the current density be uniform, and the voltage probes be located along the centreline crossing the crack plane (ASTM E647-91). For the compact tension geometry, Hicks-Pickard developed the following expression using finite element modelling (ASTM E647-91, Cho et al, 1996):

$$\frac{V}{V_0} = 0.5766 + 1.9169\left(\frac{a}{W}\right) - 1.0712\left(\frac{a}{W}\right)^2 + 1.6898\left(\frac{a}{W}\right)^3 \qquad [2.4.2]$$

This expression was verified using both analogue and experimental techniques. It is however applicable only for current input locations along the load line of the specimens and for relative crack length within the range $0.24 \leq a/W \leq 0.70$. Cho et al (1996) confirm the excellent correlation of the Hicks-Pickard solution when current probes are located along the load line of the compact tension specimen.

The attractiveness of the theoretical approach is its dependence on geometric variables and the probe positions only, being independent of material properties and applied current. However, solving for the crack length can require a fairly complex solution, as in Johnson's case. It is also limited in that actual specimens contain notches of finite width. The material is also assumed to be homogeneous, with a constant, gross cross-section of uniform electrical resistivity. Importantly, both theoretical and empirical calibrations are limited as they do not account for current or temperature fluctuations, changes in crack shape, and, crack face bridging (Druce & Booth, 1980).

2.4.3. Sensitivity and Reproducibility of the Method

An important aspect of the potential drop method concerns the positioning of the current leads and the potential leads, which both influence the sensitivity and reproducibility of the method. Sensitivity (S) may be defined as the change in output voltage for a 1% change in crack length (a_o) (Knott, 1980):

$$S = \frac{V(1.01a_0) - V(a_0)}{V(a_0)} \qquad [2.4.3]$$

High sensitivity is obtained with the current-leads near the crack plane as this produces the steepest potential gradient across the crack. However, the calibration is less reproducible when current probes are placed near the crack plane. A uniform potential distribution improves reproducibility (see Figure 2.4.2). Knott (1980) also showed mathematically that variations in probe positions up to $0.1a_0$ have less than 1% effect on the sensitivity (S) making slight errors in probe positioning and effects due to probe wire thickness less significant. The sensitivity also increases as the notch sharpness increases, i.e. ellipticity decreases in curved notches, or, the angle becomes more acute in the case of V-notches.

2.4.4. Problems with Crack Face Contact or Bridging Effects

A specific problem with the PD method is the underestimation caused by crack face contact or bridging. This limits the usefulness of both theoretical and experimental calibrations. The common method of controlled-sectioning (saw-cutting) of the sample to simulate the growing crack becomes dubious when it is applied to narrow cracks where crack face contact is likely. A preferred method is to grow the crack by fatigue and measure the crack length optically. However, optical measurements may not account for curvature in the crack front. The ASTM Standard E647-91 advises using other methods to validate the crack length measured by the PD method. If the alternative method cannot be used while testing, it recommends measuring the initial and final crack sizes after testing. The PD method is thus more likely to underestimate the average crack length. Crack face touching would therefore cause an underestimation in the crack length measured by PD. This would be enhanced in coarse microstructures in which crack face irregularity is greater, as well as, environments that promote good electrical contact, e.g. vacuum.

Freeman & Neate (1980) advise that calibrations may be used with reasonable confidence in the absence of bridging effects, provided that the initial voltage of the notched sample that is used in calculations, is the voltage recorded at the start of crack initiation. If bridging does occur, the measured potential can be markedly reduced. Bridging is more likely in low ductility materials where crack tip opening displacements are small and the probability of crack face contact is higher. Factors that reduce the crack tip displacement also promote bridging, e.g. the applied load, the specimen geometry, and, the initial notch length. Halliday & Beevers (1980) state that crack face contact and crack extension can occur simultaneously in some materials under certain conditions such that, a conducting path is always present behind the crack front. It may be possible to account for this error if this underestimation is of a reproducible nature.

Some contention remains about the application of the method for monitoring crack growth in ductile materials with high crack growth resistance. Curry & Milne (1980) highlight conflicting reports about the use of the PD method in ductile materials. They state that the method is unable to resolve the contribution to the specimens resistance from different failure mechanisms, in particular, plastic effects at the crack front. Successful reports involve measurements in metallic materials with shallow *R*-curves, i.e. low work-hardening capacity. Okumura et al (1989) add that the method is successful when crack tip plasticity is small. In metallic materials with steeply rising *R*-curves, the method has been less successful. They add that the method must distinguish between increasing plasticity, and, crack extension to be applicable. Recently, Grabulov (1999) claimed success in measuring both static and dynamic *J-R* curves in high-strength steels. probably because these are not significantly ductile materials.

2.4.5. Application of the Potential Drop Method in Ceramic Materials

The application of the PD technique in ceramic materials appears to be very limited, probably due to their poor conductance. Few attempts have been made to apply the method to ceramics. Stalder et al (1983) devised a method for application to plastics and ceramics which entailed spraying a graphite suspension over the specimen surface to form a rectangular shaped area coated by a thin (~5μm), conductive layer in the crack extension region.

The coated region is then connected on either side by silver ink electrodes which allow the resistance change of the layer to be measured as the crack extends. Stalder et al (1983) found the method correlated well with optical measurements to within ~1%. Interestingly, it was noted that graphite particles in the sprayed suspension caused bridging behind the crack tip if the particles were larger than the local COD. Kobayashi et al (1983) also developed an externally mounted 'crack gauge' for measuring crack length in alumina specimens. Browne (1989) used a DC potential drop method to verify a newly developed test method for measuring *R*-curve behaviour in coarse-grained ceramics. Using graphite as the control material, Browne (1989) showed that the crack length measurements made by PD measurements using an experimental calibration (saw-cut) approach and that measured optically, were in excellent agreement.

2.4.6. Some Considerations in using the Potential Drop Method

Two instrumental variants of the PD method are available, the DCPD (direct current) and ACPD (alternating current) methods. The DCPD method relies on the change in material resistance with crack growth while the ACPD method usually measures the impedance change of the material. Both methods are similar in principle except that a higher current is needed in the DCPD method. In metallic specimens, the ACPD method has the advantage that a 'skin effect' occurs with the current flowing in the surface regions of the specimen. Therefore, the DCPD method requires higher input current (10-100 A) compared to ACPD (~0.1-1A). However, this effect really only resides at high AC frequencies and is stronger in magnetic materials (Wei & Brazill, 1980).

Equipment should be capable of measuring potential ranging from a few microvolts to several volts. Wojcik (1995) cautions that the voltage drop generated across highly conductive materials using allowable current levels is very small, of the order of microvolts. One therefore requires instrumentation capable of measuring in the nanovolt range. Electrical noise from equipment can be of the same order of magnitude as the output signal. The PD method can be used to detect crack initiation, however, this depends on how discontinuous the event is. Cleavage or shear cause sudden increases in resistance and should therefore be easily detectable (Knott, 1980).

CHAPTER 3

AIMS & OBJECTIVES

The *R*-curve concept and its application in characterising the toughening mechanisms that contribute to crack growth resistance in carbon materials was discussed in detail in the previous chapter. It was also explained that a limited number of studies on *R*-curve behaviour in polycrystalline graphite have been carried out. The review in Section 2.3 explained the influence of microstructural characteristics, with the grain size being a most influential factor controlling the *R*-curve behaviour of ceramic materials.

This review also highlighted the significant variation in the *R*-curve behaviour of carbon materials that has been reported and the apparent reasons for these variations. One important variable that influences the *R*-curve profile is the method of crack length measurement that is employed such that different methodologies can produce marked differences in the *R*-curve profile. The mechanisms that are thought to contribute to *R*-curve behaviour were also described in detail. This study therefore attempts to improve the current understanding of *R*-curve behaviour in polycrystalline, nuclear graphites by:

1. Comparing the *R*-curve behaviour of nuclear graphites with different structural characteristics, one difference being average grain size.
2. Relating differences in the *R*-curve behaviour of these nuclear graphites to structural differences to obtain a better understanding of the crack growth resistance mechanisms in polycrystalline graphite.
3. Applying different methodologies and test configurations to assess the *R*-curve behaviour of the nuclear graphites, and comparing the effectiveness of these methods.
4. Placing a specific emphasis on using the potential drop technique to measure and compare the *R*-curve behaviour of these materials. This method of crack length measurement has not been widely applied for *R*-curve assessment in graphite, and, ceramics in general.
5. Evaluating the *R*-curve behaviour of oxidised nuclear graphite in relation to the microstructural degradation caused by oxidation. This is an aspect of particular concern in gas-cooled graphite moderated reactors.

It is also the aim of this study to investigate the usefulness of the nano-indentation technique for measuring the elastic modulus of the nuclear graphites before and after oxidation. A potential advantage of the method over conventional methods used to determine the elastic modulus is the small size of test specimens. This might afford a unique advantage for determining the elastic modulus change in reactor graphite due to irradiation and oxidation.

3.1. Materials Selection

In meeting the aims of the study, four nuclear graphites were selected. The materials and their main characteristics are outlined below:

1. PGA graphite

   A coarse grained, needle-coke graphite formed by extrusion (average grain size≈1mm). It is in use in some British AGR's.

2. Gilsocarbon graphite (grade IM1-24)

   A coarse-grained, Gilsocoke graphite in which the filler grains are spherically shaped (average grain size≈0.5mm). The spherical grains coupled with a moulding process lend it near-isotropic properties. This graphite is mainly used in modern British AGR's.

3. IG110 graphite

   A fine-grained, isotropic graphite formed by isostatic pressing (average grain size≈20μm). It is one of the nuclear grades on test as part of the development of the Japanese HTR (High Temperature Reactor) by JAERI (Japanese Atomic Energy Research Institute).

4. UcarC graphite (grade PMX123)

   This extruded fuel-sleeve graphite is made from coal-tar pitch coke and coal tar pitch binder. It has an average grain size of ~0.22mm with a maximum grain size of ~0.8mm. It is impregnated during fabrication.

All four materials are of commercial importance and provide a wide range in nuclear graphite properties. Grades 3 and 4 have been earmarked as candidate materials for the South African PBMR. The *R*-curve behaviour of the PGA grade was not assessed since a small quantity of material was available for test purposes.

CHAPTER 4

CHARACTERISATION OF THE NUCLEAR GRAPHITES

The four grades of nuclear graphite materials selected for this study were described briefly in the previous chapter. It was pointed out that the selection of materials covers a wide range of typical nuclear graphite structure-property combinations. It was necessary for the purposes of this study to characterise these materials to obtain a baseline of their structure and properties from which to compare these materials. The starting point for characterising and comparing the different materials was their microstructural characteristics.

SECTION 4.1: MICROSTRUCTURAL CHARACTERISATION

4.1.1. Preparation of Specimens

As indicated by Nightingale (1962), careful polishing of polycrystalline graphite is necessary given the fragility of the porous, brittle graphite structure. Normal metallographic techniques tend to damage the surface of the material. This is avoided by resin impregnation of the specimens, which helps to strengthen the graphite structure, making surface preparation easier and more meaningful.

Samples of each graphite were mounted for surface preparation in plastic moulds (diameter=25mm, height=20mm) using Struers Epofix resin. The samples are placed upside down in the mould such that, the bottom surface remains exposed thereby forming the preparation surface. Impregnation of the samples was done simultaneously, by mounting the specimens under vacuum.

The sample and mould was placed in a dessicator and evacuated after which resin is introduced into the container through a tap in a glass funnel located on top of the dessicator lid. The resin is left to settle and penetrate well into the sample pores under vacuum. Thereafter, the vacuum is released through a tap in the vacuum line and the mould removed. The resin is allowed to harden overnight. The curing time of the resin may be shortened by heating the mounted sample in an oven at a moderate temperature.

Table 4.1. Procedure used to polish the mounted graphite samples.

Step No.	Grinding/Polishing Medium	Wheel Speed (rpm)	Pressure (lbs/sample)
1	wet grinding on p400 SiC	120	5
2	9μm diamond to smoothen surface	60	5
3	3μm alumina as a first polishing step	60	2.5
4	Finish using alumina Masterpolish	60	2.5

Note: Samples are cleaned ultrasonically in water after each step.

The impregnated samples were ground and polished using an automated Buehler Motopol polishing system. The procedure used to prepare the mounted samples is one that is generally applicable to all types of carbon materials, as outlined in Table 4.1. The polished specimens were examined using reflected light microscopy, polarised light microscopy, and, SEM.

Polarised light microscopy is routinely used to study the structure of graphite materials. The combination of polarised light and a tint plate helps to reveal anisotropy within filler particles and, the orientation of these particles in the graphite block. Both Nightingale (1962) and Edwards (1989) provide detailed explanations of the workings of polarised light microscopy.

The SEM is also routinely used to resolve structural features at much higher magnification than light microscopy, with the advantage of being able to view surface topography. To examine the graphite structures in detail, sections from fractured specimens of each material were also prepared for SEM using routine preparatory techniques.

4.1.2. Optical & Electron Microscopy

In discussing polarised light microscopy of the graphite structures, it is worth noting the significance of the different interference colours produced by the interaction of the polarised light with the graphite lamellae. Basal planes oriented perpendicular to the plane of polarisation, appear purple when the retarder plate is inserted into the optical path. Planes oriented at angles to the plane of polarisation appear blue or yellow, the two colours being indicative of

filler particles oriented at about 90° to each other (Edwards, 1989). Because the areas observed are much larger than the relatively perfect crystallites, small mis-orientations between crystallites are not resolved optically. Being non-textured, the resin filling the pores appears purple under the sensitive tint and does not change colour under the polarised light. Poorly aligned regions also show little colour change (Nightingale, 1962).

The microstructure of the four nuclear graphite materials are represented in **Figures 4.1– 4.4**. The reflected light micrographs, polarised light micrographs, and, SEM micrographs for each material are combined in each figure to allow for a better comparison.

The PGA graphite microstructure in reflected and polarised light is shown in **Figures 4.1a** and **4.1b** respectively. Large, needle-coke filler grains are clearly seen. In polarised light, the texture within the needle-coke grains is evident from the directional orientation of the interference colours within these grains. Grains oriented at 45° to the vertical axis (clockwise in the plane of the paper), appear blue and grains lying at 90° to these blue grains appear yellow. Grains lying at intermediate angles appear pink-purple. The anisotropy of the needle-coke grains is exemplified by the colour change of the large central grain. Due to its curvature, the colours change from yellow to blue, and vice versa, as the lamellae within this grain change orientation. Towards the centre of this curved grain, the colour is pinkish-purple, similar to those grains oriented at intermediate angles. Fine, longitudinal cracks, and pores, are also evident in the larger grains.

The SEM micrographs of the PGA graphite fracture surface reveals the appearance of the needle-coke grains more clearly, as in **Figure 4.1c**. The exact location of the binder phase or matrix is difficult to specify, whereas the large needle-coke grains are easily distinguishable. However, in **Figure 4.1c**, it may be that the binder phase can be distinguished from the larger filler particles as an agglomeration of smaller graphitized particles, with no particular texture, that supports the large filler grains. The highly textured needle-coke grains in the PGA graphite are highlighted in **Figure 4.1d**.

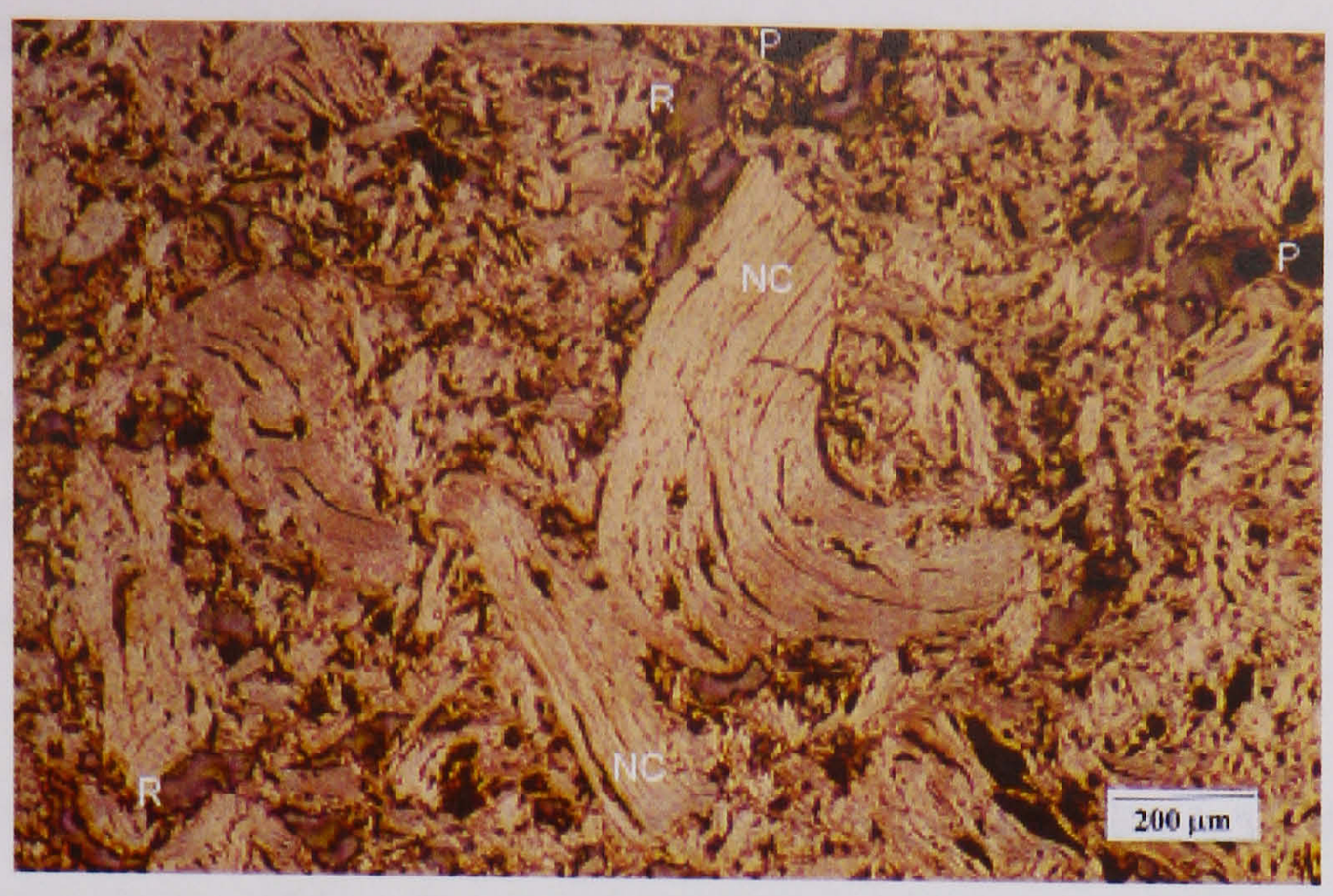

a

b

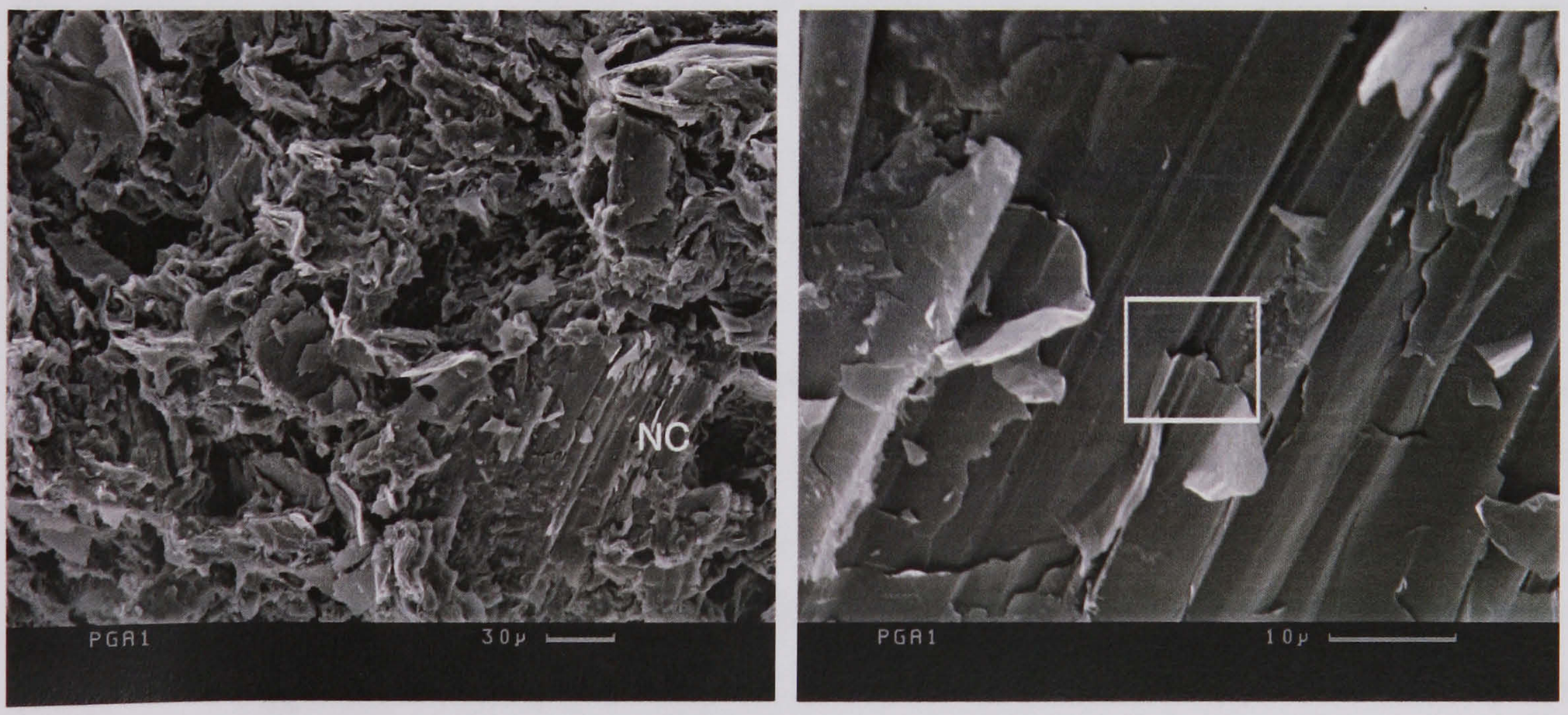

c d

Figure 4.1. Micrographs of PGA graphite: (a) reflected light; (b) polarised light (crossed polars, 1λ retarder plate); (c) SEM image showing the fine graphite flakes surrounding a large coke grain; (d) magnified view of the grain; NC = needle-coke grain, P = pore, R = resin.

The microstructure of Gilsocarbon graphite in reflected and polarised light is shown in **Figure 4.2a** and **Figure 4.2b** respectively. The Gilsocarbon graphite is comprised of large, spherical, Gilsocoke filler grains that exceed 1mm in diameter in some instances. Contained in the Gilsonite-coke grains are circumferential or lenticular cracks. In some grains, radial cracks are also apparent. Both the lenticular and radial cracks are narrow, opening quite widely towards their centre.

In the Gilsocarbon structure, the binder phase appears to be more readily distinguishable than that in the PGA graphite, this being the fine granular region between the large filler grains. Another distinctive feature of the Gilsocarbon structure is the globular pores, which tend to be distributed between the large filler grains. The globular pores are generally resin-filled but the lenticular cracks are not, signifying that they are closed.

In polarised light (**Figure 4.2b**) the fine granular binder region between the grains appears as a fine array of blue and yellow specks. The large spherical grains display texture associated with their curvature. Quadrants of these spherical grains that lie at approximately 45° to the vertical axis, (clockwise in plane of paper) appear blue while opposing quadrants appear yellow. However, the colours are not as strong as in the case of the needle-coke grains in the PGA graphite for example, suggesting that the texture, i.e. orientation of the basal layers, within these grains is not as strong. Resin-filled pores are seen to be purple and non-filled pores are black in colour.

Some of the finer features of the Gilsocarbon microstructure deserve greater attention, in particular the mosaic type of structure observed in some regions between the grains and on the periphery of many grains. The mosaic structure is highlighted in **Figure 4.2c** and **Figure 4.2d**. In some cases, this coarse-structured region on the periphery of the filler grains appears relatively wide, being of the order of about 50μm in the example shown in **Figure 4.2d**. Magnified images in polarised light reveal a coarser, randomly oriented texture within the mosaic region compared to that within the rest of the binder phase.

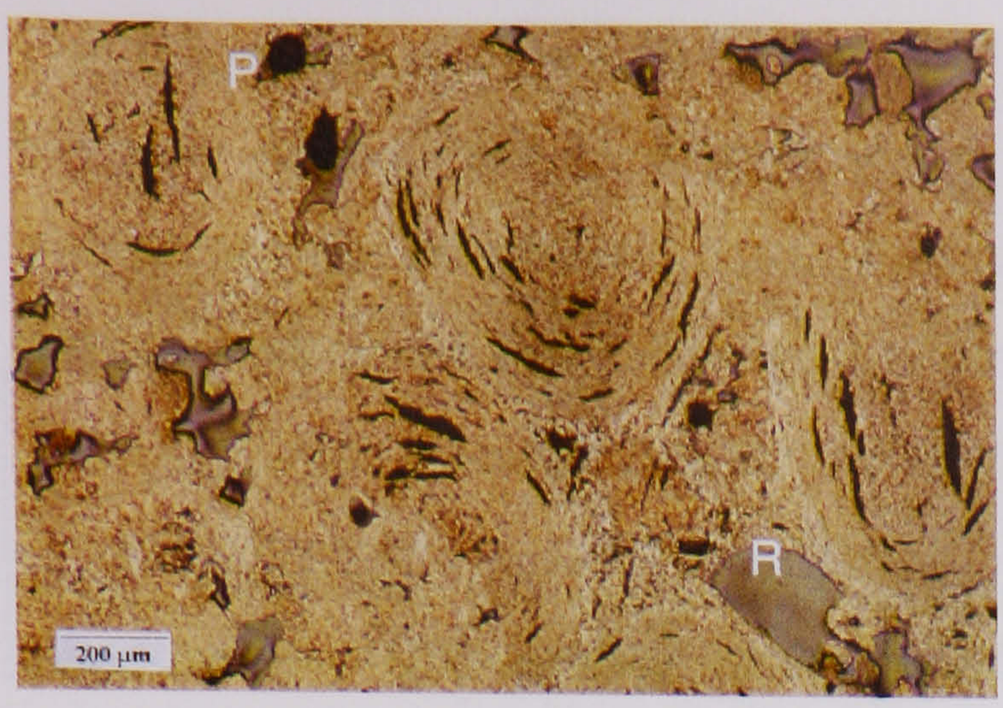

a

b

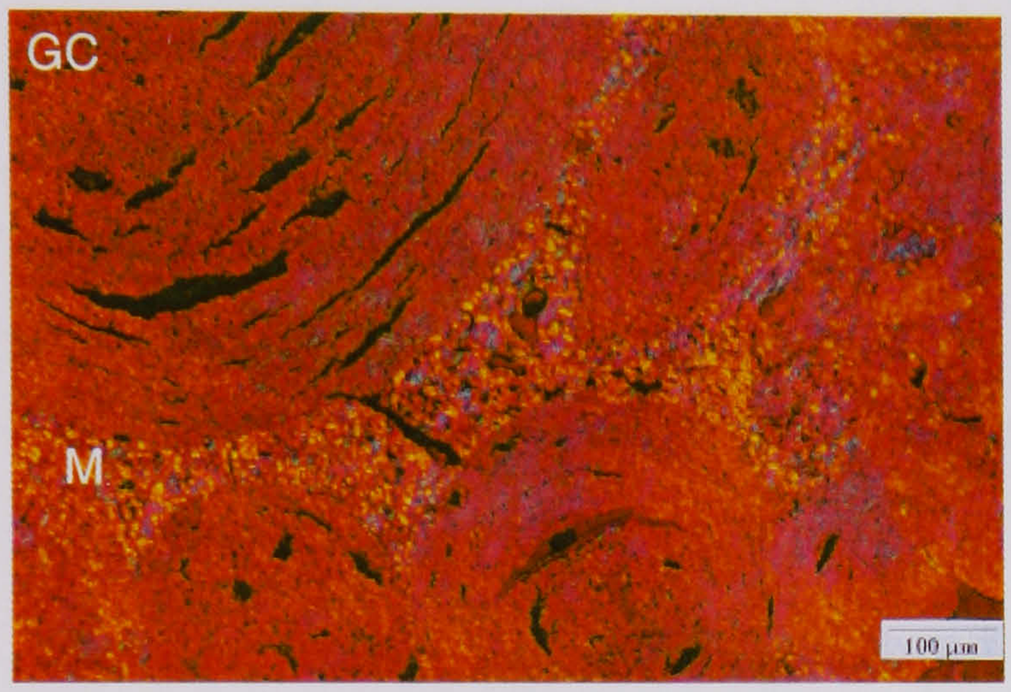

c

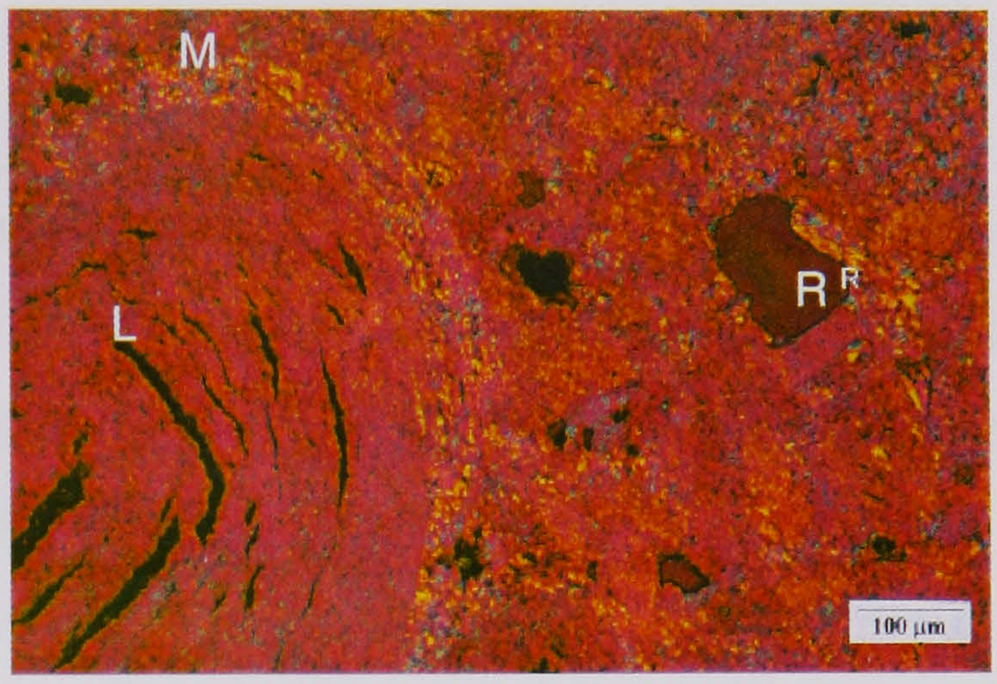

d

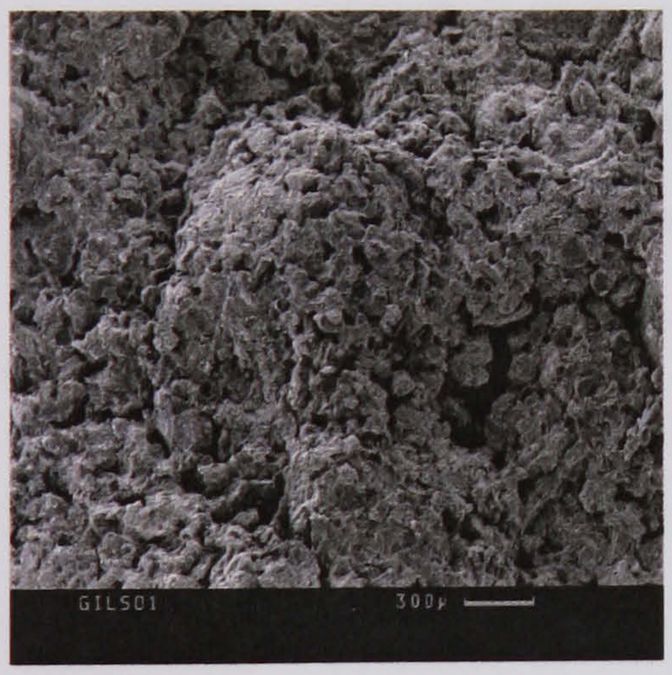

e

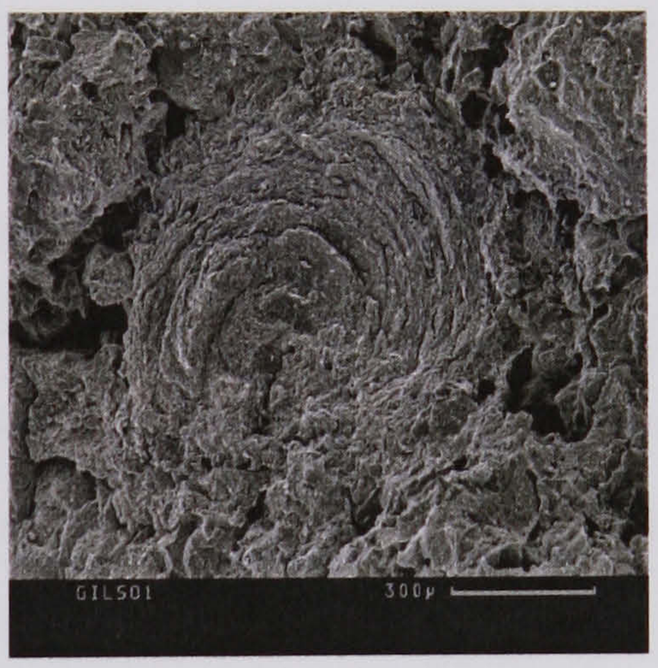

f

g

Figure 4.2. Gilsocarbon graphite structure: (a) reflected light; (b) polarised light (crossed polars, 1λ retarder plate); (c) mosaic structure; (f) mosaic on grain periphery (e) SEM images: fine grains around a Gilsocoke grain; (ii) section through a fractured grain; (iii) Magnified view of grain periphery highlighting mosaic region;

GC = Gilsocoke grain, P = pore, R = resin, M = mosaic, L = lenticular crack.

The Gilsocarbon structure is revealed more vividly by the SEM micrographs in **Figures 4.2e-4.2g**. In **Figure 4.2e**, it is seen that the binder comprises an agglomeration of smaller grains that surround the larger, Gilsocoke grain. The porous nature of the Gilsocarbon matrix is well exposed in this micrograph. Transgranular fracture of a large, spherical coke grain (**Figure 4.2f)** reveals an onion skin structure within the grains. The porosity surrounding the filler grain is clear seen. The smaller grains seem to agglomerate around the large filler grains binding them together.

Figure 4.2g magnifies the onion skin structure revealing two interesting features. The lenticular cracks within the filler grains appear to be gaps between the layers that make up the onion skin structure, and, the texture within the mosaic structure is more random compared to the inner layers of the filler grain. This correlates with the polarised light micrographs of the mosaic region, as shown in **Figures 4.2c** and **Figure 4.2d**.

The IG-110 graphite structure is shown in **Figures 4.3a-4.3c**. This is clearly a much finer structure than that of PGA and Gilsocarbon graphite. In reflected light (**Figure 4.3a**), it is difficult to distinguish the orientation and texture within the fine needle-coke particles that surround the large needle-coke grains, the latter occurring less frequently throughout the structure. In polarised light (**Figure 4.3b**), the smaller needle-coke grains become more clearer, developing similar colours to those seen in PGA and Gilsocarbon graphite. Fine pores of somewhat regular size and shape are dispersed throughout the structure.

The fine-gained structure of the IG-110 graphite is magnified by the SEM micrograph in **Figures 4.3c**, showing the very fine-grained material surrounding the coarser grains. It is difficult to distinguish any binder phase in this structure but it would appear that the fine grained material surrounding the large coke grains forms the matrix. In **Figure 4.3d**, it is seen that this fine-grained material really comprises small graphite flakes. The fine, open porous structure of the IG-110 graphite is also made evident in these micrographs.

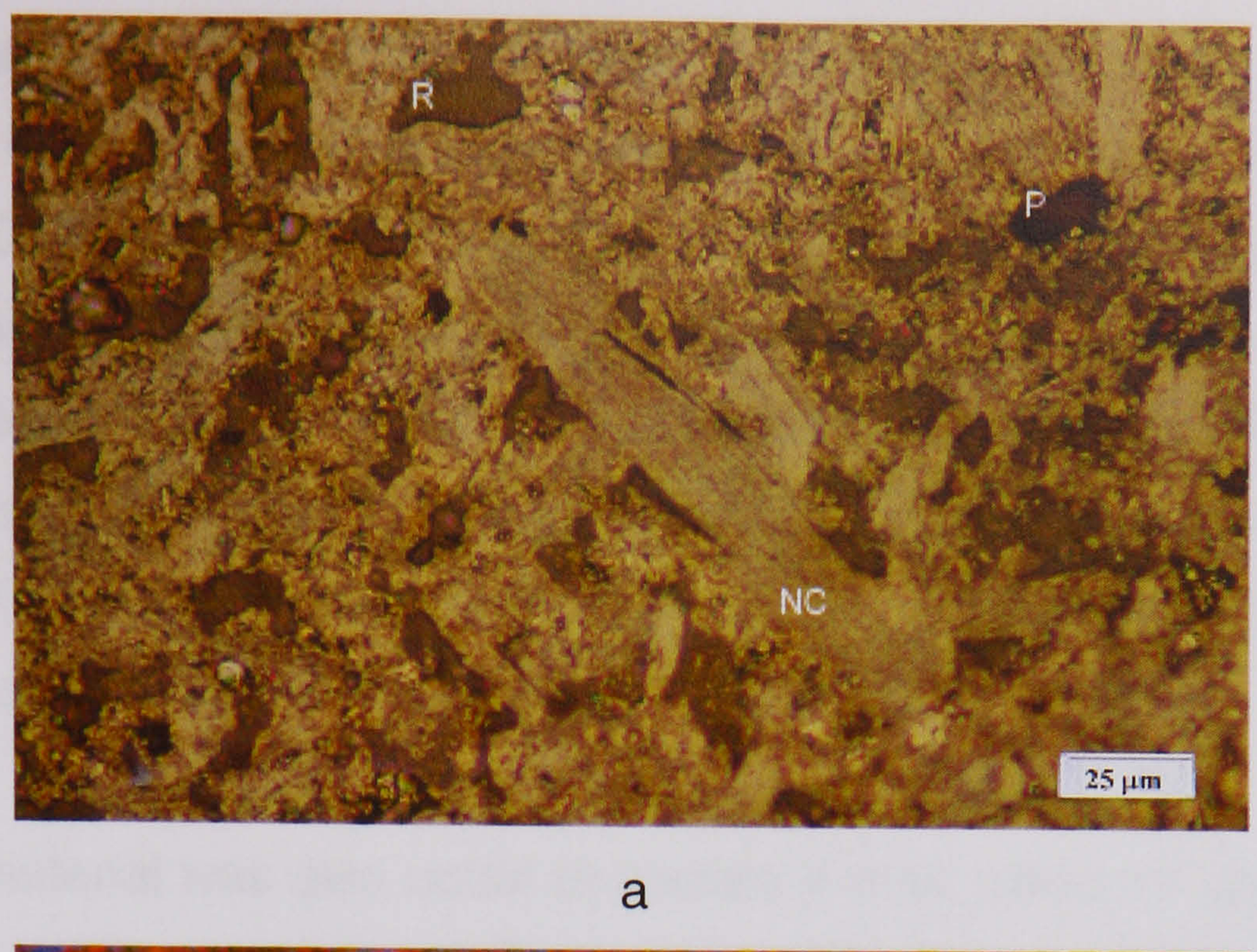

a

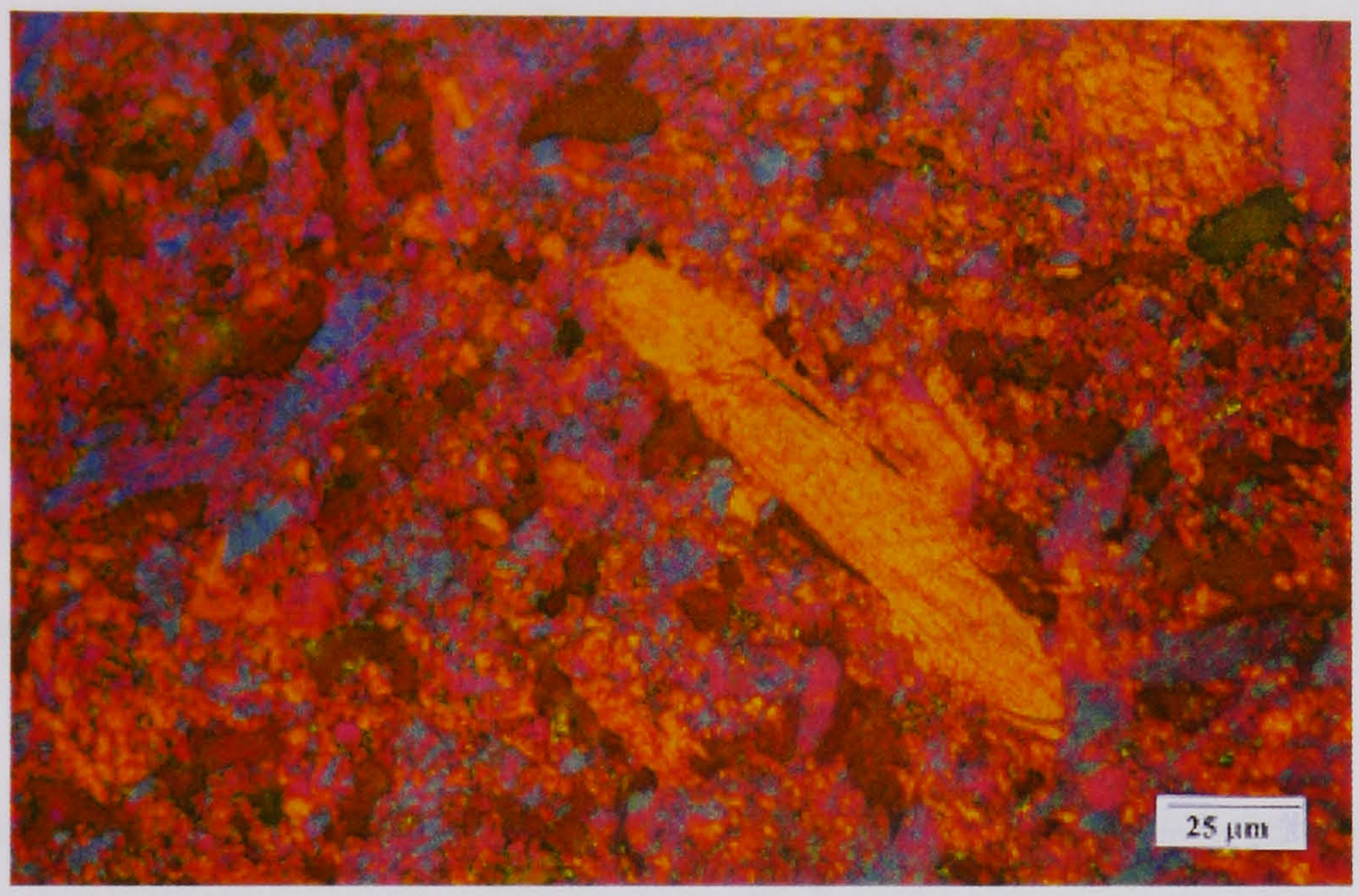

b

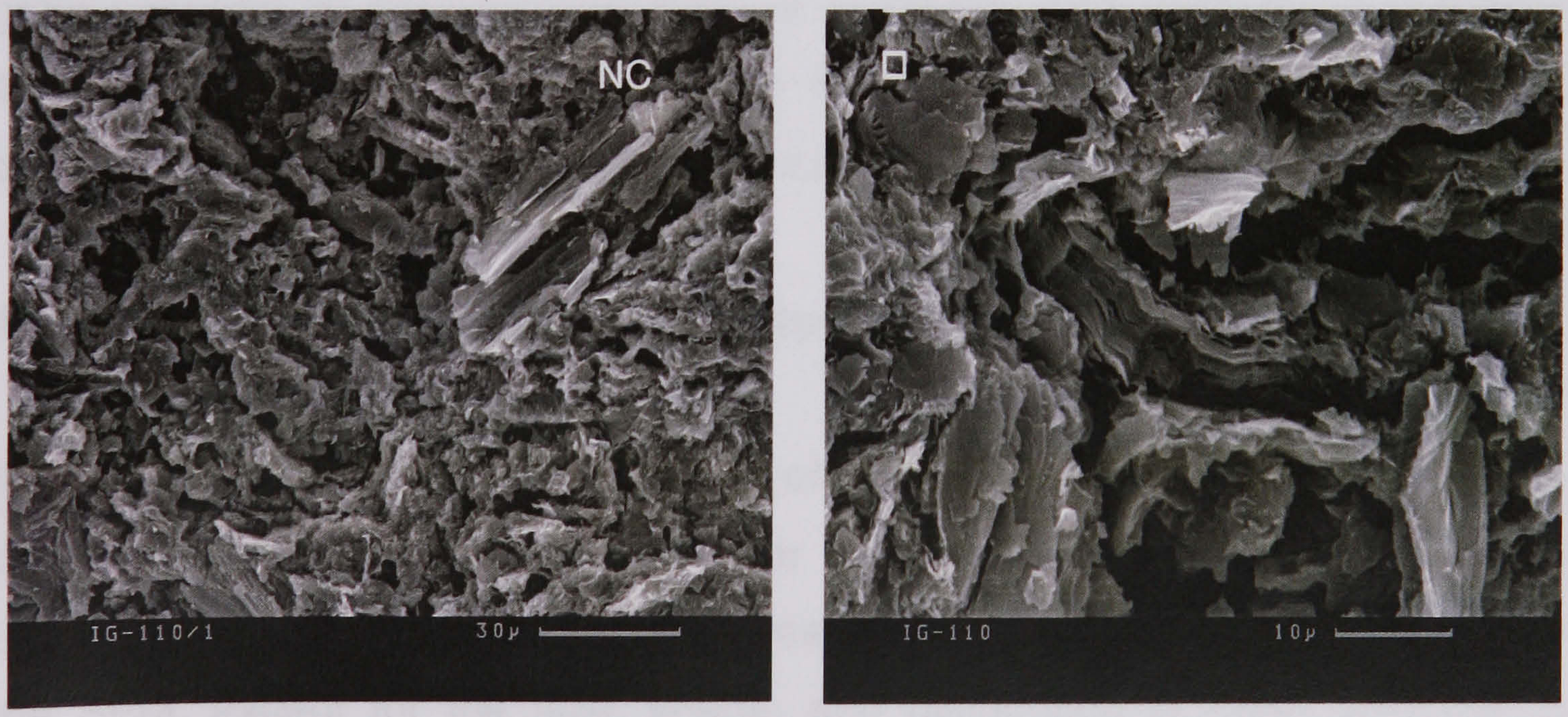

c d

Figure 4.3. Micrographs of IG110 graphite structure: (a) reflected light; (b) polarised light (crossed polars, 1λ retarder plate); (c) SEM image showing larger needle-coke grain surrounded by fine grains; (d) Close-up view of the fine graphite flakes; NC = needle-coke grain, P = pore, R = resin.

The UcarC graphite structure is represented in **Figures 4.4a-4.4f**. In reflected light (**Figure 4.4a**), it is difficult to distinguish the pitch-coke filler grains making up the UcarC structure, with the exception of the odd, over-sized grain. The finer grains become more apparent under polarised light (**Figure 4.4b**), as does their orientation relative to each other. The surrounding matrix appears to be extremely fine judging from its isotropic, purple or pinkish-red colour. However, the apparent isotropy of the matrix may be an interference effect from the impregnant used to densify this material.

The UcarC material was also noted to contain a wide variety of pore sizes and shapes, with a fair proportion of slit-shaped or elliptical pores that appeared to be grouped together, as shown in **Figure 4.4c-4.4d**. The size of the different pore types also varied widely, with some of the large, irregular pores exceeding a mean diameter of 1mm. It is thought that the slit-shaped pores originate during the devolatilisation process that follows re-impregnation and baking. A pore channel is shown by SEM in **Figure 4.4e** and exposes the deposit lining the pore walls, the origin of this deposit being the impregnant carbon.

The fractograph in **Figure 4.4e** suggests that the relatively large coke grains in the UcarC graphite are surrounded by a fine binder phase. The large, coke grain exposed by transgranular fracture in **Figure 4.4e** suggests that most of the fracture in the UcarC occurred in the fine matrix, hence the scarcity of exposed coke grains observed in the micrograph.

4.1.3. Etching of Polished Graphite Specimens

An attempt was also made to examine etched specimens to determine whether the graphite structure could be better resolved using SEM. Because the polished graphite surface does not reveal detail about the graphite structure in the SEM, except for the size, shape, and distribution of pores and cracks, etching could help reveal microstructural features. The possibility existed that etching would reveal additional features not seen using polarised light microscopy, or, SEM of polished samples or fracture surfaces. To examine this possibility, polished samples of Gilsocarbon graphite were etched by two different techniques, i.e. chemical etching and thermal etching.

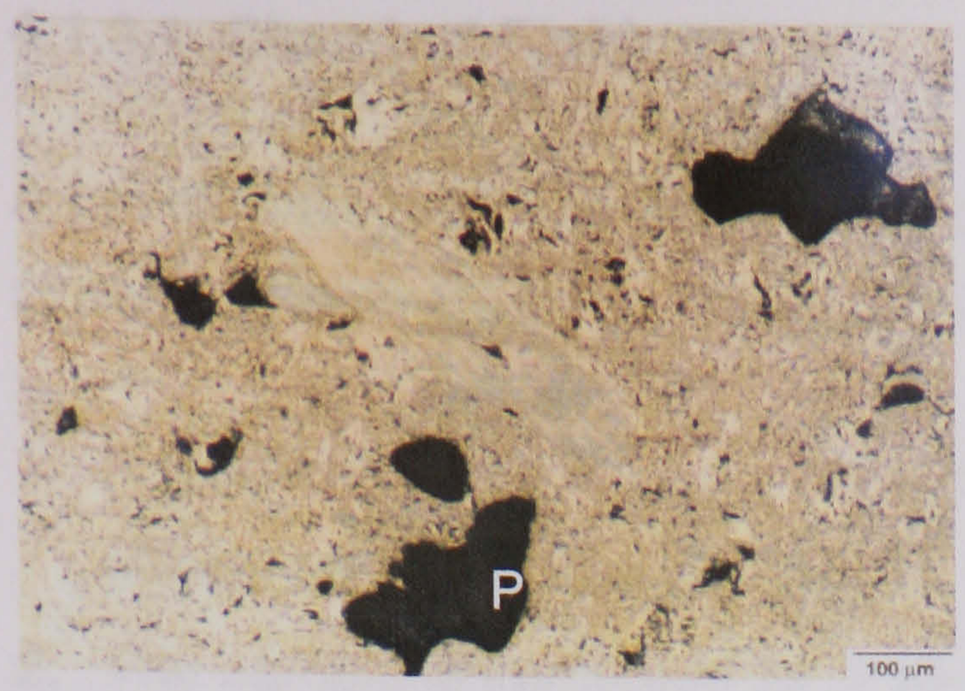

a

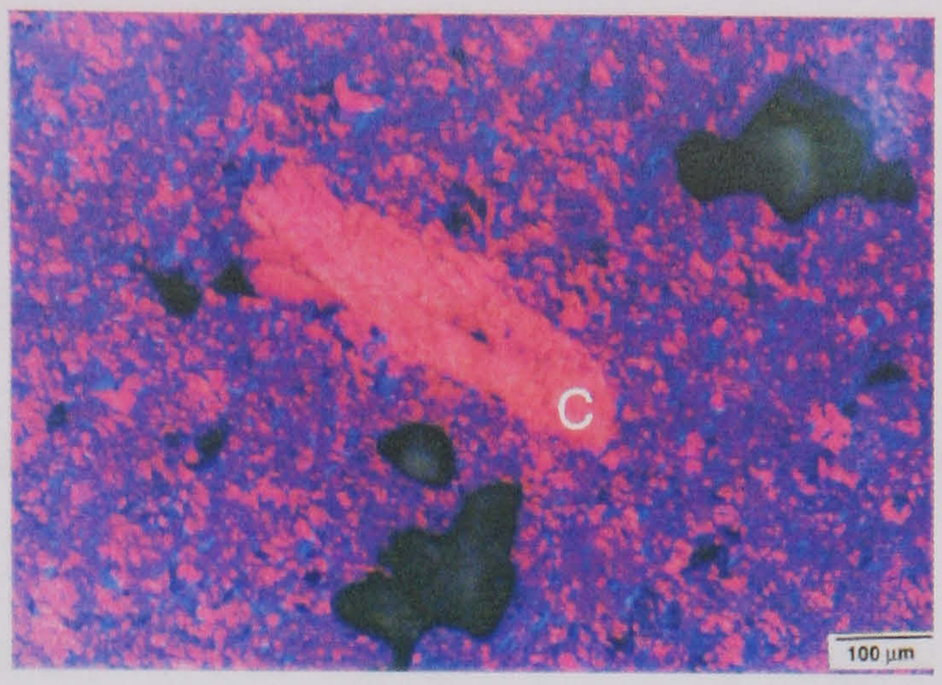

b

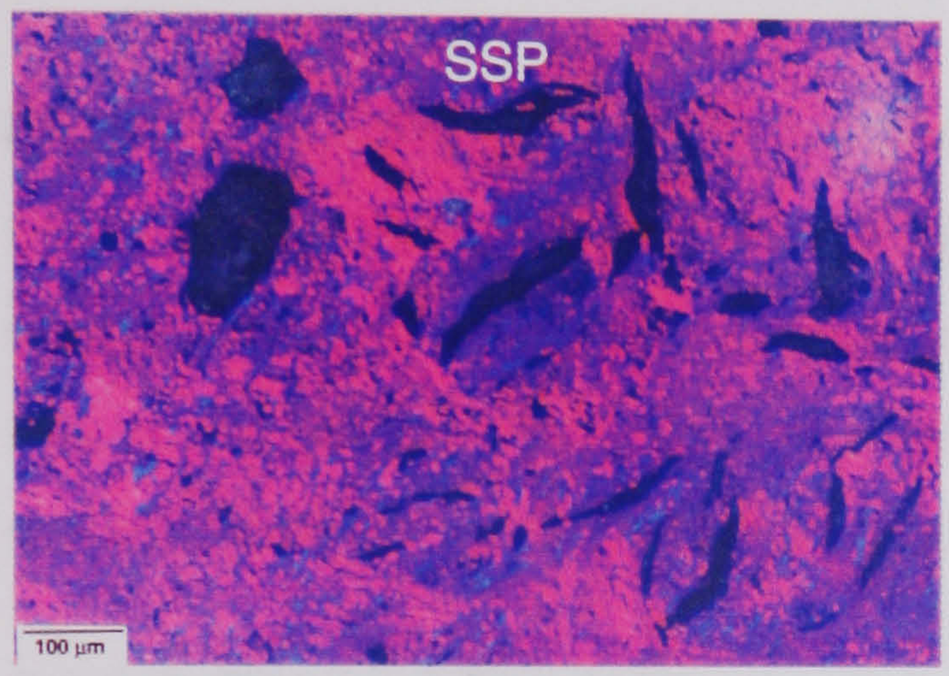

c

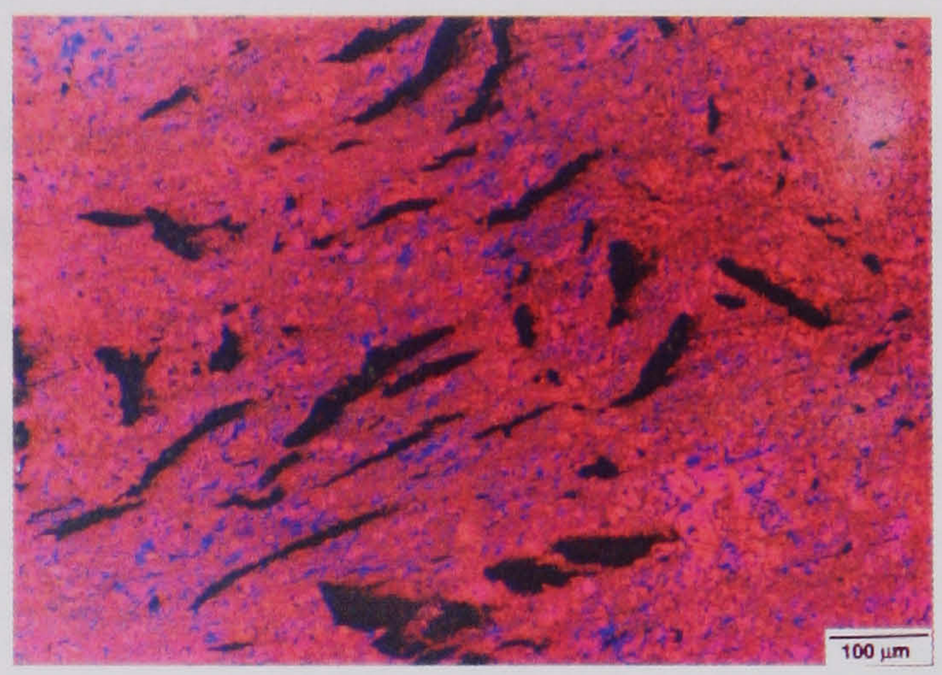

d

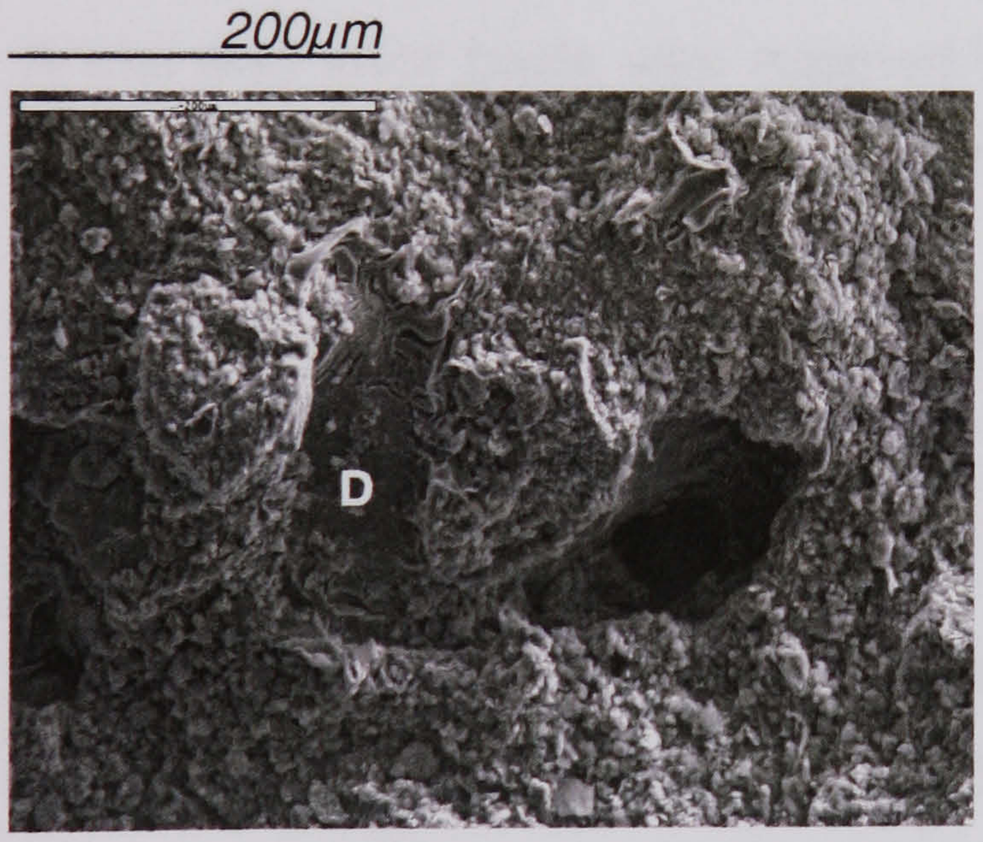

e

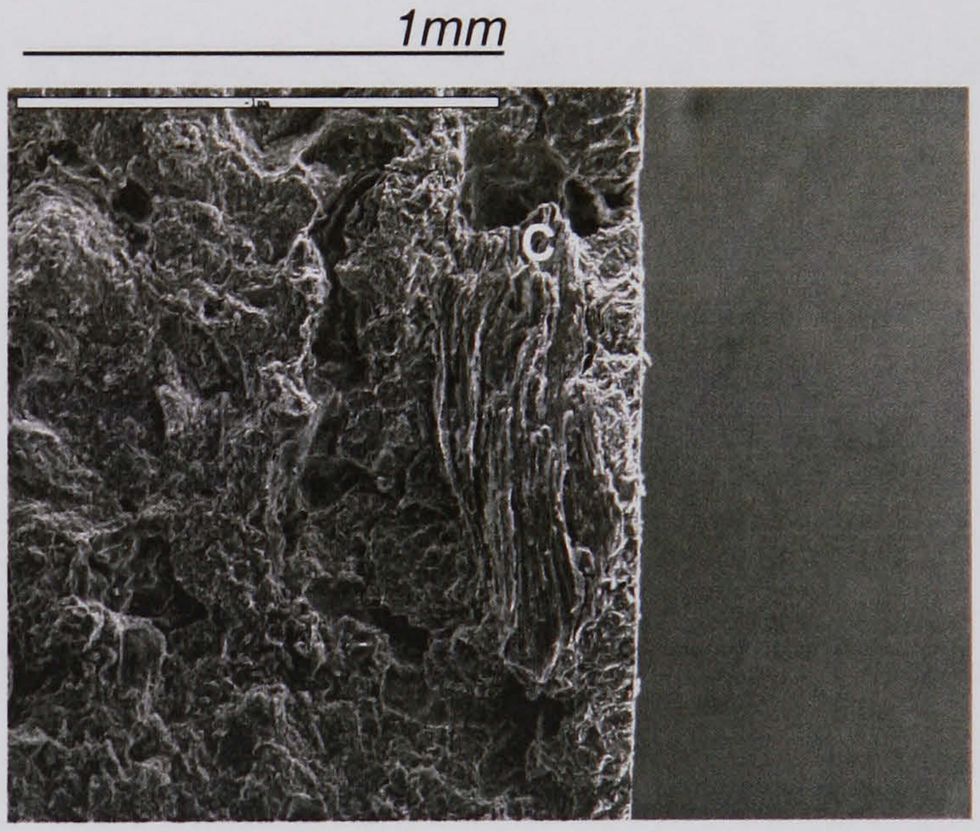

f

Figure 4.4. Micrographs of UcarC graphite structure: (a) reflected light; (b) polarised light showing filler grain orientation (crossed polars, 1λ retarder plate); (c) a variety of pore size and shapes; (d) magnified view of slit-shaped pores; (e) close-up view of deposit in a pore; (f) SEM image showing fine granular appearance of the fracture surface and a large coke grain;
C = coke grain, P = pore, SSP = slit-shaped pore, D = deposit.

4.1.3.1. Chemical Etching

A hot chromic acid was used for chemical etching. This method has been used to reveal the structure of cokes (Legin-Kolar, 1992), and, involves the following:

1. A chromic acid solution (10g potassium dichromate in 50 ml of 85% phosphoric acid) is gently heated to 130-135 °C.
2. The sample is immersed for 5-10 minutes in the hot acid and then quenched in a large beaker of water, to dilute the carcinogenic chromate (Cr^{6+}) ions.
3. Rinse sample in water-ethanol (5% by volume) mixture and leave to dry.

Figures 4.5a and **4.5b** show that the polished Gilsocarbon sample only shows pores and lenticular cracks in the SEM. After chemical etching the Gilsocoke grains and lenticular cracks appear more exposed (**Figure 4.5c**). However, closer examination indicates that the etchant may cause excessive removal of surface material as shown by the pocky surface in **Figure 4.5d**.

4.1.3.2. Thermal Etching

A trial and error basis was adopted in which polished Gilsocarbon specimens were simply oxidised in air at different temperatures and times (see Table 4.2).

Table 4.2. Temperatures and times used for thermal etching.

Temperature (°C)	300	400	500	600	650
Time (minutes)	30	30	15	15	15, 30

After oxidising polished samples at 300, 400 and 500 °C for the chosen times, the surface was found to be relatively unchanged. At 600 °C for 10 minutes, this changed slightly, and, after 30 minutes at 650 °C the topography shown in **Figure 4.5e** developed. Interestingly, extremely fine lenticular cracks appear that were not apparent in the polished surface (**Figure 4.5f**). Although the oxidative etch exposes the lenticular cracks better, localised areas appear to oxidise preferentially (**Figure 4.5f**), due to the exothermic C-O_2 reaction.

The preferential attack of the graphite surface observed with both etching techniques appeared to limit their usefulness. The techniques were therefore not applied to the remainder of the nuclear graphite materials. A more detailed investigation may help to expand the usefulness of these techniques.

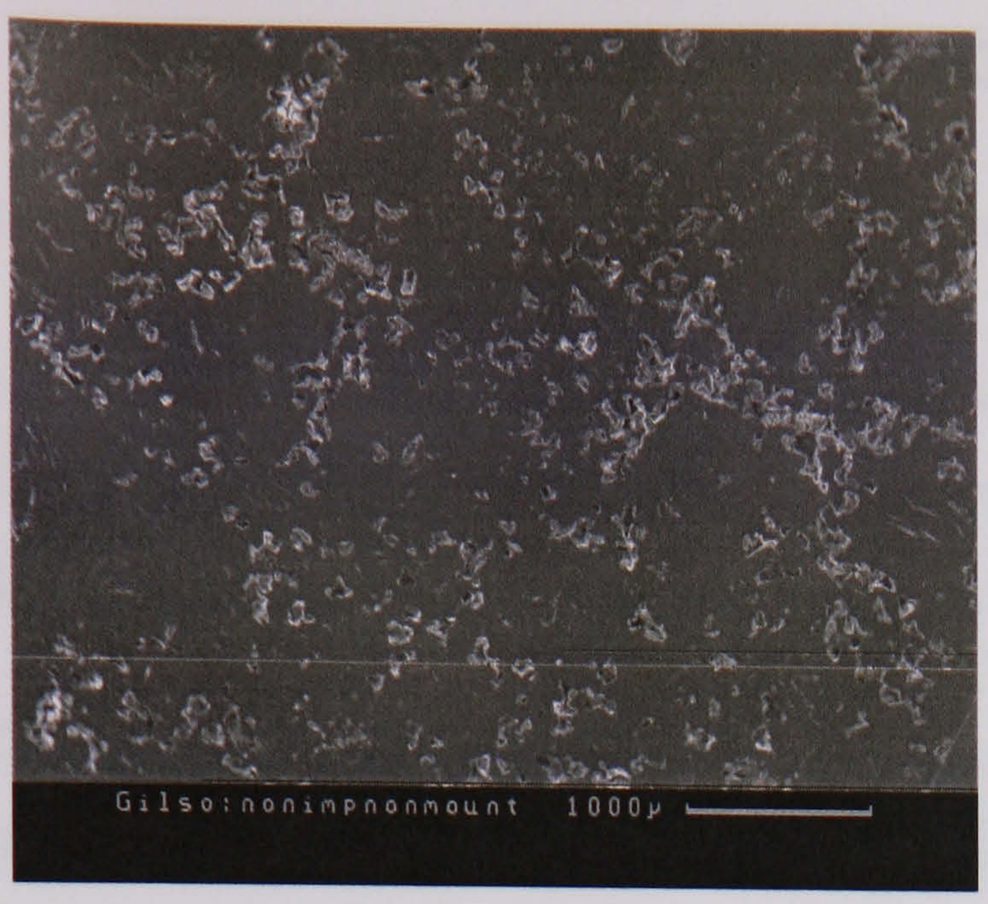

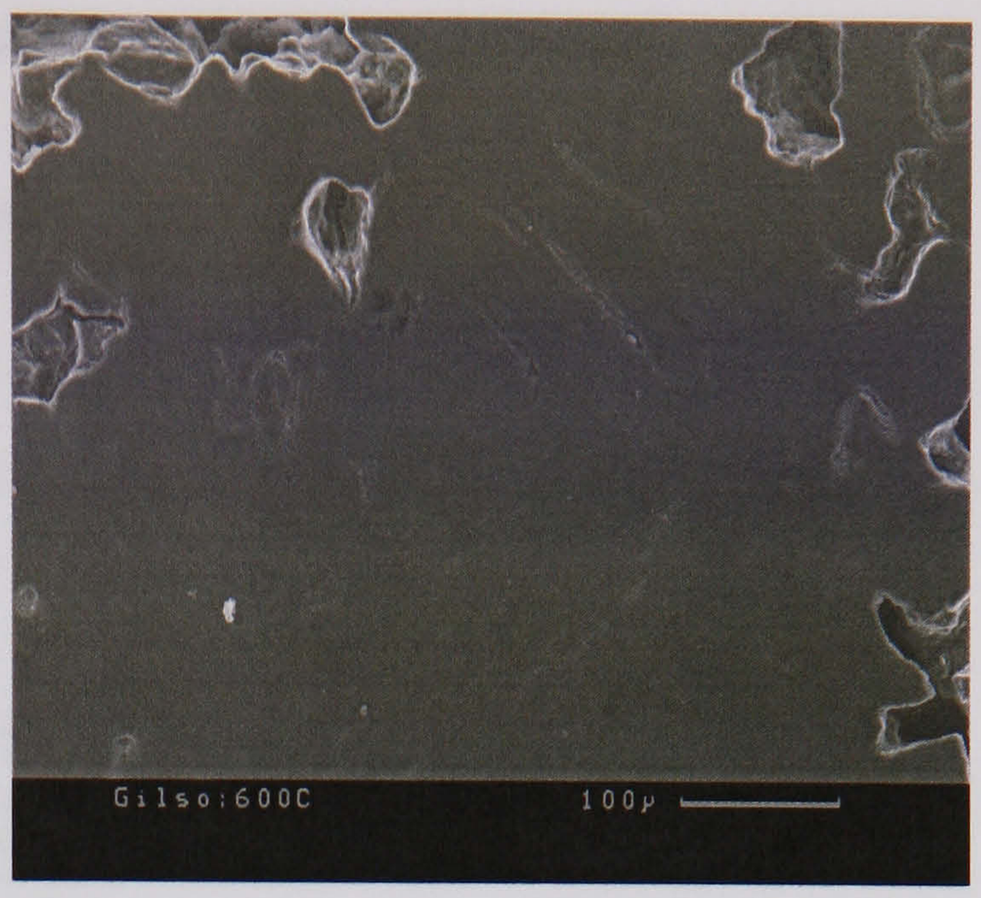

a

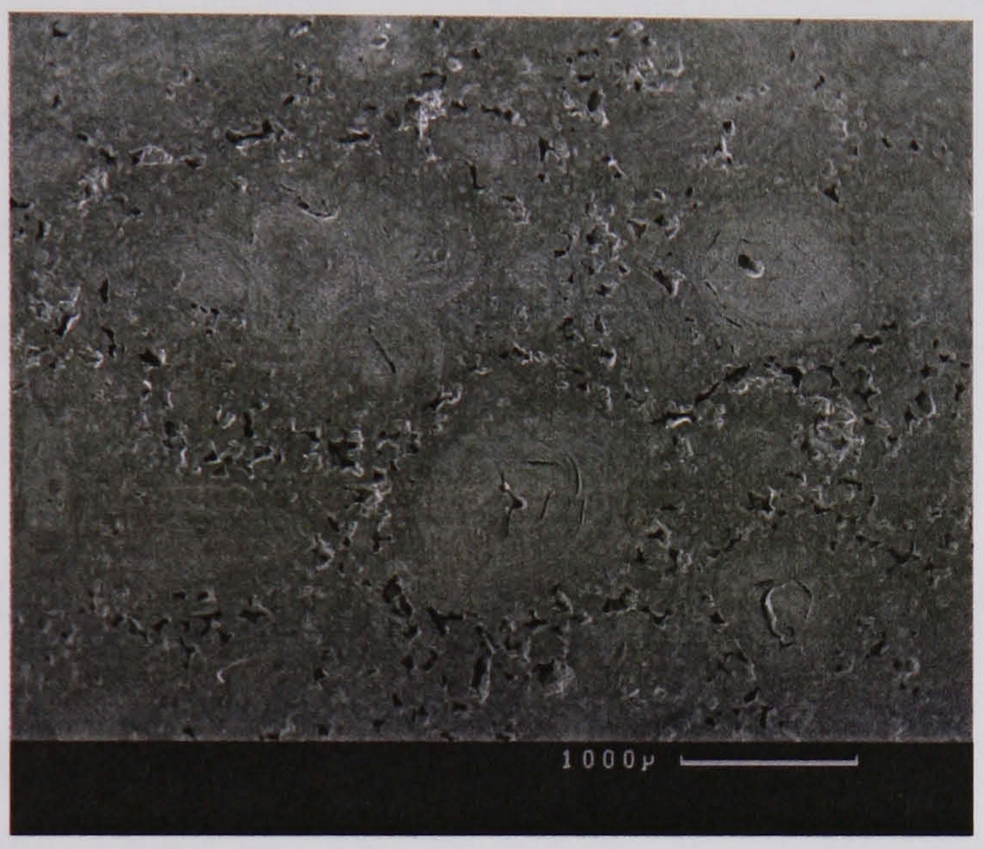

b

c

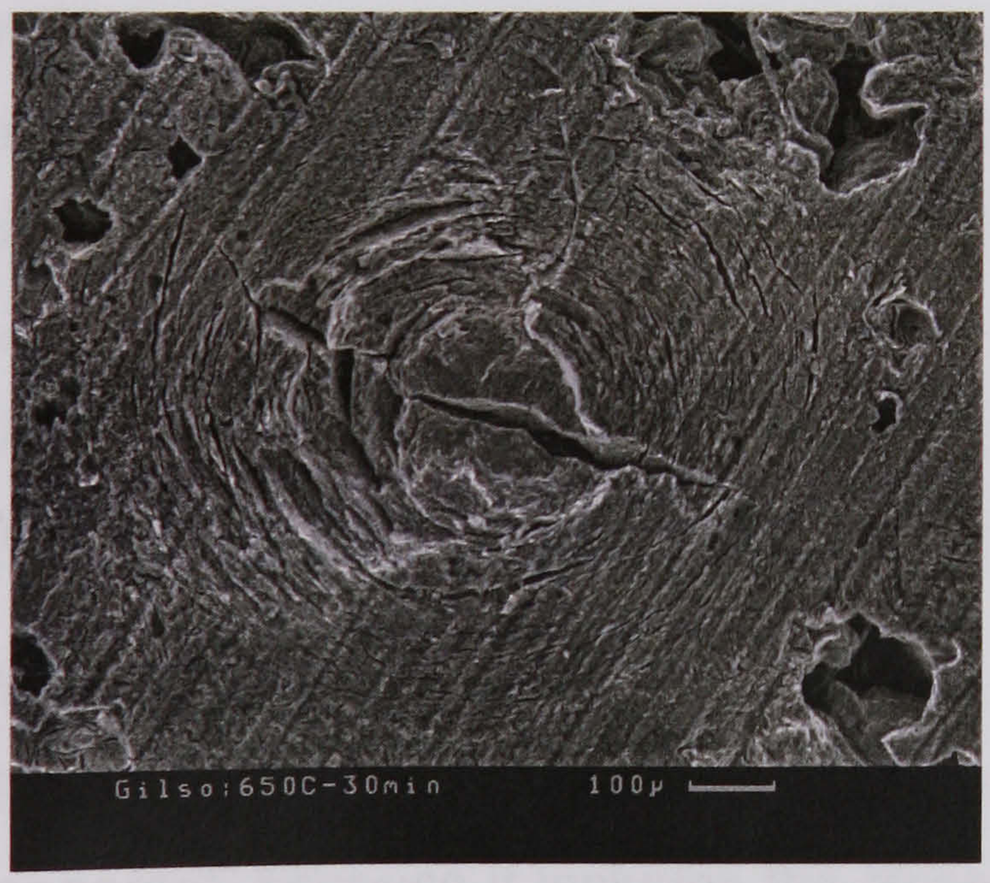

d

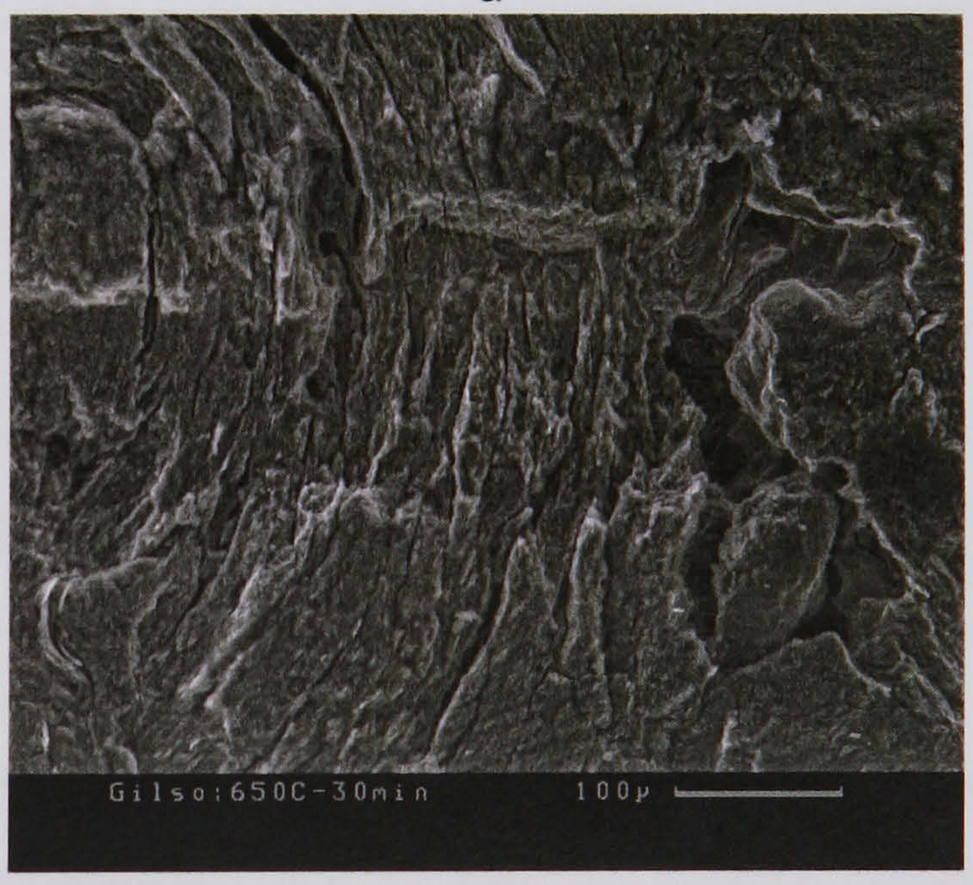

e f

Figure 4.5. SEM images of polished and etched Gilsocarbon graphite: (a) as-polished surface; (b) magnified view of the polished surface; (c) chemically-etched in hot chromic acid; (d) close-up of the chemically-etched surface showing pocky appearance; (e) thermally-etched surface; (f) close-up of thermally-etched surface showing preferential attack in localised areas.

SECTION 4.2: DENSITY AND POROSIMETRY MEASUREMENTS

It was of interest to compare the graphites in terms of the following parameters:

1. Bulk density, apparent solid density, and, 'true' density.
2. Apparent porosity, and, 'true' porosity.
3. Open, closed, and, 'true' porosity.

These parameters are routinely used to characterise porous materials. Definitions of these parameters are given in British Standard BS 7134 (1989), these definitions being applicable to this study.

The density and porosity of the nuclear graphite materials was compared using mercury densitometery and helium pycnometry. Mercury porosimetry was used to compare the pore size distribution in these materials. The methods used are described in the following sections.

4.2.1. Density and Porosity Measurements

Bulk Density (ρ_B)

The bulk density (ρ_B) may be defined as the mass per unit volume of particles including the open and closed pores. This was measured with a Doulton densitometer. This is a mercury displacement method, in which the mercury displacement volume is used to determine ρ_B of the sample. Bulk density was also measured by mercury porosimetry (see Section 4.2.2). This is done at low pressure by measuring the volume of mercury that encloses the sample without penetrating the pores (McEnaney & Mays, 1995).

Apparent Solid Density (ρ_S)

This is the density of solid material making up the porous body and is termed 'apparent' because it includes the closed porosity. It may also be termed 'solid carbon density' (McEnaney&Mays, 1995). A Micromeritics Accupyc 1330 pycnometer was used to measure ρ_S. Pycnometry is a displacement method that uses helium as the penetrant, which is able to penetrate most of the open pores in carbons due its small atomic diameter. The ρ_S-values were also derived from mercury porosimetry (see Section 4.2.2) by subtracting the total volume of mercury intruded from the bulk volume.

True Density (ρ_T)

This refers to the density of the solid material that makes up the porous material and is determined from the density of very finely ground powder samples. The ρ_T-values were measured by helium pycnometry using powder samples that were ground to a nominal aperture size of -45 μm (350 mesh) as specified by BS 7134. It is assumed that grinding exposes the closed porosity.

Apparent or Open Porosity (P_A)

This is the percentage of open porosity in the bulk porous body excluding the closed porosity. The total cumulative volume of mercury intruded in mercury porosimetry tests may be used as a measure of the apparent porosity. Alternatively, P_A may be calculated from the ratio of the total, open pore volume in the porous body to its bulk volume (BS 7134: 1989):

$$P_A = \left(\frac{1}{\rho_B} - \frac{1}{\rho_S}\right)\rho_B x100 \qquad [4.2.1]$$

'True' Porosity (P_T)

This is simply the sum of the apparent porosity and the closed porosity. Again, the assumption is made that all the closed porosity is exposed by grinding. The P_T-value may be calculated using the relation (BS 7134),

$$P_T = \left(\frac{1}{\rho_B} - \frac{1}{\rho_T}\right)\rho_B x100 \qquad [4.2.2]$$

Closed Porosity (P_C)

This is simply the difference between the true porosity and apparent porosity:

$$P_C = (P_T - P_A) = \left(\frac{1}{\rho_S} - \frac{1}{\rho_T}\right)\rho_B x100 \qquad [4.2.3]$$

4.2.2. Measurement of Pore Size Distribution by Mercury Porosimetry

Mercury porosimetry was performed using a Micromeritics Autopore II porosimeter, which uses a non-contact design for measuring the mercury displacement volume (see Figure 4.6), i.e. a coaxial plate is located outside the capillary stem. The instrument uses three pairs of capacitance plates mounted at specific positions along the mercury column to measure the volume of mercury penetrating the material. As the mercury is pressurised into the pores of the sample, the hydraulic pressure exerted and the mercury displaced in the calibrated capillary tube is monitored.

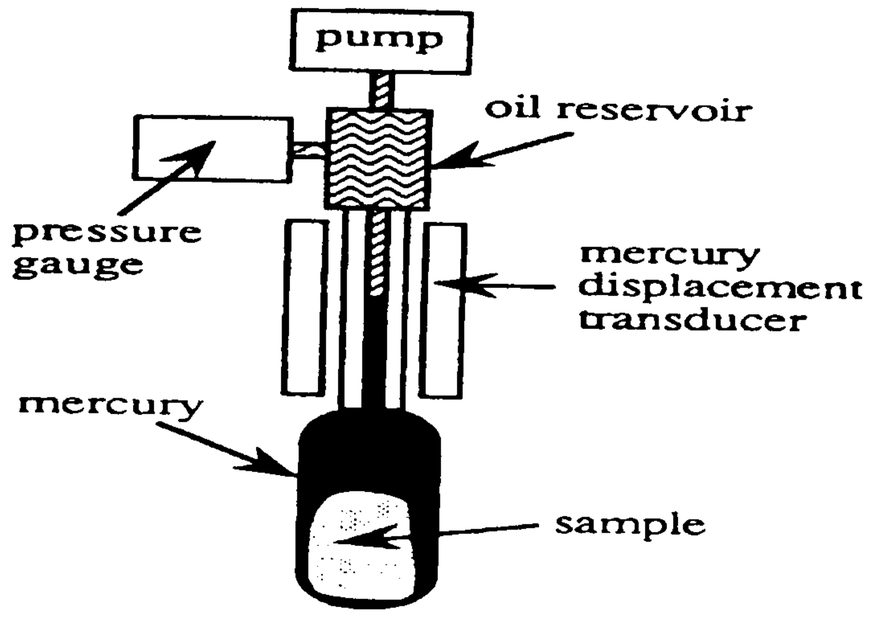

Figure 4.6. A typical mercury porosimeter (McEnaney & Mays, 1995).

In the contact method the resistance change of a coaxial platinum wire fixed inside the capillary stem measures the mercury displacement volume.

Pressure is needed to overcome the non-wetting ability of the mercury due to its large contact angle ($\theta \approx 140°$). Given the differential intrusion pressure (Δp), the pore entrance radius (r) is obtained by the equation (McEnaney & Mays 1995):

$$r = \frac{2\gamma \cos \theta}{\Delta p} \qquad [4.2.4]$$

The surface tension of the mercury, γ is typically ~480 mJm^{-2}. The equation is based on a non-intersecting, cylindrical-pore model. Given the pressure range of a typical porosimeter, i.e. 0.1-400 MPa, pore diameters between 3.5nm-15µm can be measured (γ=480 mJ m^{-2}, θ=140°). This falls within the meso-macropore range. Measurement of the total porosity by mercury porosimetry is not recommended in carbons where the micropore volume or closed porosity is high because internal damage can occur at the high intrusion pressures needed in such materials (McEnaney & Mays, 1995). Other limitations of mercury porosimetry are (McEnaney & Mays, 1995 and Byrne & Marsh, 1995):

1. The value of γ can vary significantly with contamination of the mercury.
2. The contact angle (θ) is found to vary between 130-150°, and, may vary, depending on whether the mercury advances or retreats.
3. The cylindrical pore model is highly idealised since real pores are rarely uniform. The model also neglects pore networks and slit-shaped pores.
4. It measures only the dimensions of pore entrances.
5. It is unsuited to measuring micro- or mesoporosity, as structural damage, occurs at high, mercury intrusion pressures.
6. Mercury retention causes hysteresis in the depressurisation cycle.

4.2.2. Results of Density and Porosimetry Tests

The results of the density and porosity tests are presented in Table 4.3. Where applicable, the mercury displacement measurements are compared with the measurements made by helium pycnometry. It is seen that the bulk density values measured by mercury densitometry agree well with those obtained from mercury porosimetry. The UcarC graphite has the highest bulk density, which is probably due to its being impregnated, with Gilsocarbon and IG110 showing similar ρ_B-values.

The apparent solid densities (ρ_S) measured by helium pycnometry are markedly lower than those obtained by porosimetry, with the exception of PGA graphite where this trend is reversed. This unlikely result is probably due to internal damage caused at the higher end of the mercury, intrusion pressure range. Excessively high mercury pressures can cause closed porosity to open thus allowing an unwanted volume of mercury to penetrate the sample. This results in anomalous results being obtained by mercury porosimetry.

The 'true' density for all the materials is quite similar, PGA graphite being the exception by approaching the theoretical density of 2.256 gcm^{-3} very closely. This is consistent with its apparent solid density (helium pycnometry) which is also the highest of all the materials tested. This reflects the high degree of crystallinity of the PGA material. It is well known that the helium density of graphitizing carbons approaches the theoretical maximum towards the higher end of the heat treatment temperature range. Petroleum cokes can approach values that are about 5% below the theoretical maximum (Blackman, 1970).

The apparent porosity or P_A-values obtained by helium pycnometry do not correlate well with the mercury porosimetry values. Although both show the same trend, the porosimetry results are generally higher than those from pycnometry, which is unlikely since helium has more penetrability. Again, the trend is reversed for PGA graphite, the reason for this being unclear. The higher P_A-values obtained by mercury porosimetry provides further evidence of intrusion damage. This makes the apparent solid densities and apparent porosities obtained by porosimetry unreliable when comparing the different graphites. It is interesting to note that the P_A-values from porosimetry match the true porosity values quite closely suggesting that much of the closed porosity in these samples were opened by high intrusion pressure.

Table 4.3. Results of mercury densitometry, helium density and mercury porosimetry tests*.

GRADE	Bulk Density ρ_B (g cm^{-3})		Apparent Solid Density ρ_s (g cm^{-3})		True Density ρ_T, (g cm^{-3})	Apparent/Open Porosity P_A (%)		Closed Porosity P_C (%)	True Porosity P_T (%)
	Mercury Densitometry	Mercury Porosimetry	Helium Pycnometry	Mercury Porosimetry	Helium Pycnometry	Helium Pycnometry	Mercury Porosimetry		
PGA	1.70	1.70	2.13	2.01	2.24	20.3	15.5	4.0	24.3
Gilso	1.75	1.78	2.02	2.19	2.18	13.3	18.8	6.5	19.8
IG-110	1.75	1.77	2.05	2.20	2.18	14.6	19.8	5.1	19.7
UcarC	1.84	1.86	2.00	2.17	2.20	7.8	14.5	8.5	16.3

* All tests done at room temperature

Terms and Definitions used according to BS 7134: Section 1.2 (1989):

Open porosity:	Pores that are connected with the atmosphere directly or via one another.
Closed porosity:	Pores that are not penetrable by a fluid or connected with the atmosphere.
Bulk density:	The ratio of the mass of the dry material of the porous body to its bulk volume
True density:	Ratio of the mass of the dry material, i.e. powder sample, to the volume of solid material in the porous body
Apparent solid density:	The ratio of the mass of the dry material of the porous body to its apparent solid volume, viz. the sum of the volume of the closed pores and the volume of the solid material in the porous body.
True porosity:	Ratio of the volume of open and closed pores to the bulk volume, as determined using powder samples.
Apparent porosity:	The ratio of the total volume of open pores in a porous body to its bulk volume, i.e. excluding closed pores.

The high P_T-value of PGA graphite implies that it is the most porous graphite. It also appears to have the most open structure given its low percentage of closed porosity. The UcarC material is seen to have the lowest P_T-value with the highest percentage of closed porosity (P_C), which is expected because it has been impregnated.

Gilsocarbon graphite also shows a relatively high percentage of closed porosity, which must be related to the presence of extensive lenticular cracks within the filler grains. It was shown in Section 4.1 that these cracks are generally closed. Gilsocarbon graphite and IG-110 graphite show similar 'true' porosity levels, close to about 20%.

As with mercury densitometry tests, the specimens need not have a specific geometry or dimensions, except that the sample is within a certain size. The pore size distribution of the nuclear graphites is shown in Figure 4.7 as a cumulative open-pore volume distribution, i.e. cumulative amount of mercury intruded [$cm^3\ g^{-1}$], versus, the open-pore entrance diameter (μm). The IUPAC-defined boundary between meso- and macropores is also shown in Figure 4.7.

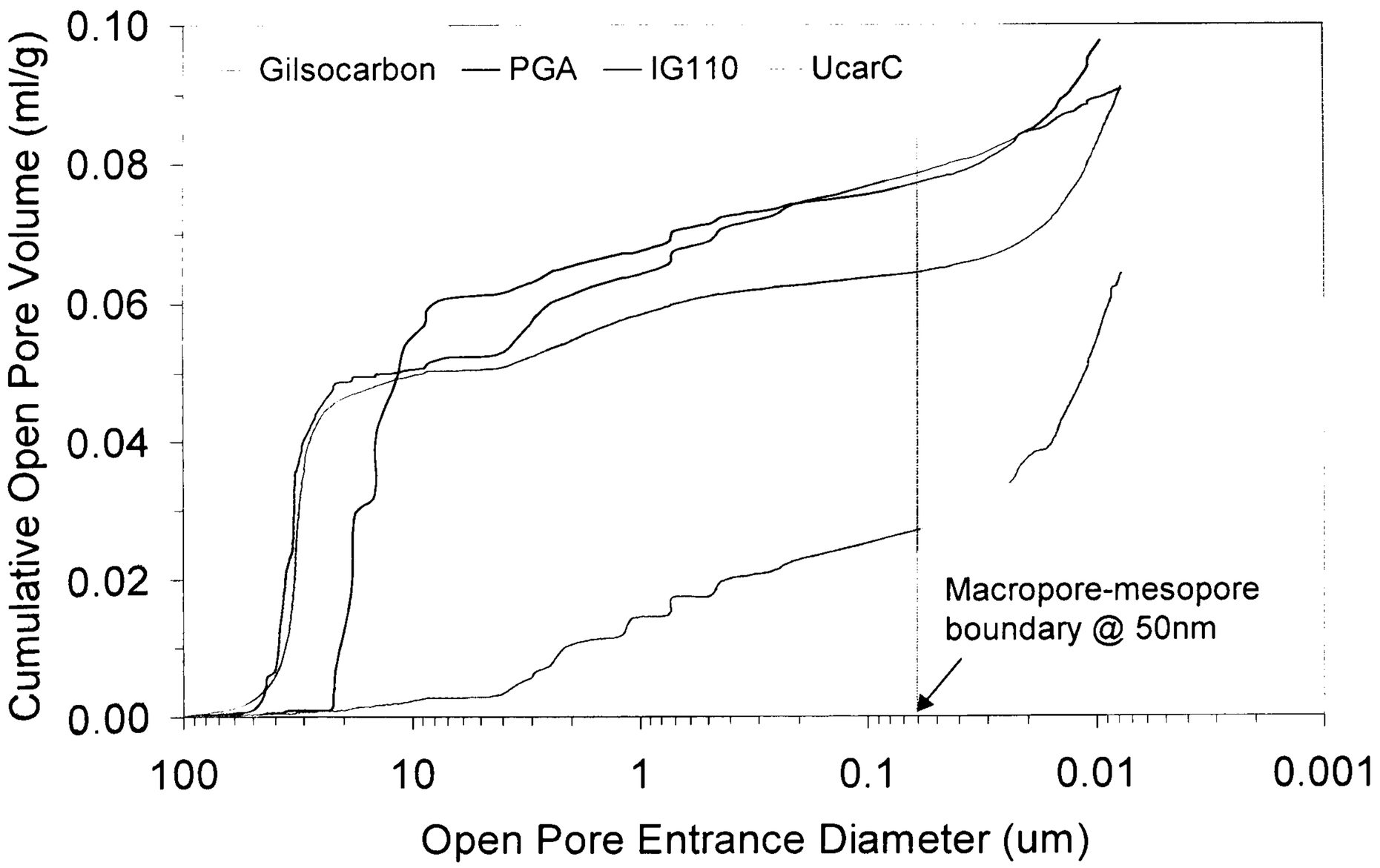

Figure 4.7. Pore size distribution in the nuclear graphite materials.

All three samples show a narrow, unimodal distribution within the macropore region. The IG-110 graphite appears to have the largest volume of open porosity given that it shows the highest cumulative volume of mercury intruded of the four graphite samples. The UcarC graphite shows a bimodal distribution that covers a broad range in the pore size extending over both the mesopore and macropore range. However, it can be seen that the UcarC graphite has a very low volume of open porosity compared to the other graphites. The low cumulative volume of mercury intruded in the UcarC sample may be due to pore closure caused by impregnation. Although this material was microscopically seen to have a wide range of pore sizes, with a fair proportion of large pores, the pores size distribution does not reflect this.

SECTION 4.3: XRD ANALYSES OF THE NUCLEAR GRAPHITES

The importance of XRD in characterising graphitic structures was highlighted in Section 2.1. Because nuclear graphite ranks amongst the most crystalline of carbon materials, the degree of crystallinity is an important aspect to consider when comparing different grades of nuclear graphite. XRD analyses was therefore important for further characterising the graphite materials and comparing them in terms of their degree of crystallinity. PGA graphite, which is made from a premium-grade, needle-coke filler having excellent graphitizability, was used as a control material against which the crystallinity of the experimental materials was compared. The peak width used for crystallite size calculations was derived by different methods to determine if these methods have a significant influence on the measured crystallite size.

4.3.1. Determination of Crystal Lattice Parameters

To compare the crystallinity of the nuclear graphites, three types of samples were prepared for analyses:

1. Non-sieved powder samples.
2. Sieved (-350 mesh) powder samples.
3. Bulk solid samples.

These samples were prepared in order to evaluate the effect of grinding the powder sample to –45μm, which is typically recommended for crystal lattice measurements, on the broadening of the 002-peak profile, in addition to other broadening factors. It was nonetheless useful to evaluate the consistency of the crystal lattice spacing measured with the different samples.

To obtain the non-sieved powder samples, pieces of each grade of graphite were crushed manually using a clean porcelain mortar and pestle. After crushing, the powder samples were dried at 110 °C in an oven for at least 2 hours. The dried powder was then compacted into a standard sample holder used for XRD powder analyses. To prepare the sieved powder samples, the non-sieved powder was crushed until all the powder passed through a –350 mesh sieve. The bulk solid samples were thin, rectangular pieces that could be fit into the standard, sample holder window.

All the samples were analysed using CuK_α-radiation at 40 kV and 30 mA. The samples were scanned between 15°–90° 2θ using a scanning speed of 0.025° 2θ sec^{-1} and a step size of 0.05° 2θ. This angular range was adequate for detecting all the major (00*l*) and (*hkl*) peaks that were needed to calculate the required lattice parameters and crystallite dimensions. Using the angular position of the 002, 004, and 006 peaks at the maximum intensity, values for the *d*-spacings were calculated using the Bragg equation. The *a*-spacing was calculated using the angular position of the 110 peak at maximum intensity.

Typical XRD profiles obtained for the non-sieved graphite powder samples are shown collectively in Figure 4.8, with the crystal lattice planes and their reflections labelled accordingly in the figure. The profiles are plotted on a log-intensity scale because the high relative intensity of the 002 peak makes the higher order peaks less distinguishable on the linear scale. It is seen that the PGA peaks appear more pronounced than those of the other graphites.

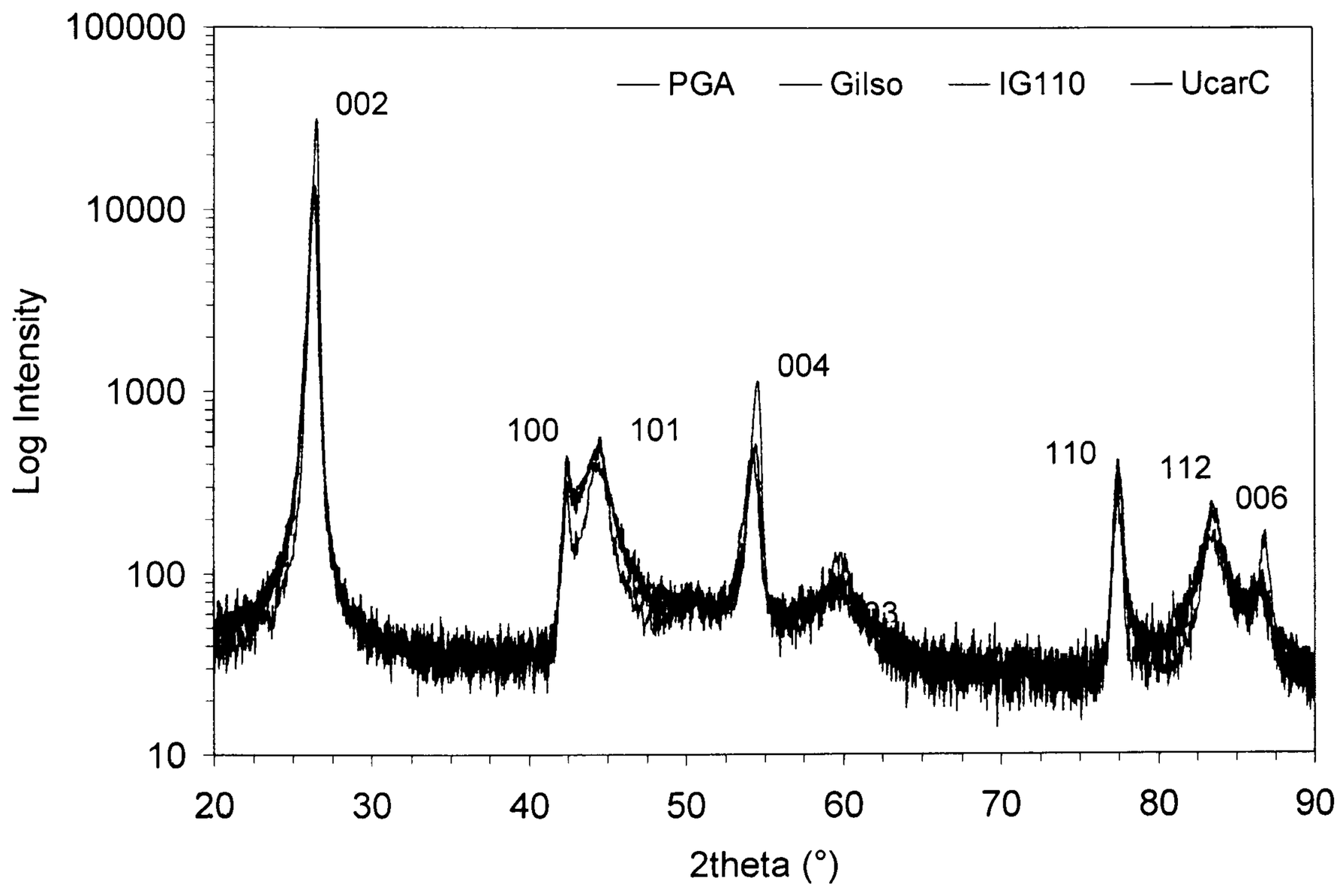

Figure. 4.8. Typical XRD profiles of the nuclear graphite materials (log-scale).

The lattice parameters, i.e. the *a*-spacing and *d*-spacing, are presented in Table 4.5. Also included in Table 4.4 are the critical 2θ-values of these peaks. It can be seen that the four nuclear graphite samples have similar *d*-spacing with PGA graphite approaching the perfect lattice value more closely, i.e. 3.3539 Å.

Table 4.4. Measured lattice parameters of the nuclear graphite samples.

	2θ-value (°)				Calculated *d*-spacing (Å)				
	Non-Sieved Samples								
GRADE	$2\theta_{002}$	$2\theta_{004}$	$2\theta_{006}$	$2\theta_{110}$	d_{002}	d_{004}*	d_{006}*	$d_{Average}$	d_{110}*
PGA	26.475	54.525	86.825	77.425	3.3638	3.3632	3.3625	3.3632	2.4633
Gilsocarb	26.275	54.225	86.475	77.475	3.3890	3.3803	3.3734	3.3809	2.4619
IG110	26.325	54.425	86.625	77.425	3.3827	3.3689	3.3687	3.3734	2.4633
UcarC	26.375	54.375	86.675	77.475	3.3764	3.3717	3.3671	3.3717	2.4619
	Sieved Samples (-45μm)								
GRADE	$2\theta_{002}$	$2\theta_{004}$	$2\theta_{006}$	$2\theta_{110}$	d_{002}	d_{004}*	d_{006}*	$d_{Average}$	d_{110}*
PGA	26.525	54.575	86.825	77.475	3.3576	3.3603	3.3625	3.3601	2.4619
Gilsocarb	26.425	54.275	86.525	77.575	3.3701	3.3775	3.3718	3.3731	2.4592
IG110	26.425	54.375	86.525	77.475	3.3701	3.3717	3.3718	3.3712	2.4619
UcarC	26.525	54.475	86.825	77.525	3.3576	3.3660	3.3625	3.3620	2.4606
	Bulk Solid Samples								
GRADE	$2\theta_{002}$	$2\theta_{004}$	$2\theta_{006}$	$2\theta_{110}$	d_{002}	d_{004}*	d_{006}*	$d_{Average}$	d_{110}*
PGA	26.475	54.525	86.775	77.425	3.3638	3.3632	3.3640	3.3637	2.4633
Gilsocarb	26.475	54.425	86.225	77.575	3.3638	3.3689	3.3812	3.3713	2.4592
IG110	26.375	54.425	86.475	77.425	3.3764	3.3689	3.3734	3.3729	2.4633
UcarC	26.425	54.425	86.875	77.475	3.3701	3.3689	3.3609	3.3666	2.4619

d_{004}*, d_{006}* = *d*-values calculated using the angular position of the 004, 006 peaks

d_{110}* refers to the *a*-value calculated using the angular position of the 110 peak

The degree of graphitization (*g*) of the materials was also compared using the equation (Nightingale, 1962):

$$\bar{g} = \frac{3.440 - d_{002}}{3.440 - 3.354} \qquad [4.3.1]$$

A perfect graphite structure has $g = 1$, and, a turbostratic structure, $g = 0$. The d_{002}-value used to calculate *g* for the graphite samples was determined from the maximum intensity of the 002 peaks. An average value of d_{002} was used, this being the average obtained from the XRD profiles of the three sample types, i.e. non-sieved powder, sieved (-45μm) powder, and, bulk solid sample.

Table 4.5. Degree of graphitization (*g*) of the nuclear graphite samples.

Grade	Average *d*-spacing (d_{002}, Å)	Degree of Graphitization (*g*)
PGA	3.3617 (± 0.0036)	0.91
Gilsocarb	3.3743 (± 0.0131)	0.76
IG110	3.3764 (± 0.0063)	0.74
UcarC	3.3680 (± 0.0096)	0.84

The calculated *g*-values in Table 4.5 show that the PGA graphite has the highest *g*-value followed by UcarC, with Gilsocarbon and IG110 graphite being similar. Crystal lattice dimensions of graphitic materials approach the perfect lattice dimensions, as the degree of graphitization increases, which is the case for PGA. This correlates with the XRD profiles shown in Figure 4.8 where the PGA peaks are seen to be sharper than those of the other graphites.

Close examination of the (00*l*) peaks, in particular the 002 peaks (shown in Figure 4.9), displayed an asymmetric profile irrespective of type of graphite or the sample type, i.e. bulk solid or powder. The 002 peak for PGA graphite demonstrates significantly higher intensity and reduced asymmetry reflecting the higher order in the PGA structure. This asymmetry of the (00*l*) peaks is a well-known feature in the XRD spectra of graphite (Blackman, 1970). It is a line broadening effect caused by disorder in the crystallite layer stacks.

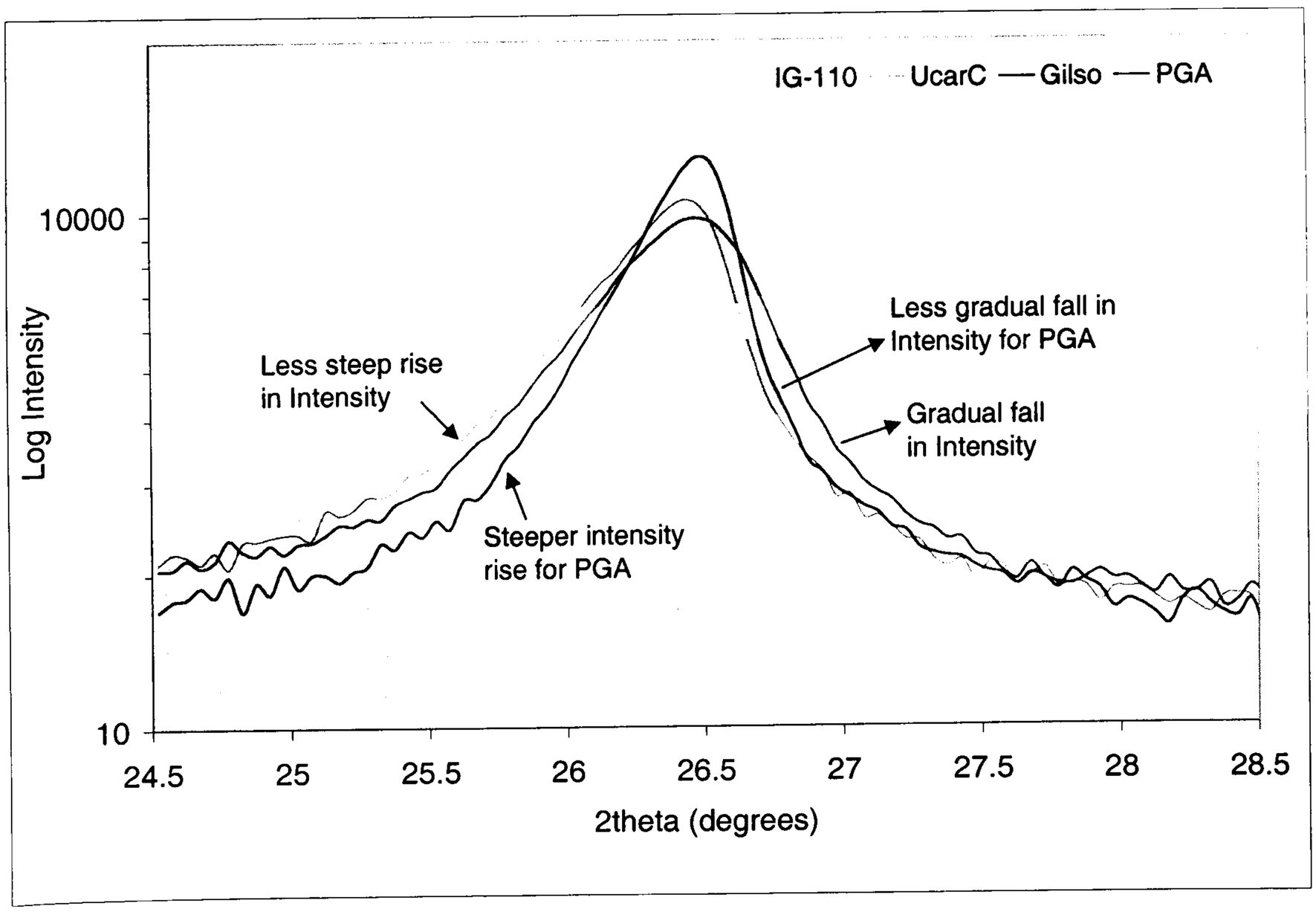

Figure 4.9. XRD profiles of 002 peaks indicating their asymmetric profile.

4.3.2. Determination of Crystallite Size

As explained in Section 2.1, various approaches are adopted for measuring the true width (β) of the XRD peak, which is needed for calculating the crystallite size. Ruland (1968), however, points out that a "precise determination of the crystallite size is difficult and time consuming and even the reputedly more accurate methods are not without shortcomings". In this study, the more tedious methods for calculating β were therefore avoided. There was however, an interest in comparing the simpler methods. In doing so, four different approaches were used to measure the 002 and 110 peak widths, which are used to determine L_c and L_a respectively. These were:

1. Manual measurement of the 'half-breadth' or FWHM:
   Manual measurement of the peak width at half the maximum intensity, i.e. the half-breadth or FWHM. This is the most common approach applied by many researchers. The angular width at half the maximum intensity is taken as the value of β (Cullity 1956, Ruland 1968).

2. Calculation of the integral breadth, or, 'integral line breadth' (B_{int}). This is apparently more accurate than the FWHM (Ruland, 1968):

$$B_{\text{int}} = \frac{\int I(2\theta)\, d\theta}{I_{\max}} \qquad [4.3.2]$$

   $I(2\theta)\, d\theta$ = area under the diffraction curve between θ_1 and θ_2

   I_{max} = maximum intensity of the diffraction profile

3. Calculating the width after subtraction of the instrumental broadening:
   Here, the instrumental broadening (b) is determined using a standard, typically high purity, single crystal silicon, which is said to have an infinite crystallite size. Therefore, broadening observed with the standard can be taken as purely instrumental. By multiplying the integral breadth with the broadening factor, the true width (β) is obtained (Ruland, 1968):

$$\beta = B_{\text{int}} \cdot \left(\frac{b}{B_m} \right) = (ib).B_{\text{int}} \qquad [4.3.3]$$

   ib = instrumental broadening factor = b/B_m

   b = peak width of standard, i.e. due to instrumental broadening

   B_m = experimentally obtained broadening from test sample

PAGE

MISSING

IN

ORIGINAL

Table 4.6. Crystallite size of the sieved, non-sieved, and, bulk solid samples before stripping of the $K\alpha_2$-component.

Sample Type	**L_c (Å)**			**L_a (Å)**		
Non-sieved Powder	**FWHM**	**Integral Breadth**	**$\beta = B_{int}$ x *ib***	**FWHM**	**Integral Breadth**	**$\beta = B_{int}$ x *ib***
PGA	291	231	288	281	148	185
Gilsocarbon	196	158	198	240	135	169
IG-110	218	169	211	221	150	188
UcarC	222	170	212	245	144	180
Sieved Powder (-45µm)	**L_c (Å)**			**L_a (Å)**		
PGA	272	219	274	204	137	171
Gilsocarbon	189	145	182	184	124	155
IG-110	208	165	206	184	129	161
UcarC	195	152	191	151	110	137
Bulk Solid Sample	**L_c (Å)**			**L_a (Å)**		
PGA	352	280	350	248	192	240
Gilsocarbon	203	164	205	175	129	161
IG-110	214	189	236	229	166	207
UcarC	269	203	253	209	154	193

In Table 4.7, the crystallite dimensions obtained after stripping the XRD peaks of the $K\alpha_2$-component are presented. For comparison, the peak width used in these crystallite size calculations was also determined by the three methods applied to the non-stripped profiles.

The results show that the crystallite size of the materials is of a similar magnitude, except for PGA graphite, which has larger L_a and L_c values. Whilst the PGA graphite has L_c-values of the order of about 300 Å the other graphite samples display L_c-values of about 200 Å. The L_a-values between the graphite samples are also quite similar, including that of PGA graphite.

Table 4.7. Crystallite size of graphite samples after $K\alpha_2$-stripping of peaks.

Sample Type	L_c (Å)			L_a (Å)		
Non-sieved Powder	**FWHM**	**Integral Breadth**	**$\beta = B_{int} \times ib$**	**FWHM**	**Integral Breadth**	**$\beta = B_{int} \times ib$**
PGA	302	245	306	401	270	338
Gilsocarbon	176	142	177	290	195	243
IG-110	217	175	219	325	236	295
UcarC	233	177	221	312	221	276
Sieved Powder (-45µm)	L_c (Å)			L_a (Å)		
PGA	280	224	280	354	161	202
Gilsocarbon	190	152	190	257	193	242
IG-110	210	168	211	317	224	280
UcarC	199	157	196	206	179	224
Bulk Solid	L_c (Å)			L_a (Å)		
PGA	375	304	380	477	378	473
Gilsocarbon	208	170	212	239	198	247
IG-110	246	199	249	373	283	383
UcarC	257	215	269	363	283	354

Interestingly, the powder samples show markedly reduced L_a-values and L_c-values compared to the bulk solid sample, with a more substantial reduction in the L_a-values compared to the L_c-values. This points to a breakdown in the crystallite size by grinding, with preferential rupture of the crystallites perpendicular to the basal plane orientation. In comparing the different methods used to calculate the width of the 002 and 110 peaks required for the crystallite size calculation, it is seen that the half-breadth and integral breadth compare well, with the latter giving more conservative values. The crystallite dimensions derived using the instrumental broadening factor (ib=0.80) are also slightly conservative but, not remarkably different from the values obtained using the half-breadth (FWHM).

Remarkably, the L_c-values for PGA graphite increase to ~400 Å in the bulk solid sample, while the L_c-values for the powder samples approach ~300 Å, after $K\alpha_2$-stripping. This shows that the $K\alpha_2$-component has significant influence on

the calculated crystallite size, particularly in the bulk solid samples. The variation in the 002 peak widths for the different sample types is shown graphically in Figure 4.10, using PGA as example. It is seen that the peak width is markedly higher in the sieved sample, compared to the non-sieved powder sample, with the peak width being narrowest in the bulk solid sample. Included in Figure 4.10 is the profile of the 002 peak of the PGA bulk solid sample, after $K\alpha_2$-stripping, which shows clearly a further reduction in the peak width.

This demonstrates that the (00*l*) peak widths can be dramatically reduced when common line broadening effects are taken into account. This effect was consistent throughout the analyses as seen from the crystallite size obtained using the different sample types (see Tables 4.6 and 4.7).

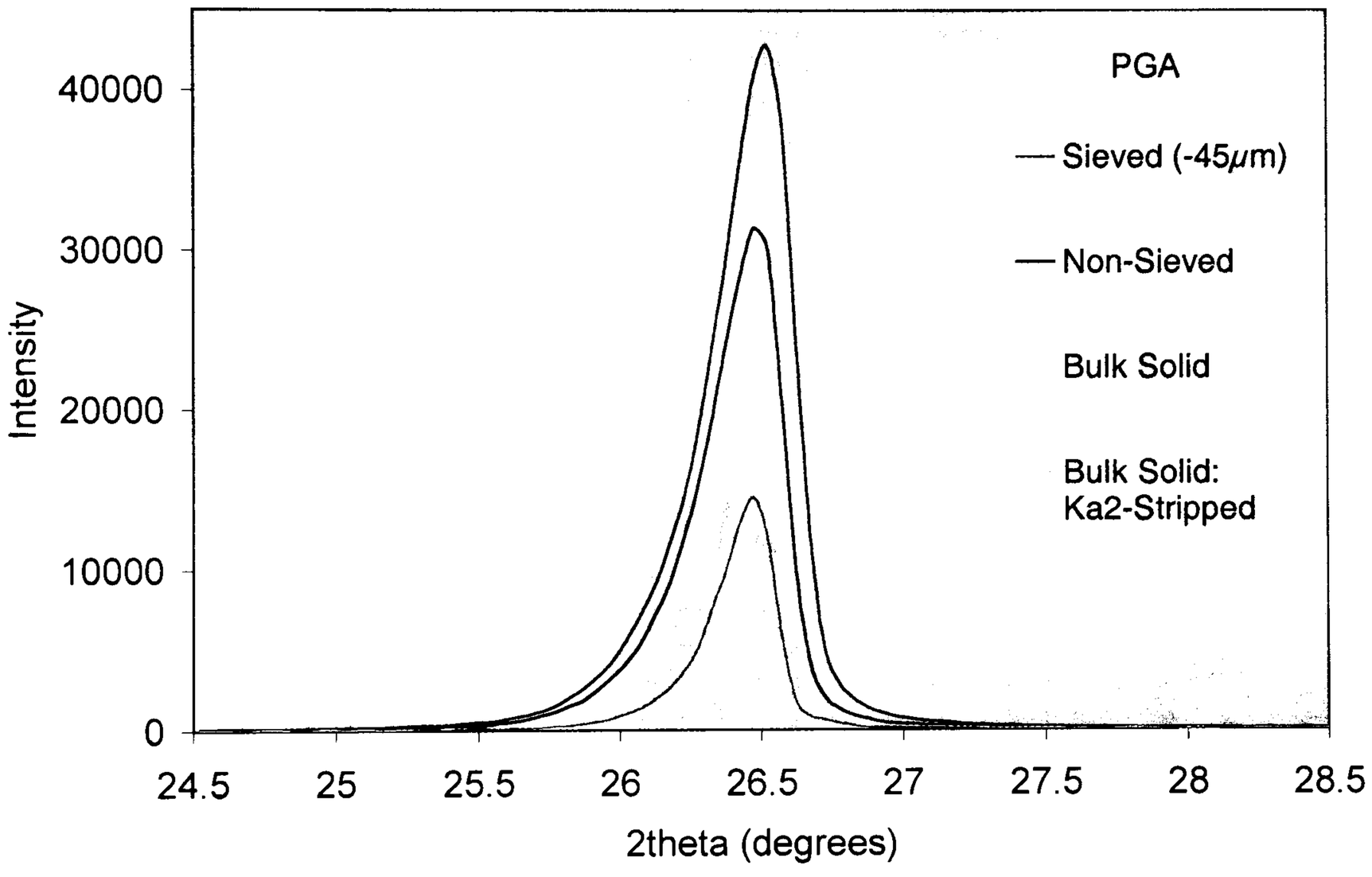

Figure 4.10. Width of 002 peak for non-sieved, sieved, and bulk solid, PGA graphite. Note the reduced width after $K\alpha_2$-stripping.

It is well known that broadening effects are promoted in graphite samples subjected to prolonged grinding (Inagaki & Iwashita, 1993). Grinding promotes disorder in the graphite crystal structure and increases lattice distortion. It is remarkable though, that such a short duration of grinding causes a significant increase in the peak width. It is therefore important to correct the experimental profile for these common broadening effects to avoid underestimating L_a and L_c. This may not be necessary with more disordered carbons.

SECTION 4.4: MEASUREMENT OF ELECTRICAL RESISTIVITY

The electrical resistivity of the nuclear graphites was compared. This is an important indicator of the crystallinity of the materials. The electrical resistivity also provides a means of assessing the uniformity of oxidation in oxidised specimens. The methods used are described below.

4.4.1. Methods used to measure the Electrical Resistivity

The ASTM Standard C611-84 was used as a guideline. This refers to the four point contact method (see Figure 4.11) for measuring the potential across a cross-sectional area (*A*) of the specimen. Using a set applied current and the measured potential across a length of the sample (*L*), the electrical resistivity (ρ) is simply calculated using the well known relation:

$$\rho = \frac{R \,.\, A}{L} \qquad [4.4.1]$$

A series of measurements was taken at increasing gauge lengths on each face of the rectangular specimens. The current was also reversed for each reading.

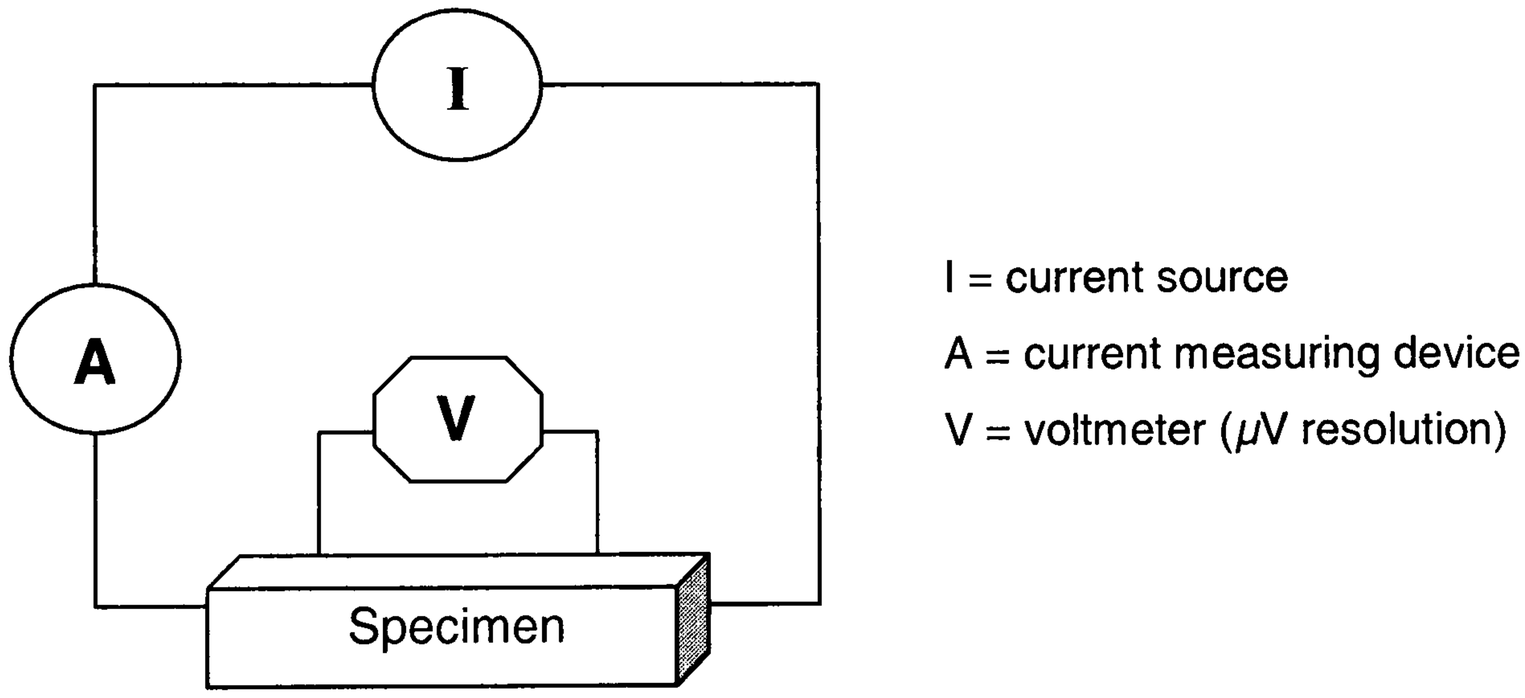

Figure 4.11. Circuit diagram for electrical resistivity measurement.

In constructing the apparatus for measuring the electrical resistivity, a number of criteria specified by ASTM C611-84 were followed. A potential measuring device with μ-volt sensitivity was used. The minimum ratio of specimen length to maximum cross-sectional dimension was kept above 6:1, and, the smallest dimension of the specimen was greater than five times the maximum grain size. Pin contacts were used to ensure that the potential contact area was not greater than 0.5% of the distance between the potential contacts. The gap between potential and current probes was larger than the maximum sample dimension.

4.4.1.1. Set-up of Test Equipment

The electrical resistivity measurements were made in two ways (see Figure 4.12). One method involved the use of a high sensitivity, Blackstar BS-401 ohmmeter. The second method involved the use of a LeCroy 9304M oscilloscope and constant DC power supply. The main reason for applying the second method was to verify this set-up for potential drop tests. The sample is held gently in a polyethylene clamp, between two oversized copper blocks used for current supply. A cover piece on the clamp has ten 1mm holes, spaced 10mm apart, which provide location points for the spring-loaded potential contacts as shown in Figure 4.12. The clamp allows a range of gauge lengths between 10-80mm. Three-point bend specimens (12x10x100mm) were tested.

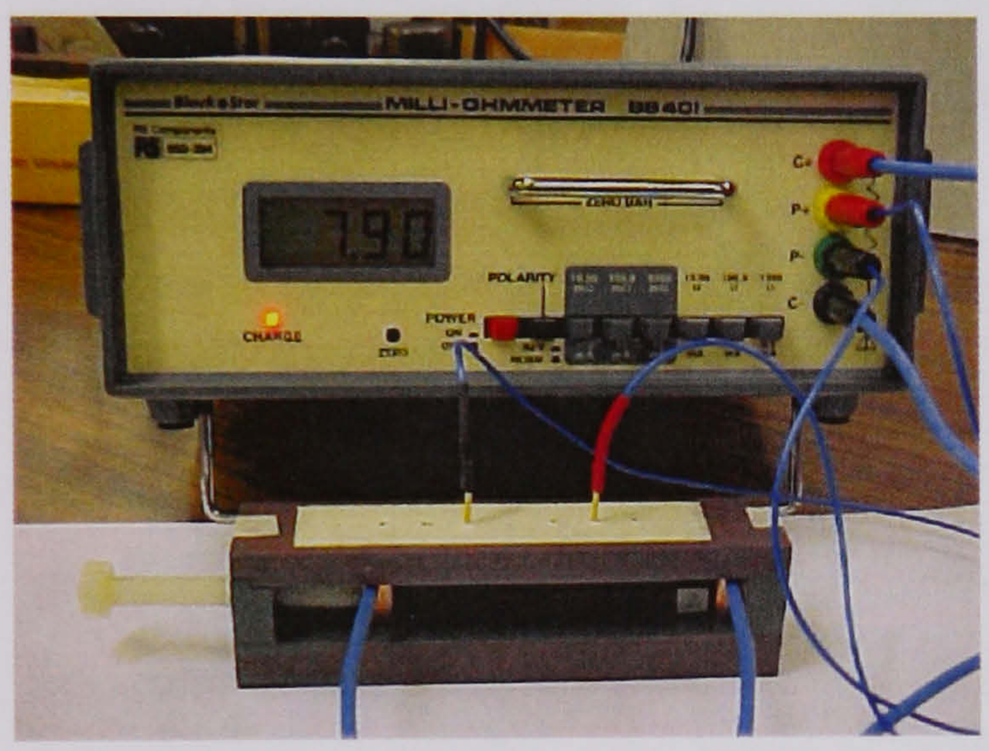

Ohmmeter set-up

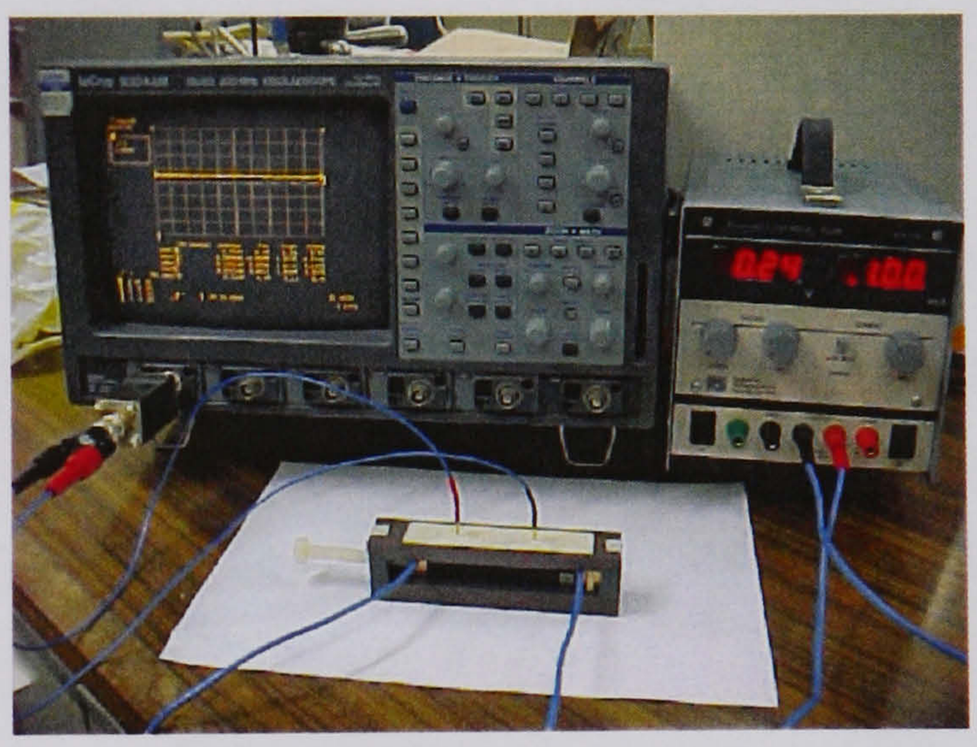

Oscilloscope and power supply

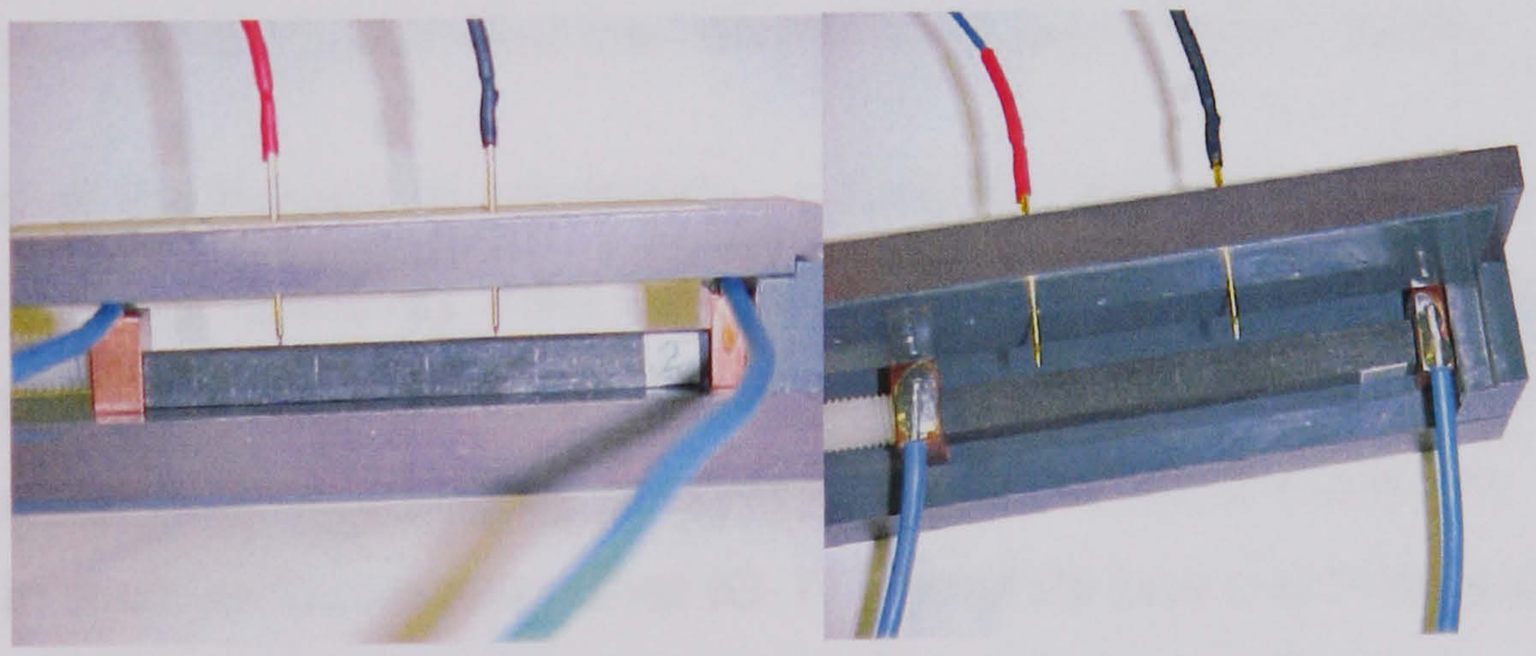

Close-up of current and potential contacts (note: graphite sample)

Figure 4.12. Set-up used to measure electrical resistivity.

The ohmmeter passes current and measures resistance simultaneously, using a fixed current of 100 mA. With the oscilloscope set-up, a 100mA current was applied and the corresponding voltage recorded. Measurements were taken at gauge lengths of 20mm, 40mm, and 60mm on three different specimens.

Readings were taken on each face of the sample for each gauge length using both forward and reverse currents. The average electrical resistivity of the graphites is presented in Table 4.8. Measurement could not be made on PGA graphite because the specimens were too short (15x15x15mm). A typical resistivity value for PGA graphite, parallel to extrusion, is given for comparison.

Table 4.8. Average electrical resistivity values of the nuclear graphites.

Grade	Average Electrical Resistivity (μΩ m)	
	Ohmmeter Measurement	Oscilloscope Measurement
Gilsocarbon	9.53 ± 0.17	9.49 ± 0.28
IG110	12.12 ± 0.08	12.12 ± 0.07
UcarC (parallel)	9.12 ± 0.03	9.18 ± 0.19
UcarC (perpendicular)	9.62 ± 0.09	9.83 ± 0.12

* PGA value (parallel to extrusion) ≈ 6.0 μΩ m (Nightingale, 1962)

The results indicate that IG110 graphite has the highest electrical resistivity, with the remaining graphites showing values between 9.0-10.0 μΩ m. The UcarC graphite has lower resistance in the direction parallel to extrusion. The relatively small difference between the two directions in the UcarC graphite may be due in part to impregnation, which densifies the material. Gilsocarbon graphite has similar electrical resistivity to UcarC graphite perpendicular to extrusion. It is also seen that the two methods give similar results.

In terms of the degree of crystallinity, clearly the more graphitic PGA has much lower electrical resistivity than the other materials. The IG-110 graphite shows markedly higher electrical resistivity. As shown in the previous section, IG-110 graphite has a similar degree of crystallinity to the other materials. It was also shown in the previous section that IG-110 graphite has a similarity porosity level to Gilsocarbon, yet it shows markedly higher electrical resistivity.

The markedly higher electrical resistivity of IG-110 graphite is probably related to its smaller grain size, which increases the number of filler grain-binder interfaces. It may also be that the nature of the filler-binder interfaces in the IG-110 graphite influences its electrical resistivity, particularly if the interfaces are not well bonded or porous.

SECTION 4.5: MEASUREMENT OF THE ELASTIC MODULUS

The elastic modulus is one of the characterising properties of polycrystalline graphite and engineering materials in general. In nuclear applications, the elastic modulus presents a vital indicator of the graphite moderator integrity, with increasing neutron fluence over the life of the reactor. Measurement of the elastic modulus is not always straightforward, particularly with polycrystalline graphite, which shows non-linear deformation behaviour. In this study, the elastic modulus of the graphite materials was needed for crack length calculations by the compliance method, as will be shown later. The bulk modulus values are also needed for comparison with the elastic modulus values obtained by nano-indentation. Two common methods were used, a sonic resonance technique and the flexural modulus measurement.

4.5.1. Sonic Modulus

The attractiveness of the sonic resonance method for measuring the elastic modulus is its simplicity and non-destructive nature. In this technique, a rod of the material is supported at its centre and made to resonate about this point. A longitudinal stress-wave travels down the specimen, being reflected at the opposite end. In the fundamental resonance condition, with the fixed centre of the rod forming a node and its ends vibrating at maximum amplitude, the wavelength is defined by twice the length of the specimen, i.e. $\lambda=2L$. The stress wave down the rod is said to travel at the velocity of sound, the velocity (v) being related to the density (ρ) and Young's modulus by:

$$E=\rho v^2 \qquad [4.5.1]$$

Since, $v=f\lambda$, the elastic modulus can be related to the resonance frequency (f) and the length of the rod (l) by:

$$E = 4l^2 f^2 \rho \qquad [4.5.2]$$

The equipment used to measure the sonic Young's modulus of the graphite materials is shown in Figure 4.13. The rod is made to resonate by applying a periodically fluctuating voltage at one end of the specimen via a charged capacitor. At the opposite end, a transducer senses the resonant condition defined by the specimen vibration.

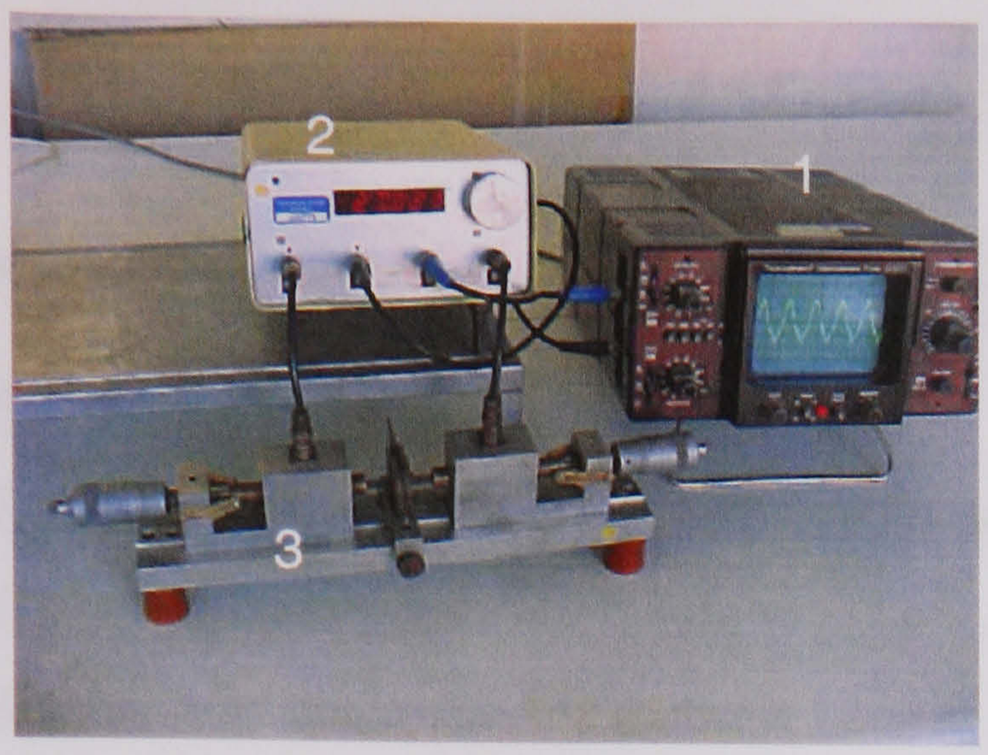

Test set-up

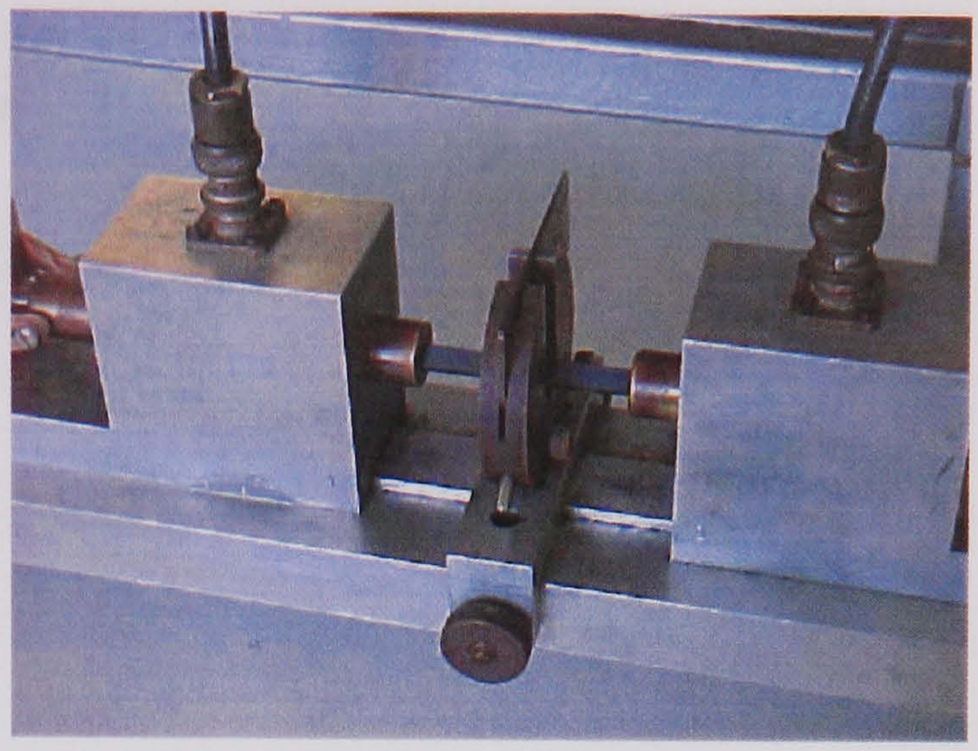

Close-up view of specimen

[1=oscilloscope; 2=frequency detector; 3=sample holder]

Figure 4.13. Arrangement of equipment for measuring the sonic modulus.

For the sonic modulus measurements, rectangular specimens were machined from rectangular half-samples that were sectioned from fractured bend specimens. The dimensions of the specimens were 7x7x45mm.

4.5.2. Flexural Modulus

It is common practice to use the slope of the initial linear portion of the stress-strain curve for calculating the elastic modulus of polycrystalline graphite given that the deformation response is non-linear. Greenstreet et al (1969), fitted the initial part of the non-linear stress-strain (σ-ε) curve with a parabolic function:

$$\sigma = a\varepsilon^2 + b\varepsilon\,, \qquad \therefore \frac{d\sigma}{d\varepsilon} = 2a\varepsilon + b \qquad [4.5.3]$$

The coefficient '*b*' then corresponds with *E*. Greenstreet et al (1970) found the flexural modulus of polycrystalline graphite to be similar to the sonic modulus. They caution that friction between the loading supports produces a bending moment that opposes the applied moment in flexural modulus tests.

Harel et al (1980) showed that there are two methods for obtaining an appropriate *E*-value. One is to use the slope of tangent to the deformation curve, and, the second involves an experimental determination of *E* from flexural tests. However, the elastic modulus in 3-point flexure is affected by the shear modulus (Harel et al 1980, Fischer et al 1980, Allard et al 1991). The flexural modulus is influenced by both the elastic-shear modulus ratio (*E/G*), and, the load span-depth ratio (*S/W*) as dictated by the relation (Allard et al 1991, Mazzei et al 2000):

$$E = E_f\left(1 + \frac{3(E/G)}{2(S/W)^2}\right) \qquad [4.5.4]$$

where,

$$E_f = \frac{S^3}{4BW^3}.m \qquad [4.5.5]$$

E = elastic modulus

E_f = flexural modulus (also referred to as applied or effective modulus)

G = shear modulus

S/W = load span-thickness ratio

m = spring constant (slope of linear portion of deformation curve)

B = specimen width; W = specimen thickness

Therefore, the effective modulus approaches the elastic modulus as E/G decreases, and, S/W increases. Practically, this requires that a large S/W ratio be used to determine E, as highlighted by Figure 4.14.

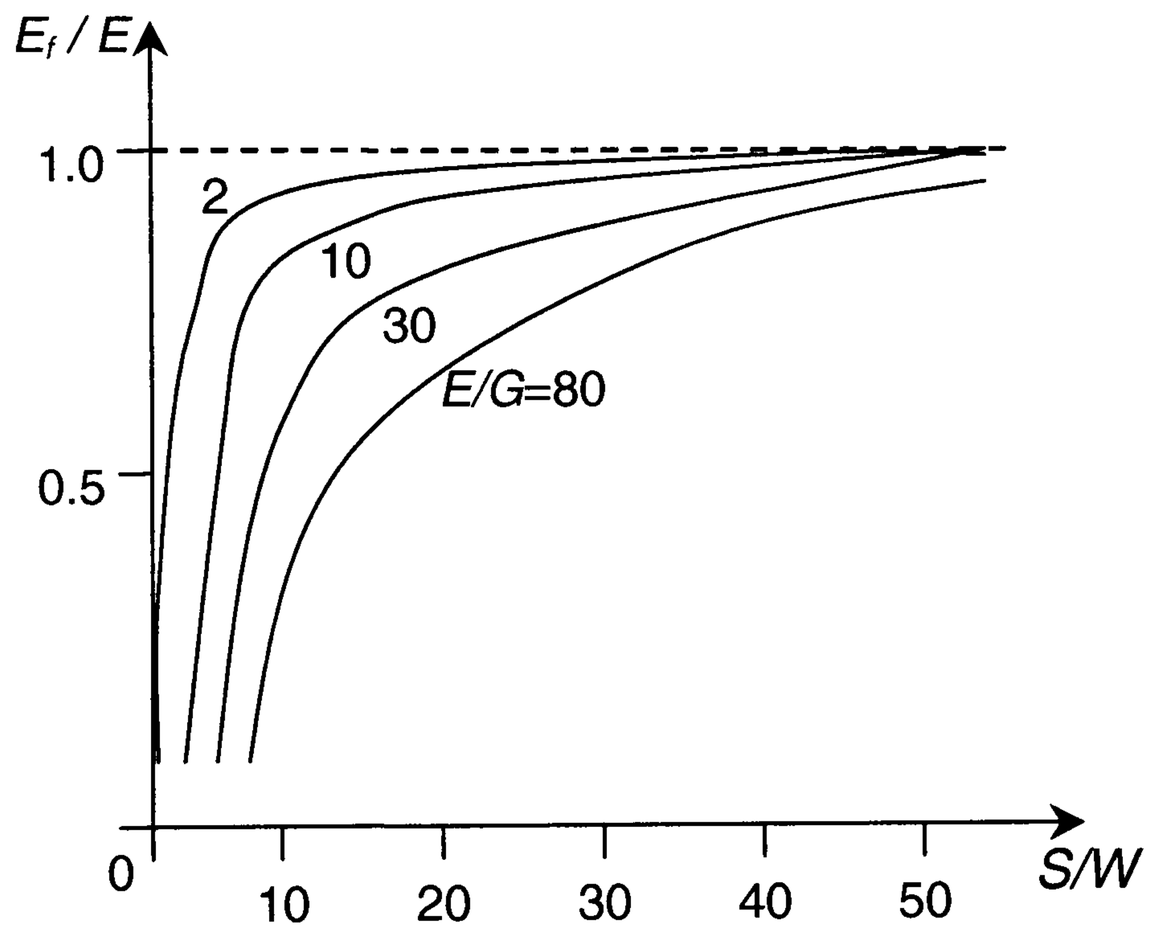

Figure 4.14. Ratio of (E_f/E) versus (E/G) and (S/W) ratios (Fischer et al, 1980).

In more anisotropic materials, the E/G ratio increases, making it more difficult to determine E, due to the requirement of a very high S/W ratio. Determining the 'true' elastic modulus can therefore be a challenge. However, Fischer et al (1980) derived mathematically, an expression for determining the elastic modulus and shear modulus using a single bend specimen, in which only two S/W ratios and their corresponding spring constants are required. The method requires that the spring constant be determined at two different S/W ratios. Using the experimental data so determined, E and G can be calculated from the expressions (Fischer et al, 1980):

$$E = \frac{m_1 m_2}{4B}\left|\frac{A1}{A2}\right| \qquad G = \frac{m_1 m_2}{B}\left|\frac{A1}{A2}\right| \qquad [4.5.6]$$

$$|A1| = \frac{S_1 S_2^3 - S_2 S_1^3}{W^3} \qquad |A2| = \frac{m_1 S_1 - m_2 S_2}{W} \qquad |A3| = \frac{m_1 S_1^3 - m_2 S_2^3}{W^3} \qquad [4.5.7]$$

S_1, S_2 = load spans

m_1, m_2 = spring constants at S_1, S_2

Fischer et al (1980) showed their method to produce excellent correlation with modulus values obtained by other methods using glass-fibre reinforced composite test specimens. It was thus of interest to determine the elastic modulus according to Fischer et al's method (1980) given its simplicity and compare the values obtained with the effective modulus.

To measure the flexural modulus of the specimens, they were tested in 3-point bending using $S/W = 8$ (96mm) and a cross-head speed of 0.100mm/min. To preserve the specimens for further testing, tests were stopped at ~20% of the estimated fracture load. The load-displacement response was recorded on an *X-Y* plotter using a low displacement range to magnify the initial linear portion of the load-displacement curve, from which the value of *m* required for calculating E_f was obtained. To obtain the elastic modulus by Fischer et al's (1980) method, the same specimens were tested using another *S/W* ratio, and, the *E*-values and *G*-values calculated using Equations [4.5.6] and [4.5.7]. The two *S/W*-ratios were chosen relative to the specimen width (10mm) and thickness (12mm), either ratio giving *S/W*=8 when the specimen is tested on the relevant side. The average modulus values, obtained from three specimens are shown in Table 4.9, including the calculated *E/G* ratios and the sonic modulus measurements.

Gilsocarbon and UcarC (parallel) have similar elastic moduli based on their E_f values. Considering the *E*-values for Gilsocarbon and UcarC (parallel), however, this may not be the case. It is also seen that the *E*-values for UcarC (parallel) and UcarC (perpendicular) appear quite similar, unlike the flexural modulus values, which are significantly different. The flexural modulus (E_f) values are significantly lower than the sonic modulus values, with the latter being lower than the *E*-values obtained by Fischer et al's (1980) method.

Table 4.9. Elastic modulus values obtained by the different methods.

Material	E_{sonic} (GPa)	E_f (GPa)	E (GPa)	E/G
Gilsocarbon	11.35 ± 0.04	10.52 ± 0.14	14.41 ± 2.17	14.1 ± 3.7
IG110	8.20 ± 0.16	7.41 ± 0.09	9.48 ± 0.05	11.3 ± 0.3
UcarC (perpendicular)	11.06 ± 0.39	9.35 ± 0.24	13.18 ± 0.92	16.5 ± 3.0
UcarC (parallel)	11.81 ± 0.18	10.75 ± 0.30	13.46 ± 0.72	10.7 ± 4.3

The variation between the different measurements may be due to shear loading effects. Friction at support rollers may also cause a lower flexural modulus to be recorded. This would increase as the load span is reduced. Overall, the results consistently show that the IG110 graphite has the lowest stiffness, followed by UcarC graphite perpendicular to extrusion.

The calculated *E*-values would suggest that the 'true' modulus values of these materials might be higher than that recorded by simple flexural testing or the sonic resonance method. However, the calculated *E/G* ratios are quite large suggesting that higher *S/W*-ratios may be needed to obtain flexural modulus values that approach Young's modulus for the graphites. The practical feasibility of using much higher *S/W*-ratios is questionable.

It is not certain to what extent the calculated *E/G* ratios are reliable since, the *E/G* ratio of UcarC appears to be the highest when flexed perpendicular to the extrusion direction. The *E/G* ratio for UcarC should be higher parallel to extrusion because the *E/G* ratio increases with increasing anisotropy (see Figure 4.15). The isotropic IG110 graphite also shows a higher *E/G* ratio than UcarC parallel to extrusion, which also seems unlikely. This aspect of the mathematical approach by Fischer et al (1980) requires more rigorous examination.

SECTION 4.6: SUMMARY

Microstructural examination highlighted important structural differences between the selection of nuclear graphites characterised in this part of the study. Grades PGA (average grain size≈1mm) and Gilsocarbon(≈0.5mm), and, UcarC(≈0.22mm) were seen to comprise much larger filler grains than IG-110 (≈20μm). The large needle-coke grains in PGA graphite display a high degree of texture. Polarised light microscopy and XRD analyses showed the PGA grade to be more highly graphitised than the other grades.

Gilsocarbon graphite showed some texture within the spherical Gilsocoke grains. In the fine-grained IG-110 graphite, texture becomes evident at higher magnifications under polarised light, with the larger needle-coke grains mainly showing orientation. The UcarC graphite is similar to the PGA graphite in that it also comprises large, highly textured, needle-coke grains. However, XRD analyses indicated that the degree of graphitisation of the UcarC grade is lower than that of the PGA grade, being similar to the Gilsocarbon and IG110 grades. These three grades were similar in terms of the interlayer spacing and crystallite size measured by XRD. However, the electrical resistivity of IG110 grade was markedly higher than Gilsocarbon or UcarC, mainly due to its fine grain size.

It was not easy to distinguish clearly the binder phase in the graphite structures, using both optical, and, electron microscopy. The binder regions between the filler particles appear as a mass of very-fine grained material in the SEM, and, as fine blue-yellow regions with random orientation under polarised light. The binder phase may be regarded as the mass of very fine graphitized particles surrounding the large, more notably textured grains. This distinction is however not always clear since the binder and matrix blend well in many instances.

It was confirmed using both polarised light and SEM, that the mosaic structure observed in the Gilsocarbon structure is a region of coarser, randomly oriented particles, often located on the periphery of the filler grains and sometimes in the binder. Both chemical and oxidative etching appear to expose the Gilsocarbon grains and lenticular cracks within these grains more clearly but seem to cause undesirable attack of the surface implying that they may be difficult to control.

Mercury porosimetry indicated that the UcarC graphite has markedly higher density than the other grades due to its being impregnated. This also makes UcarC the least porous material with the highest percentage of close porosity. PGA graphite showed the highest open porosity. The 'true' density of the graphites was not markedly different, PGA being an exception with a value close to the theoretical maximum, re-emphasising its highly graphitic nature. There were some anomalies in the mercury porosimetry results suggesting that internal damage may have been caused at high intrusion pressures.

Porosimetry indicated that PGA, IG110, and, Gilsocarbon graphite had unimodal pore size distributions, while the UcarC grade showed a bimodal distribution. The higher open pore volume of PGA, Gilsocarbon, and, IG-110 supports observations made by fractography which show that these graphites have a relatively open pore structure. The high open-pore volume in the IG110 graphite points to the existence of a fine, interconnected pore network. The lower open-pore volume of UcarC is again a clear sign of impregnation.

A comparison of different methods used for measuring the peak width that is used for crystallite size calculations by the Scherrer equation revealed that all the methods gave similar results. Interestingly, the crystallite size measured using bulk solid specimens was significantly larger than that obtained using conventional powder analyses, because grinding physically reduces the crystallites, in addition to promoting structural disorder. The measured crystallite size was also substantially reduced by the $K\alpha_2$-radiation. It is thus recommended that peak broadening due to grinding and non-monochromatic, radiation are avoided to prevent underestimating the crystallite size.

Sonic modulus measurements were higher than flexural modulus values, probably due to experimental error in the flexural modulus tests. The UcarC graphite had highest stiffness along the extrusion direction as expected. Impregnation probably also contributes to the higher stiffness of the UcarC grade. Mathematical calculation of the Young's modulus produced elastic moduli that were significantly higher than the experimentally obtained values. The reliability of the mathematical approach requires further study given that the *E/G*-ratio for IG-110 was higher than that of UcarC (parallel) to extrusion, which seems an unlikely result since IG-110 is an isotatically pressed graphite.

CHAPTER 5

DEVELOPMENT & APPLICATION OF THE POTENTIAL DROP METHOD

The development and application of the potential drop technique for *R*-curve measurement is detailed in this section. The machining and preparation of specimens for potential drop measurements are included as part of the developmental work. Various aspects that were evaluated in the development of the method form a large part of this chapter. Calibration procedures are also described as part of the developmental work.

5.1. Preparation of Specimens

5.1.1. Machining the Specimens

Graphite is a non-hazardous material with the exception that a very fine dust is generated during machining making dust extraction necessary. Due to a lack of dust extraction facilities as well as very high machining costs, an alternative machining route was devised (see Figure 5.1). A slice of the material, of slightly larger thickness than that required for the final specimen thickness, is cut from the large block supplied by the manufacturer. This slice is then sectioned using a mini-band saw with a dust extraction nozzle that is connected to a domestic vacuum cleaner. A limited amount of dry milling is done only to level the slice and reduce it to the desired thickness.

During milling, a vacuum cleaner nozzle is mounted above the work-piece to reduce the dust. After milling, the levelled slice is sectioned into sample lengths using the band-saw. The sample lengths are cut to a width slightly larger than that required for the finished specimen. The rough cut faces of these lengths, which are roughly parallel having been cut with the guide, are attached to the underside of an aluminium wheel specifically designed to adapt to a Buehler Motopol grinding/polishing machine. The sample lengths are attached to the wheel using a combination of masking tape and double-sided tape. In a series of grinding steps, the sample is carefully ground until opposite faces are parallel and the specimen is of the required width and thickness. The compact tension specimens are prepared in a similar way but require drilling for the pin-holes. An advantage of this technique is that the specimen can be polished if required.

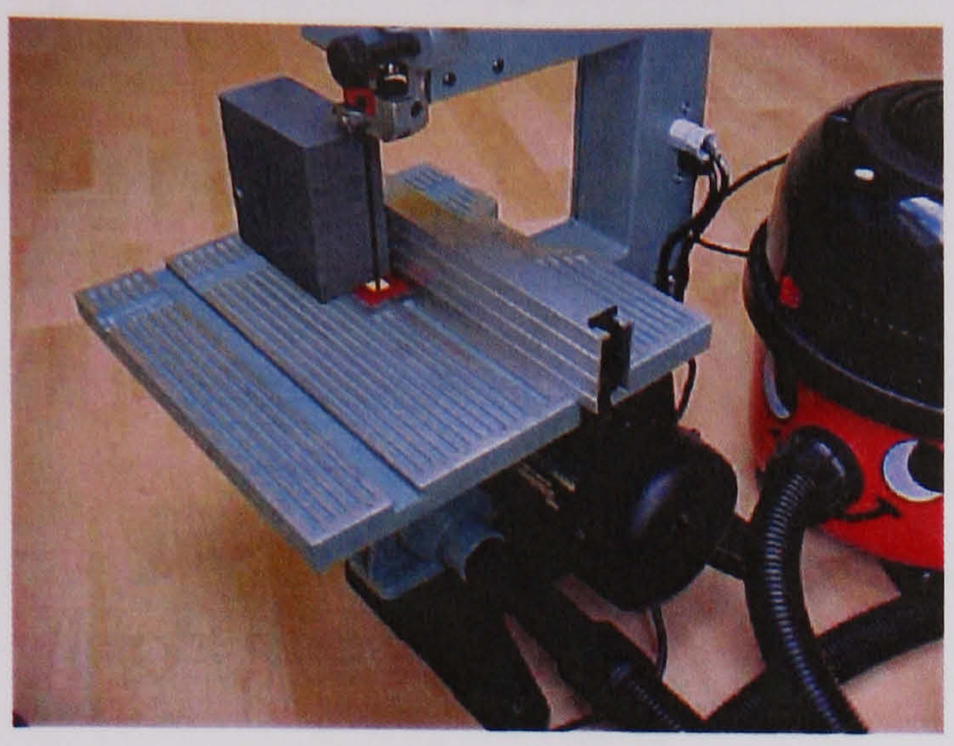

1. Cutting a slice from a large block.

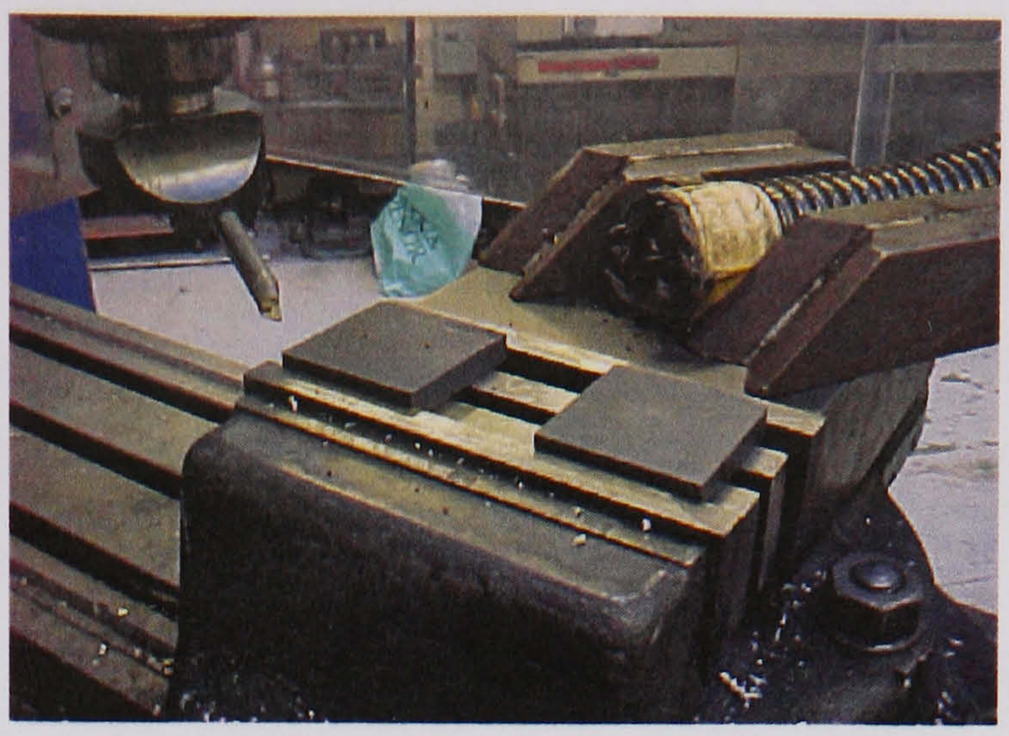

2. Levelling opposite faces of the slice.

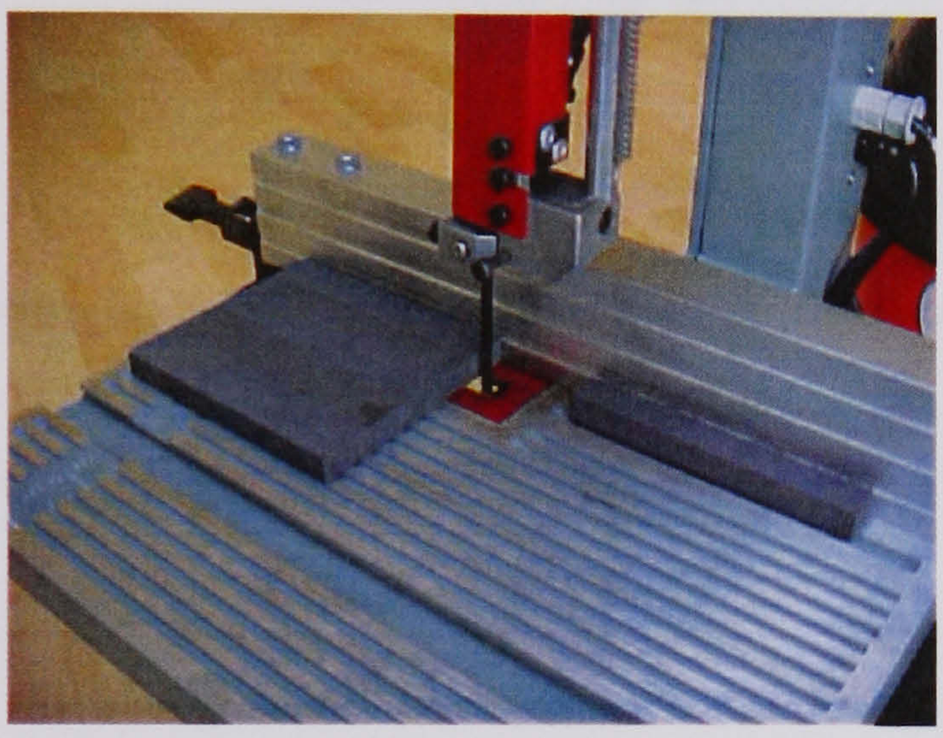

3. Sample lengths cut from the slice.

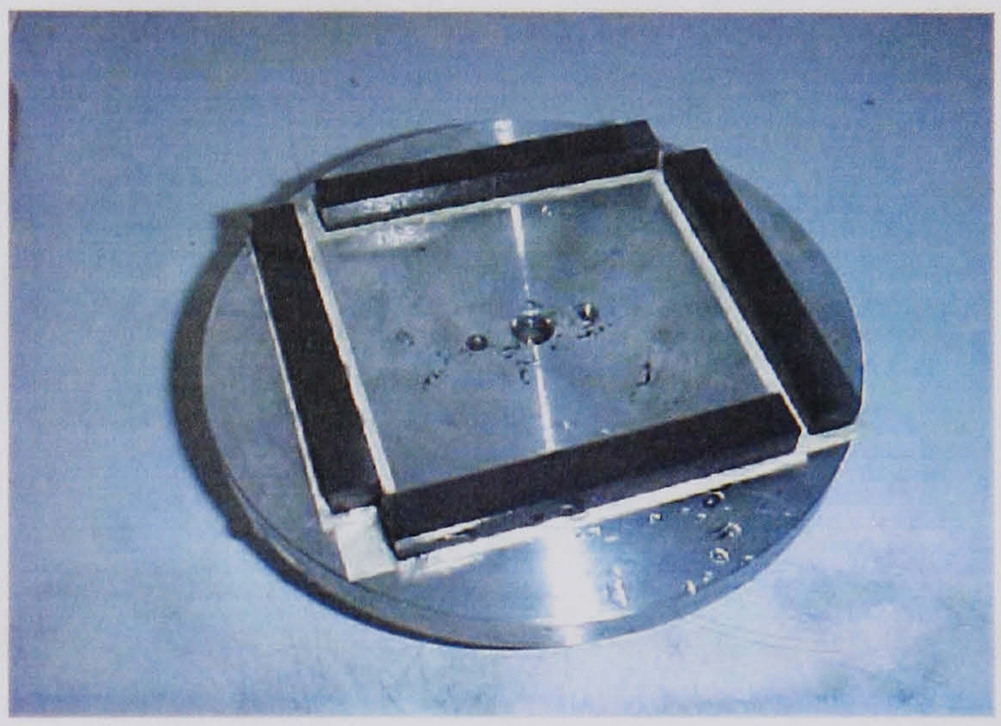

4. Sample lengths attached to the disc.

5. Grinding samples to final dimension.

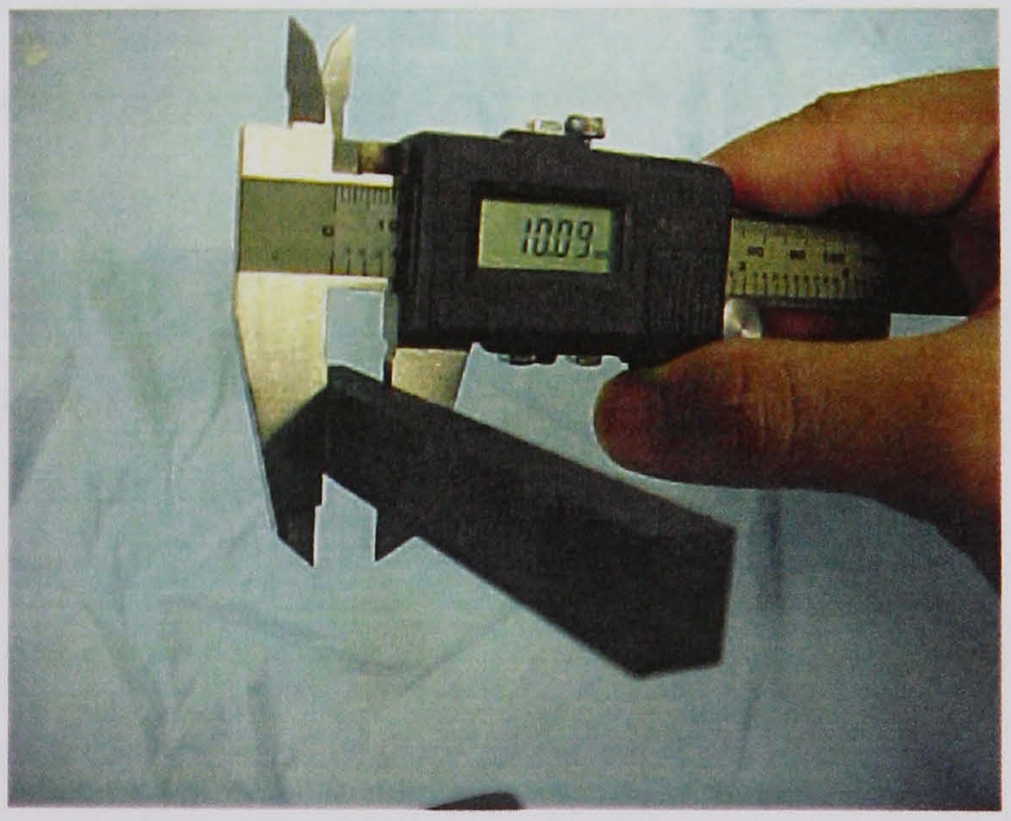

6. A finished specimen.

Figure 5.1. Procedure used to machine the specimens.

5.1.1.1. Accounting for the Extrusion Direction in the UcarC Graphite

As it was expected that the UcarC graphite might display directional properties due to it being extruded, the UcarC specimens were cut such that the crack path was parallel or perpendicular to the extrusion direction. That is, the fracture path traverses parallel or perpendicular to the preferred orientation of the filler grains. This is shown schematically in Figure 5.2.

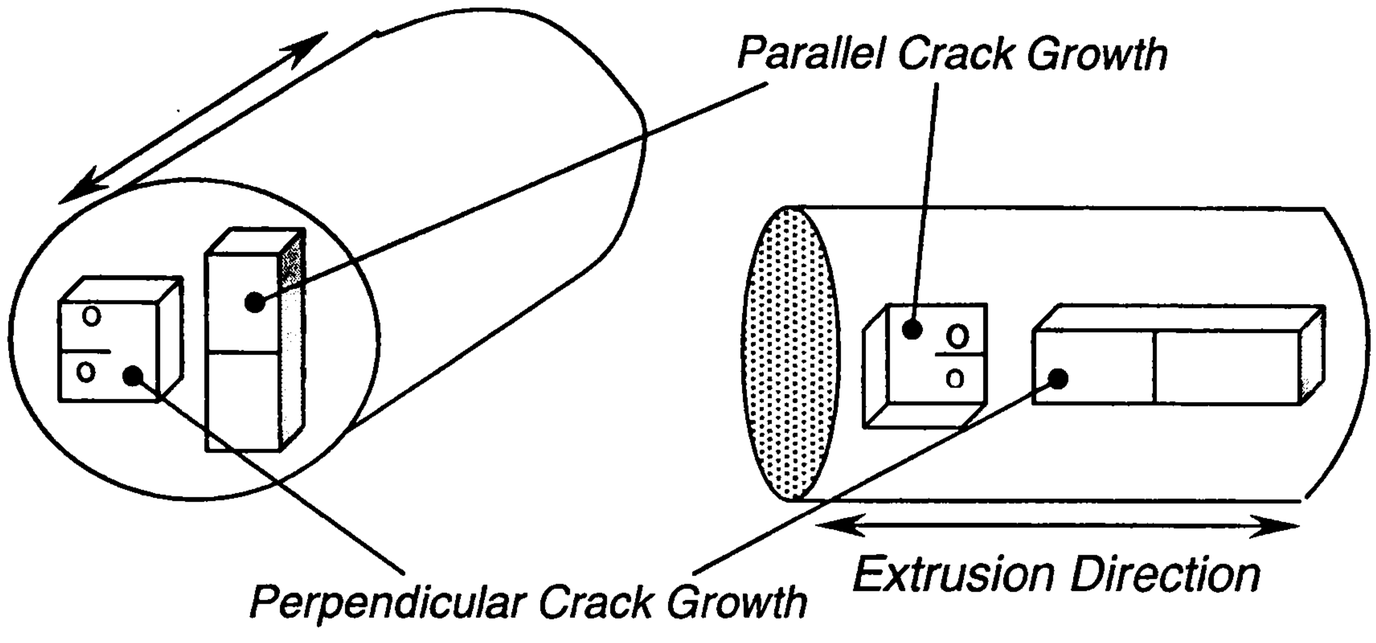

Figure 5.2. Orientation of notch relative to the extrusion direction in UcarC graphite.

5.1.2. Wiring the Specimens

Several criteria were important for wiring the specimens for potential drop tests:

1. Current and voltage probes had to be securely fixed to the specimens without any mechanical fixing.
2. The location and positioning of these probes had to be consistent for all the specimens to ensure reproducibility.
3. The current input area had to be large to avoid concentrating the charge density and causing localised heating effects.
4. Thin voltage probe wire was needed to help reduce any error caused by imprecise location of the voltage probes.

Following some preliminary work, a suitable procedure was developed to satisfy these criteria. The procedure is illustrated in Figure 5.3. Thin (0.25mm diameter), silver-plated, copper-wire with a maximum current rating of ~3A is used for the current and voltage probes. The wires are fixed to the specimen using a conductive epoxy solder (Circuit Works Conductive Epoxy CW2400). Each end of the specimen is coated with a layer of silver paint (RS 186-3230 Conductive Paint) prior to soldering the wires.

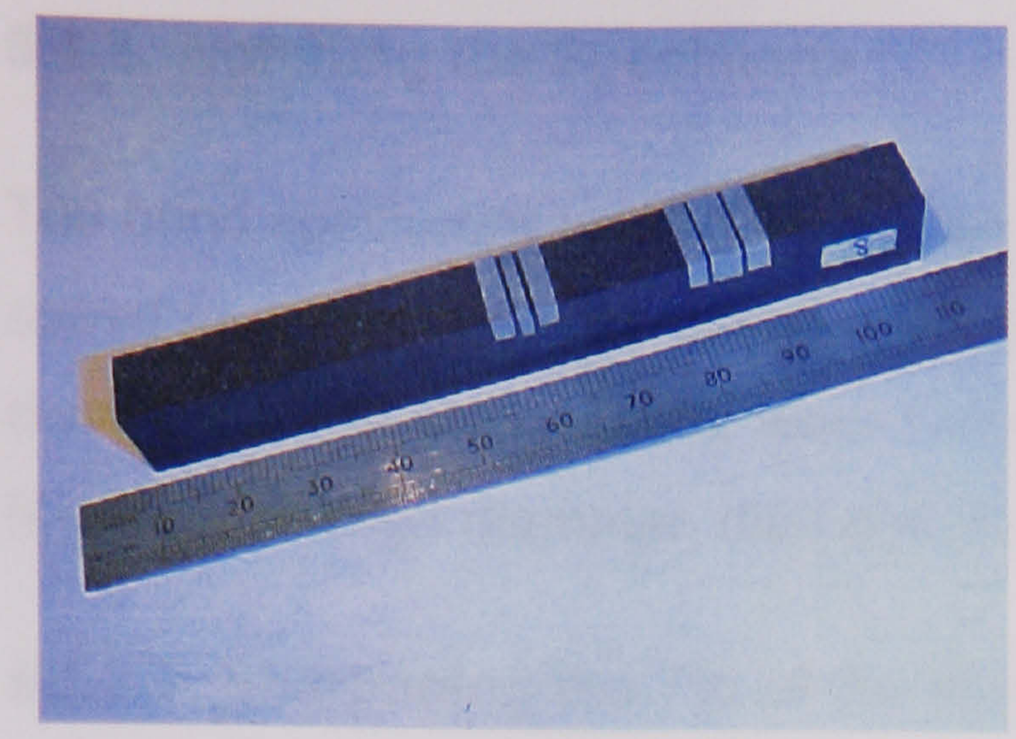

1. Masked voltage probe locations.

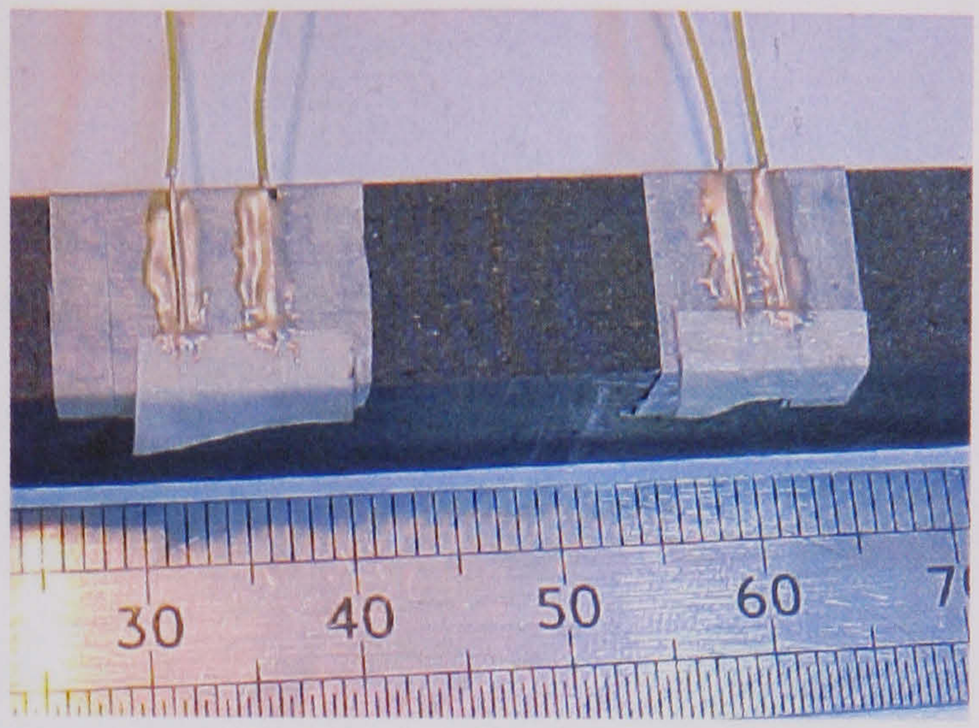

2. Wires soldered over the silver paint.

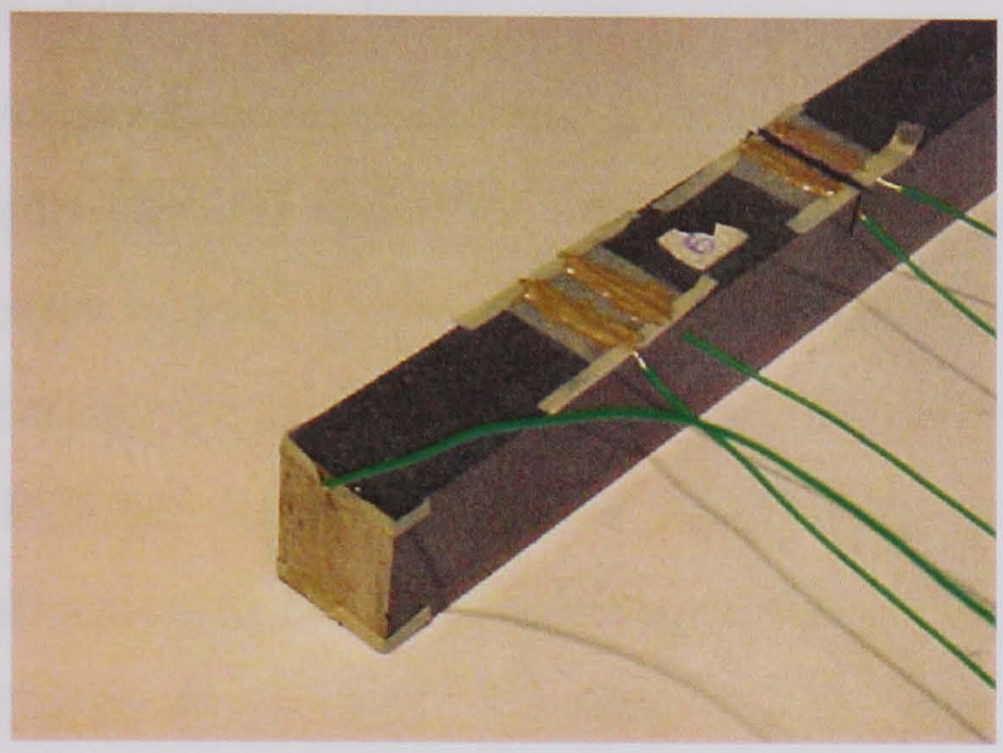

3. Completed bend specimen.

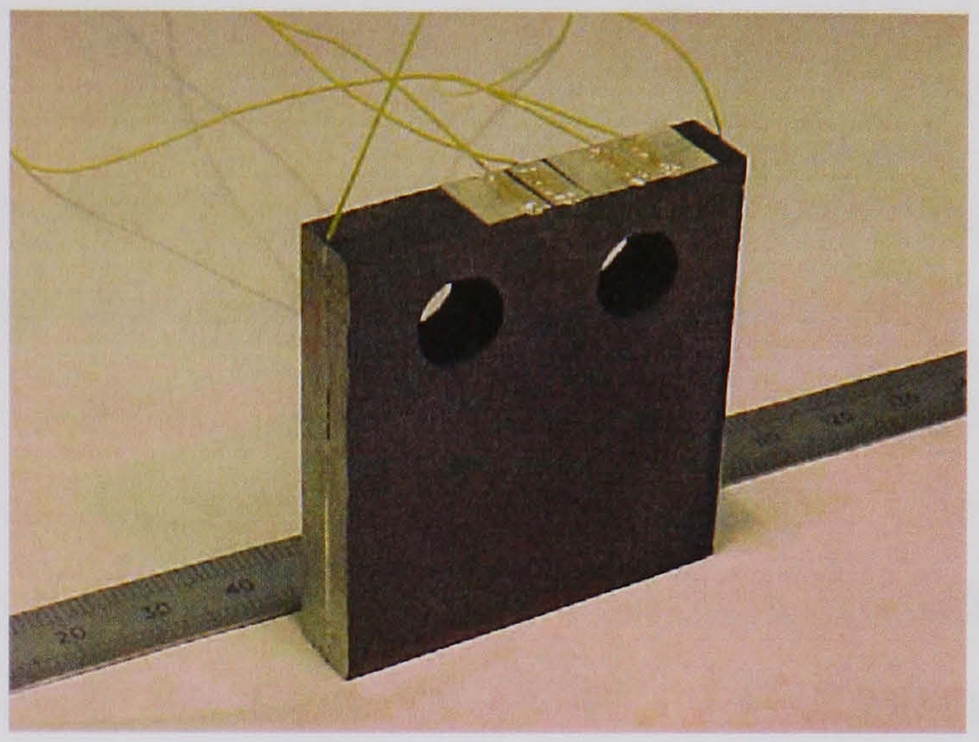

4. Completed compact tension specimen.

Figure 5.3. Wiring the specimens for the potential drop tests.

As the epoxy solder is costly, it is more cost effective to apply a layer of silver paint over the current and voltage probe sites first. The silver paint penetrates the porous graphite surface more effectively than the epoxy solder and helps to spread the current input area. The silver paint is cured, before the wires are soldered in place, by heating at 110 °C for 15 minutes which optimises its conductivity. The epoxy solder is also cured at 110 °C for 15 minutes to improve its adhesive strength and conductivity. Whereas curing the silver paint is not important to sample integrity, curing of the epoxy solder is.

Although the wire has a very low current rating of ~3A, it offers the advantage of avoiding mechanical fixing of the probes. The current probes on the bend specimens were fixed at the two ends of the specimen because this produces a uniform field, which is said to improve reproducibility of the method. Since a uniform field distribution cannot be obtained in the compact tension specimens, the current probes on these specimens were positioned along the two edges, either side of the notch, as shown in Figure 5.3.

5.1.3. Notching the Specimens

The bend specimens were notched using a milling machine fitted with a variable speed motor for driving a diamond-impregnated cutting wheel (t=0.25mm). The compact tension specimens were notched on an Elliot 4100 grinding machine fitted with a large diameter, diamond impregnated cutting wheel (t=0.8mm).

5.1.3.1. Sharpening the Tip of the Notch

In preliminary tests, using a travelling microscope to observe crack growth in polished bend specimens, it was apparent that cracks grew from the blunt notch with varying stability. More often, cracks grew in an unstable manner from the blunt notch. Crack initiation was rapid with the crack propagating well over half the specimen thickness before the crack seemed to stabilise. It was therefore decided to sharpen the notch tips to encourage stable crack growth. The effectiveness of sharpening the notch tip with a razor blade is well-documented (Sakai et al 1988, Hiramatsu & Okada 1998, Kostopoulos 1998). To sharpen the notch, a jig was designed to be fitted alongside the notch-cutting machine (see Figure 5.26). The bottom end of the jig forms a clamp for holding the sharpening tool. This allowed the depth of sharpening to be controlled.

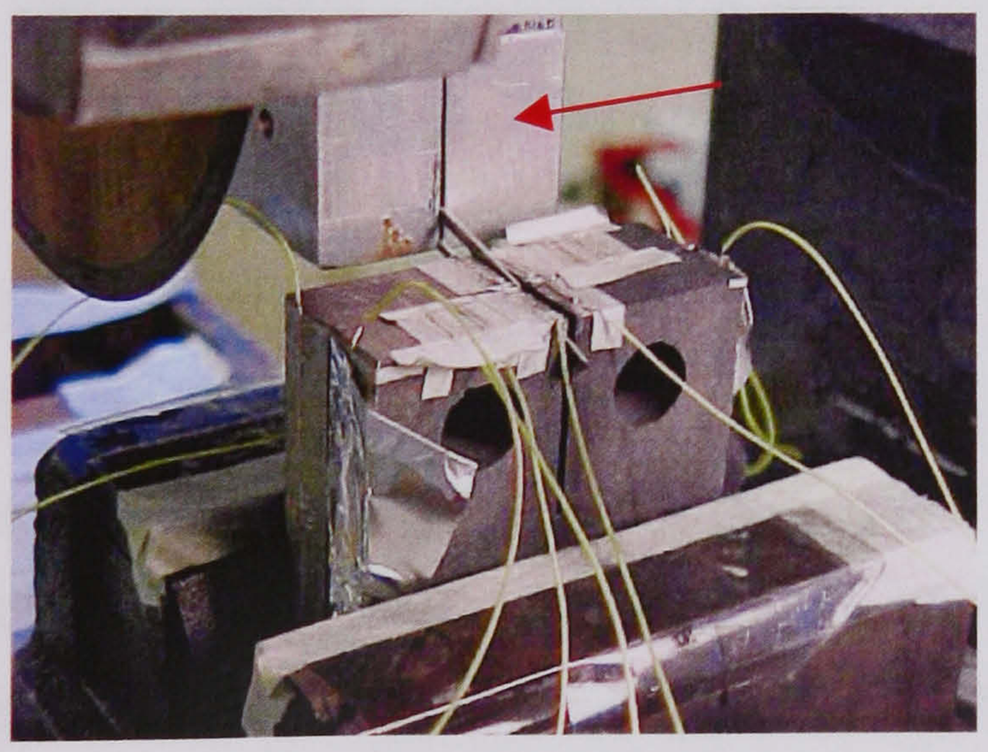

Compact tension specimen

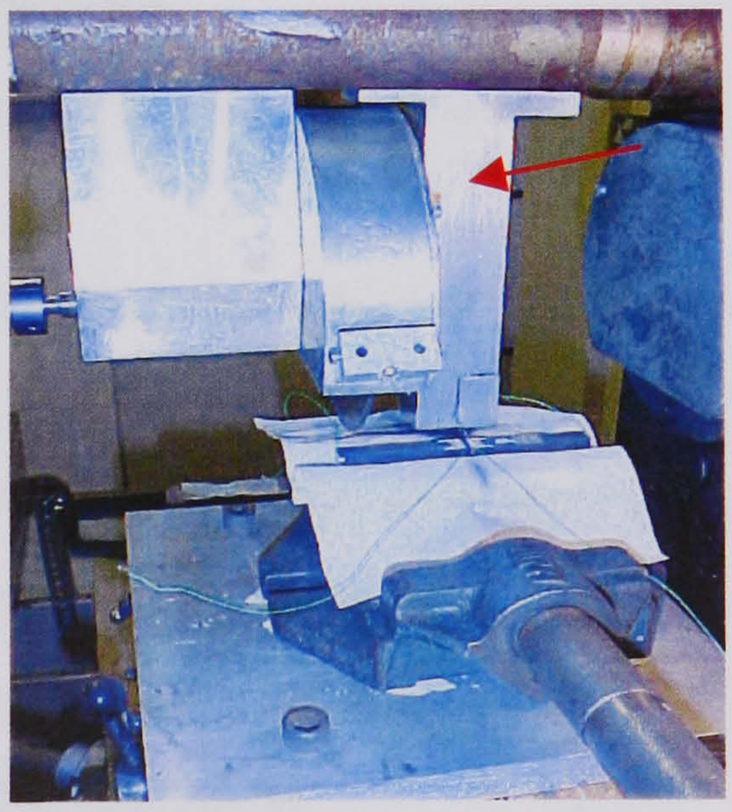

Bend specimen

Figure 5.4. Jig used for notch-tip sharpening.

Trial runs showed that the notch could only be sharpened by ~0.4-0.5mm because the sharpened edge of commercial blades is only ~0.5-0.6mm wide. Beyond this, the blade is uniformly thick and acts like a wedge causing premature failure of the specimen. One limitation of this method is that it may not be applicable to hard materials, unless a suitably hard sharpening tool is used.

5.2. Improvements to the Initial Test Set-up and Test Conditions

The initial test set-up used for potential drop measurements is shown in Figure 5.5. This set-up consists of a Mayes SM-50 mechanical test machine, a constant current DC power supply (max. output~3A), a PC for capture and storage of data, and, a LeCroy 9304M oscilloscope. Load, displacement, and, voltage data is fed to the PC via the GPIB (general purpose interface board) of the oscilloscope. This initial set-up was used to investigate and improve various aspects of the technique.

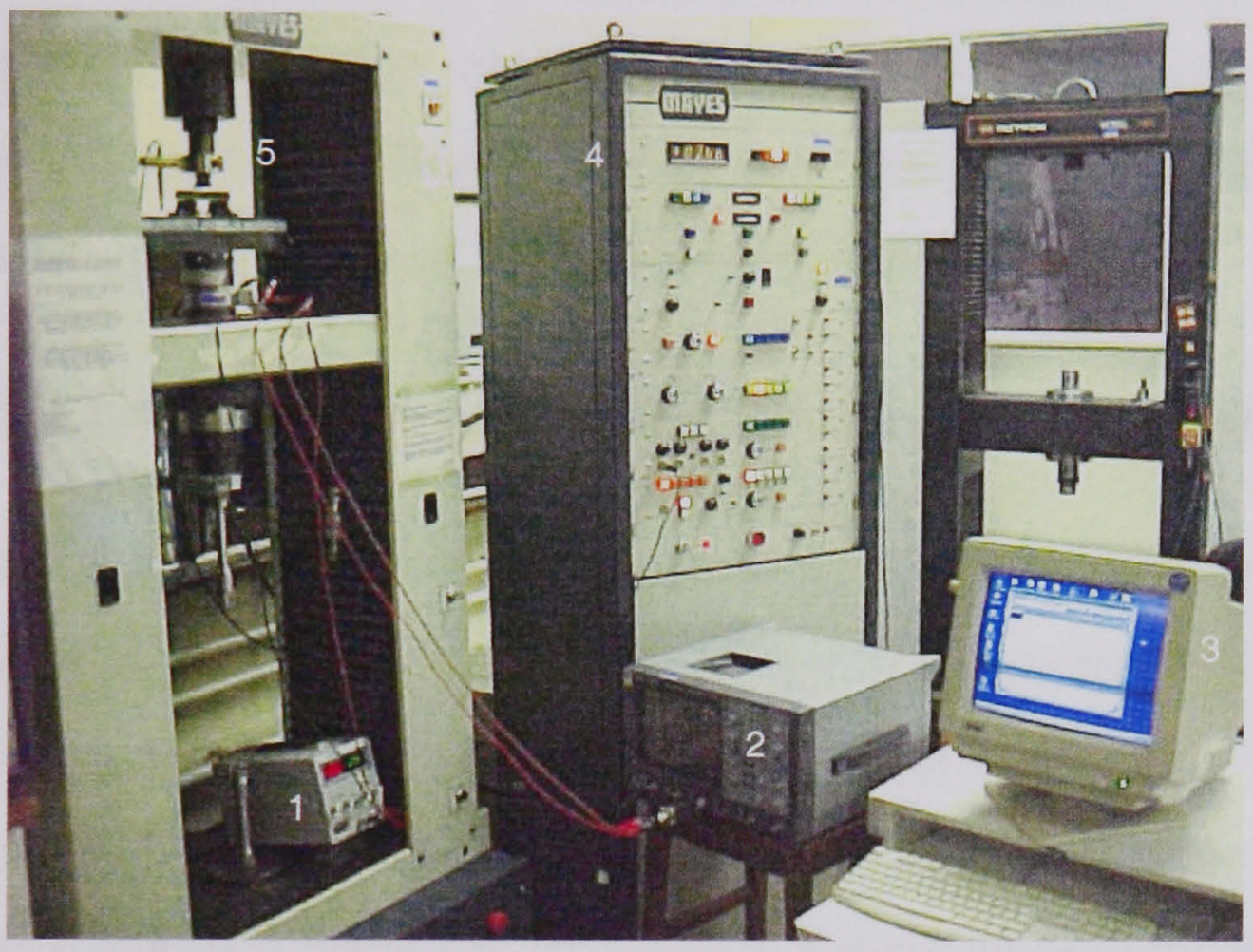

Figure 5.5. Initial test set-up used for potential drop measurements.

This initial set-up was improved by employing only the LeCroy 9304M storage oscilloscope for data capture. This removed the need to interface with the PC and allowed tests to be observed on-screen. Previously, the success of the data transfer and capture process could only be confirmed after the test. The oscilloscope stores data in binary form and this requires conversion to ASCII format using proprietary LeCroy Scope Explorer software.

An important factor for promoting stable crack growth is to reduce the speed of testing. The normal analogue control on the Mayes SM-50 allows a minimum speed of 0.200mm/min. This is relatively high considering that researchers employ lower speeds of ~0.005 mm/min (Sakai et al, 1988). To achieve lower test speeds, the analogue control was substituted by a digital ramp control (see Figure 5.6). This allowed much lower test speeds to be achieved.

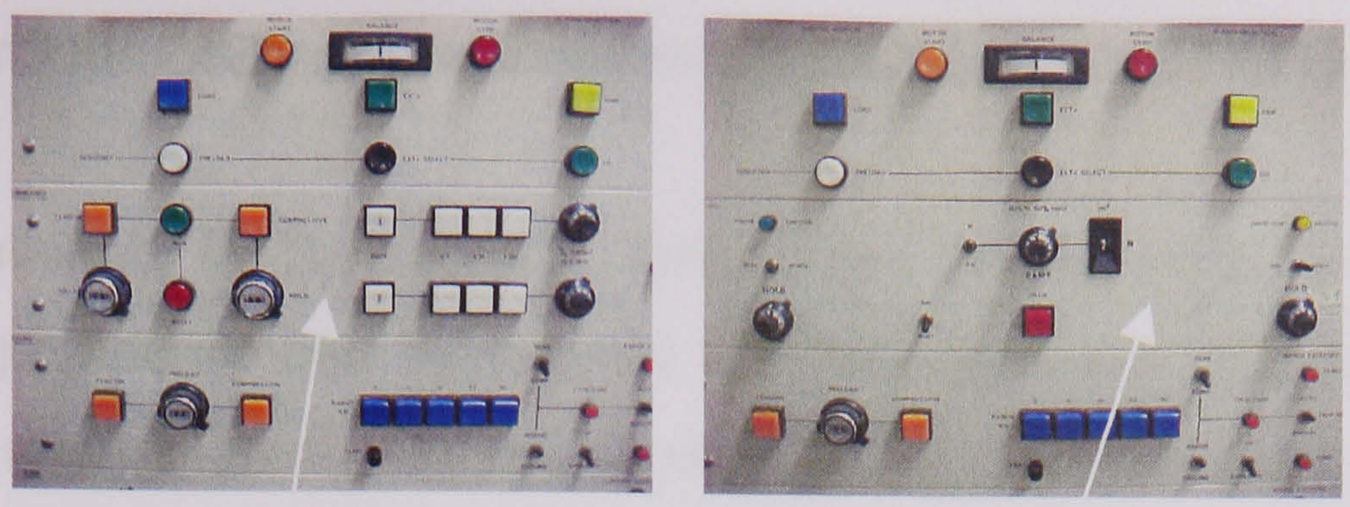

Analogue control Digital ramp control

Figure 5.6. Replacement of analogue ramp control by digital ramp control.

5.3. Aspects Evaluated in the Development of the PD Method

Various aspects of the method were investigated with the aim of developing the set-up and test conditions that would provide optimum sensitivity and reproducibility. The following sections outline the aspects that were evaluated and the outcome of these investigations.

5.3.1. Resolution of the Test Set-up and Equipment

To evaluate the sensitivity of the method to crack propagation, a simple test was performed. Gilsocarbon bend specimens of thickness W=14mm were prepared with voltage probes spaced at 5mm either side of the notch. A current of 1A DC was passed while the specimen was sectioned in a controlled manner in 0.025mm intervals and the potential drop monitored. This represented the smallest depth of cut possible with the available equipment. Figure 5.7 shows the voltage change with cut depth and clearly indicates that the equipment is able to detect crack increments of at least 0.025mm.

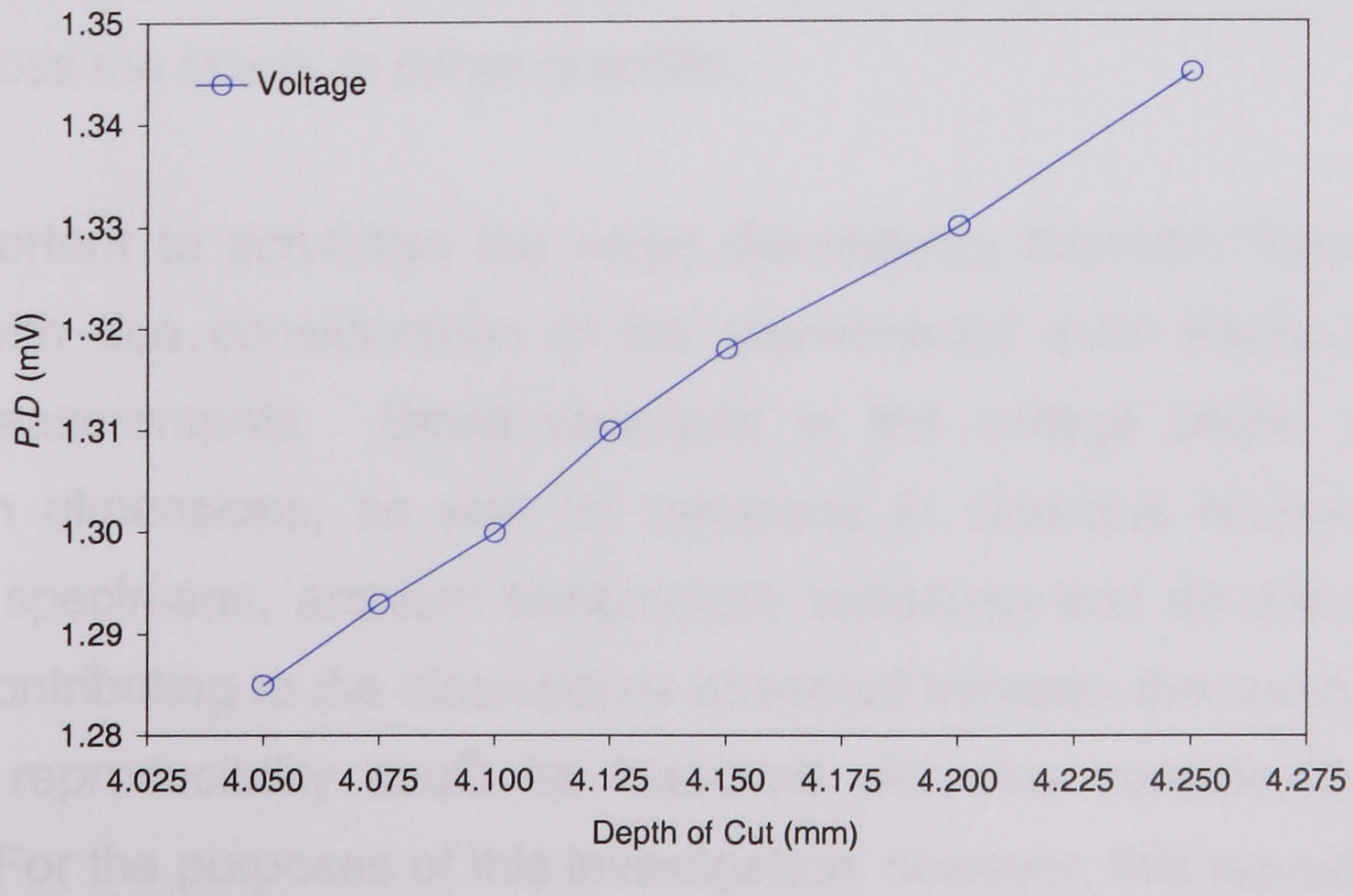

Figure 5.7. Potential drop (*PD*) in a Gilsocarbon, bend specimen with 0.025mm cuts.

5.3.2. Reproducibility of the Experimental Calibration Method

It was explained in Section 2.4 that, either a theoretical or experimental calibration procedure can be applied with the potential drop method. In this study, the experimental method of saw-cutting specimens to simulate crack growth was opted for in favour of the theoretical method mainly due to its simplicity. It was however uncertain as to how reproducible the experimental calibration technique would prove. It was understood from literature that the reproducibility of the method diminished when the voltage probes are placed closer to the notch plane. There was also a concern that data obtained from calibration specimens might not be directly applicable to test specimens given the porous, heterogeneous nature of the graphite material.

To confirm the reproducibility of the experimental calibration method, bend specimens of Gilsocarbon (W=14mm) and IG110 (W=12mm) graphite were sectioned and the potential drop measured using voltage probes located at 30mm, 10mm, and, 5mm across the notch. In this way, the reproducibility of the calibration method was tested for two different grades of graphite using voltage probes placed at closer proximity to the notch plane.

The result of these tests is shown in Figures 5.8 and 5.9 for the Gilsocarbon and IG110 specimens respectively. The calibration curves obtained for both graphites appear highly reproducible, even when the voltage probes are placed quite close to the notch. There was no significant difference in the reproducibility of the curves obtained with the voltage probes placed at 30mm or 5mm across the notch, in either graphite.

It is important to scrutinise the small discrepancy between these calibration curves with due consideration of the experimental error involved in making these measurements. Small variations in the voltage probe position and specimen dimensions, as well as variations in electrical resistivity between different specimens, ambient temperature variations and electrical noise, are factors contributing to the discrepancy observed between the curves. It is likely that the reproducibility could be improved with due consideration of these factors. For the purposes of this investigation, however, this reproducibility was considered adequate.

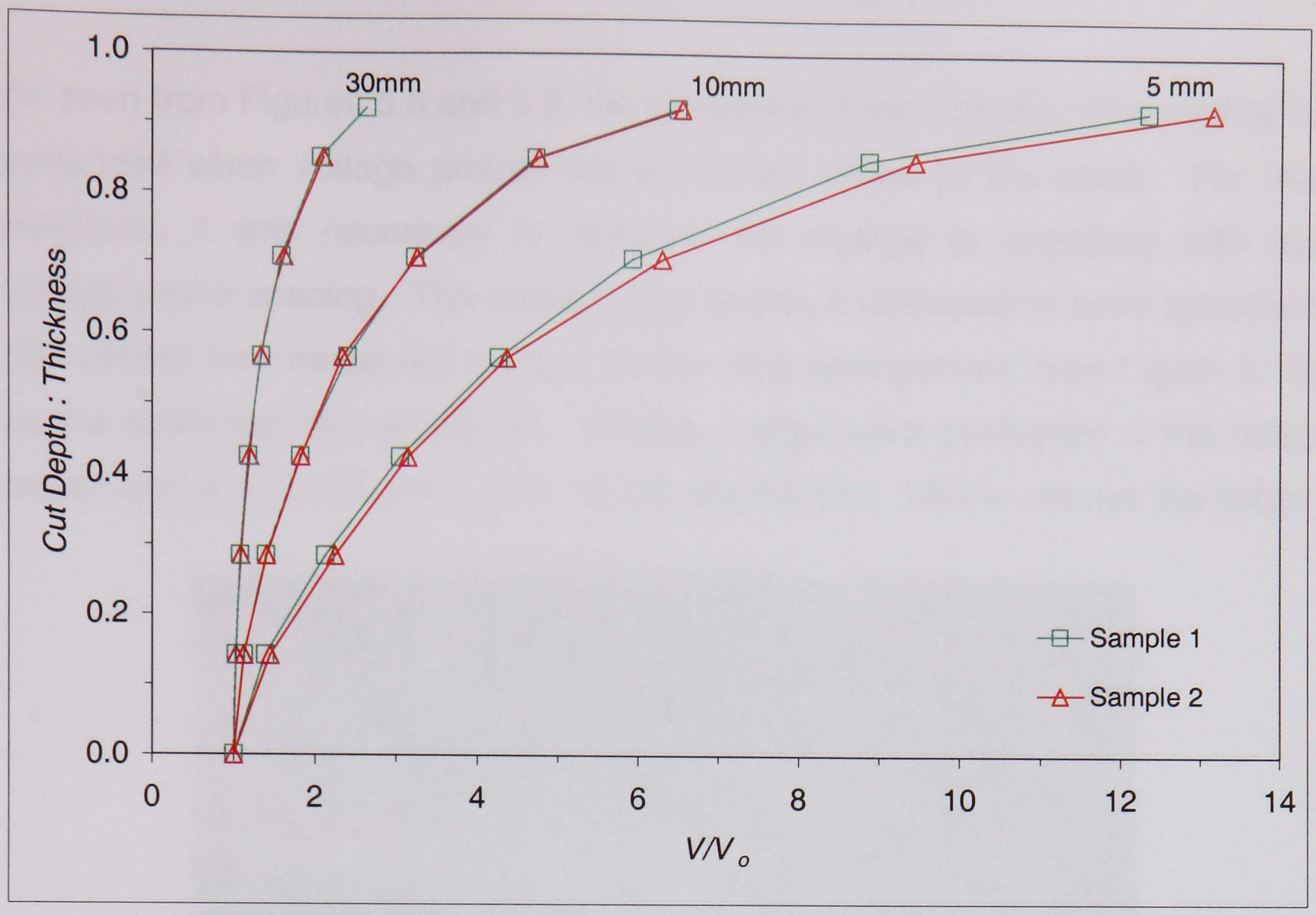

Figure 5.8. Reproducibility of calibration curves for different voltage probe spacing: Gilsocarbon graphite, W=14mm, *i*=1A.

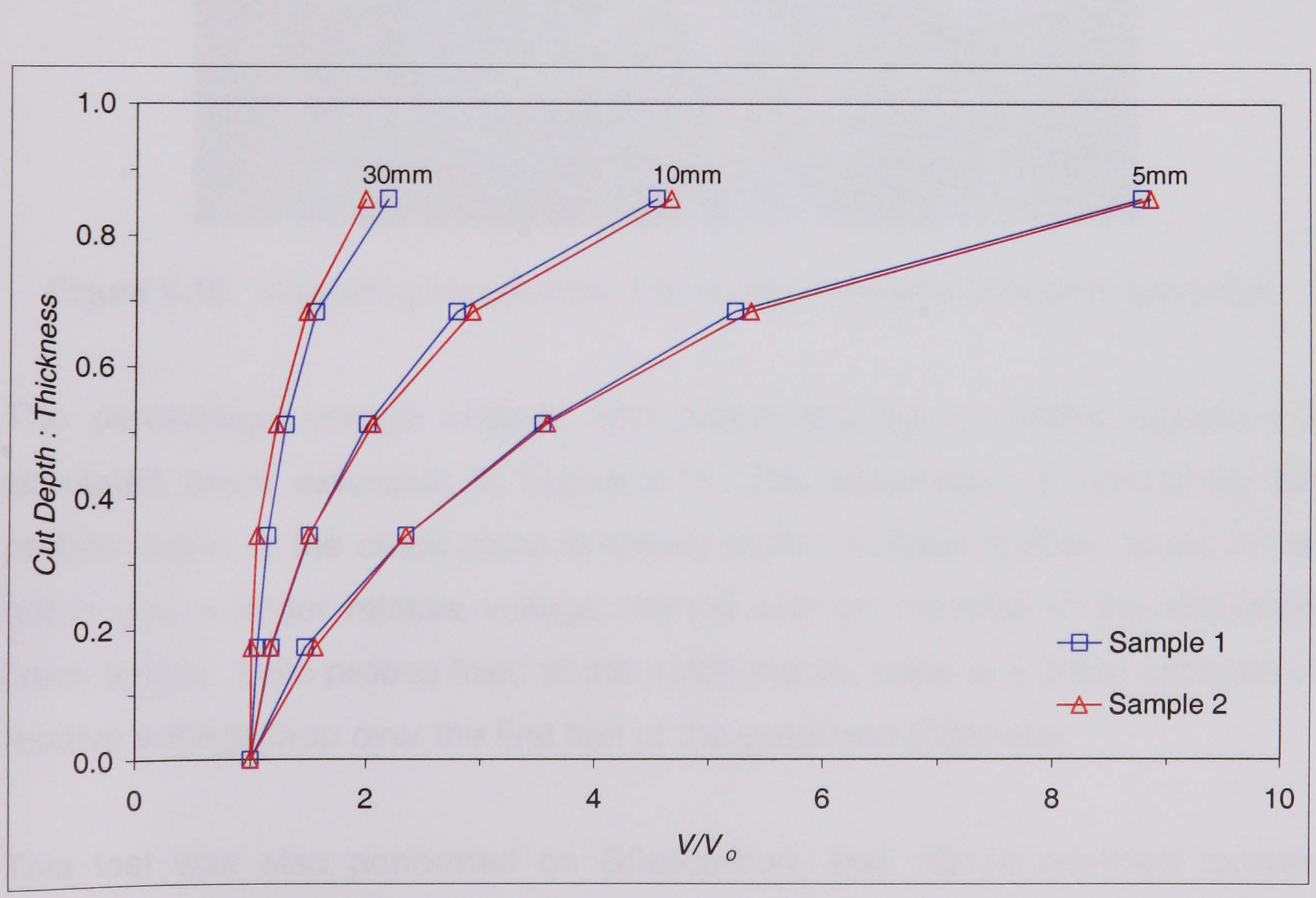

Figure 5.9. Reproducibility of calibration curves for different voltage probe spacing: IG110 graphite, W=12mm, *i*=1A.

5.3.3. Effect of Voltage Probe Spacing on Sensitivity

As seen from Figures 5.8 and 5.9, the sensitivity of the potential drop method is enhanced when voltage probes are positioned closer to the notch. For test purposes, it was necessary to compare the change in sensitivity with the voltage probe spacing. The voltage drop across a Gilsocarbon bend specimen (W=14mm) was measured using a multi-probe arrangement (see Figure 5.10) as the specimen was sectioned. Voltage probes were positioned at the notch mouth and at a spacing of 2, 3, 5, 10, 30, 60, 80, and, 100mm across the notch.

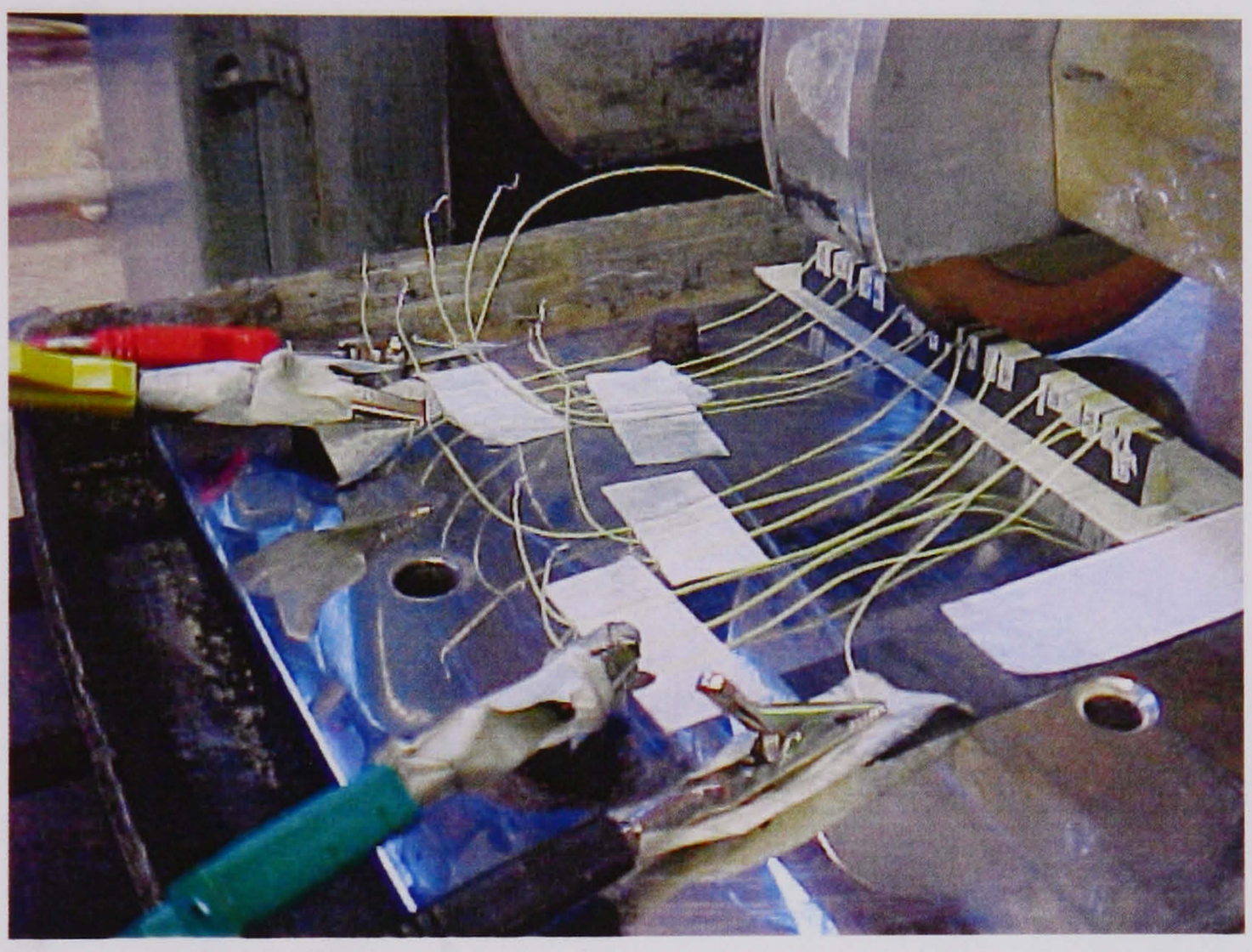

Figure 5.10. Measuring the potential drop across the multi-probe bend specimen.

The percentage voltage change with probe spacing is plotted against the simulated crack extension in Figure 5.11. The advantage of positioning the probes closer to the crack plane is clearly seen. Voltage probes closer to the notch give a larger relative voltage change with an increase in the simulated crack length. With probes fixed at the notch mouth, there is a linear increase in relative voltage drop over the first half of the specimen thickness.

This test was also performed on Gilsocarbon, and, IG110 compact tension specimens (W=32mm). Voltage probes were positioned at 2mm, 10mm, and, 20mm across the notch. Figure 5.12 shows that sensitivity in the compact tension specimens also increases when the voltage probes are positioned closer to the notch.

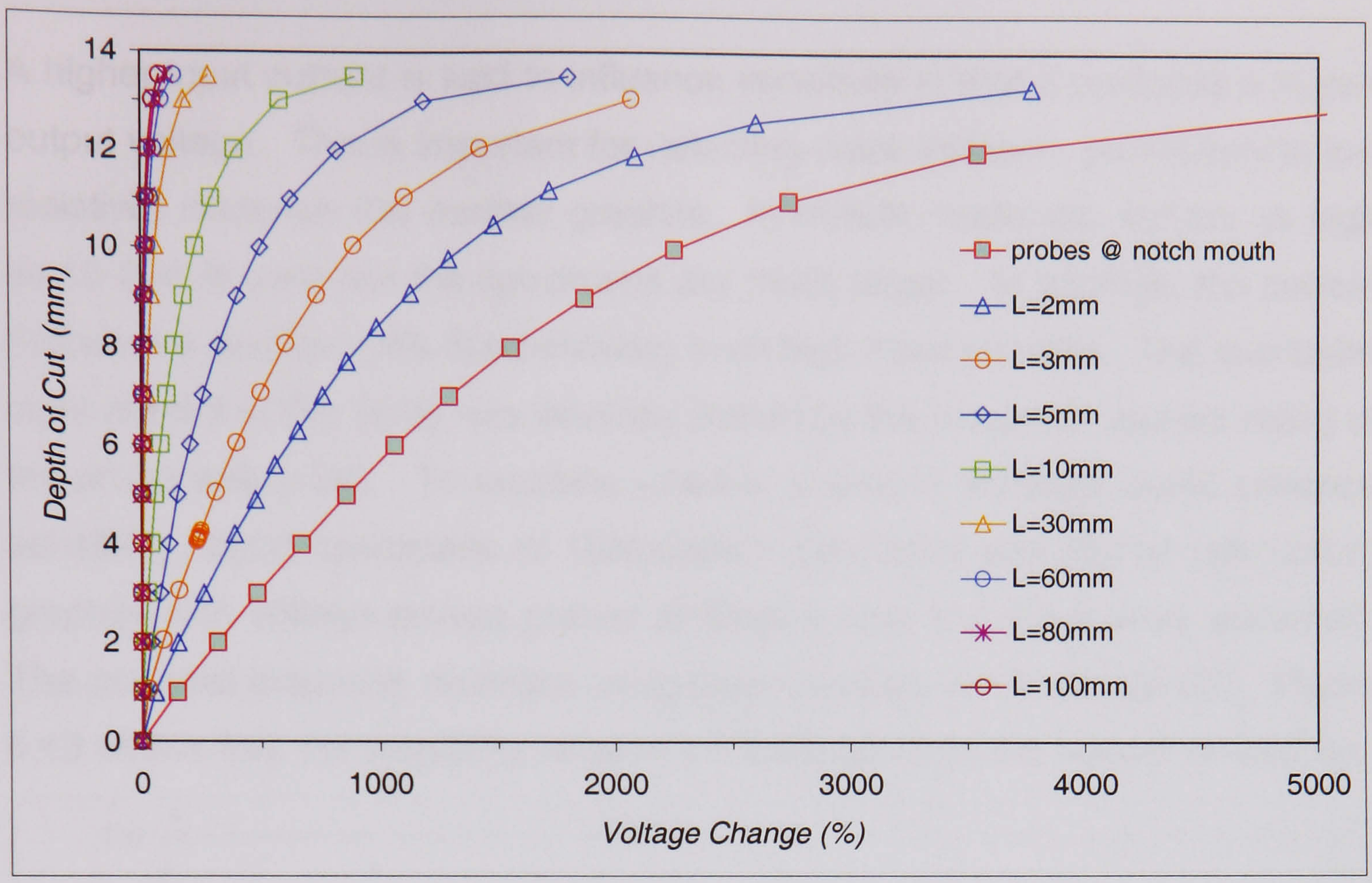

Figure 5.11. Change in sensitivity with different voltage probe spacing: Gilsocarbon bend specimen, *W*=14mm, *i*=1A DC.

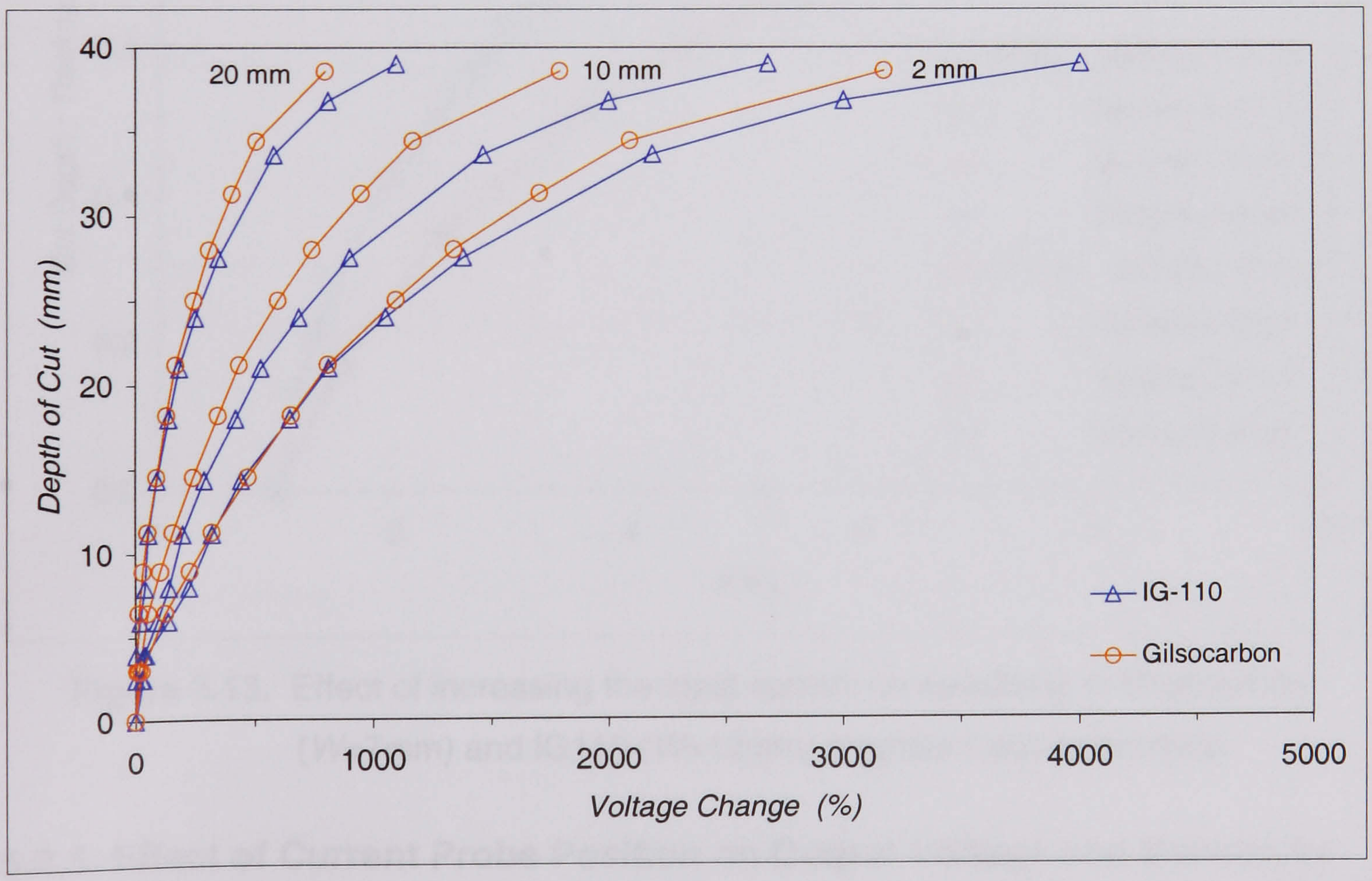

Figure 5.12. Change in sensitivity with different voltage probe spacing: Gilsocarbon and IG110 compact tension specimens, *W*=32mm, *i*=1A DC.

5.3.4. Effect of Input Current on Sensitivity

A higher input current is said to influence sensitivity in that it produces a higher output voltage. This is important for detecting crack initiation, particularly in low resistivity materials like nuclear graphite. In metallic materials, current as high as 10-20A is used but the specimens are much larger. In addition, the current probes are mechanically fixed allowing such high input currents. The maximum input current in this study was severely limited by the maximum current rating of the probe wire (~3A). To examine whether a current increase would enhance sensitivity, bend specimens of Gilsocarbon (W=7mm) and IG110 (W=12mm) graphite with voltage probes placed at 5mm across the notch were sectioned. The potential drop was recorded using input currents of 1A and 2A DC. Figure 5.13 shows that the sensitivity remains unchanged when the current is doubled.

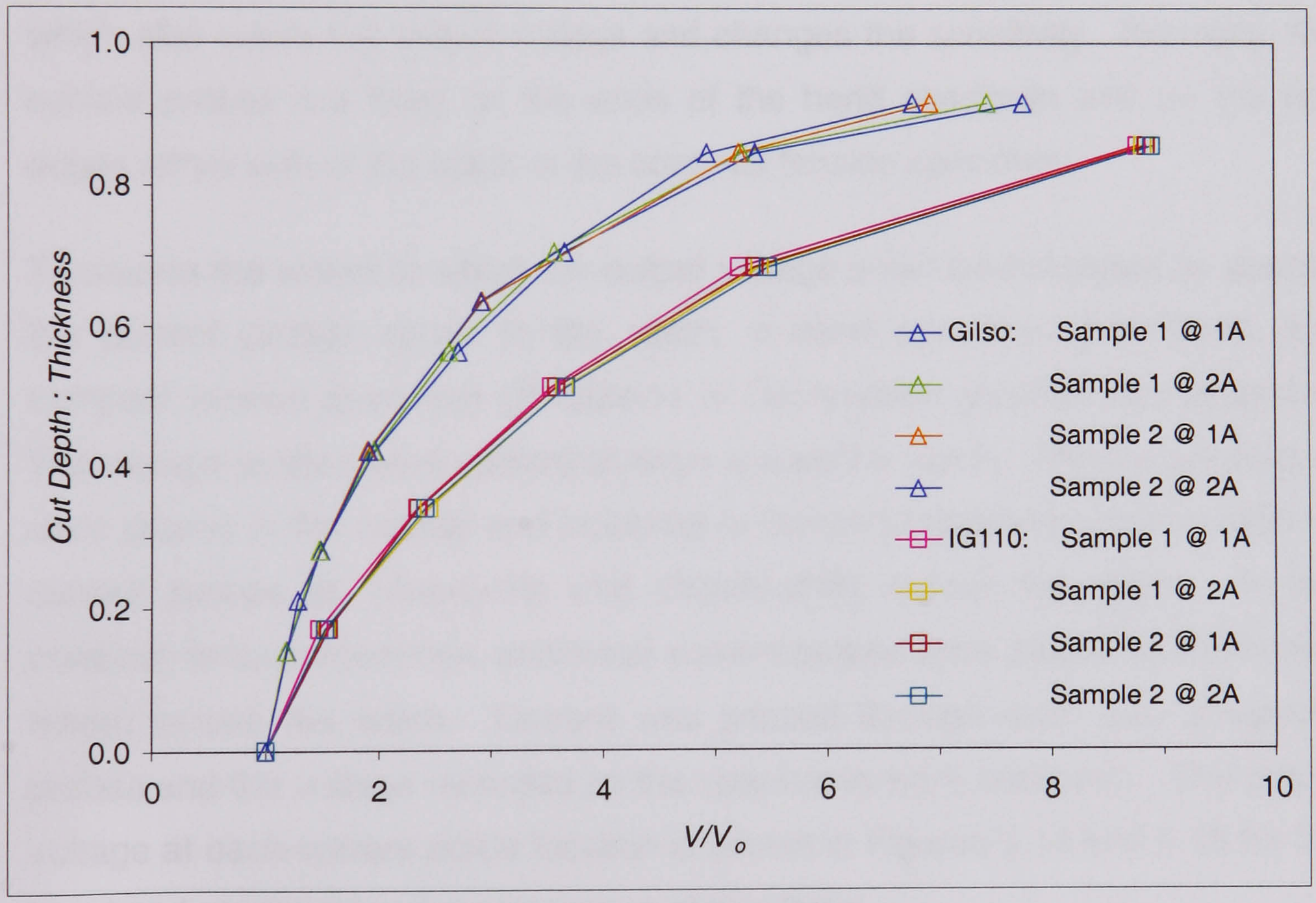

Figure 5.13. Effect of increasing the input current on sensitivity in Gilsocarbon (W=7mm) and IG110 (W=12mm) graphite bend specimens.

5.3.5. Effect of Current Probe Position on Output Voltage and Sensitivity

In Figure 5.7, it may have been noted that the output voltage produced in the graphite specimens is very low, being only a few milli-volts for i=1A DC. Typical output voltages, taken across un-notched and notched specimens current are shown in Table 5.1, where the low voltage levels are obvious.

Table 5.1. Output voltage ranges in the graphite specimens (i=1A DC).

Specimen Type	Probe Spacing (mm)	Output Voltage Range (mV)
Bend specimen (un-notched)	4	0.50 - 0.60
Bend specimen (a_0=0.35W)	4	1.00 - 1.10
Compact Tension (un-notched)	4	0.70 – 0.80
Compact Tension (a_0=0.35W)	4	1.50 – 1.60

It was also seen in Figure 5.13 that raising the current did not enhance the sensitivity. Alternative ways were therefore sought by which the output voltage or sensitivity could be increased. One option is to increase the voltage probe spacing, which raises the output voltage but sacrifices the overall sensitivity. Another option was to position the current input probes closer to the notch, which also raises the output voltage and changes the sensitivity. Normally, the current probes are fixed on the ends of the bend specimen and on the two edges either side of the notch in the compact tension specimen.

To assess the extent to which the output voltage could be increased by placing the current probes closer to the notch, a bend specimen (W=14mm) and compact tension specimen (W=32mm) of Gilsocarbon graphite was prepared. The voltage probes were spaced at 4mm across the notch. The current probes were placed in the normal end positions in the bend specimen, with additional current probes at 14mm(=W) and 28mm(=2W) across the notch. In the compact tension specimen, additional current probes were placed at 20mm and 30mm across the notch. Current was passed through each pair of current probes and the voltage recorded as the specimens were sectioned. The output voltage at each current probe location is shown in Figures 5.14 and 5.15 for the bend and compact tension specimens respectively.

In both specimen types, the extent of the output voltage increase could not warrant the placement of current probes closer to the notch given that the increase was only of the order of a few milli-volts. More importantly, the actual gain in sensitivity with current probes placed closer to the notch was reduced. This is shown in Figure 5.16 for the compact tension specimen, where the current probes at the ends produce the highest sensitivity. There was therefore little improvement to be had, with current probes closer to the notch.

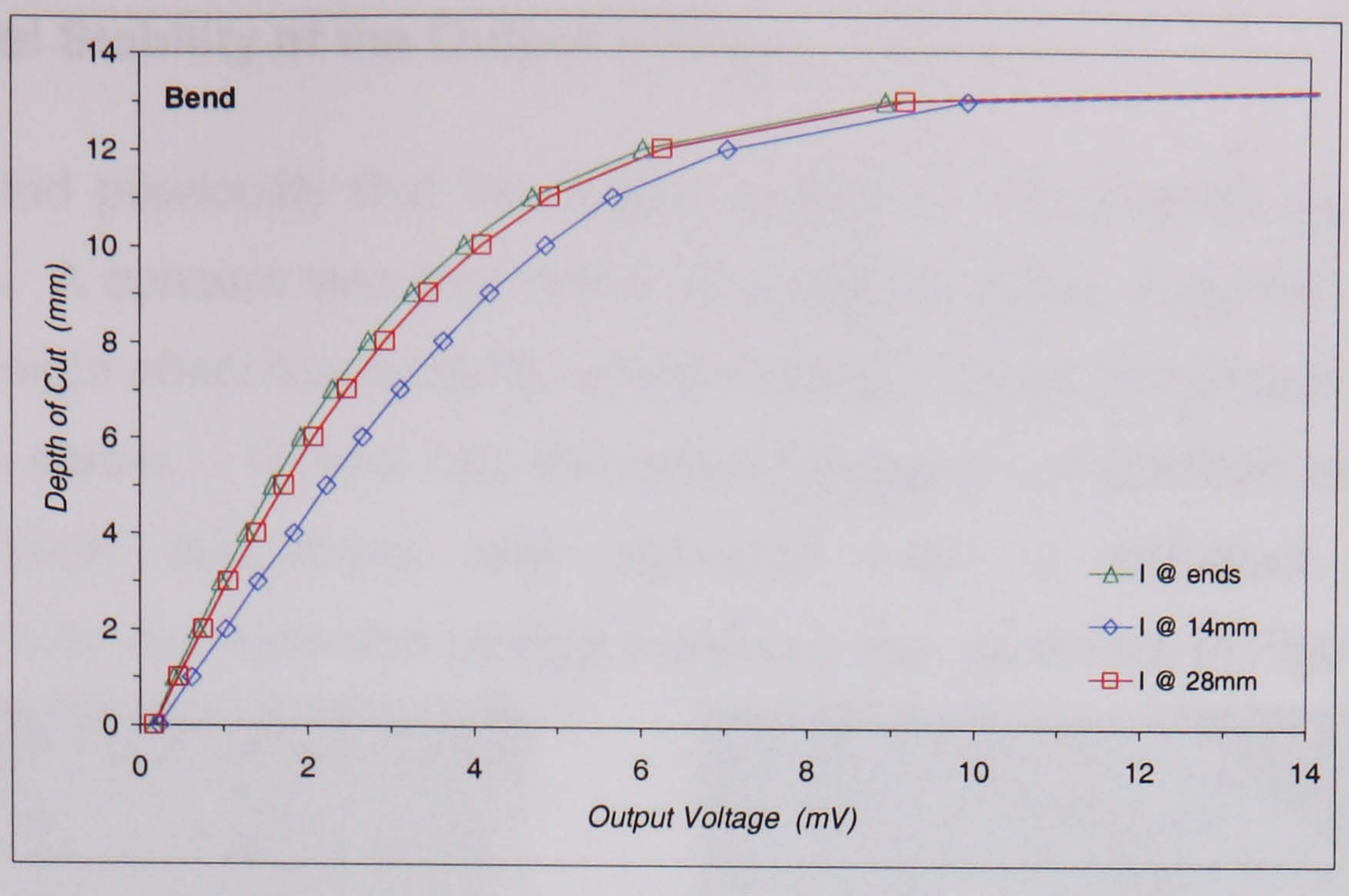

Figure 5.14. Effect of current probe position on the output voltage: Gilsocarbon bend specimen, *W*=14mm, *i*=1A DC.

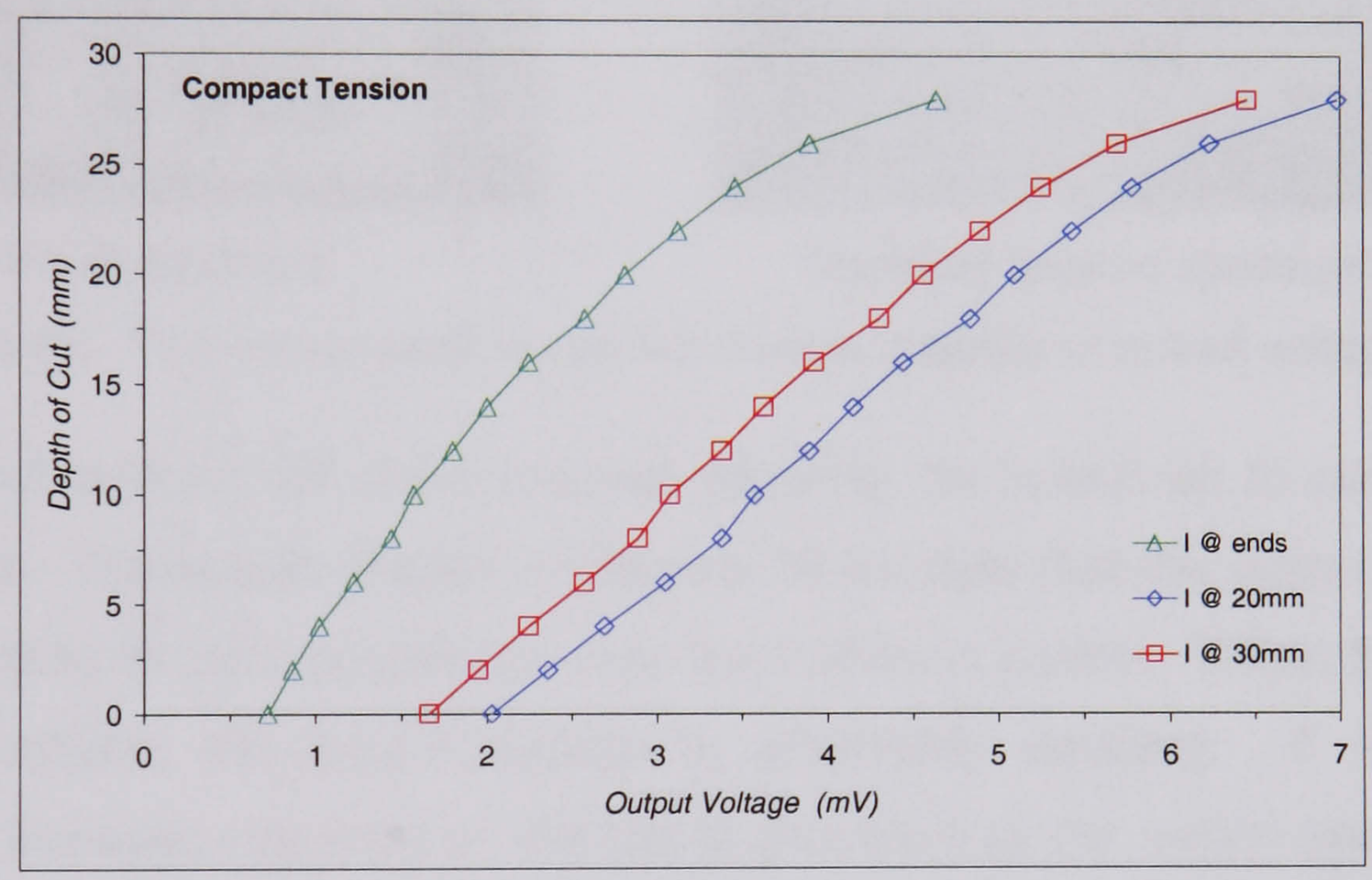

Figure 5.15. Effect of current probe position on the output voltage: Gilsocarbon compact tension specimen, *W*=32mm, *i*=1A.

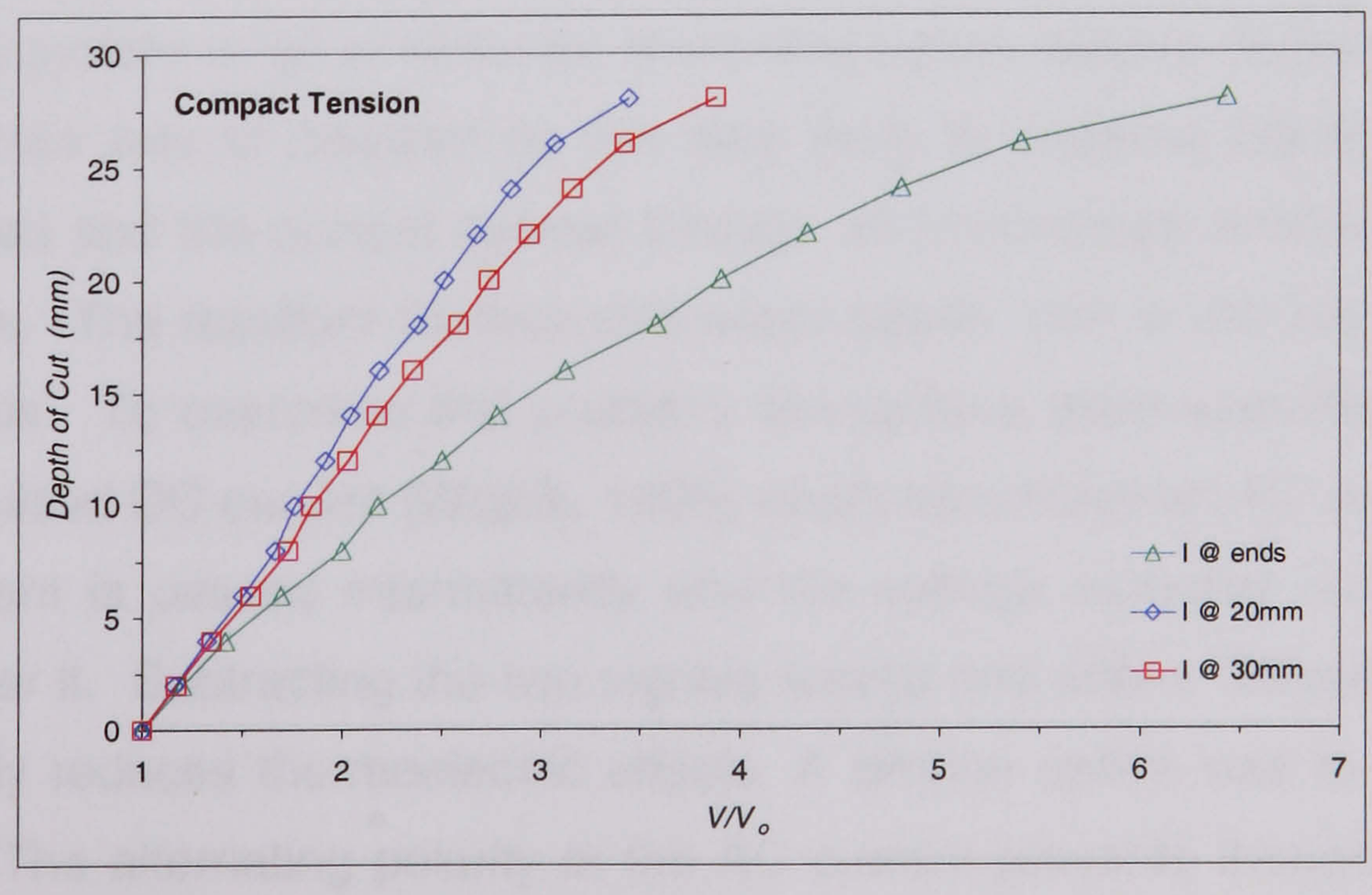

Figure 5.16. Effect of current probe position on the sensitivity: Gilsocarbon compact tension specimen, *W*=32mm, *i*=1A.

5.3.6. Thermal Stability of the Output Voltage

It was indicated previously that the output voltage in the graphite specimens was very low. A concern was that drift in the output voltage, over the duration of the tests, might affect the reliability of the method. It was thus important that the system is stable. To test this, the output voltage in un-notched bend and compact tension specimens was recorded over a half-hour period. Temperature was also recorded using a thermocouple, as shown in Figure 5.17.

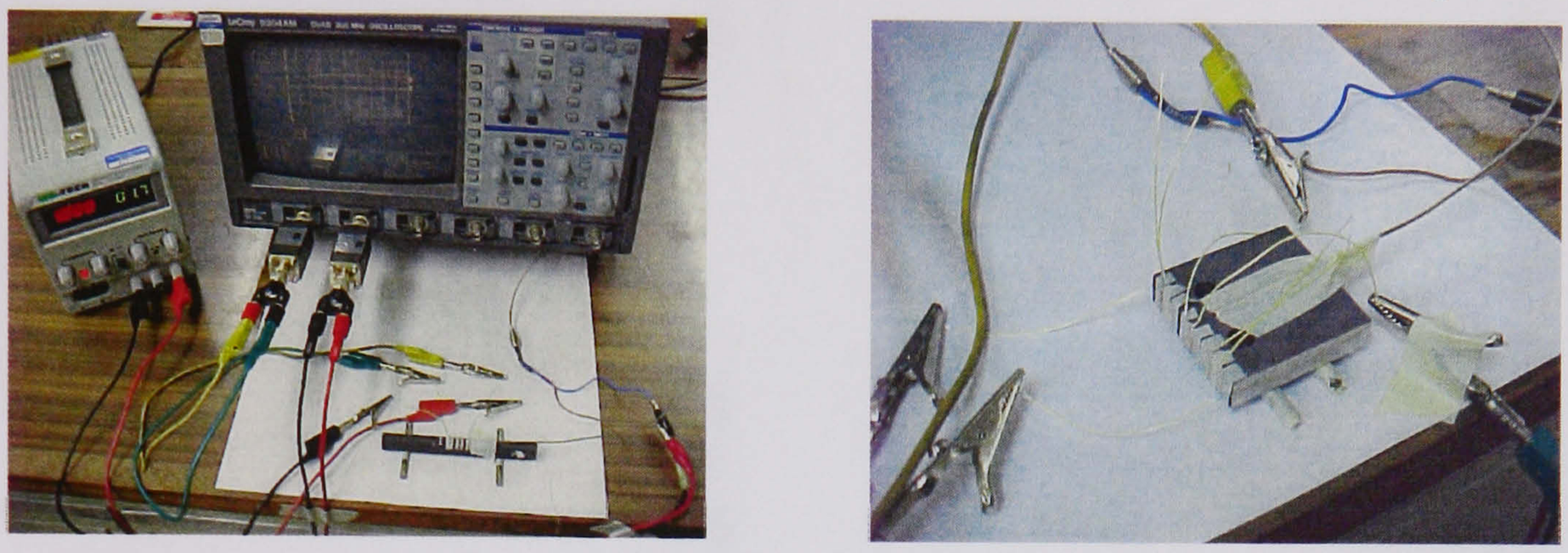

Bend specimen

Compact tension specimen

Figure 5.17. Test set-up used to monitor thermal stability of output voltage.

Currents of 1A and 2A DC were applied, allowing the specimen to cool down between tests. The results shown in Figure 5.18 indicate that the output voltage fluctuates slightly in both specimens over the half-hour period. When the input current is doubled, the output voltage is effectively doubled. A dramatic temperature increase occurred in the bend specimen at 2A, which seemed to stabilise after 15 minutes. In the compact tension specimen, the temperature rose slightly during the test period. The results suggest that the voltage could stabilise if the system is left to stand for some time before testing. However, the temperature rise was of concern as this was likely to become worse as the crack extended and the current passed through an increasingly smaller cross-sectional area. The resultant thermal drift would cause error in the low, output voltage signals. To overcome this problem, two options were available. One was to use pulsed DC current (Wojcik, 1995) which resembles an AC current in that the current is passed intermittently and the voltage recorded during the pulse and after it. Subtracting the two signals leaves one with a 'filtered' signal and effectively reduces thermoelectric effects. A simpler option was to use an AC current. The alternating polarity of the AC current prevents thermoelectric effects, at the current-voltage probe junctions.

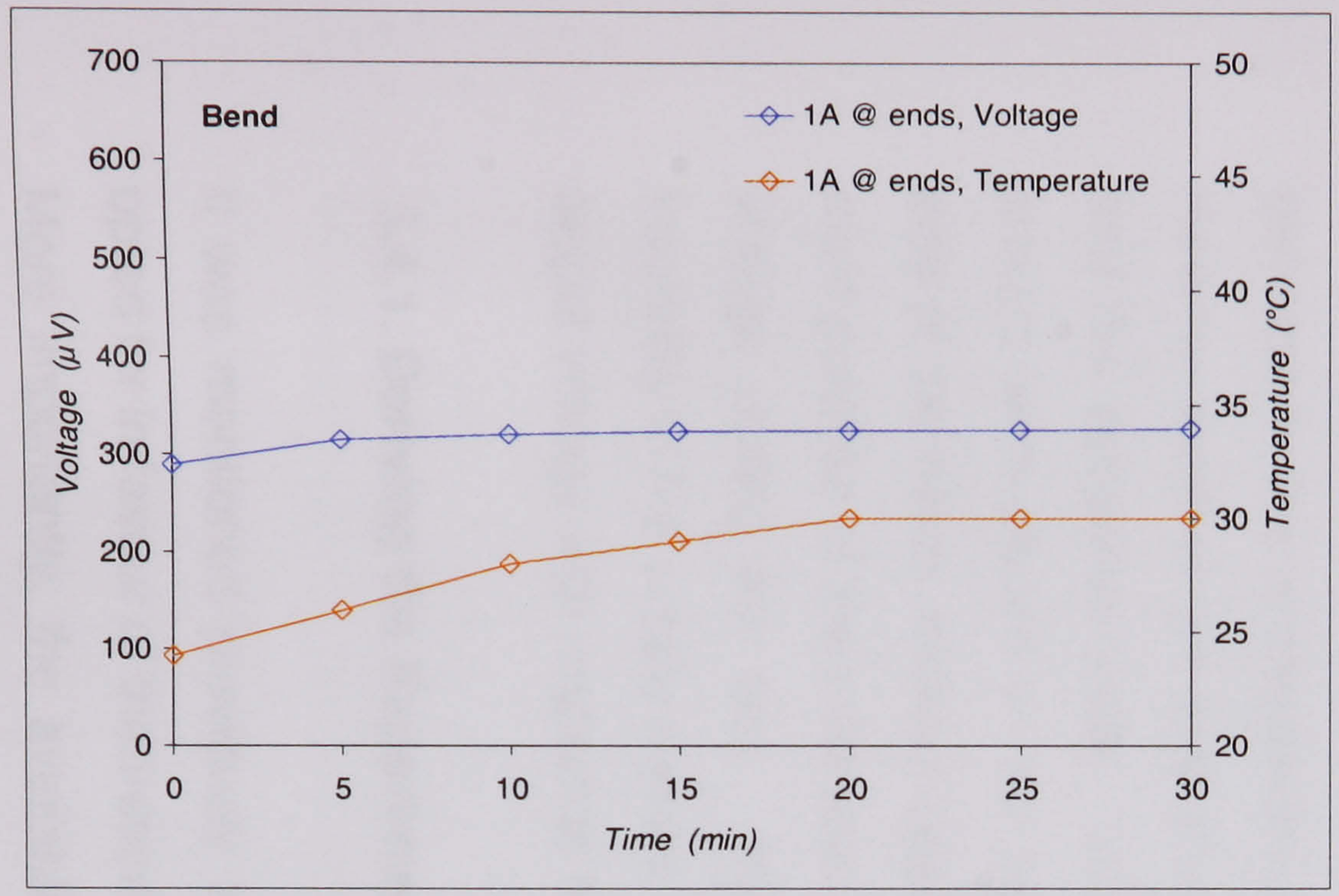

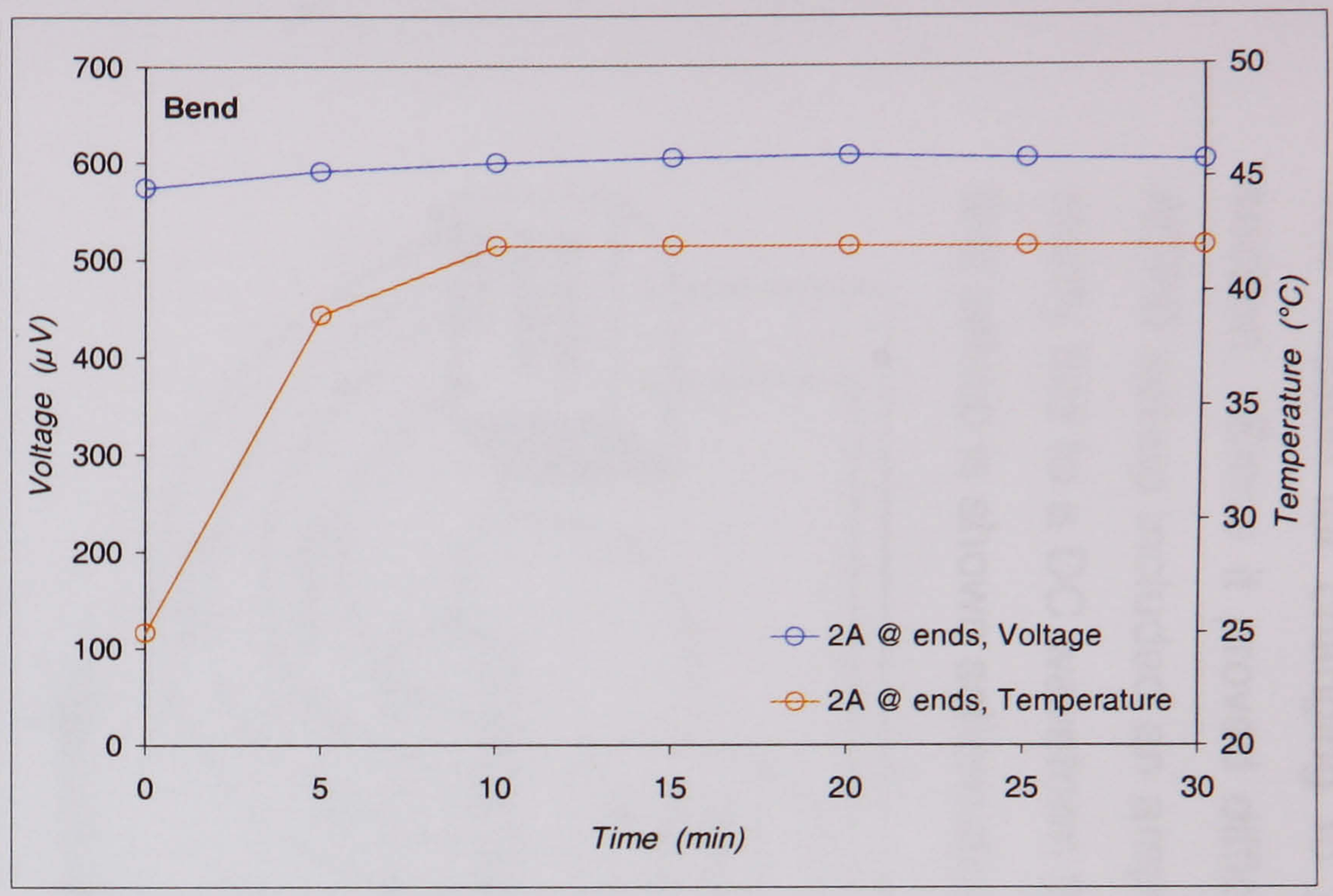

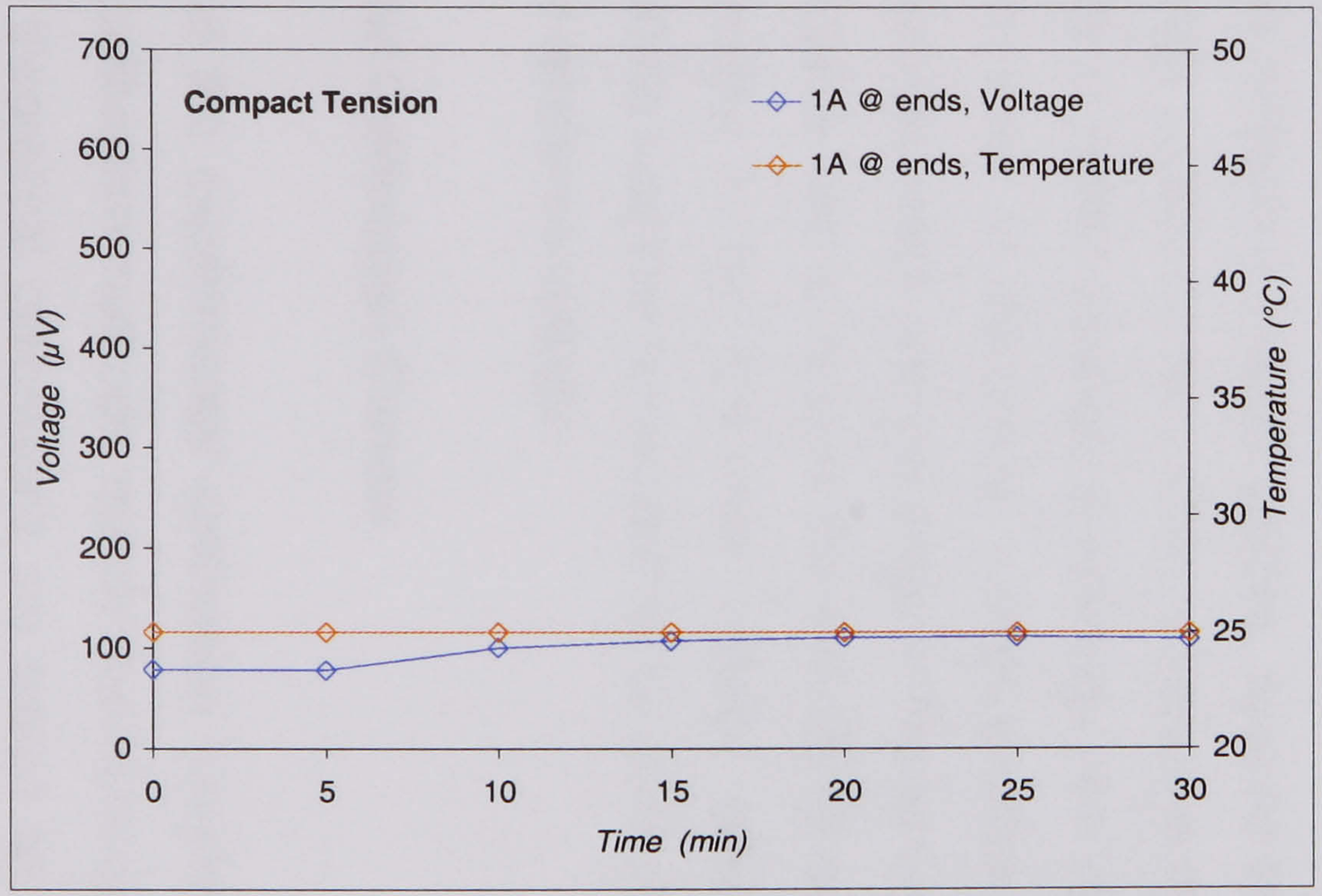

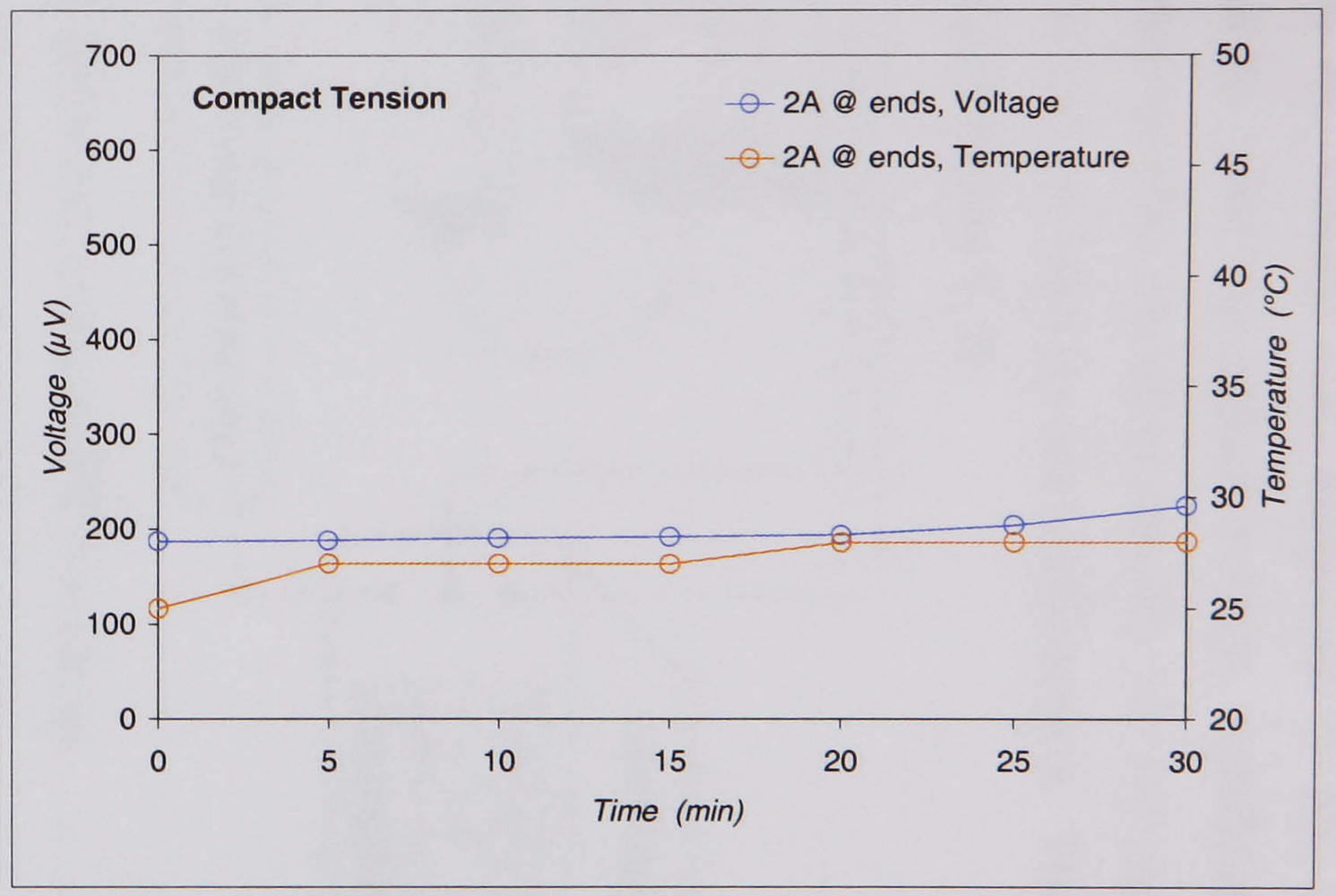

Figure 5.18. Thermal stability of the output voltage: Gilsocarbon bend (*W*=12mm) and compact tension (*W*=32mm) specimens, 1A & 2A DC.

5.4. The ACPD Method and its Application for R-curve Measurement

The reason for changing to an AC current was explained in the previous section. Since it proved difficult to raise the output voltage significantly, the ACPD set-up included an amplifier-rectifier circuit to amplify the AC signal and rectify this to a DC waveform that can be read by the oscilloscope. The ACPD test set-up is shown schematically in Figure 5.18.

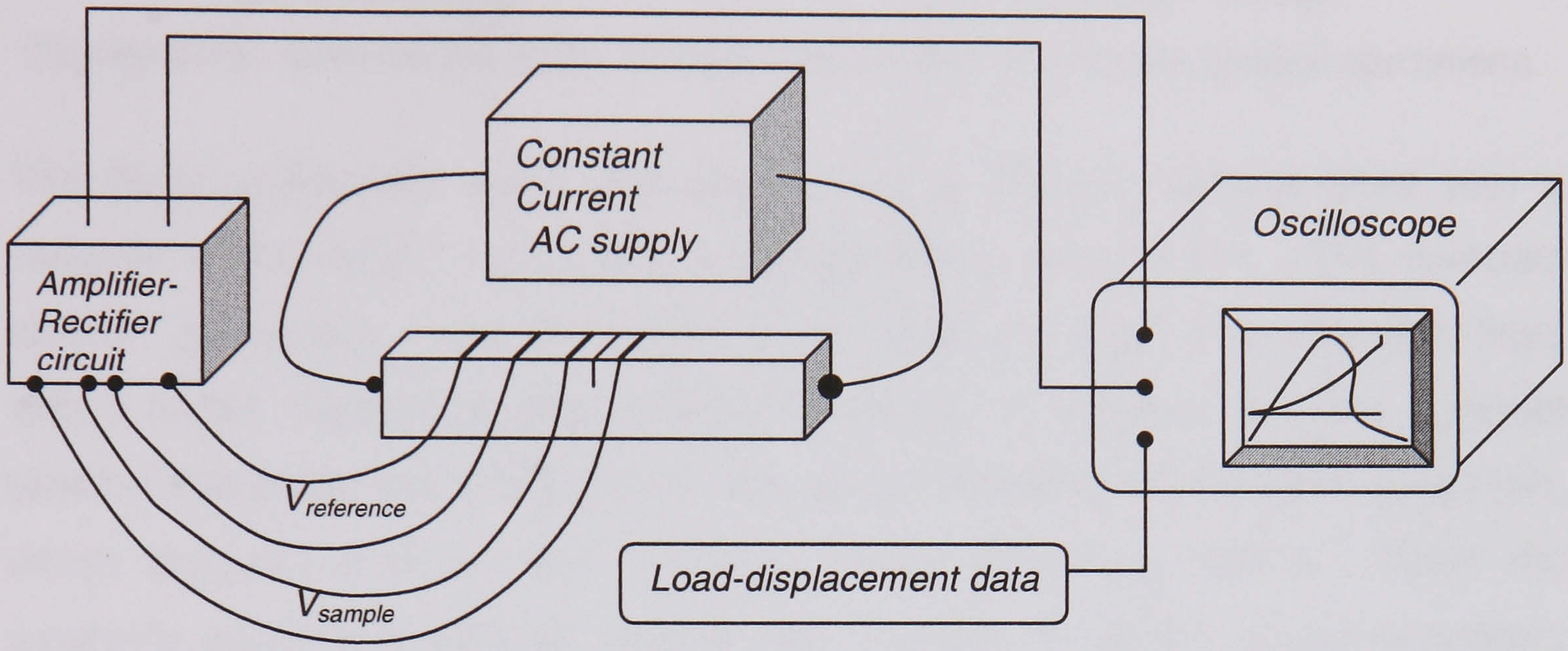

Figure 5.18. Schematic of the ACPD test set-up.

Included in this arrangement are reference voltage probes, spaced the same distance apart as the output voltage probes (4mm), midway between the notch and the specimen ends. In the compact tension specimens, the reference probes were placed on the same edge as the output voltage probes, on one side of the notch, midway between the notch and the edge of the sample. The main purpose of the reference probes was to monitor the stability of the output voltage during the test. Instability in the reference voltage would imply instability in the supply current, which could be accounted for by normalising the output voltage with respect to the reference voltage.

5.4.1. Deriving the Experimental Calibration Curves

It was mentioned previously that the experimental calibration technique was opted for in favour of theoretical calibration methods, mainly due to its simplicity. More importantly, the available theoretical calibrations are based on specific arrangements of the current-voltage nodes, which do not readily simulate the arrangements used in this study. The dimensions of the test and calibration specimens, which had to obviously be similar, are shown in Figure 5.19.

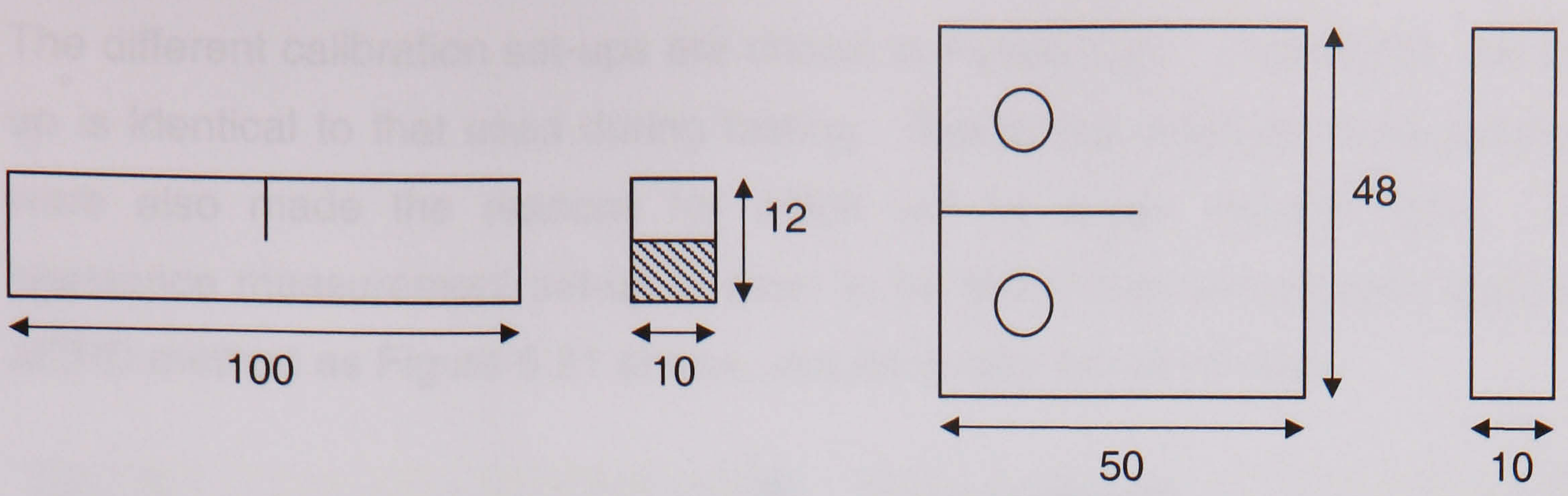

Bend Specimen

Compact Tension

Figure 5.19. Dimensions (mm) of the 3-point bend and compact tension specimens.

The bend specimens were calibrated using a milling machine fitted with a variable speed motor for driving a cutting wheel (t=0.25mm). The compact tension specimens were calibrated on an Elliot 4100 grinding machine fitted with a larger diameter cutting wheel (t=0.8mm). A problem with the compact tension specimen was the need for controlled sectioning of the entire specimen, which required a wheel with a cutting depth exceeding 50mm. Since the available equipment allowed a maximum cut depth of ~25mm, it was necessary to cut the specimens manually to achieve deeper cuts (see Figure 5.20).

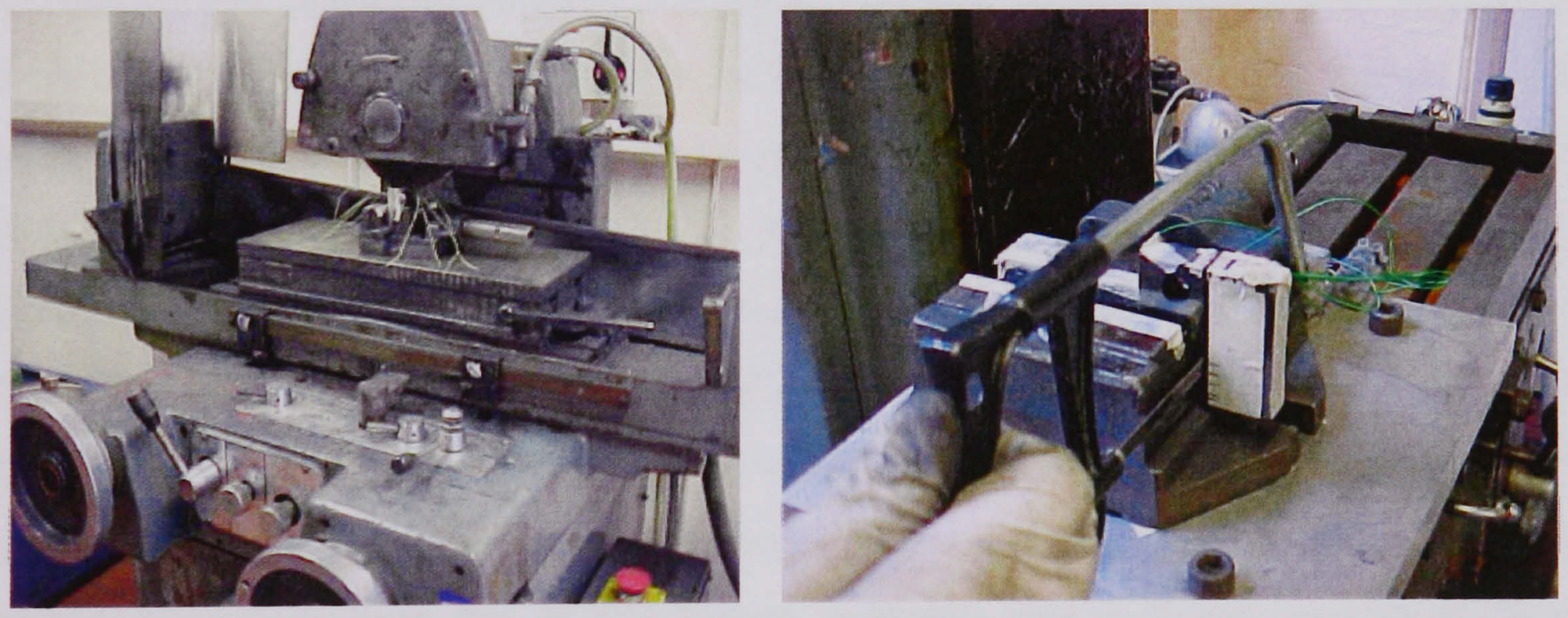

Controlled Sectioning

Graduated Manual Cutting

Figure 5.20. Two-stage sectioning for calibration of the compact tension specimen.

Three bend specimens were used to obtain an 'average' calibration curve. Only one compact tension specimen was used for calibration. A voltage probe spacing of 4mm across the notch was selected in both specimen types. This presented the best compromise between high sensitivity whilst avoiding the difficulty involved in soldering the probes closer to the notch. Since the AC current prevents thermoelectric effects, a current of 2A was used for all testing. A higher current could not be used given the 3A maximum rating of the wires.

The different calibration set-ups are shown in Figure 5.21. In principle, the set-up is identical to that used during testing. Resistance change measurements were also made the reasons for which will be made evident later. The resistance measurement set-up is seen to be much less complicated than the ACPD method as Figure 5.21 shows, requiring only the ohmmeter.

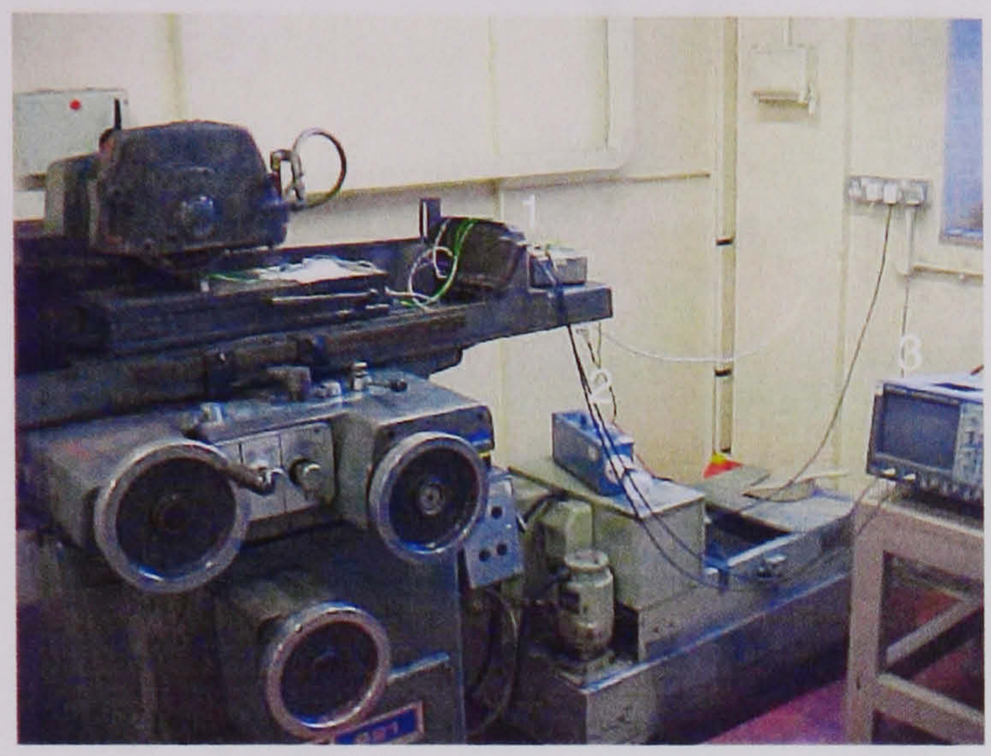

ACPD calibration: (1) amplifier-rectifier, (2) AC power-supply, (3) oscilloscope.

Using the resistance change for calibration.

Figure 5.21. Different set-ups used to calibrate specimens.

To derive the calibration curves the depth of cut was normalised with respect to specimen thickness and plotted against the normalised voltage, which is the ratio of the voltage at a particular depth to the initial voltage, i.e. V/V_o. A polynomial equation is then fit to the experimental curve. The average calibration curves for the bend specimens are shown in Figure 5.22 along with the polynomial expression and correlation coefficient, the latter indicating the good fit obtained in each case. The graphs in Figure 5.22 include calibration curves obtained by resistance measurements, these curves showing slightly higher sensitivity than the ACPD curves probably due to higher sensitivity from the ohmmeter. Importantly, the two curves show close resemblance, validating the use of the resistance change for crack length measurement.

The calibration curves for the compact tension specimens are presented in Figure 5.23. Here, it is seen that prior to manual sectioning, the calibration curves are identical. After ~0.4W, the data becomes scattered. The calibration data for the bend and compact tensions specimens remarkably appeared to lie on a master curve, as shown in Figure 5.24. The latter curve was used for calculating the crack length in the compact tension specimens.

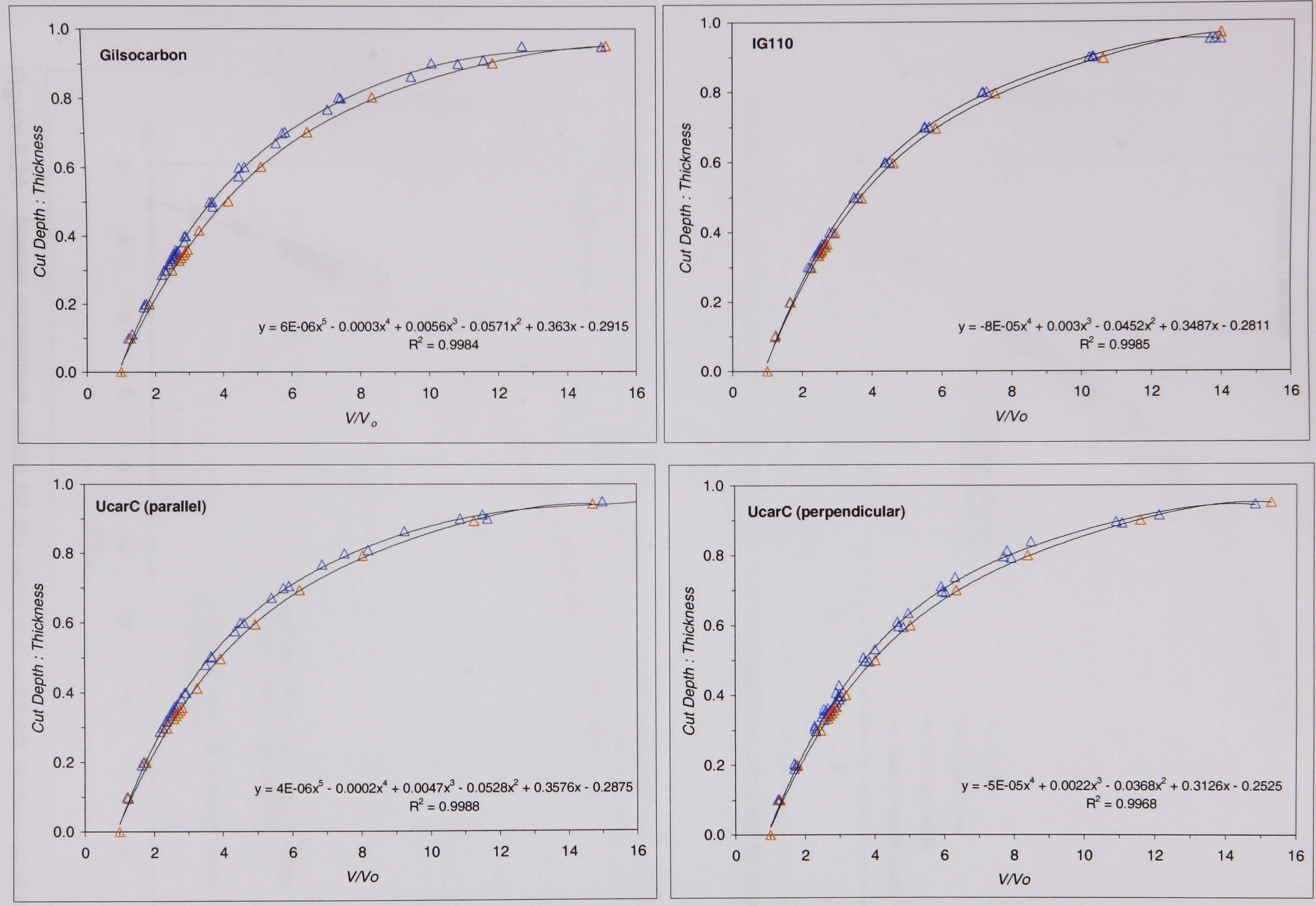

Figure 5.22. Average calibration curves for the bend specimens: Δ = ACPD, Δ = resistance measurements.

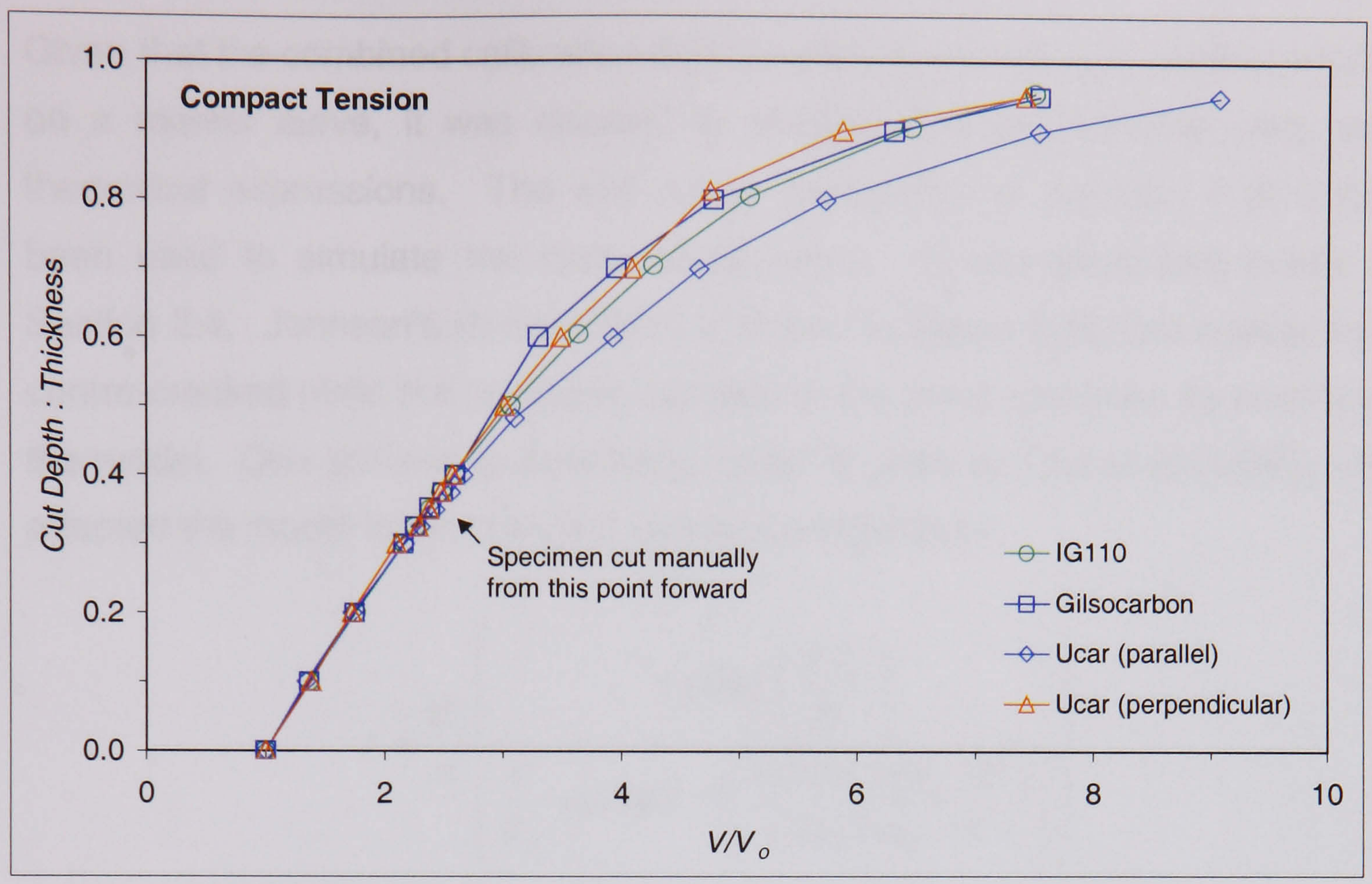

Figure 5.23. ACPD Calibration curves for the nuclear graphites: compact tension.

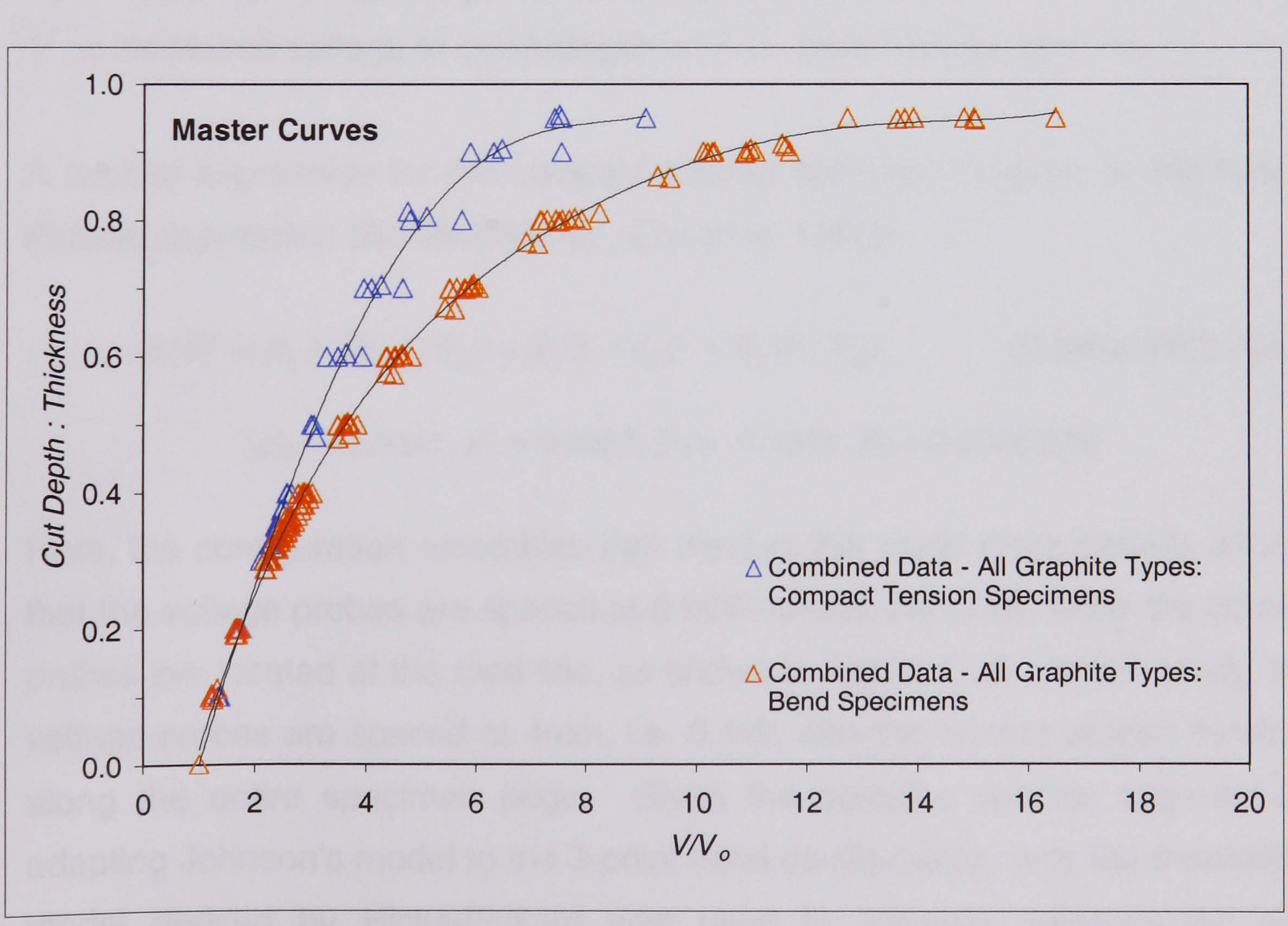

Figure 5.24. Master calibration curves for the bend and compact tension specimens obtained by combining the calibration data for all the nuclear graphites.

5.4.2. Comparison of the Experimental and Theoretical Calibration Curves

Given that the combined calibration data for each specimen type appeared to lie on a master curve, it was decided to compare the experimental data with theoretical expressions. The well-known expression of Johnson (1965) has been used to simulate the bend configuration. It was described briefly in Section 2.4. Johnson's model (1965) is shown in Figure 5.25 and applies to a centre-cracked plate but is usually adapted to the bend specimen by modifying the model. One solution to Johnson's model is given by Cho et al (1996), who adapted the model to the compact tension configuration:

$$a = \frac{W}{\pi}\left[\frac{COSH\left(\frac{\pi Y_0}{W}\right)}{\frac{V}{V_0}\,xCOSH^{-1}\left[\frac{COSH\,(\pi Y_0 / W)}{COS\,(\pi a_0 / W)}\right]}\right]$$

a = crack length; a_0 = initial crack length; W = specimen thickness

Y_0 = voltage probe spacing from notch/crack plane

V = measured voltage at crack length 'a'; V_0 = initial voltage at $a = a_0$

A simpler expression for the compact tension specimen is given by the Hicks-Pickard expression (ASTM E647-91, Cho et al, 1996):

$$a/W = B_0 + B_1(V/V_0) + B_2(V/V_0)^2 + B_3(V/V_0)^3 \qquad (0.24 \le a/W \le 0.70)$$

$$[B_0 = -0.5051,\ B_1 = 0.8857,\ B_2 = -0.1398,\ B_3 = 0.0002398]$$

Here, the configuration resembles that used in this study more closely, except that the voltage probes are spaced at 0.06W across the notch while the current probes are located at the load line, as shown in Figure 5.25. In this study, the voltage probes are spaced at 4mm, i.e. 0.1W, with the current probes running, along the entire specimen edge. Given the complex solution required for adapting Johnson's model to the 3-point bend configuration, only the theoretical model derived by Hicks-Pickard was used to compare experimental and theoretical calibration curves. This comparison is shown in Figure 5.26. The crack length calculated theoretically was based on the depth of cut made during the experimental calibration.

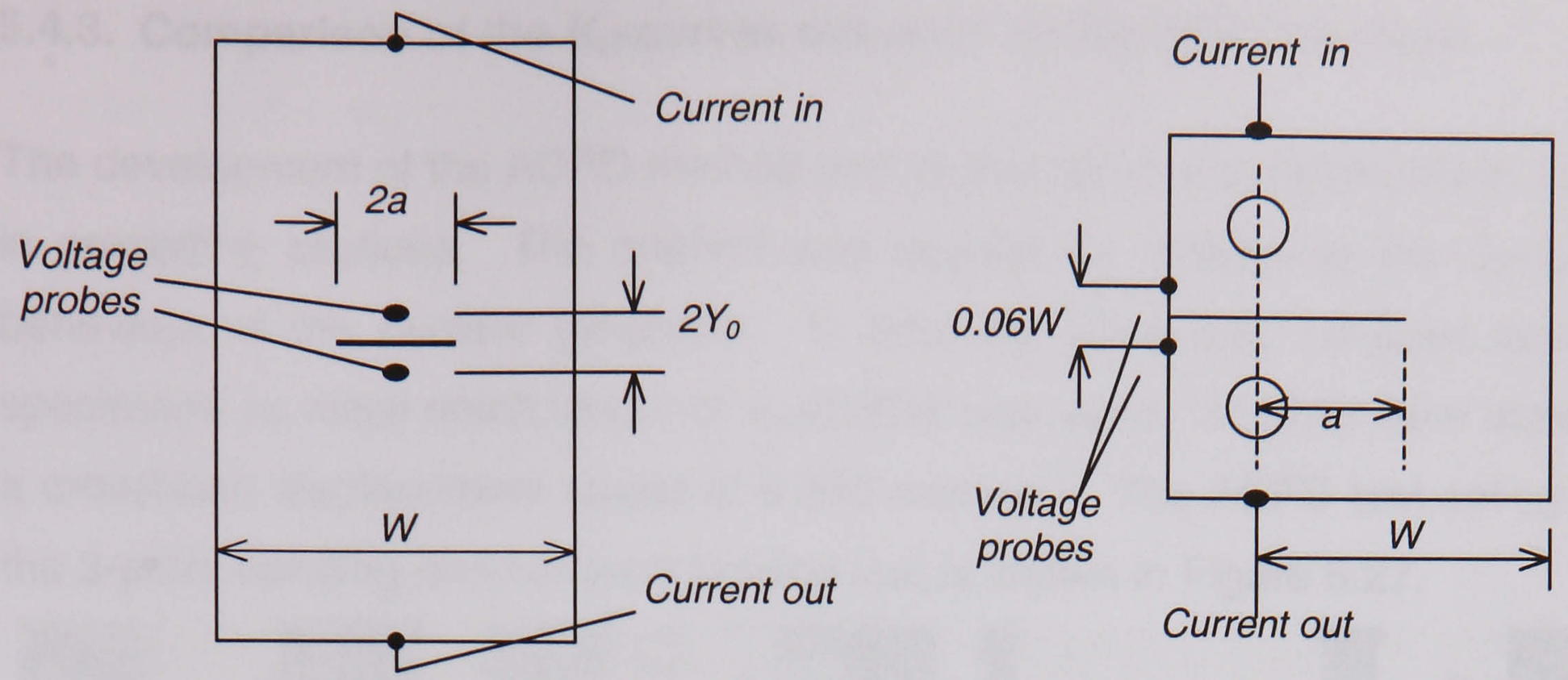

Johnson: centre-cracked plate Hicks-Pickard: compact tension

Figure 5.25. Configuration of the specimen in the theoretical model (ASTM E647-91).

It is seen that the Hicks-Pickard model and the experimental data agree quite closely. The small discrepancy is probably due to slight differences in the two configurations, e.g. the locations of the current-voltage probes. It may also be, that the graphites do not conform to the ideal material of the model. A particular limitation of the Hicks-Pickard solution is that it only applies for $0.24 \leq a/W \leq 0.7$. It is necessary for $a_0=0.24W$ otherwise the Hicks-Pickard solution is not applicable. This explains the deviation of the theoretical curve after ~0.8W. It is also seen that the model simply applied a parabolic type fit to the data.

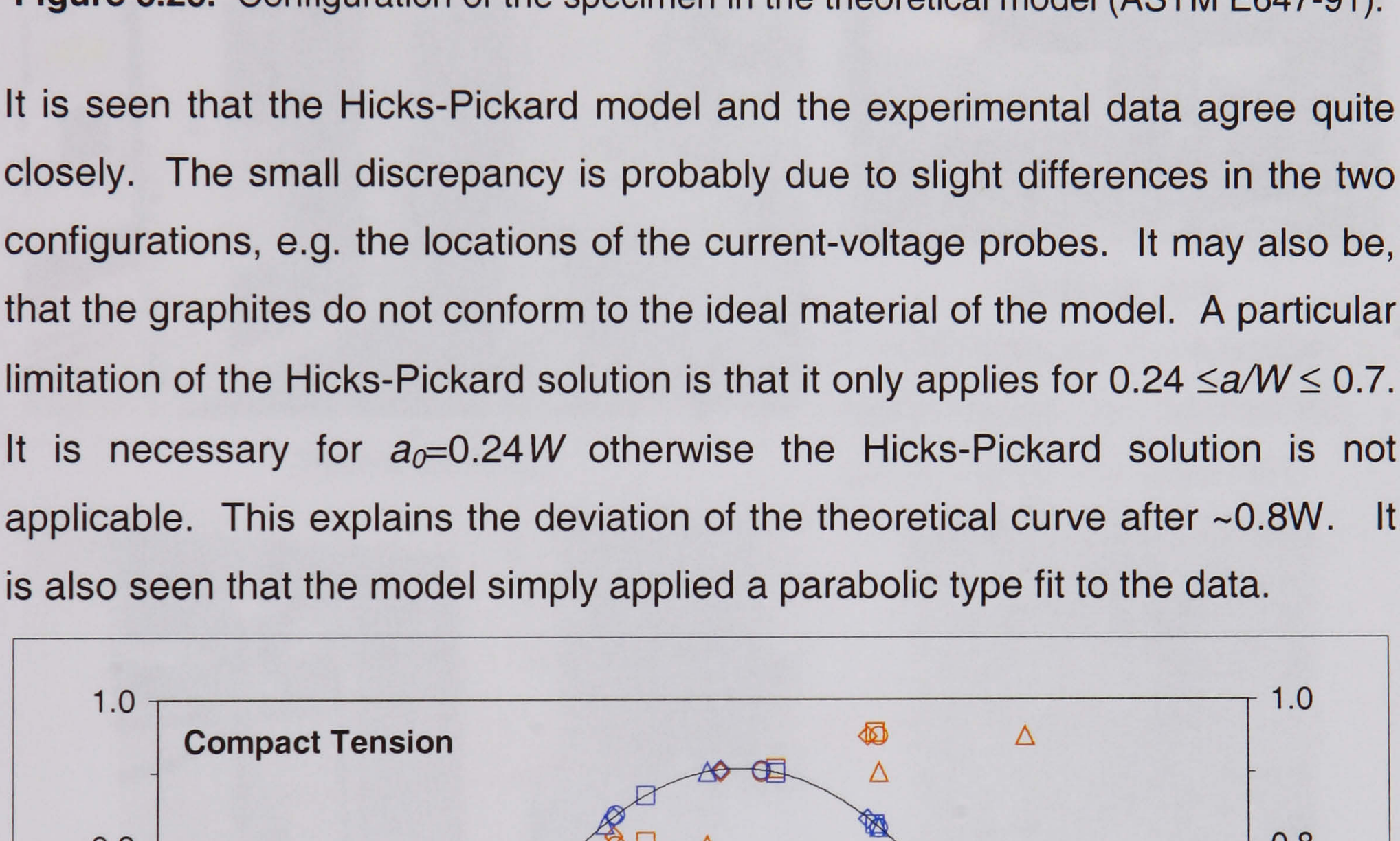

Figure 5.26. Comparison of the theoretical and experimental calibration curves for the compact tension configuration by Hicks-Pickard model (ASTM E647-91).

5.4.3. Comparison of the K_R-curves obtained by the ACPD Method

The development of the ACPD method and its operation was described in detail in preceding sections. The method was applied for comparing the K_R-curve behaviour of the nuclear graphites. In both the bend and compact tension specimens an initial notch length of a_o=0.35W was used. All tests were done at a crosshead displacement speed of 0.050 mmmin^{-1}. The ACPD test set-up for the 3-point bending and compact tension test is shown in Figure 5.27.

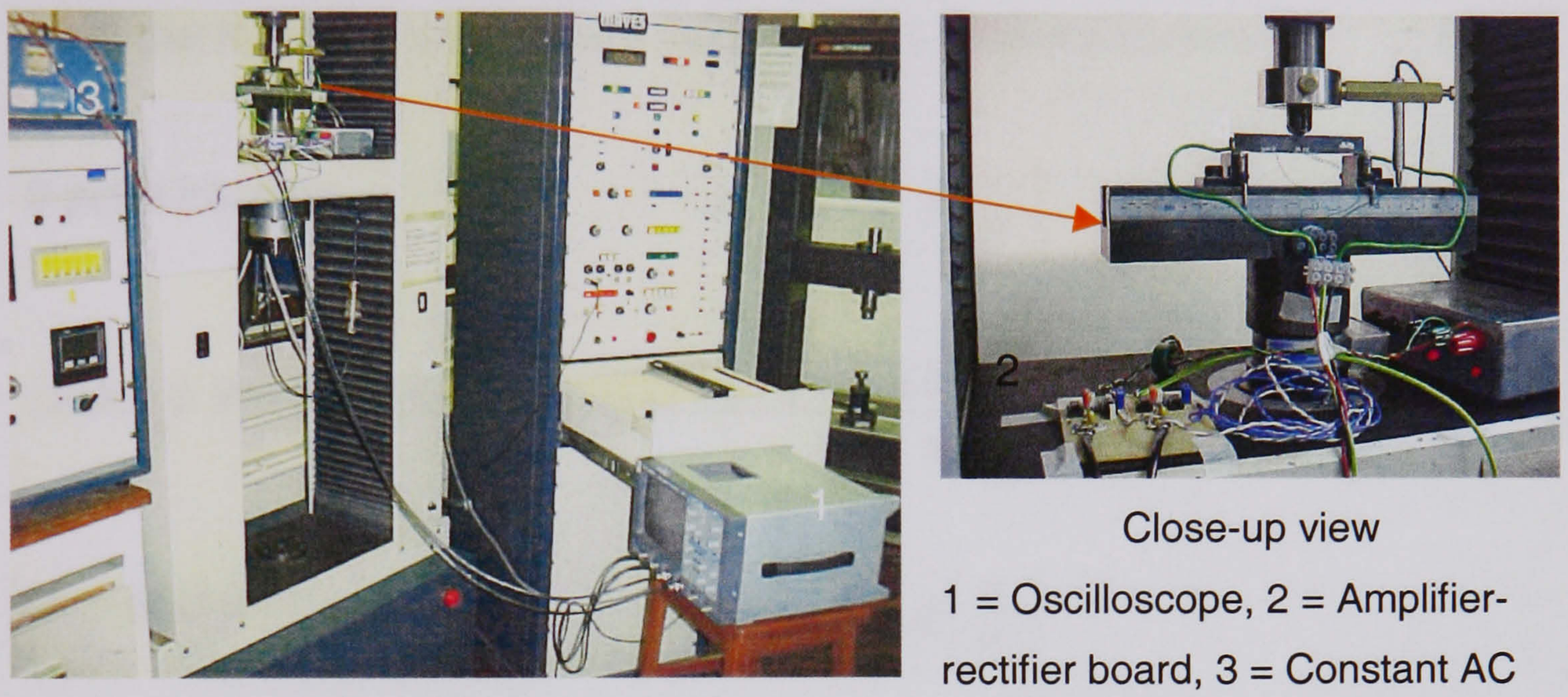

3-point bending

Close-up view

1 = Oscilloscope, 2 = Amplifier-rectifier board, 3 = Constant AC power supply, 4 = Specimen

Compact tension

Close-up view

Figure 5.27. Set-up of the ACPD test method.

The specimens were insulated electrically by masking all contact areas. Care was taken to use a smooth masking tape to minimise frictional effects. The masking was applied over the contact areas of the bend specimen, not over the bearings, to prevent the tape restricting the movement of the load bearings. In compact tension specimens, electrical isolation was achieved by masking the two loading pins.

The point of crack initiation was taken as the point where the output voltage began to increase continuously, above the highest recorded voltage prior to the continuous increase. Any voltage fluctuations prior to this were disregarded so that crack initiation was defined as a distinct event in the voltage history of the specimen. This prevented inconsistency in the crack length measurements and ensured consistency when comparing the different materials.

Using the crack length estimated by the ACPD method and the corresponding load, the K_R-curve was derived using the well-known equations:

3-point bending:
$$K_I = \frac{PS}{BW^{\frac{3}{2}}} . f\left(\frac{a}{W}\right)$$

(Sakai & Bradt, 1993):
$$f\left(\tfrac{a}{W}\right) = \frac{3\left(\tfrac{a}{W}\right)^{\frac{1}{2}}\left[1.99 - \tfrac{a}{W}\left(1 - \tfrac{a}{W}\right)\left(2.15 - 3.93\left(\tfrac{a}{W}\right) + 2.7\left(\tfrac{a}{W}\right)^2\right)\right]}{2\left(1 + 2\tfrac{a}{W}\right)\left(1 - \tfrac{a}{W}\right)^{\frac{3}{2}}}$$

Compact tension:
$$K_I = \frac{P}{BW^{\frac{1}{2}}} . f\left(\frac{a}{W}\right)$$

(Ewalds & Wanhill, 1986):
$$f\left(\tfrac{a}{W}\right) = \frac{\left(2 + \tfrac{a}{W}\right)\left[0.886 + 4.64\left(\tfrac{a}{W}\right) - 13.32\left(\tfrac{a}{W}\right)^2 + 14.72\left(\tfrac{a}{W}\right)^3 - 5.6\left(\tfrac{a}{W}\right)^4\right]}{\left(1 - \tfrac{a}{W}\right)^{\frac{3}{2}}}$$

K_I = stress-intensity factor under Mode I loading

P = load; B = specimen width; W = specimen thickness

a/W = ratio of crack length to specimen thickness

$f(a/w)$ = geometric correction factor

The geometric factors for the bend specimen and compact tension specimens are valid for ($0 < a/W < 1$) with an accuracy of about 98% (Sakai & Bradt, 1993).

Typical load-displacement curves obtained for the three graphite materials are shown in Figure 5.28 for the bend specimens. In all cases, stable crack extension was achieved throughout the entire test. The highest maximum load was achieved in Gilsocarbon graphite, with IG110 graphite showing the lowest value. The UcarC material appeared to show little difference for the two specimen orientations. Typical K_R-curves obtained by the ACPD method are presented in Figure 5.29 for the bend specimen.

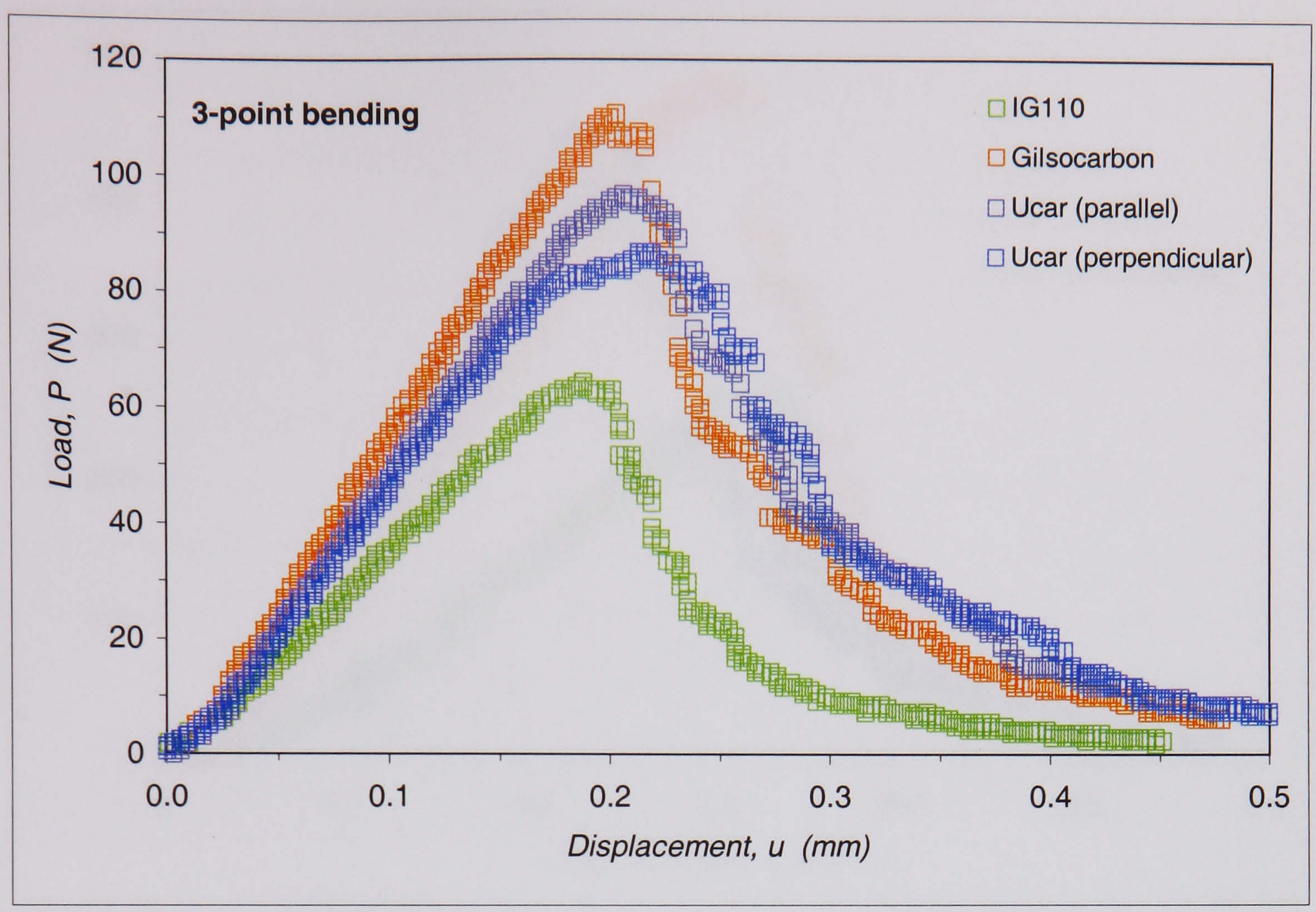

Figure 5.28. Load-displacement curves of the graphite specimens in 3-point bending.

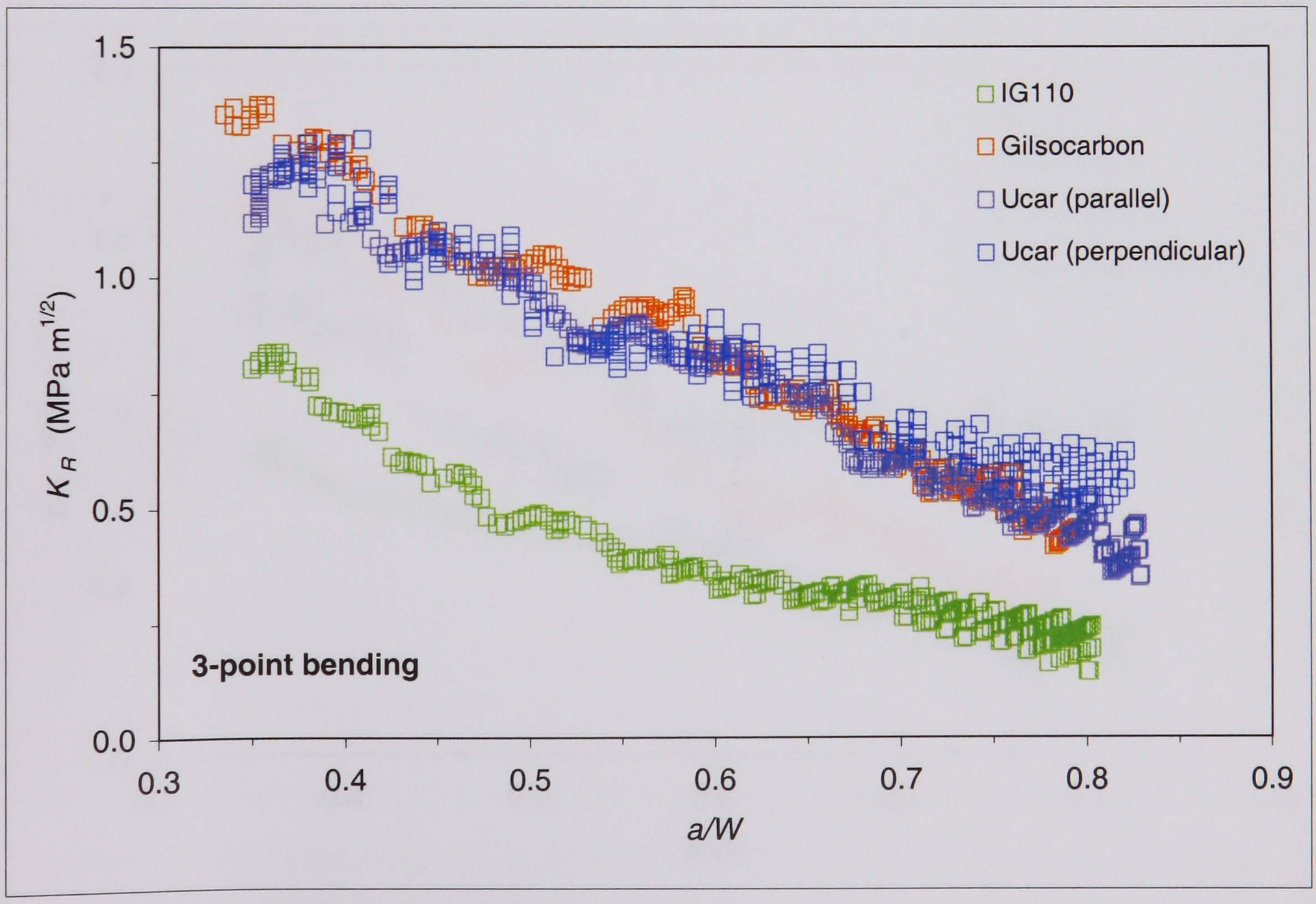

Figure 5.29. K_R-curves obtained by the ACPD method: 3-point bend specimens.

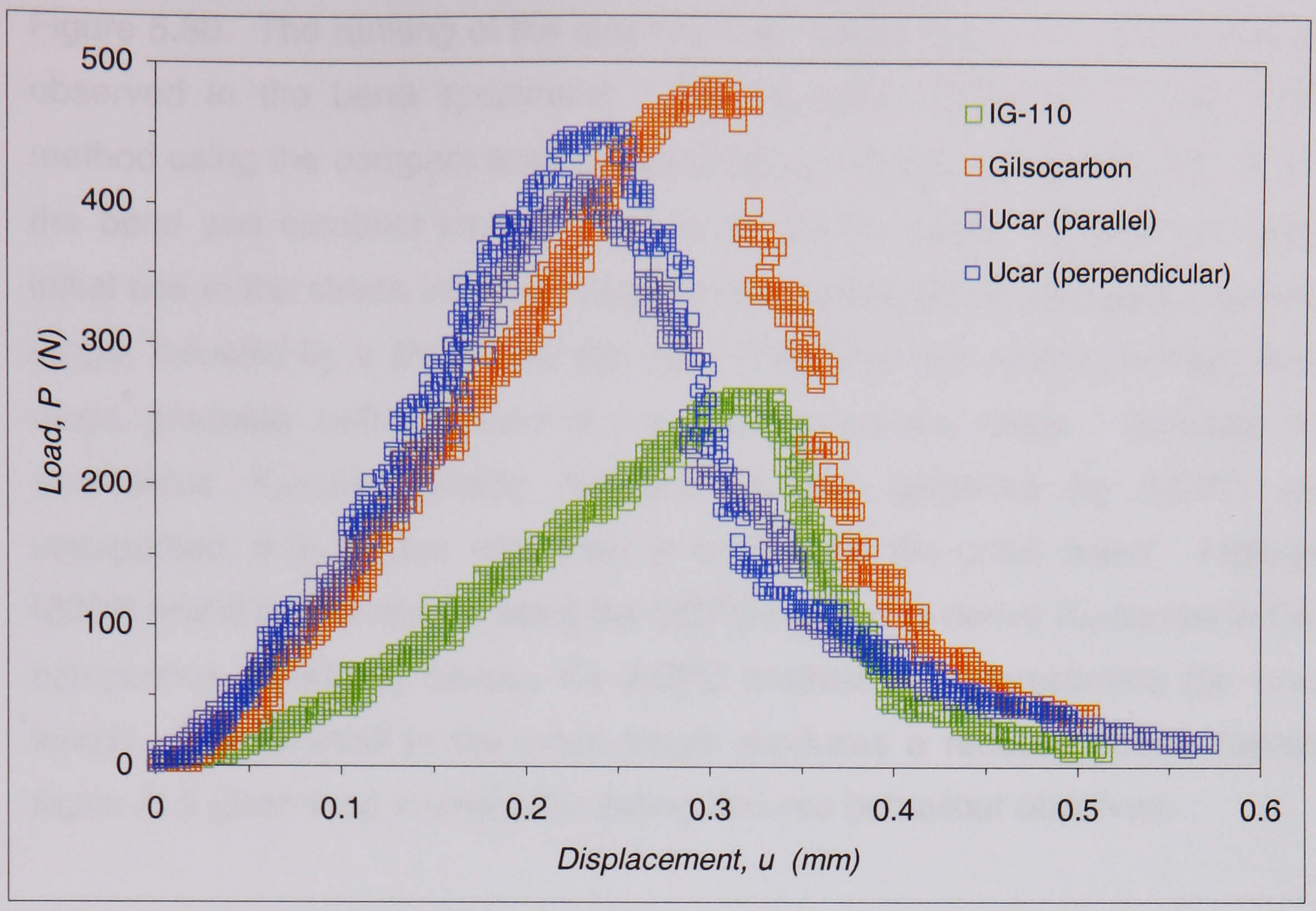

Figure 5.30. Load-displacement curves of the compact tension specimens.

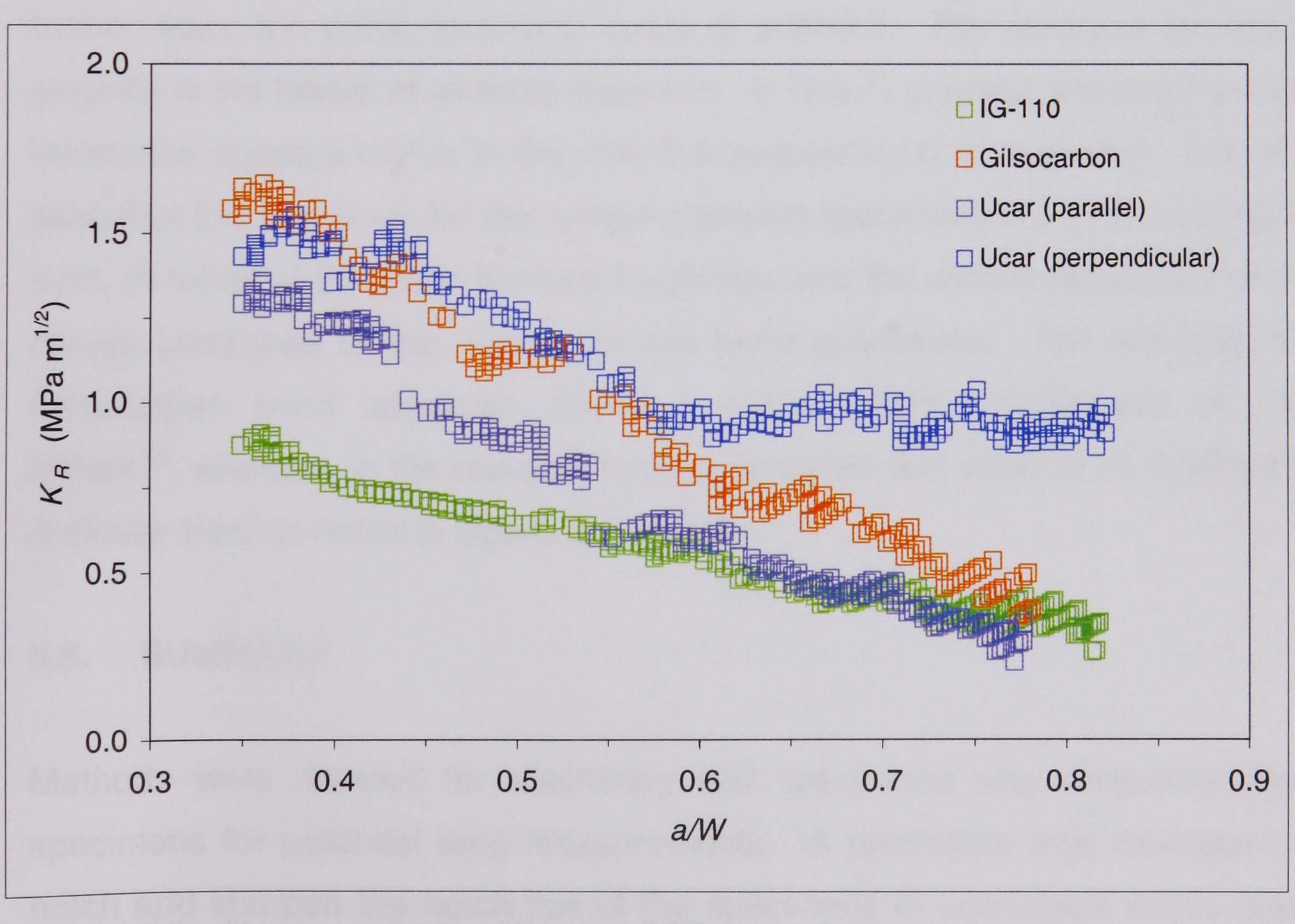

Figure 5.31. K_R-curves obtained by the ACPD method: compact tension specimens.

The load-displacement curves for the compact tension specimens are shown in Figure 5.30. The ranking of the graphite materials in this case is similar to that observed in the bend specimens. The K_R-curves obtained by the ACPD method using the compact tension specimens is shown in Figure 5.31. In both the bend and compact tension specimens, the K_R-curves show a very steep initial rise in the stress intensity factor over an extremely small crack extension range, followed by a short-lived plateau. Thereafter, the stress intensity factor drops gradually until the end of the crack extension range. Although the anomalous K_R-curve profile obtained for the graphites by ACPD was unexpected, it is a clear indication of bridging in the crack wake. Arulrajah (2002) found similar results using the DCPD method to derive K_R-curves in C/C-composites. Bridging causes the ACPD method to underestimate the crack length. The shortfall in the crack length produces a reduced stress intensity factor at a given load, causing the falling *R*-curve behaviour observed.

In both specimen types, the K_R-curve for Gilsocarbon appears to be more highly placed than that of UcarC and IG110 graphite, with this difference vanishing further down the crack extension range at $a/W \approx 0.6$. The K_R-curve for IG110 graphite is the lowest of all three materials. In UcarC graphite, the crack growth resistance appears higher in the direction perpendicular to extrusion. It is also seen that the K_R-curves for the compact tension specimens are generally higher both, in terms of the initial fracture toughness and the overall placement of the curves compared to the curves for the bend specimens. For example, the Gilsocarbon bend specimen shows a crack initiation toughness of ~1.4 $MPam^{1/2}$, whereas, in the compact tension specimen this value is ~1.6 $MPam^{1/2}$. A similar trend is noted in UcarC and IG110.

5.5. SUMMARY

Methods were devised for machining test specimens and preparing these specimens for potential drop measurements. A procedure was developed to notch and sharpen the notch tips of the specimens to encourage stable crack growth. Various improvements were made to the ACPD method to optimise test conditions for R-curve measurement. Generally, the output voltage of the specimens was low due to the low resistivity of nuclear graphite. An attempt

was made to increase the output voltage by changing the input current and the current probe positions but proved unsuccessful. Errors in the output voltage due to thermoelectric effects were avoided by using an AC current rather than the DC current.

The experimental calibration technique was found to have good reproducibility despite the structure-property variations between the different nuclear graphite materials, when the normalised voltage drop is measured as a function of the relative depth of cut. Remarkably, the normalised calibration data for both the bend and compact tension configurations were found to lie on a single calibration curve, implying that a master calibration curve could be applied to the specimen configurations.

The master curve also points to the existence of a theoretical model that could define the normalised voltage drop in the graphite specimens. Comparison of the experimental calibration data obtained from the compact tension configuration, with calculated data obtained by a theoretical expression showed close correlation between the two sets of data. However, the theoretical model has limited applicability since it applied for a specific, current-voltage probe configuration and only for a fixed initial notch length. The theoretical model also failed to describe the experimental calibration curves towards the end of the simulated crack extension range.

The success of the notch tip, sharpening procedure was cònfirmed by the load-displacement curves obtained for the bend and compact tension specimens, which all passed smoothly over the maximum load point. The K_R-curves obtained by the ACPD method all show an anomalous, falling behaviour over most of the crack extension range. Before the drop in K_R, the curves show a steep rise in K_R, over a very small, crack extension range, followed by a very short-lived plateau, and then the falling behaviour. Qualitatively, the ranking of the nuclear graphites in terms of the ACPD-derived K_R-profiles was similar in both the bend and compact tension specimens, with the K_R-curves being marginally higher in the compact tension specimens.

CHAPTER 6

COMPARISON OF *R*-CURVE BEHAVIOUR OBTAINED BY DIFFERENT CRACK LENGTH MEASUREMENT METHODS

It was pointed out that one of the aims of this study was to compare *R*-curves obtained by the ACPD method with other crack length measurement techniques. This was also necessary given the anomalous K_R-curve profiles obtained by the ACPD method, as shown in the previous chapter. In this regard, the optical method and a theoretical compliance method were adopted. In performing the optical crack length measurements, the ACPD across the fracture specimen was recorded simultaneously, to allow a direct comparison of the *R*-curves obtained by the two methods.

6.1. Simultaneous Optical and Electrical Measurements

Given the dimensions of the bend specimens, i.e. 12x10x100mm, a large 3-point bending jig was needed to ensure that $S/W \geq 8$. Accommodating this jig, in addition to the travelling microscope and pieces of the ACPD equipment was not possible on the base of the cross-head. Another problem was that the optical measurements on the 3-point bending specimens could not be made in-situ because it was not possible to use the travelling microscope effectively with the larger bending jig in place.

It was therefore necessary to load and unload the bend specimens at various displacement intervals. The specimen was removed from the jig at each interval and the optical crack length measured using a microscope with vernier-stage (see Figure 6.1). Thereafter, the specimen was returned carefully to the jig, the wire probes re-connected, and, the specimen re-loaded to a higher displacement interval. This procedure was repeated at each interval.

It was also necessary to use resistance change measurements instead of the ACPD method at each displacement interval because the oscilloscope did not have the storage capacity required for the long duration of these load-unload tests. Resistance measurement only required the use of an ohmmeter that was easily accommodated in the test set-up (Figure 6.1).

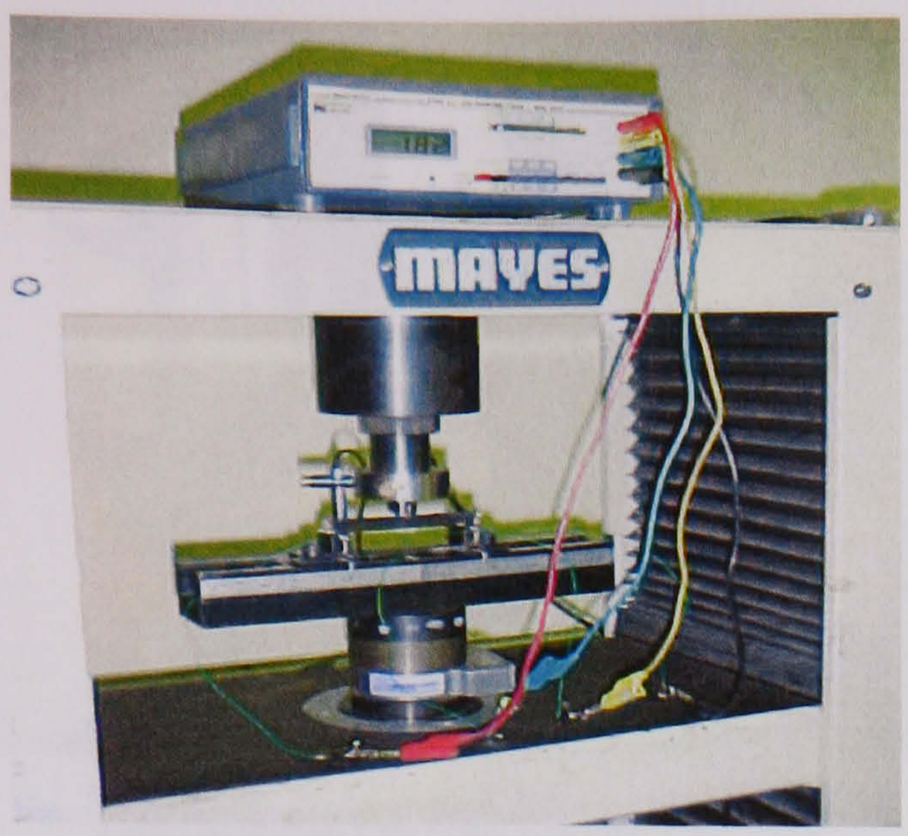

Resistance Measurement

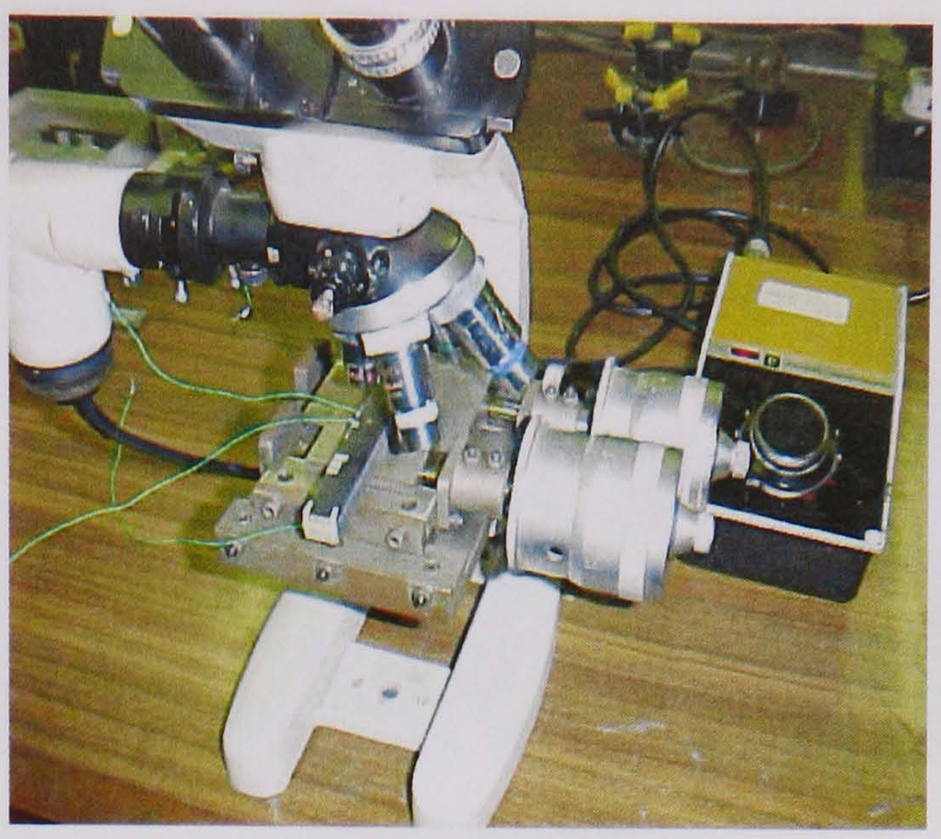

Optical measurement

Figure 6.1. Simultaneous crack length measurement in the bend specimens.

The crack length measurement using the resistance change was obtained from the calibration curve derived using the fractional change in resistance, as described in Chapter 5. A shortcoming of this approach was that the load-displacement data could not be recorded given the absence of the oscilloscope and the need to load-unload at various stages. The process of loading and unloading probably introduces some error into the measurements, as it is not possible to set-up the specimen in an identical manner each time. Nonetheless, this method allowed for a comparison between the *R*-curve derived optically with that obtained using the potential drop method.

With the compact tension specimens, it was possible to accommodate both the travelling microscope and ACPD test equipment. In this case, therefore, the potential drop was used and compared against the *R*-curve obtained optically (see Figure 6.2). With the compact tension specimens, crack length was measured in situ, whilst the cross-head was held at a pre-selected displacement interval. There was no need to load and unload.

The compact tension specimens and bend specimens were all tested using a speed of 0.050mm/min to reduce the duration of testing. Since the test had to be stalled at various intervals to make in situ measurements (see Figure 6.2), these tests lasted longer than the continuous ACPD tests. To enable storage of all the test data on the oscilloscope, it was necessary to ensure that tests were not too long. At 0.005mm/min, for example, tests would have lasted longer than 160 minutes, exceeding the time-base range of the oscilloscope.

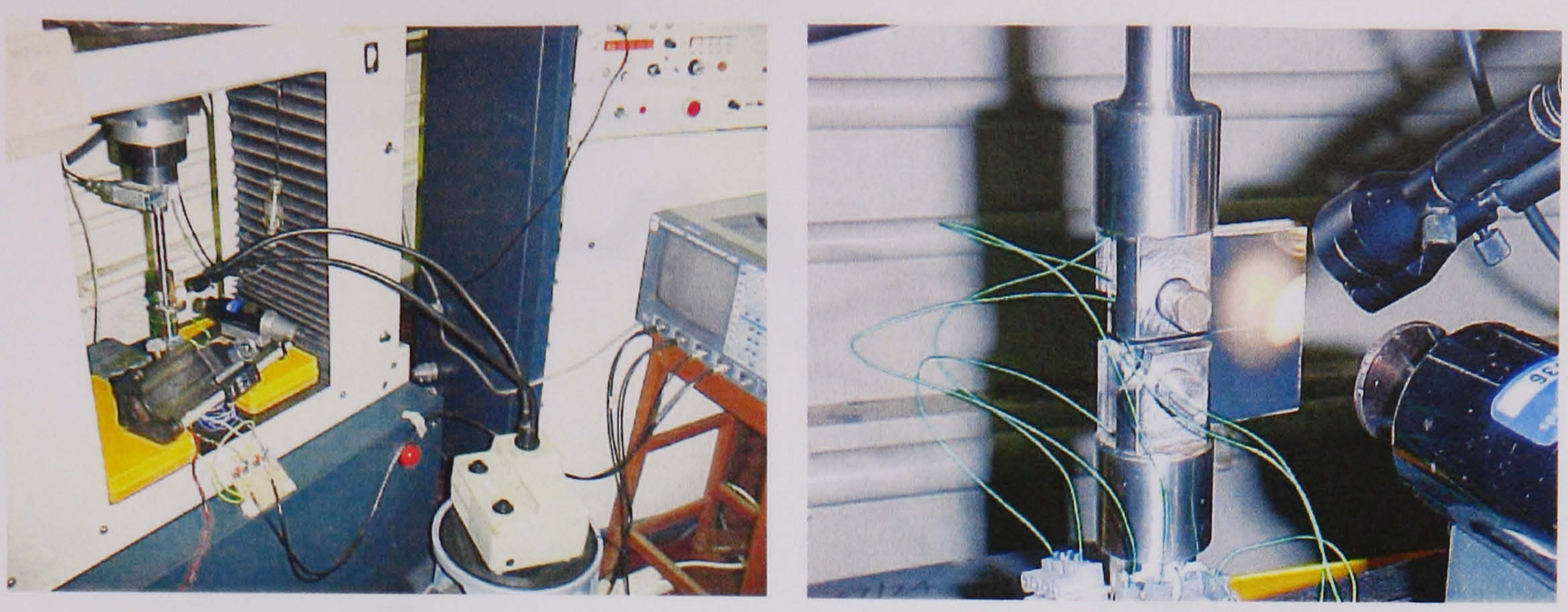

Combined ACPD-optical set-up | Close-up view

Figure 6.2. Set-up for simultaneous measurements in compact tension specimens.

A critical point in these tests was detecting the displacement interval at which crack initiation occurred. To determine the crack initiation point, an X-Y chart recorder was used to monitor the load-displacement response of the specimen. As soon as the plot began to show signs of non-linearity, the cross-head was stopped. Thereafter, the cross-head was stopped more frequently until the first sign of cracking became visible in the travelling microscope.

For the bend specimen, the crack initiation point was detected from the initial resistance change. The *X-Y* plotter had an advantage over the oscilloscope in that it allowed the load-displacement response to be scaled up considerably, thereby making it easier to detect the initial deviation from linearity. In general, it was found that the point of crack initiation corresponded with the initial drop in the output voltage, or, the initial resistance change.

To estimate the crack length from the potential drop of the compact tension specimens in these tests, a load-time-voltage plot was used. A typical plot is shown in Figure 6.3. From the plot, the voltage and load at each hold point was determined. During the hold points, whilst the optical measurements were being taken, the load was found to drop slightly and stabilise after a short period, and, the voltage was noted to fluctuate slightly. The load used to calculate the stress intensity at a given hold-point was the load taken at the instant the cross-head was stopped. The voltage reading over this hold-period, from which the crack length was calculated using the potential drop calibration curve, was the average voltage measured over the hold-period.

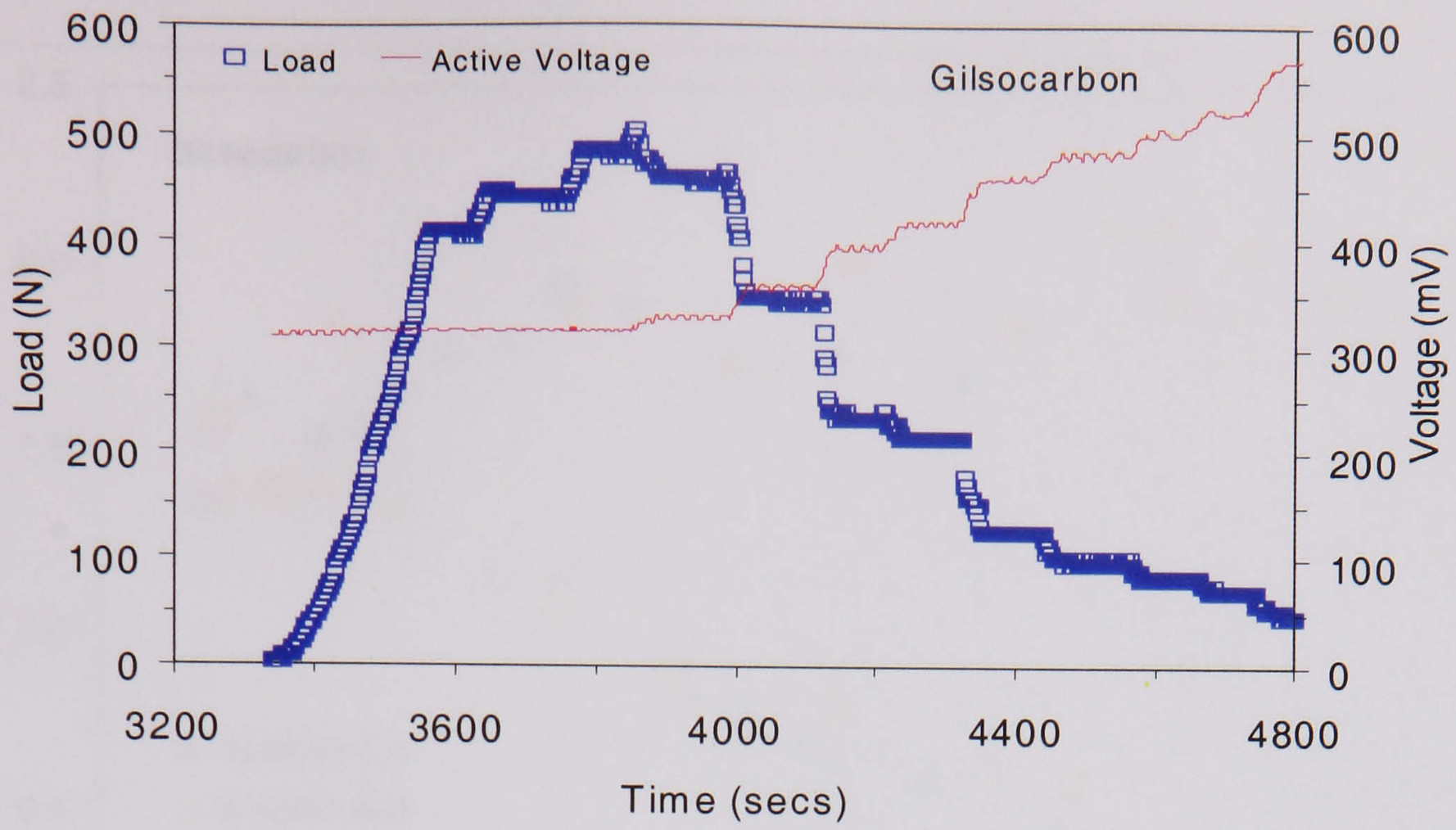

Figure 6.3. Typical load-time-voltage plot used for ACPD measurements.

Using the method described in Chapter 5, the K_R-curve of the nuclear graphites was derived for the bend and compact tension specimens using both the electrical measurements, and the optical measurements. These K_R-curves are presented in Figures 6.4 and 6.5. In each plot, both the bend test and compact tension test data are shown except for the UcarC material where the results from the two specimens are presented separately.

The results clearly indicate a difference between the K_R-curves obtained by the optical method, and, the K_R-curves derived using the electrical measurements. In all cases, the electrical measurements produced a falling *R*-curve behaviour, similar to that observed previously. The K_R-curves derived optically all show an initial rise in stress intensity factor, followed by a levelling off to a plateau region, and in some cases, a steep rise towards the end of the crack extension range. This behaviour was consistent with the K_R-curve behaviour of polycrystalline graphite reported by other workers (Sakai et al, 1988). The results also indicate that the Gilsocarbon and UcarC graphite have similar K_R-curve behaviour. The crack initiation toughness ($K_{C,init}$) in the Gilsocarbon graphite appears slightly higher at about 1.3-1.5 MPa $m^{1/2}$, compared with 1.2-1.4 MPa $m^{1/2}$ in the UcarC graphite. The plateau toughness ($K_{R,plat}$) of both materials appeared similar at about 1.7-1.8 MPa $m^{1/2}$, with Gilsocarbon displaying a slightly higher plateau. The IG110 graphite was the lowest in terms of both toughness parameters with $K_{C,\,init}$ = 0.7-0.9 MPa $m^{1/2}$, and, $K_{R,plat}$ = 1.0-1.2 MPa $m^{1/2}$.

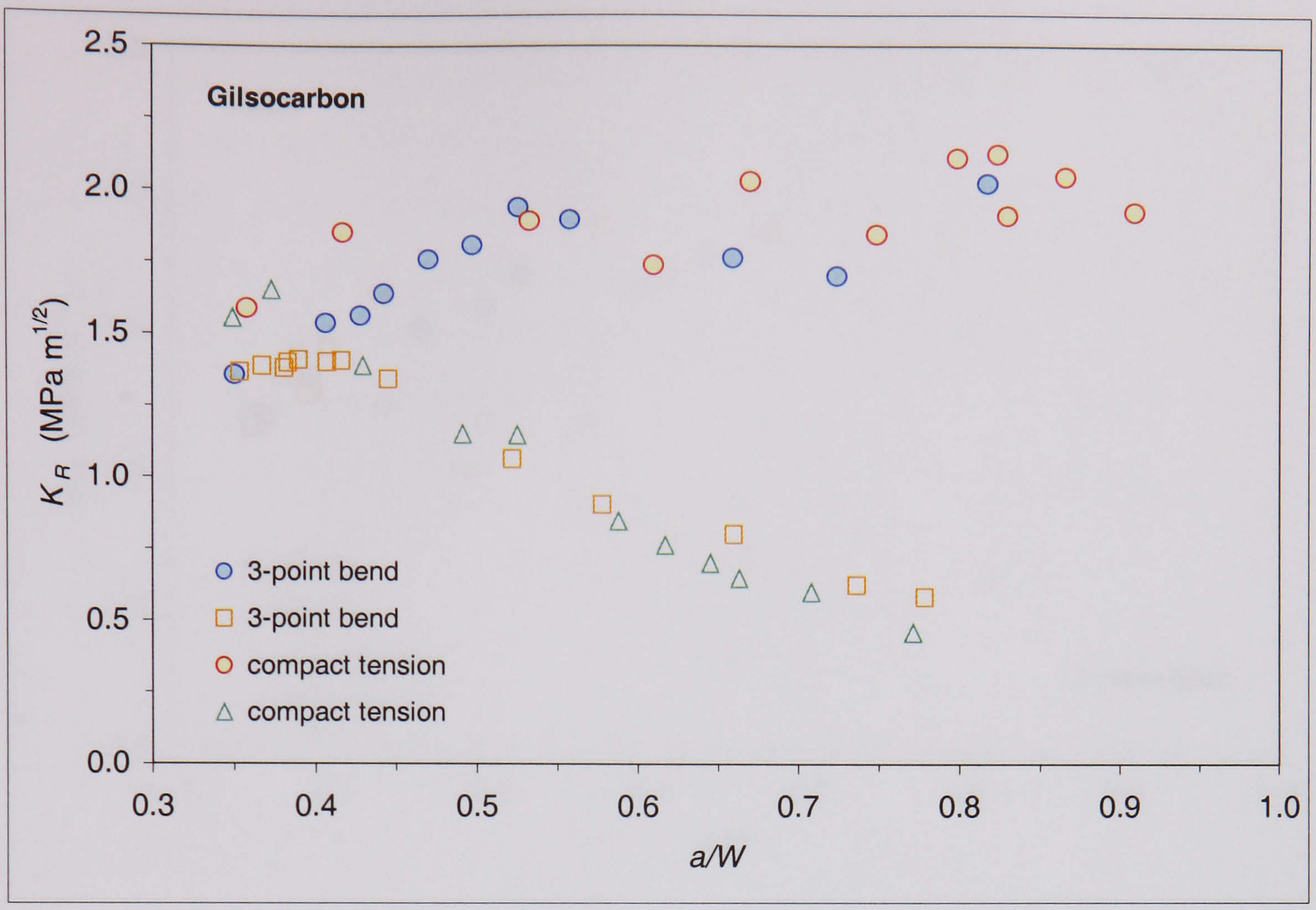

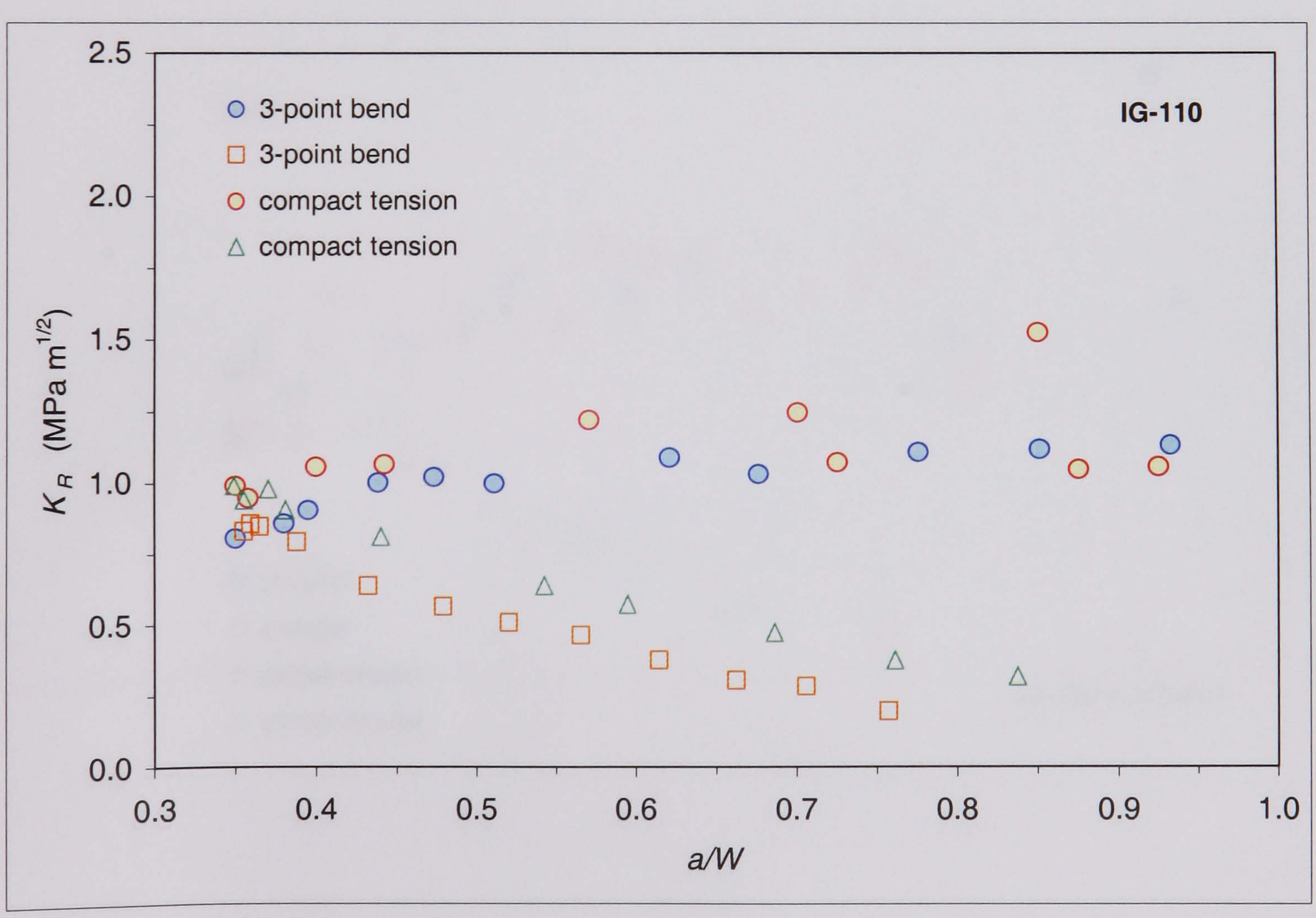

Figure 6.4. Comparison of K_R-curves for Gilsocarbon and IG110 graphite obtained by the optical, ACPD, and, resistance measurements using 3-point bend and compact tension specimens; (O = optical, Δ = ACPD, □ = resistance).

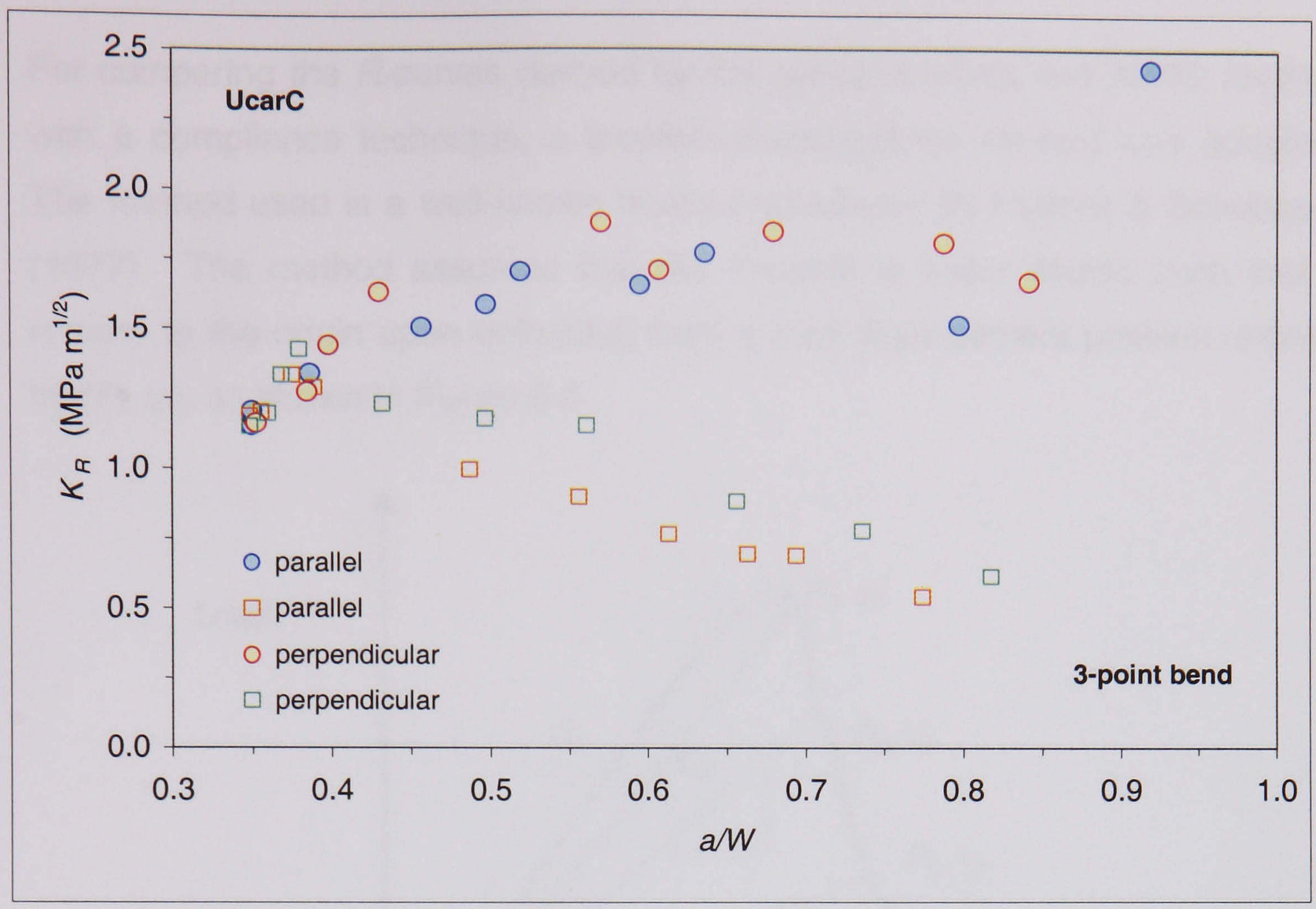

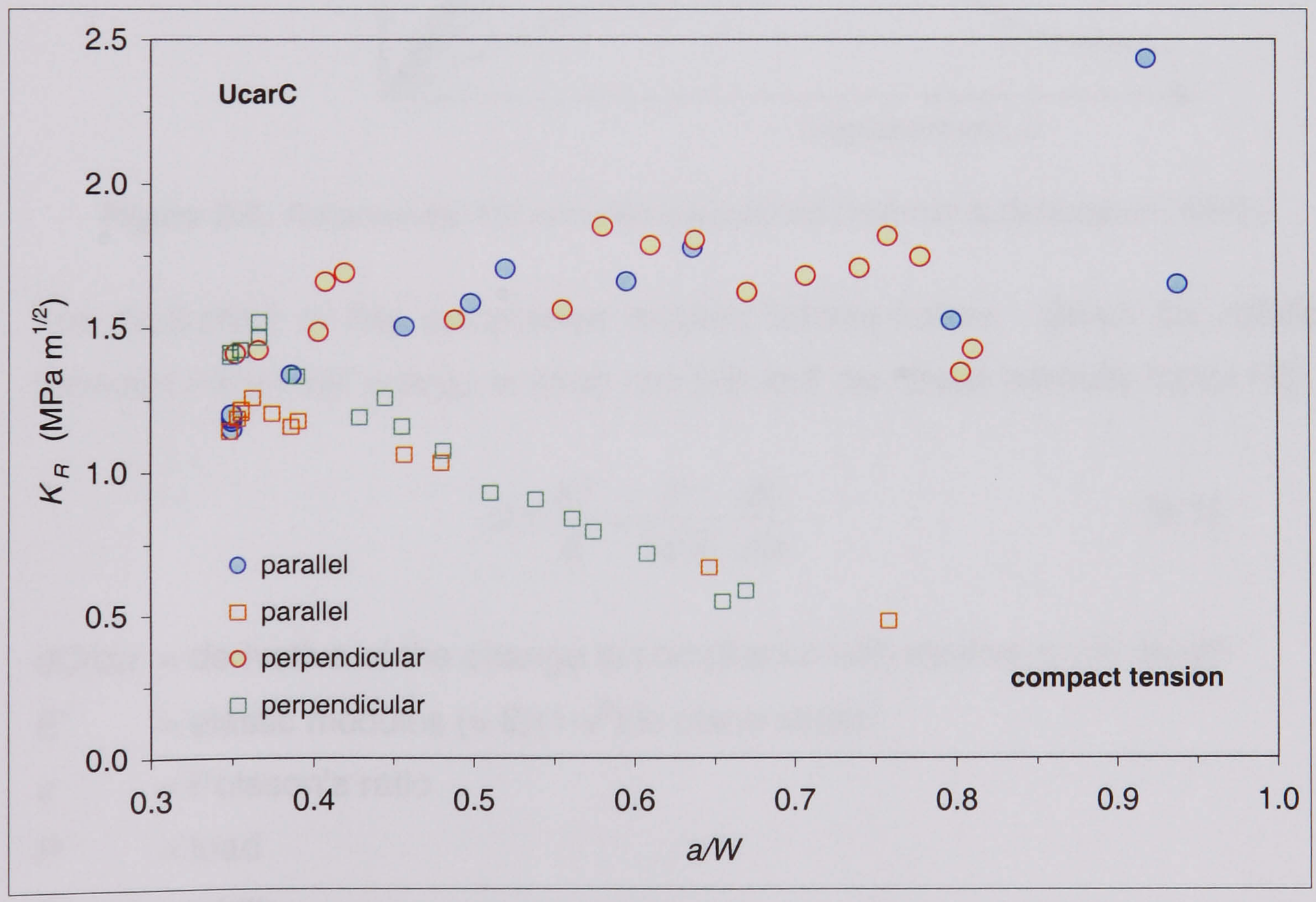

Figure 6.5. Comparison of K_R-curves for UcarC graphite, in two crack growth directions, using optical, ACPD and, resistance measurements in 3-point bend and compact tension specimens; (O = optical, □ = electrical measurements).

6.2. Measurement of *R*-curves by a Theoretical Compliance Method

For comparing the *R*-curves derived by the optical method and ACPD method with a compliance technique, a theoretical compliance method was adopted. The method used is a well-known method developed by Hubner & Schubauer (1977). The method assumes that the material is linear elastic such that it returns to the origin upon unloading from a load-displacement position defined by (P_i, u_i), as shown in Figure 6.6.

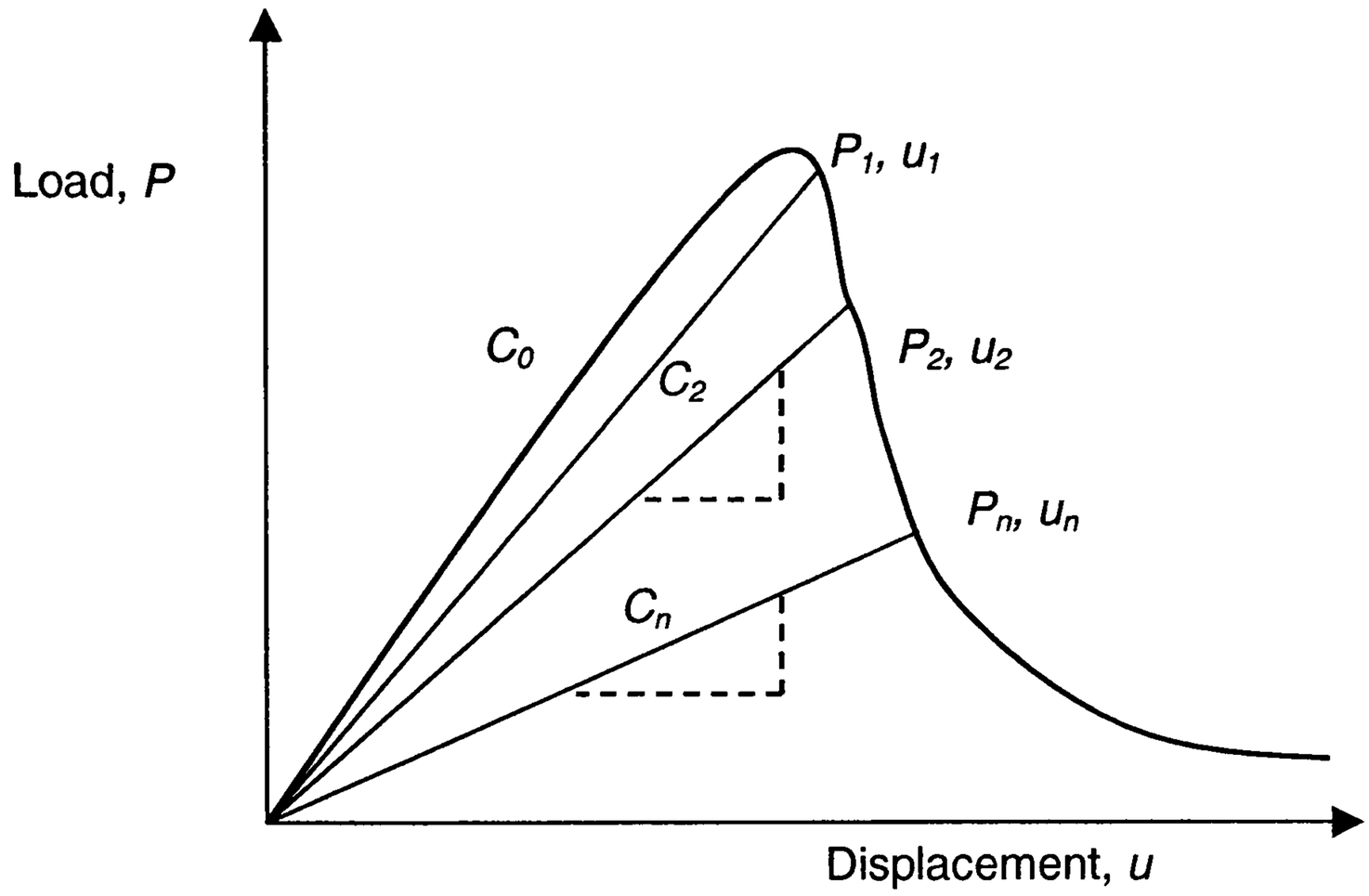

Figure 6.6. A schematic the compliance method (Hubner & Schubauer, 1977).

The derivation of this compliance method follows below. Given the relation between the elastic energy-release rate (G) and the stress intensity factor (K):

$$G = \frac{K_I^2}{E'} = \frac{P^2}{2BW} \cdot \frac{dC}{d\alpha} \qquad [6.1]$$

$dC/d\alpha$ = derivative of the change in compliance with relative crack length

E' = elastic modulus (= $E/(1-\nu^2)$ in plane strain)

ν = Poisson's ratio

P = load

B = width

The stress intensity factor for a cracked beam in 3-point bending is given by:

$$K_I = \frac{3PS}{2BW^{3/2}} \cdot Y(\alpha) \qquad [6.2]$$

Therefore,

$$G = \frac{P^2}{2BW}.\frac{dC}{d\alpha} = \frac{K_I^2}{E'} = \frac{1}{E'}\left[\frac{3PS}{2BW^{3/2}}.Y(\alpha)\right]^2 \qquad [6.3]$$

$Y(\alpha)$ = geometric correction factor

S = load span

W = thickness

It follows that,

$$\frac{dC}{d\alpha} = \frac{9S^2}{2BE'W^2}[Y(\alpha)]^2 \qquad [6.4]$$

So,

$$C - C_0 = \frac{9S^2}{2BE'W^2}\int_{\alpha_0}^{\alpha} Y^2(\alpha)d\alpha \qquad [6.5]$$

Using the as-notched compliance (C_0) and the compliance at a given load-displacement interval (C), the crack length can be calculated by solving for (α). This requires finding the α-value for the function $Y(\alpha)$ over the interval [α_0 - α] such that right hand side of Equation [6.5] equals the compliance change over this interval. Using the computed α-values, the K_R-curve can then be derived.

For the compact tension configuration, this relation alters slightly according to the stress intensity equation for this specimen configuration. In addition, the $Y(\alpha)$ function for the compact tension specimen is substituted in the expression, so that Equation [6.5] becomes:

$$C - C_0 = \frac{2}{BE'}\int_{\alpha 0}^{\alpha} Y^2(\alpha)d\alpha \qquad [6.6]$$

A distinct advantage of the radiant line method is that it only requires the experimental load-displacement data in the analysis. This poses an advantage over the experimental compliance calibration, which can be rather tedious and prone to error, particularly over the initial crack extension region when the change in compliance is small (Ouagne, 2000). However, the method is not, without its shortcomings. A particular dilemma one is faced with concerns the value of the elastic modulus to be used in Equation [6.5].

Some consideration was given to this matter in Section 4.5 where it was explained how shear loading influences the measured flexural modulus. It was also indicated that shear effects are really only eliminated at high *S/W* ratios, the required *S/W* ratio being higher in more anisotropic materials. The low flexural modulus values that were obtained are most likely due to shear effects, as well as frictional loading at support rollers. Dimensional inaccuracy of the specimens would also contribute to experimental error. Another issue concerns the elastic modulus value used for the compact tension specimen, which must experience a different load distribution than the specimens in 3-point flexure.

Given this dilemma, it was decided to use the sonic modulus values in the calculations. Intuitively, this represented a balance between the low flexural modulus values and the high values obtained by Fischer et al's method (1980). Although Fischer et al's method (1980) is supposed to produce a more representative elastic modulus, it was felt that this would not reflect the experimental situation where the shear modulus of the material must influence its stiffness. It was also found that small variations in the *R*-curve profile occur, with small differences in the elastic modulus that is used in the compliance calculation, as will be shown later.

It is worth pointing out that Hubner & Schubauer (1977) found their theoretical method to work well, probably because they tested isotropic materials, i.e. alumina and brass. It was not specified whether the brass was in the annealed or as-rolled condition. They also compared experimentally determined modulus values with sonic resonance values and found excellent correlation, again, probably due to the isotropy of their materials. In addition, their specimens were very accurately machined and tested in a specially designed fixture.

In applying the theoretical compliance method, the experimental load-displacement data for both the 3-point bend and compact tension specimens was used. In either case, the relevant geometric factor and specimen dimensions were used in the computation. A Poisson's ratio of 0.2 was assumed for all the materials, this having little influence on the overall *R*-curve profile as will be shown later. The solution to the integral of the $Y(\alpha)$-function in Equation [6.5] was derived using MathCad Version 2001 software.

The K_R-curves of the graphite materials derived by the compliance method are compared in Figure 6.7 for both the 3-point bend and compact tension specimens. For both specimen types, the ranking of the materials is similar, with IG110 graphite displaying the lowest overall toughness. In all cases, the crack growth resistance appears to be higher for the compact tension specimens than the 3-point bend specimens, suggesting an influence from the specimen type on the observed *R*-curve behaviour. There also appears to be a marked difference in crack growth resistance parallel and perpendicular to the extrusion direction in the UcarC graphite.

6.3. Comparison of the K_R-curves obtained by the Different Methods

The K_R-curves of the nuclear graphites derived by compliance are compared graphically with those obtained by the optical and ACPD methods in Figure 6.8, and Figure 6.9 for the 3-point bend and the compact tension specimens respectively. In all cases, the ACPD derived K_R-curves show a falling behaviour. The optical and compliance methods produce similar K_R-curves for each graphite type in the 3-point bend tests. However, in the compact tension specimens, the compliance-based K_R-curves tend to rise above those obtained by the optical method. The optically derived K_R-curves also show considerable scatter, which was expected given the difficulty in accurately resolving the crack tip, and, the possible influence of an irregular crack front, or, crack front bowing.

Unlike the K_R-curves obtained by the optical method, the compliance-based curves show a more gradual rise in stress intensity factor over the initial part of the crack extension range, with the plateau-like region appearing later in the *a/W*-range. The more gradual, initial rise probably stems from the tendency of the compliance method to translate the initial non-linearity in the load-displacement curve to an increment in the crack length. Some of the curves show a slight falling tendency at the end of the *a/W*-range. Qualitatively, the K_R-curves for both the 3-point bend and compact tension specimens compare well against those derived optically. However, the compliance-based K_R-curves show higher $K_{R,plat}$ values than the curves derived optically. For example, the $K_{R,plat}$ values for Gilsocarbon and UcarC rise above 2.0 MPa $m^{1/2}$ in compact tension tests, but remain just below this level in the bend tests.

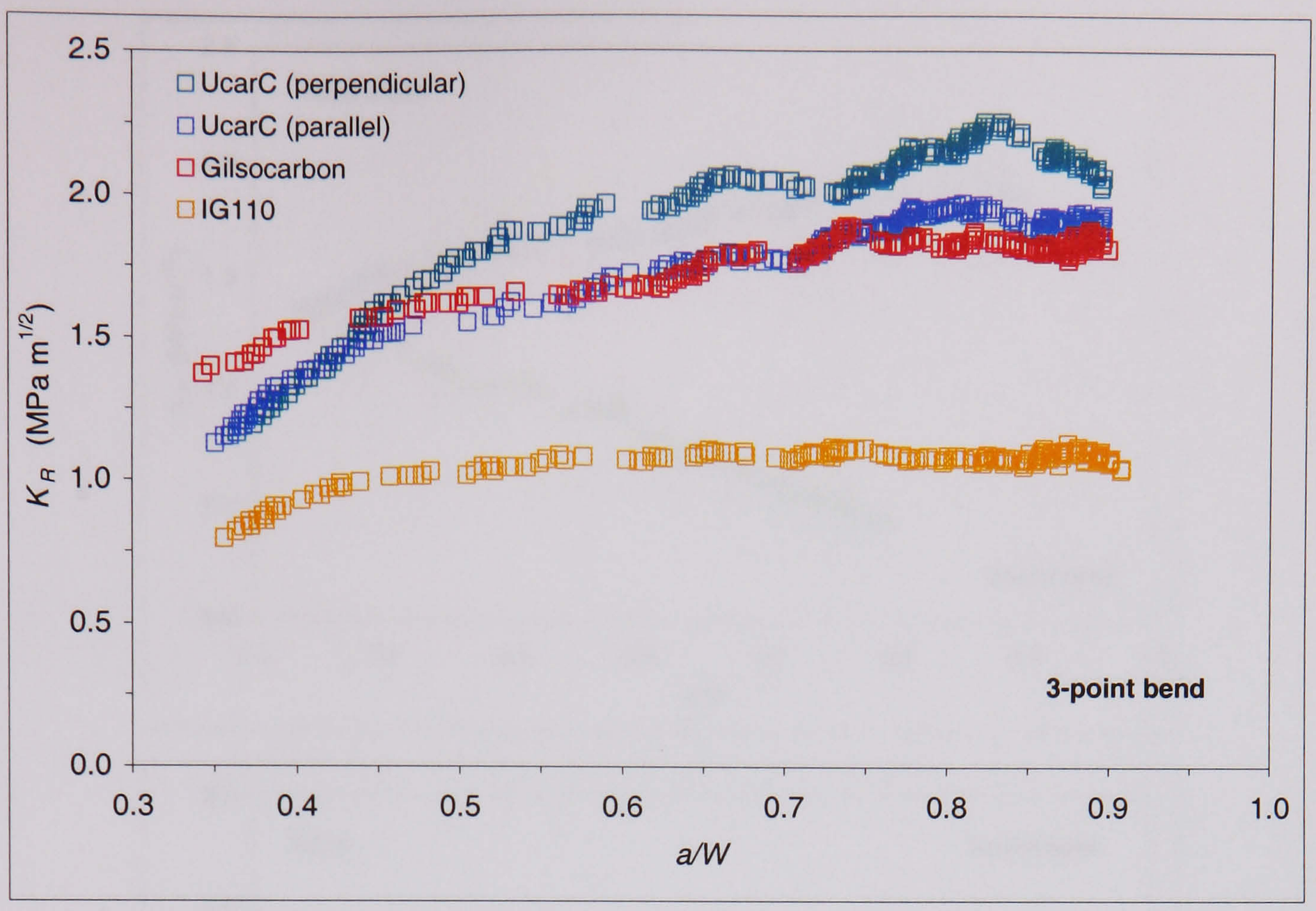

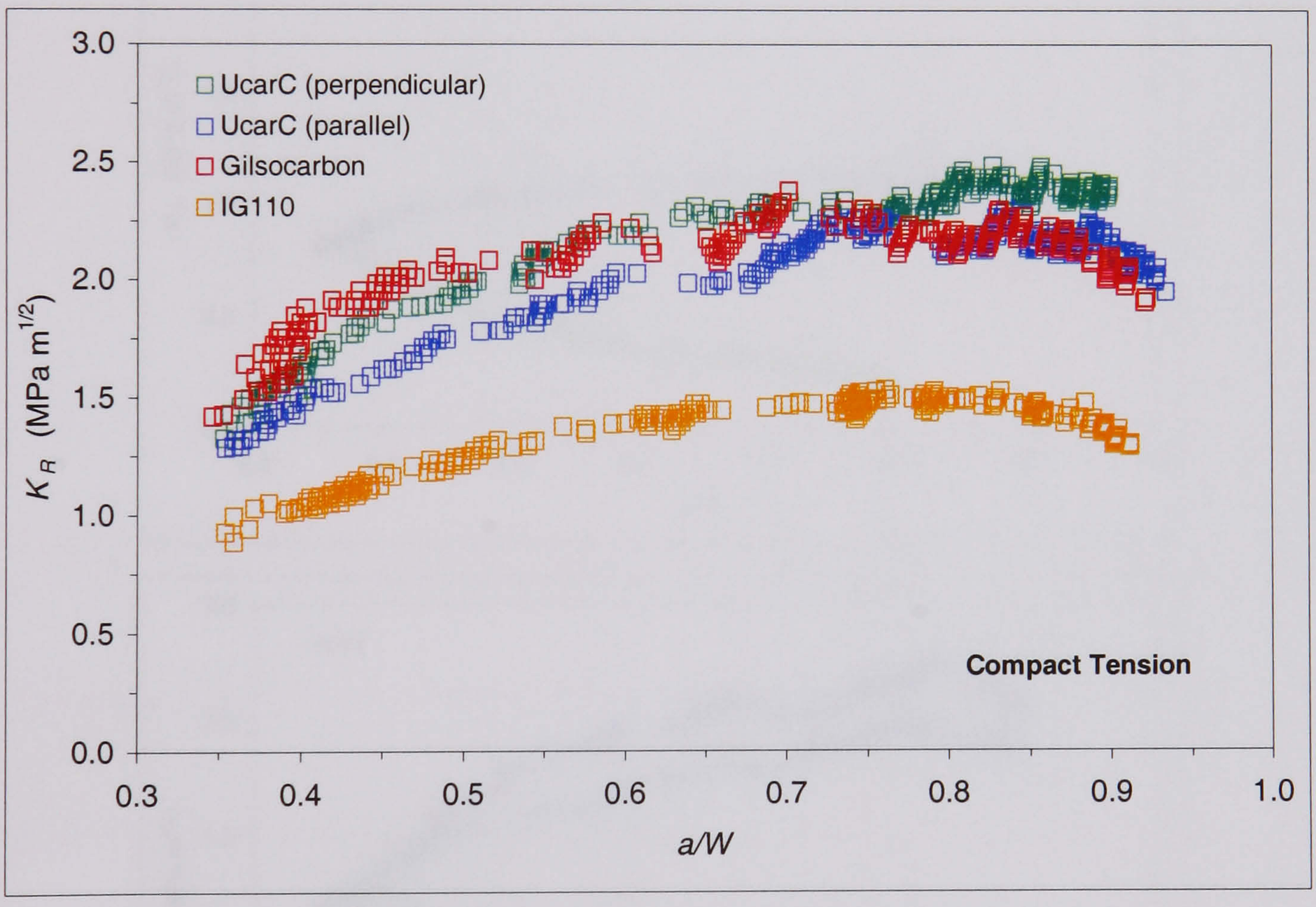

Figure 6.7. K_R-curves of the nuclear graphite materials obtained by the compliance method in the bend and compact tension specimens.

Other factors that cause scatter in the optical data are the irregular crack path and its pore-following tendency. Qualitatively, the K_R-curve ranking in Figures 6.8 and 6.9 correlates with that found by the ACPD method. That is, the Gilsocarbon graphite shows slightly higher toughness than UcarC over the initial portion of the crack extension range, with UcarC showing high toughness towards the latter part of the range. Overall, IG110 ranks the lowest.

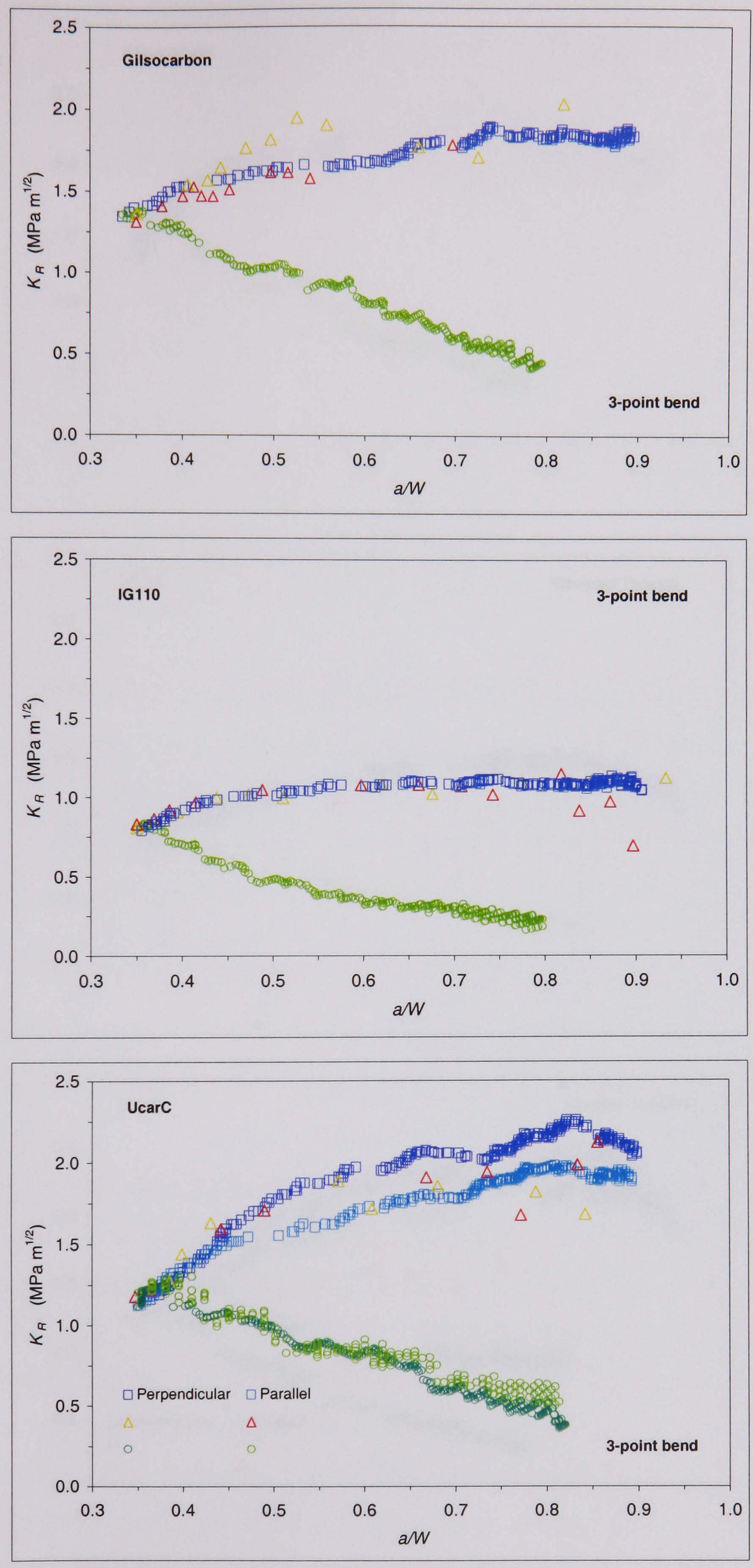

Figure 6.8. Comparison of K_R-curves for Gilsocarbon, IG110, and, UcarC graphite obtained by the optical, ACPD, and, compliance methods in 3-point bending; (□ = compliance, Δ = optical, O = ACPD).

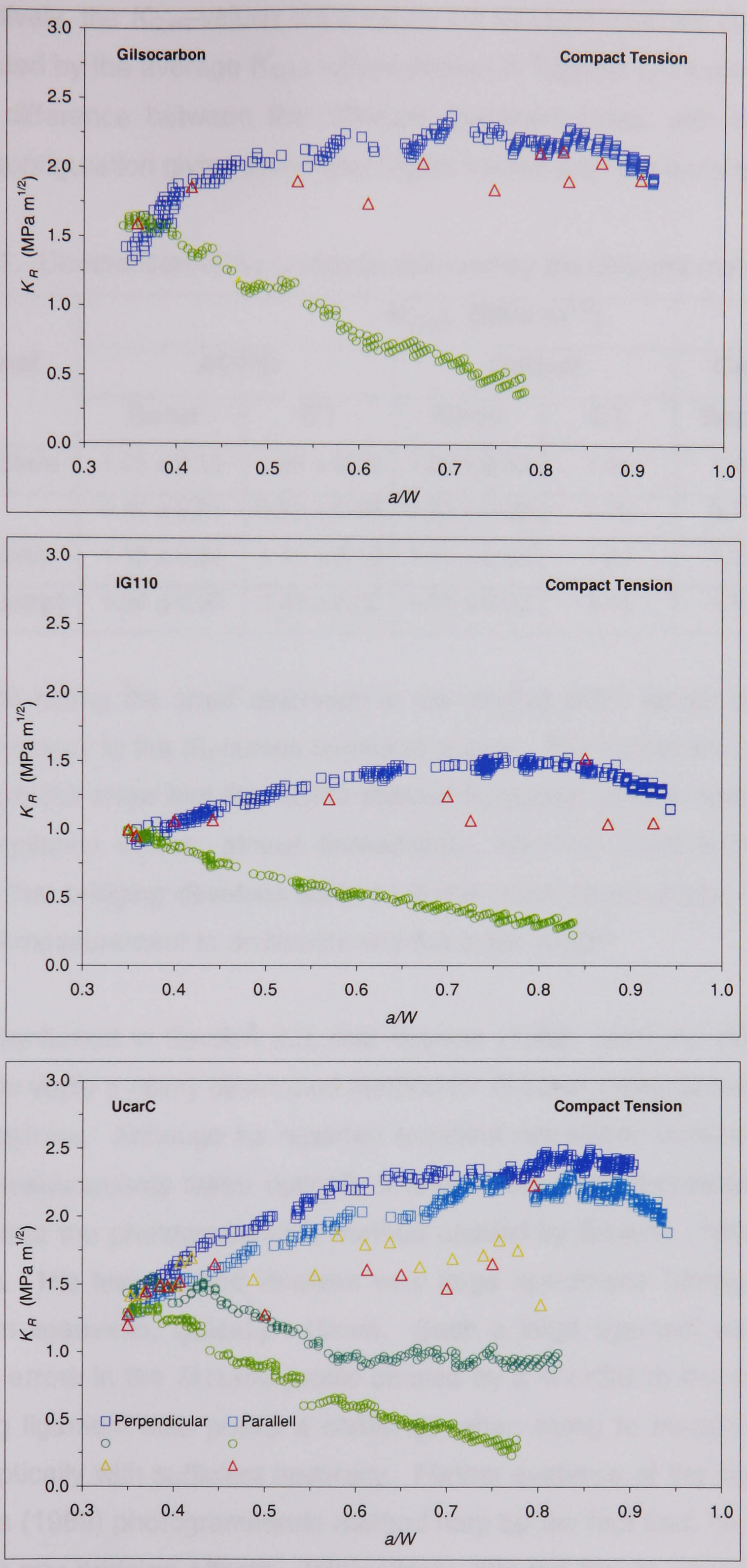

Figure 6.9. Comparison of K_R-curves for Gilsocarbon, IG110, and, UcarC graphite obtained by the optical, ACPD, and, compliance methods in compact tension; (□ = compliance, Δ = optical, O = ACPD).

Quantitatively, the $K_{C,init}$-values obtained by the different methods compare well, as indicated by the average $K_{C,init}$ values shown in Table 6.1. However, there is a slight difference between the different specimen types, with the compact tension configuration giving somewhat higher values than the bend specimen.

Table 6.1. Comparison of $K_{C,init}$ values obtained by the different methods.

Material	$K_{C,init}$ (MPa m$^{1/2}$)					
	ACPD		Optical		Compliance	
	Bend	CT	Bend	CT	Bend	CT
Gilsocarbon	1.25 ± 0.12	1.46 ± 0.13	1.33 ± 0.03	1.58	1.40	1.42
IG110	0.81 ± 0.01	0.92 ± 0.06	0.82 ± 0.02	0.99	0.79	0.89
UcarC (prll)	1.18 ± 0.04	1.17 ± 0.19	1.17 ± 0.02	1.20	1.13	1.29
UcarC (perp)	1.20 ± 0.06	1.42 ± 0.02	1.20 ± 0.03	1.41	1.15	1.32

It is worth noting the small extension in the relative crack length during which the discrepancy in the K_R-curves begins to appear. The K_R-curves in Figure 6.8 and Figure 6.9 show that the ACPD derived K_R-curves deviate from the optical and compliance curves, almost immediately, following crack initiation. This signifies that bridging develops early on in the crack growth stage, causing the electrical measurement to underestimate the crack length.

It was mentioned in Section 2.3, that Browne (1989) used the potential drop method to verify a newly developed method for *R*-curve measurement in coarse grain ceramics. Although he reported excellent correlation between the crack length measurements taken optically and that measured electrically, it seems unlikely that the photogrammetric method applied by Browne (1989) was very accurate. His test method involves very large specimens having long crack extension ligaments, typically >10mm. Such a large ligament would tend to disclose errors in the *R*-curve profile caused by a shortfall in the crack length. The long ligament also poses a challenge when trying to measure the crack length optically with sufficient accuracy. Further evidence of the inadequacy of Browne's (1989) photogrammetric method may be the fact that, he was unable to detect any bridging effects. Interestingly, this led him to conclude that the main toughening mechanism was microcracking in the frontal process zone.

6.4. Influence of Elastic Modulus and Poisson's Ratio on *R*-curve Profile

The possible influence of the elastic modulus and Poisson's ratio that is input for the compliance calculations was discussed briefly in Section 6.2. It is demonstrated here, that these parameters have little influence on the overall *R*-curve profile, within the known limits for the material being considered. *R*-curves for Gilsocarbon and IG110 graphite are compared in Figure 6.10 using different elastic modulus values and Poisson's ratios in the calculations. In both cases the sonic modulus and flexural modulus values were applied (see Section 4.5). For the Poisson's ratio, the calculations were compared using values of 0.2 and 0.3. Clearly, the *R*-curve profiles change only slightly, towards the end of the crack extension range.

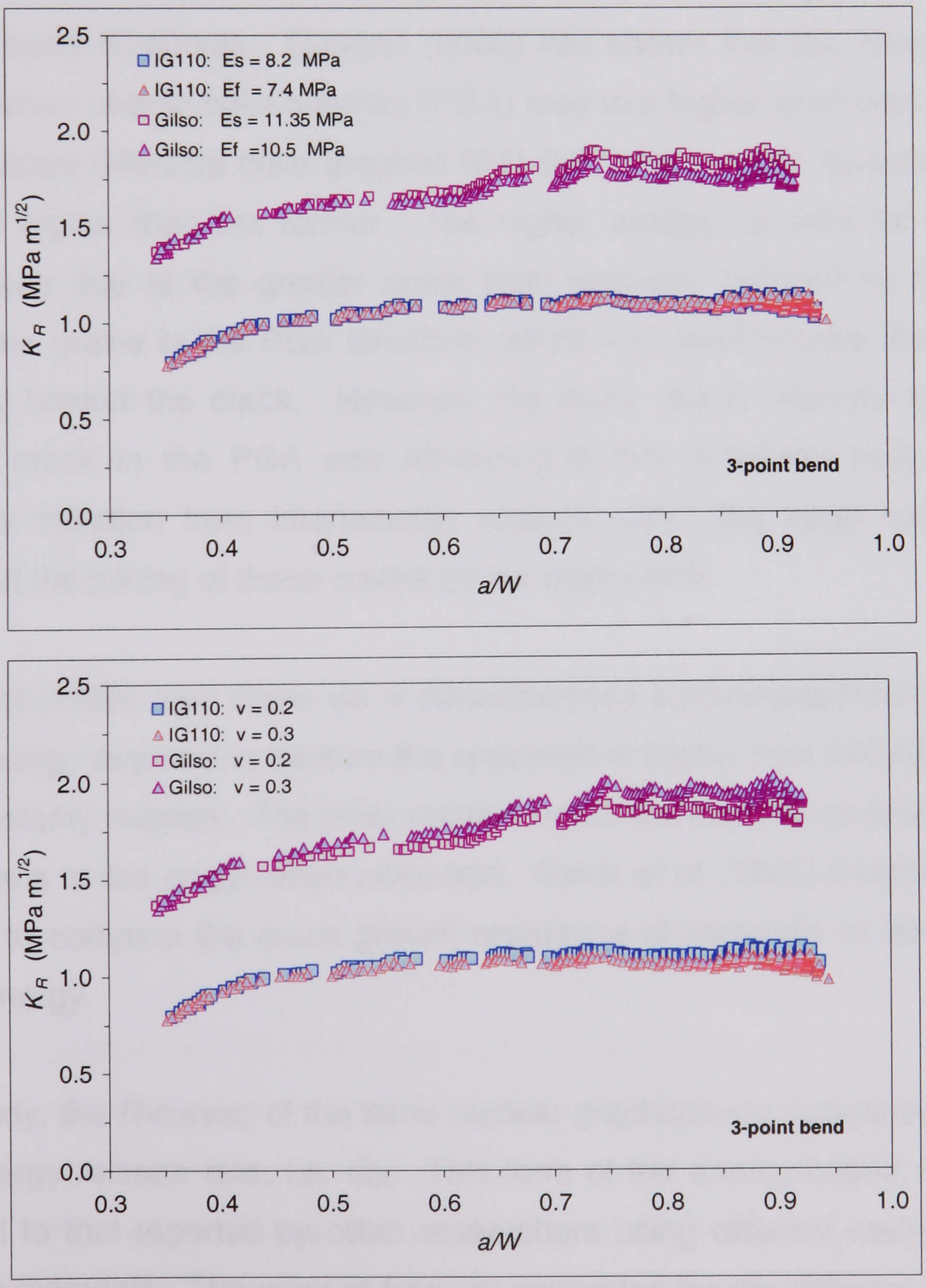

Figure 6.10. Change in K_R-curve profile with elastic modulus and Poission's ratio (E_s, E_f = sonic, flexural modulus).

6.5. Energy Considerations in Comparing the *R*-curve Behaviour

It has been reported in a number of cases, that a material with a higher K_R-curve does not necessarily demonstrate a high crack growth resistance in terms of the energy consumed during fracture. This has been reported by Sakai and Bradt (1993), who give examples of some materials that display such behaviour, e.g. partially stabilised zirconia. Polycrystalline graphite is one of the materials for which the stress intensity-based K_R-curve profile and the energy-based *R*-curve profile are similar (Sakai and Bradt, 1993).

However, it must be noted that, the energy-based *R*-curves for coarse-grained graphites do not necessarily correspond, in terms of ranking to their stress intensity-based K_R-curves. Ouagne (2000) has shown that the *R*-curve for a coarse-grained needle-coke graphite (PGA) rose to a higher level than that for a coarse-grained Gilsonite coke graphite (IM1-24), although the K_R-curve for the latter was higher than the former. The higher energy required for the PGA graphite was due to the greater crack path tortuosity induced by the large, needle-coke grains in the PGA structure, which was said to raise the bridging propensity behind the crack. However, the lower stress intensity needed to drive the crack in the PGA was attributed to the increased probability for microcrack initiation from interlamellar regions within the large needle-coke grains, and the joining of these cracks by the main crack.

Sakai et al (1988) also show via a dimensionless load-displacement method, that the energy required to fracture the specimen is higher than that obtained by Irwin's similarity relation. The latter relation treats the material as linear elastic, i.e. it returns to the origin when unloaded. Sakai et al (1988) therefore stress the need to compare the crack growth resistance of materials in terms of the fracture energy.

In this study, the *R*-curves of the three nuclear graphites are compared in terms of the energy release rate, i.e. G_R. This form of the energy-based *R*-curve is compared to that reported by other researchers using different methodologies on similar materials. The work of fracture generated for the different specimen types is also compared and discussed in relation to the material properties.

6.5.1. Comparison of the G_R-curves

The G_R-curves were simply calculated using the well-known LEFM expression:

$$G_R = K_R^2 / E'$$

Data obtained by the compliance method was used to derive the G_R-curves. Again, one is faced with the dilemma regarding the value for the elastic modulus that is to be used in the calculation of G_R. Although slight variation in the value of E' was shown to have little influence on the K_R-curves (see Figure 6.10), it does have considerable influence on the G_R-curves in that a marked difference in the fracture energy is obtained. In calculating the G_R-curves, the sonic modulus values were used, given that these values were used previously.

Figure 6.11 compares the G_R-curves for the different nuclear graphites in 3-point bending and compact tension. It is seen that the ranking of the different materials remains unchanged from that observed in their K_R-curve behaviour. Gilsocarbon consumes the highest energy over the initial crack extension region, but is superceded by the UcarC graphite. The IG110 material ranks lowest. The results also suggest that there is considerable influence from the specimen type, with the measured energy being substantially higher in the compact tension test.

It is interesting to compare these G_R-curves obtained by the analytical compliance method, with that obtained by other workers on similar graphites. The G_R-curve obtained for IG110 graphite compares well with that reported by Sakai et al (1988) for IG-11 graphite, the two materials being almost identical, except for slight variations in physical and mechanical properties. Sakai et al (1988) used the dimensionless load-displacement method to derive the *R*-curve for IG-11 graphite, with specimens of similar dimensions to that used in this study. They found the initial *R*-value for IG-11 graphite to be about 60 Jm^{-2}, and, the plateau *R*-value to be approximately 220 Jm^{-2}, with the plateau arriving sooner in the *a/W*-range. In this study, the initial *R*-value (G_{IC}) for IG110 graphite is ~100 Jm^{-2} with a plateau *R*-value ($G_{R,plat}$) of ~250 Jm^{-2}, the slightly larger grain size of IG110 being a possible reason for the marginal difference.

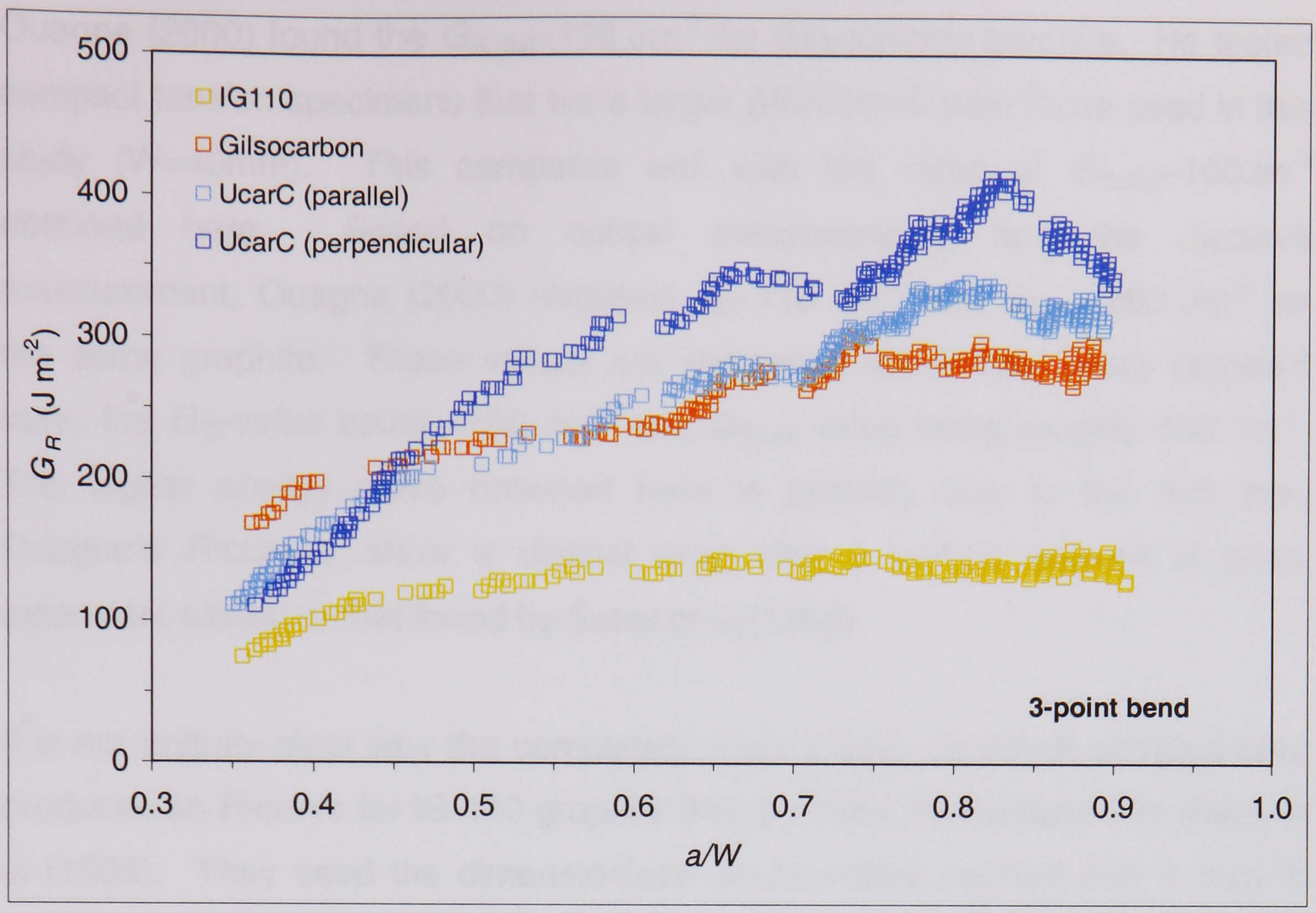

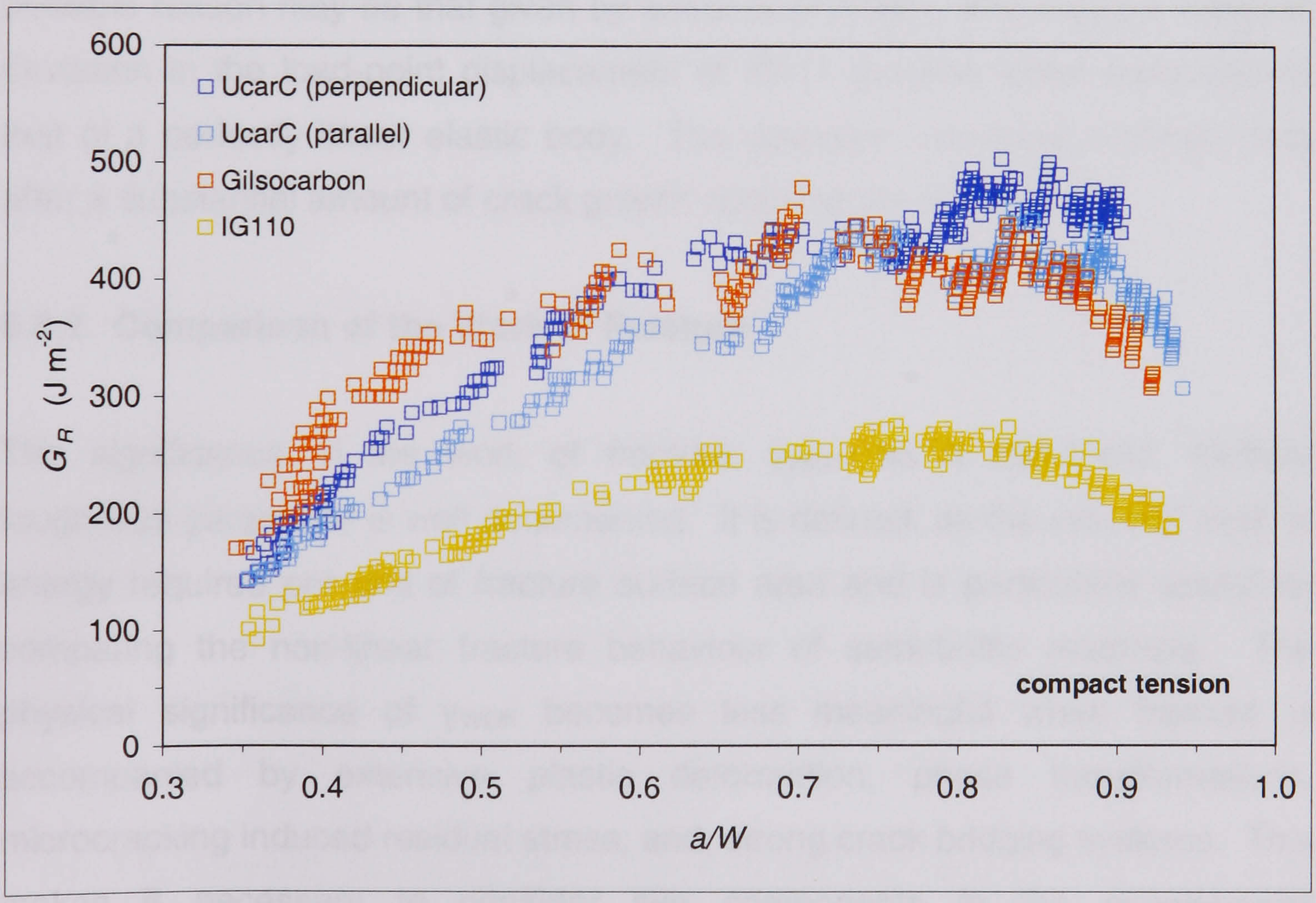

Figure 6.11. Comparison of G_R-curves in the bend and compact tension specimens.

Taking the area under the load-displacement curve up to the critical load, Ouagne (2000) found the $G_{R,plat}$~138 Jm^{-2} for Gilsocarbon graphite. He tested compact tension specimens that were larger (W=65mm) than those used in this study (W=40mm). This compares well with the value of $G_{R,plat}$~160Jm^{-2} obtained here. Based on optical measurements and the J_R-curve measurement, Ouagne (2000) obtained J_{IC}~110 Jm^{-2} and $J_{R,plat}$~260 Jm^{-2} for the same graphite. These values are somewhat lower than those obtained here, the G_{IC}-value being ~160 Jm^{-2} and $G_{R,plat}$ value being roughly 400 Jm^{-2}. The higher energy curve obtained here is possibly due to the fact that, Ouagne's *R*-curves, show a distinct drop after a certain amount of crack extension, similar to that found by Sakai et al (1988).

It is not entirely clear why the completely linear elastic approach adopted here produces an *R*-curve for IG-110 graphite that is similar that obtained by Sakai et al (1988). They used the dimensionless displacement method that is said to include the energy dissipated due to non-linear fracture mechanisms. A possible reason may be that given by Sakai et al (1988), who noted a marginal deviation in the load-point displacement of IG-11 graphite when compared to that of a perfectly linear elastic body. The deviation increased markedly only after a substantial amount of crack growth occurred, i.e. $a \approx 0.6\text{-}0.7W$.

6.5.2. Comparison of the Work of Fracture

The significance of the work of fracture, γ_{WOF}, as a non-linear, fracture toughness parameter is well documented. It is defined, as the external work or energy required per unit of fracture surface area and is particularly useful for comparing the non-linear fracture behaviour of semi-brittle materials. The physical significance of γ_{WOF} becomes less meaningful when fracture is accompanied by extensive plastic deformation, phase transformations, microcracking induced residual stress, and, strong crack bridging systems. This makes it necessary to consider two components in the experimental determination of γ_{WOF}. One component due to elastic processes and the other due to non-elastic processes such as crack bridging.

Using the area under the experimental load-displacement curves (U) and the fracture, surface area (A) the work of fracture (γ_{WOF}) is given by the relation:

$$\gamma_{WOF} = \frac{U}{2A}$$

The fracture energy values are given in Table 6.2. The results obtained in the 3-point bend specimens correlate well, in terms of the ranking of the *R*-curves for the graphites. In the compact tension tests, Gilsocarbon showed higher fracture surface energy than the UcarC material, which appeared to have similar γ_{WOF} values in the two orientations relative to extrusion. The energy requirement in the compact tension specimens is much higher than that in the bend specimens, indicating an influence from the specimen geometry on the work of fracture. The influence of the specimen geometry on the work of fracture is well-recognised (Sakai & Ichikawa, 1992).

Table 6.2. γ_{WOF} values for the different graphites and specimen types.

Material	γ_{WOF} (Jm^{-2})	
	3-point bend	Compact Tension
Gilsocarbon	143.8 ± 1.2	256.4
IG-110	71.9 ± 1.0	122.1
UcarC (parallel)	138.9 ± 1.3	246.6
UcarC (perpendicular)	170.5 ± 1.5	236.1

For a fine-grain polycrystalline graphite IG-11, which is similar to the IG-110 graphite tested here, Sakai et al (1988) obtained γ_{WOF}=76 Jm^{-2} in compact tension test specimens. This compares well, with the γ_{WOF} value obtained for the IG-110, compact tension specimens tested in this study. A reason for the somewhat higher value for IG-110 graphite may be its slightly larger grain size than the grade IG-11, i.e. ~12μm compared to ~20μm.

The effectiveness of the method used to derive the *R*-curve, can be assessed from the energy balance defined by the following equation (Nakayama 1965, Fett & Munz 1998):

$$\gamma_{WOF} = \frac{1}{2(W-a_0)}\int_{ao}^{W} R.da = \left(\frac{1}{2(\alpha-\alpha_0)}\right)\int_{\alpha o}^{\alpha} R(\alpha).d\alpha = \frac{\overline{R}}{2}$$

The more closely matched the energy envelope defined by the area under the *R*-curve ($\overline{R}$) with the work of fracture (γ_{WOF}), the more effective is the *R*-curve measurement technique in accounting for the total fracture energy. The area defined by the *R*-curve is halved to account for the total fracture surface defined by the two halves of the fractured specimen. The $\overline{R}$/2-values obtained for each material and specimen type are compared with γ_{WOF} in Table 6.3.

Clearly, the compliance method is effective in accounting for the fracture surface energy, given the closeness of the two parameters. The discrepancy in the two parameters is due to unaccountable energy losses, for example, frictional losses at the loading rollers and instability events that occur during the fracture process. This discrepancy is higher for the compact tension specimens implying that the unaccountable energy losses were greater in these tests. This may be related to the control of the crosshead during the tests. In the bend tests, crosshead movement was controlled using feedback from an external, high sensitivity transducer. In the compact tension tests, control was based on feedback from an internal transducer designed for a very wide displacement range (20-500mm). Therefore, energy losses may have been lower in the bend tests given the smoother control of these tests.

Table 6.3. Comparison between the γ_{WOF} and $\overline{R}/2$ parameters.

Material	3-point bend		Compact tension	
	γ_{WOF} (Jm^{-2})	$\overline{R}/2$ (Jm^{-2})	γ_{WOF} (Jm^{-2})	$\overline{R}/2$ (Jm^{-2})
Gilsocarbon	143.8 ± 1.2	122.3	256.4	183.8
IG-110	71.9 ± 1.0	64.30	122.1	102.9
UcarC (parallel)	138.9 ± 1.3	126.0	246.6	165.5
UcarC (perpendicular)	170.5 ± 1.5	147.0	236.1	184.7

Interestingly, Magon et al (1995) showed that the $\overline{R}/2$ values obtained in 3-point bending matched γ_{WOF} more closely than those obtained in 4-point bending. Rodrigues & Pandolfelli (1995) have shown that the value of $\overline{R}/2$ obtained by the theoretical compliance method approaches γ_{WOF} more closely than other methods such as the optical method and the load-unload technique. They concluded that the compliance method is more accurate in accounting for γ_{WOF}.

6.6. Fractographic Evidence for the Differences in R-curve Behaviour

A comparison of the *R*-curve behaviour of the nuclear graphites would not be complete without due consideration of the role of the microstructure. The influence of the microstructure on the crack growth resistance of graphite is reported in fair detail in several studies (Knibbs 1967, Sakai et al 1988, Ahlborn 1993, and, Allard et al 1991) and is well understood. It is the purpose of this section to highlight those fractographic details, which distinguish the different graphites from each other, in relation to their R-curve behaviour.

It was described previously, how the 3-point bend and compact tension specimens were prepared (see Section 5.1). It was also mentioned that the method used allowed the test specimens to be polished according to the procedure outlined in Section 4.1. This made it possible to examine the fracture path in the bend, and, the compact tension specimens using optical microscopy. Cracked sections from some of the bend specimens were cut and mounted for viewing the crack path in the SEM. Some specimens were fractured completely in order to view the fracture surfaces. The results of fractogaphy are presented in the following sections.

6.6.1. Crack Path Deflection

It was described in Section 2.3.5 how crack path deflection contributes to an increase in the crack growth resistance of carbon materials and ceramics. The role of pores and the filler grains in polycrystalline graphite, as reported by Knibbs (1967), Allard et al (1991), and, Ahlborn (1993), including other workers was also reviewed.

In this study, optical microscopy of the crack path in test specimens revealed a marked difference in the extent of crack deflection or crack path tortuosity between the different materials. This is shown in the mosaic of optical micrographs presented in Figure 6.12. Clearly, the coarse grain materials display considerable path deflection, unlike the IG-110 graphite where crack deflection is not so marked. In the 3-point bend specimens, the difference in the extent of crack deflection was similar, as shown by the electron micrographs in Figure 6.13.

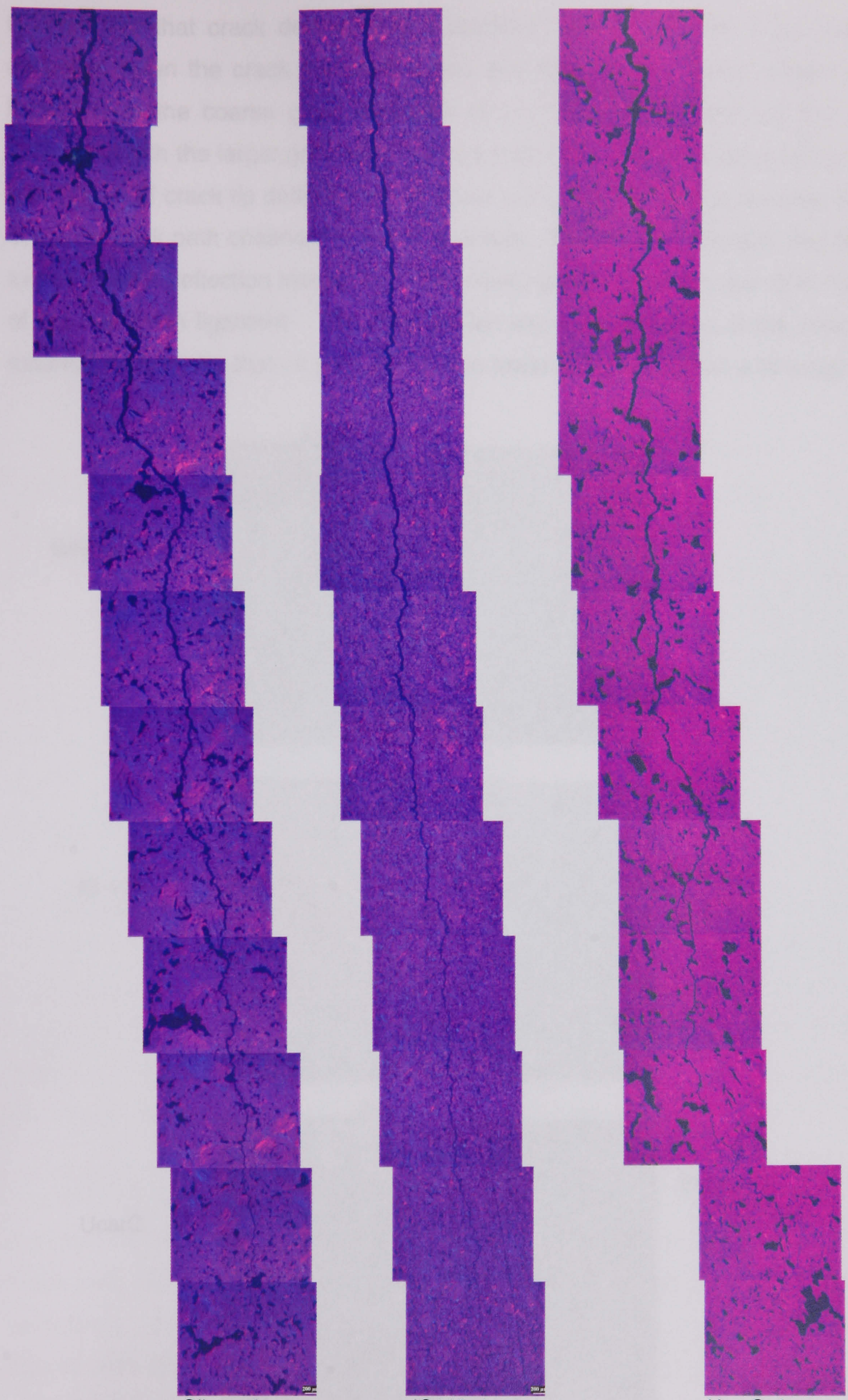

Figure 6.12. Comparison of crack path tortuosity in the compact tension specimens.

It is evident that crack deflection is a localised event along the crack path, occurring when the crack intersects pores and filler grains. There is also an indication in the coarse grain materials of an overall path deflection that is consistent with the larger grain size in these materials. The cumulative effect of a multitude of crack tip deflections that occur along the crack front develops the complex crack path observed in these materials. There is an indication that the extent of path deflection increases in the UcarC graphite towards the latter half of the specimen ligament. This may explain why the resistance of the UcarC material rises above that, of the Gilsocarbon towards the end of the *a/W*-range.

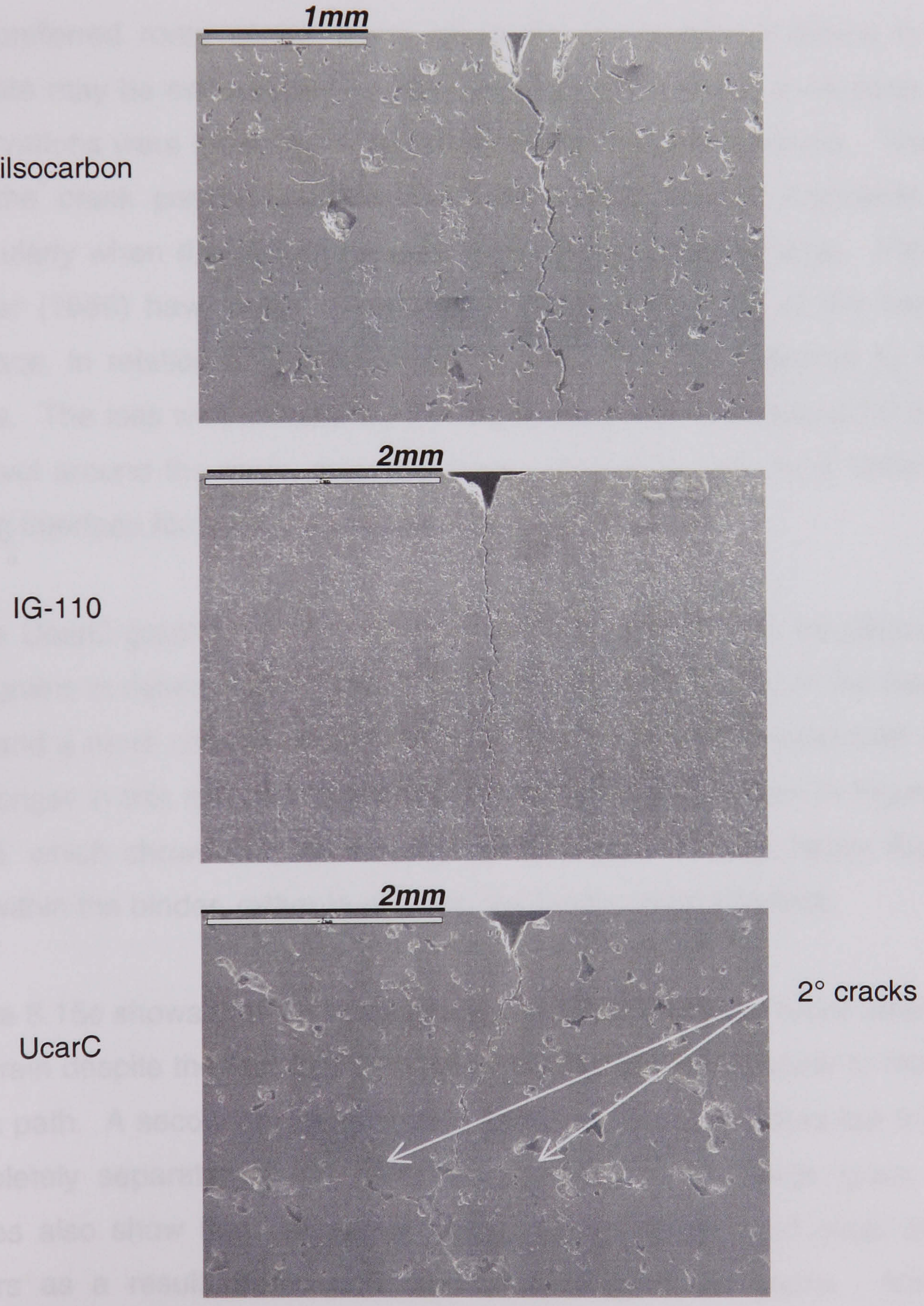

Figure 6.13. Comparison of crack path tortuosity in bend specimens.

The filler grains were found to play a varying role in deflecting the crack. In the fine grain IG-110, the crack appeared to be deflected around the filler grains in most instances (Figure 6.14). The apparent ease with which the crack is deflected in the IG110 graphite may be related to the small grain size, and, the nature of the filler-binder interface. The small grain size makes it easier for the crack to travel around the grain, rather than cause interlamellar fracture, even when the grain is oriented at a rather acute angle to the crack path (Figure 6.14a-6.14b). The ease of crack deflection around the grains promotes grain pullout, as shown in Figures 6.14b-6.14d.

The preferred route of the crack along the binder-filler interface in IG-110 graphite may be encouraged by the pores located along this interface. Similar observations were made by Allard et al (1991) in anode carbons. They noted that the crack passed easily around the poorly bonded anthracite grains, particularly when the size of the grain fell below a certain range. Patrick and Walker (1986) have noted some important characteristics of the binder-filler interface, in relation to the probability that the crack is deflected by the filler grains. The less well bonded the interface, the easier it becomes for the crack to travel around the grain, and, the more pronounced the crack deflection. A strong interface forces the crack to traverse the grain.

In the UcarC graphite, a somewhat varied role appeared to be played by the filler grains in deflecting the crack. This seemed to be related to the larger grain size and a more coherent binder-filler interface. That the binder-filler interface is stronger in this material is evident in the micrograph shown in Figure 6.15a-6.15d, which shows that the crack prefers to pass through larger filler grains and within the binder, rather than along the binder-grain interface.

Figure 6.15c shows that the crack prefers to travel along the basal orientation of the grain despite the fact that this route lies almost perpendicular to the general crack path. A secondary crack is also generated in the process but this fails in completely separating the binder-filler interface of this large grain. These figures also show that secondary cracks are generated and crack branching occurs as a result of the deflection caused by these grains. Both these processes consume fracture energy.

a. Deflection of crack along the interface of two filler grains.

b. Multiple deflection along the filler-binder interface with pullout.

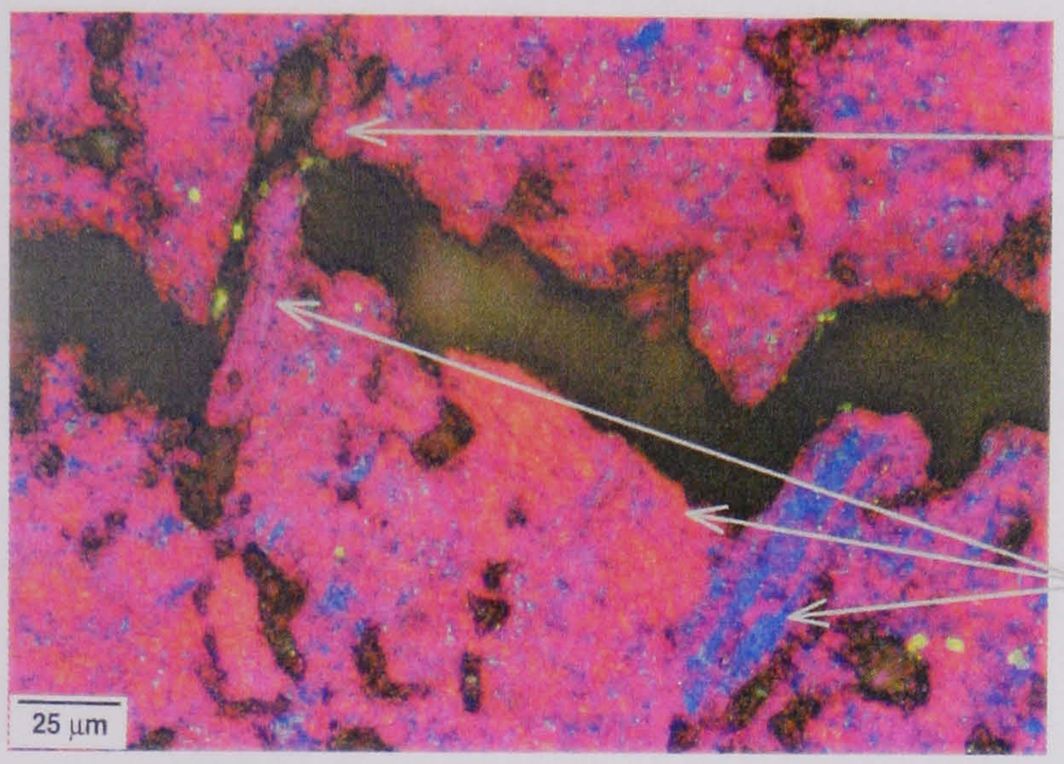

c. Crack deflection and pullout of a grain.

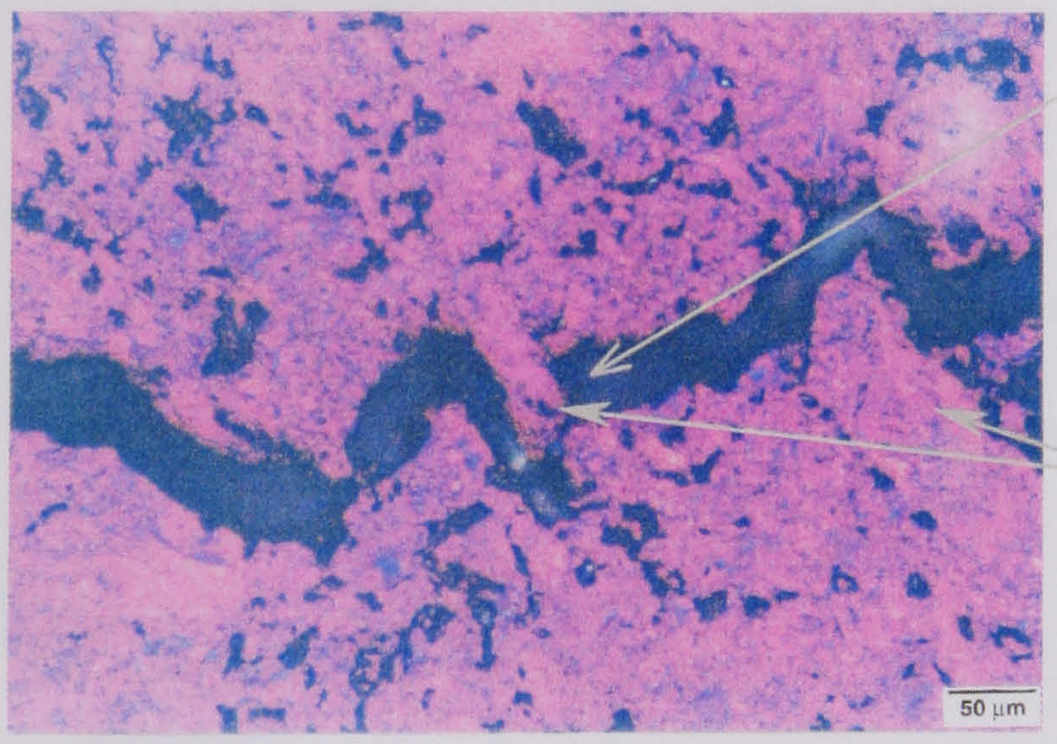

d. SEM image shows the filler grains protruding from the fracture surface.

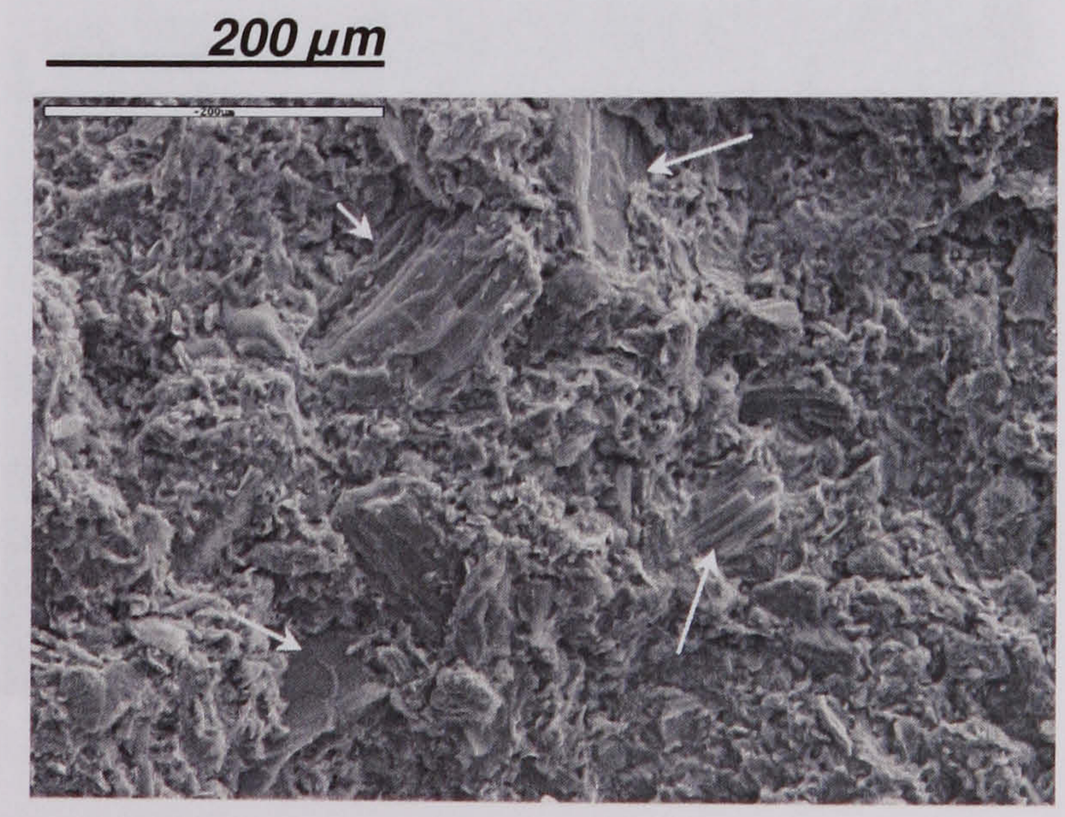

Figure 6.14. Crack deflection along binder-filler interface and grain pullout (IG-110).

a. Path through a grain and resulting deflection with 2° crack formation.

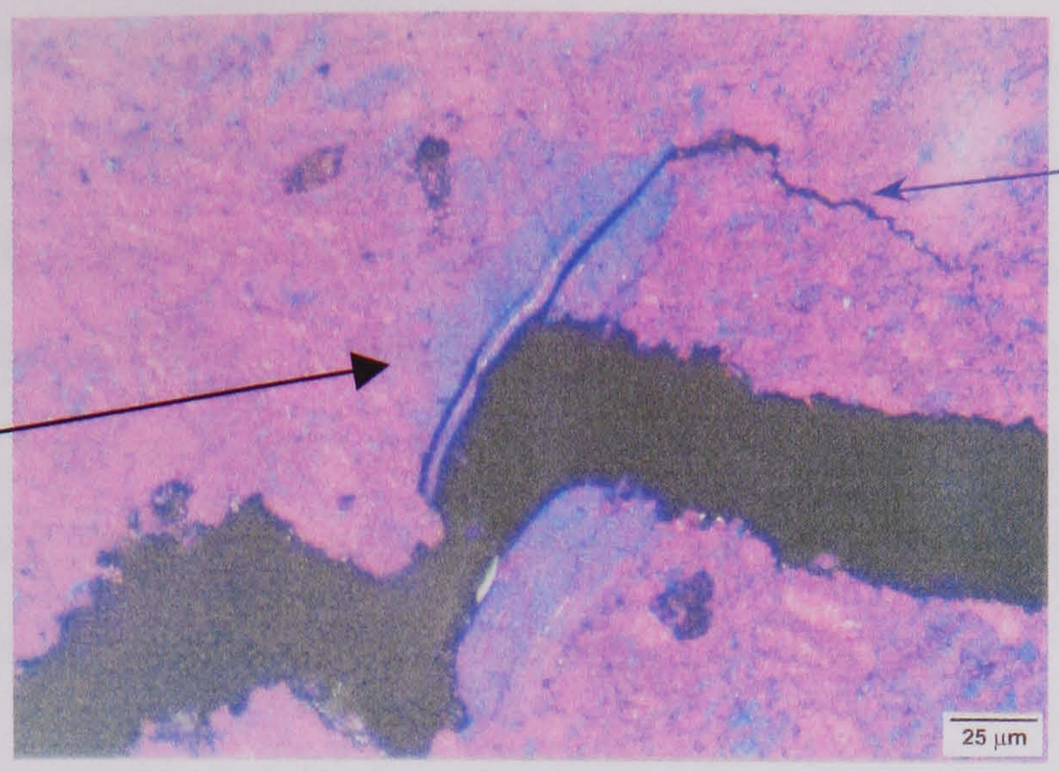

b. Obstruction of crack by grain oriented at ~90° to crack path – crack finds an interlamella path through the grain.

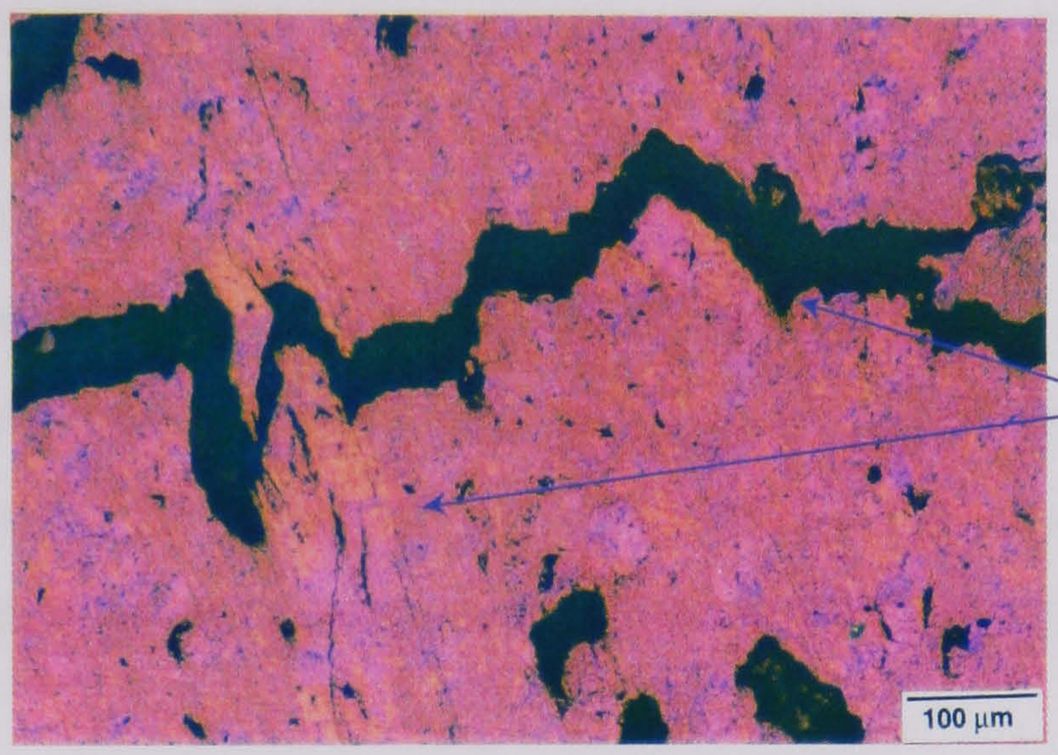

c. Extensive path deflection due to a preferred route through the basal orientation of the grain with 2° crack.

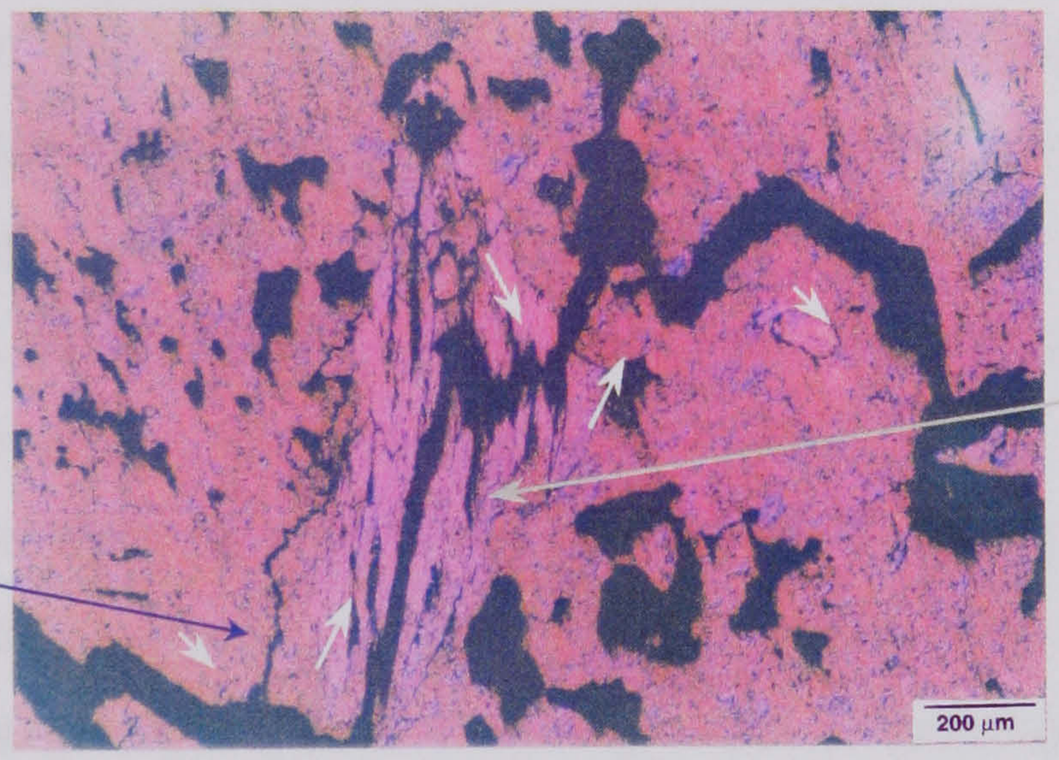

d. SEM of fracture surface indicates failure is mainly within binder phase with partial fracture of large filler grains.

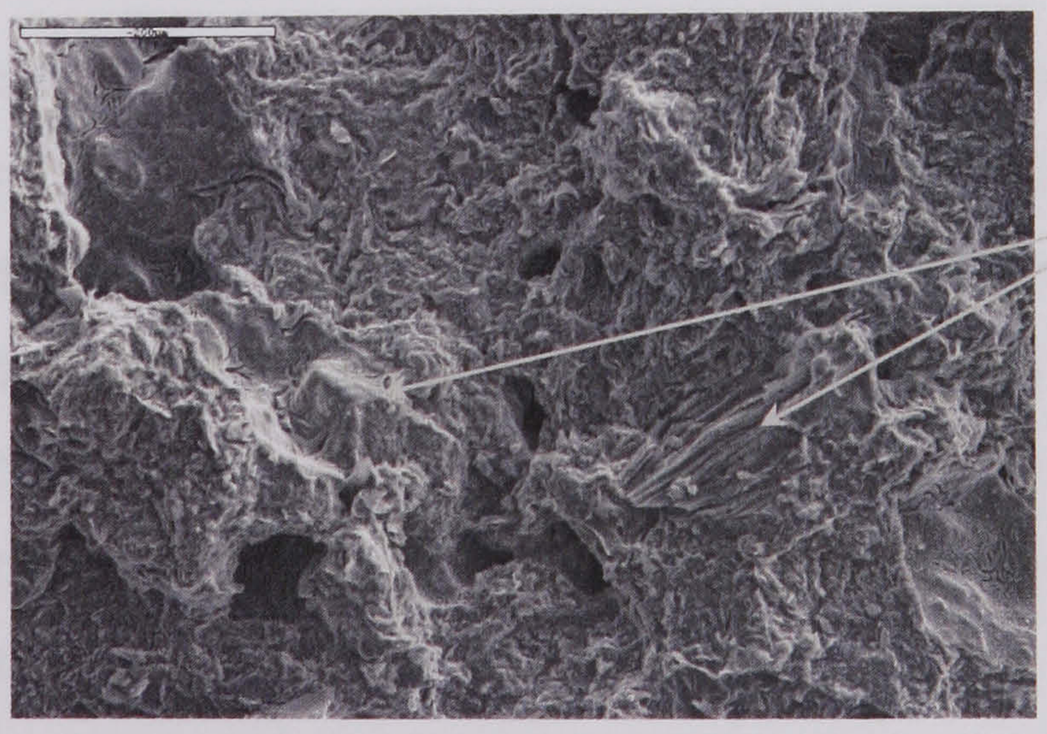

Figure 6.15. Preferred path of crack along basal orientation within filler grains in UcarC graphite; note the secondary cracks and crack branches that are generated.

It was rare to find needle-coke grains oriented perpendicular to the crack path in the UcarC specimens. Rather, the probability for the crack to be obstructed when crack growth is perpendicular to the extrusion direction must be higher. The cumulative effect of these deflections renders the overall crack path more tortuous. However, this was not obvious from the microscopic observations. It was also not certain what the role of the impregnant carbon was, but this probably helps in mechanically-binding the filler to the matrix.

In the Gilsocarbon graphite, the large spherical grains tend to have their basal orientation always aligned perpendicular to the crack. This makes it difficult for the crack to traverse the grain, except in certain instances, when the grain may be located very close to the notch tip. In such instances, the crack is forced to traverse the grain before it can propagate further, as shown in Figure 6.16a. The energy required in the process is high and may account partly for the higher initial crack growth resistance shown by the Gilsocarbon graphite.

Another reason for the higher initial resistance of Gilsocarbon graphite compared to the UcarC graphite may be that given by Ouagne (2000), who explained that crack initiation is easier in needle-coke graphite. The interlamellar regions within the needle-coke grains are likely sites for microcrack formation from which the macrocrack is more easily created. In Gilsocarbon, the spherical texture of the grains make microcracks less accessible to each other so that the macrocrack is more difficult to form via the coincidental microcrack alignment process that is a characteristic of graphite failure.

A distinctive interfacial feature in the Gilsocarbon graphite is the mosaic type structure often observed at the boundary between the spherical coke grains and the surrounding matrix. The coarser, more randomly oriented nature of the mosaic regions, and, their location at the binder-filler interface, make them a preferred region through which the crack traverses. This is illustrated by the polarised light micrograph in Figure 6.16b. In Figure 6.16c, a SEM image shows the deflection of the crack around a Gilsonite coke filler grain. This deflection can be extensive such that grain pullout results. An example of this is shown in the SEM image in Figure 6.16d, which shows that the outer layers of the onion skin structure within the Gilsocoke grain are exposed during pullout.

a. Transgranular fracture of a Gilsocoke grain located near the notch tip, giving a higher initial stress intensity (K_r) value.

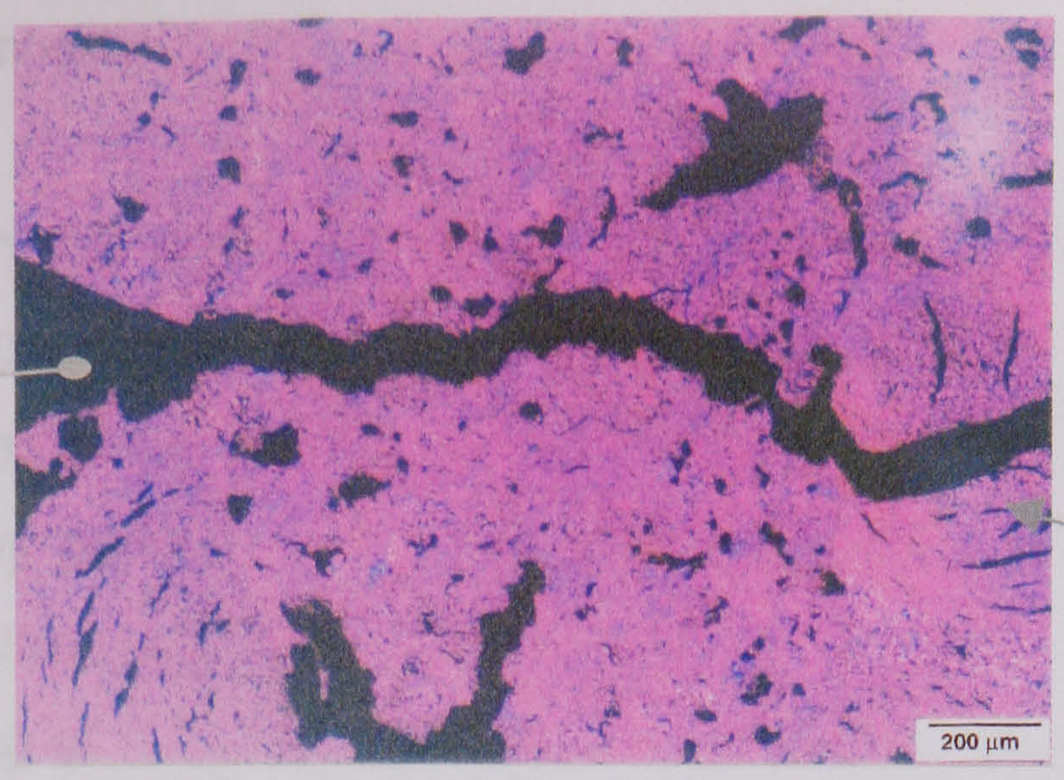

b. Partial deflection of the crack due to the presence of the mosaic phase on the periphery of the grain.

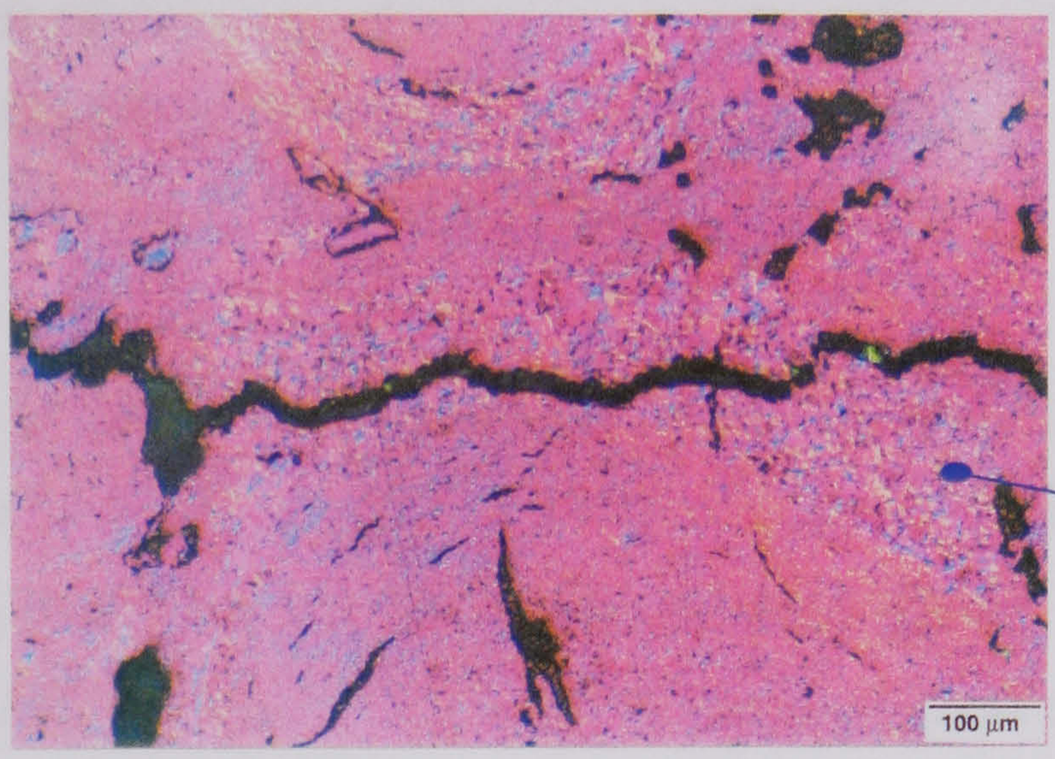

c. SEM image showing the extent to which the path of the crack may be deflected by a grain.

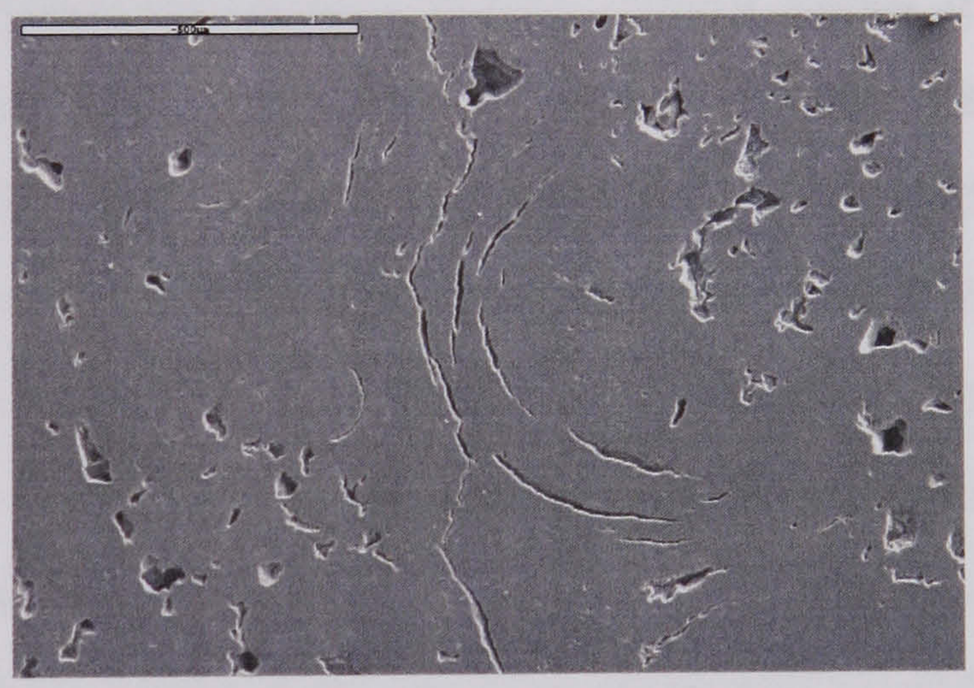

d. SEM image showing the appearance of the outer layers of a pulled out grain.

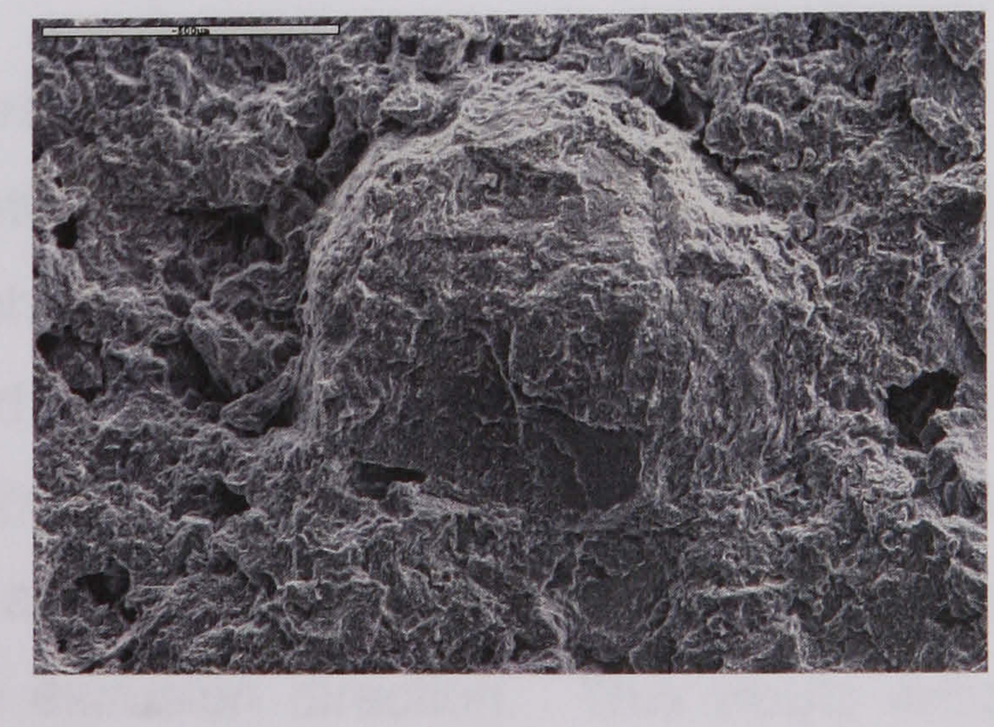

Figure 6.16. Crack path deflection in Gilsocarbon graphite.

6.6.2. Influence of Porosity

The role of porosity on the fracture resistance of polycrystalline graphite has been examined in considerable detail in numerous studies and is well documented. It is nonetheless difficult to characterise the precise nature of the complex role played by porosity. Tucker et al (1986) have described crack growth in polycrystalline graphite in terms of a perforation mechanism, analogous to the tearing of a stamp, with the crack seeking out the pores, in its search for a path of least resistance. This is a suitable analogy, as indicated by some of the micrographs in Figures 6.13-6.16, which show that there is a pore-following tendency by the crack in all three graphites.

Apart from the blunting of the crack tip upon entering the pore, an effect that is said to reduce the crack tip stress intensity, there is another noteworthy role played by the pores in enhancing the resistance of the material. This effect is most notable in the UcarC graphite and concerns the deflection of the crack by the pore. An example of this is shown in Figures 6.17a-6.17b for the Gilsocarbon and UcarC graphites respectively. From these micrographs, it is clear that the crack path can become extremely complicated by the large globular pores. The complex interaction between the crack and pores results in a combination of crack path deflection, secondary crack formation, crack branching, and, crack tip blunting. All these fracture processes enhance the crack growth resistance. Crack branching and secondary cracks were less notable in the IG-110 graphite (Figure 6.17c), implying that the size and shape of the pores play an important role in promoting crack path deflection.

Other influential features of the pores are their shape and their orientation relative to the crack path. This was noted to be a significant feature in the UcarC graphite, which showed the highest crack growth resistance of the three graphites. An elongated pore oriented perpendicular to the crack path is more likely to reduce crack tip stresses than the same pore oriented parallel to the crack path. There was an indication that the large pores in the UcarC material tend to elongate in the extrusion direction. This would enhance the stress-shielding effect of the pores, especially when the crack growth direction is perpendicular to the extrusion direction.

a. Complication of the crack path by a field of large globular pores with extensive 2° cracking from the surrounding pores - Gilsocarbon.

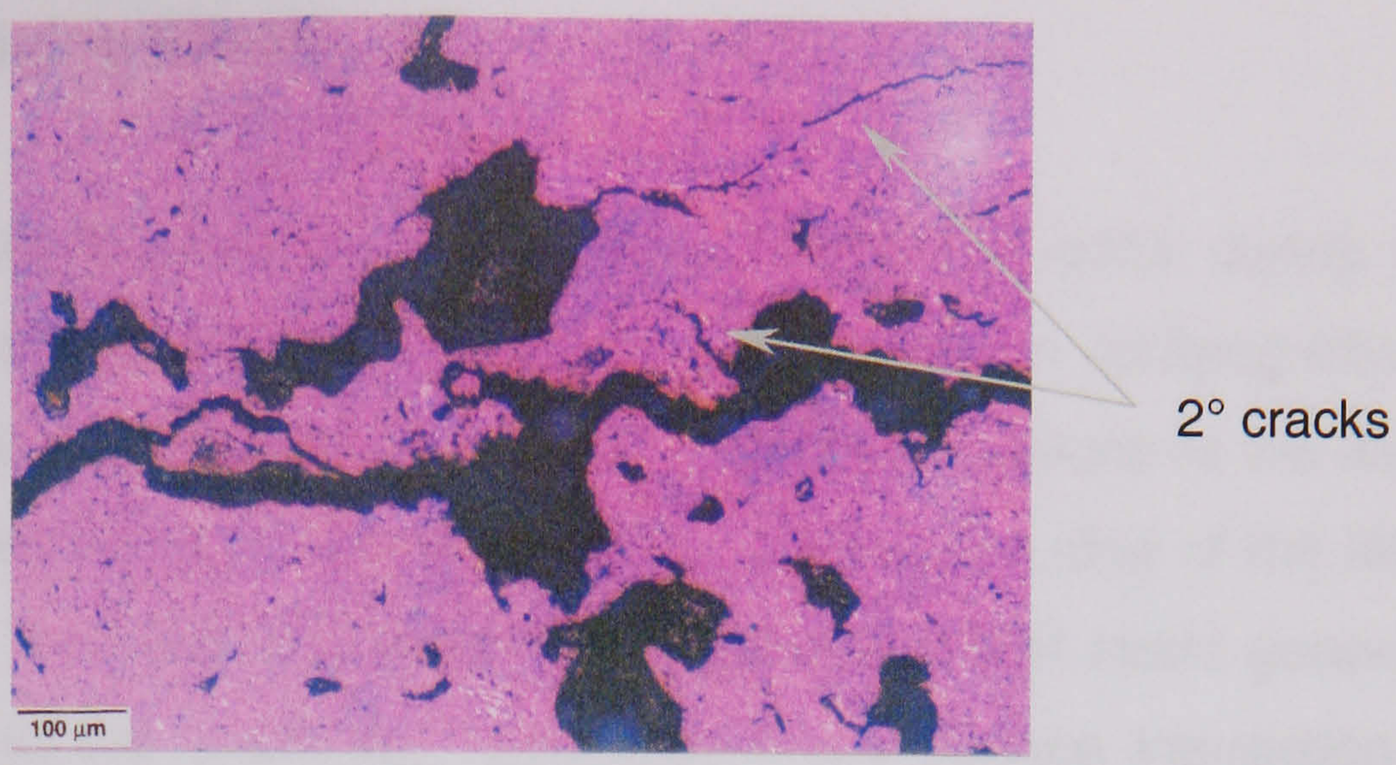

b. Complex interaction between crack and a field of large globular pores with 2° cracking from adjacent pores – UcarC.

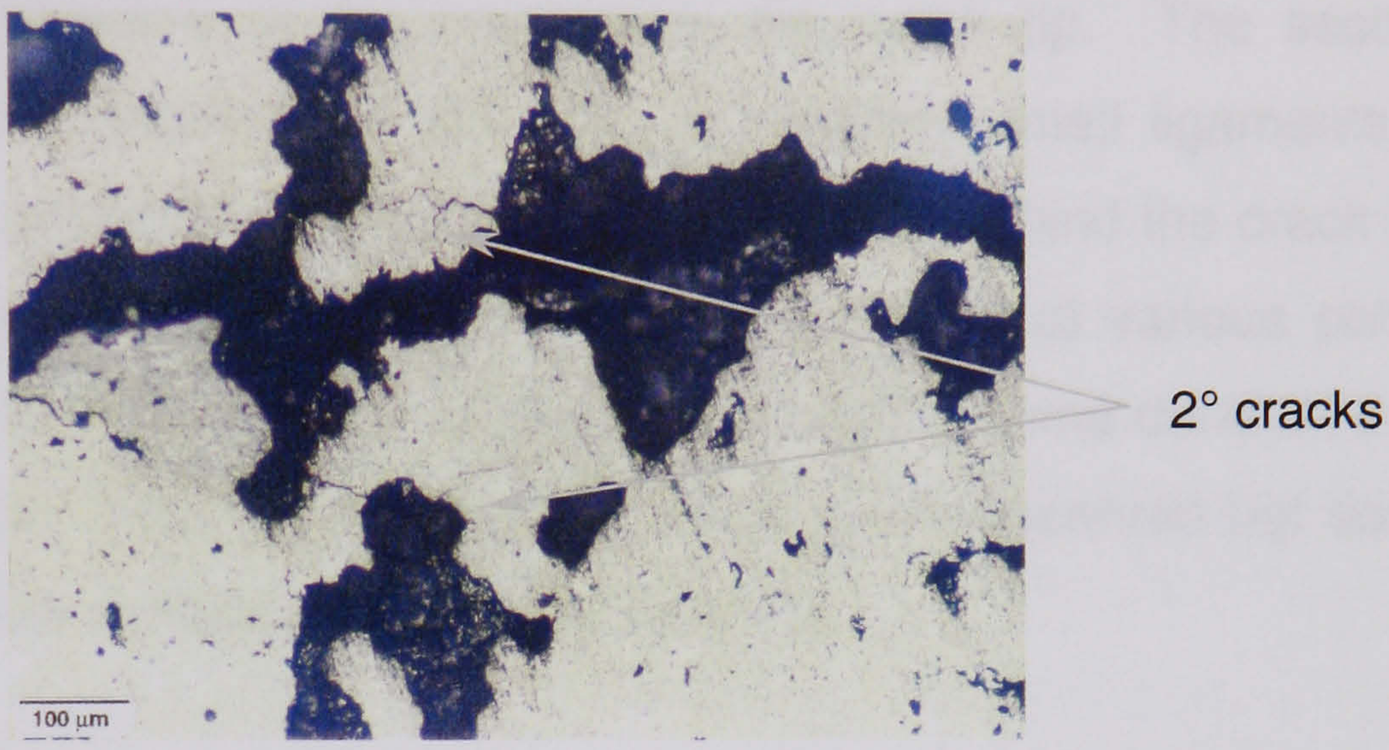

c. Crack branches in IG-110 caused by deflections in the crack path.

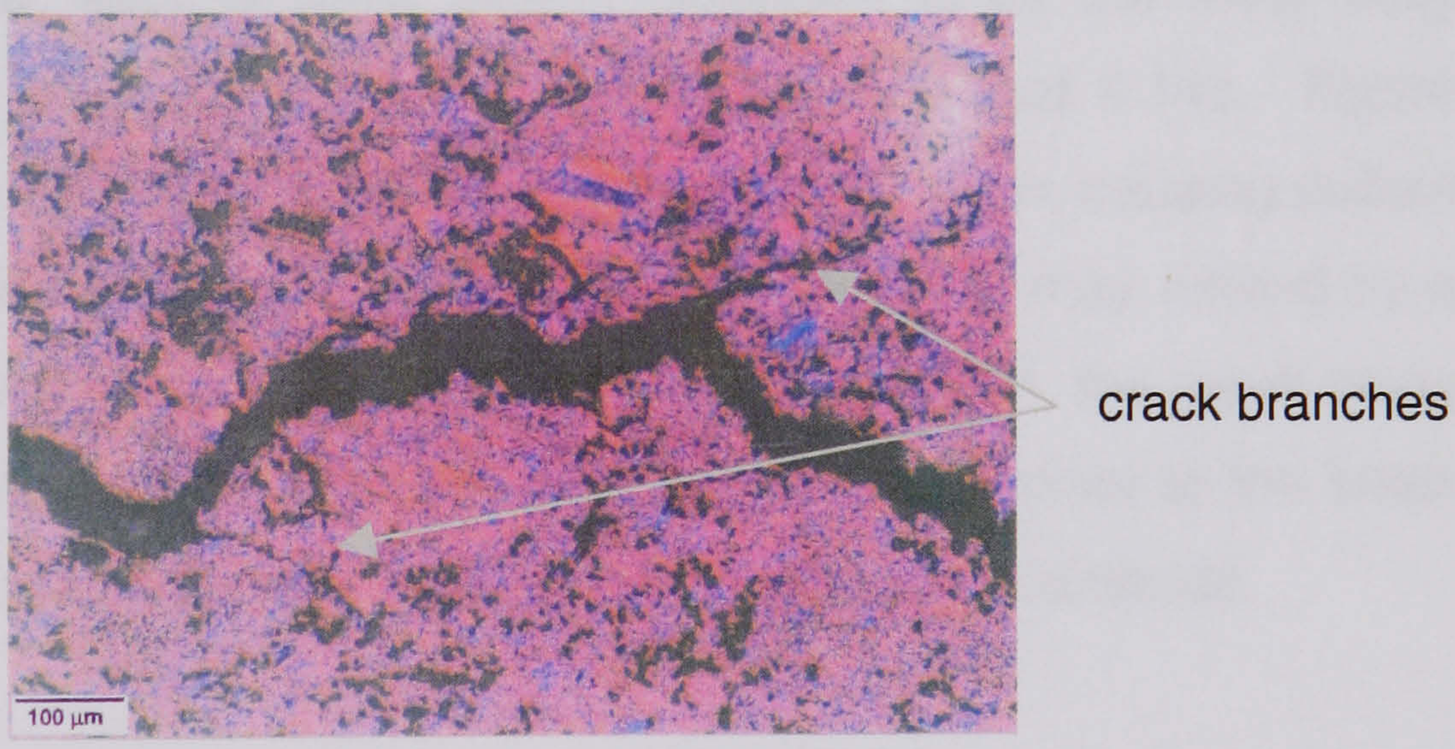

d. Pore following and crack branching in the UcarC graphite.

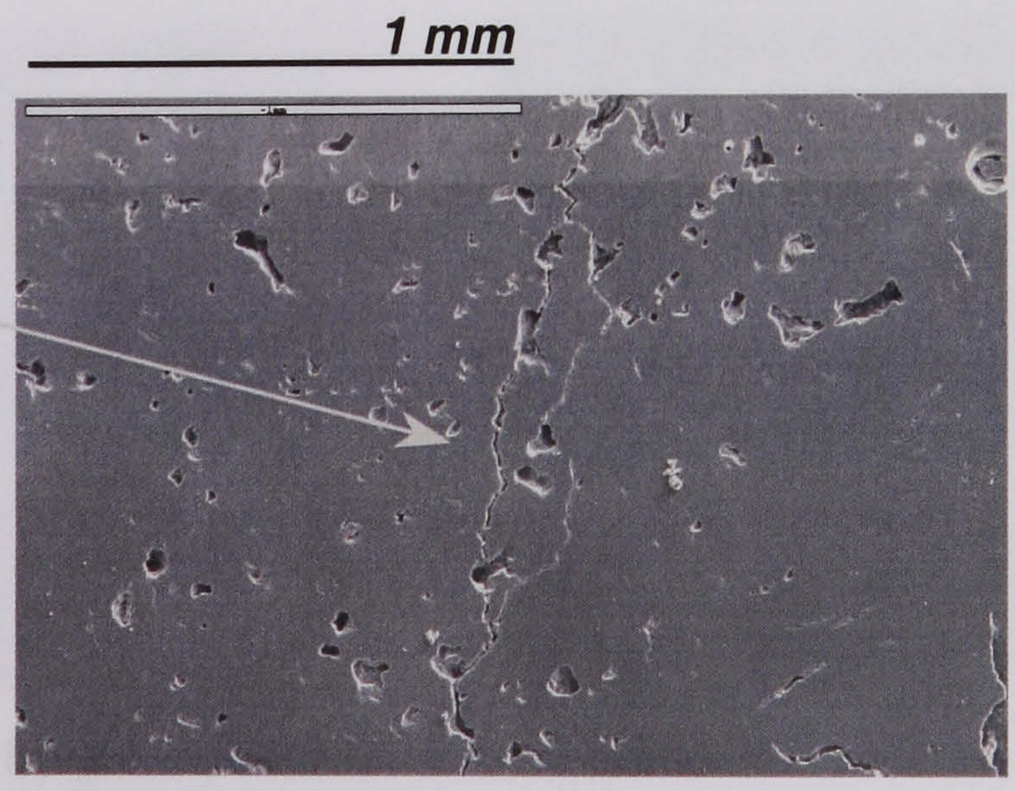

Figure 6.17. Secondary cracks and path deflection caused by crack-pore interaction.

6.6.3. Crack Tip Bridging Effects

As it was not possible to observe the development of the crack during the course of testing given the available test set-up, possible grain bridging effects could not be observed as the crack extended. From observations of the wake region in fractured specimens, it was possible to obtain some idea of the likely sources of bridging. Two features were mainly observed that could generate bridging effects behind the crack tip. One was crack surface interaction at numerous points along wake of the crack near the crack tip. The second feature was bridging constituents in the form of relatively small ligaments of material that seemed to join the mating crack surfaces just behind the crack tip. There was strong evidence that pulled out grains observed at various points along the crack path may contribute to bridging stresses for some duration over the history of the crack. Intact bridging grains were rarely observed but some observations were made confirming this phenomenon.

In the IG-110 graphite, sites of grain pullout appeared to be the most likely bridging constituents, as was highlighted in Figures 6.14b and 6.14c. Figure 6.18a reveals how the extending crack can bypass a filler grain, causing pullout and subsequent traction. Figure 6.18b shows how the crack may extend by a perforation type mechanism, involving pores ahead of the grain, the result being that an intact grain forms a bridge between the two surfaces close to the crack tip. Clearly, this grain will eventually suffer pullout as the crack extends.

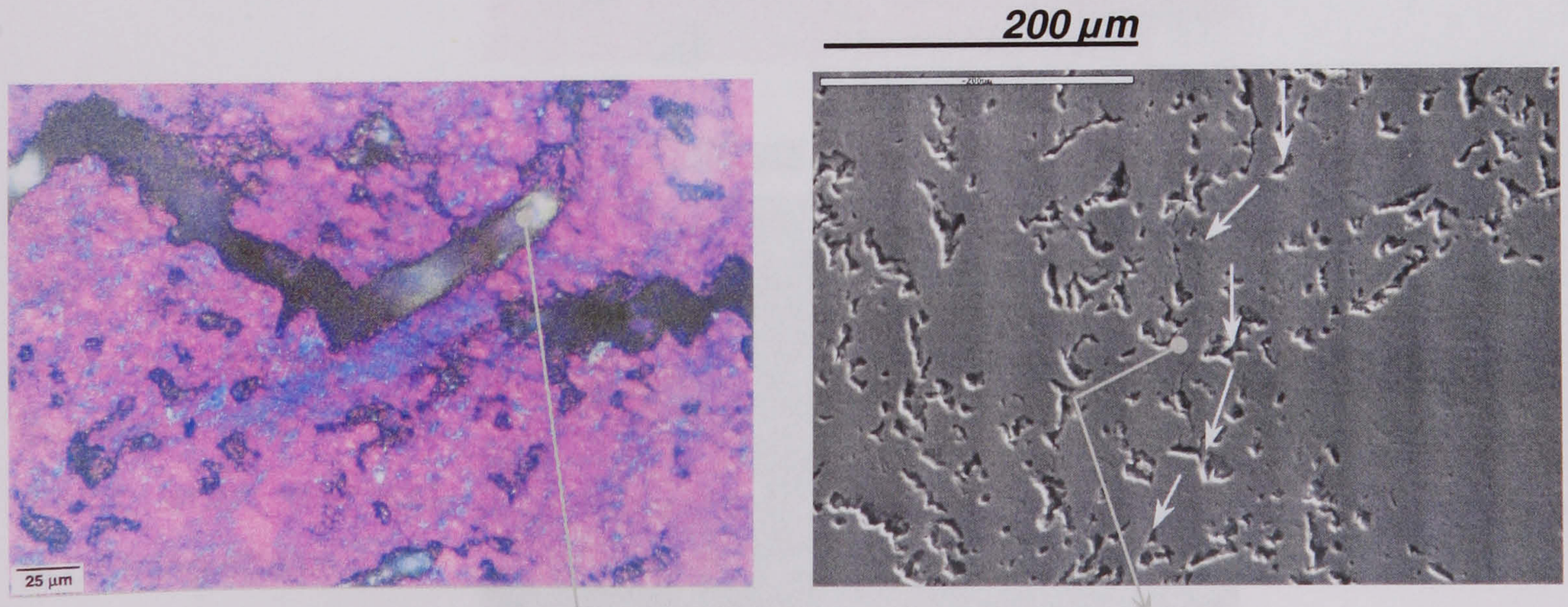

a. Crack face interaction by grain pullout.

b. Formation of a bridging grain behind tip.

Figure 6.18. Bridging constituents observed in the IG-110 graphite.

In the Gilsocarbon graphite, it was more difficult to envisage a bridging grain due to the spherical shape of the grains. Chandler et al (2002) have shown that spherically shaped grains do not contribute to bridging effects since they do not generate an interlocking effect such as elongated grains do. Although the Gilsocoke grains are not perfectly spherical, the predominantly round shape of the grains must reduce the likelihood for grain bridging. Apart from ligaments of material adjoining the mating crack surfaces (Figure 6.19a), possible grain bridges were not obvious in the Gilsocarbon graphite. However, bridging by fractured grains is possible.

It does appear however, that the path of the crack through the binder and mosaic regions surrounding the crack generates very rough crack surfaces (Figure 6.19b). It is likely that the roughness of the mating crack surfaces, coupled with the crack path tortuosity, constitute the bridging elements in the Gilsocarbon graphite. There may also be an influence from non-spherical grains that behave like elongated grains, however this was not obvious. Partially fractured grains may also perform a bridging function.

a. A bridging ligament behind the crack tip.

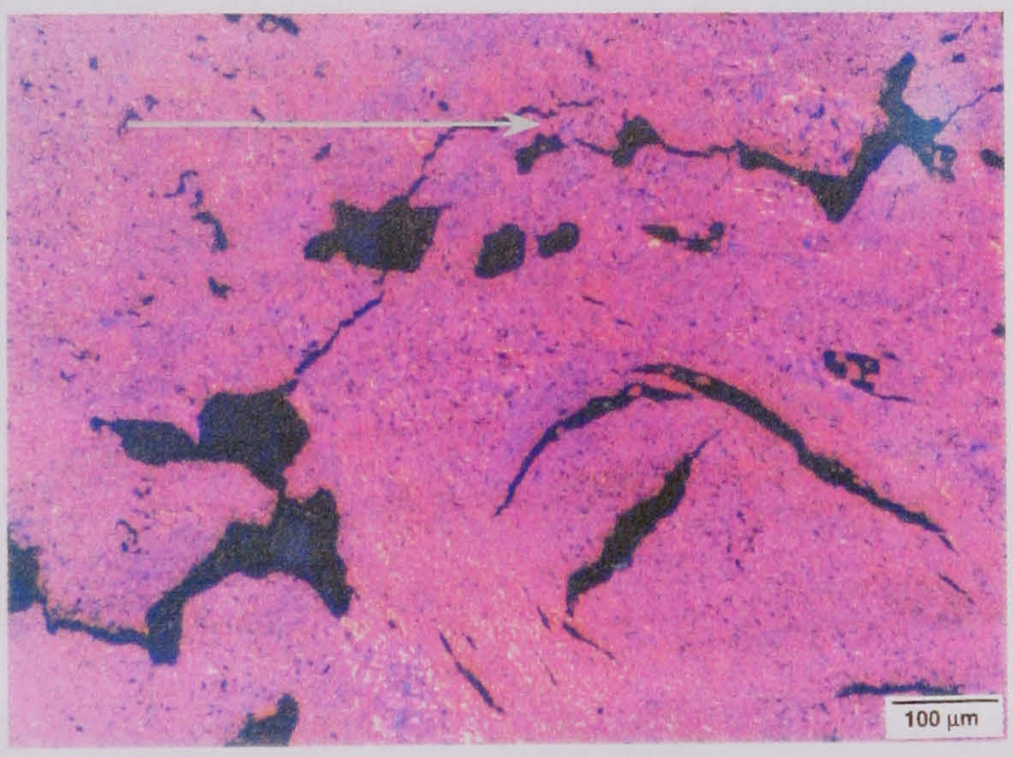

b. SEM image showing the roughness of the fracture surface in between the filler grains, which may add to bridging effects.

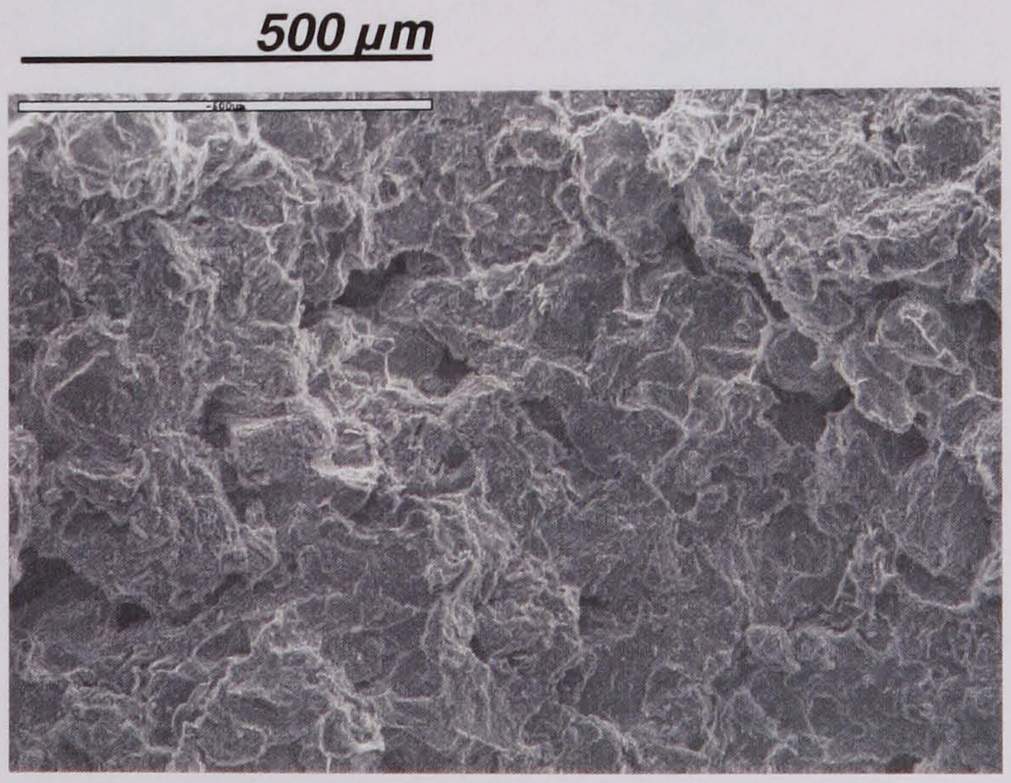

Figure 6.19. Possible sources of bridging traction in the Gilsocarbon graphite.

In the UcarC graphite, the bridging constituents appeared to be ligaments of material behind the crack, as well as bridging grains. There was also evidence of crack face interaction at numerous points along the mating crack surfaces, for some distance away from the crack tip. Examples of these features are shown in Figure 6.20. The presence of a bridging ligament is clear in Figure 6.20a, as are the interaction sites between the mating surfaces in Figure 6.20b and Figure 6.20c.

a. A bridging ligament behind the crack tip.

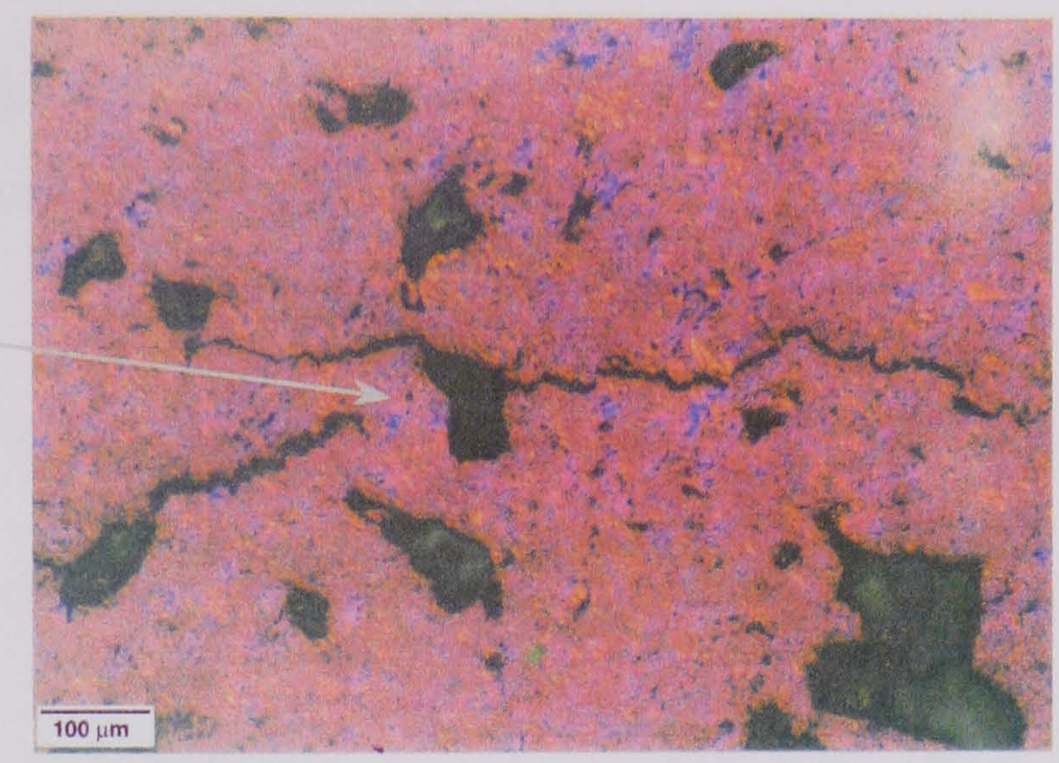

b. Interaction between the crack faces close to the crack tip.

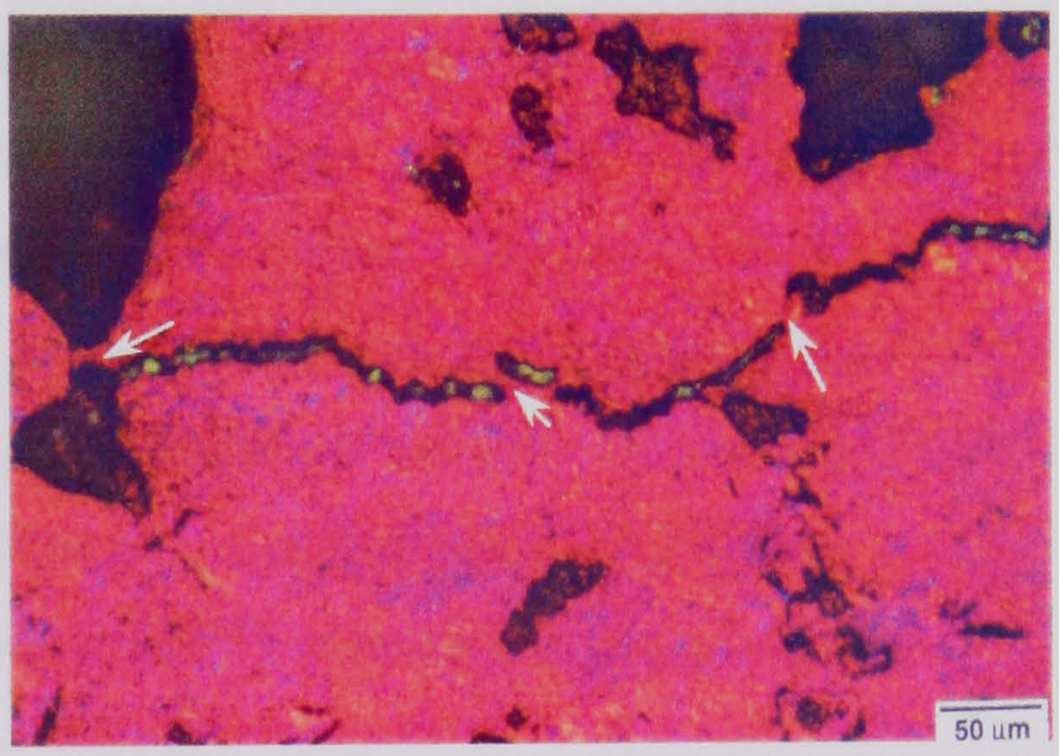

c. A bridging grain between the mating surfaces, close to the crack tip. Note the crack interaction sites.

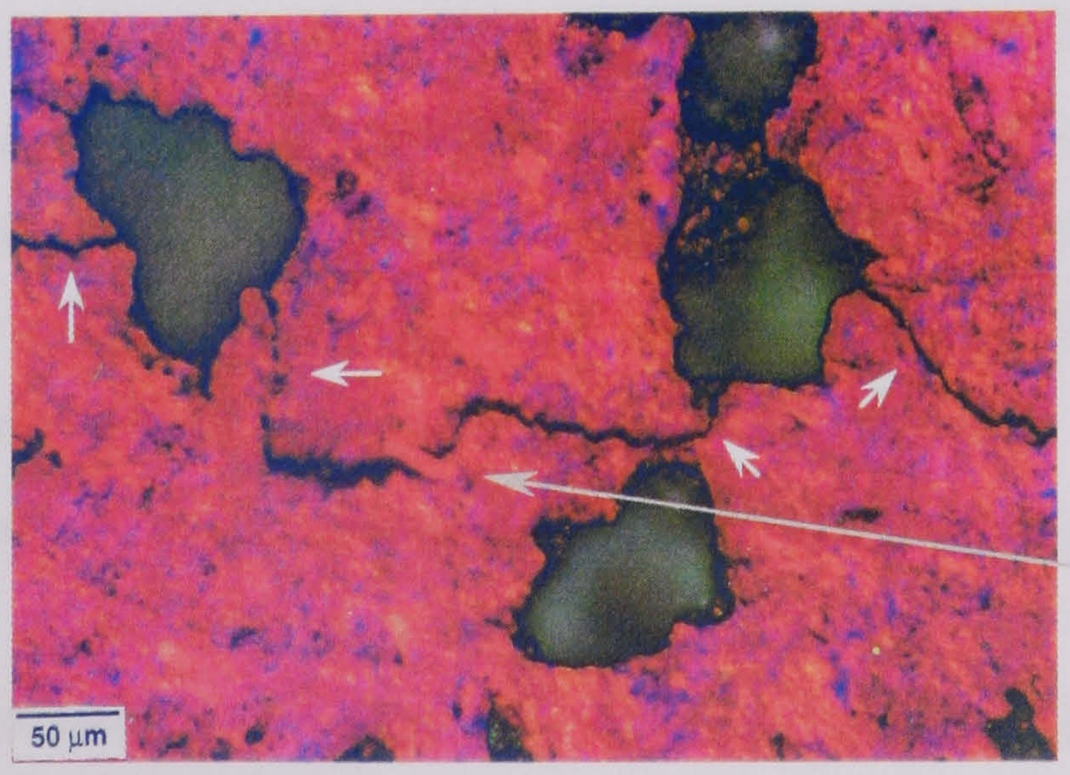

Figure 6.20. Crack bridging effects in the UcarC graphite.

Figure 6.20c shows how a relatively small filler grain forms a bridge between the mating crack surfaces, despite its low orientation angle to the crack path. It would appear from Figure 6.20c that a number of factors determine whether an elongated filler grain forms an effective bridge or not. These are:

1. The size of the grain relative to the local crack opening displacement.
2. The orientation of this grain to the crack path.
3. The nature of the filler-binder interface.

The filler grain is likely to bridge the crack more effectively, if it is appropriately sized, favourably oriented to the crack, and, adequately bonded along the binder-filler interface.

6.7. SUMMARY

Simultaneous optical and electrical measurements of the crack length, using 3-point bend and compact tension specimens, revealed a difference in the experimentally obtained *R*-curves obtained by the two methods. The application of a theoretical compliance method for calculating the relative crack length was described, and, some of the possible limitations of the method were discussed. The K_R-curves obtained by the compliance method compared well with those obtained optically, confirming the anomaly in the falling K_R-curve behaviour obtained by the ACPD and resistance measurements.

A comparison of the crack length measurements obtained by the different techniques revealed a serious underestimation in the crack length obtained from the electrical methods. The optical and compliance method was found to produce very similar results, a factor that validates the usefulness of the theoretical compliance method for crack length measurement. It was further demonstrated that the compliance method is relatively unaffected by small discrepancies in the elastic modulus or Poisson's ratio that is used in the calculation of the crack length. Qualitatively, all the crack length measurement techniques produced the same ranking for the different nuclear graphites, in terms of their crack growth resistance.

In quantitative terms, the Gilsocarbon and UcarC graphite showed similar resistance, with the former exceeding the latter over the initial part of the crack extension range. The results also indicate a slightly higher resistance in the UcarC material for crack growth perpendicular to extrusion. There was also some indication, particularly from the compliance-based *R*-curves, that the specimen geometry influences the *R*-curve behaviour. This is evident from the higher crack growth resistance and crack initiation toughness observed in the compact tension specimens compared to the 3-point bend tests. The γ_{WOF} values also show that compact tension specimens require more fracture energy.

The effectiveness of the compliance method was confirmed by the good correlation obtained between the γ_{WOF}-values and the energy envelope defined by the G_R-curve. Remarkably, the energy-based G_R-curves, based on the compliance derived K_R-curves, compared well with *R*-curves obtained by other workers using graphical methods, which reputedly account for non-linear fracture processes that are ignored using Irwin's similarity rule. The ranking of the G_R-curves of the different graphites was identical to the ranking of the K_R-curves, with IG-110 showing the lowest resistance to crack propagation.

Fractographic examination provided clear evidence to support the observed differences in *R*-curve behaviour between the three graphites. The most obvious difference noted was the complexity of the crack path, which was highest in the UcarC graphite. Coupled with extensive crack branching, secondary crack formation and pore blunting this gave the UcarC graphite the highest crack growth resistance. The higher crack initiation resistance in Gilsocarbon graphite was related to the increased difficulty for microcrack initiation and coincidental alignment of these cracks to form the macrocrack.

In the needle-coke graphites there was clear evidence of bridging effects, however, this was not so obvious in the Gilsocarbon graphite. It would appear however that the size of the bridging constituents is limited by the crack opening displacement since little evidence was found of bridging by very large grains. Bridging also seemed to be caused by ligaments of material that remained intact in the region just behind the crack tip. These ligaments probably detach when the local COD increases sufficiently. It was not clear to what extent frictional forces due to crack face interaction contribute to the overall bridging.

CHAPTER 7

USING THE DIFFERENCE IN CRACK LENGTH AS A MEASURE OF THE BRIDGING ZONE LENGTH

As shown in the previous chapter, the ACPD measurement underestimates the crack length, producing a falling *R*-curve behaviour. It became of interest to examine the extent of this underestimation when compared against the crack length obtained by the optical and compliance measurement techniques. The main objective was to evaluate whether the difference in the crack length measurement could be used to assess the development of the bridging zone. It was also of interest to see whether the difference in crack length could be used as a physical measurement of the length of the bridging zone. Possible variations in this 'apparent' bridging zone length between the different graphites could then be related to differences in their observed *R*-curve behaviour.

7.1. Evaluation of the Difference in Crack Length

The assumption is made that the crack length obtained by the ACPD methods gives a physical measure of the crack length that excludes the bridging zone length, defined by the relevant crack face interaction in the wake of the crack. The difference obtained in subtracting the crack length obtained by electrical measurements, i.e. a_{ACPD} *or* $a_{resistance}$, from the optical crack length ($a_{optical}$) or compliance crack length ($a_{compliance}$) measurements, is taken to be the length of the bridging zone (l_{br}). This is shown schematically in Figure 7.1.

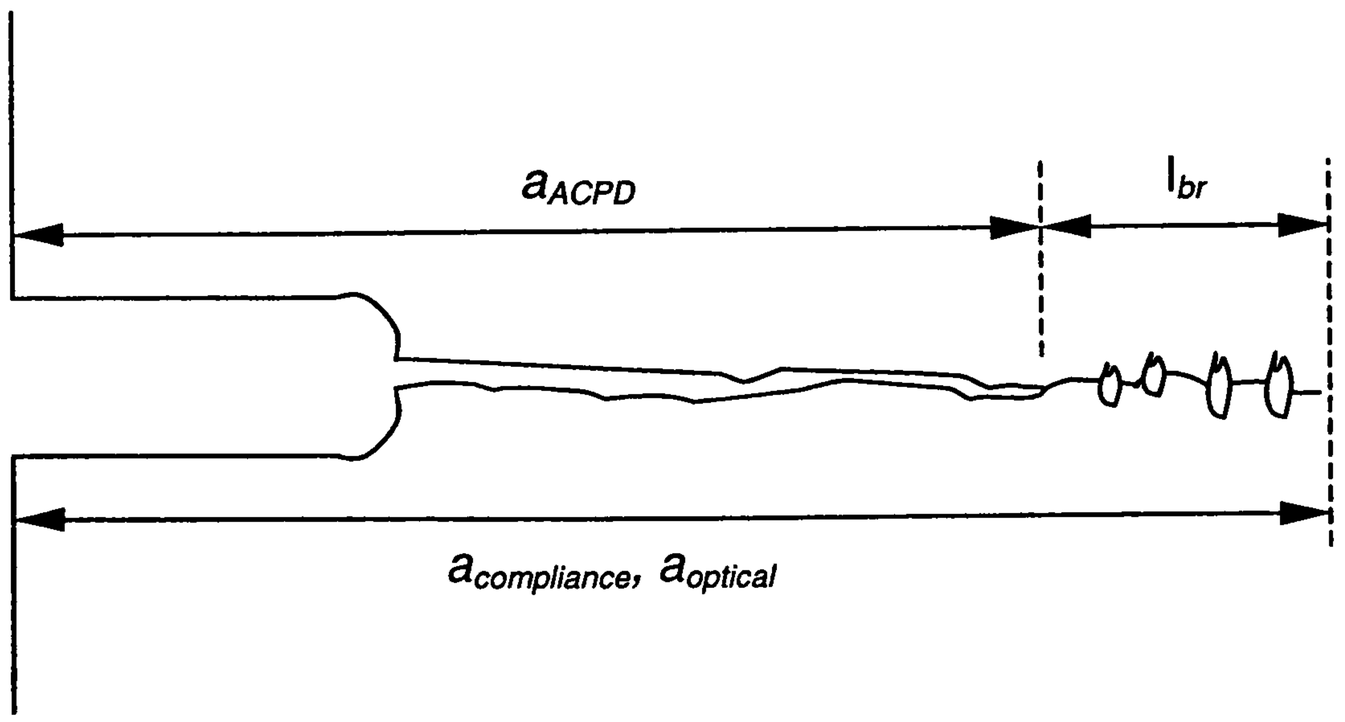

$$l_{br} = a_{optical} - a_{ACPD} = a_{compliance} - a_{ACPD}$$

Figure 7.1. Schematic definition of the bridging zone length, l_{br}, obtained from the difference in crack length measurements.

The crack length obtained by electrical measurement was simply subtracted from the optical or compliance measurements. It is arguable whether this assumption can be made. However, as will be shown, the differences obtained between these materials are consistent and may provide a means of understanding the development of the bridging zone. The possibility exists that the use of the crack length difference, as a measure of the bridging zone length, represents an overestimation of the actual zone length.

Part of the shortfall in the crack length obtained by the electrical measurements could simply be due to electrical contact from mutual contact between the crack faces, which does not necessarily contribute to the overall bridging stress. Unless this assumption is confirmed, by in-situ optical measurement or SEM measurement it is difficult to ascertain the extent to which simple, crack face contact may contribute to the measured differences. It may be even more difficult to differentiate between crack face regions that simply make contact, and, those regions which contribute to the overall bridging traction via their interaction, in the wake of the crack.

7.2. Assessing the Development of the Bridging Zone

In evaluating the development of the apparent bridging zone length, l_{br}, it is informative to firstly note the development of the crack in relation to the load-displacement response. A typical example showing the relative crack length developed according to the ACPD, optical, and, compliance methods, in relation to the load-displacement response is presented in Figure 7.2, for Gilsocarbon.

Clearly, the optical and compliance methods produce comparable results, whilst the ACPD method produces a shortfall in the crack length. In this typical case, it can be seen that the discrepancy in the crack length measurement begins to appear very early in the crack extension range, developing sooner in the 3-point bend specimen. It is also seen that the compliance method allows a continuous, assessment of the crack increment, in contrast to the scattered data given by the optical method. The compliance method therefore allows a better assessment of the development of the apparent bridging zone length, l_{br}.

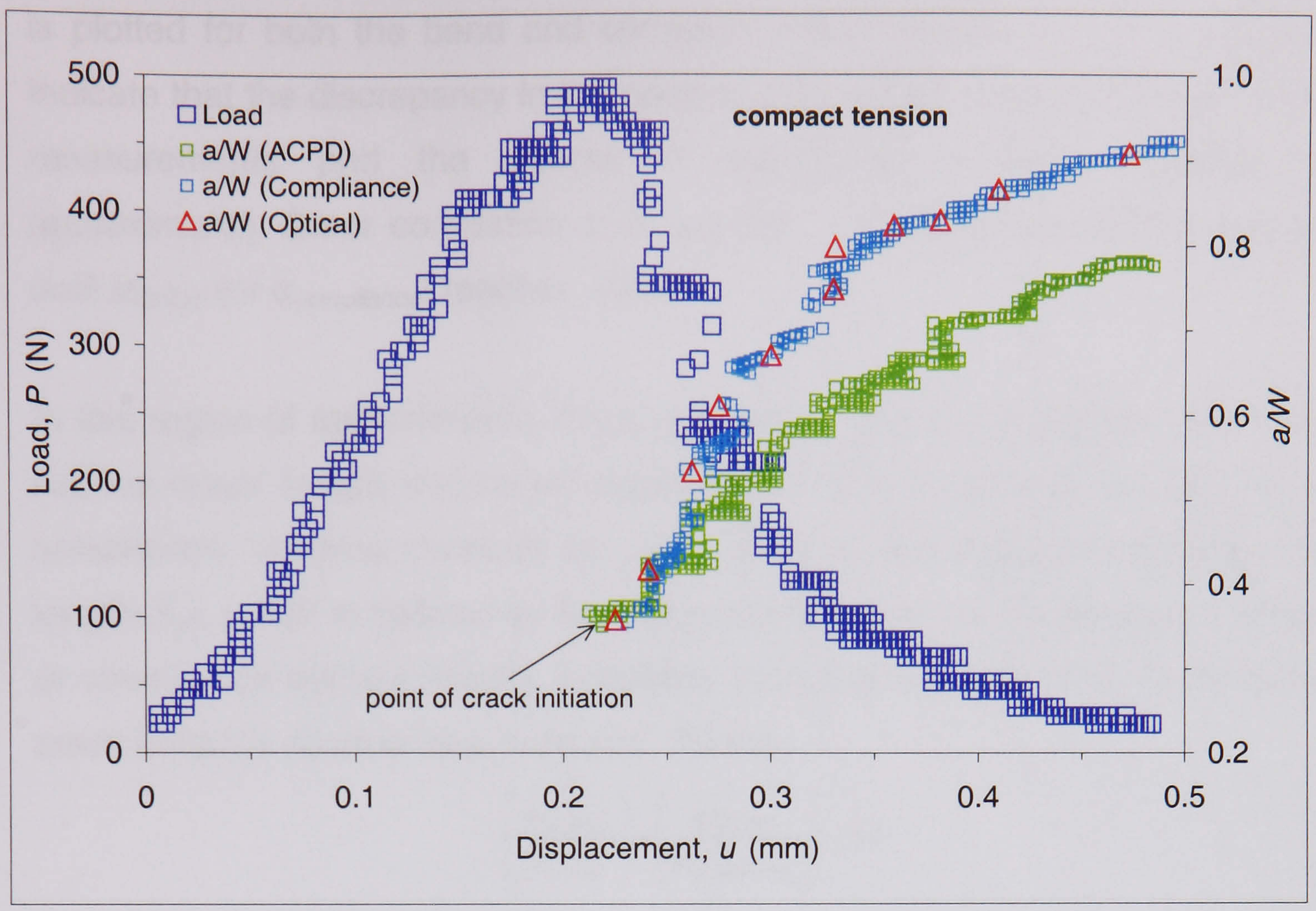

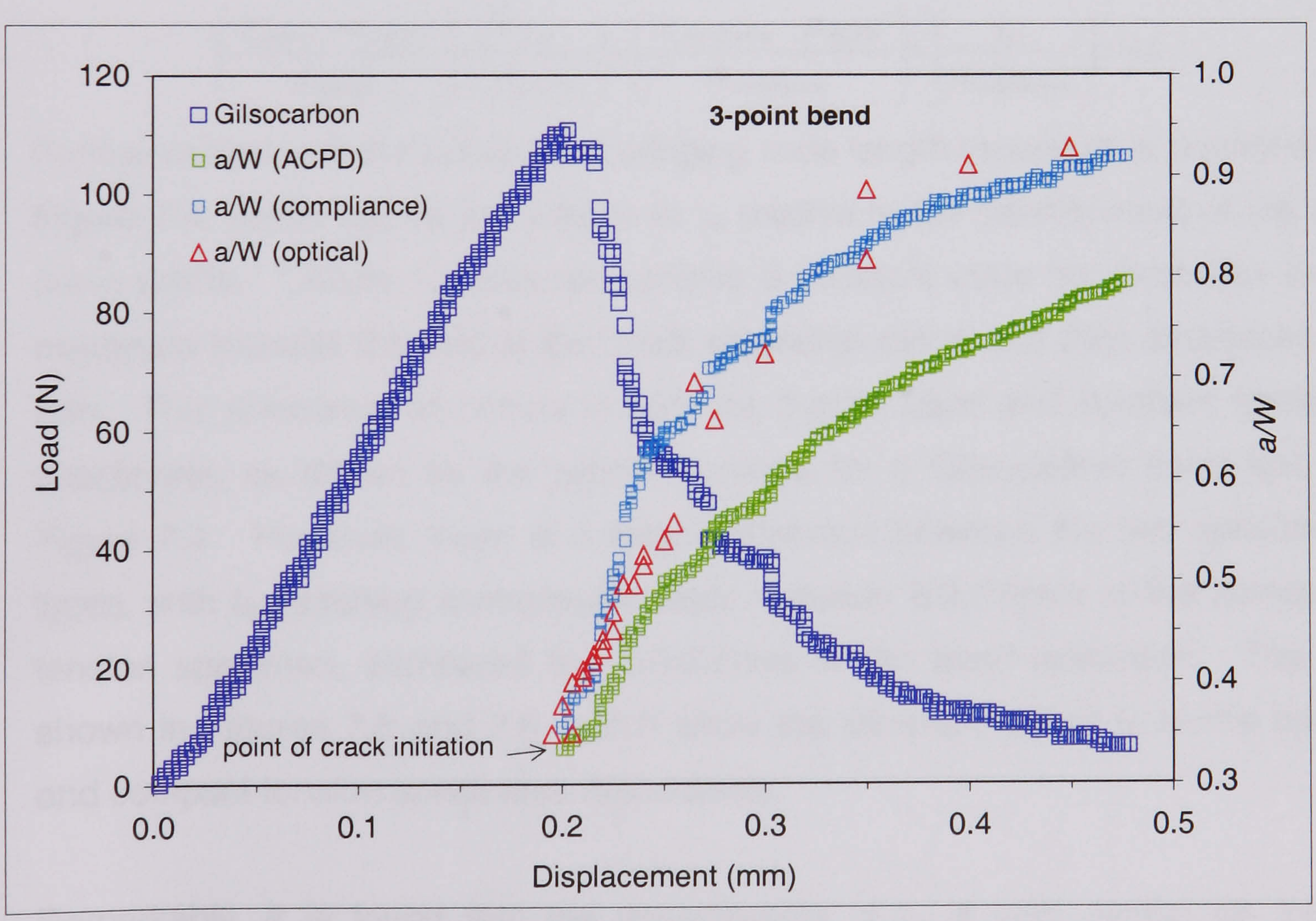

Figure 7.2. Variation in crack length measurements obtained by the different measurement techniques in relation to the load-displacement response for 3-point bend and compact tension specimens: Gilsocarbon graphite.

In Figure 7.3, the correlation between $a_{optical}$ and a_{ACPD}, or, $a_{optical}$ and $a_{resistance}$, is plotted for both the bend and compact tension specimens. These graphs indicate that the discrepancy in the relative crack length obtained from electrical measurements and the optical or compliance methods, reaches an approximately linear correlation at $\alpha_{optical}$~0.5. This linear correlation persists until $\alpha_{optical}$ (or $\alpha_{compliance}$) reaches ~0.8.

In this region of approximately linear correlation, it is found that the ratio of the relative crack length measured electrically to that measured optically, or by compliance, remains constant at ~0.8. That is, the apparent bridging zone length (l_{br}), which is defined by the difference between the electrical and optical, or compliance measurements, increases such that the ratio of l_{br} to the actual crack length is more or less constant. That is,

$$\left(\frac{\alpha_{ACPD}}{\alpha_{optical}}\right) \approx \left(\frac{\alpha_{ACPD}}{\alpha_{compliance}}\right) \approx 0.8$$

or

$$\left(\frac{\alpha_{optical} - \alpha_{ACPD}}{\alpha_{optical}}\right) \approx \left(\frac{l_{br}}{a_{optical}}\right) \approx \left(\frac{\alpha_{compliance} - \alpha_{ACPD}}{\alpha_{compliance}}\right) \approx \left(\frac{l_{br}}{a_{compliance}}\right) \approx 0.2$$

Further evidence that the apparent bridging zone length increases is provided in Figure 7.4, which shows the change in l_{br} relative to the development of the *R*-curve profile. Clearly, l_{br} does not achieve a constant value but increases to a maximum towards the end of the crack extension range and then decreases a little. This phenomenon occurs in both the 3-point bend and compact tension specimens, as shown by the typical example for a Gilsocarbon bend test in Figure 7.4. However, there is a major difference between the two specimen types, with l_{br} reaching a maximum value between 6.0-7.0mm in the compact tension specimen, compared to ~2.0-2.5mm in the bend specimen. This is shown in Figures 7.5 and 7.6, which show the development of l_{br} in the bend and compact tension specimens respectively.

Remarkably, it is found that the development of l_{br} is very similar for each graphite type, regardless of their structural differences. The magnitude of l_{br} begins to increase early in the crack extension range and continues increasing until $\alpha_{optical}$>0.8. The figures also indicate that the optically measured crack length is slightly lower than that obtained by compliance.

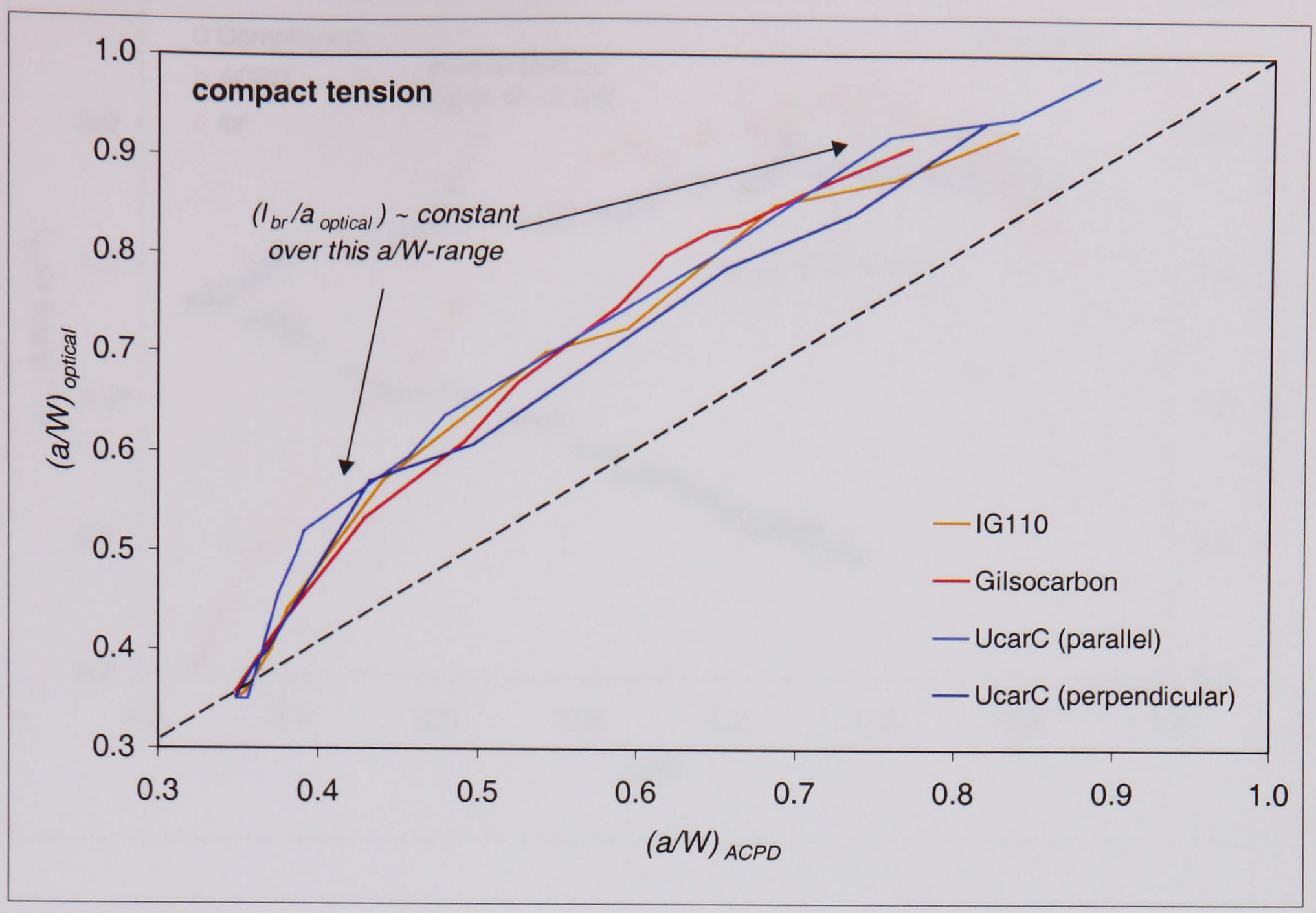

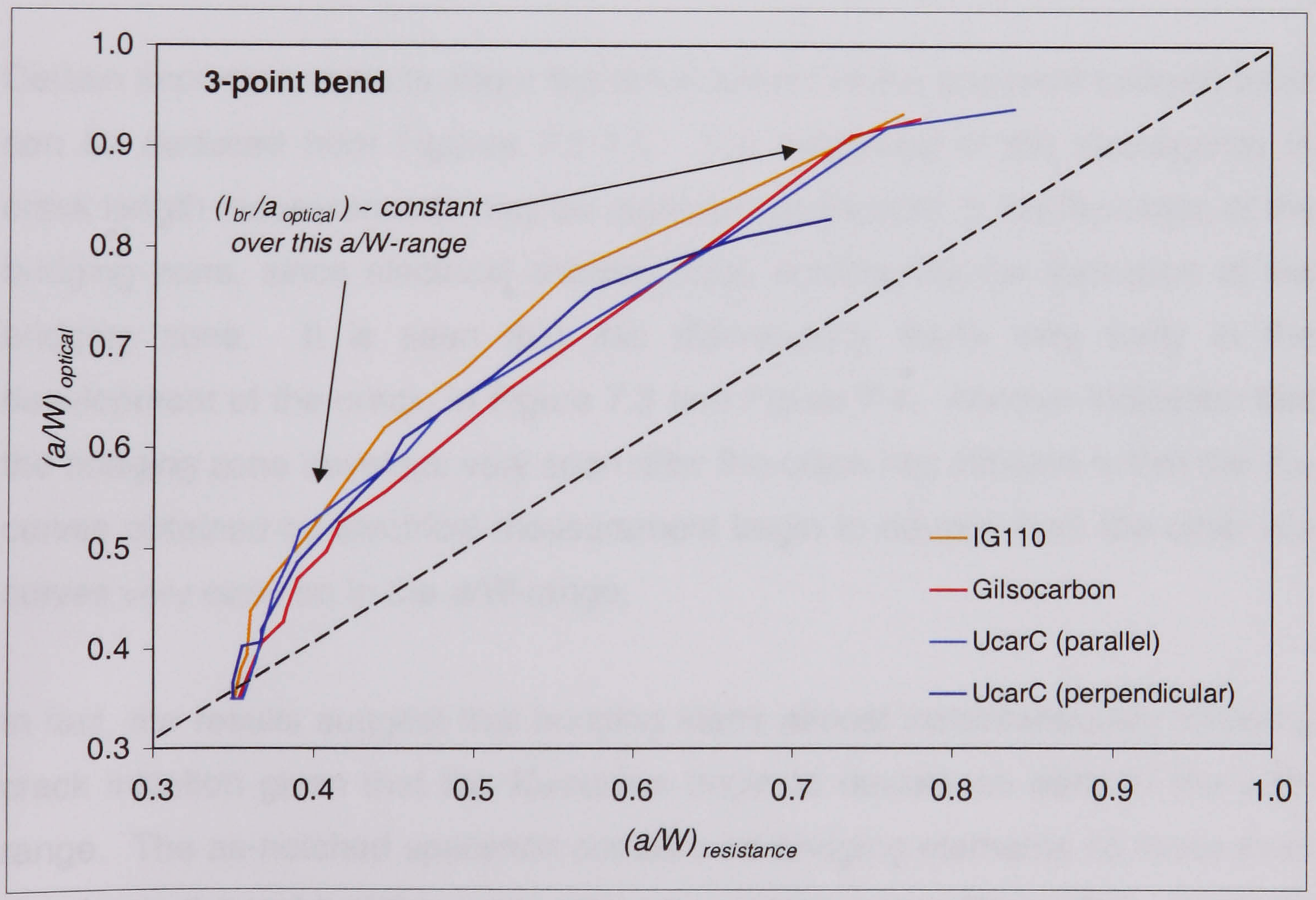

Figure 7.3. Correlation between the relative crack length obtained by electrical measurements, and that measured optically in the 3-point bend and compact tension specimens.

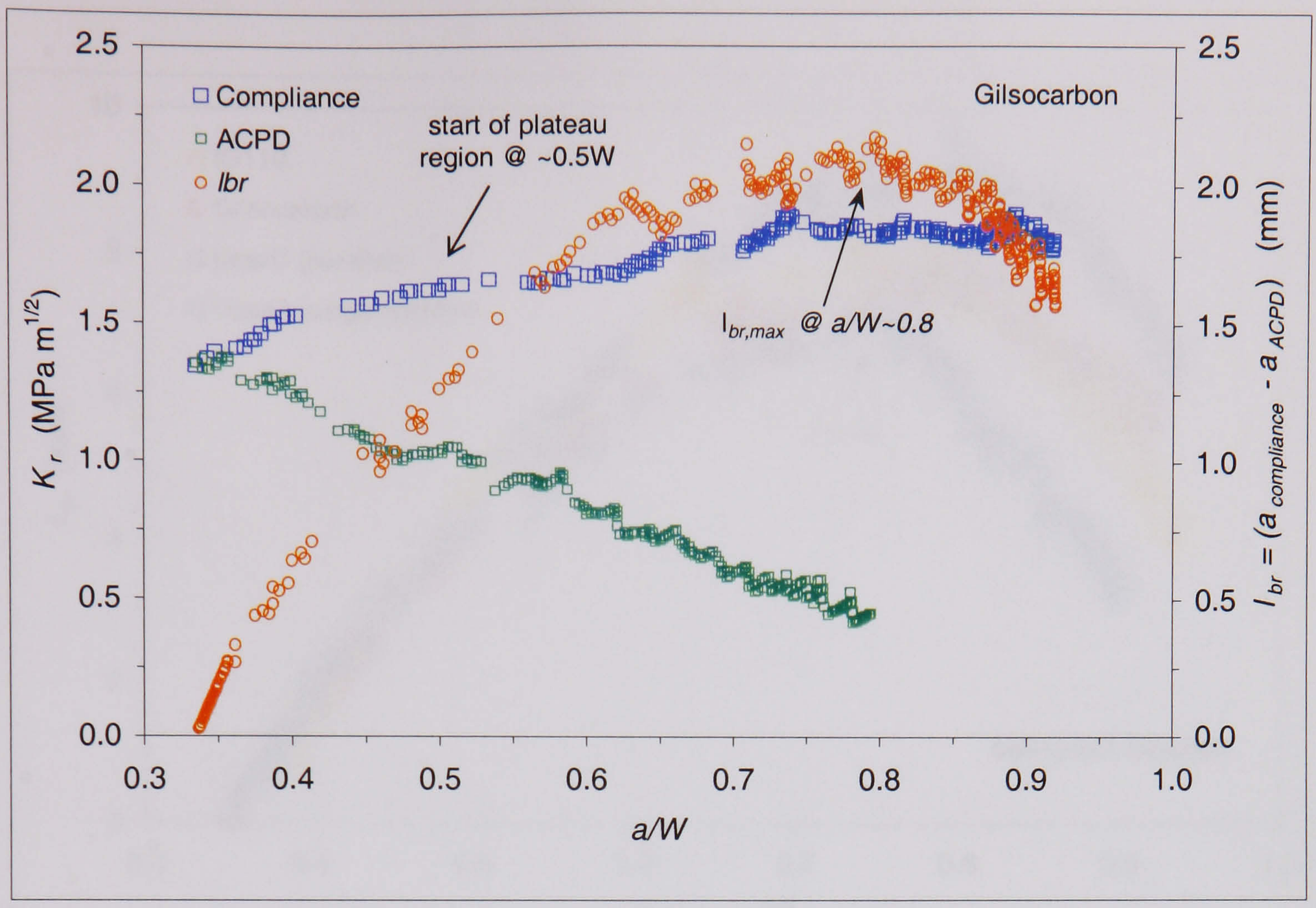

Figure 7.4. Development of I_{br} relative to the K_R-curve profile: Gilsocarbon.

Certain important aspects about the development of the apparent bridging zone can be deduced from Figures 7.3-7.6. The beginning of the discrepancy in crack length measurements may be regarded as the start of the formation of the bridging zone, since electrical shorting must accompany the formation of the bridging zone. It is seen that this discrepancy starts very early in the development of the crack, in Figure 7.3 and Figure 7.4. Another indication that the bridging zone develops very soon after the crack has initiated is that the K_R-curves obtained by electrical measurement begin to deviate from the other K_R-curves very early on in the *a/W*-range.

In fact, the results suggest that bridging starts almost instantaneously following crack initiation given that the K_R-curves begin to deviate so early in the *a/W*-range. The as-notched specimen contains no bridging elements so these must develop in the wake of the crack once it has initiated (see Figure 7.7). It is prior to the development of the bridging elements that the electrical measurements and optical/compliance measurements coincide. However, this correlation ends, due to electrical shorting, as soon as the crack is prevented from propagating in an unstable manner by the very first bridging elements.

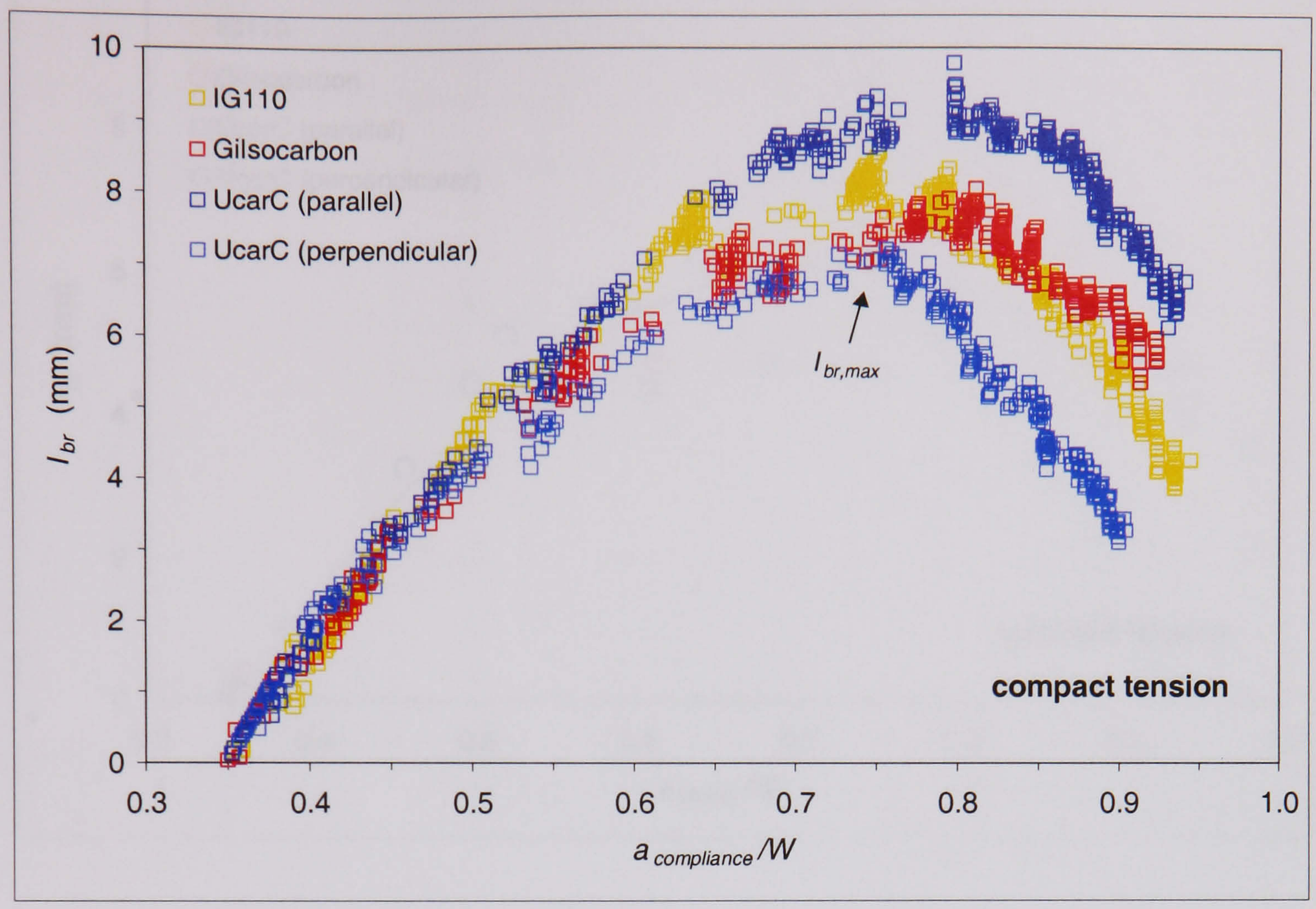

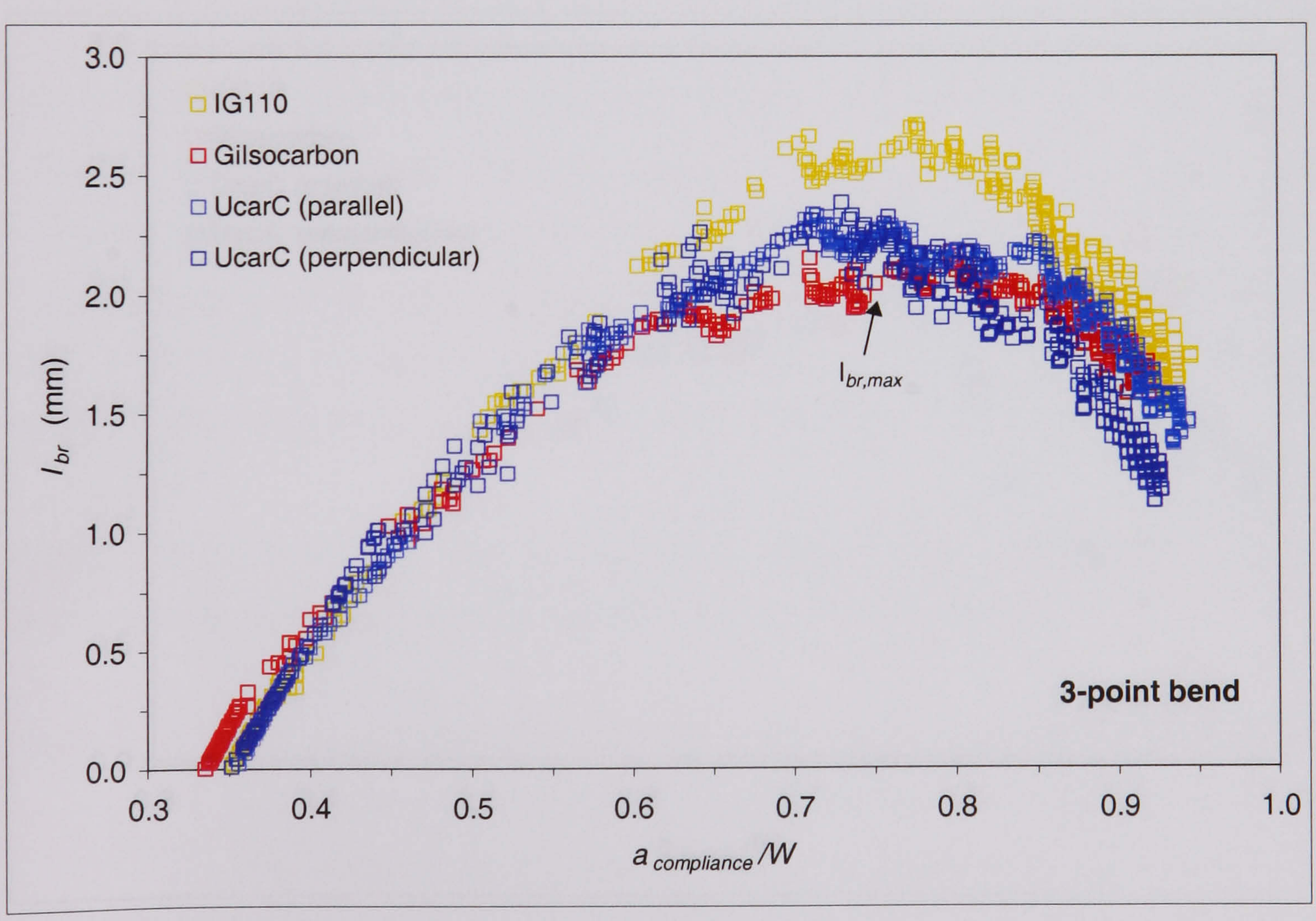

Figure 7.5. Development of the apparent bridging zone length (l_{br}) based on the difference in crack length measurements between the compliance and ACPD methods: 3-point bend and compact tension specimens.

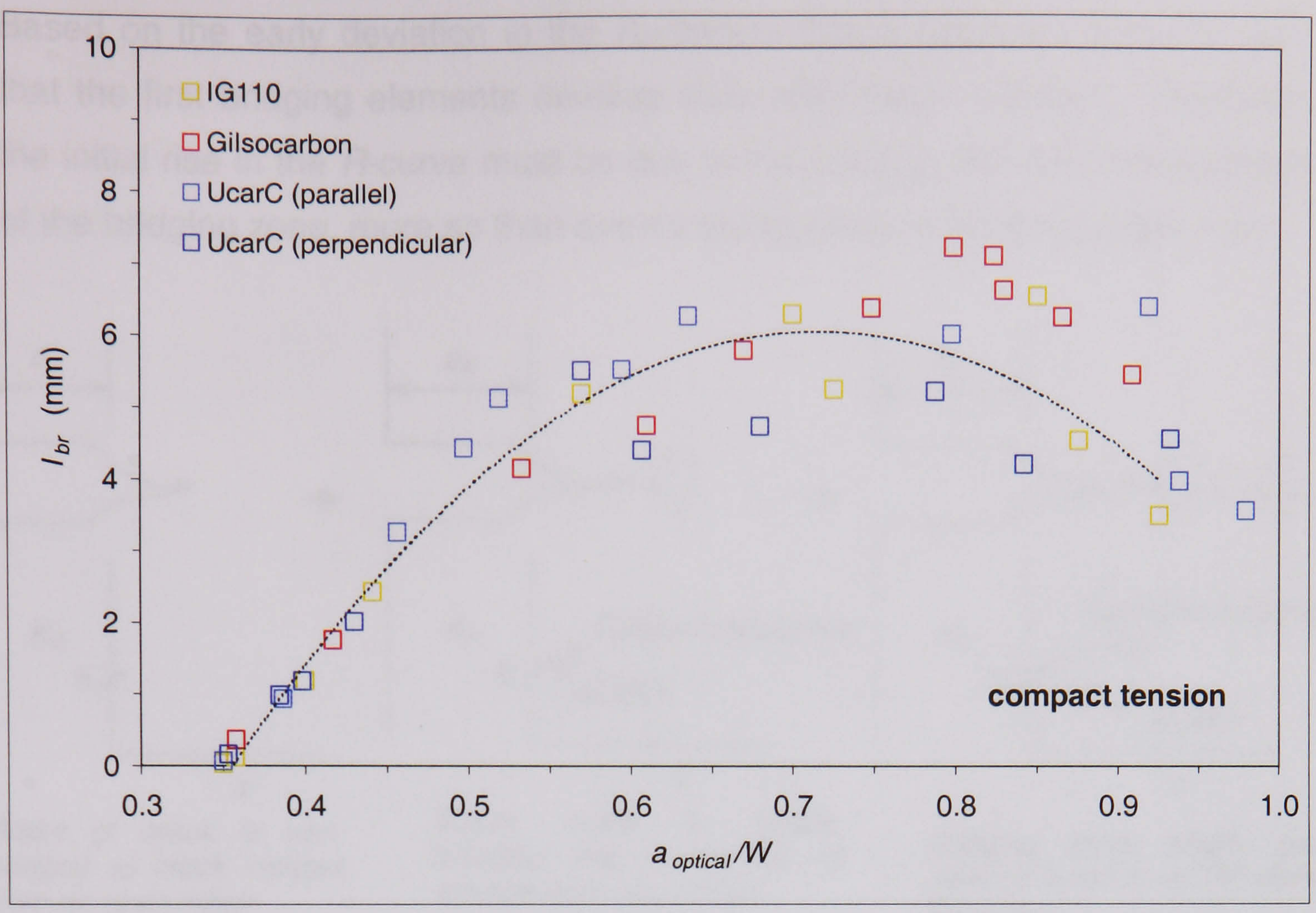

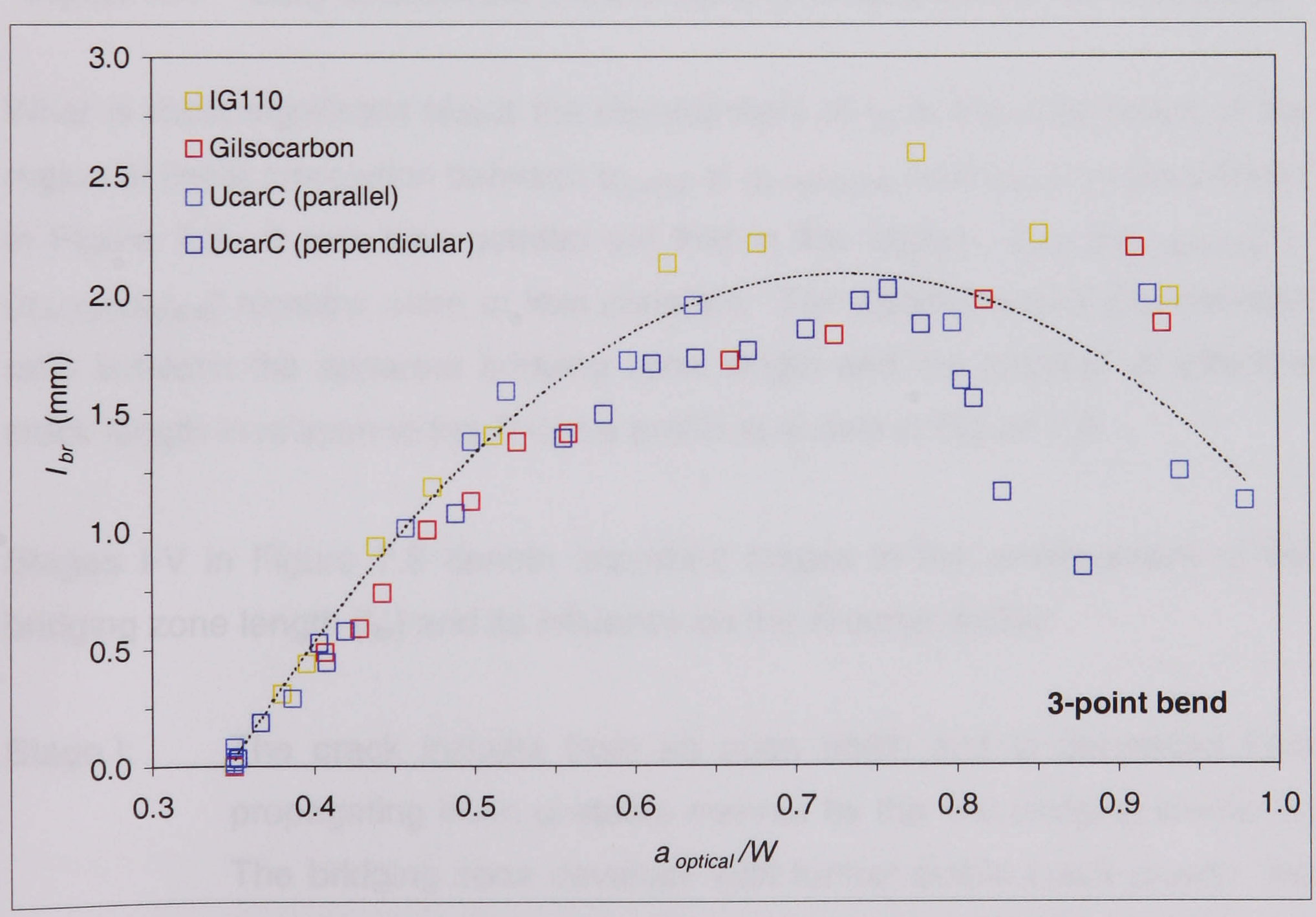

Figure 7.6. Development of the apparent bridging zone length (l_{br}) based on the difference in crack length measurements between the optical and ACPD methods: 3-point bend and compact tension specimens.

Based on the early deviation in the K_R-curves that is observed it can be said that the first bridging elements develop soon after crack initiation. Therefore, the initial rise in the *R*-curve must be due to the initial growth and development of the bridging zone, more so than events taking place in frontal process zone.

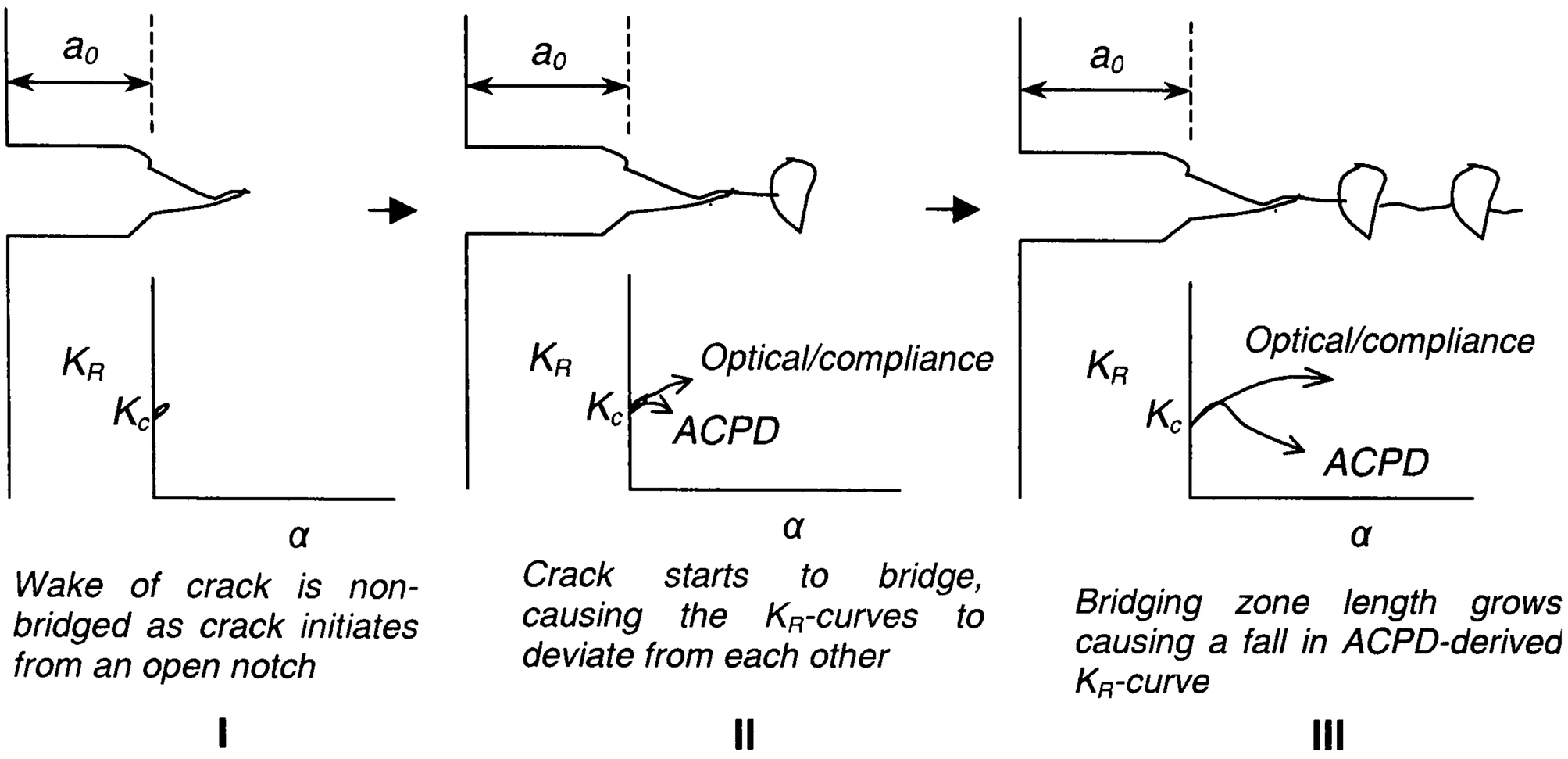

Figure 7.7. Early development of the bridging zone causes initial rise in K_R-curve.

What is most significant about the development of l_{br} is the occurrence of the region of linear correlation between $\alpha_{optical}$ or $\alpha_{compliance}$, and α_{ACPD} as was shown in Figure 7.3. It was also pointed out that in this region, ($\alpha_{ACPD}/\alpha_{compliance}$) or ($\alpha_{ACPD}/\alpha_{optical}$) remains more or less constant. The significance of this constant ratio between the apparent bridging zone length and the physical or effective crack length in relation to the *R*-curve profile is shown in Figure 7.8.

Stages I-V in Figure 7.8 denote important stages in the development of the bridging zone length (l_{br}) and its influence on the *R*-curve profile:

Stage I: The crack initiates from an open notch and is prevented from propagating in an unstable manner by the first bridging elements. The bridging zone develops with further stable crack growth, the increase in ($l_{br}/a_{optical}$) being the main cause of an initial rise in the *R*-curve. There may be a possible enlargement of the frontal process zone. However, experimental evidence for this is lacking.

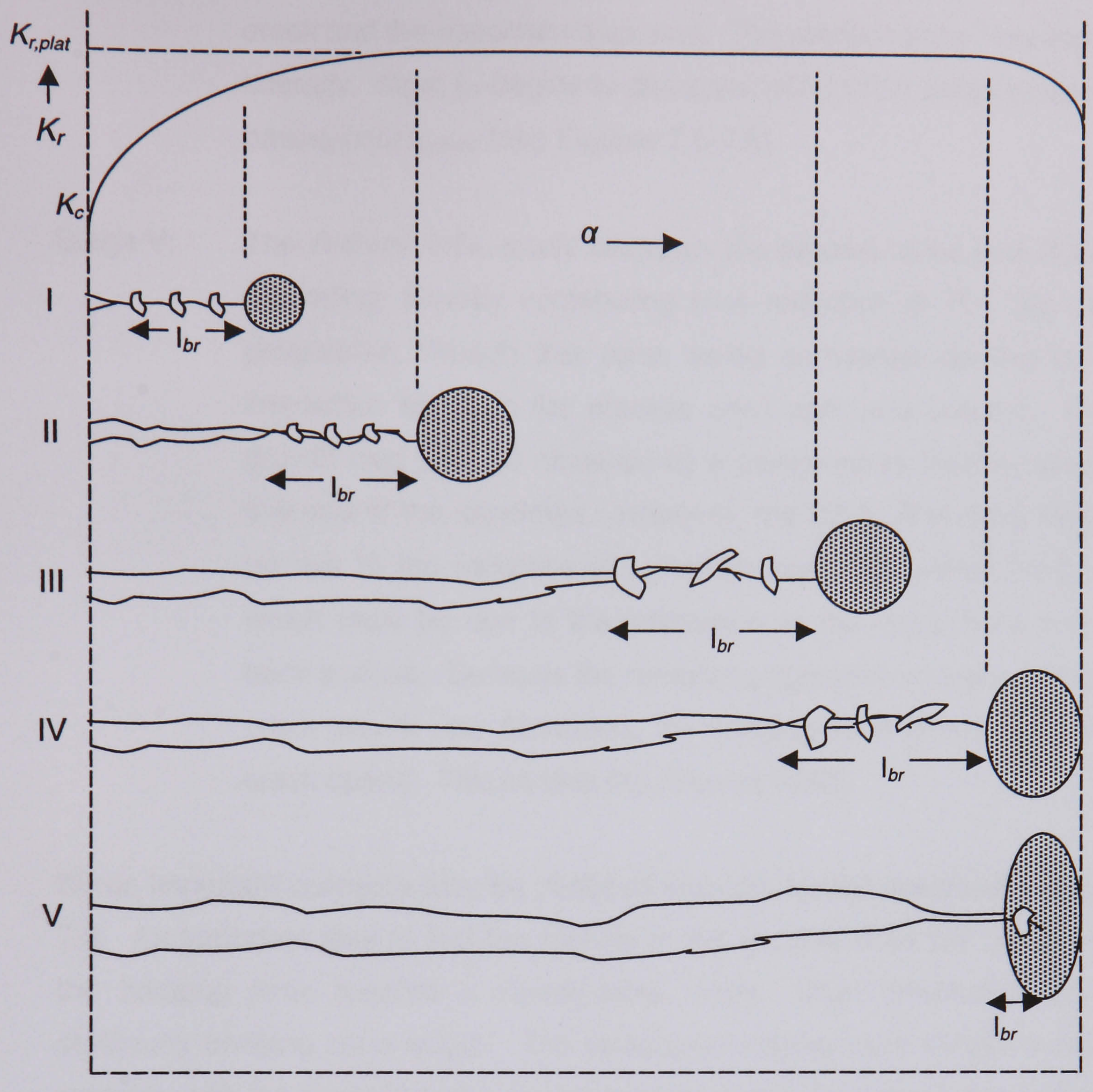

Figure 7.8. Relation between apparent bridging zone length and *R*-curve profile.

Stage II: The bridging zone has grown to a point where ($l_{br}/a_{optical}$ or $l_{br}/a_{compliance}$) is more or less constant. Now, the *R*-curve begins to plateau because the bridging zone length begins to translate relative to the crack increment thereby maintaining a constant ($l_{br}/a_{optical}$) or ($l_{br}/a_{compliance}$) ratio. This produces a plateau in the K_R-curve. The process zone also translates relative to the crack.

Stage III: The steady-state region where extension of the crack is counterbalanced by a proportional increase in the bridging zone length (l_{br}). The process zone may also translate accordingly.

Stage IV: The end of the steady-state condition and the beginning of the fall in the K_R-curve signalling the start of the interaction between the

crack and the specimen back end. The process zone may expand laterally. Now, l_{br} begins to decrease with further crack extension, having past $l_{br,max}$ (see Figures 7.5-7.6).

Stage V: The *R*-curve falls, partly because, the process zone has stopped extending, thereby contributing to a reduction in *R*. The crack progresses through this zone, being somewhat stunted by the interaction between the process zone and back surface. Crack growth may also be hindered by a compressive loading effect at this end of the specimen. However, the fall in *R* is more likely to be due to the reduction in l_{br}, which began at $a/W \approx 0.7$-0.8, and which must be due to the interaction of the crack front and the back surface. Because the remaining ligament is minimal and the crack growth rate decreases, the bridging zone diminishes as the crack opens. This causes the *R*-curve to fall.

Some important concepts may be deduced from the model described in Figure 7.8. An important idea is that the plateau in the *R*-curve does not occur when the bridging zone reaches a steady-state length, often referred to as the stationary bridging zone length. The stationary bridging zone length is said to coincide with the formation of a frontal process zone of constant size, which is also said to coincide with steady-state propagation of the crack, i.e. the plateau region on the *R*-curve. Rather, it appears that the steady-state condition is attained when the increase in the bridging zone length relative to the crack increment reaches a constant value, i.e. $(l_{br}/a_{optical}) \approx$ constant. It is the proportional increase in l_{br} relative to the increase in the crack length, which produces the steady-state condition in the crack growth, resistance curve.

The fall in *R*-curve towards the end may be viewed in terms of a drop in toughness caused by a reduction in the length of the bridging zone. This is a more likely situation than the idea proposed by Sakai et al (1988) that the *R*-curve falls mainly because the process zone stops developing with the crack extending through this zone. Allard et al (1991) envisaged the process zone to expand laterally along the back surface as depicted by Figure 7.8 (see Figure 2.3.13). They attributed the rise in their experimental *R*-curves to this apparent

enlargement of the process zone at the back surface. The depicted lateral extension of the process zone is hypothetical and may not reflect the reality given that the *R*-curve falls in some materials such as graphite. This also seems unlikely given the comparatively weak influence of the process zone on the overall toughening process as revealed by re-notching experiments.

From the development of l_{br} shown in Figures 7.4-7.6, it is seen that l_{br} reaches a maximum at a/W~0.8 and then starts to decline, in both the bend and compact tension specimens. The decrease in l_{br}, so late in the a/W-range, must be related to the coincidence between the crack front and the specimen back end. The reduction in l_{br} implies that the crack growth rate is reduced such that the electrically measured crack length approaches the optical or compliance measurements. At this point, the bridging zone behind the crack disengages at a rate faster than the rate of crack extension causing l_{br} to reduce and the *R*-curve to fall. The bridging zone that developed over the plateau region of the *R*-curve is effectively pulled apart. This also explains why the energy-based *R*-curve falls towards the end of the a/W-range.

The question arises as to why some materials show the rising *R*-curve while others show a fall towards the end of the a/W-range. This would appear to be a material dependent phenomenon. Materials that show a continuous rise in *R*, or, a late rise following the plateau region, are likely to be those in which an extensive bridging zone develops. In C/C composites, a continuous rise tends to occur due to extensive bridging between the fibres, which persists even when the crack has traversed much of the available ligament. In very coarse-grained ceramics or carbons, where the grain size is of the order of millimetres, a similar effect must occur in that bridging persists over much of the available crack growth ligament. This effect is particularly enhanced with elongated grains.

7.3. Estimating the Size of the Frontal Process Zone

Sakai et al (1988) showed a fall in K_R-curve behaviour at a/W~0.6, which they related to the frontal process zone coinciding with the specimen back end. From this, they estimated the frontal process zone length to be about 15mm in the compact tension test specimens (W=40mm).

Allard et al (1991) used a similar approach in bend specimens (W=50mm), showing that the influence of the specimen back wall manifests itself sooner, when the initial notch is deeper. They obtained an estimate of ~12mm in bend specimens using an initial notch depth of a_0=0.5W. Ouagne (2000) used the same method to estimate the process zone size in compact tension specimens (W=50, 80mm) and obtained proportionally, similar values to Sakai et al (1988).

In this study, the experimental R-curves show a falling behaviour much later in the a/W-range (>0.9W), such that a smaller process zone size is obtained compared to that reported by others. Sakai et al's (1988) estimate of about 15mm is much larger than the value of ~7-8mm obtained for the compact tension specimens (W=40mm) tested here. Clearly, the earlier fall in the R-curve in Sakai et al's case (1988) leads them to estimate a much larger process zone size. The optically derived R-curves in this work show either a rise or fall near the end of the a/W-range. Because this occurs late in the a/W-range, the R-curve profile is susceptible to errors in the crack length measurement and the influence of the geometric factor, both of which cause scatter in the data.

7.4. Relation between l_{br}, COD, and, R-curve Behaviour

It was pointed out earlier that a substantial difference in the magnitude of l_{br} was obtained between the 3-point bend and the compact tension specimens. This difference in the size of the apparent bridging zone (l_{br}) may offer an explanation as to why the R-curve profile shows a dependence on the test specimen geometry. In the compact tension specimens, more energy is needed to overcome the bridging stresses that develop within the bridging zone thereby resulting in a higher R-curve profile. Therefore, the crack growth resistance obtained using compact tension specimens appears higher than that in the bend specimens. The higher energy required to overcome the bridging stress in the compact tension specimens would also explain why the work of fracture is higher in these specimens compared to the bend specimens.

Sakai et al (1988) estimated the stationary bridging zone length (Δa^*) from the intersection point between the rising part and the plateau region on the K_R versus $\sqrt{\Delta a}$ curve and obtained $\Delta a^* \approx$ 1.7mm. The stationary bridging zone

length is said to coincide with the formation of a steady-state wake zone, which also coincides with steady-state propagation of the crack, i.e. the plateau region on the *R*-curve. In energy terms, the energy release rate or crack driving force is said to equal the crack growth resistance at this stage.

Ouagne (2000) obtained much longer bridging zone sizes at 9mm and 13mm in compact tension specimens with W=50mm and W=80mm. However, he estimated the bridging zone length taking the crack increment over which the *R*-curve initially rises to the plateau level to indicate the bridging zone length. It is not entirely certain whether this is appropriate since the calculation of the stationary-bridging zone length requires that K_R be plotted against $\sqrt{\Delta a}$. Ouagne's estimate is therefore likely to be smaller than reported, i.e. ~3-4mm.

Allard et al (1991) found $\Delta a^* \approx 2.3$mm in anthracite based carbons of coarse grain size ranging between 5-12mm. Clearly, the application of the concept that a steady-state bridging zone length occurs produces a shorter bridging zone length to that measured in this study using the difference in crack length. In this study, the bridging zone length is shown to increase.

It is not entirely clear why the two specimen types show such a large difference in l_{br}-values. This may be due to a difference in the stress-distribution profiles in the two specimen types. The size of the bridging zone is generally considered to be due to the roughness of the crack surfaces and the development of the COD (Reichl & Steinbrech, 1988). Interestingly, Reichl and Steinbrech (1988) have noted that the COD is a function of the type of test and crack geometry. This may explain the longer bridging zone length (l_{br}) obtained in the compact tension specimens in which the COD may be smaller than that in the bend specimens. This is however speculative and requires investigation.

A remarkable feature of the results presented here is that the development of l_{br} appears to be similar in all the graphite materials, despite their significant structural differences, particularly the difference in the average grain size. It was also found that the maximum l_{br} reached was similar in all the materials. This may imply that the bridging zone length (l_{br}) might not be a useful indicator of differences in the *R*-curve response between the different graphites.

Instead, the extent of crack path deflection, and the size and nature of the bridging constituents within this zone seem likely to be of more influence. A similar observation was made by Ouagne (2000) who measured similar bridging zone lengths in two different graphites using another approach. He concluded that the frictional traction and bridging constituents within the bridging zone was greater in the graphite that showed higher crack growth resistance. In effect, this meant that the crack path tortuosity within the bridged zone was higher.

Therefore, the difference in crack growth resistance between the coarse and fine grain graphite may depend more strongly on the bridging stress distribution that develops. The bridging stress gradient is likely to be higher in coarser grained materials where a higher COD would be needed to overcome the bridging elements. The COD may thus be more influential in determining the bridging stress profile that develops at various stages in the growth of the bridging zone. Grimes et al (1990) state that the COD is the critical component governing the bridging traction, not the crack length. They show that a small COD value relative to a coarse grain size contributes to grain bridging. Reichl and Steinbrech (1988) indicate that when the COD at a particular interaction site is larger than the crack surface roughness, which is related to the grain size of the material, bridging no longer becomes possible. Tandon & Faber (1998) state that a smaller COD is required for transgranular fracture than when a bridging grain undergoes full de-bonding and pullout without fracturing. In principle, this concept can be extended to materials with different grain sizes. In coarser materials, a large COD is needed to achieve pullout.

Sakai et al (1988) equated the critical COD (~12μm) with the mean filler grain size of the graphite which was ~15μm. Allard et al (1991) found a critical COD of ~11μm for anthracite-based carbons with grain size ranging between 5-12mm. They concluded that the bridging constituents in their materials could not be the grains, as Sakai et al (1988) had proposed, given the order of magnitude difference in the grain size of the materials. They concluded that fracture in their materials must be transgranular rather than intergranular so that, the critical bridging element corresponded more with the binder phase or a portion of the fractured grain rather than an entire grain. However, they had no fractographic evidence to prove this.

The fractographic evidence found here supports the view of Allard et al (1991) in that, the COD is unlikely to coincide with the average grain size, particularly when the grain size become coarser. Microscopy of the crack path indicates that the local COD behind the crack is far smaller than the average grain size. It is also observed that the larger grains hardly ever undergo pullout, but fracture instead. The nature of the binder-filler interface would also determine whether pullout occurred or not.

The maximum size of grain that can be pulled out within the constraints of the local COD may also be limited. Grain shape must also play a role. It was noted that the spherical Gilsocarbon grains were easily pulled out despite their fairly, large grain size. It seems that the critical COD is that COD, which is needed to just disengage the bridging element at the end of the bridging zone. This may not require that the entire grain be pulled out. Instead, the grain may partially be disengaged or fractured and still cause bridging. The combination of increased crack path tortuosity within the bridging zone and the higher COD that is required for pullout in coarser materials would raise their *R*-curve profiles.

7.5. SUMMARY

Based on the hypothesis that the shortfall in crack length obtained by the ACPD method provides a measure of the length of the bridging zone, it is found that the apparent bridging zone length increases continuously as the crack propagates. This apparent bridging zone length appears to be similar in all the nuclear graphites but larger in the compact tension specimens compared to the bend specimens. The development of the apparent bridging zone length relative to the crack length suggests that it is the bridging zone length that translates relative to crack extension rather than the process zone translation which causes the *R*-curve to plateau.

This was shown by considering the ratio of the apparent bridging zone length to the actual crack length, which reaches a more or less constant value early in the crack extension range. The attainment of this constant ratio appears to coincide with the beginning of the plateau in the *R*-curve. The fall in the *R*-curve towards the end of the crack extension range is also well accounted for

for by this hypothesis. This fall was attributed to a reduction in the apparent bridging zone length that occurs towards the backend of the specimen. The disengagement of existing bridging elements within the bridging zone and a discontinuation in the further development of this zone, towards the backend of the specimen, would appear to be responsible for the fall in the R-curve. In materials that show a rising R-curve the bridging zone must extend over most, if not all, of the available crack growth ligament. Thus, bridging elements remain partially or fully engaged even when the crack approaches the specimen end.

The process zone size estimated in this study was found to be substantially, smaller than that estimated by other workers for graphites and carbon materials. However, the difference stems mainly from the profile of the experimentally measured R-curve, in particular, the point at which the curve begins to fall. The difference in the length of the apparent bridging zone between the bend and compact tension specimens also provides an explanation as to why the fracture energy, and hence the R-curve, is higher in the compact tension configuration. That a similar bridging zone length was obtained for all the graphites, regardless of their grain size and shape, implies that the extent of crack path tortuosity within this zone determines the bridging stress gradient.

There would appear to be a complex relation between the bridging stress distribution developed within the bridging zone, the microstructure, and, the test specimen geometry which may also influence the COD. The relation between the COD and the propensity for bridging is well recognised but is an area that requires investigation. Recently, Ramos (2002) used the weight function method (Fett & Munz, 1998) to calculate the bridging stress profile in coarse-grained alumina-SiC refractory material containing different amounts of graphite flake. Ramos (2002) has shown that the calculated bridging zone length correlates well with the apparent bridging zone length obtained by the shortfall in crack length measured by the PD method. He also found that the bridging zone length was reduced when the local COD increased, the increase in COD occurring with higher proportions of graphite. Fractography indicated that the graphite flake encourages crack deflection and pullout, which extends the length of the bridging zone but, reduces the overall bridging stress gradient.

CHAPTER 8

INFLUENCE OF THE NOTCH CONFIGURATION ON THE *R*-CURVE PROFILE

Certain aspects of *R*-curve measurement were considered in more detail during the course of this study in order to acquire a better understanding of *R*-curve measurement techniques. The two aspects discussed here are both concerned with the influence of the notch configuration on the *R*-curve profile. The first aspect concerns the importance of notch sharpness or pre-cracking on the *R*-curve, and, the second aspect concerns the use of chevron-notched bend specimens for *R*-curve measurement.

8.1. Influence of Notch Sharpness on the *R*-curve Profile

It was mentioned in Chapter 5 that preliminary observations of crack initiation using blunt-notched specimens revealed that cracks often propagated in an unstable manner from the notch tip. It was therefore of interest to compare the stability of crack growth between as-notched and sharpened specimens. This is also important in demonstrating the need to sharpen or pre-crack the specimen.

8.1.1. Theoretical Background

Munz et al (1980) state that notch preparation in straight-through, notched specimens is a critical factor, that is responsible for the variation in K_{IC}-values obtained since the notch does not represent a real crack. Damani et al (1996) recognise the need for a standardised fracture toughness test, but are in favour of the straight-through notched 3-point bend specimen, citing various advantages in this respect. Amongst the most important of these are its proven reproducibility in round-robin tests, its cost effectiveness and simplicity, and, the large body of accumulated data.

Damani et al (1996) show that, the measured K_{IC} value decreases with notch width, reaching a constant value below a critical notch root radius. This constant value is said to equal the plane-strain fracture toughness that would be obtained using a proper pre-crack. They found the critical root radius to be material dependent. Brocklehurst (1978) also indicates that the limit on the effective sharpness of the notch is set by the microstructure of the material.

A common method used to reduce the notch root radius is to sharpen the notch tip using a sharpening tool. Typically, a razor blade is used (Sakai et al 1988, Kostopoulos et al 1998, Hiramatsu & Okada 1998). The extremely acute root-radius produced simulates a pre-crack very well, with the sharpened notch root having a radius <10μm (Sakai et al, 1988).

Fine grain graphite is known to show higher notch sensitivity than coarse-grained material. Bazaj and Cox (1969) found the stress-concentration factor to be 50-60% higher in fine-grained (~0.7-0.8mm) graphite compared to coarse-grained material (~8-9mm). They found experimental stress concentration factors to be lower than theoretical values, due to inherent flaws, which lower the strength of the material. Experimental values are more realistic since notch sensitivity is not a true material characteristic but depends on notch geometry.

8.1.2. Comparison of As-notched and Sharpened Specimens

For the comparison, IG110 graphite was selected because of its fine grain size. An as-notched specimen and two sharpened specimens were tested. The notch-tip sharpening procedure was described in Chapter 5. The specimens were of similar dimensions, i.e. 12x10x100mm, with an initial notch length a_0=0.35W. The nominal width of the sawn notch was ~0.250mm. The as-notched specimen was tested at a speed of 0.010 mmmin^{-1}, while the specimens with sharpened tip were tested at 0.050 mmmin^{-1}. The load displacement curves for the different specimens are compared in Figure 8.1, along with the K_R and G_R-curves. The K_R-curves were derived by the compliance method.

The load-displacement response clearly shows that the 'as-notched' specimen reaches a slightly higher maximum load than the sharpened specimens, following which it fails in a more unstable manner. This is evident from the sharp drop in load following the maximum load. By contrast, the sharpened specimens display a smooth transition past the maximum load. The K_R-curves reveal that the 'as-notched' specimen produces a higher K_{IC} value than the sharpened specimen. Overall, the K_R-curves give the impression that notch tip acuity has little effect on the measured crack growth resistance, given the similarity in the K_R-curves for the different specimens.

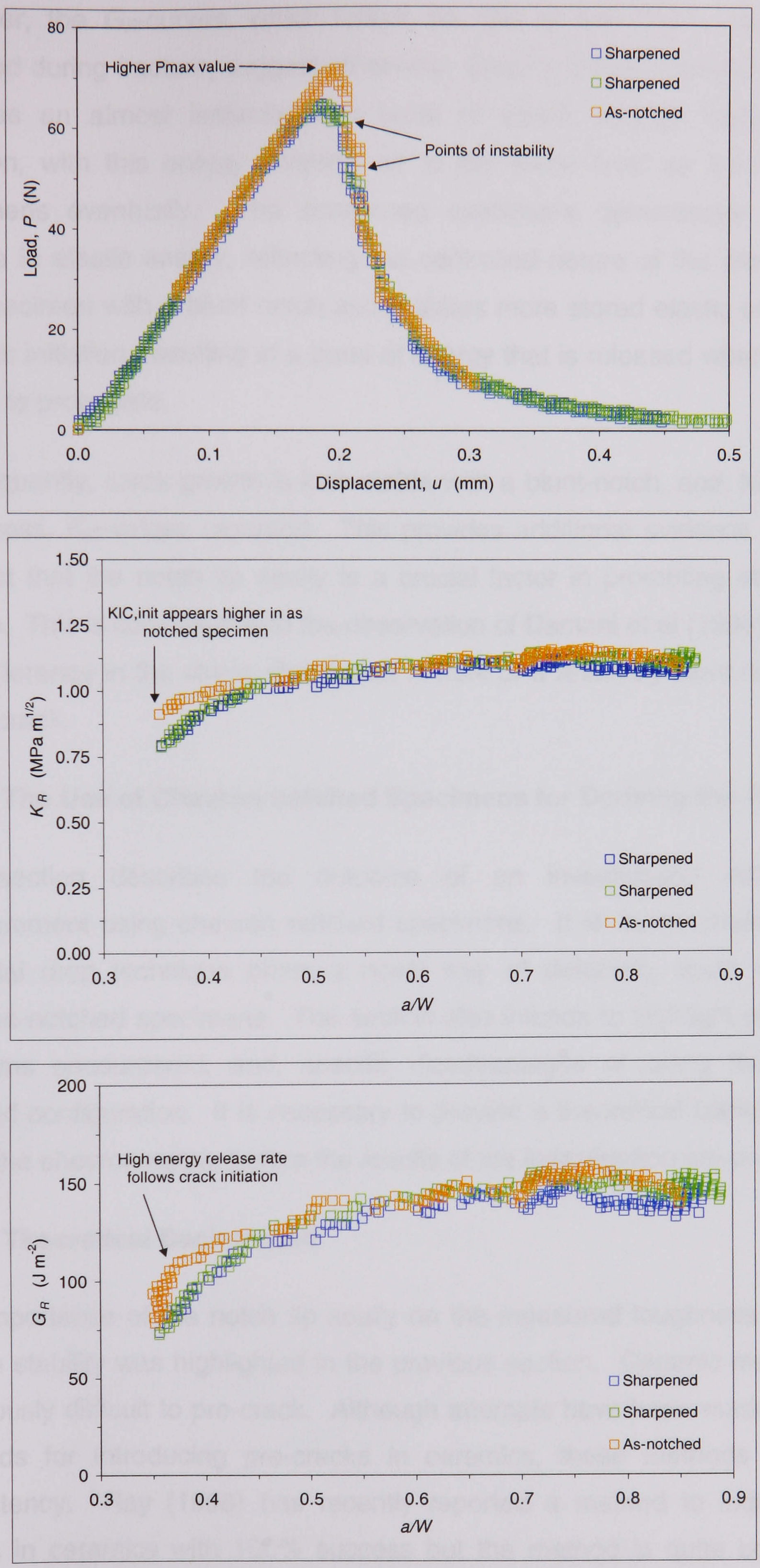

Figure 8.1. *R*-curve behaviour of 3-point bend specimens with as-notched and sharpened notch tips: (a) *P-u* curves; (b) K_R-curves; (c) G_R curves.

However, the G_R-curves, which reflect the rate of the elastic strain energy released during fracture, suggest otherwise. Clearly, the 'as-notched' specimen releases an almost instantaneous burst of elastic energy following crack initiation, with this energy levelling off to the same level as the sharpened specimens eventually. The sharpened specimens demonstrate a gradual release in elastic energy, reflecting the controlled nature of the crack growth. The specimen with a blunt notch accumulates more stored elastic energy prior to crack initiation, resulting in a burst of energy that is released when the crack begins to propagate.

Consequently, crack growth is less stable with a blunt-notch, and, higher initial toughness, K_{IC}-values recorded. This provides additional evidence to support the fact that the notch tip acuity is a crucial factor in promoting stable crack growth. This is consistent with the observation of Damani et al (1996) that there is a difference in the stress-distribution in front of a relatively blunt notch and a sharp crack.

8.2. The Use of Chevron-notched Specimens for Deriving the *R*-curve

This section describes the outcome of an investigation into *R*-curve measurement using chevron notched specimens. It is demonstrated that the potential drop technique offers a novel way of detecting crack initiation in chevron-notched specimens. The section also intends to highlight some of the problems encountered, and, specific disadvantages of using the chevron-notched configuration. It is necessary to provide a theoretical background into using the chevron-notch, before the results of the investigation are presented.

8.2.1. Theoretical Background

The importance of the notch tip acuity on the measured toughness and crack growth stability was highlighted in the previous section. Ceramic materials are notoriously difficult to pre-crack. Although attempts have been made to devise methods for introducing pre-cracks in ceramics, these methods often lack consistency. Ray (1998) has recently reported a method to induce starter cracks in ceramics with 100% success but the method is quite complicated, requiring the use of specially designed fixtures.

The chevron-notch configuration is said to provide a particular advantage in this regard in that the complications associated with trying to produce measurable pre-cracks are avoided. The crack initiates from the angular tip very early in the fracture process due to the very high stress intensity at the tip. The triangular-shaped ligament also promotes stable crack growth because the width of the ligament increases as the crack extends. This notch configuration was initially developed for testing metallic materials (Barker, 1977) but has found extensive application in testing ceramics and brittle materials in recent years.

The ASTM Standard C1421-1999 describes various chevron-notch configurations for determining the fracture toughness of advanced ceramics using 3-point and 4-point bending. A specific requirement of the standard is that the materials are macroscopically homogeneous, fine-grain ceramics. Nonetheless, the notch configurations provided by the standard are easily adapted to other materials such as carbons.

A distinctive feature of the chevron-notch configuration is the unusual form of the function describing the geometric correction factor, $Y(\alpha)$, which is shown in Figure 8.2a. Whereas the $Y(\alpha)$ function for the straight-through notch increases monotonically, the $Y^*(\alpha)$ function shows a singularity at a_0, but drops rapidly with increasing α, reaching a minimum at Y^*_{min}. For $\alpha > \alpha_1$, $Y(\alpha)$ and $Y^*(\alpha)$ are the same as the crack configurations become the same.

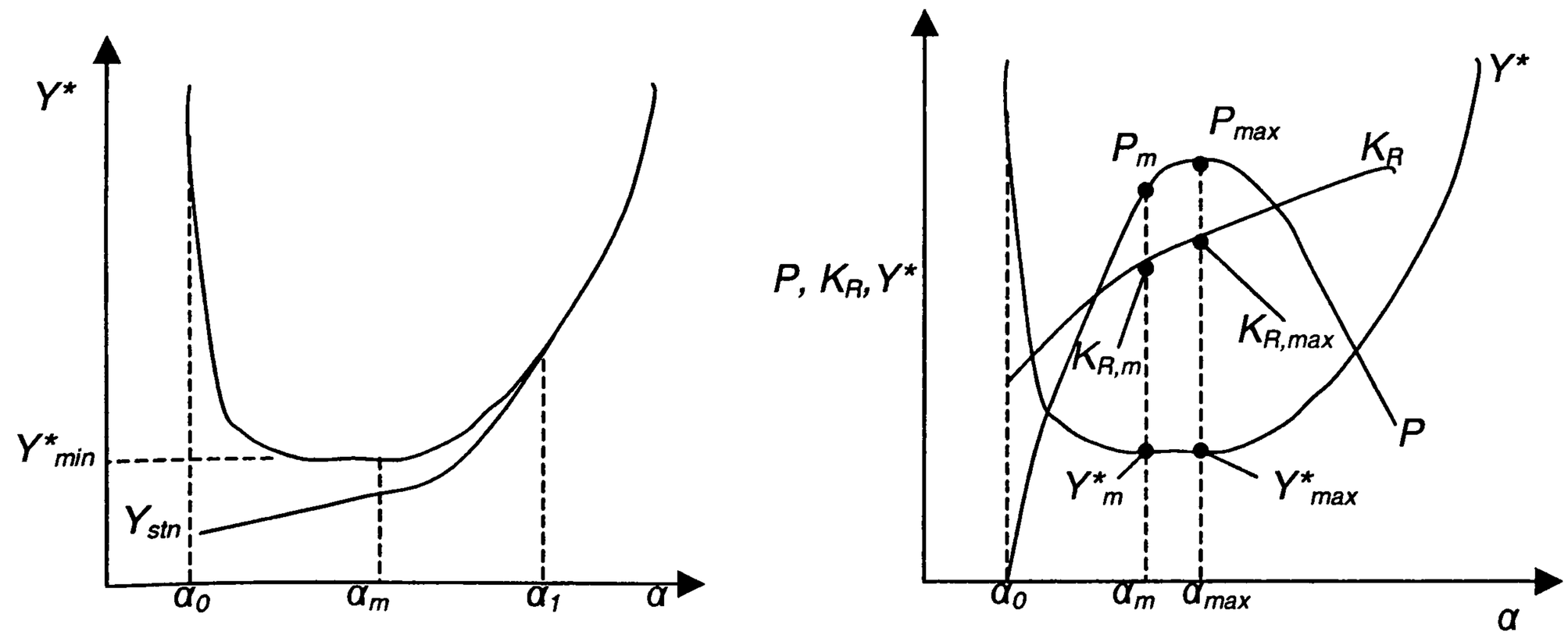

Figure 8.2. (a) Shape factors for chevron notch (Y^*) and straight-through notch (Y_{stn}) (Sakai & Bradt, 1993) (b) Variation in load (P), stress intensity factor (K_R), and, geometric factor (Y^*) for a material with rising R-curve behaviour (Munz, 1983).

One of the main aspects about ASTM C1421-1999 is that it only aims to determine fracture toughness. Fracture toughness (K_{IVB}) in the chevron-notched specimens is obtained using the expression:

$$K_{Ivb} = Y^*_{\min}\left[\frac{P_{\max}S}{BW^{3/2}}\right] \qquad [8.1]$$

It is seen from Equation [8.1] that K_{IVB} is obtained using Y^*_{min} and P_{max}. It is also seen from Figure 8.2b, that Y^* passes through the minimum Y^*_{min} as the load passes through the maximum, P_{max}. The standard therefore assumes that at P_{max}, the inferred crack length is equal to α_{min}, so that, $Y^*=Y^*_{min}$. For this assumption to be valid, the material must have a flat R-curve, that is, no crack growth resistance, and therefore, α_{min} and P_{max} coincide, making the substitution of Y^*_{min} in the fracture toughness calculation valid.

However, many ceramics show rising R-curve behaviour so that the crack length at P_{max} is no longer independent of the material. Therefore, α_{min} and P_{max} do not necessarily coincide because, stable crack growth occurs prior to the maximum load being reached. Since it is difficult to measure the extent of stable crack growth that occurs prior to P_{max} in the chevron-notch specimen given the inaccessibility of the notch tip, the value of Y^* to be used in Equation [8.1] becomes uncertain. This is because Y^*_{min} and P_{max} no longer coincide.

Munz (1983) has shown graphically the implications of using the chevron-notch configuration in a material with rising R-curve behaviour. As shown in Figure 8.2b, the rising R-curve behaviour results in a K_{IVB} value that lies between K_{IRm} and K_{IRmax}. Munz (1983) explains that the amount of crack extension prior to P_{max} in a rising R-curve material also depends on the specimen size and notch geometry, generally increasing with the specimen size. Therefore, K_{IVB} calculated in the standard way should increase with increasing specimen size.

Because P_{max} is reached after considerable stable crack growth has occurred, K_{IVB} must lie in the upper region of the K_R-curve, and should increase for larger specimens where the extent of stable crack growth before P_{max} is greater. For example, K_{IC} tends to be larger in double-cantilever beam specimens compared to straight-through bend specimens because the total amount of crack extension at P_{max} is greater in the former specimen type.

8.2.1.1. The Straight-through Crack Assumption (STCA)

To adapt the chevron-notch configuration to *R*-curve measurement, it is necessary to develop a numerical solution for the trapezoidal shaped notch that is generated once the crack propagates from the tip of the chevron notch. Figure 8.3 shows the notch geometry and its relevant dimensions.

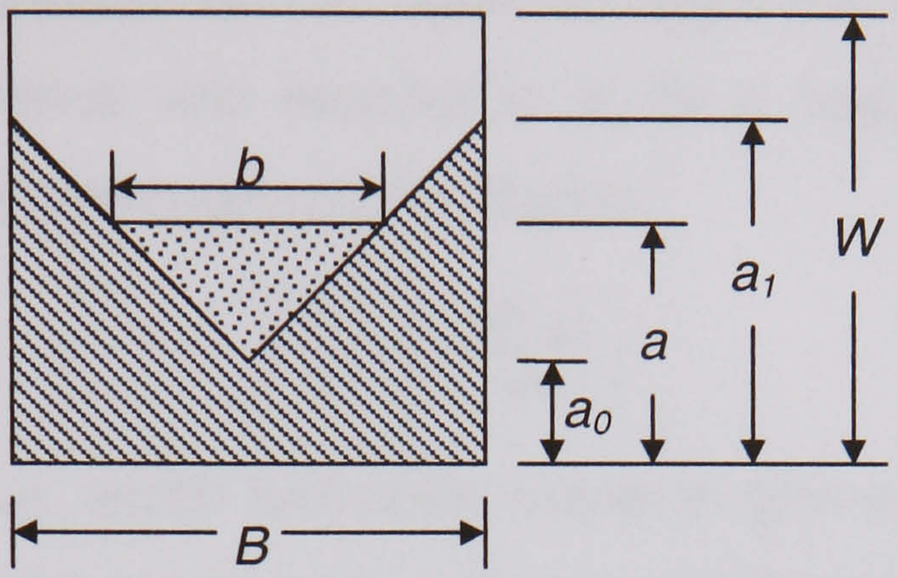

Figure 8.3. Section through the chevron-notch geometry and relevant dimensions.

The shaded area defines the trapezoidal-notched that is produced when the crack propagates. Solving numerically for this notch geometry is complex. This is simplified by the use of the "straight-through crack assumption" (STCA). This assumption treats the trapezoidal crack front as if it were a straight-through notch, making use of a geometric factor to simplify the problem. Munz et al (1980) present the derivation of the STCA as follows:

The length of the crack front, *b*, at crack extension, *a*, is given geometrically by:

$$b = B\left[\frac{(a - a_0)}{(a_1 - a_0)}\right] = B\left[\frac{(\alpha - \alpha_0)}{(\alpha_1 - \alpha_0)}\right] \qquad [8.2]$$

The energy needed to drive the crack a distance *da* is given by:

$$dG = dU = \left(\frac{P^2}{2W}\right)\left(\frac{dC_{tr}}{d\alpha}\right)da \qquad [8.3]$$

The increment in crack surface area is given by *dA=b.da*, so the work done in extending the crack is *dW*, which can be obtained from the relation:

$$dW = G_{IC}dA = \left(\frac{K_{IC}^2}{E'}\right)dA \qquad [8.4]$$

Since *dU=dW* during crack extension, K_{IC} can be obtained by equating expressions [8.3] and [8.4] such that,

$$K_{IC} = P\left[\frac{(dC_{tr}/d\alpha)E'}{2Wb}\right]^{1/2} = \frac{P}{BW^{1/2}}\left[\frac{1}{2}\frac{dC'_{tr}}{d\alpha}\frac{(\alpha_1 - \alpha_0)}{(\alpha - \alpha_0)}\right]^{1/2} \qquad [8.5]$$

By definition, the dimensionless compliance is given by $C'_{tr}=E'BC_{tr}$, and, the stress intensity factor coefficient for the chevron-notch is given by Y^* where,

$$Y^* = \left[\frac{1}{2}\frac{dC'_{tr}}{d\alpha}\frac{(\alpha_1-\alpha_0)}{(\alpha-\alpha_0)}\right]^{1/2} \qquad [8.6]$$

Munz et al (1980) state the calculation of K_{IC} using Equation [8.6] requires the compliance function C_{tr} to be known. Given the complexity of determining such a function, a first approximation can be obtained under the **assumption** that the derivative of the compliance with respect to α, for a trapezoidal notch is the same as that for a straight-through notch. That is,

$$\left(\frac{dC'_{tr}}{d\alpha}\right)=\left(\frac{dC_{stn}}{d\alpha}\right) \qquad [8.7]$$

This constitutes the STCA, which has been shown to give a good approximation for chevron-notched bend specimens under four-point bending (Munz et al, 1980). Since the stress-intensity factor for a straight-through crack in four-point bending is given by,

$$K_{IC} = \frac{PS}{BW^{1/2}}[Y(\alpha)] \qquad (0\leq\alpha\leq1) \qquad [8.8]$$

and, the derivative of the compliance for a straight-through crack is given by:

$$\frac{dC'}{d\alpha} = 2Y^2 \qquad [8.9]$$

The stress-intensity factor for the trapezoidal notch can be expressed as:

$$K_{IC} = \frac{PS}{BW^{3/2}}[Y(\alpha)]\left[\frac{(\alpha_1-\alpha_0)}{(\alpha-\alpha_0)}\right]^{1/2} \qquad [8.10]$$

where,

$$Y^* = [Y(\alpha)]\left[\frac{(\alpha_1-\alpha_0)}{(\alpha-\alpha_0)}\right]^{1/2} \qquad [8.11]$$

Here, $Y(\alpha)$ is the geometric factor for the straight-through configuration. The Y^* function for the short-bar, chevron-notched specimen determined by the STCA is found to show excellent agreement with that determined by experimental compliance measurements (Munz et al, 1980). Therefore, the STCA provides a good approximation of the shape function for the trapezoidal notch. It can be appreciated however, that the physical reality of this assumption is poor during the initial stage of crack growth when the trapezoidal shape approximates the chevron notch and the width of the trapezoidal crack front is very small.

The problem with determining precisely the fracture toughness using chevron-notched specimens in materials that show crack growth resistance was explained earlier. One way to circumvent this problem, is to be able to detect precisely the load at which crack initiation occurs, and, obtain a measure of the crack length at the maximum load, P_{max}. However, this is difficult to achieve with the chevron-notch configuration. If the intermediate crack length at P_{max} could be determined rather than assuming $P = P_{max}$ at $\alpha = \alpha_m$, then the value of K_{IC} determined by the STCA should correspond to a value on the K_R-curve. The reason being, that at P_{max} the crack might be, fully or partially bridged, depending on the specimen thickness.

8.2.2. Deriving the K_R-curve using ACPD and Compliance Methods

To derive the K_R-curve using chevron-notch specimens and compare this with the K_R-curve obtained by the straight-through notch configuration, 3-point bend specimens of dimensions 6.95 x 6.95 x 80mm were machined. There was also an interest to compare the K_R-curves obtained using the two different crack length measurement techniques, i.e. the ACPD and compliance methods. Due to the limited usefulness of the chevron-notch configuration, which became apparent following this investigation, only Gilsocarbon graphite was tested.

8.2.2.1. Geometry of the Chevron-notch

In selecting a notch geometry for the tests, Configuration B (ASTM C1421-99) was adopted as this is the only geometry specified for three-point bending. The geometry of the other chevron-notch configurations is specified for 4-point bending. The nominal dimensions of the notch are shown in Figure 8.4.

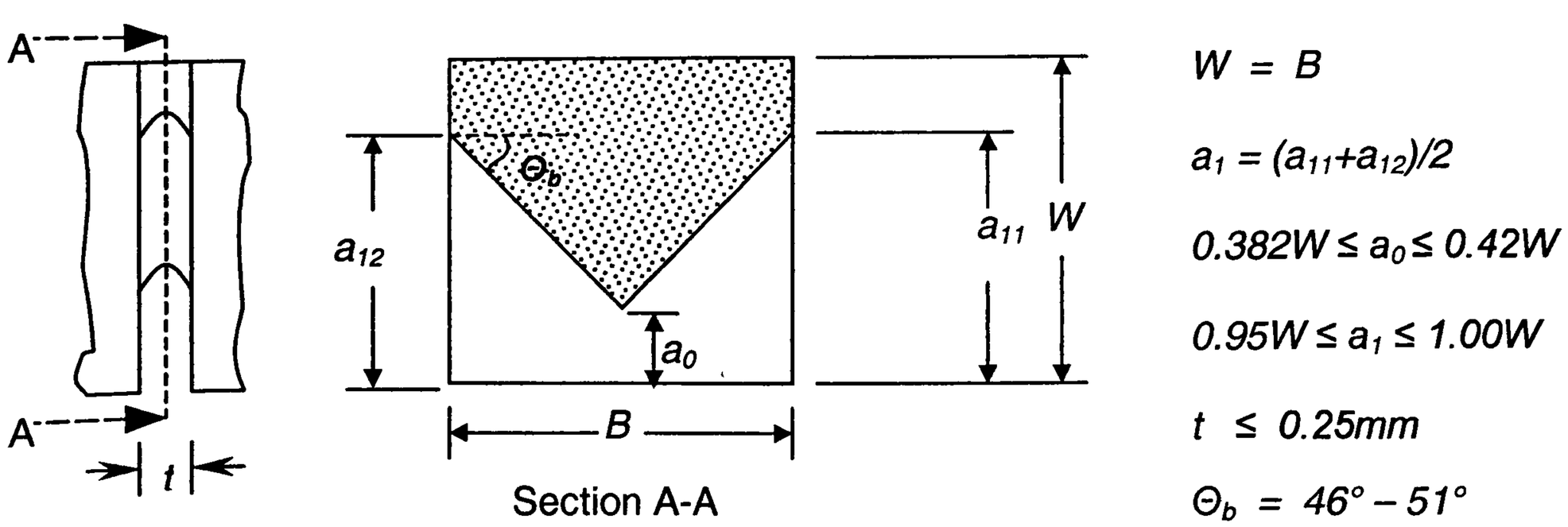

Figure 8.4. Chevron-notch geometry according to Configuration B: ASTM C1421-99.

8.2.2.2. Cutting the Chevron-notch

To cut the chevron notch in the bend specimens, a jig was designed to fit onto the worktable of a machine normally used for cutting straight-through notches (see Figure 8.5). The design of the jig is shown in Figure 8.5, which shows the angle at which the specimen is clamped. For configuration B, the base angle (θ_b) of the notch can vary between 46-51°. This determines the angle at which the notch is cut into the specimen as Figure 8.5 shows. This angle also dictates the depth of cut, which is limited by the maximum cutting depth of the wheel.

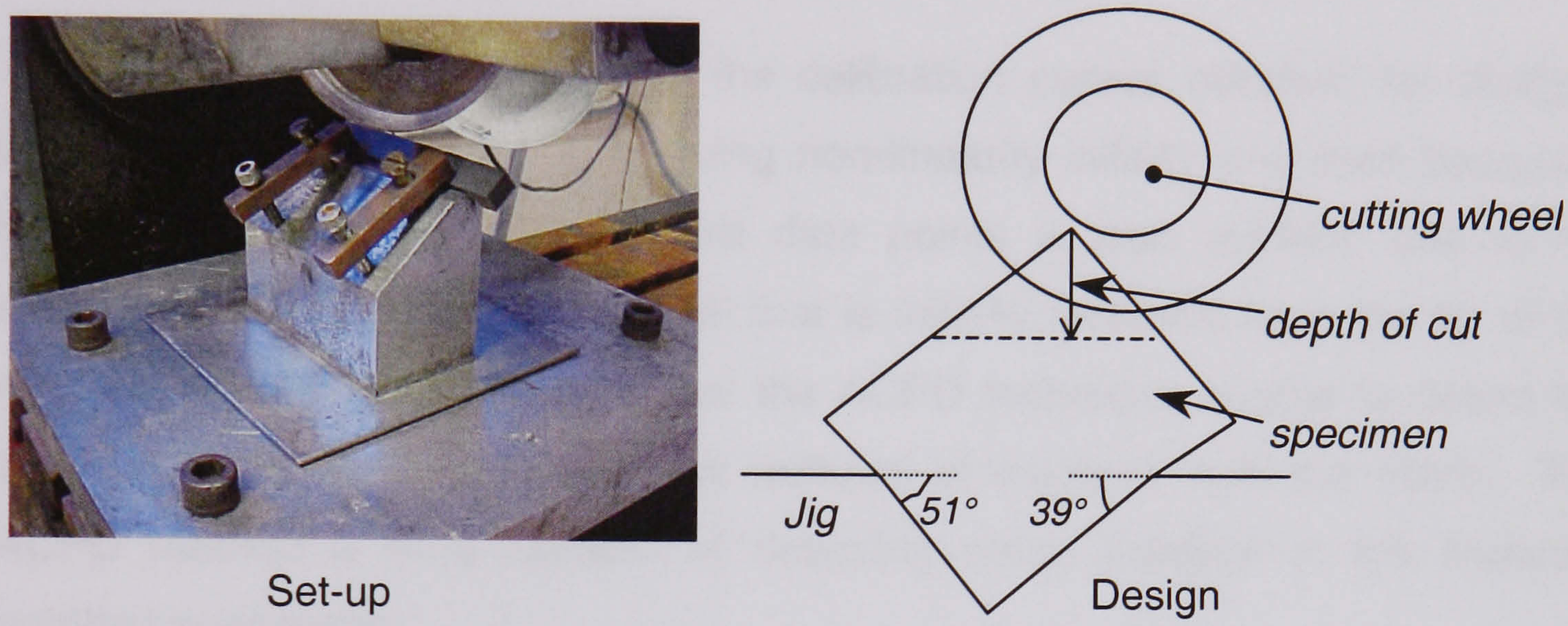

Figure 8.5. Set-up and design of the chevron-notch cutting jig.

Since the thin blade that is used to cut the notch has a short cutting depth, one is limited in the thickness of specimen that can be notched with this blade. Since the maximum cutting depth was about 5mm, the maximum thickness and width of the bend specimens that could be notched according to Configuration B was < 8mm. With the 39° cutting angle of the jig, the 6.95mm width and thickness of the specimens results in notch dimensions of a_o = 2.65mm, and, a_1=W=6.95mm. This falls within the limit of the standard for configuration B, i.e. $0.382 \leq a_0 \leq 0.420$ and $0.95 \leq a_1 \leq 1.00$.

The accuracy of the cutting angle is critical in ensuring that the final notch dimensions conform to the tolerances specified by the standard. When this angle satisfies the standard specifications, the appropriate notch dimensions in terms of a_o, a_1, etc are simply achieved by controlling the depth of cut made into the specimen that is held in the jig. To ensure that the notch width did not exceed the 0.25mm thickness specified by the standard a cutting wheel of 0.2mm nominal thickness was used.

8.2.2.3. Calibrating the Chevron-notch Specimens by the ACPD Method

Calibrating the chevron-notched specimen is somewhat more complicated given that the tip is internally displaced. Because there is uncertainty regarding the exact depth at which the cutting wheel begins to section the notch tip, one has to rely on the nominal notch dimensions for calibration. The cutting wheel is moved down a distance equivalent to the nominal a_o-value, i.e. 2.65mm for the 6.95mm thick sample. The first voltage reading is taken at this point. The calibration curve for the chevron-notched specimen is shown in Figure 8.6.

This curve differs markedly from the calibration curves obtained for straight-through notched specimens, showing non-linearity initially and then becoming linear. Some scatter in the initial data points is also evident, due to the extremely small amount of material that is initially removed from the tip of the notch. Nonetheless, it is seen that the ACPD technique is able to detect the small changes associated with the removal of material from the notch. The ACPD method is thus capable of detecting crack initiation in the chevron-notched specimens.

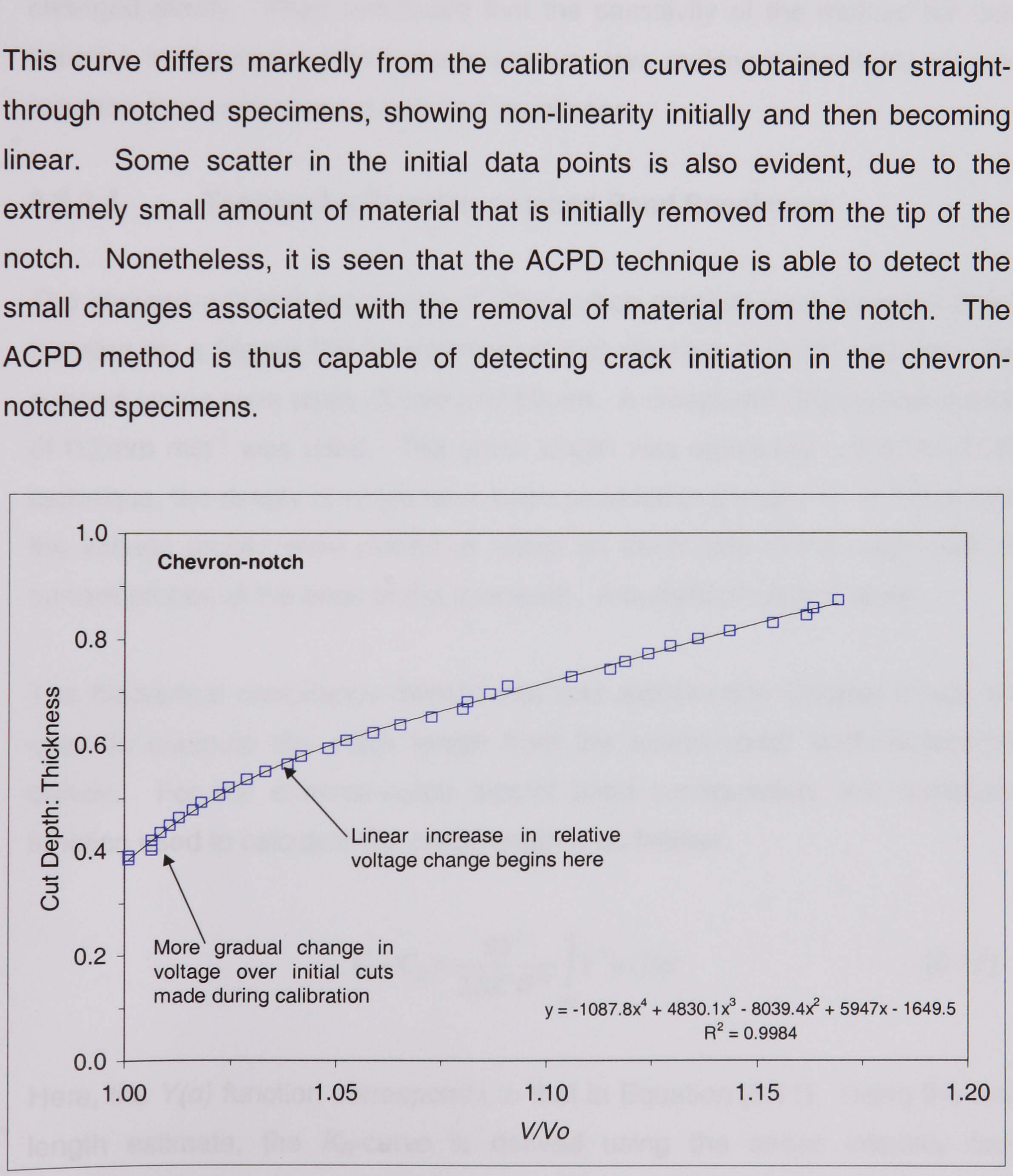

Figure 8.6. Potential drop, calibration curve for the chevron-notched bend specimen: ; W=B=6.95mm; Gilsocarbon graphite.

It is interesting to note that Troczynski & Nicholson (1985, 1986) modelled the potential drop across the chevron-notched bend specimen. They compared mathematical models with experimental data (obtained by saw-cutting graphite specimens) and found good correlation for a combination of voltage and current probe positions, as well as, varying chevron notch geometry. They noted that the potential drop across the graphite calibration specimens (W=B=10mm) ranged only between 0.1 – 2.0 mV for current input probes on the top surface of the specimens and a supply current of 200 mA. They also noted that over the initial stage of crack extension (~5% of the available ligament) the potential changed slowly. They concluded that the sensitivity of the method for crack initiation in chevron-notched specimens was low, making it unsuitable for crack initiation studies in chevron-notched specimens.

8.2.2.4. Testing the Chevron-notched Bend Specimens

The chevron-notched specimens of Gilsocarbon graphite were tested in 3-point bending on a Mayes SM-50 mechanical test machine of 50kN capacity. Two support spans were used, 30mm and 60mm. A crosshead displacement speed of 0.2mm min^{-1} was used. The crack length was measured using the ACPD technique, the details of which have been provided in Chapter 5. In these tests, the voltage probes were placed at 10mm on either side of the notch, with the current probes at the ends of the specimen. A current of 1A was used.

The theoretical compliance method that was explained in Chapter 6 was also used to compute the crack length from the experimental load-displacement curves. For the chevron-notch 3-point bend configuration, the compliance function used to calculate the crack length is as follows:

$$C - C_0 = \frac{9S^2}{2BE'W^2} \int_{\alpha_0}^{\alpha} Y^2(\alpha) d\alpha \qquad [8.12]$$

Here, the $Y(\alpha)$ function corresponds to that in Equation [8.11]. Using the crack length estimate, the K_R-curve is derived using the stress intensity factor equation based on the STCA (Equation 8.10), which was derived, in Section 8.2.1.

8.2.2.5. Comparison of the K_R-curves

The load-displacement curves obtained for the chevron notch, bend specimens using a load span of 30mm and 60mm are shown in Figure 8.7. The use of a shorter load span, results in a maximum load that is almost twice that attained at double the span. Clearly, both curves indicate that stable crack growth was achieved with a smooth transition in the load past the maximum point. The fall in load past the maximum appears to be more gradual in these specimens, than that observed in the straight through notched specimens. This points to greater crack stability, due to the increasing width of the ligament in the chevron-notched specimen. The voltage drop across the specimens starts to change at some point before the maximum load, giving a clear indication of the crack initiation event. This is useful for determining the start of the *R*-curve.

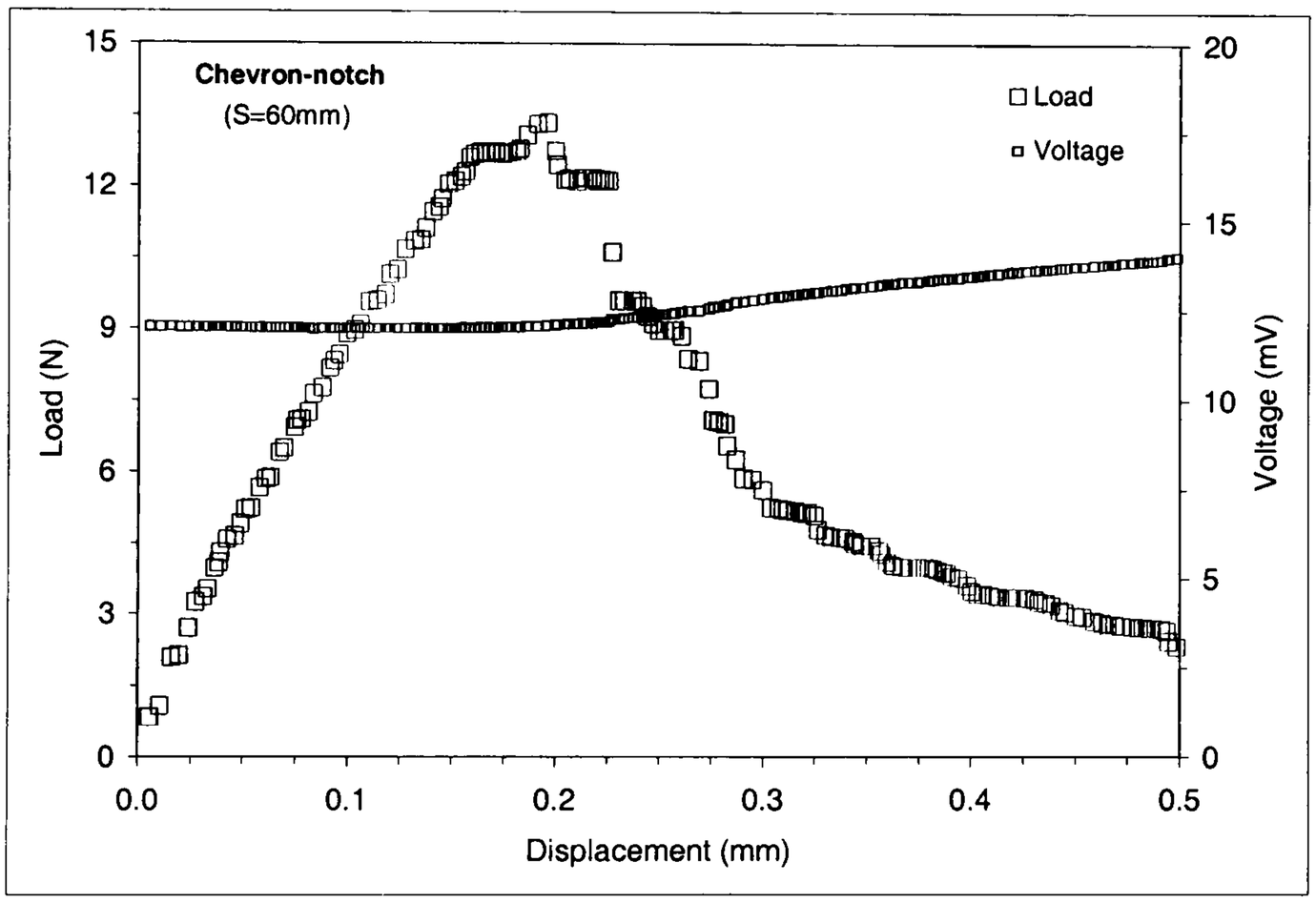

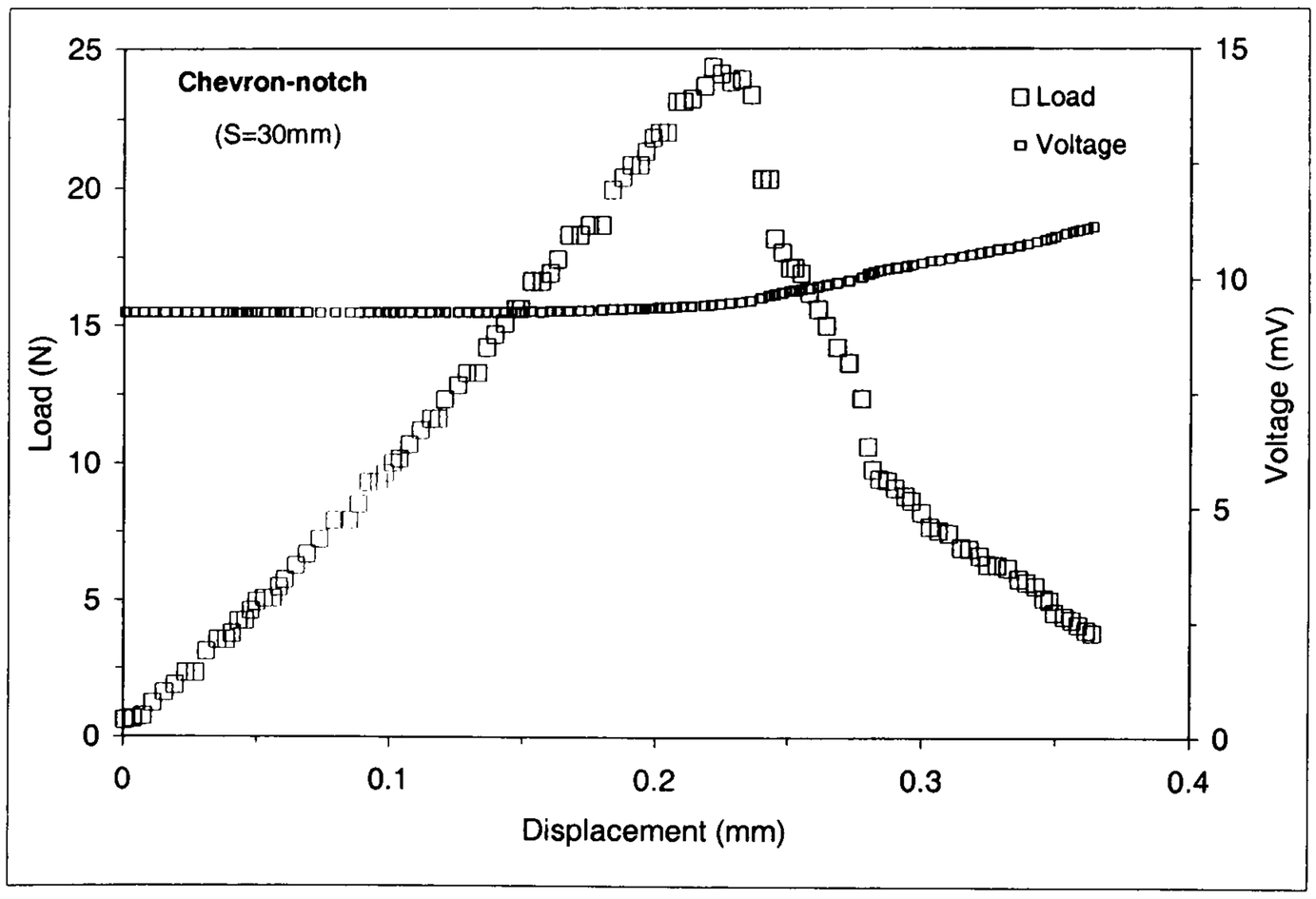

Figure 8.7. Load-displacement curves of chevron-notched 3-point bend specimens for two different load spans, 30mm and 60mm: Gilsocarbon graphite.

The *R*-curves for the specimens tested using load spans of 60mm and 30mm are shown in Figures 8.8 and 8.9 respectively. Both the compliance-derived and the ACPD-derived K_R-curves are shown. Full scale and reduced scale graphs are presented in each figure to highlight the very high, initial K_R-value that is obtained using the compliance method. The K_{IVB} values shown on the graphs were calculated using the load just prior to the initial voltage, not P_{max}, since the PD method allows one to detect the load at which crack initiation occurs. This K_{IVB} value forms the first point on the ACPD-derived K_R-curve. It is seen that a gap then occurs between K_{IVB} and the next point on the ACPD-derived *R*-curve. This is due to bridging which shorts the ACPD signal.

Electrical shorting due to crack face bridging renders the ACPD method unable to detect the initial stage of stable crack growth. It is only until the voltage changes sufficiently at P_{max} that the ACPD method starts to detect crack increments because the crack has grown sufficiently by this point. The reason why the ACPD method detects crack initiation is the absence of a bridged zone.

The inability to detect crack growth prior to P_{max}, because of crack face bridging, causes an anomaly in the ACPD-derived K_R-curve. The result is a sharp rise in stress intensity factor from the initiation point following which the K_R-curve takes the form consistent with that for the chevron-notch. Interestingly, the K_R-value of 1.88 $MPam^{1/2}$ (see Figure 8.8b) calculated using the STCA and the load at P_{max} appears to correspond with a value higher up on the K_R-curve for Gilsocarbon graphite. It was shown in the Chapter 6 (Figure 6.7) that the plateau K_R-value for Gilsocarbon bend specimens was about 1.8-2.0 $MPam^{1/2}$.

The compliance-derived K_R-curve starts at an unrealistically high K_R-value, clearly because of the strong influence of the shape function, which has a singularity for α-values close to α_0. Perhaps the compliance method is over sensitive, interpreting the initial non-linearity in the load-displacement curve to be due to crack growth. So the very steep, initial part of the compliance-derived K_R-curve may be superficial. Nonetheless, it seems likely that the ACPD-derived K_R-curve would also show this steep initial region if the ACPD method was unaffected by bridging effects.

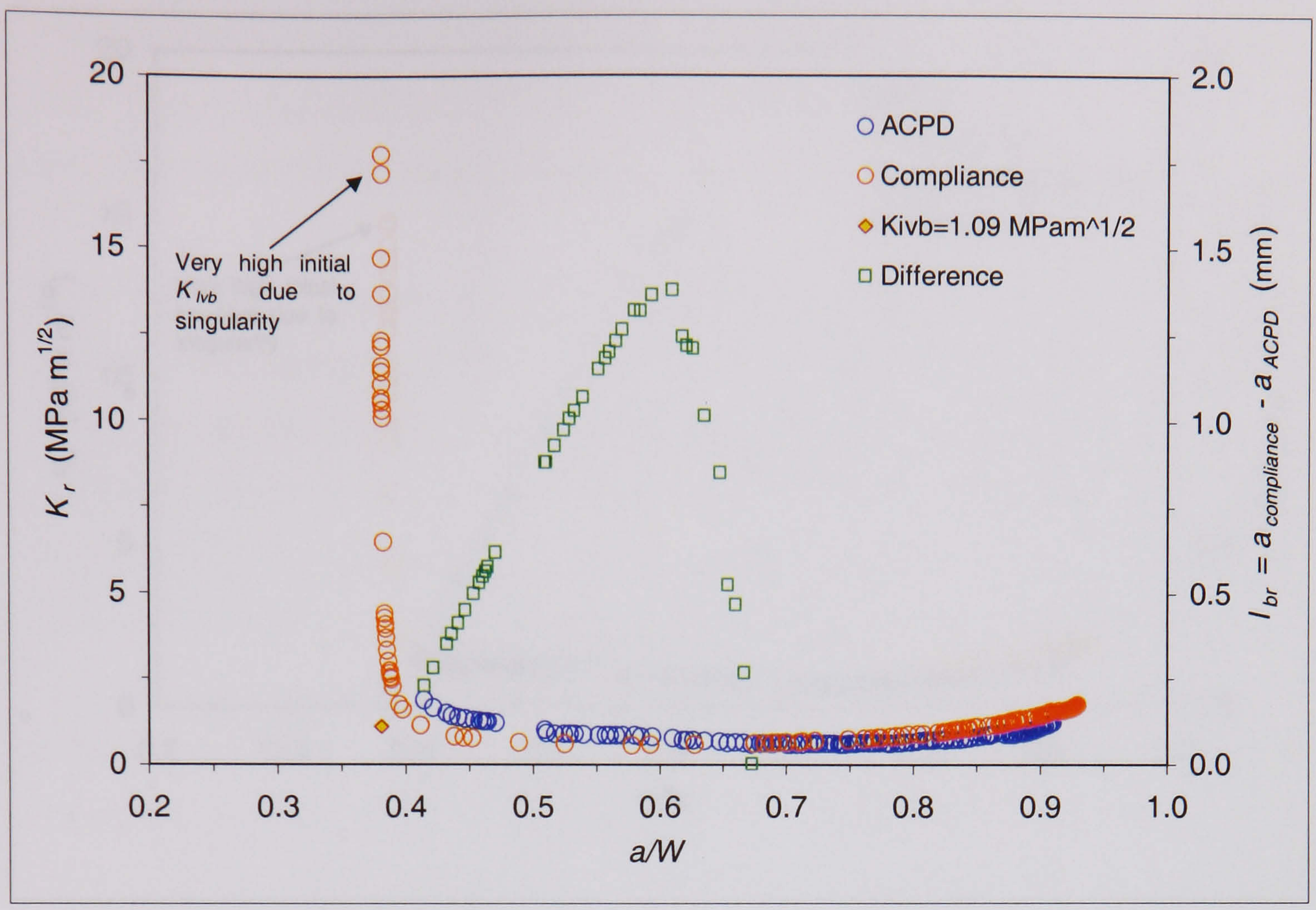

a

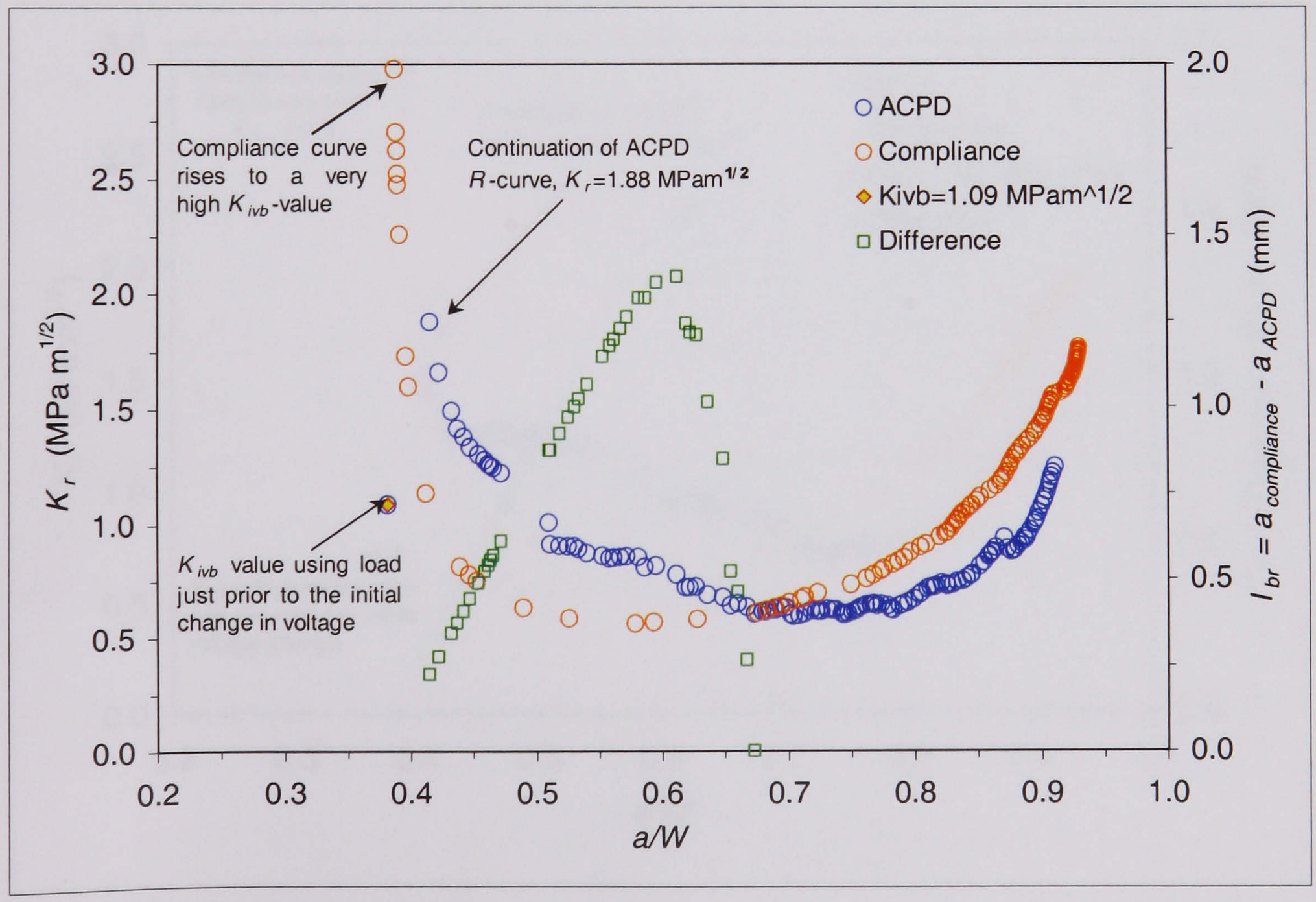

b

Figure 8.8. *R*-curve for chevron-notched 3-point bend specimen: (a) full-scale; (b) enlarged scale; Gilsocarbon graphite, *S*=60mm.

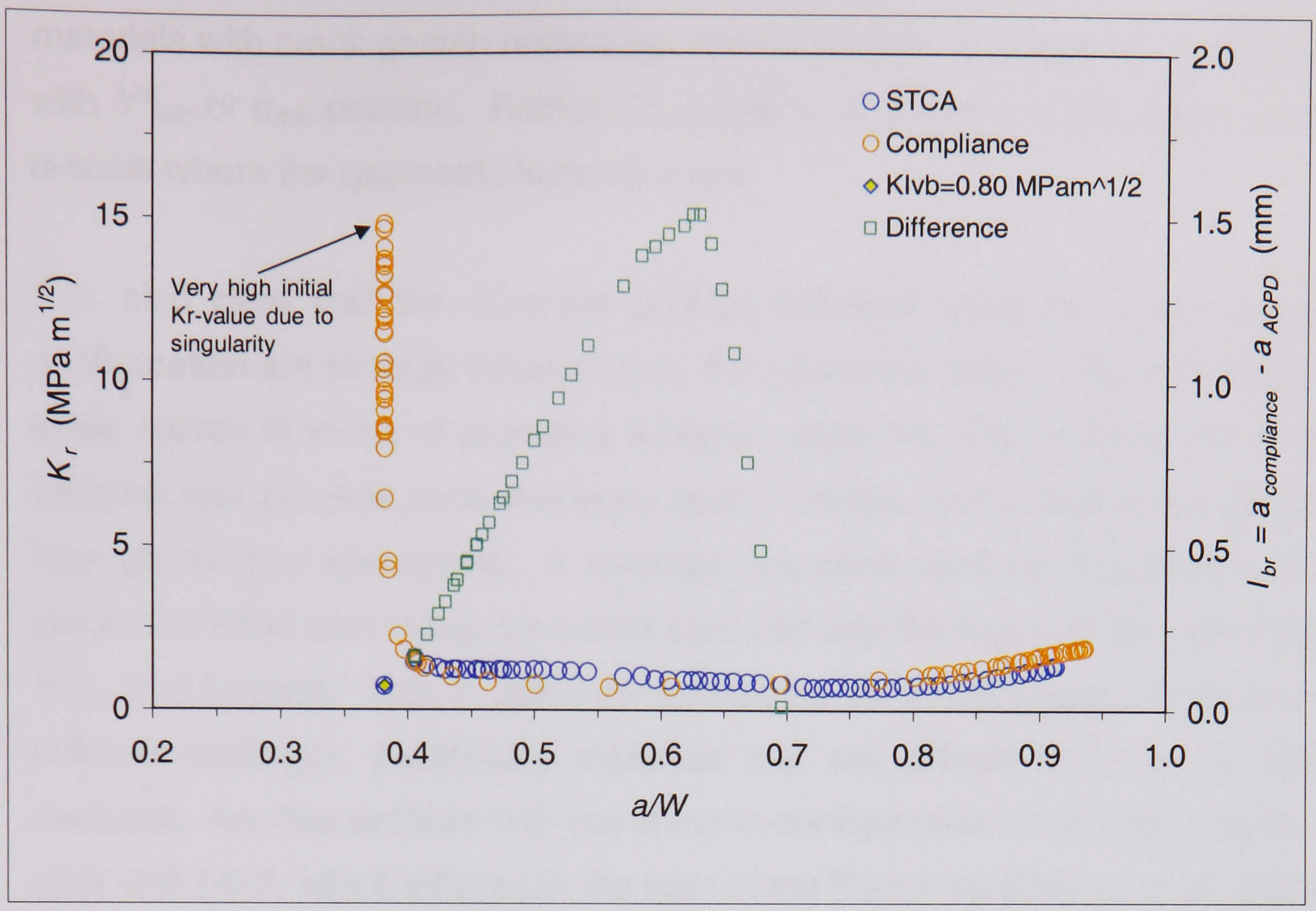

a

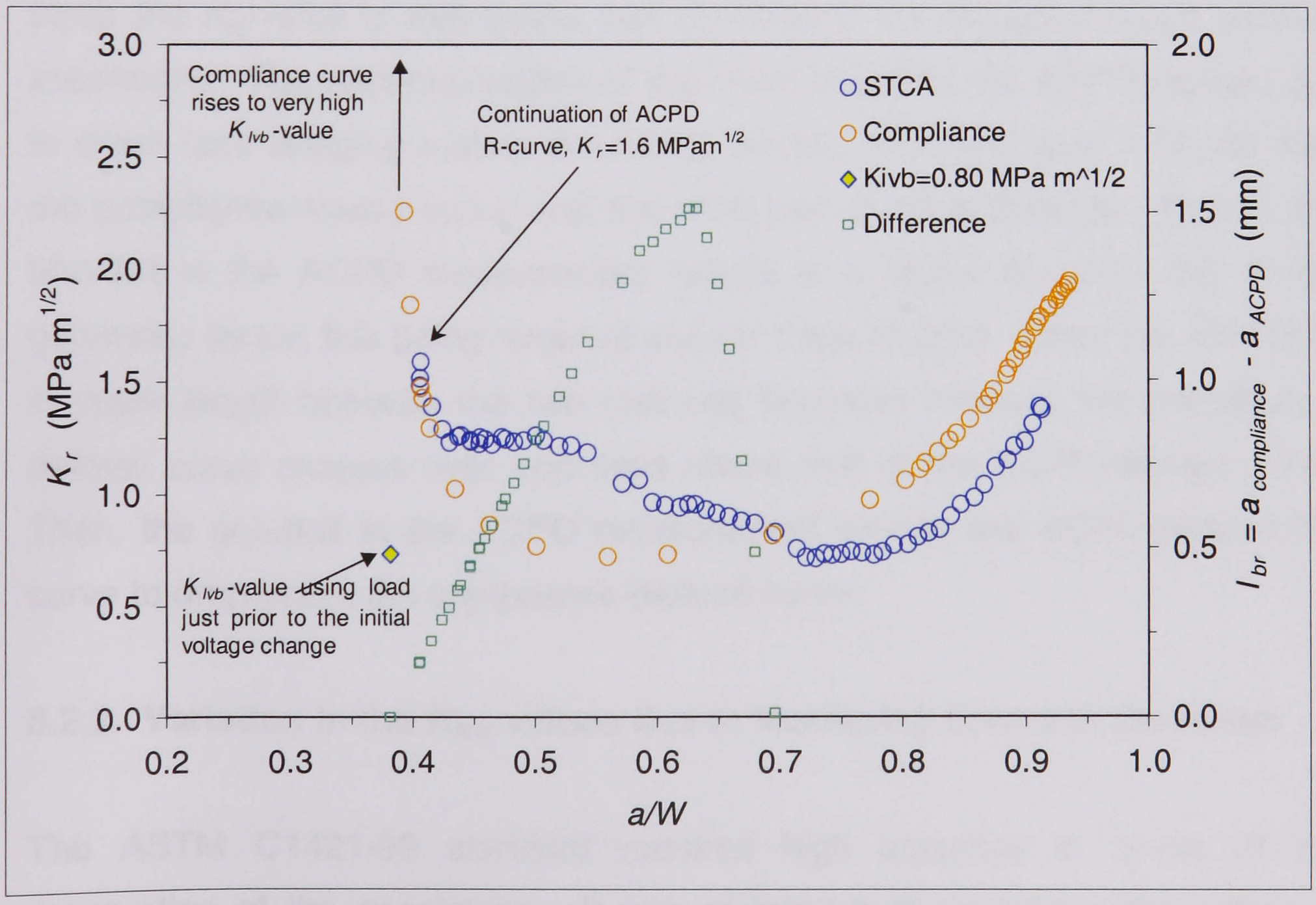

b

Figure 8.9. *R*-curve for chevron-notched 3-point bend specimen: (a) full-scale; (b) reduced scale; Gilsocarbon graphite, *S*=30mm.

More importantly, the compliance and ACPD-based K_R-curves show that, in materials with crack growth resistance, the maximum load does not correspond with Y^*_{min} or α_{min} position. Rather, P_{max} occurs at α-values much higher up the α-scale where the geometric factor is larger.

It is also clear that the K_R-curve profiles obtained using the chevron-notch configuration are strongly influenced by the geometric factor. The usefulness of these curves in terms of providing a better insight into the development of the bridging and process zone therefore seems limited, unlike that of the straight through notched specimens. A common approach used by researchers is to ignore the initial part of this curve and consider only the region of the curve from Y^*_{min} and beyond. This is useful for comparing the crack growth resistance of different materials, particularly materials that are difficult to notch by other methods. Another problem with the chevron-configuration is the steep rise in Y^* after $\alpha \approx 0.7$-0.8, which influences the form of the K_R-curves (Mazzei et al, 2000).

In this instance, the portion of the curve from Y^*_{min} onward has little significance since the K_R-value is well below that obtained in the straight-through notched specimens. The underestimation of the crack length by the ACPD method due to crack face bridging makes the ACPD-derived K_R-curve appear higher than the compliance–based curve over the initial part of the a/W-range. That is, the shortfall in the ACPD measurement results in a higher K_R-value due to the geometric factor, this being larger at shorter crack lengths. Once the difference in crack length between the two methods becomes minimal, the compliance-derived curve crosses over and rises above that of the ACPD-derived curve. Then, the shortfall in the ACPD measurement causes the ACPD-derived K_R-curve to drop below the compliance-derived curve.

8.2.3. Variation in the K_{IVB}-values due to Machining Errors in the Notch

The ASTM C1421-99 standard requires high accuracy in terms of the preparation of the specimens. It was of interest to determine the extent to which differences between the specified tolerances and actual tolerances of test specimens affected the K_{IVB} values obtained by the standard.

To examine this aspect, fracture toughness values were calculated according to the standard, using the nominal notch dimensions, and, the actual notch dimensions measured by SEM. For a 3-point bend specimen chevron-notched to configuration B, the standard lists the following tolerances (see Figure 8.4):

$\underline{B = W = 6.35 \pm 0.13\text{mm}}$:	a_0	$= 2.54 \pm 0.07$ mm	(with no over-cut)
	a_{11}, a_{12}	$= 0.95\text{-}1.00\ W$	(with no over-cut)
	t	≤ 0.25 mm	(notch width)

Clearly, the specified tolerances are quite tight. For the test specimens used in this study, the tolerances on the notch dimensions may be given as follows:

$\underline{B=W=6.95\text{mm}}$:	$0.382 \leq a_0/W \leq 0.420$,	i.e. $2.65 \leq a_0 \leq 2.92$mm
	$0.95 \leq a_1/W \leq 1.00$,	i.e. $6.60 \leq a_1 \leq 6.95$mm

A value of $a_1 = 1.00W$ was selected for the notch because, the value of K_{IVB} is said to be more or less independent of the α_0 value. However, a dependence of the K_{IVB}-value on a_1 has been found (Munz et al, 1980).

The jig used for chevron-notching the bend specimens was designed with a 39° tilt angle (see Figures 8.4 and 8.5). This is the minimum angle at which the specified notch dimensions can be obtained when $a_1=1.00W$. If a higher angle is used then, a_1 must be made $<1.00W$ to ensure that a_0 is within the allowable range. Given that $W=B=6.95$mm for the test specimens, the required notch dimensions become $a_0=2.65$mm, $a_1=1.00$W, and, $\theta_b=51°$.

It was however found by measuring fractured specimens in the SEM that, the accuracy of the notch varied. Usually, the notch tip fell slightly short of the specified value, i.e. $a_0=2.65$mm. The a_1-value also varied, being undercut or over-cut, and, sometimes being exactly equal to W. There was also evidence of misalignment of the cut in some specimens. It was difficult to obtain both a_0 and a_1 dimensions that fell within specification, implying that accurate machining is needed. Typical machining errors are shown in the SEM images in Figure 8.10. The SEM micrographs show that it was difficult to obtain the a_0-dimension precisely to specification with the experimental techniques used in this study. An a_1-dimension equivalent to ~$1.00W$ was more easily obtained.

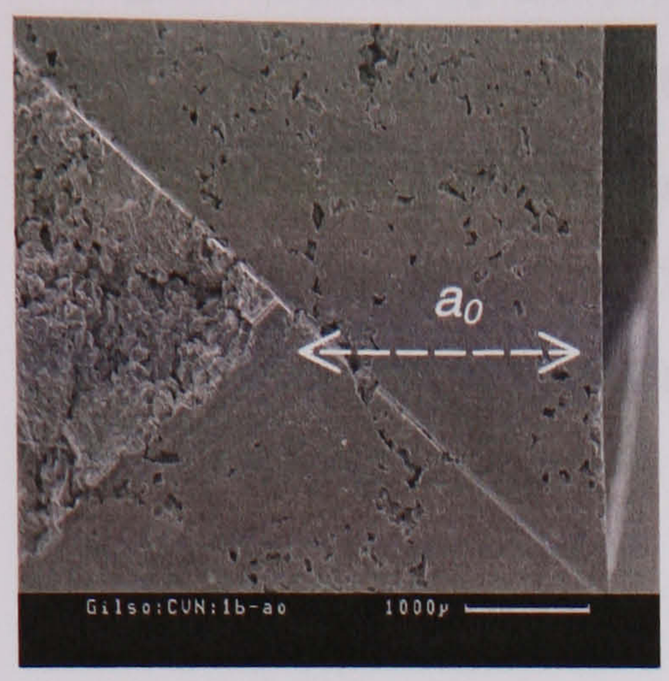

Specimen 1b

a_0, nominal = 2.65mm

a_0, measured = 2.62mm

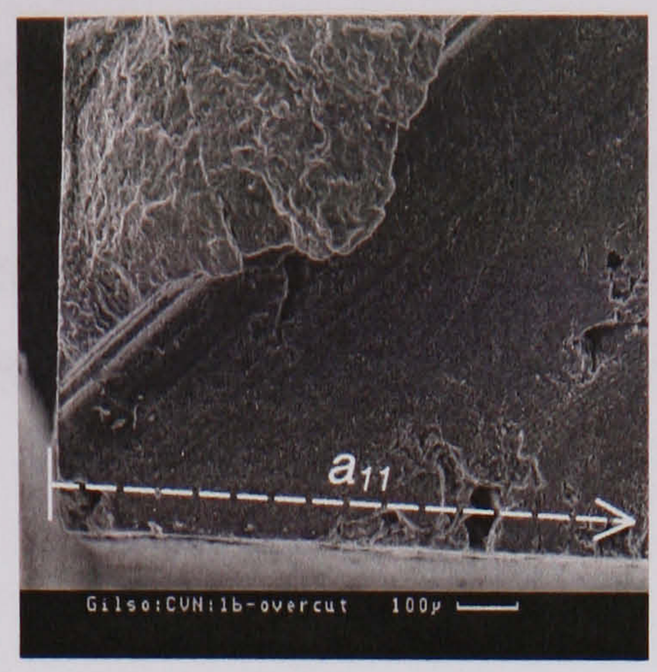

Specimen 1b

a_1, nominal = 1.00W

a_1, measured = overcut

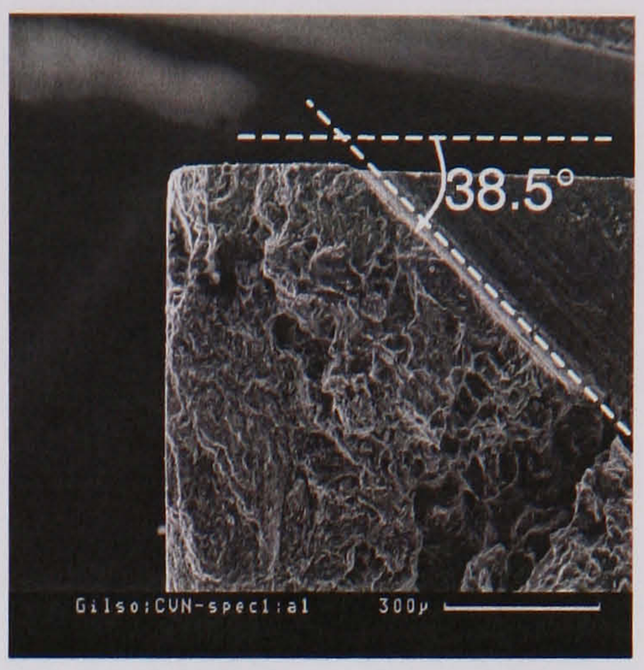

Specimen 1a

a_1, nominal = 1.00W

a_1, measured = 0.95W

Specimen 3a

a_0, nominal = 2.65mm

a_0, measured = 2.57mm

Specimen 3a

a_1, nominal = 1.00W

a_1, measured = 1.00W

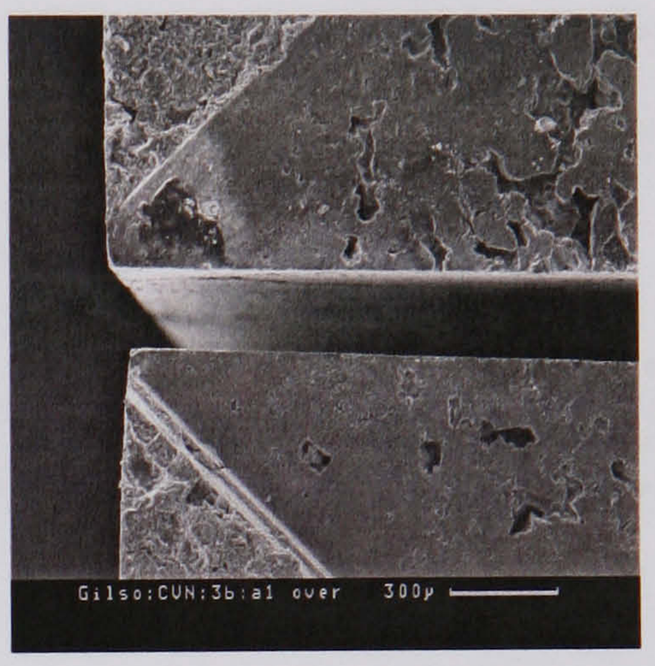

Specimen 3b

a_1, nominal = 1.00W

a_1, measured = 1.00W

Specimen 4

a_0, nominal = 2.65mm

a_0, measured = 2.78mm

Specimen 4

a_{11}, nominal = 1.00W

a_{11}, measured = 0.95W

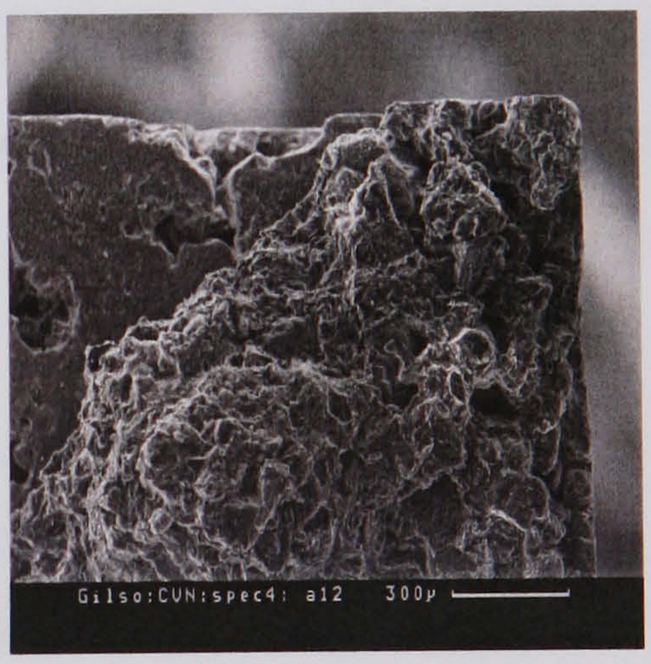

Specimen 4

a_{12}, nominal = 1.00W

a_{12}, measured = 0.94W

Figure 8.10. Typical errors in the dimensions of the chevron notched specimens.

However, the actual notch dimensions were close to specification, as the cutting angle of 38.5° (~39°) in Specimen (1a) indicates. It was not certain to what extent these errors physically influenced the calculated K_{IVB}-values. To answer this question, the K_{IVB} values were calculated using the nominal notch dimensions, and, the dimensions measured by SEM. To calculate K_{IVB}, the standard equation was used, P_{max} being the maximum load obtained in the test:

$$K_{Ivb} = \frac{P_{\max}(S_o - S_i)}{BW^{\frac{3}{2}}}\left[Y^*_{\min}\right] \qquad [8.12]$$

For 3-point bending, S_i=0.

The background to this expression was given earlier in this section. As explained, Y^* varies in a somewhat parabolic manner, the Y^*_{min}-value being used to calculate the fracture toughness on the premise that the material has a flat R-curve. For Configuration B, Y^*_{min} is given by the analytical expression:

$$Y^*_{\min} = Y^*_{\min}(a_0/W, a_1/W) = \left[\frac{0.7601 - 3.6364(a_0/W) + 3.1165(a_1/W) - 1.2782(a_1/W)^2 + 0.3609(a_1/W)^3}{1.0000 - 3.1199(a_0/W) + 3.0558(a_0/W)^2 - 1.0390(a_0/W)^3 + 0.0608(a_0/W)^4}\right]$$

$$(0.382 \le a_o/W \le 0.420) \text{ and } (0.950 \le a_1/W \le 1.00) \qquad [8.13]$$

Table 8.1 compares the K_{IVB}-values obtained using the nominal and measured notch dimensions. The discrepancy between the two measurements is seen to be small in most cases, highlighting the accuracy of the notching technique. Clearly, the discrepancy in the notch dimensions does not cause significant variation in the measured K_{IVB} values, considering the fact that some error must originate from other sources, e.g. operator error.

Table 8.1. K_{IVB}-values obtained using nominal and measured dimensions.

Specimen No.	Nominal Dimensions			Measured Dimensions		
	a_0	a_1	K_{IVB}	a_0	a_1	K_{IVB}
1a*	2.65	6.95	**1.20**	2.30	6.60	**1.03**
1b*	2.65	6.95	**0.93**	2.62	6.95	**0.93**
3a*	2.65	6.95	**0.75**	2.57	6.95	**0.73**
4*	2.65	6.95	**1.20**	2.78	6.58	**1.18**
7	2.65	6.95	**1.20**	2.60	6.90	**1.19**

* see SEM micrographs in Figure 8.10

8.3. SUMMARY

An investigation of the influence of notch tip acuity on the K_R-curve and G_R-curve profiles showed that blunt-notched specimens accumulate a higher degree of stored elastic energy prior to crack initiation. By contrast, specimens with a sharpened notch root fracture in a more stable manner. The G_R-curve for the blunt-notched specimen displays an instantaneous release of stored elastic energy following crack initiation, resulting in a higher K_{IC}-value. The energy required to propagate a crack from a blunt notch therefore exceeds that required with a more acute notch tip radius or a pre-crack.

Important aspects of using the chevron-notched configuration in 3-point bend specimens were highlighted. Particular attention was placed on the shortcomings involved in using the chevron notch for *R*-curve measurement. The methods used to cut the chevron notch and calibrate chevron-notched specimens for ACPD measurements were also explained. The K_R-curve profiles obtained by the ACPD, and, compliance methods was found to be strongly influenced by the shape function, Y^*. It was also shown that the singularity in the Y^* function at low α-values produces an anomaly in the K_R-curve profile such that an abnormally high K_R-value is initially obtained. The ACPD method was useful for detecting crack initiation from the chevron notch.

The K_{IVB}-values calculated according to ASTM C1421-99 were significantly lower than the K_{IC} values obtained in straight through notched specimens. The initial K_R-value obtained using the STCA and crack increment based on the ACPD calibration produced values that were compatible with plateau K_R-values obtained in straight-through notched specimens. Crack face bridging was evident from the discrepancy between the ACPD-derived and compliance-derived K_R-curves. It was also found that errors in the notch dimensions had little influence on the K_{IVB}-values calculated using the standard method. However, these values were generally lower than the K_{IC}-values obtained using straight through notched bend and compact tension specimens.

CHAPTER 9

R-CURVE BEHAVIOUR IN OXIDISED NUCLEAR GRAPHITE

The attractiveness of gas as a coolant in graphite moderated reactors is its ability to provide excellent heat transfer at relatively low operating pressures. However, reactor efficiency depends strongly on the operating temperature, this being limited by the corrosiveness of the coolant gas. Oxidation prevention is thus important to reactor safety and moderator service life. Significant research has been done on the mechanisms that control oxidation and the influence of oxidation on the strength of nuclear graphite. However, little study has been made regarding the change in crack growth resistance of nuclear graphite, which occurs with oxidation. One of the aims of this study was therefore, to evaluate the effect of oxidation on the *R*-curve behaviour of nuclear graphite. The following sections outline the research undertaken in this respect.

9.1. Selection of Oxidation Conditions

In selecting appropriate conditions for oxidising fracture specimens, the main criterion was to achieve uniform oxidation. Uniform oxidation is attainable at lower temperatures where gas reactivity is low and unreacted gas can reach the interior of the material, thus establishing a constant, gas concentration profile. That is the oxidation rate is controlled by the reactivity of the solid. With non-uniform oxidation, a concentration gradient of the reactant gas prevails. Although gas-graphite reactivity mainly depends on the temperature, the reactivity between different grades of nuclear graphite also varies with the starting materials used in their fabrication. Structural differences such as the accessible pore volume also influence the reactivity.

An idea of the practically useful oxidation conditions can be obtained by considering the conditions used by other researchers, as shown in Table 9.1. Of the range of conditions listed in Table 9.1, the simplest involves oxidation in air around 500°C. However, the C-O_2 reaction can be highly exothermic, making it difficult to control, whilst the endothermic nature of the C-CO_2 reaction makes it a more attractive option for oxidising test specimens. According to Nightingale (1962) nuclear graphite begins to oxidise at ~300 °C in air, but in CO_2 oxidation begins at ~600°C.

Table 9.1. Typical oxidation conditions used by various researchers.

Study	Nuclear Graphites	Oxidant	Temp (°C)	Reference
1	Great Lakes H440, Poco AXF-5Q, Stackpole 2020	Air (open tube) CO_2-He (flowing) H_2O in He (flowing)	500 - 750 800 - 1000 900 - 1000	Thrower et al (1982)
2	Grades 580, 3499, KK-16	Dry flowing air	500	Zhao et al (1981)
3	Grades H451, PGX & IG-11	Air 2% O_2-N_2 2% H_2O in He	400 - 650 600 - 900 550 - 900	Eto & Growcock (1983)
4	PGA, IM1-24	CO_2 – 5% CO	900	Pickup, McEnaney & Cooke (1986)
5	Grades 580, 3499, KK-16, 4029	Dry flowing air	500	Wood et al (1980)

Thermodynamic data for the C-CO_2 reaction indicates that the reaction begins above 625°C. Uniform oxidation conditions are said to prevail to temperatures as high as 900°C. However, the positive enthalpy of the C-CO_2 reaction means that a positive equilibrium constant is achieved only at high temperatures exceeding ~800°C (Nightingale, 1962). Therefore, although CO_2 appeared to be the most suitable oxidant, the oxidation rate at temperatures below 800°C was not certain. A series of preliminary oxidation tests were necessary therefore, to establish how quickly samples could be oxidised at temperatures below 800°C since lower temperatures favour uniform oxidation conditions.

A mixture of CO_2-N_2 (1:1) gas was used at a flow-rate of 0.1litre/min for either gas. Gases were mixed before entry to the furnace. Preliminary oxidation tests were done on small samples that were supported on a platform made by stranding thin steel wire around an alumina boat cut out of an alumina tube. Specimens were oxidised in a tube furnace at 650, 700, 750, 800, and, 850 °C. Typical results from preliminary tests are given in Table 9.2, which shows that the oxidation rate between 650-800°C is slow. Longer oxidation times are needed for IG-110 graphite probably due to its finer pore size, with longer time being needed for UcarC graphite which has a low oxidation rate even at 850°C. The UcarC graphite is impregnated during manufacture, which must enhance its oxidation resistance.

Table 9.2. Typical oxidation rates for the graphites at different temperatures.

Graphite	Oxidation Rates (g hr^{-1})				
	650°C	700°C	750°C	800°C	850°C
Gilsocarbon	0.0014	0.0015	0.0022	0.0025	0.0059
IG110	-	0.0013	0.0015	0.0021	0.0028
UcarC	-	-	-	0.0010	0.0018

Given the slow oxidation rates and the added limitation that only three bend specimens could be oxidised simultaneously within the available furnace space, it was necessary to employ as high an oxidation temperature as possible using CO_2 as the oxidant. The impregnated UcarC graphite also posed a problem given its much lower oxidation rate compared to the other graphites. Although it was initially intended to oxidise specimens to high percentages, in excess of 10% mass loss, these problems limited the number of samples that could be oxidised uniformly within the available time. The highest oxidation level that was achieved within the available time was around 5% mass loss in the UcarC.

Prior to oxidation, the specimens were dried for 24 hours in an oven at 110°C. The specimens were weighed and stored in a dessicator before transferring to the oxidation furnace. The weight loss of the specimens was simply determined from the difference in the mass before and after oxidation. A typical oxidation cycle is shown in Figure 9.1. To reduce the oxidation period but still encourage uniform oxidation, test specimens were oxidised at 750°C to achieve ~1% mass loss and at 850°C to reach ~5% mass loss.

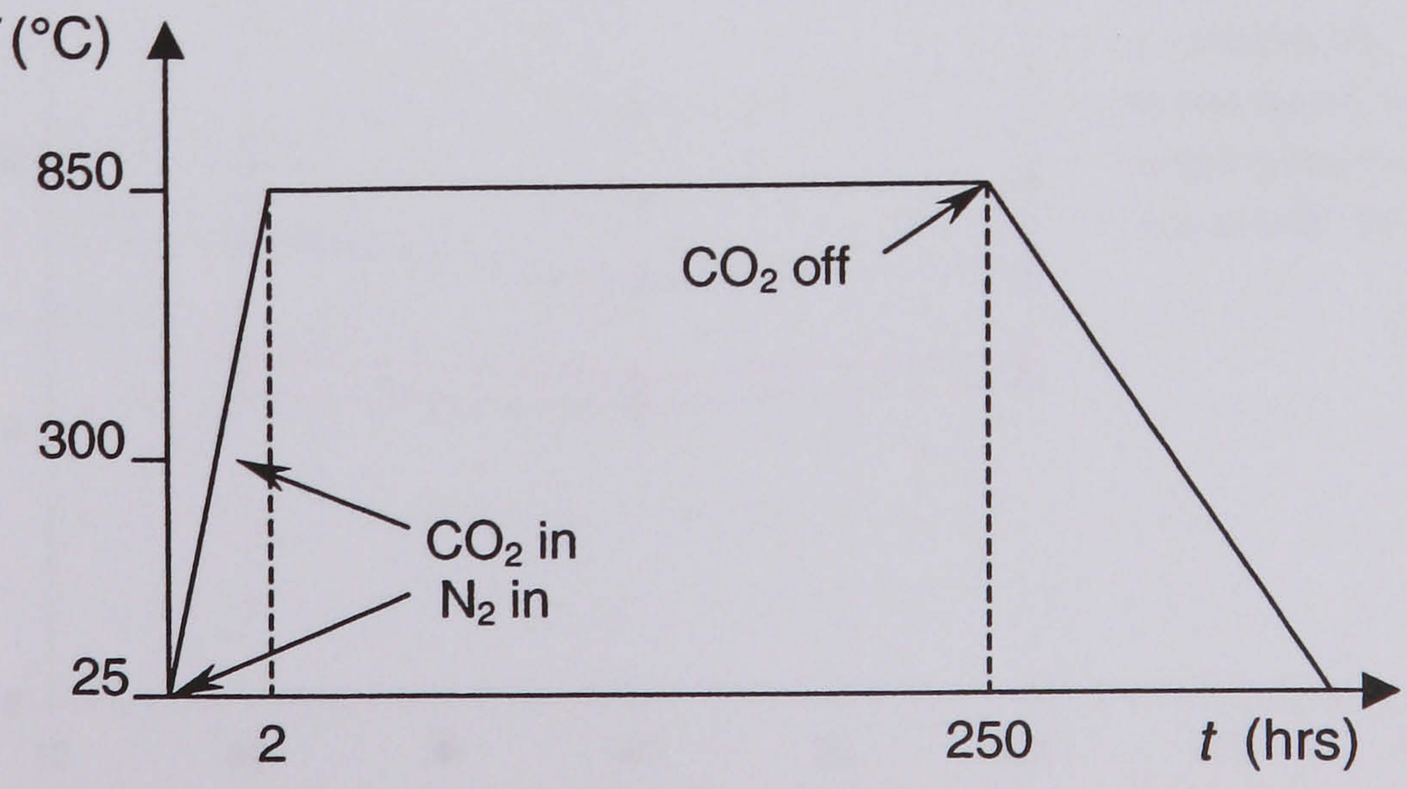

Figure 9.1. Typical cycle used for oxidising the bend specimens.

9.2. Using Electrical Resistivity to assess the Uniformity of Oxidation

Electrical resistivity measurements were performed on the oxidised bend specimens as a means of assessing the uniformity of oxidation. The idea was that oxidation could be regarded as uniform if the resistivity was constant along the length of the specimen. Measurements were made at gauge lengths of 20, 40, and, 60mm before and after oxidation. The results presented in Figure 9.2 show that a significant change in resistivity occurs even at a low oxidation level of 1%. The roughly constant resistivity along the length of the specimens suggests that the oxidation was uniform. Slightly higher values are obtained at the shortest gauge length (10mm), possibly due to perturbation between the probes. The through thickness uniformity of the oxidation was not assessed.

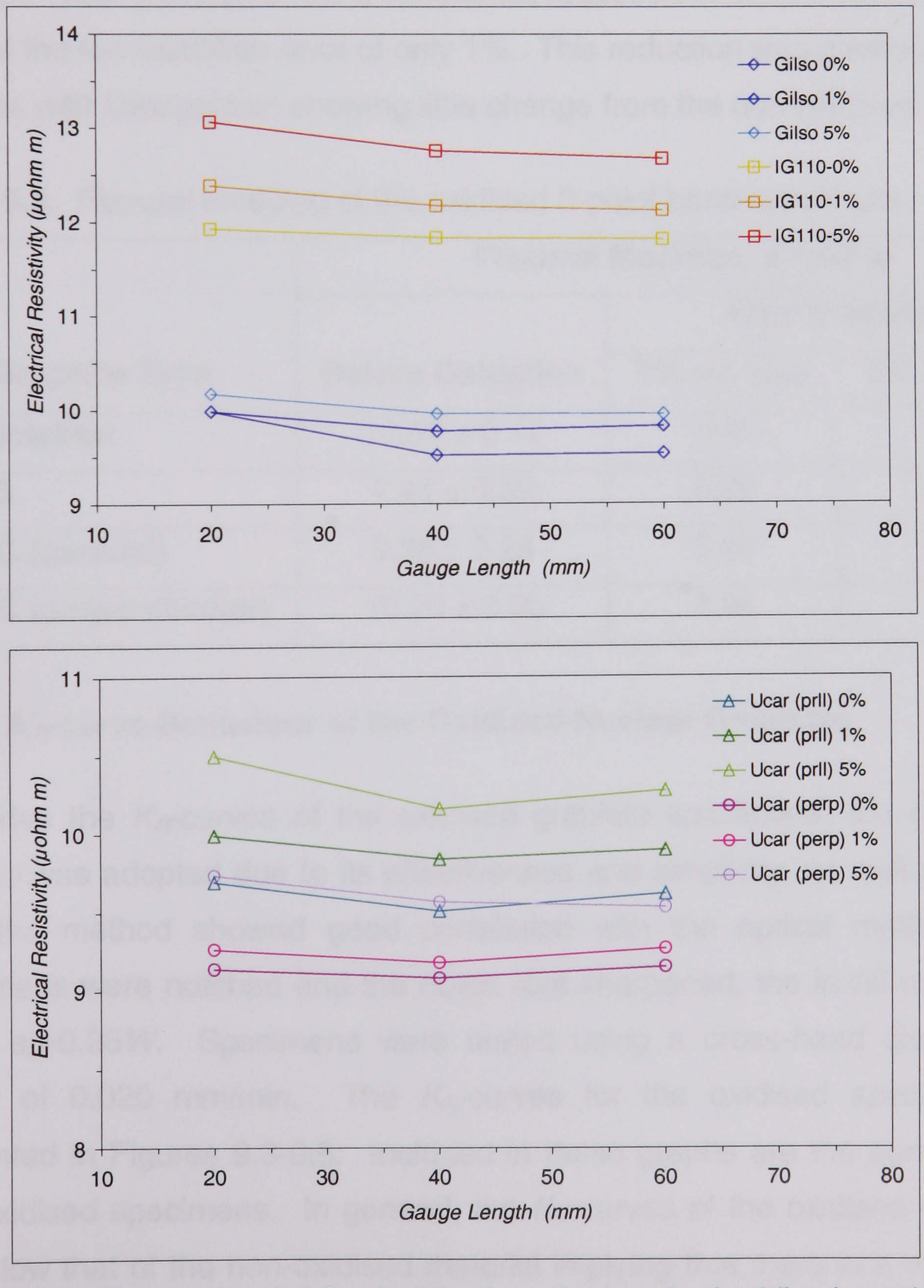

Figure 9.2. Electrical resistivity change along the length of oxidised specimens.

9.3. Elastic Modulus of Oxidised Graphites

The method used to measure the flexural modulus of the 3-point bend specimens was described in Section 4.5. The same methodology was applied for measuring the flexural modulus of the oxidised 3-point bend specimens. A span-width ratio of S/W=8 was used, with a cross-head displacement speed of 0.100mm/min. A magnified X-Y plot of the load-displacement (P-u) curve was used to obtain the slope of the tangent to the initial linear portion of the P-u curve that is used in calculating the flexural modulus. To preserve the oxidised specimens, they were tested up to a maximum load of about 20N only. Higher load was avoided to prevent damage to the oxidised specimens, given their fragility. Table 9.3 shows that a substantial reduction in flexural modulus occurs even at the low oxidation level of only 1%. This reduction was greatest in IG110 graphite with Gilsocarbon showing little change from the non-oxidised value.

Table 9.3. Flexural modulus of the oxidised 3-point bend specimens.

Graphite Type	Flexural Modulus, E_f (GPa)		
	Before Oxidation	After Oxidation	
		1% wt. loss	5% wt. loss
Gilsocarbon	10.52 ± 0.14	10.00	9.55
IG110	7.41 ± 0.09	5.88	3.10
UcarC (parallel)	9.35 ± 0.24	6.29	5.96
UcarC (perpendicular)	10.75 ± 0.30	8.44	7.10

9.4. K_R-curve Behaviour of the Oxidised Nuclear Graphites

To derive the K_R-curves of the oxidised graphite specimens, the compliance method was adopted due to its effectiveness and simplicity, as well as the fact that, the method showed good correlation with the optical method. Test specimens were notched and the notch root sharpened, the initial notch depth being a_0=0.35W. Specimens were tested using a cross-head displacement speed of 0.020 mm/min. The K_R-curves for the oxidised specimens are presented in Figures 9.3-9.5. Included in these graphs are the curves for the non-oxidised specimens. In general, the K_R-curves of the oxidised specimens fall below that of the non-oxidised material implying that there is a reduction in crack growth resistance with oxidation.

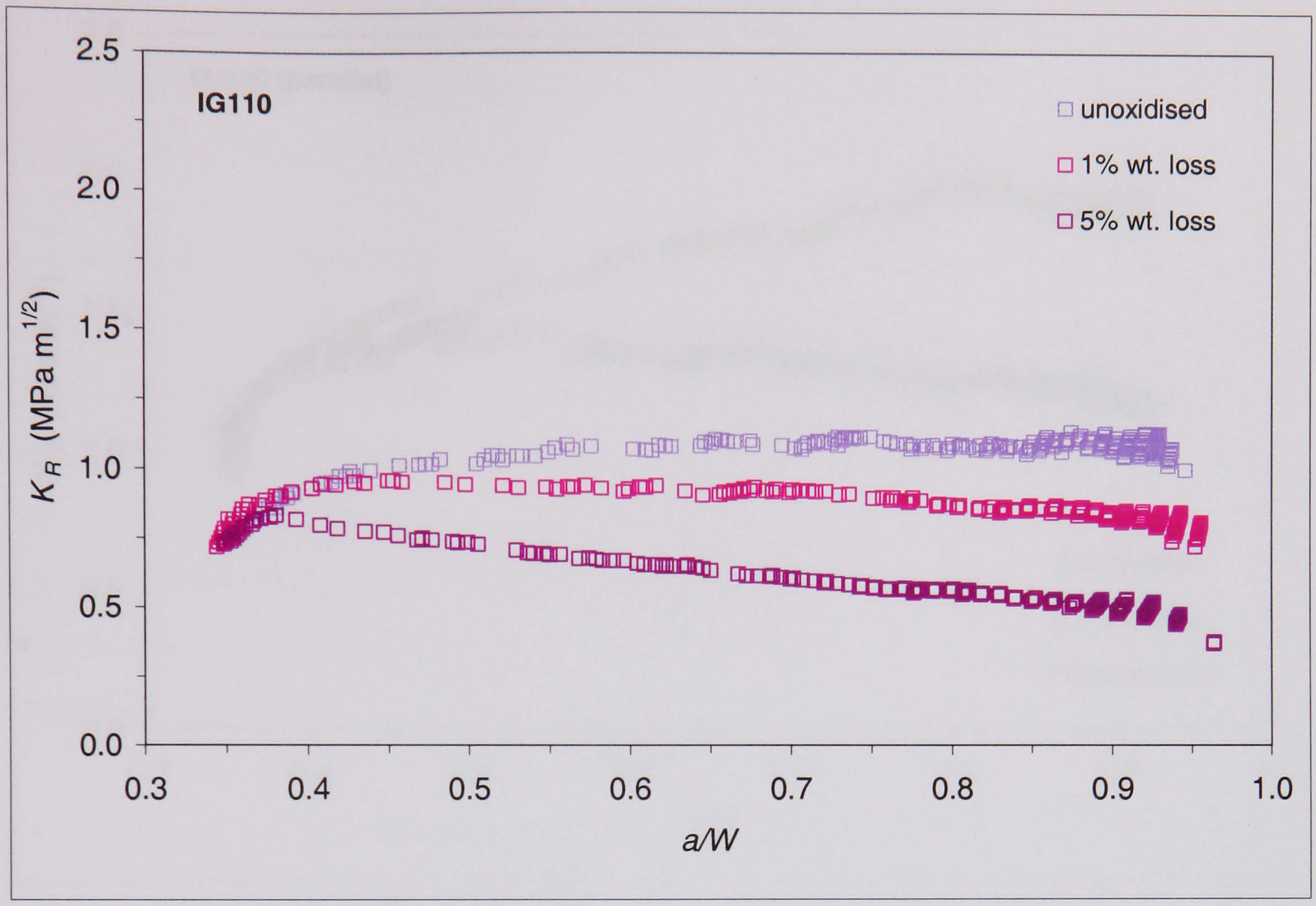

Figure 9.3. K_R-curves of oxidised and non-oxidised IG110 graphite in 3-point bending.

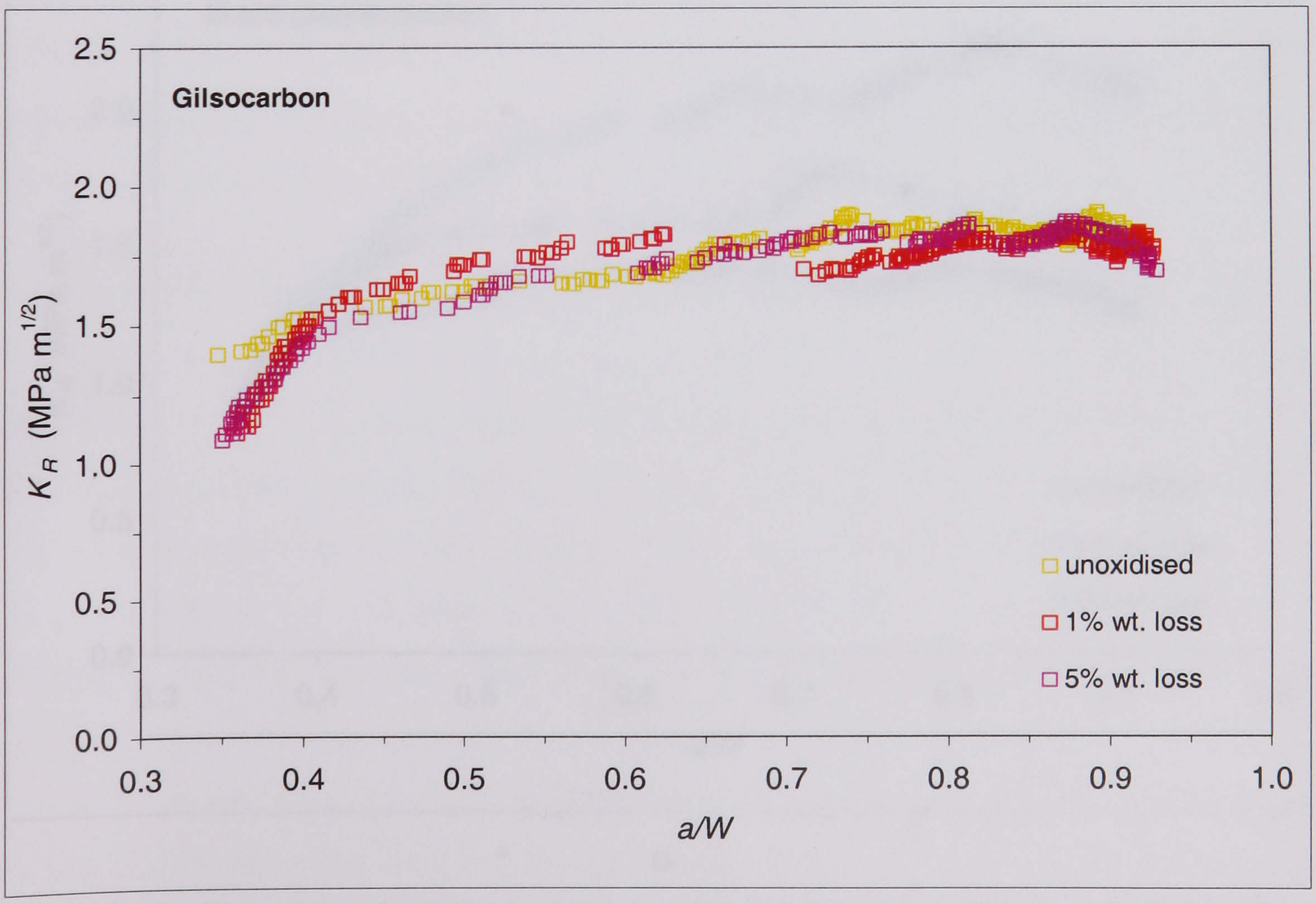

Figure 9.4. K_R-curves of oxidised and non-oxidised Gilsocarbon in 3-point bending.

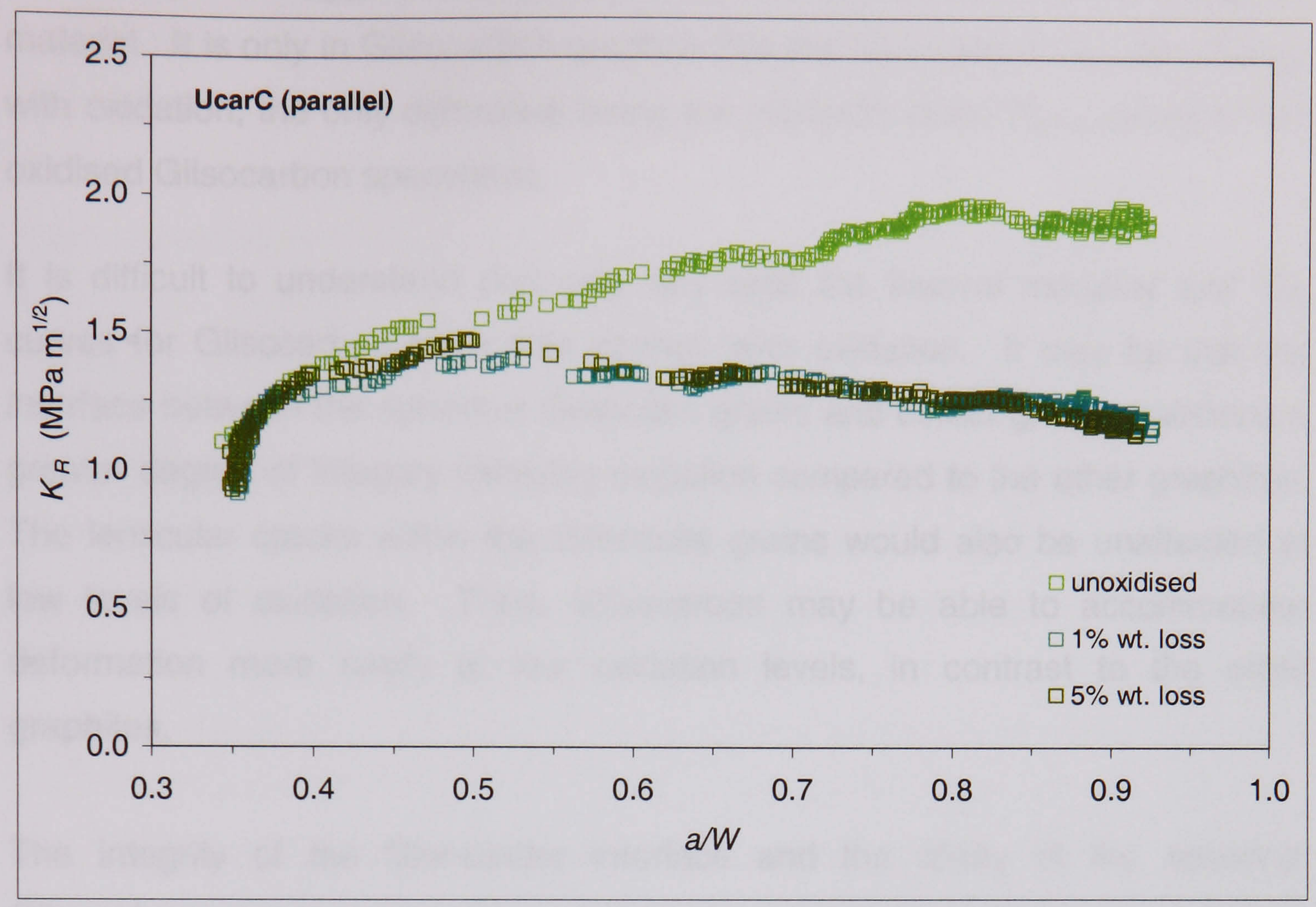

a

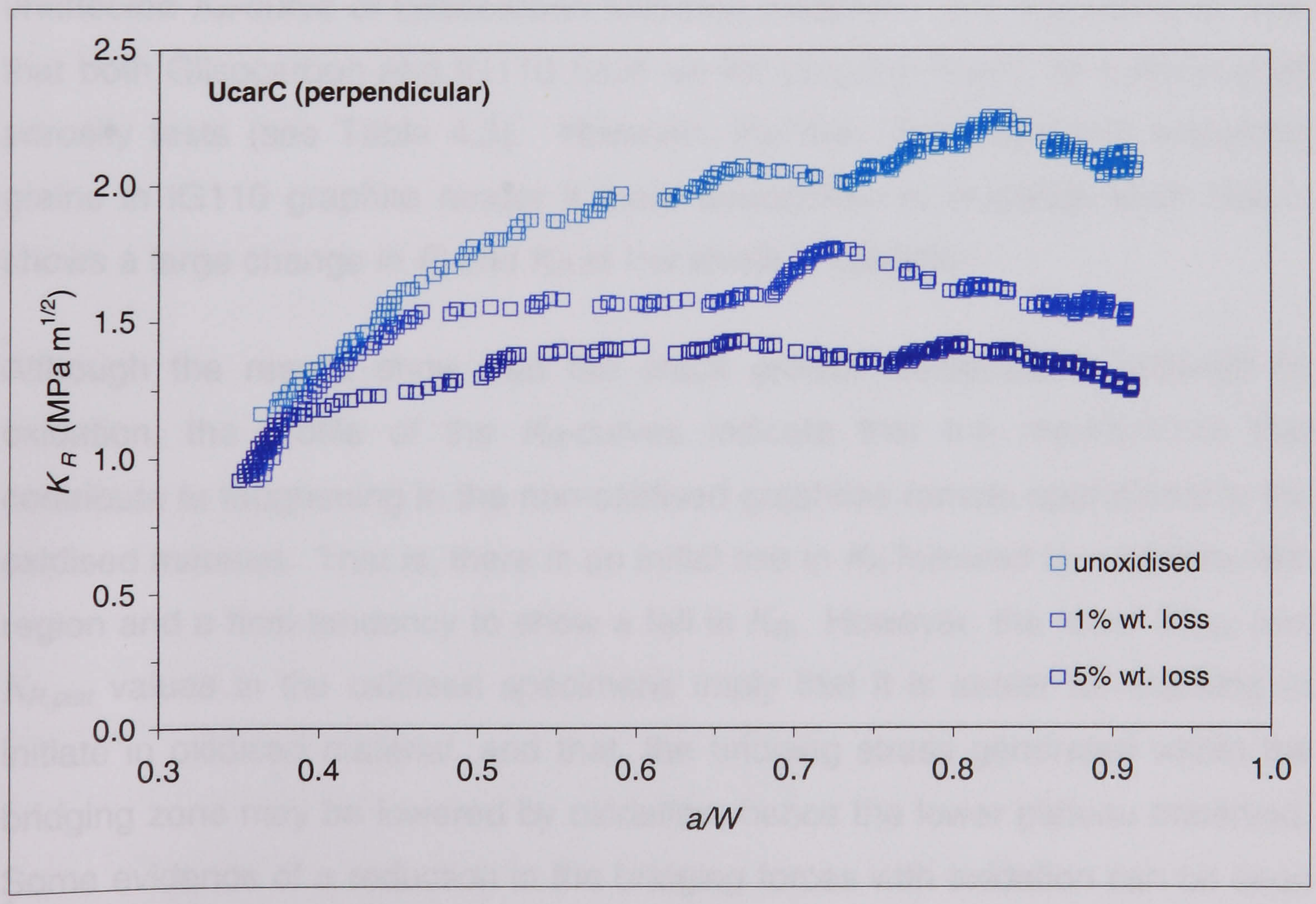

b

Figure 9.5. K_R-curves of oxidised and non-oxidised UcarC graphite in 3-point bending.

The lower crack growth resistance of the oxidised materials is evident from their lower $K_{R,init}$ and $K_{R,plat}$ values, both of which fall below that of the non-oxidised material. It is only in Gilsocarbon graphite that the K_R-curves show little change with oxidation, the only difference being the markedly lower $K_{R,init}$ values in the oxidised Gilsocarbon specimens.

It is difficult to understand precisely why both the flexural modulus and K_R-curves for Gilsocarbon show little change with oxidation. It may be that the interface between the spherical Gilsocoke grains and binder grains maintains a greater degree of integrity following oxidation compared to the other graphites. The lenticular cracks within the Gilsocoke grains would also be unaffected at low levels of oxidation. Thus, Gilsocarbon may be able to accommodate deformation more easily at low oxidation levels, in contrast to the other graphites.

The integrity of the filler-binder interface and the ability of the spherical Gilsocoke grains to reduce the probability for coincidental microcrack alignment (Ouagne, 2000) may be an important factor contributing to the relatively unaffected K_R-curve of Gilsocarbon following oxidation. It is interesting to note that both Gilsocarbon and IG110 have similar porosity levels, as confirmed by porosity tests (see Table 4.3). However, the fine, grain size and elongated grains in IG110 graphite render it more susceptible to oxidation such that is shows a large change in E_f and K_R at low levels of oxidation.

Although the results show that the crack growth resistance is reduced by oxidation, the profile of the K_R-curves indicate that the mechanisms that contribute to toughening in the non-oxidised graphites remain operational in the oxidised material. That is, there is an initial rise in K_R followed by a plateau-like region and a final tendency to show a fall in K_R. However, the lower $K_{R,init}$ and $K_{R,plat}$ values in the oxidised specimens imply that it is easier for cracking to initiate in oxidised material, and that, the bridging stress generated within the bridging zone may be lowered by oxidation, hence the lower plateau observed. Some evidence of a reduction in the bridging forces with oxidation can be seen in the IG110 graphite oxidised to 5% weight loss. Here, a plateau does not occur. The K_R-curve falls gradually after showing an initial rise to a maximum.

It is worth pointing out that despite the reduction in crack growth resistance following oxidation, the coarser grained materials still display practically useful toughness levels. In contrast, the fine-grained IG110 graphite appears to lose most of its toughening ability at a low oxidation level of 5%. This may be another characteristic on which to base the selection of the graphites. The observed reduction in crack growth resistance will clearly increase as the extent of oxidation increases with the coarse-grained materials still showing some resistance compared to IG110, which seems likely to develop a flat *R*-curve.

Ouagne's study (2000) of *R*-curve behaviour in oxidised nuclear graphites indicates that Gilsocarbon graphite continues to show crack growth resistance, even at oxidation levels exceeding 10%. Ouagne (2000) also found that the stress-intensity-based K_R-curve and the energy-based *R*-curve were reduced by oxidation. However, his *R*-curves and K_R-curves for the same materials display a marked difference in profile in that, the *R*-curves fall after showing a plateau whilst the K_R-curves rise following the plateau.

Ouagne (2000) attributed the earlier onset of a fall in *R*-curve to an enlarged process zone caused by increased porosity and microcracking, whose interaction with the specimen backend manifests itself sooner. The crack progresses through an already damaged zone causing a drop in *R*. He attributes the rise in the K_R-curve after the plateau formation to the geometric funtion ($Y(\alpha)$) that is used in calculating the stress intensity factor. However, this reason put forward by Ouagne (2000) is difficult to reconcile with the fact that his K_R -curves show a continual, gentle rise at high oxidation levels (>10%). The K_R -curves obtained in this study show a drop in K_R following the plateau, which is consistent with the profile of the energy-based *R*-curves and consistent with *R*-curve profiles reported by Ouagne (2000).

It is not certain to what extent microcracking in the frontal process zone may contribute to the toughening that is still observed in the oxidised graphites. It seems unlikely that an increase in microcracking propensity following oxidation could play a significant role towards toughening. An increase in the microcrack density in the frontal process zone is likely to make crack initiation easier, and, assist the crack in finding a fracture path of lower resistance. The same holds true for the concept that the process zone enlarges with increasing oxidation.

9.5. Comparison of the G_R-curves of the Oxidised Nuclear Graphites

As explained in several instances throughout this study, it is necessary to compare the crack growth resistance of materials in terms of both the K_R-curve (stress-intensity based form) and *R*-curve (energy-based form). This is because a lower K_R-curve does not necessarily correspond with a lower *R*-curve. That is, materials that show a relatively low stress intensity factor may still require a high fracture energy (Sakai, 1988). Using Irwin's similarity rule ($G=K^2/E'$), the *R*-curves of the oxidised graphites were computed in terms of the elastic, energy release rate (G_R). Figures 9.6-9.8 compare the G_R-curves for the oxidised and non-oxidised material. The graphs expose a serious shortcoming of the Irwin similarity rule, as well as a limitation of the theoretical compliance method for crack length measurement.

With the exception of the UcarC specimens in which crack growth was perpendicular to extrusion (Figure 9.8b), it is seen that the G_R-curves of the oxidised specimens rise above that of the non-oxidised material. This anomalous result is thought to be due to two factors. Firstly, the theoretical compliance method requires the input of the elastic modulus for the calculation of the crack length. Error in the flexural modulus measurement of the oxidised specimens would lead to error in the crack length measurement and hence the K_R-curve and G_R-curve profile of the oxidised specimens. Non-uniform oxidation of the specimens would also add to such error.

More importantly though, it is the failing of the Irwin similarity rule in accounting for the non-linear fracture processes, i.e. toughening mechanisms, that produces the anomalous result. Dividing the square of the stress intensity factor by the elastic modulus is a simplistic approach that ignores the contribution from non-linear toughening mechanisms on the *R*-curve profile. Indeed, this approach causes the reduced flexural modulus of the oxidised specimens to produce G_R-curves that appear higher than the non-oxidised materials, which is an unlikely scenario. Although the Irwin similarity approach was found to give G_R-curves in non-oxidised material, that were comparable to *R*-curves obtained by other workers using different methodologies, it fails to produce comparable results when the material is oxidised. This is a direct result of its dependence on the elastic modulus.

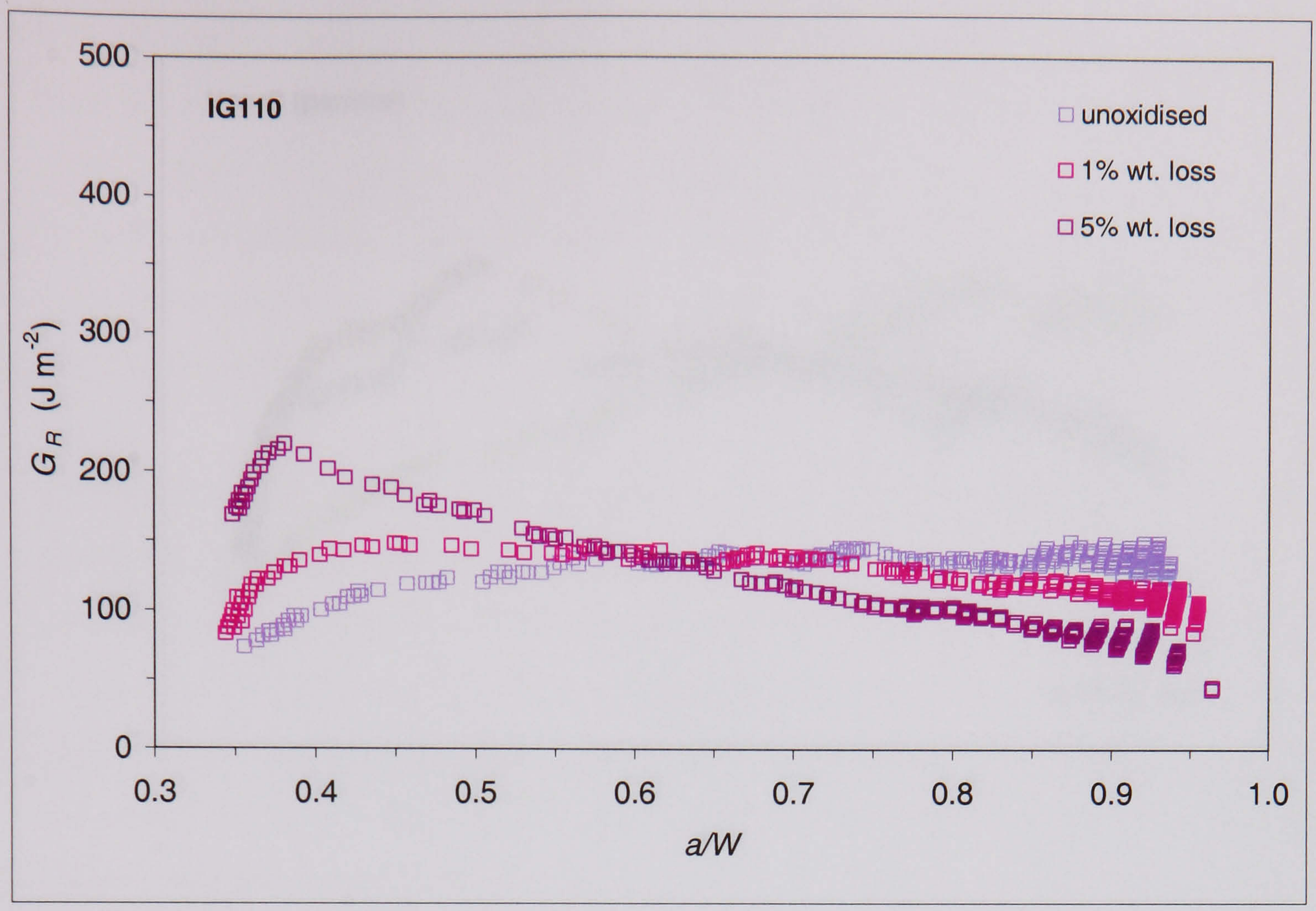

Figure 9.6. G_R-curves of oxidised and non-oxidised IG110 graphite in 3-point bending.

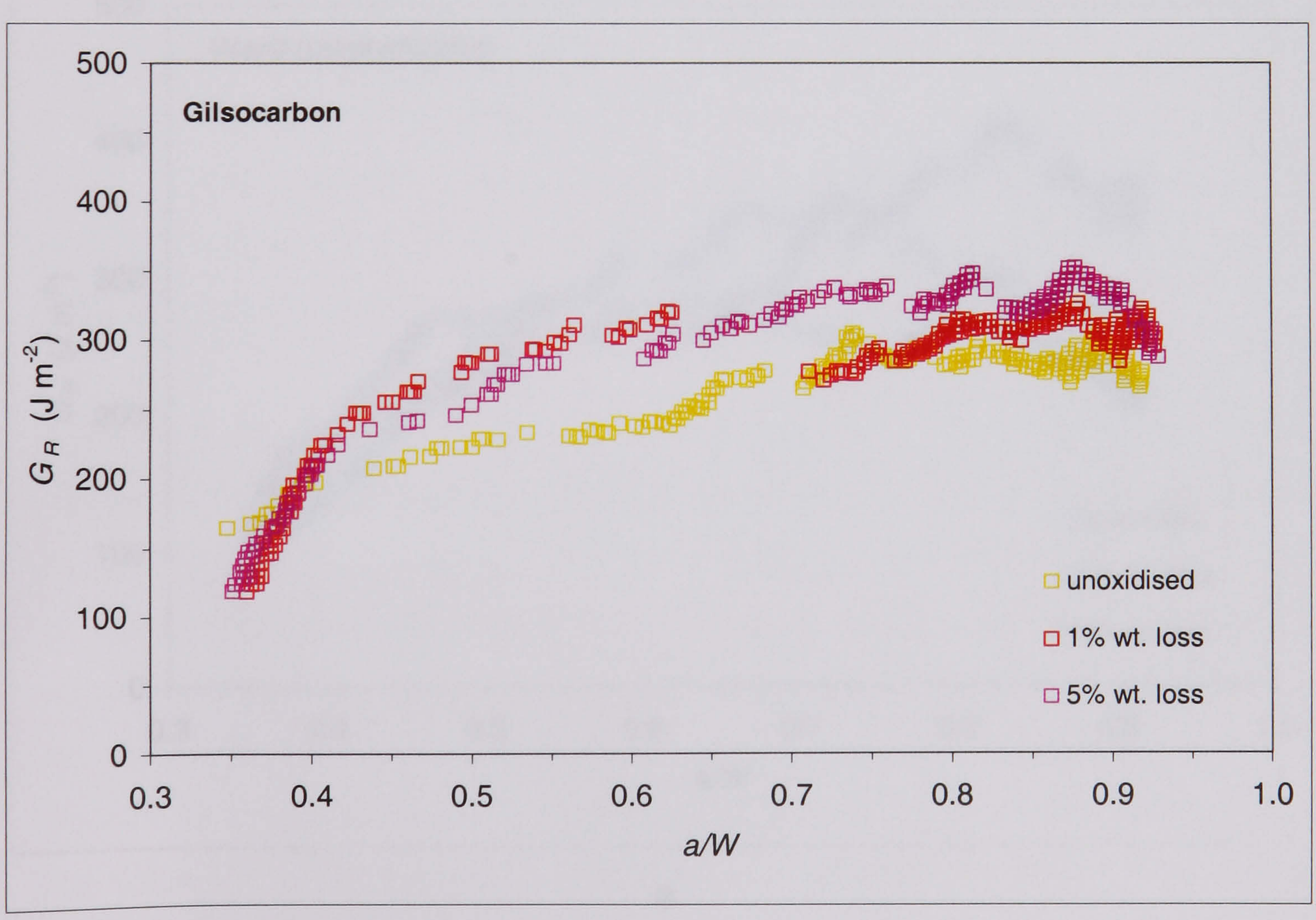

Figure 9.7. G_R-curves of oxidised and non-oxidised Gilsocarbon in 3-point bending.

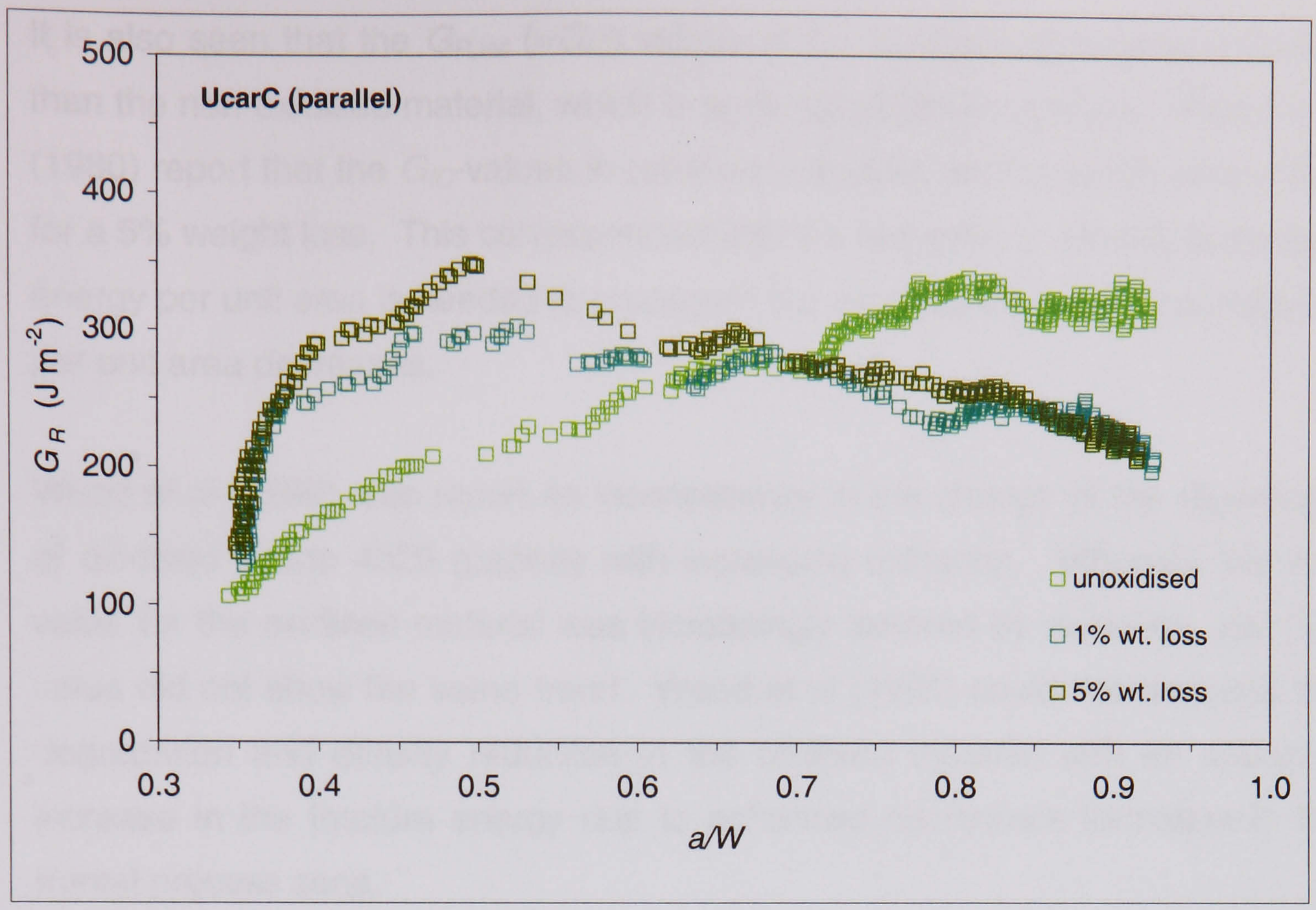

b

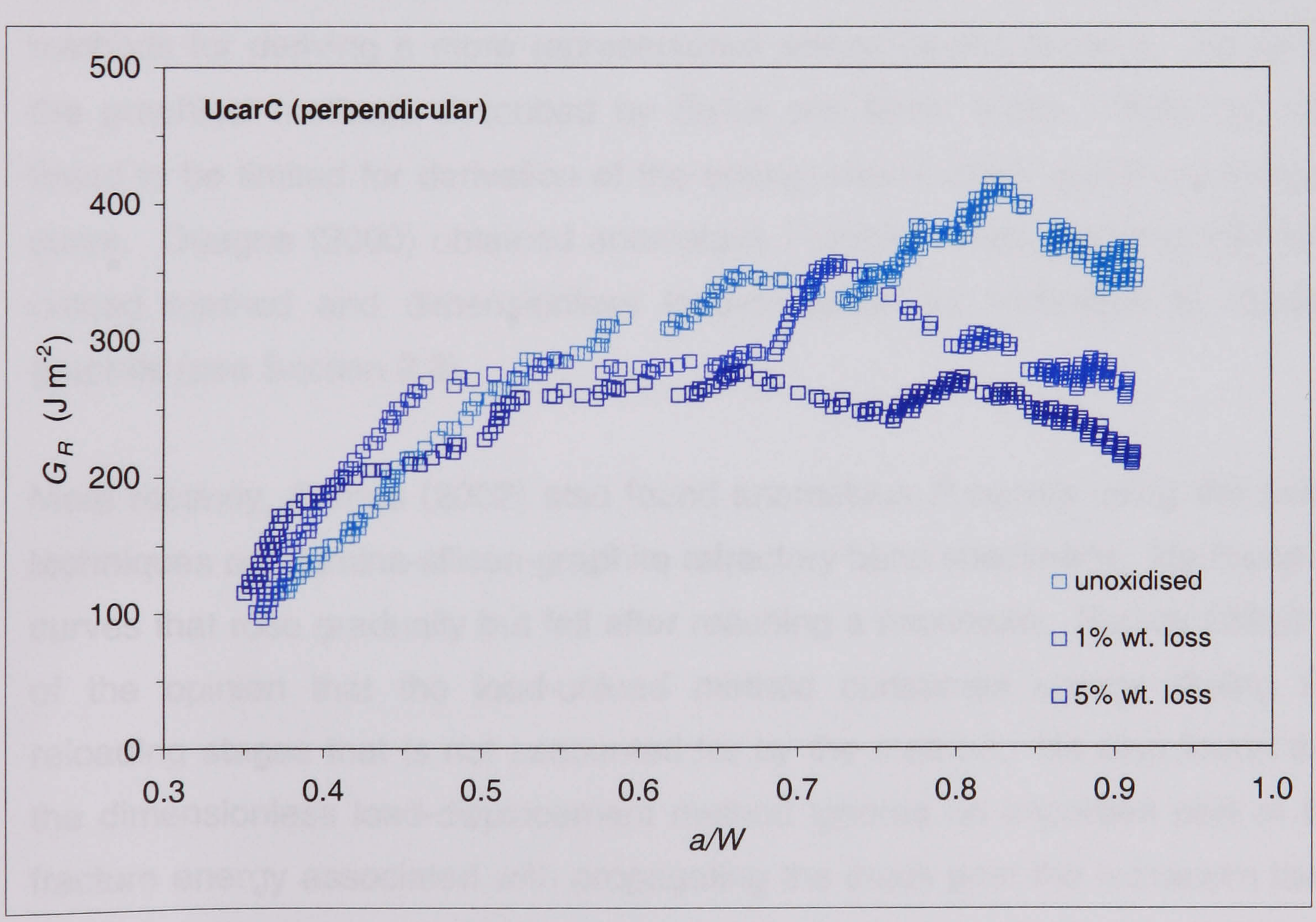

a

Figure 9.8. G_R-curves of oxidised and non-oxidised UcarC graphite in 3-point bending.

It is also seen that the $G_{R,init}$ (=G_{IC}) values of the oxidised specimens is higher than the non-oxidised material, which is again an anomalous result. Wood et al (1980) report that the G_{IC}-values in oxidised materials decreased by about 30% for a 5% weight loss. This corresponded with the reduction in density since less energy per unit area is needed to propagate the crack as the amount of material per unit area decreases.

Wood et al (1980) also report an inconsistency in the change of the G_{IC}-values of oxidised Grade 4029 graphite with increasing oxidation. Whereas the K_{IC}-value for the oxidised material was increasingly lowered by oxidation, the G_{IC}-value did not show the same trend. Wood et al (1980) could not reconcile the degradation and density reduction in the oxidised material with an apparent increase in the fracture energy due to enhanced microcrack formation in the frontal process zone.

This is the main reason why Sakai (1988) has stressed the use of alternative methods for deriving a more representative energy-based *R*-curve. However, the graphical methods described by Sakai and Bradt (1986, 1989) are also found to be limited for derivation of the energy-based crack growth, resistance curve. Ouagne (2000) obtained anomalous *R*-curves when applying the load-unload method and dimensionless load-displacement technique to nuclear graphite (see Section 2.3).

More recently, Ramos (2002) also found anomalous *R*-curves using the same techniques on alumina-silicon-graphite refractory bend specimens. He found *R*-curves that rose gradually but fell after reaching a maximum. Ramos (2002) is of the opinion that the load-unload method consumes energy during the reloading stages that is not accounted for by the method. He also found that the dimensionless load-displacement method ignores an important part of the fracture energy associated with propagating the crack past the maximum load. The reliability of the graphical methods also depends on the method of crack length measurement. A variation in the *R*-curve profile is also likely depending on the test specimen configuration that is used.

9.6. Fractography of the Oxidised Test Specimens

Numerous studies have considered the relation between microstructural changes with oxidation and the reduction in mechanical properties such as strength and fracture toughness, in nuclear graphite. These studies report a wide variation in the structural changes caused by oxidation, with the nature and extent of the change depending on the oxidation conditions, the oxidant used, and, the structure and properties of the graphite itself. Thrower et al (1982, Part II) noted that the influence of oxidation on the strength of the graphite depends not only on the reactant gas but the microstructure of the material as well. Radiolytic and thermal oxidation are found to have different effects on the development of the pore structure (Burchell et al, 1986).

The general observation in most studies is that oxidation occurs preferentially in the binder since pores in the binder phase are more accessible to the oxidising gas. Cracks therefore propagate almost entirely in the binder or along the binder-filler interface in oxidised materials, with corrosion of filler particles occurring at higher oxidation levels. It is also recognised that a high density of small pores is more conducive to crack initiation than a few large pores. Oxidation that produces a large number of small pores causes a greater strength reduction than that which produces a small dispersion of large pores. The removal of filler grains has less influence on the modulus compared to the removal of inter-granular binder, which is more detrimental.

Pickup et al (1982) report a reduction in the fracture toughness of Gilsocarbon and PGA graphite with oxidation (CO_2-CO) due solely to a reduction in E and γ caused by an apparent increase in narrow, slit-shaped pores in the binder phase. They regarded the high aspect ratio pores as more detrimental than the enlargement of the general pore structure in the graphite. Despite the preferential formation of the narrow, slit-like pores, they found no evidence of a change in fracture mechanism with oxidation.

Since low levels of oxidation have an etching effect on the graphite structure, it was not necessary to polish the bend specimens to examine the crack path in the SEM. The notched portion of the specimens was sectioned, cleaned ultrasonically in water, dried, and, mounted for SEM.

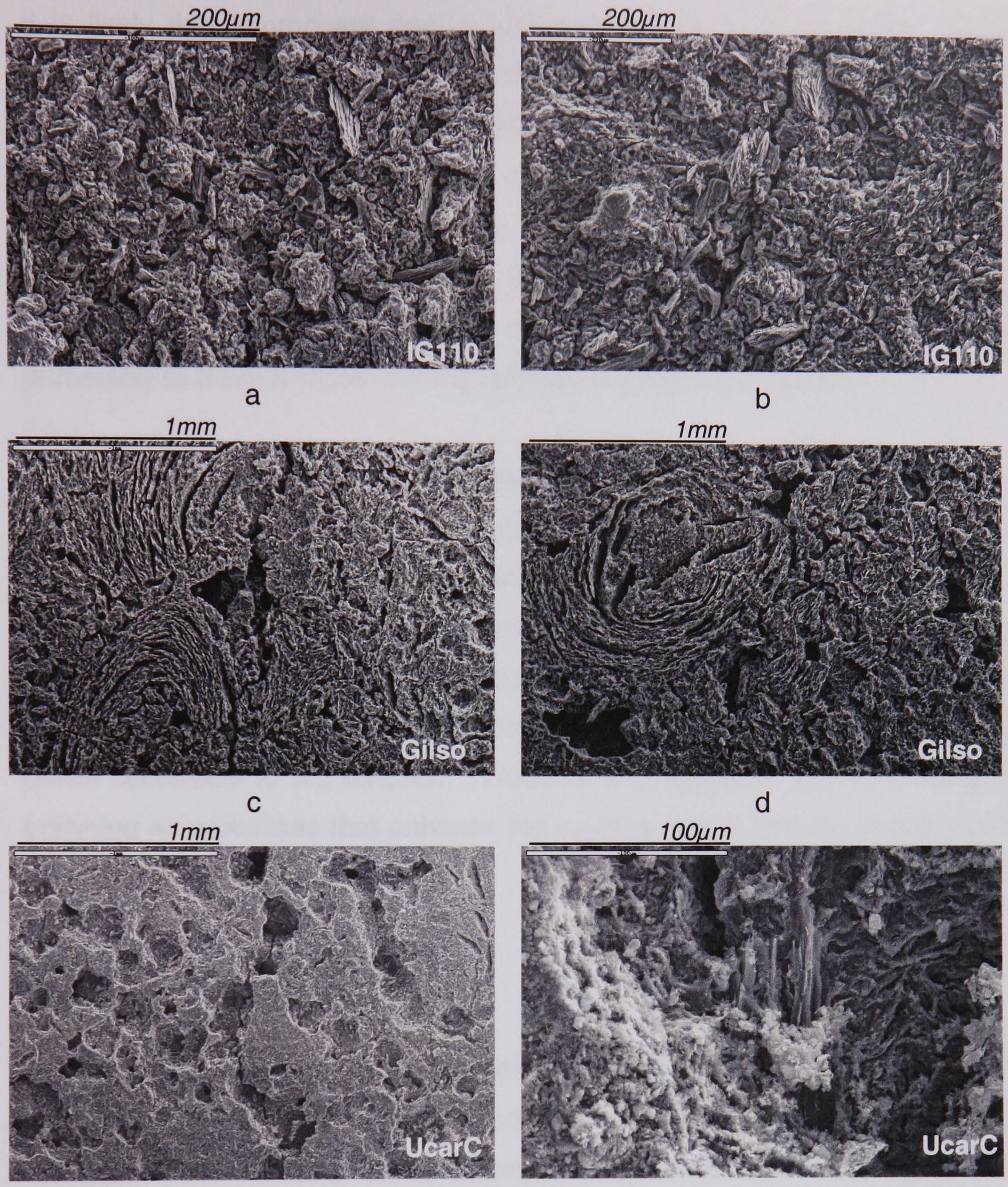

Figure 9.9. Fracture path in oxidised 3-point bend specimens.

Examination of the fracture path in the oxidised bend specimens indicated a notable increase in porosity, as expected. This is shown by the SEM images of the fracture path in Figure 9.9 for the IG110, Gilsocarbon, and, UcarC graphites oxidised to 5% mass loss. In the IG110 graphite, preferential oxidation of the binder phase exposes more of the filler grains, particularly those grains with the basal edges perpendicular to the surface (see Figures 9.9a-9.9b).

It is likely that impregnant carbon within the pores is preferentially oxidised leading to the notable enlargement of the pores. This also exposes the filler grains that are held intact by the binder material (Figure 9.9f). In general, the SEM images indicate that notable crack deflection occurs in the oxidised specimens and this must contribute towards the R-curve behaviour that is observed in the oxidised materials. Ouagne (2000) states that a reduction in the extent of material that must be cleaved due to oxidation means that the probability of crack bridges forming behind the crack tip is reduced.

Although these SEM images are taken on the surface of the specimens, they must give a fair representation of the internal structural changes. Surface oxidation is known to occur preferentially but the extent to which this influences the observations made here is uncertain. It is worth noting that Eto and Growcock (1983) found a sharp rise, in the burn-off profile at the surface of oxidised specimens, citing that machining made a large number of smaller pores accessible to the oxidant. Wood et al (1980) also cite machining and polishing as processes that enhance the surface reactivity through deformation of carbon material at the surface.

9.7. SUMMARY

The conditions used to oxidise the test specimens are described and reasons for selecting the experimental conditions are cited. Since the selected conditions produced very low oxidation rates, specimens could only be oxidised to a level of 5% mass loss. The impregnated UcarC graphite showed the lowest oxidation rate of the three materials posing a problem when trying to achieve high oxidation losses within a practical time.

The K_R-curves of the oxidised graphites are generally lowered by oxidation, except for Gilsocarbon, which showed similar behaviour at all oxidation levels. This may be related to the lower relative decrease in the flexural modulus of the Gilsocarbon material with oxidation compared to the other materials where the relative decrease in modulus is greater. The lower relative, modulus decrease in Gilsocarbon suggests that the binder-filler interface in Gilsocarbon is less

affected by oxidation than in IG110 and UcarC graphite, which may be indicative of a more coherent binder-filler interface in Gilsocarbon.

The K_R-curve profiles of the oxidised materials show that crack growth resistance mechanisms remain operational but diminish with increasing oxidation. A loss of binder phase and the resultant increase in porosity must lower the fracture energy, as well as, the bridging stress that is generated within the bridging zone. There may be a reduction in crack deflection with oxidation since the crack is able to find paths of lower resistance, however this was not clear. The ranking of the G_R-curves does not correlate with that of the K_R-curves since the Irwin similarity rule fails to account for the non-linear toughening mechanisms that contribute to *R*-curve behaviour. The dependence of the similarity principle on the elastic modulus also causes its failure since the modulus of the oxidised material decreases with oxidation, producing G_R-curves for oxidised materials that are higher than that of the non-oxidised material.

CHAPTER 10

NANO-INDENTATION BEHAVIOUR OF THE NUCLEAR GRAPHITES

It was mentioned that one aim of this work was to evaluate the usefulness of the nanoindentation technique in studying the deformation behaviour of polycrystalline graphite. A particular interest was to compare the elastic modulus obtained by nanoindentation with that measured by conventional, bulk modulus measurements. One of the attractions of the method is the ability to test very small specimens. This presents a distinct advantage with nuclear graphites since the Young's modulus change with irradiation and oxidation could be monitored using small samples. Following the theoretical background given in the next section, the method is described and the outcome of this study presented in the remainder of this chapter.

10.1. Theoretical Background

In nano-indentation, the deformation response of a small volume of material is measured using a continuous, load-displacement sensing device. The popularity of the method has increased over the last decade (Pharr, 1992), and, it is now routinely used to perform small-scale, mechanical property measurements at depths of only a few microns (Hay et al, 1999). The method has been used to study elastic and plastic deformation in brittle materials (Kanari et al, 1997).

10.1.1. Measurement of the Elastic Modulus using Nanoindentation

Much of the development of the nanoindentation technique has centred on elastic modulus and hardness measurements in metallic materials. To validate the usefulness of the technique, researchers often compare experimentally obtained modulus values with bulk modulus values. Differences between the two values have been attributed to a range of variables that are thought to originate from the complex interaction between the indenter and the material. There remains an ongoing effort to understand and quantify these variables. The most popular method for obtaining the elastic modulus by nanoindentation is founded on the work of Sneddon (1965). He derived an expression relating the load (P) and displacement (h) of a rigid, flat, cylindrical punch indenting an isotropic, elastic half-space, viz.

$$P = \left(\frac{4\mu.a}{1-\nu}\right)h \qquad [10.1]$$

μ = shear modulus

a = radius of the cylindrical punch

ν = Poisson's ratio

The projected area (A) of the punch, in contact with the elastic half-space is given by $A = \pi a^2$. The shear modulus, Poisson's ratio, and elastic modulus are inter-related by $E = 2G(1+\nu)$. Differentiating P with respect to h leads to a popularly used equation (Oliver & Pharr 1992, Pharr et al 1992),

$$S = {}^{dP}\!/_{dh} = \frac{2\sqrt{A}}{\sqrt{\pi}}\frac{E}{(1-\nu^2)} \qquad [10.2]$$

This equation relates the elastic modulus (E) of the material to the initial slope of the unloading curve, this slope being defined as the stiffness, S ($=dP/dh$). This concept is illustrated in Figure 10.1.

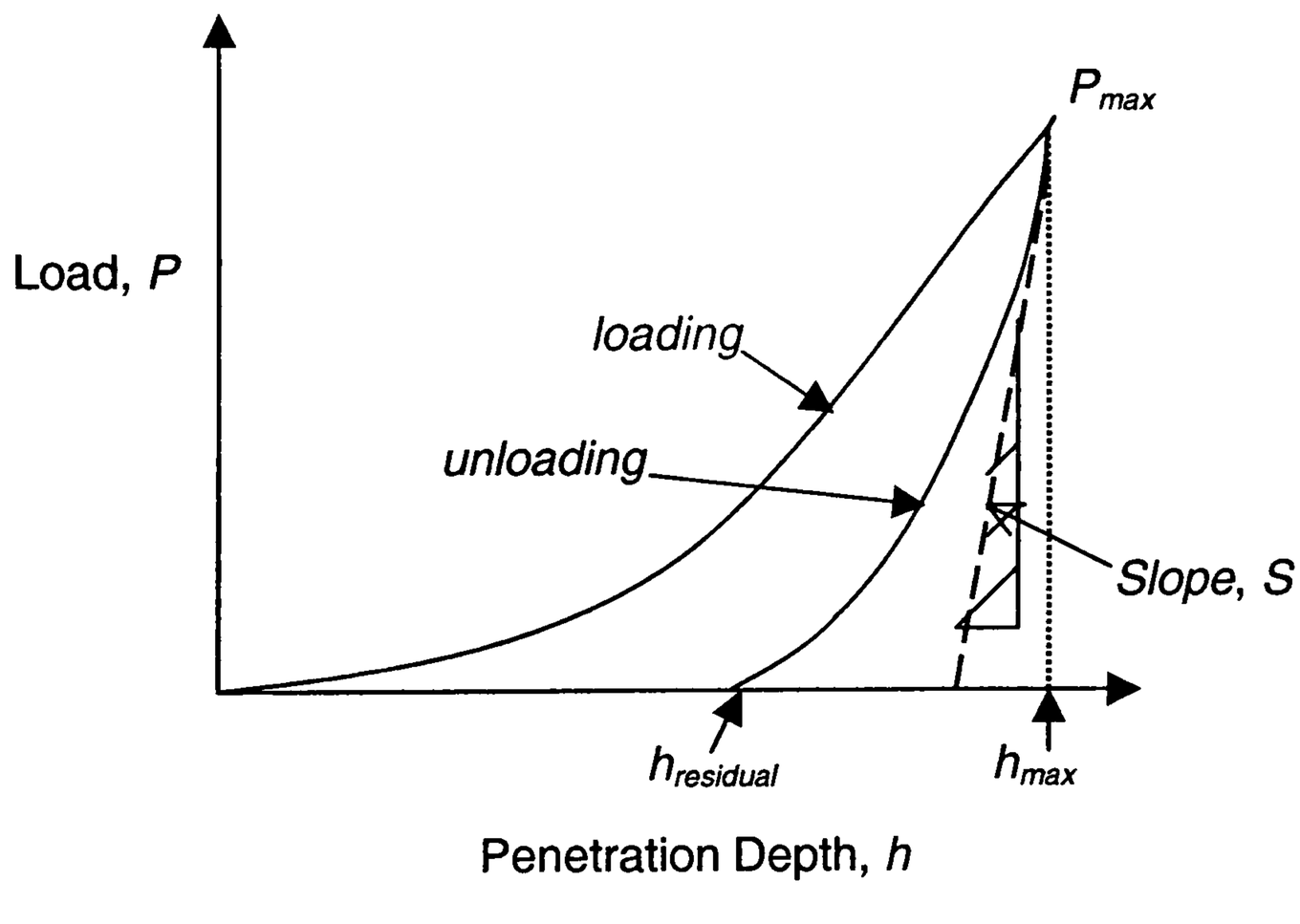

Figure 10.1. Deriving the stiffness from the unloading curve (Oliver&Pharr, 1992).

An important assumption made in this model is that the contact area between the indenter and the specimen remains constant over the portion of the unloading curve used in the analysis. The method also requires that the contact area (A), and, Poisson's ratio (ν), be known to an approximation at least.

10.1.2. Nano-Indentation Response of Different Materials

In general, the shape of the load-unload curve varies depending on the deformation behaviour of the material as shown schematically in Figure 10.2. Metals typically show large residual deformation such that their unloading-curve drops rapidly from the maximum displacement position.

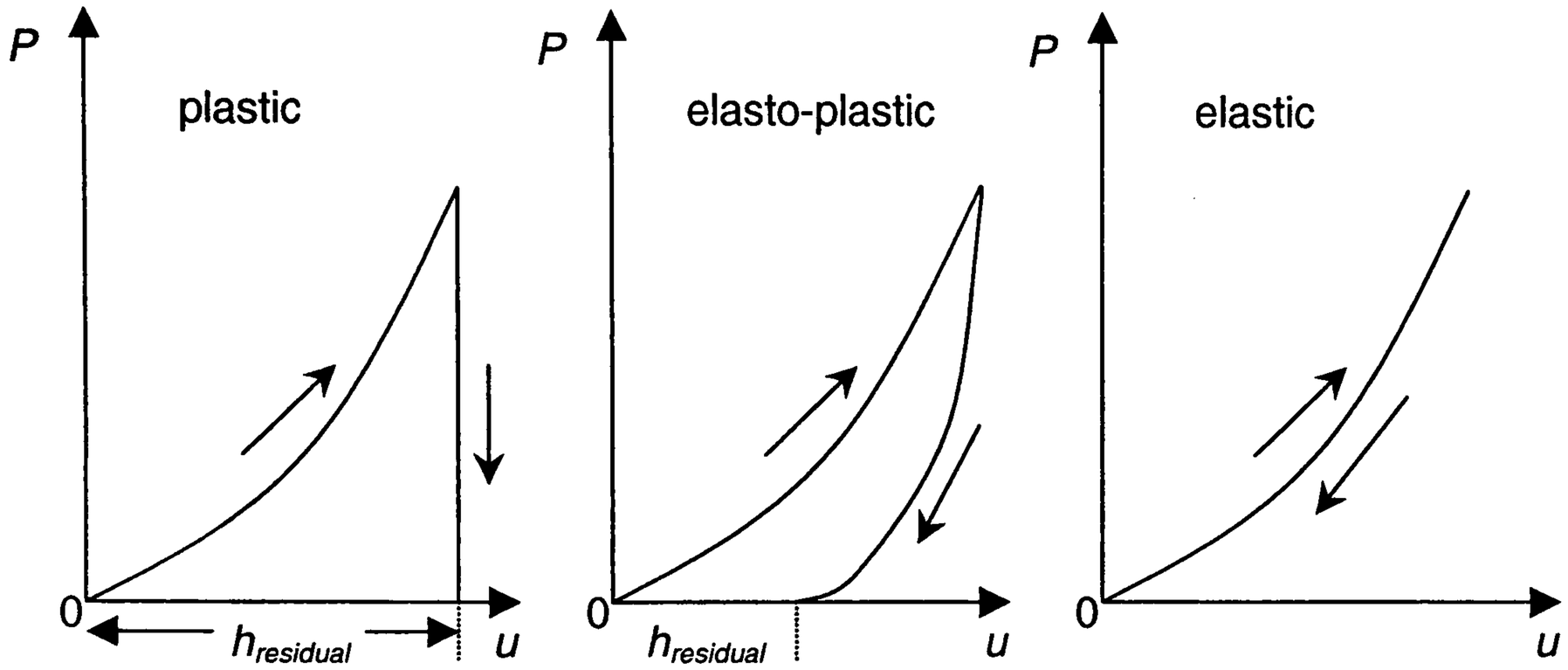

Figure 10.2. Different types of load-unload behaviour (Sakai & Nowak, 1992).

Elasto-plastic materials show a varying degree of elastic recovery whilst the indentation in purely elastic materials would recover completely with the unloading-curve returning to the origin. The work of plastic deformation, given by the area of the hysteresis loop, is therefore negligible for elastic materials resulting in the loading and unloading curves coinciding with each other. The area of this loop is largest in plastic materials. The elastic work of deformation is given by the area outside the hysteresis loop, between the unloading curve and the maximum displacement point.

10.1.3. Accuracy of the Method

There has been considerable debate regarding both the accuracy, and universality, of the popular Equation [10.2] used to calculate *E*. One aspect of contention is the geometry of the indenter tip itself. Whereas Sneddon (1965) derived his solution for a cylindrical, flat punch, in practice, the indenter tip is usually a square- or triangular-based pyramid. Pharr et al (1992) have shown that Equation [10.2] is universal, being applicable to indenters of any geometry that may be described by a solid of revolution or a smooth (infinitely differentiable) function. For example, spheres, cones, parabaloids and

ellipsoids of revolution. The use of axisymmetric indenters in practice, e.g. Vickers or Berkovich indenters that are square or triangular-based pyramids respectively, has been justified on the basis that the unloading curve for materials is often linear, particularly over the initial unloading region. This, therefore, approximates the flat punch behaviour modelled by Sneddon (1965). Doerner and Nix (1986) report linear unloading over almost the entire unloading cycle in metal samples. Pharr et al (1992) disagree highlighting power law unloading behaviour in many materials, using metals and ceramics that show non-linear, unloading behaviour as examples.

Pharr et al (1992) have also suggested that Equation [10.2] may be applicable in the case of axisymmetric indenters, due to the unique relationship between the contact stiffness, contact area, and, elastic modulus described by this equation. They point out that the geometry of the actual impression is related to the indenter geometry and the elastic-plastic properties of the material in a complex way, making a complete analysis of the unloading process difficult. Stilwell and Tabor (1961) showed that the diameter of a conical indentation remains unchanged upon withdrawal of the indenter, but decreases in depth due to elastic rebound, this rebound being related to the elastic constant.

Recently, Cheng and Cheng (1997) claimed that the Equation [10.2] is applicable to elastic and elastic-plastic contact. This is supported by King (1987) who showed that Equation [10.2] could still be applied for Vickers or Berkovich indenters provided a suitable geometric factor was included in the calculation to account for the indenter shape. Other workers have also made similar observations (Hay et al, 1999).

It is also possible to obtain hardness measurements using nano-indentation. Conventionally, hardness is calculated by dividing the applied load (P) by the actual contact area made by the indenter. In nano-indentation, the hardness is really the mean pressure of contact (p_m) (Kanari et al, 1997), given by:

$$p_m = \frac{P_{\max}}{A_a} = 0.192(\cot^2 \alpha).\left(\frac{P_{\max}}{h_{\max}{}^2}\right) \qquad [10.3]$$

P_{max} = maximum load

A_a = apparent or projected area of contact based on indenter geometry

h_{max} = maximum penetration depth; α = included angle of indenter

10.2. Nano-Indentation Behaviour of Carbon Materials

Few studies have been done on carbon materials. Kanari et al (1997) performed tests on isotropic, nuclear graphite (IG-11) using a load range between 0.050 mN-20 mN. The bulk elastic modulus for IG-11 graphite is 9.8 GPa. They obtained an average indentation modulus of 10.7±4.64 GPa, the large standard deviation reflecting the large scatter in the data. Kanari et al (1997) also noted significant scatter in the hardness values, spanning over one order of magnitude. This was attributed to inherent inaccuracies in the measurement technique and unevenness of the sample surface but most importantly the large number of voids and defects in the material.

Another important observation by Kanari et al (1997) was the apparent sensitivity of the hardness (mean indentation pressure) to the surface finish of the samples. On samples polished with p2000 emery paper, it was noted that mean pressures rose to values as high as 300-400 MPa (0.3-0.4 GPa). This was attributed to densification of material at the surface of the graphite, caused by the polishing procedure. On samples finished by a micro-milling process (average surface roughness=2-3 μm) with little densification of surface material the mean indentation pressure dropped to ~50 MPa.

They also noted anelastic hysteresis upon reloading even at the lowest end of the loading range, i.e. 0.05 mN. This behaviour was related to Jenkins' (1962) deformation model where energy is consumed by plastic deformation of filler grains in an elastic carbon network.

Marx and Riester (1999) also used nano-indentation to compare the elastic modulus, the hardness and stiffness, of different C/C-composites. They found distinctive differences in the measured parameters for the different materials studied but concluded that statistical analysis of the data was necessary to improve the reproducibility and reliability of the results.

Akatsu et al (2000) performed nanoindentation tests on highly oriented graphite tape and noted that the indentation modulus and hardness decreased with heat treatment temperature. This was attributed to a progressive removal of crystallite boundary restraint with increasing heat treatment temperature.

Akatsu et al (2000) view crystallite boundary restraint as a possible reason for the extreme elastic recovery shown by the graphite tape during unloading.

In another study, Hoffman et al (2000) used nano-indentation to characterise pyrolitic carbon layers formed on Poco AXF-5Q graphite. Microscopy showed that two types of pyrocarbon formed, a dense, smooth, homogeneous type, and, a rough, less dense porous type. Nano-indentation revealed the homogeneous pyrocarbon layer to be more stiff (E=24.4±0.8 GPa) than the porous layer (E=8.8±1.9 GPa). The homogeneous layer also showed much higher hardness (3.6±0.2 GPa) than the porous layer (0.9±0.2 GPa). The unloading curve for the homogeneous material displayed almost complete elastic recovery, with a small hysteresis loop, whilst the porous pyrocarbon layer showed much larger hysteresis and lower elastic recovery. Hoffman et al (2000) found these differences despite the fact that the layers were often contained in narrow bands of ~100 μm or less, highlighting the localised nature of the variation in the elastic modulus and hardness of carbon materials.

10.3. Operation of the Nano-Test 300

Before presenting the results of nano-indentation tests, it is necessary to explain briefly the workings of the instrument. A 'Nano-Test 300' machine designed by Micro-Materials Ltd (UK) was used for tests. The machine measures the movement of a diamond-tipped stylus (1) in contact with the specimen surface (2) (see Figure 10.3). Control, calibration, and test selection, is done via a PC-controlled interface operating on proprietary software.

The stylus consists of a pendulum (3) rotating on a frictionless pivot. Being a solid, cylindrical length of alumina ceramic, the pendulum is designed to be lightweight, but stiff enough to accommodate a maximum load of 500 mN. The frictionless pivot contains four stainless steel springs in an X-clamp that is very compliant in rotation. Movement of the stylus is controlled by energising a coil mounted at the top of the pendulum, which is achieved by passing a current through the coil (4). By induction, the energised coil is attracted toward the permanent magnet (4), thereby moving the diamond tip towards the specimen surface. A parallel-plate capacitor (5) on the stylus measures displacement via the capacitance change, with a maximum depth sensitivity of 1-1.5 μm.

A limit stop (6) prevents the maximum outward movement of the stylus being exceeded. The pendulum position is balanced by a system of moveable weights (7). Sample movement is achieved by three, DC motor-driven, micrometer stages (8) in an X-Y-Z path. The entire mounting base is supported on an anti-vibration mounting consisting of four, inflatable rubber bladders (9). The entire unit is enclosed in a temperature-controlled enclosure (10) as indicated by Figure 10.3. This also helps to minimise acoustic disturbances.

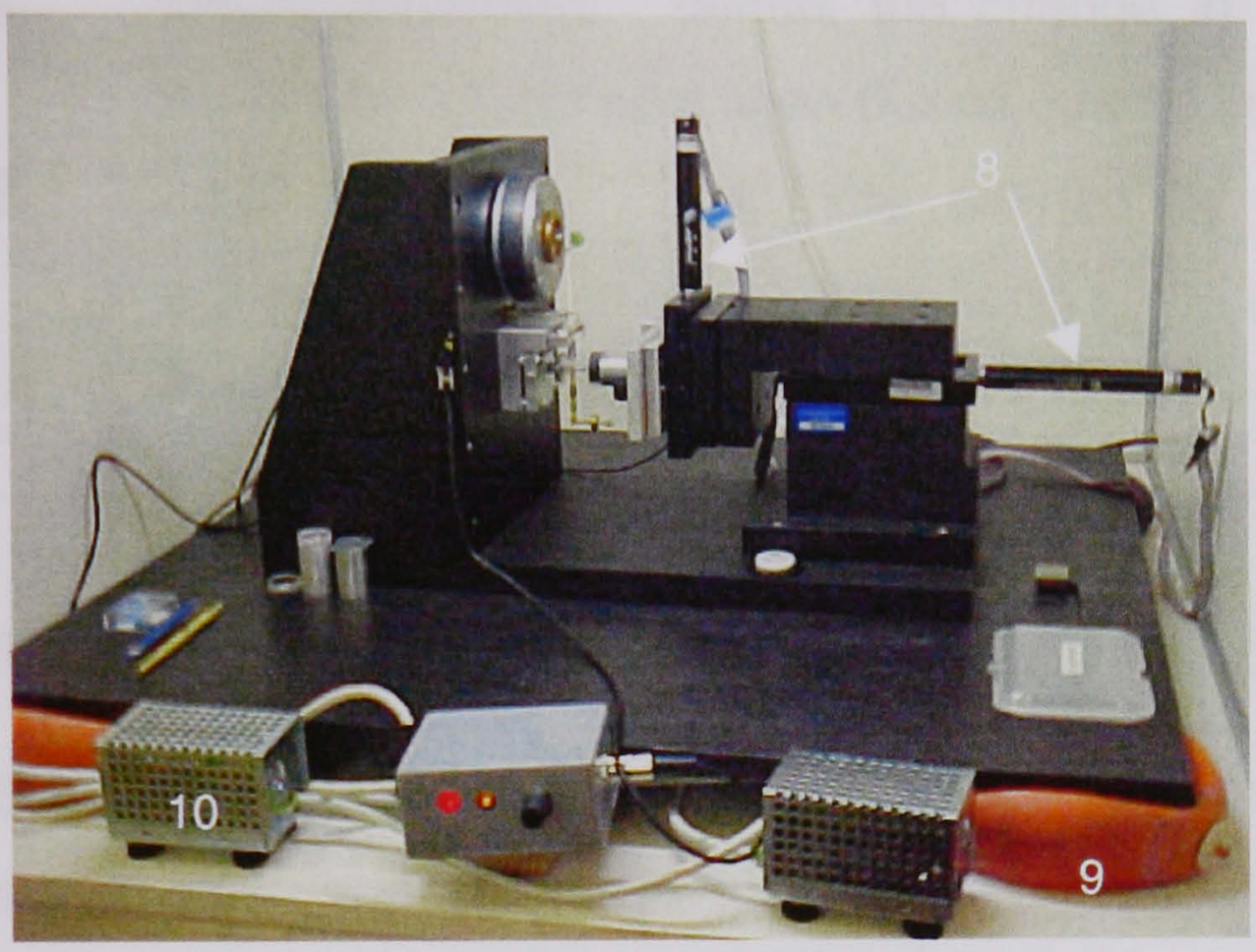

Set-up of the Nano-Test 300 indenter

PC-controlled interface

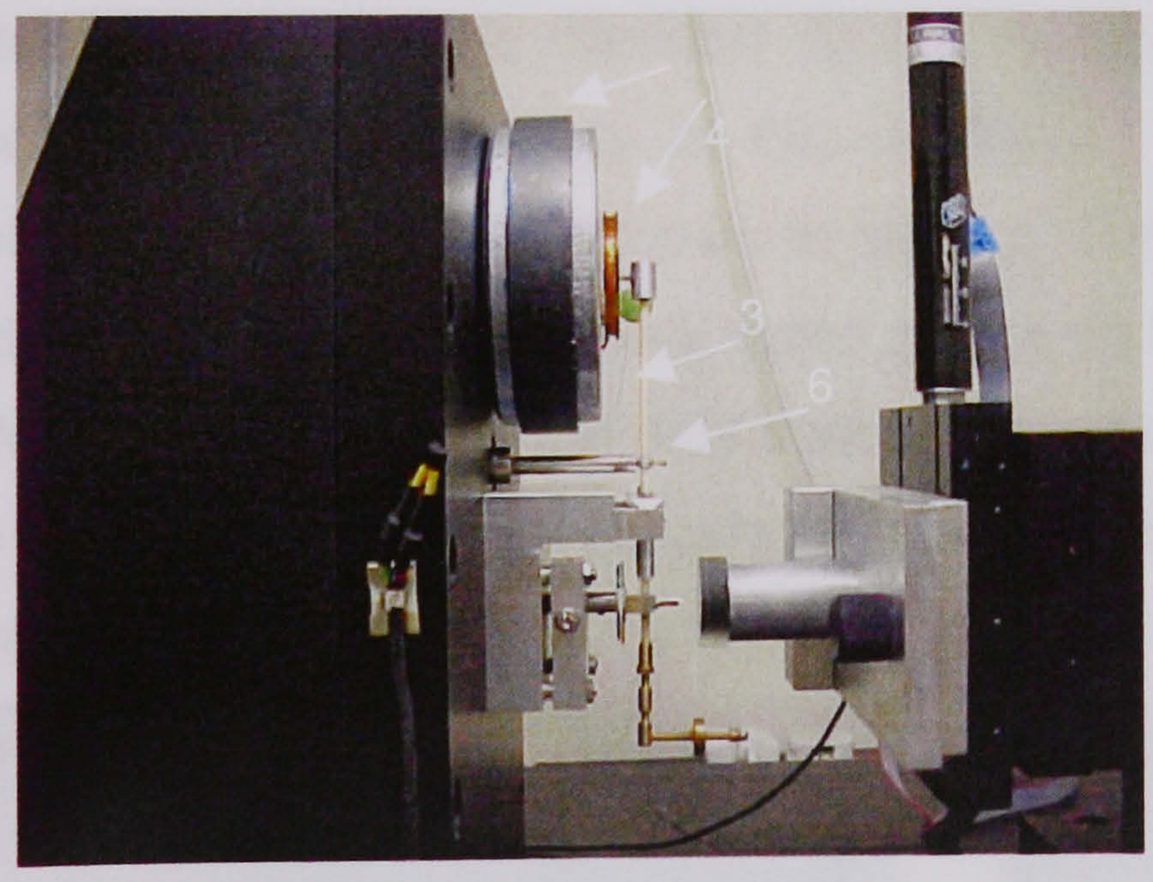

Arrangement of nano-indenter components

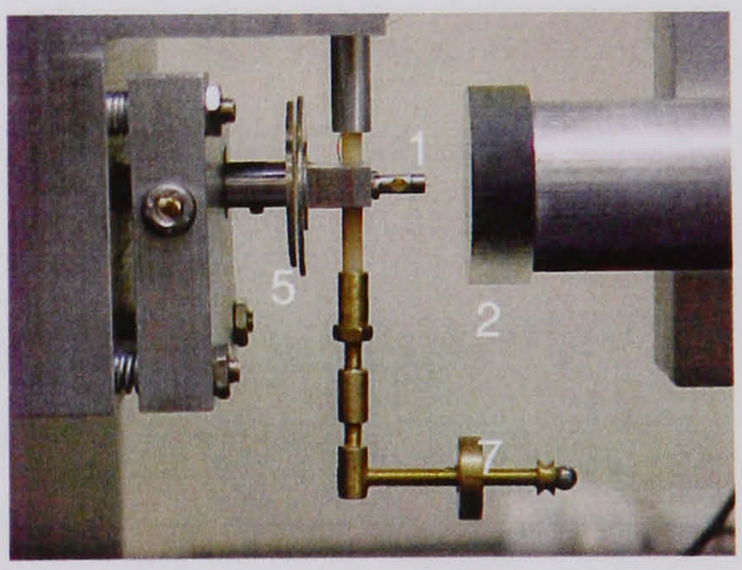

Magnified view of the indenter

1 = diamond-tipped stylus
2 = resin-mounted specimen
3 = pendulum (alumina rod)
4 = coil and magnet
5 = parallel plate capacitor
6 = limit stop
7 = adjustable weight
8 = stage control motors
9 = inflatable rubber bladders
10 = heater for temperature control

Figure 10.3. Layout of nano-indentation test equipment.

10.3.1. Calibrating the Nano-Test 300 Nano-indenter

The 'Nano-Test' machine requires various calibrations before measurements can be performed. These calibrations are done routinely, their frequency being dictated by the usage of the machine, and, are described briefly as follows:

1. Zero Load calibration: measures the minimum coil voltage needed to generate the force required, for the pendulum to contact the limit stop.
2. Depth calibration: relates the change in capacitance to the distance moved by a hard specimen (fused quartz) in contact with the pendulum.
3. Load calibration: the force exerted by the pendulum is measured against a set of known masses hung at the bottom of the pendulum.
4. Frame Compliance calibration: establishes the compliance of the load frame using a fused quartz standard of known hardness, i.e. 8-10 GPa.

10.3.2. Diamond Tip Cleanliness and Specimen Preparation

Samples are attached to the sample-holder using super-glue, Indian wax, or, acrylic resin, the main idea being to have a thin, stiff adhesive layer that does not affect the system compliance. The surface roughness of the specimen and the cleanliness of the diamond tip are important in determining the ultimate accuracy and consistency of the results. Therefore, specimens must be polished to a high standard prior to testing. The diamond tip can be cleaned by indenting a hard material, e.g. fused quartz, at high load, which would have the effect of pushing back the debris away from the diamond tip. Alternatively, the tip can be cleaned by immersing it in alcohol and gently brushing towards the tips with a soft brush followed by blow-drying or an air spray (see Figure 10.4).

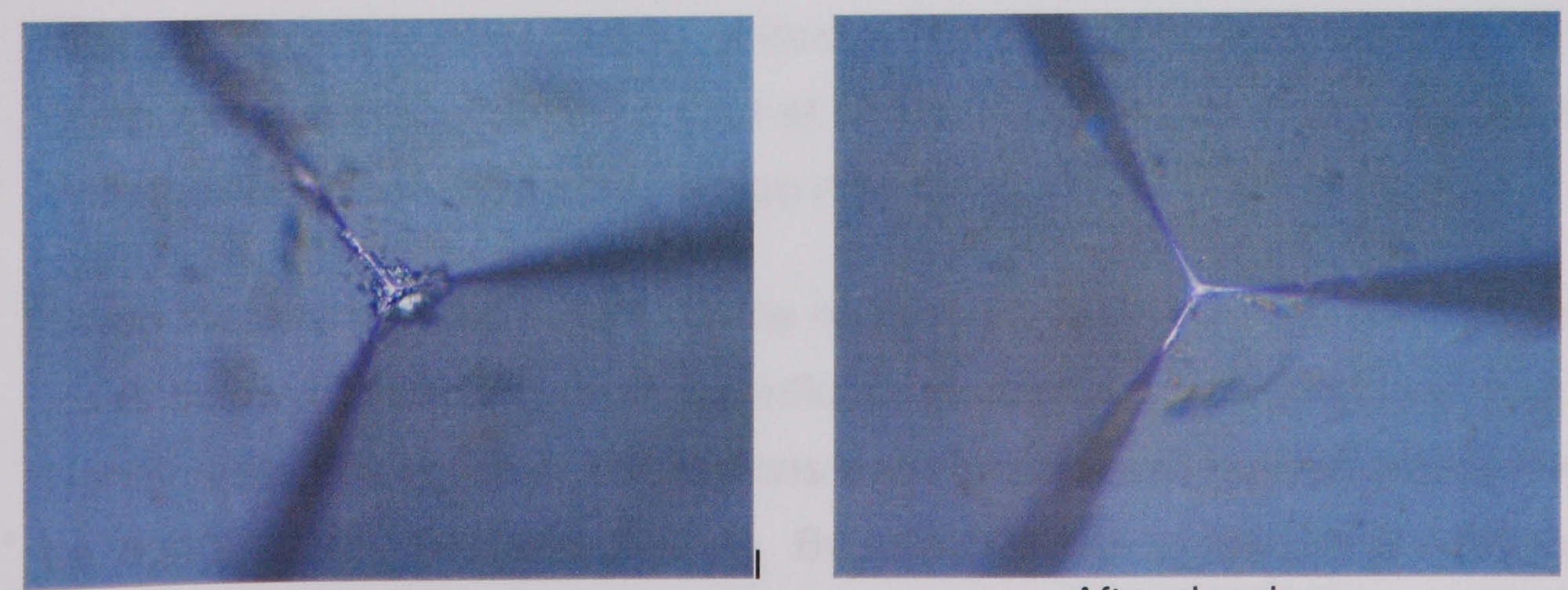

Before cleaning After cleaning

Figure 10.4. Appearance of Berkovich indenter tip before and after cleaning.

10.4. Nano-Indentation Behaviour of the Nuclear Graphites

As pointed out initially, the nano-indentation technique allows minute samples to be tested provided these can be attached satisfactorily, and, a suitable indentation area can be located accurately. In this investigation, rectangular samples were cut from larger sections, taking cognisance of the specimen orientation relative to the forming direction. All samples were polished. Initially, the specimens were vacuum impregnated with Struers Epofix resin since resin-impregnation makes polishing easier and provides a superior finish.

However, preliminary tests indicated that the resin impregnant influences the behaviour of the material and the elastic modulus measurements. There was some indication that the resin-impregnant stiffened the porous graphite structure, however this effect was not reproducible. Another problem was that some indentations were coincident with resin-filled pores, becoming evident in the load-displacement response of resin-impregnated specimens. A mixed response occurred, probably due to the resin and graphite being in close proximity. Therefore, test specimens were not impregnated for polishing because the resin seemed to stiffen the porous graphite structure.

To compare the average, elastic modulus values with bulk modulus values, the indenter was programmed to perform a series of indentations in a grid pattern. Indentations were spaced 50μm apart with a higher maximum load being applied after every 10 indentations. Although there was some merit in applying increasingly higher loads, the maximum load that can be applied is limited by the material hardness since the indenter has a maximum penetration depth, beyond which it is designed to unload. The maximum load attainable for a given material is therefore the load at which the maximum depth is achieved. With the NanoTest 300, the maximum indenter depth is ~2000nm (2μm).

Given that the maximum depth in the nuclear graphites was always attained at loads below 100mN, it became superfluous to apply loads in excess of 100mN. Nonetheless, the series of indentations were made at increasingly higher loads, i.e. 5, 10, 20, 50, 100, and, 200mN. By using a range of loads and a relatively large distance between indentations, it was hoped that the structural variation in the graphites would be adequately represented in the analyses.

10.4.1. Load-Penetration Depth Response

A typical set of load-penetration depth curves obtained for the nuclear graphites at different loads is shown in Figure 10.5, for IG-110 graphite. This family of curves demonstrates typical characteristics, regarding the deformation behaviour of the graphites, using the nano-indentation technique. All the curves show an-elastic hysteresis with the unloading curve returning almost completely to the origin, the amount of residual deformation being small. This behaviour is typical of carbon materials, as reported by others (Kanari et al 1997, Hoffman et al 2000). The curves obtained at each load rarely coincide. Instead, there is a scattered load-displacement response regardless of the maximum load applied, with the maximum load and penetration depth reached, and the amount of hysteresis varying considerably. The maximum penetration depth is reached at loads ranging between 40-50mN, except in some instances where the maximum depth is reached at a lower load. The waviness of the curves at 5mN arises from an instability of the indenter at very low load and indentation depth.

The response of the IG110 graphite shown in Figure 10.5 is typical of all the nuclear graphite materials tested. Figure 10.6 compares the load-penetration depth curves of the different materials at 100mN, which well exceeds the load needed to achieve the maximum penetration depth. Clearly, the response in each material is quite scattered, making it difficult to compare the different graphites. Some distinctions are notable nonetheless.

The residual penetration depth in PGA graphite appears to be the highest at ~1000nm, while that in the Gilsocarbon was the lowest at <500nm. The larger residual depth in PGA graphite correlates with the extent of hysteresis in PGA, which is greater than that of the other graphites. The maximum load reached is lowest in the PGA graphite, indicating that this material deforms more easily when indented. This may be related to the fact that the crystallite boundary restraint diminishes as the degree of graphitisation increases such that the extent of permanent deformation increases (Akatsu et al, 2000). Akatsu et al (2000) showed that the permanent deformation in highly oriented graphite tape increased with increasing graphitisation. The IG-110 graphite shows the least scattered response, which may be interpreted as a sign of greater structural uniformity and probably stems from its finer grain size and isotropic nature.

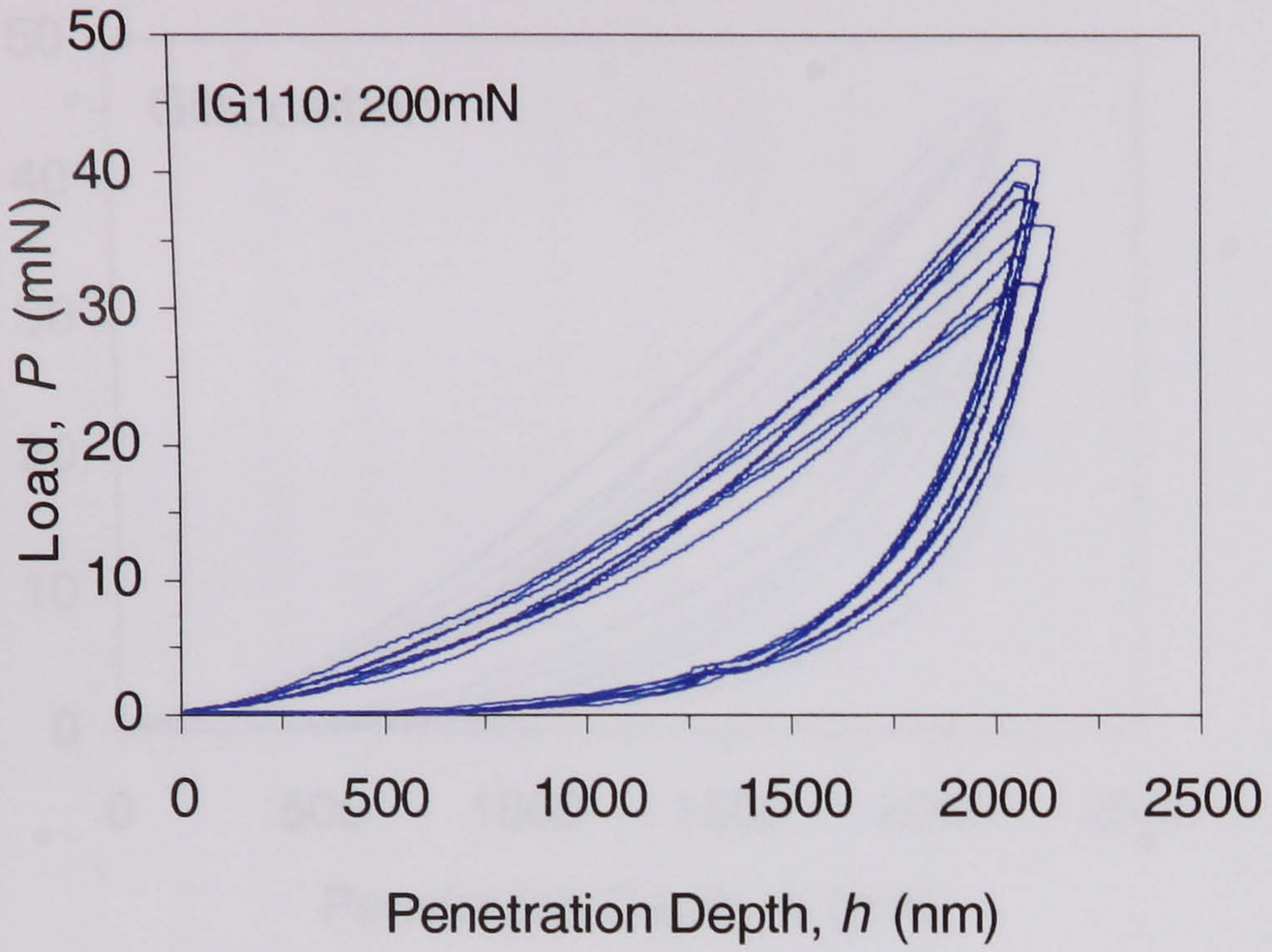

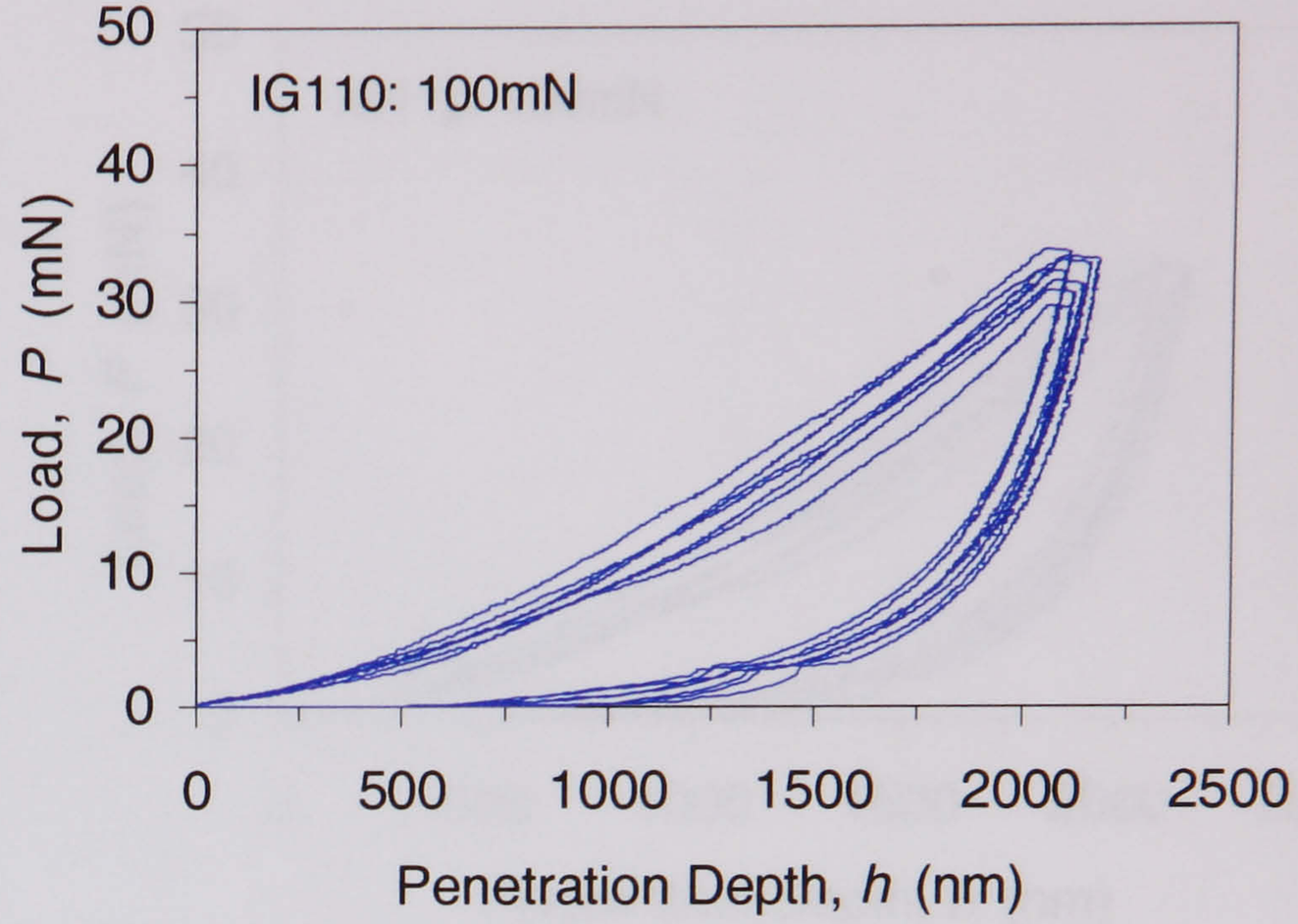

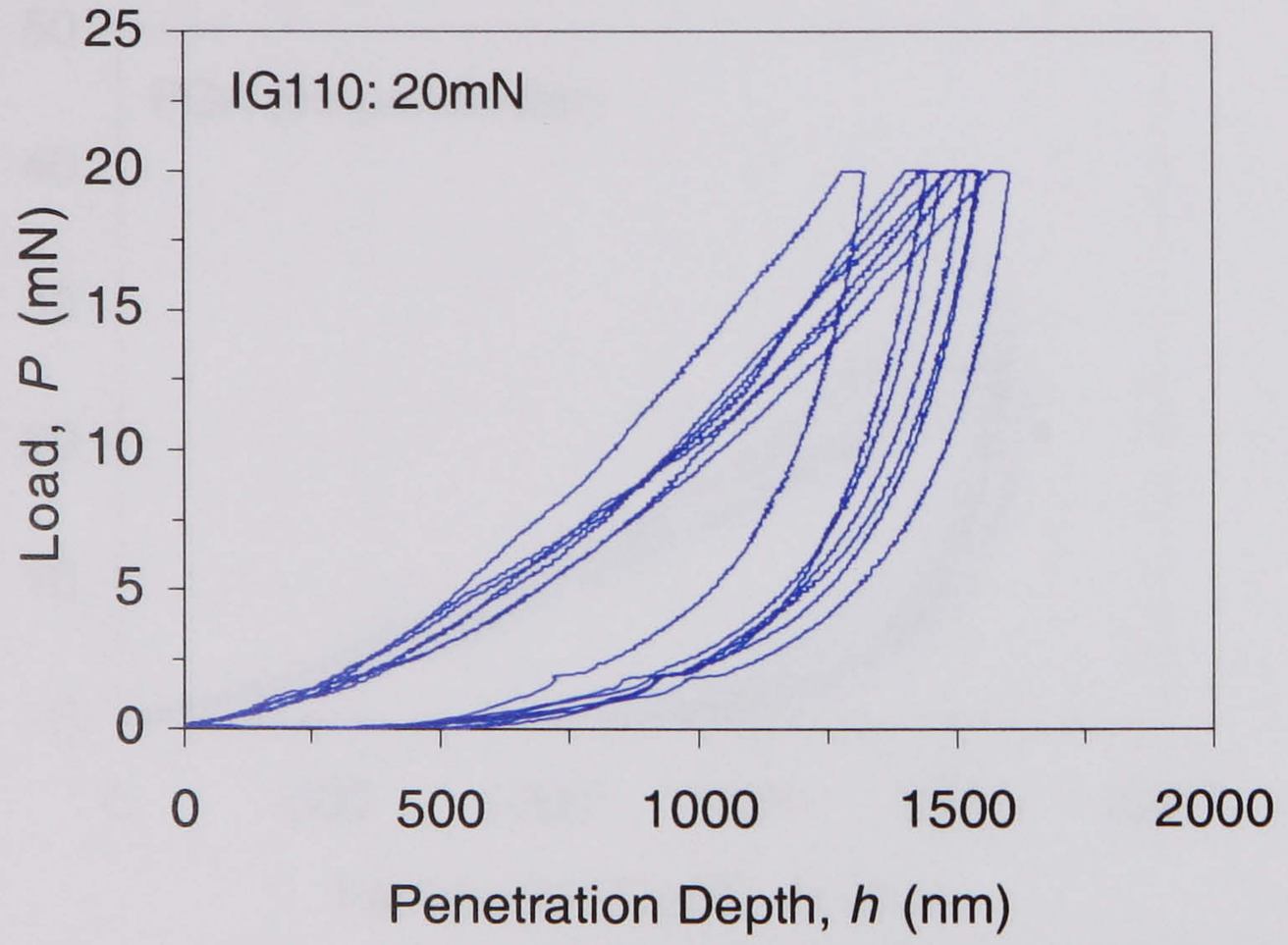

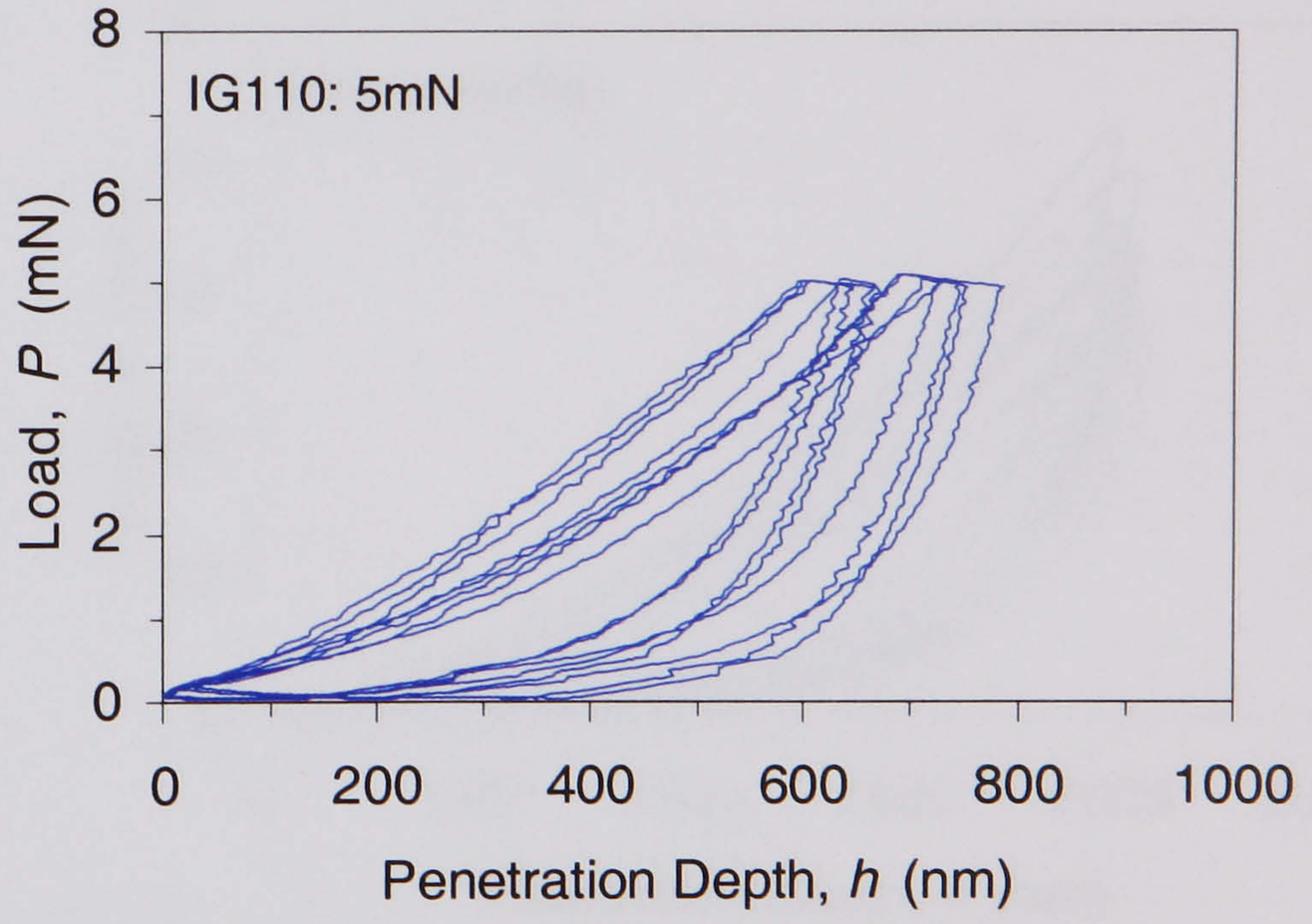

Figure 10.5. Load-displacement behaviour at different loads: IG110 graphite.

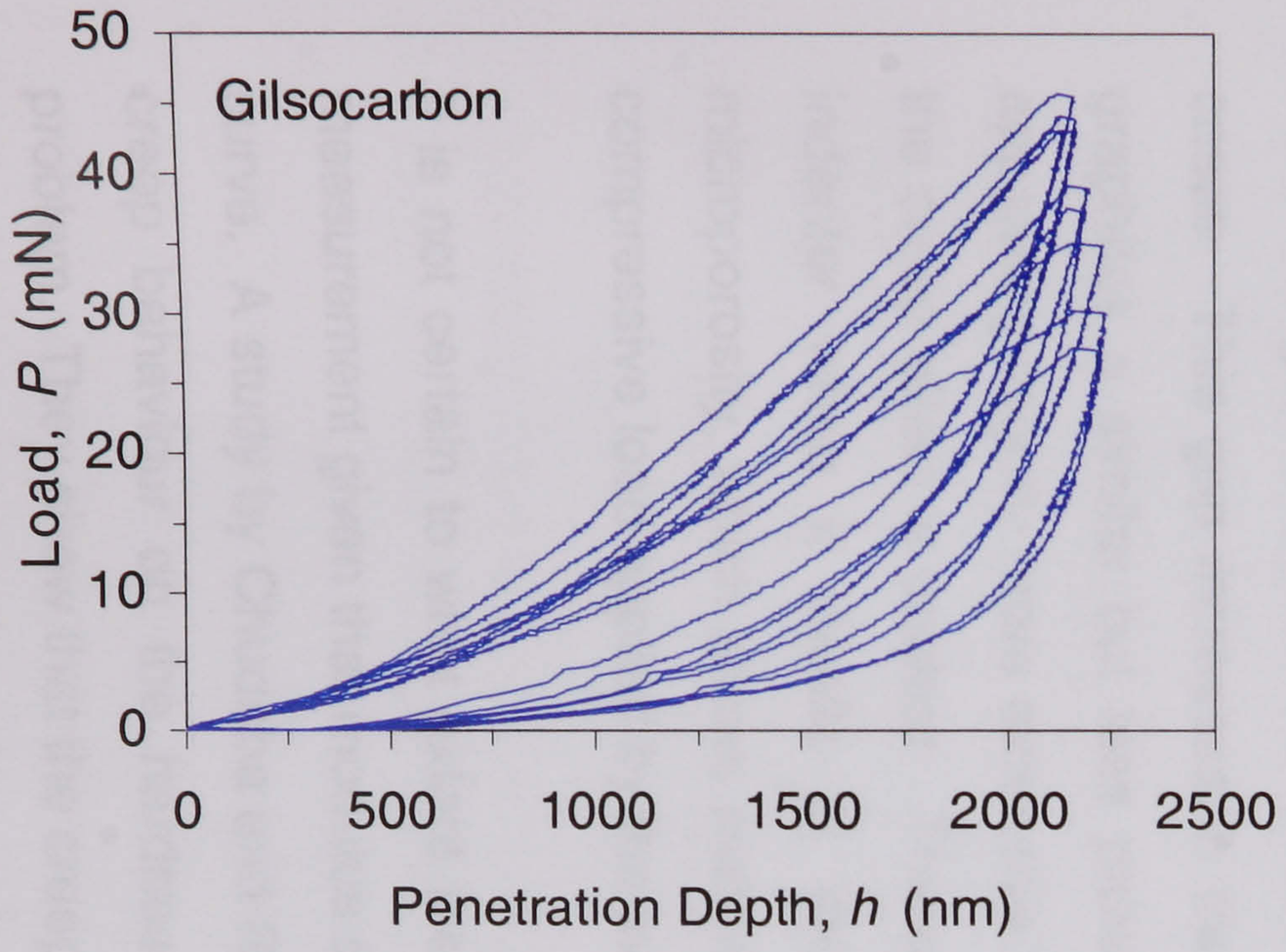

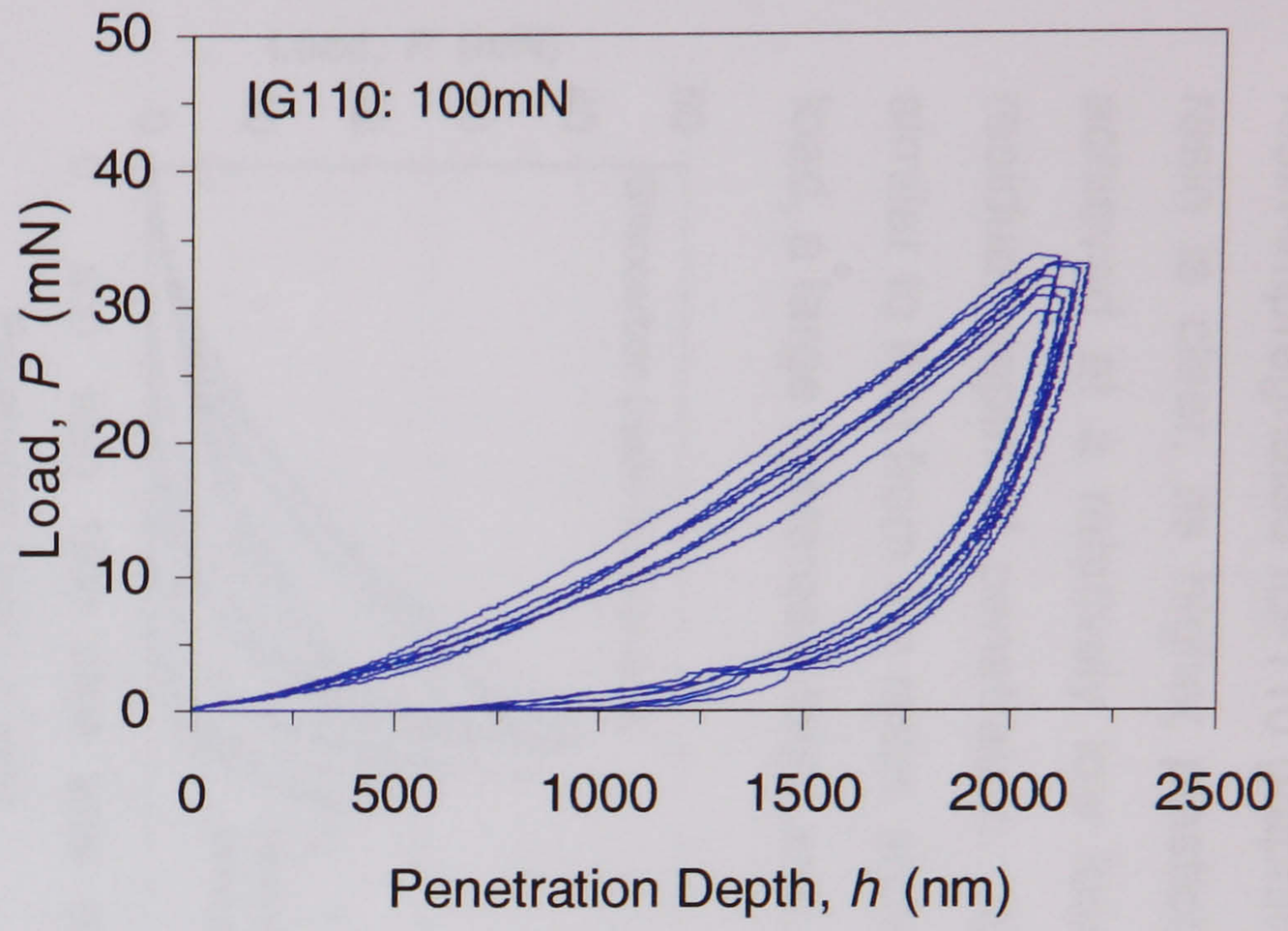

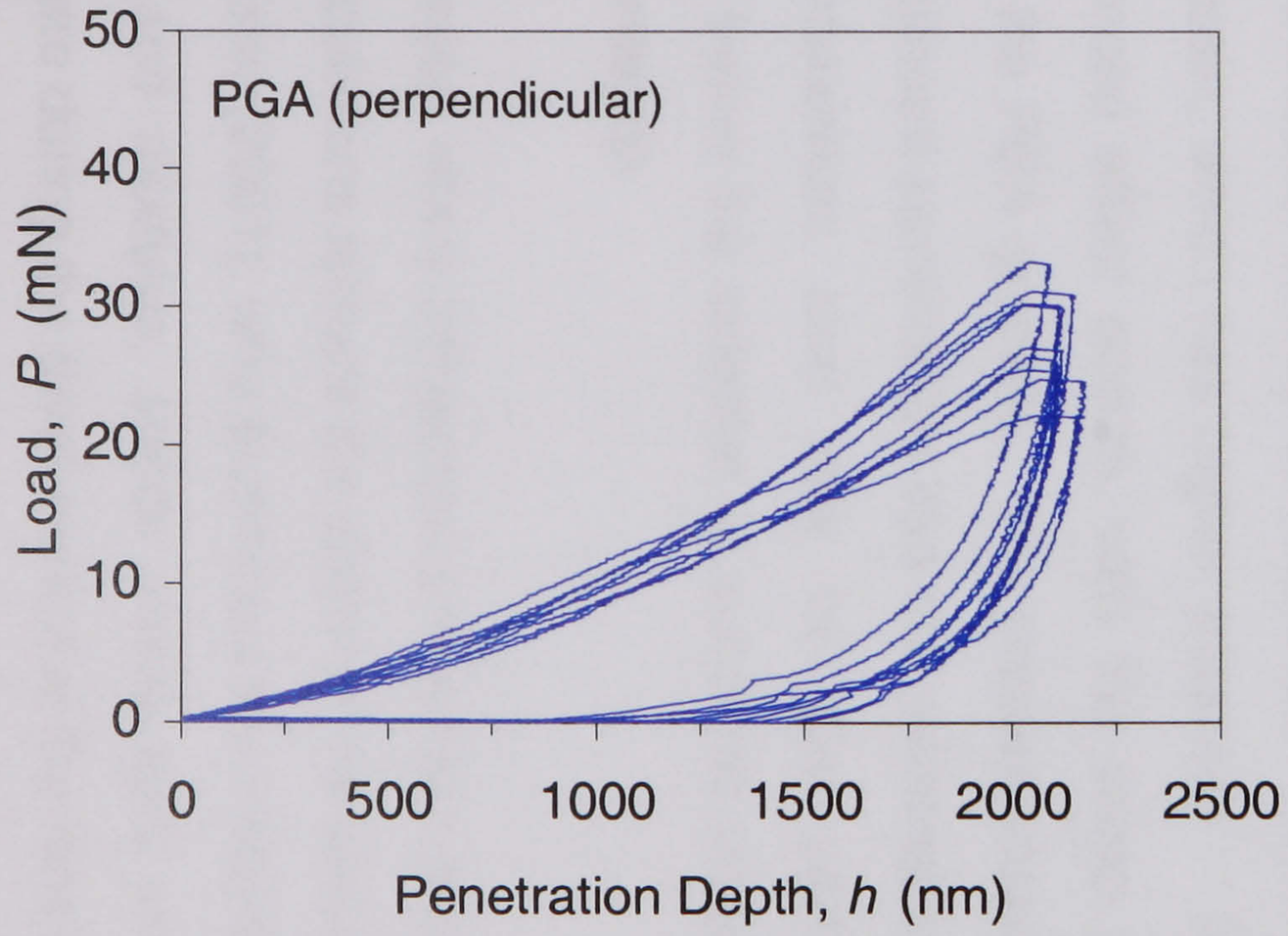

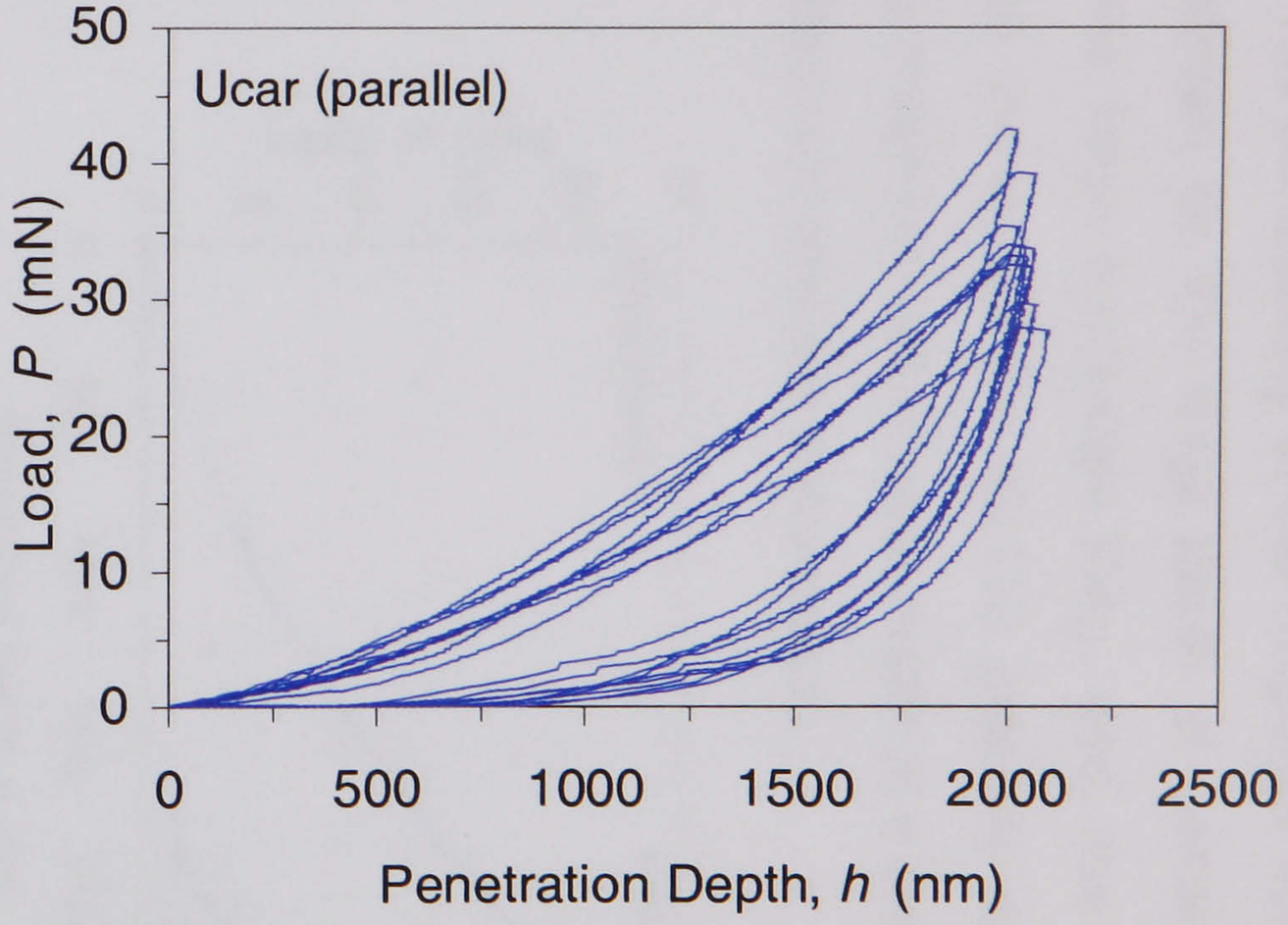

Figure 10.6. Comparison of load-displacement curves of the different nuclear graphite materials at 100 mN load.

To show the influence of the resin in resin-impregnated graphite, the response from Epofix resin is shown in Figure 10.7, along with the response obtained on resin-impregnated IG-110 graphite. The consistency of the response from the resin is clear, its higher plasticity shown by the large depth of penetration achieved at a relatively low load, the large hysteresis loop, and, the large residual depth of penetration. Some curves for the IG-110 graphite appear similar to that from the resin, showing maximum penetration depth at a reduced load, a large hysteresis loop, and, substantial residual deformation.

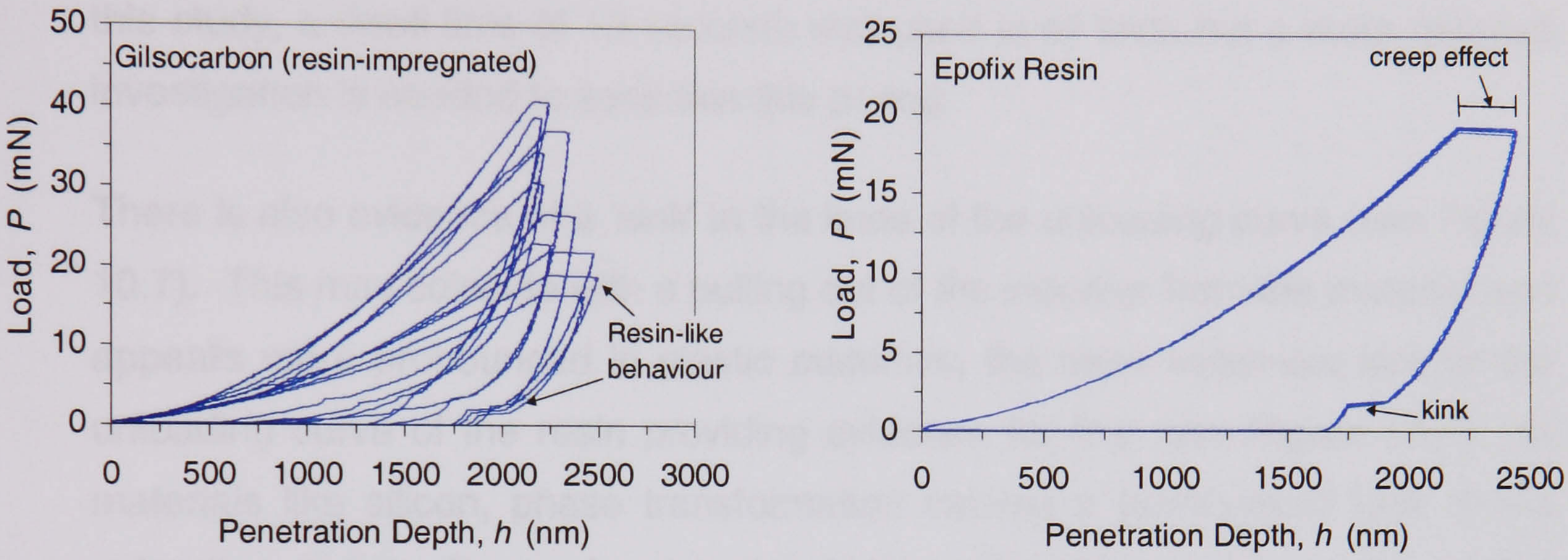

Figure 10.7. Comparison of response from Epofix resin and resin-impregnated IG110 graphite. Note the similarity between some of the IG110 curves and that of the resin.

There is also a time-dependent deformation effect, analogous to creep, evident from the gap between the load and unload curves at maximum load, in all cases. This gap increases in the resin, which has higher plasticity. In the graphites a similar but less pronounced effect occurs, with the creep effect appearing slightly more extensive in the PGA graphite. The precise reason for the creep effect is unclear. The continued penetration into the material by the indenter when it dwells at the maximum load may be due partly to microporosity, which allows material below the indenter to succumb under the compressive load applied by the indenter tip.

It is not certain to what extent the creep effect influences the elastic modulus measurement given that modulus calculations require the slope of the unloading curve. A study by Chudoba and Richter (2001), who examined the influence of creep behaviour on the hardness and modulus, sheds some light on this problem. They show that the creep rate during the dwell period at the maximum load depends on both the material and test conditions, particularly the load rate.

The increment in the maximum penetration depth due to creep can cause >20% error in the hardness value. The unloading curve also develops a bowed shape when the dwell period is too short causing an abnormally high unloading stiffness to be recorded the result being an anomalous, high elastic modulus. Chudoba and Richter (2001) therefore recommend that the dwell period be ascertained relative to the material being tested to obtain reliable data. They caution that routine nano-indentation testing often involves the use of a dwell time of 10 seconds or less to shorten test times but this may be too short. In this study, a dwell time of 15 seconds was used in all tests but a more detailed investigation is needed to ascertain this period.

There is also evidence of a 'kink' in the knee of the unloading curve (see Figure 10.7). This may coincide with a pulling out of the indenter from the material and appears more pronounced in plastic materials, the more extensive kink in the unloading curve of the resin providing evidence for this (see Figure 10.7). In materials like silicon, phase transformation causes a pronounced kink in the unloading curve. It may be that the 'kink' in the unloading response of the graphites is related to the shear transformation of the graphite structure. However, this seems unlikely given the extensive 'kink' observed in the resin where it is doubtful that a structural transformation may be responsible.

10.4.2. Calculation of the Elastic Modulus and Hardness

The proprietary software for the Nano-Test 300 allows the elastic modulus and hardness (in GPa) to be calculated, amongst other options. Two models are used in calculating these parameters, that of Doerner and Nix (1986), and, the more popular model of Oliver and Pharr (1992). The models differ mainly in the way the slope of the unloading curve, i.e. the stiffness *S,* and, the projected area of contact are calculated. Whilst Doerner and Nix (1986) assume the unloading slope is linear Oliver and Pharr (1992) consider the unloading slope to be non-linear, the latter being the more realistic situation.

The Nano-Test 300 software performs the linear or non-linear fit to the unloading curves that defines the stiffness, *S*, in Equation [10.2]. About 80% of the unloading curve are used in the curve fit. The last 20% is discarded, one reason being the uncertainty in the displacement data at low load and displacement depth. In calculating the projected area of contact, A_a, Oliver and

Pharr's model (1992) requires a value for the geometric factor ε, which varies with the type of indenter. For the Berkovich indenter, a value of $\varepsilon = 0.75$ is used, which according to their model applies for an indenter whose shape can be defined by a paraboloid of revolution. The triangular Berkovich indenter is thus assumed to have a rounded profile in this model. The hardness (or mean indentation pressure, H) is calculated from the ratio of the maximum load (P_{max}) and projected area of contact (A_a) as expressed by Equation [10.3].

To compare the elastic modulus of the graphites obtained by nano-indentation, the indenter was programmed to perform a series of indentations in a straight line using an increasingly higher load after every ten indentations. Indentations were spaced 100μm apart in order to cover a relatively large area of the material thereby obtaining a representative measure of the structural variation. The range of loads applied was 10, 50, and, 100mN. The average elastic modulus obtained for the nuclear graphites are shown in Table 10.1, and are compared against the bulk, flexural modulus values.

Whilst the average modulus values appear to approach the bulk modulus values the results must be viewed with some caution. The data obtained by nano-indentation do provide a qualitative comparison between the graphites. However, the data are not consistent given that the indentation moduli are not as distinguishing as the flexural modulus values. The nano-indentation method manages to sense a difference in the modulus of PGA graphite for indentation direction parallel and perpendicular to the extrusion direction. However, it fails to reveal the directional nature of the elastic modulus in the UcarC graphite.

Although the indentation moduli seem to correlate well with the bulk moduli, the similarity in the average values for oxidised and non-oxidised materials is a strong indication that the method is susceptible to localised microstructural inhomogeneities, e.g. porosity. Whereas, the flexural modulus values show a substantial drop following oxidation, the nano-indentation values do not reduce significantly following oxidation. Only the IG-110 graphite showed a slight reduction in the indentation modulus after 5% oxidation. This result is not surprising given that the technique performs measurements on regions smaller than the grains.

Table 10.1. Average elastic modulus and hardness values obtained by nano-indentation.

Grade	Flexural Modulus (GPa)			Average Elastic Modulus (E) & Hardness (H) by Nano-indentation (GPa)						
	Non-Oxidised	Oxidised		Load (mN)	Non-Oxidised		Oxidised			
		1% wt. loss	5% wt. loss				1% wt. loss		5% wt. loss	
	E_f	E_f	E_f	P_{max}	E	H	E	H	E	H
PGA (prll)	-	-	-	10	6.5 ± 1.1	0.23 ± 0.02	-	-	-	-
				50	6.6 ± 0.6	0.20 ± 0.02	-	-	-	-
				100	5.6 ± 0.9	0.21 ± 0.03	-	-	-	-
PGA (perp)	-	-	-	10	9.7 ± 1.8	0.57 ± 0.14	-	-	-	-
				50	7.9 ± 1.5	0.30 ± 0.05	-	-	-	-
				100	7.8 ± 1.7	0.25 ± 0.04	-	-	-	-
Gilso-carbon	10.5 ± 0.1	9.9	9.5	10	10.3 ± 0.4	0.47 ± 0.05	11.0 ± 0.5	0.56 ± 0.05	10.9 ± 0.7	0.46 ± 0.06
				50	8.5 ± 0.3	0.34 ± 0.01	9.6 ± 0.5	0.41 ± 0.03	8.8 ± 0.5	0.33 ± 0.02
				100	8.9 ± 0.4	0.39 ± 0.02	9.4 ± 0.5	0.47 ± 0.05	8.3 ± 0.5	0.30 ± 0.03
IG-110	7.4 ± 0.1	5.8	3.1	10	8.6 ± 0.5	0.34 ± 0.04	8.1 ± 0.8	0.35 ± 0.05	7.6 ± 0.6	0.40 ± 0.04
				50	7.5 ± 0.5	0.29 ± 0.02	6.2 ± 0.4	0.25 ± 0.02	6.4 ± 0.7	0.25 ± 0.02
				100	8.0 ± 0.5	0.33 ± 0.03	7.3 ± 0.4	0.29 ± 0.02	7.9 ± 0.6	0.35 ± 0.03
UcarC (prll)	10.7 ± 0.3	6.3	6.0	10	9.8 ± 0.7	0.47 ± 0.08	11.1 ± 0.6	0.59 ± 0.08	11.3 ± 1.5	0.74 ± 0.19
				50	9.1 ± 0.8	0.43 ± 0.07	9.7 ± 0.6	0.47 ± 0.04	9.5 ± 0.7	0.44 ± 0.09
				100	10.0 ± 0.9	0.54 ± 0.10	9.1 ± 0.6	0.46 ± 0.04	9.4 ± 0.7	0.42 ± 0.05
UcarC (perp)	9.3 ± 0.2	8.4	7.1	10	9.9 ± 0.7	0.48 ± 0.04	9.6 ± 1.0	0.57 ± 0.08	9.2 ± 1.2	0.61 ± 0.13
				50	9.6 ± 0.6	0.42 ± 0.03	8.4 ± 1.0	0.40 ± 0.05	8.5 ± 1.1	0.38 ± 0.05
				100	9.7 ± 0.5	0.42 ± 0.02	9.2 ± 0.8	0.38 ± 0.05	8.5 ± 1.1	0.43 ± 0.05
Epofix Resin	-	-	-	50	4.82 ± 0.0	0.16 ± 0.00	-	-	-	-

Note: PGA graphite was not oxidised due to lack of test material.

It is arguable that, the average indentation moduli of the different graphites are actually similar, within the limit of the standard deviations, with the exception of PGA graphite. This again suggests that the measurement is influenced by the volume of surface material around the indentation site rather than the bulk. Both the modulus and hardness appear higher at lower load, implying that there is some dependence on the maximum load applied. A smaller volume of material with a smaller defect population must be sampled at lower loads so that a higher modulus is obtained.

It is also remarkable that the standard deviations are generally small given the scatter observed in the load-unload response of the graphites. This implies that there is a consistency in the unloading stiffness, which may be related to the fact that, the indenter responds to the compliance of a volume of material around the indentation site rather than the bulk compliance. Hence, the degree of graphitisation, the extent of microporosity and microcracks, and, the orientation of filler grains to the indenter travel, must influence the measurement (see Figure 10.8, Section 10.4.3). Grain size would also affect the compliance of the volume of material around the indentation site.

The hardness values are less remarkable with some indication that a higher hardness corresponds with higher stiffness. Again, PGA graphite is the exception showing the lowest hardness. The factors that control the hardness are not clear but may be related to the type of filler coke that is used since the UcarC graphite (coal tar pitch-coke) shows the highest hardness. Overall, the hardness values are rather high, suggesting that there may be densification of surface material caused by sample preparation, as noted by Kanari et al (1997). The homogeneity of the Epofix resin is clear from the zero standard deviation for this material.

A statistical analysis of a large number of measurements could provide more distinguishing results but it is doubtful whether such an analysis could give as clear a distinction as the bulk modulus values. Unlike homogeneous materials where the small volume of material sampled around the indentation may be representative of the bulk, non-homogeneity in the polycrystalline graphite structure appears to prevent such a representation from being achieved.

10.4.3. Influence of the Microstructure on the Indentation Modulus

Figure 10.8 presents an idealised, conceptual view of the microstructural features that are thought to influence the elastic modulus and hardness measured by nano-indentation.

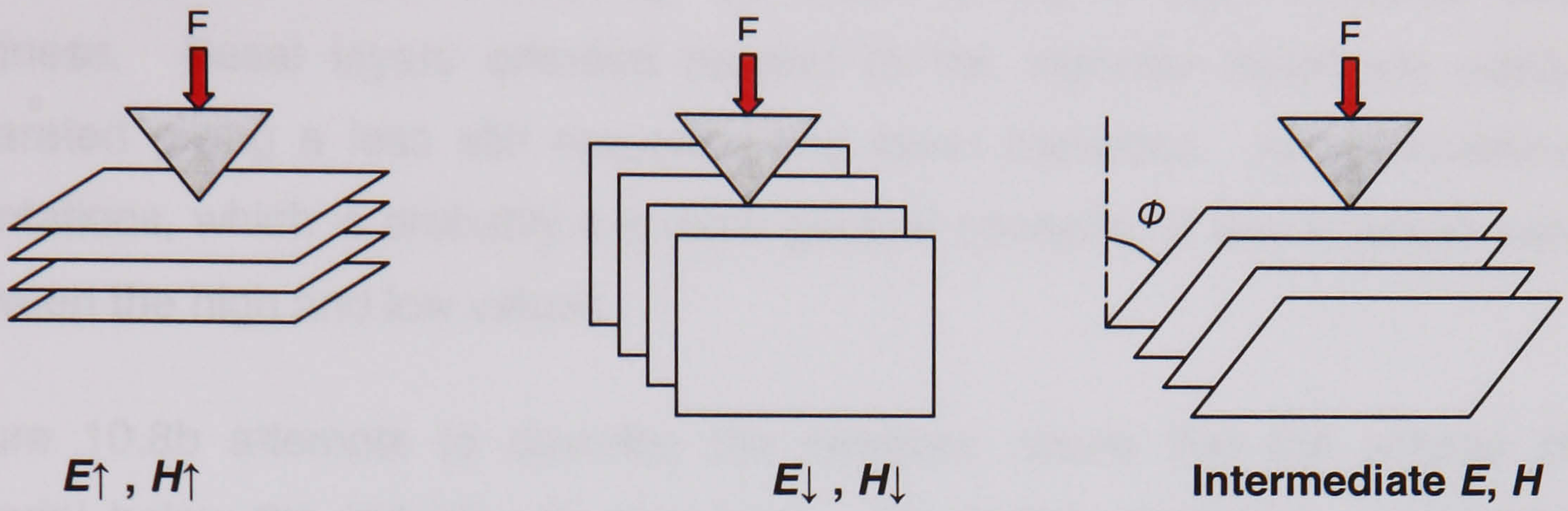

a. General orientation of basal planes relative to indentation direction

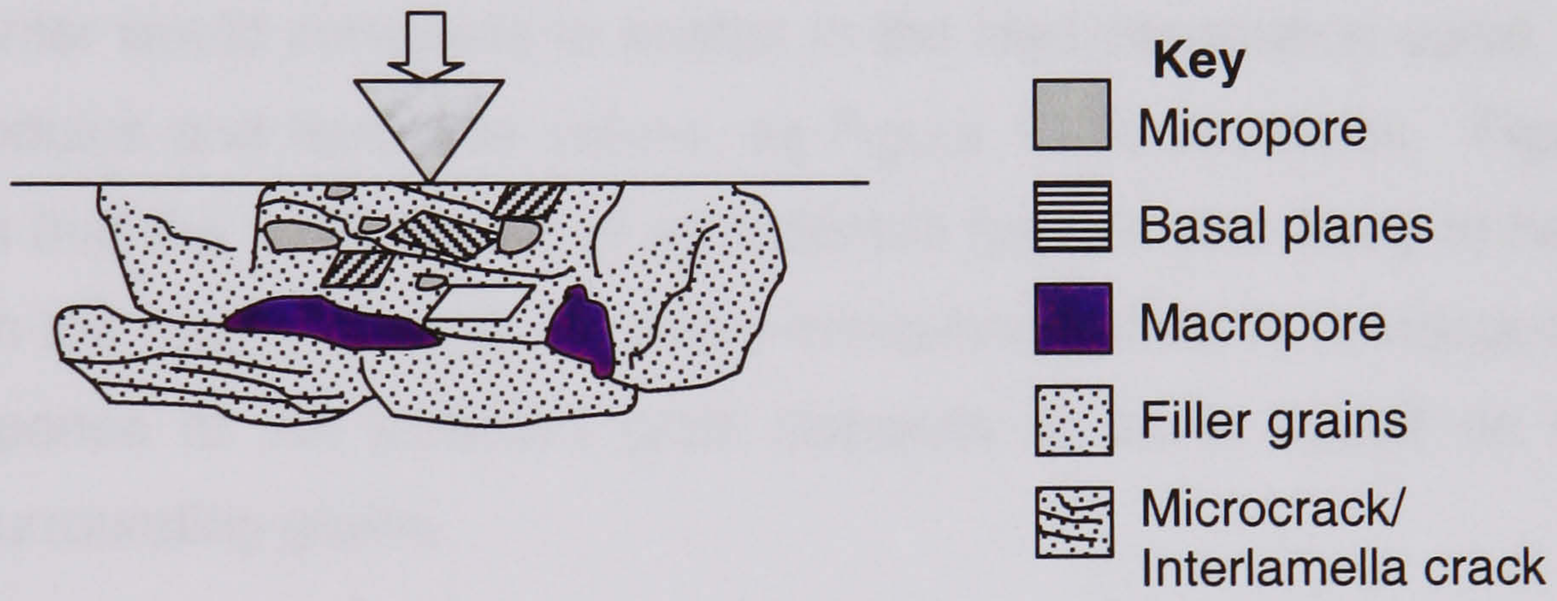

b. Microstructural features

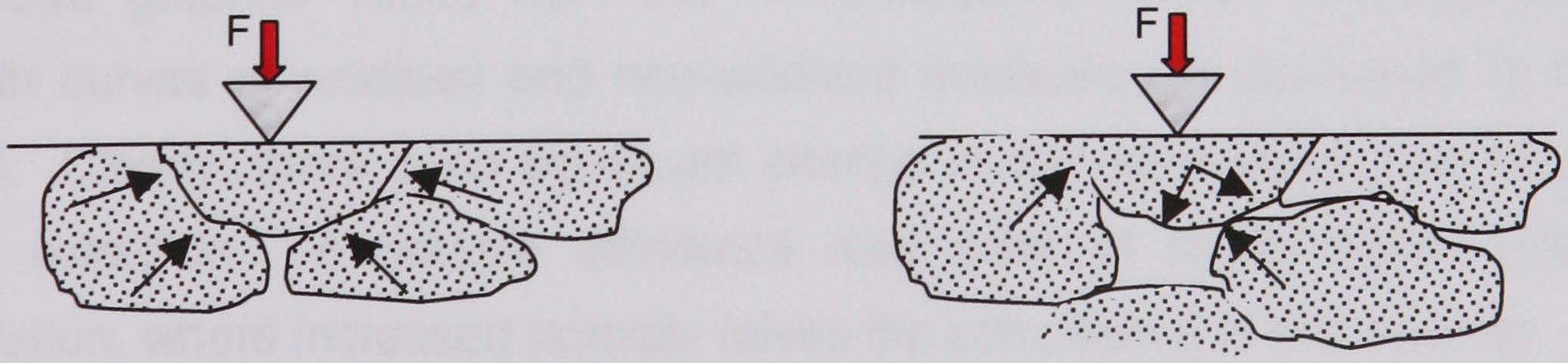

c. Micro-compliance of the volume of material around indentation site

Figure 10.8. Conceptual view of the factors that influence the indentation modulus.

Essentially, the nature of the volume of material around the indentation site is seen to play a significant role in determining the final modulus (*E*) and hardness (*H*) that is obtained. Figure 10.8a indicates how the general orientation of the crystallite population below the indenter tip may influence the measurement. For basal plane orientation perpendicular to the indenter travel, the *a*-axis tensile modulus would effectively dominate, giving a high modulus and hardness. Basal layers oriented parallel to the indenter travel are easily separated giving a less stiff response and lower hardness. At intermediate orientations, which is probably the more general scenario, *E* and *H* would vary between the high and low values.

Figure 10.8b attempts to describe the complex nature that the volume of material below the indenter tip may have. Crystallite orientation, micropores and mesopores, microcracks and interlamellar cracks combine to have a complex influence on the measured value. In general, the defect structure below the indenter would contribute to scatter in the load-penetration curve, as well as the modulus and hardness values, as Figure 10.8b illustrates. Figure 10.8c indicates that the 'compliance' of an indented grain is also likely to have an influence on the measurements. A micro-compliance effect is envisaged in which the response of the indented grain depends to some extent on the support from surrounding grains.

10.4.4. Load-penetration Depth Response of Oxidised Graphites

It was important to assess whether the nano-indentation behaviour of the oxidised graphite varied from the non-oxidised material. Load-penetration depth curves of oxidised and non-oxidised materials are compared in Figure 10.9. Clearly, there is no significant change in the nano-indentation response with oxidation. A notable difference may arise at much higher levels of oxidation, where increased porosity raises the compliance of the material.

10.5. Comparing the methods of 'Oliver & Pharr' and 'Doerner & Nix'

There was some interest in comparing the indentation modulus obtained using the methods of Oliver and Pharr (1992) and Doerner and Nix (1986). As explained earlier, the former method derives the stiffness using a non-linear fit to the unloading curve whereas the latter method assumes a linear fit.

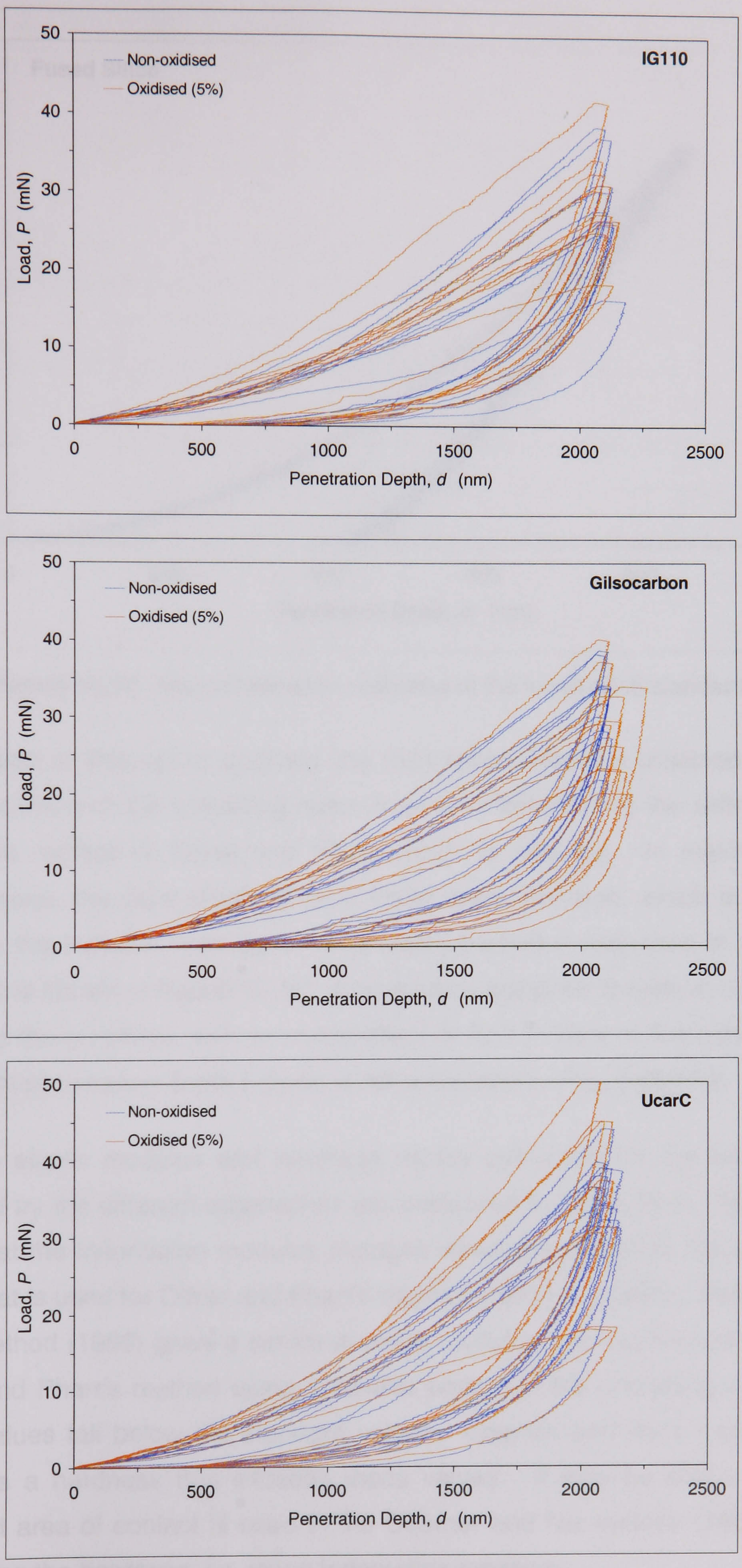

Figure 10.9. Nano-indentation behaviour in oxidised and non-oxidised graphites.

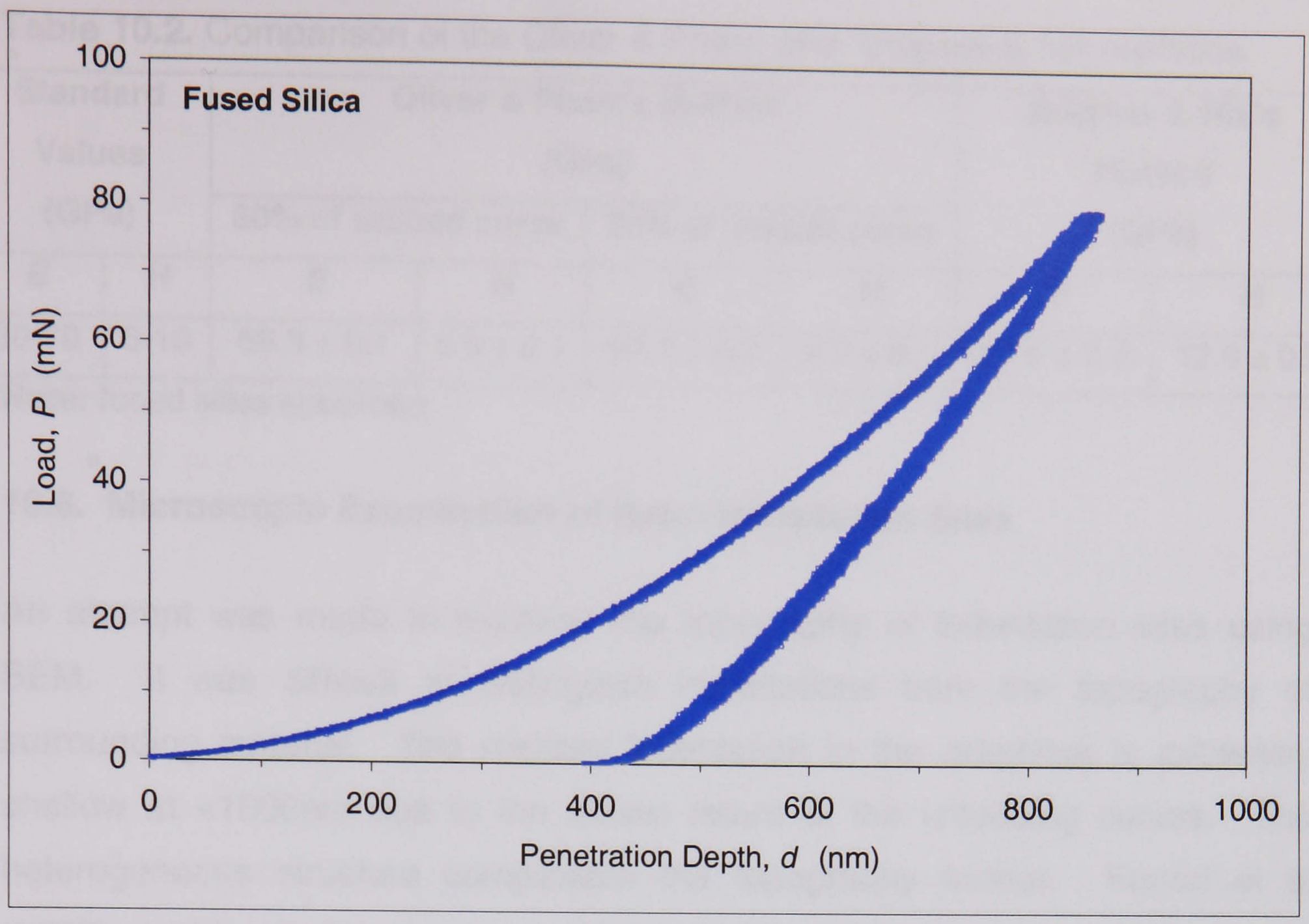

Figure 10.10. Nano-indentation response of the fused silica standard.

It was also of interest to evaluate the indentation modulus obtained when a smaller portion of the unloading curve is used in determining the stiffness (S), when the method of Oliver and Pharr (1992) is adopted. In making these comparisons, the data obtained on a fused silica standard, which is used to calibrate the indenter, was used. The load-penetration response of the silica standard is shown in Figure 10.10. A consistent response is seen in contrast to that from the graphites, with no creep effect or kink evident in the curves. The maximum penetration depth (~2μm) is not exceeded at P_{max} (~80mN).

Average elastic modulus and hardness values calculated for the fused silica standard by the different approaches are compared in Table 10.2. The results show that the indentation modulus changes when the portion of the unloading curve that is used for Oliver and Pharr's method (1992) is smaller. Doerner and Nix's method (1986) gives a similar average modulus value to that obtained by Oliver and Pharr's method using a smaller portion of the unloading curve but, these values fall below the standard values. Doerner and Nix's method also produces a hardness that exceeds these values. It may be that a smaller, apparent area of contact is used in the Doerner and Nix method (1986) when calculating the hardness, i.e. mean indentation pressure.

Table 10.2. Comparison of the Oliver & Pharr, and, Doerner & Nix methods.

Standard Values (GPa)		Oliver & Pharr's Method (GPa)				Doerner & Nix's Method (GPa)	
		80% of unload curve		25% of unload curve			
E	***H***	***E***	***H***	***E***	***H***	***E***	***H***
68-70	8-10	69.3 ± 0.1	8.9 ± 0.1	67.1 ± 0.2	9.3 ± 0.1	67.6 ± 0.0	12.0 ± 0.2

Note: fused silica specimen

10.6. Microscopic Examination of Nano-Indentation Sites

An attempt was made to examine the topography of indentation sites using SEM. It was difficult to distinguish indentations from the topography of surrounding material. The residual indentation in the graphites is extremely shallow at <1000nm due to the elastic return of the unloading curves. The heterogeneous structure complicates the topography further. Kanari et al (1997) could not detect nano-indentations in IG-11 graphite. Using micro-hardness indentation and topographic SEM, they noted significant elastic recovery in micro-indentation sites. Since the Nano-Test 300 was not equipped with a microscope, the indentation sites could not be located precisely. Indentation sites were traced in the SEM by making a series of indentations on resin-mounted specimens, starting in the resin, near the periphery of the graphite sample. The resin leaves a sizeable impression making it easy to trace the indentations travel. Figure 10.11 shows a line of indentations in the resin near the resin-graphite (IG110) boundary. Residual indentations in the resin are clear however, no indications are clear in the graphite surface.

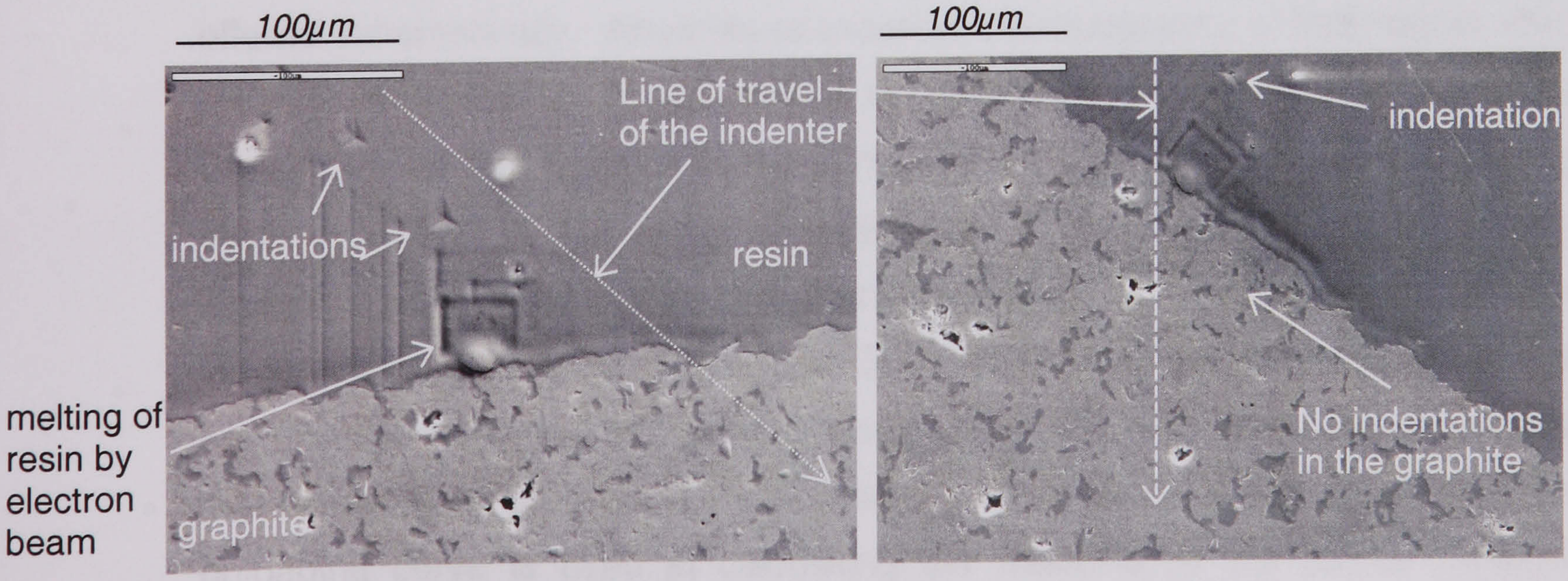

Figure 10.11. SEM images of the residual indentations.

10.7. SUMMARY

The theoretical background to the nano-indentation technique is given and the operation of the Nano-Test 300 machine outlined. A brief review is made of the limited nano-indentation tests done on carbon and graphite materials, including the theoretical models used in determining the elastic modulus. Important assumptions and shortcomings made in applying the technique, regarding indenter geometry for instance, are highlighted.

All the nuclear graphites displayed a similar anelastic, load-penetration depth response in that the unloading curve returns almost completely to the origin with significant hysteresis in the load-unload cycle. The main variation in the response between these materials was found in the extent of residual penetration depth after unloading, the amount of hysteresis, and, the reproducibility of the load-unload response. PGA graphite had the largest residual penetration depth and hysteresis loop with IG110 showing the most consistency in its load-unload curves.

The calculated average, elastic modulus values for the graphites were not as distinguishing as the bulk, flexural modulus in revealing differences between the materials. It was also found that the method failed to sense the bulk modulus changes that accompany oxidation or extrusion. It was therefore deduced that the method is susceptible to localised microstructural inhomogeneity, which causes scatter in the modulus measurements. The load-unload behaviour of the oxidised materials did also not differ from that of the non-oxidised materials.

Some explanation of the structural features that are thought to cause scatter is offered schematically. Attempts to examine the topography of indentation sites proved unsuccessful. It was difficult to resolve indentations from the general topography of the graphite surface mainly because of the extensive elastic recovery shown by the graphite material during unloading. Two well-known models used in calculating the elastic modulus and hardness from nano-indentation data, i.e. the methods of Oliver and Pharr (1992) and Doerner and Nix (1986), are compared using a fused silica standard. The results indicate that the methods produce similar modulus results when a smaller portion of the unloading curve is used in calculating the modulus by the former method. However, the latter method produced average values that fell outside those specified for the standard specimen.

CHAPTER 11

DISCUSSION & CONCLUDING REMARKS

A characterisation study of the nuclear graphites showed that the microstructure of the materials differed significantly. A major difference was the size and shape of the filler grains and the pores. Both the filler grains and pores combined to play an important role in controlling the crack growth resistance of the materials. Large pores tended to blunt the crack whilst pores located at the binder-filler interface made it easier for the crack to travel along this interface. The bonding between the filler and binder appeared to also dictate the path taken by the crack.

The degree of crystallinity, of which there was little difference between the candidate materials, made no obvious contribution to the observed differences in *R*-curve behaviour. The electrical resistivity of the finer grained IG110 was significantly higher, primarily due to its small grain size. Despite its fine grain size, IG110 displayed a markedly lower elastic modulus than the coarser grades. This may be due to the network of fine pores in IG110, particularly the pores along the filler-binder interface, which lower the stiffness of the matrix in which the filler grains are supported.

Impregnation increased the density of UcarC graphite and reduced its open pore volume, the latter appearing to have a dramatic effect in enhancing the oxidation resistance of the material. Both the elastic modulus and crack growth resistance of Gilsocarbon graphite showed little change even at 5% burn off. It seems likely that low levels of oxidation are confined in the binder surrounding the large filler grains in Gilsocarbon, with the binder-filler interface being little affected. Hence, the large filler grains remain supported in a relatively stiff matrix. This results in little change in the elastic modulus, with continued crack deflection around the grains maintaining the crack growth resistance.

Application of the potential drop method exposed a serious shortcoming of the technique when applied to material with rising *R*-curve behaviour. Clearly, crack face bridging places a serious limitation on the method when it is used to measure crack length. Developmental work on the potential drop method

applied in this study also showed that the method is not as straightforward as one may expect. Complications arise in trying to achieve meaningful and accurate experimental calibration data, with theoretical calibrations having limited applicability to specific test geometry and crack length ranges.

The attractiveness of the potential drop method is further diminished when compared against the simplicity and effectiveness of the optical method and the theoretical compliance technique. The latter technique proved the most simple, but is dependent to some extent on the elastic modulus value used in calculating the effective crack length. Whilst the elastic modulus of many materials is easily measured, this is not so with many heterogeneous materials, especially composites. Another complication with the compliance method is the change in elastic modulus with oxidation. It would be difficult to ascertain a meaningful elastic modulus value for oxidised graphite unless the material is uniformly oxidised.

The potential drop technique may nonetheless have particular merit in being able to provide a measure of the apparent bridging zone length. This could allow the unique capability of comparing bridging zone lengths in different materials. It was mentioned in Section 7.5 that a preliminary study indicated that there is some correlation between the bridging zone length calculated by the weight function method (Fett & Munz, 1998) and that measured by the potential drop technique (Ramos, 2002). This study revealed that the potential drop method might provide a useful means of studying the development of the bridging zone during the course of crack growth.

The results surprisingly show that the apparent bridging zone does not attain a so-called 'steady-state' length but rather grows as the crack extends to a maximum value. This provides further evidence to support the hypothesis of a crack bridging toughening mechanism, in contrast to the less convincing hypothesis that a microcracked, frontal process zone causes rising *R*-curve behaviour. It is surprising though, that this apparent bridging zone length is similar in all the graphites, regardless of their grain size. It seems reasonable to expect a smaller crack opening displacement in a material with a larger grain size, which in turn should result in a shorter bridging zone length. However, the

results of this study are not definitive enough to confirm this and it may be necessary to investigate whether the potential drop technique is capable of revealing such differences. It would be interesting to compare physical COD measurements with apparent bridging zone lengths in different materials to evaluate this possibility.

It could also be noted throughout this study, how the *R*-curve profile was influenced by various factors such as the specimen type, the crack length measurement technique, and, the notch configuration. An attempt was made to clarify the complexities involved in using the chevron-notched configuration for *R*-curve derivation. More importantly, it was shown how strongly the R-curve obtained using the chevron-notch configuration is influenced by its shape function. This makes it difficult to ascertain the influence of any crack growth, resistance mechanisms on the *R*-curve obtained using this notch type. Apart from ranking different materials, this notch configuration is felt to have limited application for studying the development of bridging effects in relation to the *R*-curve profile.

An investigation of the structural characteristics of the nuclear graphites using nanoindentation produced some interesting findings. The load-penetration depth behaviour of the graphites was similar to that reported in other studies on carbon and graphite materials. However, the occurrence of a creep effect at the maximum load appears unreported and may offer an interesting means of studying creep effects in carbon materials. Expectedly, the indentation modulus values were not as definitive as the bulk modulus measurements in distinguishing the different nuclear graphites. Clearly, the extremely small volume of material sampled by the technique is non-representative of the bulk. Even when the material was oxidised, this remained the case. This may nonetheless allow a means of measuring the properties of small elements of the material, which could then be related to the bulk, an important aspect for modelling the bulk material properties.

CHAPTER 12

FUTURE RESEARCH AREAS

Several research areas are thought to be potentially useful in future research work. These future research areas are outlined below.

R-curve Behaviour

1. Simultaneous measurement of the crack opening displacement (COD) and the apparent bridging zone length (l_{br}) in materials of different grain size may reveal whether the COD in coarser grained materials is larger than in fine grained material. This would also indicate whether l_{br} is shorter in coarser grained material thus confirming some of the concepts discussed here.

2. Devising a method to measure l_{br} optically, or in the SEM, with simultaneous measurement of l_{br} using the potential drop method. This would confirm the accuracy of the l_{br} values obtained by potential drop. A difficulty with this approach however, would be the optical measurement of the l_{br}. It may be difficult to define the bridging zone optically.

Nano-Indentation Tests

1. It may be instructive to perform indentations around a crack in a fracture specimen to establish whether there exists a zone of reduced modulus. This would require indentation equipment with a stage microscope so that the positions of indentations are made with some degree of accuracy. It may be easier to use a homogeneous, fine-grained material, such as alumina to avoid the susceptibility of the method to structural inhomogeneities.

2. With a stage microscope, it may be possible to measure the properties of localised regions, thus helping to identify regions of varying elastic modulus. Properties of localised regions could be used to model the bulk.

3. Evaluating the nano-indentation response of irradiated graphites may afford the opportunity to monitor elastic modulus changes with irradiation. It also offers the possibility of studying material property changes with irradiation.

CHAPTER 13: BIBLIOGRAPHY & REFERENCES

Ahlborn K, Chou T, Kagawa Y, Okura A (1993). Influence of Heat Treatment Temperature on the Crack-Growth Resistance of a Fine-grained Carbon. Carbon **31 (1)**, pp. 205-212.

Akatsu T, Lu S, Appleyard S P, Rand B (2000). Nanoindetation Behaviour of Mesophase-derived Carbon and Graphite Materials. Abstracts (Vol. I), 1st World Conference on Carbon, Berlin, Germany.

Aladekomo J B, Bragg R H. Structural Transformation induced in Graphite by Grinding: Analysis of 002 XRD Line Profiles. Carbon **28 (6)**, pp. 897-906.

Allard B, Rouby D, Fantozzi G (1991). Fracture Behaviour of Carbon Materials. Carbon **29 (3)**, pp. 457-468.

Alexander L (1950). Geometrical Factors affecting Contours of X-ray Spectrometer Maxima. Journal of Applied Physics **(21)**, pp. 126-136.

Alexander L E, Klug H P (1950). Determination of Crystallite Size with the X-Ray Spectrometer. Journal of Applied Physics **(21)**, pp. 137-142.

Alexander L E, Klug H P (1974). XRD Procedures for Polycrystalline and Amorphous Materials (2nd Ed). John Wiley & Sons, New York.

Arulrajah A A (2002). Fracture Characterisation of C/C Composites. PhD Thesis, Department of Materials, University of Leeds, UK.

ASTM Standard C611-1984, Electrical Resistivity of Manufactured Carbon and Graphite Articles at Room Temperature.

ASTM Standard E399-1990, Standard Test Method for Plane-Strain Fracture Toughness of Metallic Materials.

ASTM Standard E647-91, Measurement of Fatigue Crack Growth Rates.

ASTM Standard C1421-1999, Determination of Fracture Toughness of Advanced Ceramics at Ambient Temperature.

Austen I M (1980). Measurement of Crack Length and Data in Corrosion Fatigue. In *Measurement of Crack Length and Shape during Fracture and Fatigue.* Ed. Beevers C J, pp. 164-189, Chameleon Press, London.

British Standard BS 7134 (1989): Section 1.2: Testing of Engineering Ceramics: Methods for determination of density and porosity.

Babu V S, Seehra M S (1996). Modelling of Disorder and XRD in Coal-based Graphitic Carbons. Carbon **34 (10)**, pp. 1259-1265.

Bacon G E (1956). A Method for determining the Degree of Orientation of Graphite. Journal of Applied Chemistry **(6)**, pp. 477-481.

Bacon G E (1958). Interlayer Spacing of Graphite. Acta Crystallographica **(4)**, pp. 558-561.

Barker L M (1977). A Simplified Method for Measuring Plane Strain Fracture Toughness. Engineering Fracture Mechanics **9 (2)**, pp. 361-369.

Bazaj D K, Cox E E (1969). Stress-concentration Factors and Notch Sensitivity of Graphite. Carbon **7**, pp. 689-697.

Blackman L C F (1970). Modern Aspects of Graphite Technology. Academic Press, London.

Brocklehurst J E (1977). Fracture of Polycrystalline Graphite. In *Chemistry & Physics of Carbon* **13**. Ed. Thrower P A & Walker P L, pp. 145-280, Marcel Dekker, New York.

Browne D J (1989). Fracture Characteristics of Coarse-grained Ceramics. PhD Thesis, Dept. of Mechanical Eng., University of Newcastle upon Tyne, UK.

Browne D J, Chandler H W (1987). Computer Design of a Controlled Fracture Test. British Ceramic Transactions **(86)**, pp. 202-205.

Buch J D (1975). Mechanical Behaviour Model for Graphite. ASTM STP 605: Properties Related to Fracture Toughness, ASTM Technical Publications.

Burchell T D, Pickup I M, McEnaney B, Cooke R G (1986). Relationship between Microstructure and Elastic Modulus Reduction in Thermally and Radiolytically Corroded Nuclear Graphite. Carbon **24 (5)**, pp 545-549.

Burchell T D (1986). Studies of Fracture in Nuclear Graphite. PhD Thesis, Department of Nuclear Materials, University of Bath, UK.

Byrne J F, Marsh H. In *Porosity in Carbons*, Chapter 1: Introductory Overview. Ed. J W Patrick, pp. 42-44, Edward Arnold, London.

Chandler H W, Merchant I J, Henderson R J, Macphee D E (2002). Enhanced Crack-bridging by Unbonded Inclusions in a Brittle Matrix. Journal of the European Ceramic Society **22**, pp. 129-134.

Cheng C-M, Cheng Y-T (1997). On the initial unloading slope in Indentation of Elastic-Plastic Solids by an Indenter with an Axisymmetric Profile. Applied Physics Letters **71 (18)**, pp. 2623-2625.

Cho C C, Kim I S, Kim S S, Choe S J, Hur B Y (1996). Studies on Effects of Calibration Methods and Current Position on DCPD Method for Crack Length Measurement. Analytical Science & Technology **10 (4)**, pp. 300-306.

Chudoba T, Richter F (2001). Investigation of Creep Behaviour under Load during Indentation Experiments and its influence on Hardness and Modulus. Surface and Coatings Technology **148**, pp. 191-198.

Cullity B D (1956). Elements of XRD. Addison-Wesley, USA.

Curry D A, Milne I. The Detection and Measurement of Crack Growth during Ductile Fracture. In *Measurement of Crack Length and Shape during Fracture and Fatigue*. Ed. Beevers C J, pp. 401-434, Chameleon Press, London.

Damani R, Gstrein R, Danzer R (1996). Critical Notch-Root Radius Effect in SENB Fracture Toughness Testing. Journal of the European Ceramic Society **16**, pp. 695-702.

Doerner M F, Nix W D (1986). Interpreting Data from Depth-Sensing Instruments. Journal of Materials Research **1 (4)**, pp.601-609.

Druce S G, Booth G S (1980). Effect of Errors in the Geometric and Electrical Measurements on Crack Length Monitoring by the Potential Drop Technique. In *Measurement of Crack Length and Shape during Fracture and Fatigue*. Ed. Beevers C J, pp. 136-163, Chameleon Press, London.

Ebrahimi M E, Chevalier J, Fantozzi G (2000). Slow Crack-growth Behaviour in Alumina Ceramics. Journal of Materials Research 15 (1), pp. 142-147.

Edwards I A S (1989). In *Introduction to Carbon Science*, Chapter 1: Structure in Carbons. Ed. Marsh H, Butterworths, London.

Eto M, Growcock F B (1983). Effect of Oxidising Environment on the Strength of H451, PGX and IG-11 Graphites. Carbon **21 (2)**, pp. 135-147.

Evans A G, Faber T (1984). Crack Growth Resistance in Microcracking Brittle Materials. Journal of the American Ceramic Society **67 (4)**, pp. 255-260.

Ergun S (1976). Analysis of Coherence, Strain, Thermal Vibration and Preferred Orientation in Carbons by XRD. Carbon **14**, pp. 139-150.

Ewalds H L, Wanhill R J H (1984). Fracture Mechanics, Edward Arnold, UK.

Fett T (1991). Influence of Bridging Stresses on Specimen Compliances. Journal of Materials Science Letters **10**, pp. 1211-1216.

Fett T, Munz D (1998). In *Ceramics: Mechanical Properties, Fracture Behaviour, Materials Selection*. Ed. R Hull, Springer, New York.

Fischer S, Roman I, Harel H, Marom G, Wagner H D (1981). Simultaneous Determination of Shear and Young's Moduli in Composites. Journal of Testing and Evaluation, pp. 303-307.

Franklin R E (1951). The Structure of Graphitic Carbons. Acta Crystallographica **4**, pp. 253-261.

Freeman B L, Neate G J (1980). Measurement of Crack Length at Elevated Temperatures using the DC Potential Drop Technique. In *Measurement of Crack Length and Shape during Fracture and Fatigue*. Ed. Beevers C J, pp. 435-459, Chameleon Press, London.

Freiman S W (1988). Brittle Fracture Behaviour of Ceramics. Ceramic Bulletin **67 (2)**, pp. 392-402.

Grabulov V K (1999). New Procedure for Evaluating Material Resistance Curves under Static Loading Conditions by Applying the Potential Drop Method. Journal of the Serbian Chemical Society. **64 (3)**, p221-233.

Gregg S J, Tyson R F S (1965). Kinetics of Oxidation of Carbon and Graphite by Oxygen at 500-600 °C. Carbon **3**, pp. 39-42.

Greenstreet W L, Smith J E, Yahr G T (1969). Mechanical Properties of ECGR-Type AGOT Graphite. Carbon **7**, pp. 15-45.

Greenstreet W L, Smith J E, Yahr G T, Valachovic R S (1970). The Mechanical Properties of Artificial Graphites as Portrayed by Uniaxial Tests. Carbon **8**, pp. 649-663.

Grimes R E, P K Girish, Laurent G, White K W (1990). Elevated-Temperature R-curve Behaviour of a Polycrystalline Alumina. Journal of the American Ceramic Society **73 (5)**, pp. 1399-1404.

Halliday M D, Beevers C J (1980). The DC Electrical Potential Drop Method for Crack Length Measurement. In *Measurement of Crack Length and Shape during Fracture and Fatigue*. Ed. Beevers C J, pp. 85-112, Chameleon Press, London.

Harel H, Marom G, Fischer S, Roman I (1980). Effect of Re-inforcement Geometry on Stress-Intensity Calibrations in Composites. Composites, pp. 69-72.

Hart P E (1971). The Effect of Prestressing on the Thermal Expansion and Young's Modulus of Graphite. Carbon **10 (2)**, pp. 233-236.

Hay J C, Bolshakov A, Pharr G M (1999). Critical Examination of the Fundamental Relations used in the Analysis of Nanoindentation Data. Journal of Materials Research **14 (6)**, pp.2296-2305.

Hellan K (1985). Introduction to Fracture Mechanics, McGraw-Hill, New York.

Hiramatsu K, Okada A (1998). In-situ Observation of Stable Crack Growth in SENB Specimens for R-curve Evaluation. Ceramic Engineering & Science, Proceedings of 22nd Annual Conference **19 (4)**, pp. 335-340.

Hoffman G, Wiedenmeyer M, Freund M, Beavan L, Hay J, Pharr G M (2000). Investigation of the Relation between Position within Coater and Pyrolitic Carbon Characteristics using Nano-indentation. Carbon **38**, pp. 645-653.

Hubner H, Schuhbauer H (1977). Experimental Determination of Fracture Mechanics Stress-Intensity Calibration in 3-point Bending. Engineering Fracture Mechanics **9**, pp. 403-410.

Iwashita N, Inagaki M (1993). Relations between Structural Parameters obtained by Powder XRD of various Carbon Materials. Carbon **31 (7)**, pp. 1107-1113.

Ioka I, Yoda S (1990). Acoustic Emmission for Polycrystalline Graphite under Compressive Loading. Carbon **28 (4)**, pp. 489-495.

Ioka I, Yoda S (1990). Changes in Mechanical Properties of Graphites Parallel and Perpendicular to Compressive Prestress. Carbon **28 (1)**, pp. 159-164.

Ishiyama S, Eto M (1997). Fracture Toughness Tests of Nuclear Graphites. Extended Abstracts (Vol. II), 23rd Biennial Conference on Carbon, Penn State University, USA.

Jenkins G M (1962). Analysis of the Stress-Strain relationships in Reactor Grade Graphite. British Journal of Applied Physics **13**, pp. 30-32.

Jenkins G M, Williamson G K, Barnett J T (1965). The Role of Crystal Structure in determining the Mechanical Properties of Graphite. Carbon **3**, pp. 1-6.

Jenkins G M (1973). Deformation in Polycrystalline Graphite. In *Chemistry & Physics of Carbon* **11**. Ed. Walker P L Jr. & Thrower P A, pp. 189-242, Marcel-Dekker, New York.

Jiang X X (1997). Fabrication, Microstructure and Properties of Unidirectional C-fibre Re-inforced SiC Dual-matrix Composites. PhD Thesis, Department of Materials, University of Leeds, UK.

Johnson H H (1965). Materials Research and Standards, pp. 442-445.

Kanari M, Tanaka K, Baba S, Eto M (1997). Nano-indentation Behaviour of a 2-D C/C Composite for Nuclear Applications. Carbon **35 (10-11)**, pp. 1429-1437.

King R B (1987). Elastic Analysis of some Punch Problems for a Layered Medium. International Journal of Solid Structures **23 (12)**, pp. 1657.

Knehans R, Steinbrech R (1982). Memory Effect of Crack Resistance during Slow Crack Growth in Notched Al_2O_3 Bend Specimens. Journal of Materials Science Letters **1**, pp. 327-329.

Knibbs R H (1967). Fracture in Polycrystalline Graphite. Journal of Nuclear Materials **24**, pp. 174-187.

Knott J F (1980). The use of Analogue & Mapping Techniques with Particular Reference to Detection of Short Cracks. In *Measurement of Crack Length and Shape during Fracture and Fatigue*. Ed. Beevers C J, pp. 113-135, Chameleon Press, London.

Kobayashi A S, Emery A F, Liaw B M (1983). Dynamic Fracture Toughness of Reaction-bonded Silicon-nitride. Journal of the American Ceramic Society **66**, pp. 151-153.

Kostopoulos V, Markopolous Y P, Pappas Y Z, Peteves S D (1998). Fracture Energy Measurements of 2-D C/C Composites. Journal of the European Ceramic Society **18**, pp. 69-79.

Lawn B R, Wilshaw S (1975). Fracture in Brittle Solids. Cambridge University Press.

Legin-Kolar M (1992). Optical and Crystallographic Structure of Pitch Cokes. Carbon **30 (4)**, pp. 613-618.

Li M, Tsukimura M, Sakai M (1999). Crack-face Grain Interlocking/Bridging of a Polycrystalline Graphite: The Role in Mixed Mode Fracture. Carbon **37**, pp. 1633-1639.

Magon M F A, Rodrigues J A, Pandolfelli V C (1995). Characterisation of R-curve Behaviour for MgO-C Refractories. Proceedings, pp. 478-483, 39th Congress on Ceramics, Brazil.

Marsh H, Fiorino K (1997). In *Introduction to Carbon Technologies*: Chapter 12: Manufacture of Carbon Anodes. Ed. Marsh H, Heintz E A, Reinoso F R, University of Alicante Pub., Spain.

Marshall P, Priddle E K (1973). The Influence of Specimen Size and Mode of Loading on the Fracture of Graphite. Carbon **11**, pp. 627-631.

Marx D T, Reister L (1999). Mechanical Properties of C/C-composite Components determined using Nano-indentation. Carbon **37**, pp. 1679-1684.

Mazzei A C, Rodrigues J A, Pandolfelli V C (2000). Alumina-mullite-zirconia Composites obtained by Reaction Sintering, Part I: Microstructure & Mechanical behaviour. Journal of Materials Science **35**, pp. 2807-2814.

Mazzei A C, Rodrigues J A, Pandolfelli V C (2000). Alumina-mullite-zirconia Composites obtained by Reaction Sintering, Part II: R-curve Behaviour. Journal of Materials Science **35**, pp. 2815-2824.

McEnaney B (2001). Some Aspects of Deformation and Fracture in Carbons. Proceedings, International Carbon Conference, Lexington, USA.

McEnaney B, Mays T J (1995). In *Porosity in Carbons*, Chapter 4: Characterisation of Macropores in Carbons. Ed. Patrick J W, Edward Arnold, London.

Munz D, Bubsey R T, Shannon J L (1980). Fracture Toughness Determination of Al_2O_3 using Four-point Bend Specimens with Straight-through and Chevron-notches. Journal of the American Ceramic Society **63 (5-6)**, pp. 300-305.

Munz D (1983). Effect of Specimen Type on the Measured Values of Fracture Toughness of Brittle Ceramics. In *Fracture Mechanics of Ceramics* **6**, pp. 1-26. Ed. Bradt R C, Plenum Press, New York.

Nakayama J (1965). Direct Measurement of Fracture Energies of Brittle Heterogeneous Materials. Journal of the American Ceramic Society **48 (11)**, pp. 583-587.

Nightingale R E (1962). Nuclear Graphite. Academic Press, London.

Oku T, Eto M (1973). The Effect of Compressive Prestressing on the Mechanical Properties of Some Nuclear Graphites. Carbon **11**, pp. 639-647.

Okumura N, Venkatasubramanian T V, Unvala B A, Baker T J (1981). Application of ACPD Technique to the determination of R-curves of Tough Ferritic Steels. Engineering Fracture Mechanics **14**, pp. 617-625.

Oliver W C, Pharr G M (1992). An Improved Technique for Determining Hardness and Elastic Modulus using Load-Displacement Sensing Indentation Experiments. Journal of Materials Research **7 (6)**, pp.1564-1583.

Opperman W, Hofstotter P, Keller H P (1997). Long-term Installations of the DCPD method in four Nuclear Power Plants. Nuclear Engineering & Design **174**, pp. 287-292.

Ouagne P (2000). Fracture Property Changes in Polycrystalline Graphite with Irradiation and Oxidation. PhD Thesis, Department of Nuclear Materials, University of Bath, UK.

Ouagne P, Neighbour G B, McEnaney B (2002). Crack Growth Resistance in Nuclear Graphites. Journal of Physics D: Applied Physics **35 (9)**, pp. 297-934.

Patrick J W, Sorlie M, Walker A (1989). Strength-structure Relationships in Baked Carbon Materials. Carbon **27 (3)**, pp. 469-474.

Patrick J W, Walker A (1995). In *Porosity in Carbons*, Chapter 7: Porosity and Strength of Carbon Materials. Ed. Patrick J W, Edward Arnold, London.

Peng T C (1979). Oxidation Effects on the Tensile Strength of ATJS Graphite and Vitreous Carbon. Carbon **17**, pp 157-174.

Pharr G M, Oliver W C, Brotzen F R (1992). Generality of the Relationship among Contact Stiffness, Contact Area, and Elastic Modulus during Indentation. Journal of Materials Research **7 (3)**, pp. 613-617.

Pickup I M, McEnaney B, Cooke R G (1986). Fracture Processes in Graphite and the Effects of Oxidation. Carbon **24 (5)**, pp. 535-543.

Ramos V P N (2002). The R-curve Behaviour of Alumina-SiC-Graphite Refractory Composites by Different Methodologies, Doctoral Research, Department of Materials, University of Leeds, UK.

Rand B, Hosty A J, West S (1989). In *Introduction to Carbon Science*, Chapter 3: Physical Properties of Pitch. Ed. Marsh H, Butterworths, London.

Ray A K (1998). A New Technique for Pre-cracking Ceramic Specimens in Fatigue and Fracture. Journal of the European Ceramic Society **18**, pp. 1655-1662.

Reichl A, Steinbrech R W (1988). Determination of Crack Bridging Forces in Alumina. Journal of the American Ceramic Society **71 (6)**, pp. C299-C301.

Reinoso R F (1997). In *Introduction to Carbon Technologies*: Chapter 2: Activated Carbons. Ed. Marsh H, Heintz E A, Reinoso F R, University of Alicante Pub., Spain.

Reynolds W N (1968). Physical Properties of Graphite. Elsevier, New York.

Rodrigues J A, Pandolfelli V C (2000). R-curve Behaviour of MgO-Carbon Refractories. Ceramica **46**, pp. 40-47.

Ruland W (1968). XRD Studies of Carbon and Graphite. In *Chemistry & Physics of Carbon* **4**, pp. 1-84.

Sakai M, Bradt R C (1986). Graphical Methods for determining the Non-linear Fracture Parameters of Silica and Graphite Refractory Composites. In *Fracture Mechanics of Ceramics* **7**, pp. 127-142, Plenum, New York.

Sakai M (1988). Fracture Mechanics of Refractory Materials. Taikabutsu (Overseas) **8 (2)**, pp. 4-12.

Sakai M, Yoshimura J, Goto Y, Inagaki M (1988). R-curve Behaviour of a Polycrystalline Graphite: Microcracking and Grain Bridging in the Wake Region. Journal of the American Ceramic Society **71 (8)**, pp. 609-616.

Sakai M, Bradt R C (1989). Dimensionless Load-Displacement Relation and its Application to Crack Propagation Problems. Journal of the American Ceramic Society **72 (3)**, pp. 388-394.

Sakai M, Nowak R (1992). Fracture Toughness and Brittleness of Ceramic Materials. Australian Ceramic Society **2**, pp. 922-931.

Sakai M, Ichikawa S (1992). Work of Fracture of Brittle Materials with Micro-cracking and Crack Bridging. International Journal of Fracture **55**, pp. 65-79.

Sakai M, Bradt R C (1993). Fracture Toughness Testing of Brittle Materials. International Materials Reviews **38 (2)**, pp. 53-78.

Sakai M, Kurita H (1995). Deformation & Fracture in the Frontal Process Zone & Crack-face Contact Region of Polycrystalline Graphite. Fracture of Brittle Disordered Materials, Ed. Baker G, Karihaloo B L, E&FN Spon Pub., UK.

Seehra M S, Pavlovic S (1993). XRD, Thermal Expansion, Conductivity & Microscopy of Coal-based Graphite. Carbon **31 (4)**, pp. 557-564.

Seldin E J (1966). Stress-strain Properties of Polycrystallinte Graphites in Tension and Compression at Room Temperature. Carbon **4**, pp. 177-191.

Smith M C (1964). Effects of Prestrain on the Tensile Properties of Graphite. Carbon **2**, pp. 269-274.

Sneddon I N (1965). Relation between Load and Penetration in the Axisymmetric Boussinesq Problem for a Punch of Arbitrary Profile. International Journal of Engineering Science **3 (47)**, pp. 47-57.

Stalder B, Bequelin P, Kausch H H (1983). Simple Velocity Gauge for measuring Crack Growth. International Journal of Fracture **22**, pp. R47-R50.

Stilwell N A, Tabor D (1961). Elastic Recovery of Conical Indentations. Proceedings of the Physics Society **78**, pp. 169-179, London.

Tandon S, Faber K T (1998). Influence of Loading Rate on Crack Bridging Processes in Alumina. Acta Materiala **46 (100)**, pp. 3547-3555.

Taylor R, Brown R G, Gilchrist K, Hall E, Hodds A T, Kelly B T, Morris F (1967). The Mechanical Properties of Reactor Graphite. Carbon **5**, pp. 519-531.

Thrower P A, Bognet J C, Mathew G K (1982). Influence of Oxidation on Structure & Strength of Graphite-Part I: Materials of Different Structure. Carbon 20 **(6)**, pp. 457-462.

Thrower P A, Bognet J C, Mathew G K (1982). Influence of Oxidation on Structure & Strength of Graphite-Part II: Materials of Different Impurity Content. Carbon **20 (6)**, pp. 457-462.

Troczynski T B, Nicholson P S (1986). Sensitivity of the Potential Drop Technique for Crack Length Measurement in a Chevron-notched Specimen. Journal of the American Ceramic Society **69 (7)**, C136-137.

Troczynski T B, Nicholson P S (1985). Analysis of the Potential Drop Technique for Crack Length Measurement in a Chevron-notched Specimen. Journal of the American Ceramic Society **64 (9)**, pp. 1272-1275.

Tucker M O, Rose A P G, Burchell T D (1986). The Fracture of Polygranular Graphites. Carbon **24 (5)**, pp. 581-602.

Wei R P, Brazill R L (1980). An AC Potential System for Crack Length Measurement. In *Measurement of Crack Length and Shape during Fracture and Fatigue*. Ed. Beevers C J, pp. 190-201, Chameleon Press, London.

Wege E (1984). Graphite and ParaCrystalline Carbon (Chapter 6). In *Process Mineralogy of Ceramic Materials*. Ed. Baumgart W, Dunham A C, Amstutz G C, Ferdinand Enke Pub. Stuttgart, pp. 125-149.

Wojcik A G (1995). Potential Drop Methods for Crack Characterisation. Materials World, pp. 379-381.

Wood J L, Bradt R C, Walker P L Jr (1980). Oxidation Effects on Toughness and Slow Crack Growth in Polycrystalline Graphites. Carbon **18**, pp. 179-189.

Wood J L (1981). Effect of Oxidation on the Flexural Strength of Graphite. Carbon **19** (Letters to editor), pp. 61-62.

Zhao J, Wood L, Bradt R C, Walker P L Jr (1981). Oxidation Effects on CTE and Thermal Shock Fracture Initiation in Polycrystalline Graphites. Carbon **19 (6)**, pp. 405-408.